SCHOLARLY PUBLICATIONS

A CURRENT AWARENESS BULLETIN
OF RESEARCH OUTPUT

@DTU

(35th Edition)

NOVEMBER 2015

BY: CENTRAL LIBRARY

DELHI TECHNOLOGICAL UNIVERSITY
(FORMERLY *DELHI COLLEGE OF ENGINEERING)*
GOVT. OF N.C.T. OF DELHI
SHAHBAD DAULATPUR, MAIN BAWANA ROAD
DELHI 110042

PREFACE

This is the **Thirty Fifth** Issue of Current Awareness Bulletin started by Delhi Technological University, Central Library. The aim of the bulletin is to compile, preserve and disseminate information published by the faculty, students and alumni for mutual benefits. The bulletin also aims to propagate the intellectual contribution of Delhi Technological University (DTU) as a whole to the academia.

The bulletin contains information resources available in the internet in the form of articles, reports, presentations published in international journals, websites, etc. by the faculty and students of DTU. The publications of faculty and student which are not covered in this bulletin may be because of the reason that the full text either was not accessible or could not be searched by the search engine used by the library for this purpose.

The learned faculty and students are requested to provide their uncovered publications to the library either through email or in CD, etc to make the bulletin more comprehensive.

This issue contains the information published during **November 2015**. The arrangement of the contents is alphabetical. The full text of the article which is either subscribed by the university or available in the web is provided in this bulletin.

Central Library

CONTENTS

1. A Novel Approach for the Recognition of Hand Gestures from Very Low Resolution Images, ***3.Dinesh Vishwakarma***, ***3.Rockey Maheshwari*** & ***3.Rajiv Kapoor***, ECE, DTU

2. Application of Taguchi Experimental Design for the Optimization of Effective Parameters on the Neemoil Methyl Ester (Biodiesel) Production, ***3.R. S. Mishra***, ***3.Amit Pal*** & ***3.Anand Prakash Mall***, Mechanical Engineering, DTU

3. Average Bit Error Probability of MRC Combiner in Log Normal Shadowed Fading ***3.Rupender Singh***, ***3.S.K. Soni*** & ***3.P. K. Verma***, ECE, DTU

4. Biomedical and Clinical Importance of Mussel-Inspired Polymers and Materials, Nagendra Kumar Kaushik, Neha Kaushik , Sunil Pardeshi, ***3.Jai Gopal Sharma*** , Seung Hyun Lee and Eun Ha Choi, Biotechnology, DTU

5. !-cycle Compatible Splitting Signed Graphs S(S) and !(S), ***3.Rashmi Jain***, ***3.Sangita Kansal*** & Mukti Acharya, Applied Mathematics, DTU

6. CFD Analysis and Optimization of Geometrical Modifications of Ahmed Body, ***8.Sagar Sharma***, ***8.Saurabh Banga***, ***8.Rohit Singh Dungriya***, ***3.Mohammad Zunaid***, ***3.Naushad Ahmad Ansari*** & Suresh Lal, Mechanical Engineering, DTU

7. Clean Development Mechanism in India, ***3.Abhishek Pandey*** & ***3.Abhinav Jain***, Environmental Engineering, DTU

8. Constant Torque Operation of Wound Rotor Induction Motor using feedback mechanism in a Rectifier Fed Induction Motor Drive, ***3.Anmol Aggarwal***, ***3.JN Rai***, & ***3.Maulik Kandpal***, Electrical Engineering, DTU

9. Detection of Enterobacter sakazakii from Commercial Children Dry Milk, Mohammed Mosa Jaffaar, Mohammed K.Shebli, Abdul Khaliq Abbas Mussa,Bayan Hassan Hadi, ***3.Allaa M. Aenab*** & ***3.S. K. Singh***, Environmental Engineering, DTU

10. Economic assessment of use of pond ash in pavements, ***3.Raju Sarkar*** and A.R. Dawson, Civil Engineering, DTU

11. Effect of Homogeneous Catalysts on Production of Biodiesel from Crude Neem Oil Feedstock and Cost Analysis of Biodiesel Production, ***3.R. S. Mishra***, ***3.Amit Pal*** & ***3.Anand Prakash Mall***, Mechanical Engineering, DTU

12. Efficacy of Heavy Metals in Management of Fusarium Udum and Fusarium Oxysporum F.Sp.Ciceri, Ankita Shukla and ***3.Rajeev Kumar Mishra***, Environmental Engineering, DTU

13. Energy and Exergy Analyses of a new Solar Assisted Ejector Cooling and Power Cycle by using Refrigerants R141b, R600, R601 and R601a, Surendra Kumar Agrawal & ***3.Rajesh Kumar***, Mechanical Engineering, DTU

14. Energy-Exergy Performance Comparison of Vapour Compression Refrigeration Systems using Three Nano Materials Mixed in R718 in the Secondry Fluid and Ecofriendly Refrigerants in the Primary Circuit and Direct Mixing of nano Materials in the Refrigerants, ***3.R. S. Mishra***, Mechanical, Production & Industrial and Automobile Engineering, DTU

15. Exergy and Parametric Analyses of a Solar Driven Ejector Cooling and Power Cycle Operating with Butane as a Refrigerant, Surendra Kumar Agrawal & ***3.Rajesh Kumar***, Mechanical Engineering, DTU

16. Experimental Analysis on Forced Draft Solar Dryer with Phase Change Material, ***3.Prashant Kumar***, Mechanical Engineering, DTU

17. High speed neuron implementation using Vedic mathematics***, 3.Yamuna SV***, ***3.Anshika***, ***3.Nidhi Goel*** & ***3.S.Indu***, ECE, DTU

18. Identification of Sustainability Indicators and Evaluation of Transportation Corridors during Construction Using Fuzzy VIKOR Method, ***3.Shishir Bansal***, Sameer Verma and ***3.Santosh K. Singh***, Environmental Engineering, DTU

19. Investigation of Surface Morphology in EDM process using Response Surface Methodology, Ravinder Kumar, Surabhi Lata, Ramakant Rana, Pankaj Kumar, Abhinav Kumar, Lakshay Kumar, Jitender Kumar Verma & ***3.Roop Lal***, Mechanical and Automation Engineering, DTU

20. Investigations on effect of Incorporation of Photovoltaic System With Combined Cycle Gas Turbineplant, Naimul Hasan, ***3.B.B .Arora***, J.N. Rai, Mechanical Engineering, DTU

21. INVESTMENT BEHAVIOR OF ENGINEERS: AN EMPIRICAL STUDY, ***6. Priya Kansal*** & ***3.Dr. Seema Singh***, Humanities, DTU

22. Isolation and Characterization of Potential Phosphate Solubilizing Bacteria from the rhizoplane of Kukrail forest, Lucknow, Faria Fatima, Neelam Pathak & ***3.Smita Rastogi Verma***, Biotechnology, DTU

23. Emerging Cool White Light Emission from Dy3+ doped Single Phase Alkaline Earth Niobate Phosphors for Indoor Lighting Applications, ***3.Amit K. Vishwakarma***, ***3.Kaushal Jha***, ***3.M. Jayasimhadri***, ***3.B. Sivaiah***, ***3.Bhasker Gahtori***, D. Haranathb, Applied Physics, DTU

24. Magnetic adsorbents for the treatment of water/wastewater— A review, ***3.Dhruv Mehta***, Siddharth Mazumdar, ***3.S.K. Singh***, Environmental Engineering, DTU

25. Literature review of multi-aspect research works carried out on the concept and implementation of GSCM, ***7.1.Sheetal Soda***, Anish Sachdeva and Rajiv Kumar Garg, Production Engineering, DTU

26. Material Flow and Microstructural Studies in Friction Stir Welding / Processing of Aluminium: A Literature Review, ***3.V.Jeganathan Arulmoni***, ***3.R.S. Mishra***, ***3.Ranganath M. S***, Mechanical and Production & Industrial Engineering, DTU

27. Oxygen stress: impact on innate immune system, antioxidant defence system and expression of HIF-1a and ATPase 6 genes in Catla catla, Samar Pal Singh, ***3.Jai Gopal Sharma***, Tauqueer Ahmad & Rina Chakrabarti, Biotechnology, DTU

28. Relaxing Weighted Clustering Algorithm for Reduction of Clusters and Cluster Head, ***3.Vijayanand Kumar***, Computer Science, DTU

29. Sentiment Analysis of Mobile Reviews using Sentiwordnet, ***3.Gaurav Dudeja*** and ***3.Kapil Sharma***, Computer Science, DTU

30. Single CDBA Based Voltage Mode Bistable Multivibrator and Its Applications, Rishi Pal, ***3.Rajeshwari Pandey***, ***3.Neeta Pandey*** & Ramesh Chandra Tiwari, Electronics and Communication Engineering, DTU

31. Thermal Performance Improvements of Vapour Compression Refrigeration System Using Eco Friendly Based Nanorefrigerants in Primary Circuit, ***3.R.S. Mishra***, ***3.Rahul Kumar Jaiswal***, Mechanical Engineering, DTU

32. Thermodynamic Analysis of Heat Pipe Using Ammonia, Water and Ethanol with a View to Being Used in Refrigeration, ***3.Ankit Dwivedi*** & ***3.R. S. Mishra***, Mechanical Engineering, DTU

33. Thermodynamics Analysis of a Solar Operated Combined Power and Ejector Cooling Cycle with Environmentally Benign Fluids, Devendra Kumar Gupta & ***3.Rajesh Kumar***, Mechanical Engineering, DTU

34. X-ray Diffraction Analysis of Severely Cold Deformed Hypereutectoid Steel Wire, ***7.1.S.S. Bargujer***, N.M. Suri & R.M. Belokar, Thermal Engineering, DTU

1. Vice Chancellor	***1.1. Ex Vice Chancellor***
2. Pro Vice Chancellor	***2.1. Ex Pro Vice Chancellor***
3. Faculty	***3.1. Ex Faculty***
4. Teaching-cum-Research Fellow	
5. Alumni	
6. Research Scholar	***6.1. Ex Research Scholar***
7. PG Scholar	***7.1. Ex PG Scholar***
8. Undergraduate Student	***8.1. Ex Undergraduate Student***

A Novel Approach for the Recognition of Hand Gestures from Very Low Resolution Images

Dinesh Vishwakarma, Rockey Maheshwari, Rajiv Kapoor
(dkvishwakarma@dce.ac.in, rockeymahesh93@gmail.com, rajivkapoor@dce.ac.in)
Department of Electronics and Communication Engineering
Delhi Technological University, Delhi, INDIA-110042

Abstract- ***In this paper, a simple and effective approach for the recognition of hand gestures from very low resolution images is proposed. Enhancement of the low resolution images has always been the key focus in the processing of the digital images. Images with resolution as low as*** $[\mathbf{50 \times 50}\ \boldsymbol{pixels}]$ ***are also considered for recognition. The gestures under consideration here are the number of fingers (one, two, three, four or five) raised by the person. The low resolution gesture image captured from web camera, mobile phone, or low cost cameras is processed systematically to output the number of fingers raised. Simple concepts of the geometry of the hand have been used for the recognition of hand gesture from the input low resolution images. The proposed method extracts the hand gesture directly from the low resolution image without the need of reconstruction to a high resolution image or use of any classifier. The proposed method is based on the generation of a mask for the image which is critical in the recognition of the hand gesture. This method is tested on publically available dataset of Marcel-Triesch. The high accuracy of the experimental results show the superior performance of the proposed method for the recognition of hand gesture from low resolution images.***

Keywords: Geometry, Hand Gesture, Mask Generation, Low Resolution

I. INTRODUCTION

The recognition of hand gestures has become an area of active research in the field of computer vision and machine learning. Hand gesture recognition plays a central role in the interaction between the digital and physical world. Over the years, the human machine interaction has evolved from the physical touch to virtual gesture based interactions. The hand gesture recognition system have many applications such as automation, smart systems, virtual gaming etc. Application of hand recognition system in smaller devices require smaller digital storage space requirement, simpler and very fast processing. Our main focus for this method has been to accommodate all these features so that the designed system can be used under all constraints of the system.

Many difficulties are faced during the recognition of hand gestures such as background complexity, blurring of image, orientation of the gesture. With the increasing digital information required to be stored in system, the focus of the developers is to reduce the space required for the functionalities of the system. This supports the concept of using low resolution images which occupies lesser space for the purpose of gesture recognition.

The main focus of the proposed method is the development of a simple, robust, and effective method for the recognition of hand gestures. Thus, the proposed method does not include the use of any classifier as classifiers needs training time and their execution time also increases. Information extracted is based on the geometrical structure of the hand and not on colour, size or brightness. This ensures the methods reliability and efficiency in the cases of low lighting conditions. The orientation of the hand gesture is also taken into consideration so that the hand gesture need not to be necessarily in upright position. This is an extra advantage of the proposed method.

The rest of the paper is as follows. Section 2 highlights the previous work carried out for the gesture recognition. Section 3 describes the technical details of the proposed method. The experimental results obtained by the application of the proposed method are discussed in Section 4. The work that can be done in this field to further improve robustness of the system are explained in Section 5. Lastly, the paper is concluded and the references for the paper are cited.

II. RELATED WORK

Many researchers in the past have proposed the use of different algorithms for the recognition of human hand gesture from images. Zhenyao Mo et al [1] brought the concept of using depth images for the recognition of the hand gesture. Siddharth S. Rautaray et al [2] presented a gesture recognition system for dynamic user interface with the use of multiple algorithms such as Harr like features, Camshaft, Lucas kanade etc. Lae-Kyoung Lee et al [3] used the extraction of the fingertip for the Human-Robot interaction. Paulo Trigueiros et al [4] compared the efficiency of the various classifiers for the recognition of gestures on two different datasets. All these efforts show the importance of the effective hand gesture recognition in the present world. Many attempts have also been made in the enhancing of the low resolution images using various techniques. Nobuhide Okabayashi et al [7] used the method of removing quantization error in frequency domain from the low resolution image to generate the high resolution

images. Md Iqbal Qureshi et al [5] introduced the combined concept of Particle Swarm Optimization and discrete wavelet transform for the enhancement of low resolution images which can be further used for various functionalities. Myung-Cheol Roh et al [6] recognized gestures from low resolution videos. In [8], for the recognition of the hand gesture from the images, the shape parameters of the hand are extracted. This concept of shape parameters of the hand is developed further to decrease the recognition time of the gesture and improve the accuracy of the system. The above discussed methods have the limitation that they require either the reconstruction of the low resolution image to a higher resolution or the recognition of the hand gesture requires the use of classifiers which involves the training of the system and hence slows the performance.

III. PROPOSED METHOD

This section explains in detail the various steps involved in the recognition of the hand gesture from the low resolution images. The low resolution images that can be recognized can have a resolution of as low as $[50 \times 50\ pixels]$.

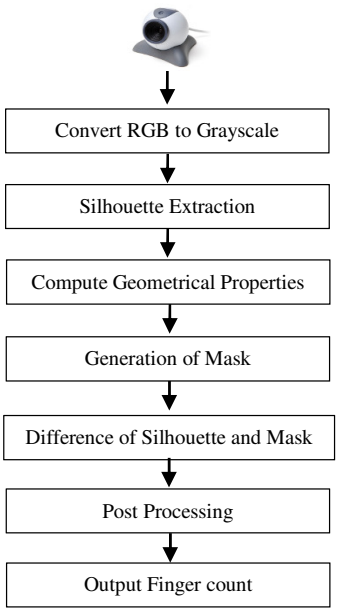


Figure 1: The work flow diagram for the proposed method for the recognition of the hand gesture from the low resolution images.

Figure 1 shows the step by step working of the proposed method. These steps are explained one by one further in this section.

A. *Pre-processing*

The low resolution image containing the hand gesture needs to be pre-processed before the generation of the mask for the gesture. This involves the conversion of the RGB image to grayscale. The next important step for the recognition of hand gesture is the extraction of silhouette of hand.

Extraction of Binary Silhouette: To extract the binary silhouette from the grayscale image, the concept of histogram is used. Image is a 2–dimensional function and thus functions representing an image will be a 2-D function. Let $R(x, y)$ represent the grayscale gesture image. The histogram of grayscale image, $R(x, y)$ determines the binary image based on a threshold value. If the value of $R(x, y)$ is greater than the threshold value then it is give a value equal to '0' in binary image else '1'. This is shown by equation 1.

Let the threshold value for the grayscale image, $R(x, y)$ calculated dynamically be $'t'$. Now,

$$B(x, y) = 1 \quad ,if \quad R(x, y) < t$$

$$B(x, y) = 0 \ ,else \tag{1}$$

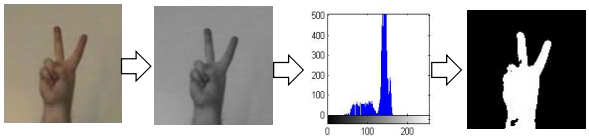


Figure 2: Steps of Pre-processing

After the formation of binary image, the next step is the application of morphological operations to improve the quality of the silhouette. The application of these morphological operations ensures that all the discontinuities from the binary image are removed. For these operations, the size of the structuring element taken is very small because of the low resolution of the image which makes the information content of the image in very small regions. Next, we generate of the mask for the binary image.

B. *Mask Generation*

Mask generation is the most critical step in the proposed method for the gesture recognition. The mask for the binary image, $B(x, y)$ is calculated based on the geometrical structure of the binary image.

The centroid of the silhouette represents the center of mass for the silhouette. It is calculated by the image moment as in [9],

$$G_{p,q} = \sum_i \sum_j i^p j^q \, V(i, j) \tag{2}$$

Where, $V(i, j)$ is the intensity of the coordinate (i, j) and the centroid $(\alpha, \beta)$is given as:

$$\alpha = \frac{G_{1,0}}{G_{0,0}}$$

$$\beta = \frac{G_{0,1}}{G_{0,0}} \quad (3)$$

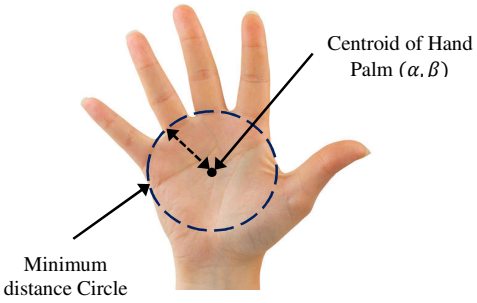


Figure 3: Hand Palm showing the minimum distance calculations

Once the centroid (α, β) of the binary image, $B(x, y)$ is obtained, the smallest distance of the boundary of the silhouette from this centroid point is calculated as per the equation 4. This minimum distance is taken in all directions from the centroid and the area thus formed represents the mask for the binary silhouette. This area usually covers the palm region of the hand and thus forms the base of the mask. Further, morphological operations are performed on the mask thus obtained to incorporate and small section near the boundary of the silhouette.

$$\lambda = sqrt(|x_s - \alpha|^2 + |y_s - \beta|^2) \quad (4)$$

From equation 4, a set of distances is computed where (x_s, y_s) is the surface coordinate of palm and the minimum distance is used to mark a circle which helps in the formation of mask.

Let $M(x, y)$ represent the mask for the binary image, $B(x, y)$. A sample mask obtained is shown in figure 3.



Figure 4: The mask generated for the gesture shown in figure 2.

C. *Mask Subtraction*

Once the mask is obtained the next step is the extraction of the remaining information from the binary image. This is done by subtracting the mask obtained in previous step from the binary silhouette of the gesture.

$$S(x, y) = B(x, y) - M(x, y) \quad (4)$$

Here, $S(x, y)$ is the subtracted image. Now, all the information about the hand gesture is contained in the binary image, $S(x, y)$.



Figure 5: Silhouette left after the removal of mask.

As it can be seen, the binary image, $S(x, y)$ still requires some further processing before the count of fingers can be obtained from it.

D. *Post-processing*

Post-processing is required to remove all small unwanted regions present in the binary image. For this morphological operations are applied to the image to enhance it information content.



Figure 6: The final binary image after the processing for the gesture recognition.

Figure 5 shows the binary image after the application of mask subtraction and morphological operations.

E. *Gesture Recognition*

The final step is the recognition of the hand gesture i.e. the count of the number of fingers raised by the person in the image.

From the figure 5, it can be observed that the number of fingers raised by the person is the number of white objects present in the binary image, $F(x, y)$. To count the number of white objects present in the binary image the region properties of the image are calculated. This returns the number of white objects present in the image which is equal to the number of raised fingers.

IV. EXPERIMENTAL RESULTS

The proposed method is tested on the publically available dataset of Marcel-Triesch. The standard dataset of Marcel-Triesch has hand gestures with a resolution of $[50 \times 50]$ pixels. The dataset also consists of many gestures which have are based on the shape of hand and thus are not considered for the experimentation results. The gestures that are used for the recognition are one, two and all five fingers raised. A similar concept for the recognition can be applied on dataset with three or four fingers raised.

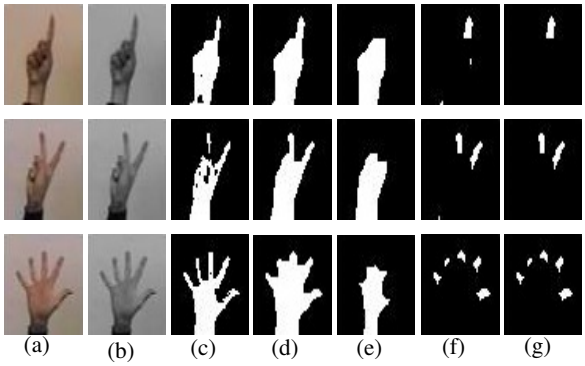


Figure 7: Different stages of the proposed method are shown pictorially in the figure.

Figure 6 shows three sample cases, one each for one, two and five fingers raised from the Marcel-Triesch dataset to explain the working of the proposed algorithm step by step. Figure 6(a) shows the original low resolution image.

The proposed method is tested for accuracy on the marcel-Triesch dataset considering only the relevant gestures that are one finger raised, two fingers raised, and five fingers raised. The results obtained on the low resolution images of the dataset are shown in table1.

TABLE 1: EXPERIMENTAL RESULTS ON STANDARD DATASET.

Hand Gesture	**One Finger Raised**	**Two Fingers Raised**	**Five Fingers Raised**
Total No. of Hand Gestures	65	57	76
Correct Detection	64	55	74
False Detection	1	2	2
Accuracy	98.46%	96.49%	97.37%
Average Accuracy : 97.47%			

The average accuracy obtained for the standard dataset of hand gestures is 97.47% which is considered as a high recognition rate. This recognition rate is comparable to the hand gesture recognition rate of other algorithms.

A. Comparison with the techniques of others

The accuracy obtained by the application of our method is compared with the accuracy of previously proposed methods for the recognition of hand gestures.

TABLE 1: STATE-OF-ART COMPARISON OF ACCURACY OF DIFFERENT METHODS

Methods	**Accuracy**
S. Marcel [10]	93.70%
D.K. Vishwakarma [9]	93.50%
A. Just [11]	92.79%
Our Method	**97.47%**

Table 2 shows the comparison of various methods proposed previously for the hand gesture recognition. These methods are not necessarily applied on low resolution images and thus the accuracy of 97.47% of our system is a great advantage as this is modifiable for higher resolution images also.

V. FUTURE WORKS

The proposed method recognizes the hand gesture from very low resolution images. The method is made robust to both the lighting conditions as well as the orientation of the hand gesture by taking into consideration the geometrical structure of hand. Hand gestures recognized by this method are the number of fingers raised by the person i.e. one, two, three, four or five fingers. Further work can be done in this area to accommodate even a larger number of gestures which considers the shape of hand or the motion trajectory of hand.

This idea of the recognition of the hand gesture can be extended further to generate sets of code from multiple images to develop even a larger number of applications for the human machine interaction. A great example of this is presented in [9]. Thus, a system can be easily designed to understand a large number of sequences as required in the applications.

VI. CONCLUSION

With the rapid pace of development and digitalization of the systems, the gesture recognition has gained a huge popularity for the human machine interface. Hand gesture recognition from low resolution images not only saves a huge storage space but also reduces the processing time of the system. The proposed system has an execution time of less than a sec (approx. 0.865 sec, running on i5 2.50 MHz processor with 4 GB RAM, MATLAB 2012a) which makes it feasible for real time implementation in different systems. The method is robust for the variable illumination conditions and orientation of the hand gesture. Furthermore, the average accuracy of the proposed system is 97.47% which shows a superior performance of our method as compared to the existing techniques used for gesture recognition.

REFERENCES

[1] Zhenyao Mo and Ulrich Neumann, "Real-time Hand pose Recognition Using Low-Resolution Depth Images", *In Proceedings of the IEEE Computer Society Conference, 2006.*

[2] Siddharth S. Rautaray and Anupam Agrawal, "Design of Gesture Recognition System for Dynamic User Interface".

[3] Lae-Kyoung Lee, Su-Yong An and Se-Young Oh, "Robust Fingertip Extraction with Improved Skin Color Segmentation

for Finger Gesture Recognition in Human-Robot Interaction", *In Proceedings of IEEE World Congress on Computational Intelligence, 2012.*

[4] Paulo Trigueiros, Fernando Ribeiro and Luis Paulo Reis, "A comparison of machine learning algorithms applied to hand gesture recognition".

[5] Md Iqbal Quraishi, Krishna Gopal Dhal, J Paul Choudhury, Kamal Pattanayak and Mallika De, "A Novel Hybrid Approach to Enhance Low Resolution Images Using Particle Swarm Optimization", *In proceedings of 2nd IEEE International Conference on Parallel, Distributed and Grid Computing,* pp. 888-893, 2012.

[6] Myung-Cheol Roh and Seong-Whan Lee, "Gesture Detection in Low-Quality Video", *In proceedings of 18th International Conference on Pattern Recognition,* 2006.

[7] Nobuhide Okabayashi, Hideya Takahashi, Tahito Aida and Hiromitsu Hama, "High-Resolution Image Restoration from Low-Resolution Images, Preprocessing for Pattern Recognition", 2004.

[8] Meenakshi Panwar, "Hand Gesture Recognition based on Shape Parameters", *In proceedings of International Conference on Computing, Communication and Applications,* pp. 1-6, 2012.

[9] D.K. Vishwakarma and Rajiv Kapoor, "Simple and intelligent system to recognize the expression of speech-disabled person", *In proceedings of 4th International Conference on Intelligent Human Computer Interaction,* 2012.

[10] Sebastien Marcel, "Hand Posture Recognition in a Body-Face centered Space", *In proceedings of International Gesture Workshop,* 2009.

[11] Agnes Just, Yann Rodrigues and Sebastien Marcel, "Hand Posture Classification and Recognition using the Modified Census Transform", *In proceedings of 7th International Conference on Automatic Face and Gesture Recognition,* 2006.

All in-text references underlined in blue are linked to publications on ResearchGate, letting you access and read them immediately.

Volume 3, Issue 3 (2015) 490-497 ISSN 2347 - 3258
International Journal of Advance Research and Innovation

Application of Taguchi Experimental Design for the Optimization of Effective Parameters on the Neemoil Methyl Ester (Biodiesel) Production

R. S. Mishra, Amit Pal, Anand Prakash Mall
Department of Mechanical Engineering, Delhi Technological University, New Delhi, India

Article Info

Article history:
Received 07 July 2015
Received in revised form
20 July 2015
Accepted 28 August 2015
Available online 15 September 2015

Keywords
Optimization,
Taguchi Method,
Analysis of Variance (ANOVA) Method,
Neem Oil Methyl Ester (Biodiesel)

Abstract

ANOVA analysis showed that the temperature had the highest effect on the biodiesel yield followed by catalyst amount, methanol to oil molar ratio and reaction time. The result of this work using Taguchi Method showed that the maximum yields were obtained at lowest factor values. This will definitely have economic advantage on neem oil biodiesel production as low energy cost, low catalyst amount, low methanol/oil molar ratio, and low temperature are able to produce high biodiesel yield.

1. Introduction

The use of alternative fuels instead of conventional fossil fuels is becoming increasingly significant due to decreasing petroleum reserves and increasing greenhouse gases, all of which lead to global warming, ozone depletion and political and health concerns (Fukuda et al., 2001). Plant oils have been used as alternative fuels for many years, since they are renewable and readily available. However, these oils cannot be used directly as fuel sources in diesel engines due to: (a) high viscosity which leads to poor fuel atomization during the injection process, (b) low volatility and (c) polymerization which results in deposit formation, incompletion combustion and poor emissions (Ma and Hanna, 1999; Meher et al., 2006). To overcome these disadvantages, oils can be converted into fatty acid methyl esters (FAME) which are also known as biodiesel. Biodiesel is an alternative fuel that is non-toxic, completely biodegradable and renewable and can be adapted easily without any modification to diesel engines.

Several processes have been developed for biodiesel production, such as pyrolysis, micro emulsification and transesterification. The chemical change of the products from the reactants caused by the thermal energy in the presence of air or nitrogen sparging is called a pyrolytic process. These products are similar to the petroleum-derived fuel. However, during the pyrolysis process, the removal of oxygen leads to reduce the environmental benefits (Ma and Hanna, 1999). The problem of the high viscosity of the substrates has been investigated using microemulsions with solvents (methanol, ethanol and 1-butanol) to meet the international standards of petroleum-derived fuels. However, an increase of lubricating oil viscosity, irregular injector needle sticking, incomplete combustion and heavy carbon deposits were reported in the laboratory screening endurance test. Therefore, transesterification process plays a vital role, in order to overcome these disadvantages.

Corresponding Author,
E-mail address: anandwrites@gmail.com
All rights reserved: http://www.ijari.org

The process of displacing alcohol from an ester to form another ester is called transesterification. Transesterification is the most simple and efficient method to produce biodiesel by using acids, alkalis, or enzymes as catalysts. Triglycerides with high free fatty acid and water contents are not essential for a biodiesel conversion process using an acid catalyst. However, the reaction rates are slower than those of the alkali catalytic process (Freedman et al., 1986). The alkali-catalysis transesterification process has been widely used in the biodiesel industry, because it gives a high yield of conversion of fatty acid methyl esters from triglycerides at low temperatures and pressures in a relatively short reaction time of 4-10 hours. However, it has several drawbacks including product separation, soap formation and negative environmental impacts such as greenhouse gas, CO, hydrocarbons, NOx and particles in exhaust emissions (Nielsen et al., 2008).

Neem is a tree in the family ‘maliaceae’ which grows various parts in Bangladesh. It’s scientific name ‘Azadirachtaindica’. The evergreen tree is large, reaching 12 to 18 meters in height with a girth of up to 1.8 to 2.4 meters. The seeds have 40% oil which has high potential for the production of biodiesel. It has a higher molecular weight, viscosity, density, and flash point than diesel fuel. Neem oil is generally light to dark brown, bitter and has a strong odor that is said to combine the odors of peanut and garlic [M.A. Fazal et al., 2011].

Neem comprises mainly of triglycerides and large amounts of triterpenoid compounds. It contains four significant saturated fatty acids, of which two are palmitic acid and two are stearic acid. It also contains polyunsaturated fatty acids such as oleic acid and linoleic acids [Muthu et al., 2010]

2. Taguchi Method to Optimize the Process Parameters:

Taguchi method is based on performing evaluation or experiments to test the sensitivity of a set of response

variables to a set of control parameters (or independent variables) by considering experiments in "orthogonal array" with an aim to attain the optimum setting of the control parameters. Orthogonal arrays provide a best set of well balanced (minimum) experiments. Table2 (a) Shows eighteen standard orthogonal arrays along with the number of columns at different levels for these arrays. An array name indicates the number of rows and columns it has, and also the number of levels in each of the columns. For example array L4 (23) has four rows and three "2 level" columns. Similarly the array L18 (2137) has 18 rows; one "2 level" column; and seven "3 level" columns. Thus, there are eight columns in the array L18. The number of rows of an orthogonal array represents the requisite number of experiments. The number of rows must be at least equal to the degrees of the freedom associated with the factors i.e. the control variables. In general, the number of degrees of freedom associated with a factor (control variable) is equal to the number of levels for that factor minus one. For example, a case study has one factor (A) with "2 levels" (A), and five factors (B, C, D, E, F) each with "3 level". Table 2(b) depicts the degrees of freedom calculated for this case. The number of columns of an array represents the maximum number of factors that can be studied using that array.

Table: 1(a). Standard orthogonal arrays

Orthogonal array	Number of rows	Maximum number of factors	Maximum number of columns at these levels			
			2	3	4	5
L4	4	3	3	-	-	-
L8	8	7	7	-	-	-
L9	9	4	-	4	-	-
L12	12	11	11	-	-	-
L16	16	15	15	-	-	-
L16'	16	5	-	-	5	-
L18	18	8	1	7	-	-
L25	25	6	-	-	-	6
L27	27	13	-	13	-	-
L32	32	31	31	-	-	-
L32'	32	10	1	-	9	-
L36	36	23	11	12	-	-
L36'	36	16	3	13	-	-
L50	50	12	1	-	-	11
L54	54	26	1	25	-	-
L64	64	63	63	-	-	-
L64'	64	21	-	-	21	-
L81	81	40	-	40	-	-

The signal to noise ratios (S/N), which are log functions of desired output, serve as the objective functions for optimization, help in data analysis and the prediction of the optimum results. The Taguchi method treats the optimization problems in two categories: static problems and dynamic problems. For simplicity, the detailed explanation of only the static problems is given in the following text. Next, the complete procedure followed to optimize a typical process using Taguchi method is explained with an example.

Table: 1(b). The degrees of freedom for one factor (A) in "2 levels" and five factors (B, C, D, E, F) in "3 levels"

Factors	Degrees of freedom
Overall mean	1
A	2-1 = 1
B, C, D, E, F	5 × (3-1) = 10
Total	12

Static Problems

Generally, a process to be optimized has several control factors (process parameters) which directly decide the target or desired value of the output. The optimization then involves determining the best levels of the control factor so that the output is at the target value. Such a problem is called as a "STATIC PROBLEM". This can be best explained using a P-Diagram (Figure 2(a)) which is shown below ("P" stands for Process or Product). The noise is shown to be present in the process but should have no effect on the output. This is the primary aim of the Taguchi experiments - to minimize the variations in output even though noise is present in the process. The process is then said to have become ROBUST.

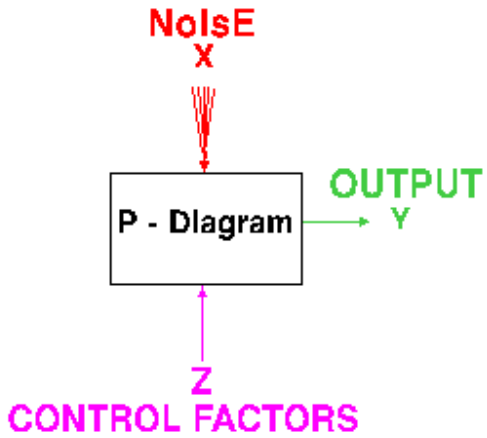


Fig: 2(a). P-Diagram for static problems

Signal to Noise (S/N) Ratio:

There are three forms of signal to noise (S/N) ratio that are of common interest for optimization of static problems.

[1] Smaller-the-better

This is expressed as

$n = -10 \text{ Log}10$ [mean of sum of squares of measured data]

This is usually the chosen S/N ratio for all the undesirable characteristics like "defects" for which the ideal value is zero. When an ideal value is finite and its maximum or minimum value is defined (like the maximum purity is

100% or the maximum temperature is 92 K or the minimum time for making a telephone connection is 1 sec) then the difference between the measured data and the ideal value is expected to be as small as possible. Thus, the generic form of S/N ratio becomes,

$n = -10\ Log_{10}$ [mean of sum of squares of {measured – ideal}]

[2] Larger-the-better

This is expressed as

$n = -10\ Log_{10}$ [mean of sum of squares of reciprocal of measured data]

This is often converted to smaller-the-better by taking the reciprocal of the measured data and next, taking the S/N ratio as in the smaller-the-better case.

[3] Nominal-the-best

This is expressed as

$$n = -10Log_{10}\left[\frac{square\ of\ mean}{variance}\right]$$

This case arises when a specified value is the most desired, meaning that neither a smaller nor a larger value is desired.

Application of Taguchi Method:

Determine the effect of four process parameters: Reaction temp (A), Catalyst Concentration (wt %) (B), Molar ratio (Methanol/Oil) (C) and Reaction time (D) on the yield of Neem Oil Methyl Ester (NOME). Also estimate the optimum setting of the above process parameters for maximum yield. Table 2(c) depicts the factors and their levels.

Table: 1(c). Factors and their levels

Factor		Levels		
		1	2	3
A	Reaction Temp (°C)	50	55	60
B	Catalyst Concentration (wt %)	1.0	1.25	1.50
C	Molar Ratio (Methanol/Oil)	4.5	6.0	7.5
D	Reaction Time(min)	55	65	75

2.1. Selection of the Design Matrix and Performing the Experiments

The present experiment is associated with four factors with each at three levels. Table 2(a) indicates that the best suitable orthogonal array is L9. Table 2(d) shows the design matrix for L9. Next conduct all the nine experiments and observe % yield of neem oil methyl ester (NOME). The summary statistic, ηi, for an experiment, i, is given by

$$n_i = -10Log_{10}\ C_i$$

where Ci refers to mean squared deviation for experiment i and the mean square refers to the average of the squares of the nine observations in the experiment i. Table 2(d) also depicts the observed value of ηi for all the nine experiments. This summary statistic ηi is called the signal to noise (S/N) ratio.

Table: 1(d). L_9 array matrix experiment table

Expt No	Column number and factor assigned				Observation, η (%)
	1 Reaction Temp (⁰ C) (A)	2 Catalyst Concentration (wt %) (B)	3 Molar Ratio (Methanol/Oil) (C)	4 Reaction Time (min) (D)	
1	1	1	1	1	37.14
2	1	2	2	2	36.85
3	1	3	3	3	36.81
4	2	1	2	3	36.68
5	2	2	3	1	36.22
6	2	3	1	2	36.42
7	3	1	3	2	35.71
8	3	2	1	3	35.83
9	3	3	2	1	35.55

Table: 1(e). Yield of Neem Oil Methyl Ester and S/N ratio (η)

Exp. No	% Yield of Neem Oil Methyl Ester (NOME)				S/N ratio (η)
	Sample 1	Sample 2	Sample 3	Mean	
1	70.8	73.9	71.3	72.0	37.14
2	65.2	70.4	74.1	69.9	36.85
3	68.9	70.2	68.8	69.3	36.81
4	66.6	69.2	69.1	68.3	36.68
5	61.8	68.5	64.4	64.9	36.22
6	65.8	67.9	65.2	66.3	36.42
7	58.2	63.5	61.9	61.2	35.71
8	57.3	66.6	63.0	62.3	35.83
9	58.2	61.4	60.4	60.0	35.55
			Mean	**66.0**	**36.35**

According to the analysis for the case of larger the better the mean squared deviations (MSD) of each experiment were evaluated using the following equation

$$MSD = \frac{1}{n}\sum_{i=1}^{n}\left(\frac{1}{y_i}\right)^2$$

Where n is the number of repetitions of each experiment and yi the yield of Neem Oil methyl ester.

Then the S/N ratio was evaluated using the equation

S/N ratio = -10 Log (MSD)

The effect of parameter level is defined as the deviation it causes from the overall mean. Hence as a first step , calculating the overall mean value of S/N ratio for the experimental region defined by the factor levels in Table 2(f).

2.2. Calculation of Factor Effects

The effect of a factor level is defined as the deviation it causes from the overall mean. Hence as a first step, calculate the overall mean value of η for the experimental region defined by the factor levels in Table 2(d) as

$$m = \frac{1}{9}\sum_{i=1}^{9} n_i = \frac{1}{9}(n_1 + n_2 + n_3 + \cdots + n_9) = 36.35$$

The effect of the temperature at level A1 (at experiments 1, 2 and 3) is calculated as the difference of the average S/N ratio for these experiments (mA1) and the overall mean. The same is given as

The effect of temperature at level

$$A_1 = m_{A1} - m = \frac{1}{3}(n_1 + n_2 + n_3) - m$$

Similarly,

The effect of temperature at level

$$A_2 = m_{A2} - m = \frac{1}{3}(n_4 + n_5 + n_6) - m$$

The effect of temperature at level

$$A_3 = m_{A3} - m = \frac{1}{3}(n_7 + n_8 + n_9) - m$$

Using the S/N ratio data available in Table 1(d). The average of each level of the four factors is calculated and listed in Table 2(f). These average values are shown in Figure 2(b) they are separate effect of each factor and are commonly called main effects.

Table: 1(f). Average η for different factor levels

Factor		Levels		
		1	2	3
A	Reaction Temp (°C)	36.93*	36.44	35.69
B	Catalyst Concentration (wt %)	36.51*	36.30	36.26
C	Molar ratio(Methanol/Oil)	36.46*	36.36	36.24
D	Reaction Time(min)	36.30	36.32	36.44*

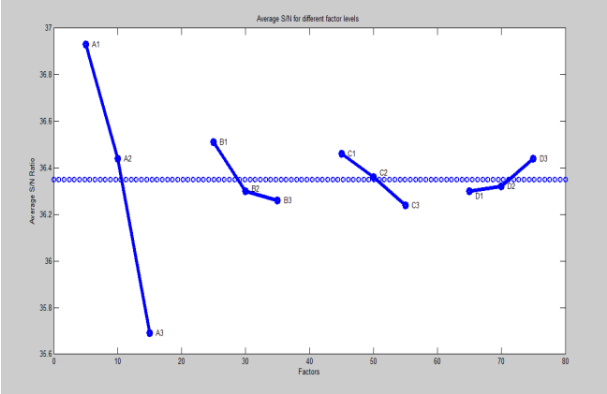


Fig: 1(b). Plots of factor effects

2.3. Selecting Optimum Factor Levels

Our goal in this experiment is to maximize the yield of Fatty Acid Methyl Ester (FAME). Since –log depicts a monotonic decreasing function, we have to maximize η. Hence the optimum level for a factor is the level that gives the highest value of η in the experimental region. From Figure 2(b) and the Table 2(f), it is observed that the optimum settings of reaction temp, catalyst concentration (wt %), molar ratio (methanol/oil) and reaction time are A1, B1, C1 and D3. Hence we can conclude that the setting A1B1C1D3 can give the highest η for Neem Oil Methyl Ester.

2.4. Developing the Additive Model For Factor Effects

The relation between η and the process parameters A, B, C and D can be approximated adequately by the following additive model:

$$n(A_i + B_j + C_k + D_l) = m + a_i + b_j + c_k + d_l + e$$

Where the term m refers to the overall mean (that is the mean of η for the experimental region). The terms ai, bj, ck and dl refer to the deviations from μ caused by the setting Ai, Bj, Ck, and Dl of factors A, B, C and D, respectively. The term e stands for the error. In additive model the cross-product terms involving two or more factors are not allowed. The above equation is utilized in predicting the S/N ratio at optimum factor levels.

2.5. Analysis of Variance (ANOVA)

Different factors affect the yield of NOME to a different degree. The relative magnitude of the factor effects are listed in Table 2(f). A better feel for the relative effect of the different factors is obtained by the decomposition of variance, which is commonly called as analysis of variance (ANOVA). This is obtained first by computing the sum of squares.

$$Total\ Sum\ of\ Squares = \sum_{i=1}^{9} n_i^2 = ((37.14)^2 + (36.85)^2 + \cdots \ldots + (35.55)^2) = 11898.80$$

$$Sum\ of\ Squares\ Due\ to\ Mean = (Number\ of\ Exp.)\ X\ m^2 = 9\ X\ (36.35)^2 = 11891.90$$

$$Total\ Sum\ of\ Squares (Sum\ of\ Squares\ of\ all\ 9\ Experiments) = \sum_{i=1}^{9} (n_i - m)^2 = 2.54$$

Sum of Squares due to factor A

$$= [(Number\ of\ Experiments\ at\ level\ A1) \times (m_{A1} - m)^2] + [(Number\ of\ Experiments\ at\ level\ A2) \times (m_{A2} - m)^2] + [(Number\ of\ Experiments\ at\ level\ A3) \times (m_{A3} - m)^2]$$

$$= [3 \times (36.93 - 36.35)^2] + [3 \times (36.44 - 36.35)^2] + [3 \times (35.69 - 36.35)^2] = 2.34$$

Sum of Squares due to factor B

$$= [(Number\ of\ Experiments\ at\ level\ B1) \times (m_{B1} - m)^2] + [(Number\ of\ Experiments\ at\ level\ B2) \times (m_{B2} - m)^2] + [(Number\ of\ Experiments\ at\ level\ B3) \times (m_{B3} - m)^2]$$

$$= [3 \times (36.51 - 36.35)^2] + [3 \times (36.30 - 36.35)^2] + [3 \times (36.26 - 36.35)^2] = 0.11$$

Sum of Squares due to factor C

$$= [(Number\ of\ Experiments\ at\ level\ C1) \times (m_{C1} - m)^2] + [(Number\ of\ Experiments\ at\ level\ C2) \times (m_{C2} - m)^2] + [(Number\ of\ Experiments\ at\ level\ C3) \times (m_{C3} - m)^2]$$

$$= [3 \times (36.46 - 36.35)^2] + [3 \times (36.36 - 36.35)^2] + [3 \times (36.24 - 36.35)^2] = 0.07$$

Sum of Squares due to factor D

$$= [(Number\ of\ Experiments\ at\ level\ D1) \times (m_{D1} - m)^2] + [(Number\ of\ Experiments\ at\ level\ D2) \times (m_{D2} - m)^2] + [(Number\ of\ Experiments\ at\ level\ D3) \times (m_{D3} - m)^2]$$

$$= [3 \times (36.30 - 36.35)^2] + [3 \times (36.32 - 36.35)^2] + [3 \times (36.44 - 36.35)^2] = 0.03$$

So the sum of squares due to factor A, B, C and D computed as 2.34, 0.11, 0.07 and 0.03, respectively. Now all these sum of squares are tabulated in Table 2(g) this is called as the ANOVA table.

Table: 2(g) ANOVA table for η (S/N Ratio)

Factor	Degree of freedom	Sum of squares	Mean square =Sum of squares/Degree of freedom	F	Contribution (%)
A	Reaction Temp (°C)	2	2.34	1.170	46.8	92.12
B	Catalyst Concentration (wt	2	0.11	0.055	2.2	4.33
C	Molar Ratio (Methanol /Oil)	2	0.07	0.035	1.4	2.76
D	Reaction Time (min)	2	0.03	0.015	0.6	0.79
Error		0	0			
Total		8	2.54			
(Error)		(4)	0.10	0.025		

In the present study, the degrees of freedom for the error will be zero. Hence an approximate estimate of the error sum of squares is obtained by pooling the sum of squares corresponding to the factors having the lowest mean square. The parameters C and D are used to estimate the error sum of squares. They account for four degrees of freedom and their sum of squares is 0.10. Referring to the sum of squares in table, the parameter A makes the largest contribution 92.12% to the total sum of squares. The factors B, C and D make 4.33 %, 2.76% and 0.79% each. The larger the contribution of a particular parameter to the total sum of squares, the larger the ability is of that factor to influence S/N ratio. Moreover, the larger F-value, the larger will be the factor effect in comparison to the error mean square.

Degrees Of Freedom

The degrees of freedom associated with the grand total sum of squares are equal to the number of rows in the design matrix.

The degree of freedom associated with the sum of squares due to mean is one.

The degrees of freedom associated with the total sum of squares will be equal to the number of rows in the design matrix minus one.

The degrees of freedom associated with the factor will be equal to the number of levels minus one.

The degrees of freedom for the error will be equal to the degrees of freedom for the total sum of squares minus the sum of the degrees of freedom for the various factors.

In the present experiment, the degrees of freedom for the error will be zero. Hence an approximate estimate of the error sum of squares is obtained by pooling the sum of squares corresponding to the factors having the lowest mean square. As a rule of thumb, the sum of squares corresponding to the bottom half of the factors (as defined by lower mean square) are used to estimate the error sum of squares. In the present experiment, the factors C and D are used to estimate the error sum of squares. Together they account for four degrees of freedom and their sum of squares is 0.10.

2.6. Interpretation of ANOVA Table

The major inferences from the ANOVA table are given in this section. Referring to the sum of squares in Table 2(g) the factor A makes the largest contribution to the total sum of squares [(2.34/2.54) x 100 = 92.12%]. The factor B makes the next largest contribution (4.33%) to the total sum of squares, whereas the factors C and D make only 2.76% and 0.79% contribution respectively. The larger the contribution of a particular factor to the total sum of squares, the larger the ability is of that factor to influence η. Moreover, the larger the F-value, the larger will be the factor effect in comparison to the error mean square or the error variance.

2.7. Prediction of η Under Optimum Conditions

In the present experiment, the identified optimum condition or the optimum level of factors is A1B1C1D3. The value of η under the optimum condition is predicted using the additive model as

$$\eta_{opt} = m + (m_{A1} - m) + (m_{B1} - m) + (m_{C1} - m) + (m_{D3} - m) + e$$

$$= 36.35 + (36.93 - 36.35) + (36.51 - 36.35) + (36.46 - 36.35) + (36.44 - 36.35) + 0 = 37.29$$

Reaction Temp (^{0}C)	50	55	60	Catalyst Concentration (Wt %)	1	1.25	1.50
S/N ratio (η)	36.93	36.44	35.69	S/N ratio (η)	36.51	36.30	36.26
Molar Ratio (Methanol/Oil)	4.5	6.0	7.5	Reaction Time(min)	55	65	75
S/N ratio (η)	36.46	36.36	36.24	S/N ratio (η)	36.30	36.32	36.44

Table: 2(h). Main effects plot of the control parameters

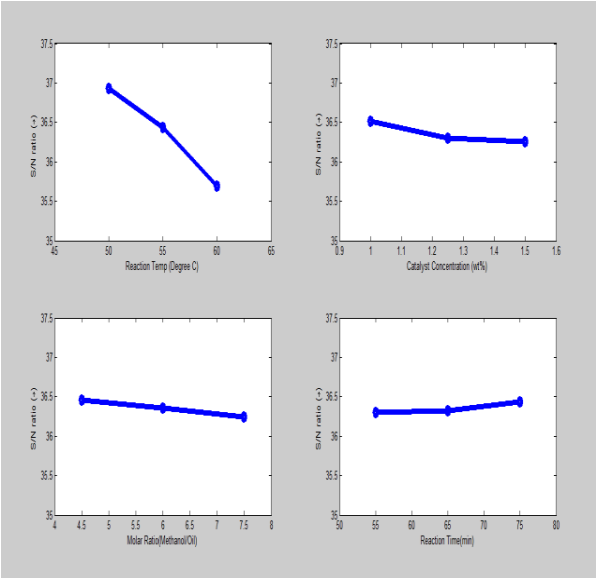


Fig: 2(c). Main effects plot of the control parameters

2.8 Conclusion

Result of the Proposed Optimized Experimental Condition

The optimum conditions to achieve effective performance for the production of neem oil methyl ester and the contri¬butions of each parameter to the S/N ratio under the optimal conditions are shown in Table 2(i)

Table: 2(i). Optimum conditions for settling the control parameters and their contributions:

Parameters		Level	Level description	Contribution
A	Reaction Temperature	1	50°C	0.58
B	Catalyst Concentration	1	1.0 wt %	0.16
C	Methanol to Oil Molar Ratio	1	4.5:1	0.11
D	Reaction Time	3	75 min	0.09
Total contribution from all parameters 0.94 Current grand average of performance 36.35 Expected result under optimum conditions 37.29				

The calculated S/N ratio corresponding to nine set of experiments given in Table 2(d). The average S/N ratios of parameter at each level for neem oil methyl ester are shown in Table 2(f). Also the main effect plot for S/N ratio is shown in Fig 2(c). The average S/N ratio for maximum percentage yield of neem oil methyl ester is obtained at level 1 (Reaction Temperature 50^{0}C), level 2 (Catalyst conc. 1.0%by wt), level 3 (Methanol to oil molar ratio 4.5:1) and level 4 (reaction time 75min). i.e., the optimum parameter setting for high percentage yield of neem oil methyl ester is A1B1C1D3. The results of ANOVA for S/N ratios are given in Table 2(g). The percentage of yield of neem oil methyl ester has been significantly improved using Taguchi Method.

The Taguchi method, which uses a set of orthogonal arrays for performing the fewest experiments, was employed to design experimental trials, with an ANOVA performed to more system¬atically analyze the relative importance of each experimental parameter on the production of neem oil methyl ester.

The reaction temperature, catalyst concentration and methanol to oil molar ratio were found to be significant parameters affecting the production of neem oil methyl ester. The contribution of the reaction temperature on the production process was larger than that of any other parameter. The yield of neem oil methyl ester obtained with the optimal experimental parameters was greater than that obtained from experiment no.1, which gave the highest yield from the experimental trials, and the theoreti¬cally expected value.

The experiments conducted under the optimized conditions showed a meaningful enhanced process performance. The Ta¬guchi method provided a systematic and efficient mathematical approach to evaluate and optimize the process for the produc¬tion of neem oil methyl ester, using only a few well-defined ex¬perimental sets for the optimization of the parameters.

Cost Analysis:

Sl. No.	Component	Cost (Rs.)
1	Sodium Hydroxide (Catalyst)	23/kg
2	Potassium hydroxide (Catalyst)	36/kg
3	Neem oil (Feedstock)	150/ litre
4	Methanol (Alcohol)	35/ litre
5	Glycerin (By product of Biodiesel)	75/ litre
Sl. No.	Component	Cost (Rs.)
1	Neem Oil – 100 ml	15
2	Two step transesterification Cost - 65 ml (45 ml +	2.275

	20 ml) of Methanol [4.5 Methanol/Oil Molar Ratio]	
3	Catalyst KOH 1.0 gm	0.036
4	Recovery (Glycerin 50 ml)	3.75
5	Total Cost (1 + 2 + 3 – 4)	17.311 – 3.75 = 13.561

Biodiesel production from 1 litre Neem Oil=0.70 Litre

So Cost of Biodiesel per litre = [(13.561 /100)*1000] / 0.70 = 193.73 Rs.

The cost of the biodiesel production can be minimized as possible to recover the used methanol. Recycling of methanol again and again in mass production and commercial use, the cost must be come to the lowest amount. Also the by-product such as glycerin and soap play an important role to minimize the cost.

3. Inference

From all the experimentation performed above, it can be clearly observed that Neem Oil Methyl Ester (NOME) can be obtained by two step transesterification process only as the FFA content of neem oil is large. By using single step transesterification, the yield will be very less and in some case NOME cannot be obtained.

Taking together all these results, the optimized biodiesel yield of 74.30% was produced at reaction time of 75 min, catalyst amount of 0.50 g, temperature of 50°C, and methanol/oil molar ratio of 4.5.

ANOVA analysis showed that the temperature had the highest effect on the biodiesel yield followed by catalyst amount, methanol to oil molar ratio and reaction time

The result of this work showed that the maximum yields were obtained at lowest factor values. This will definitely have economic advantage on neem oil biodiesel production as low energy cost, low catalyst amount, low methanol/oil molar ratio, and low temperature are able to produce high biodiesel yield.

This was in agreement with the works of Awolu and Layokun, Meher et al., Jeong et al. and Marchetti and Errazu.

4. Recommendations

In the optimization of parameters, KOH catalyst has been used with different concentration (1.0%, 1.25% and 1.5%) with the other parameters like methanol to oil molar ratio, reaction temperature and reaction time.

So, we can further do the optimization by using different catalyst types (NaOH, KOH and $NaOCH_3$), catalyst concentration, reaction temperature and methanol to oil ratio with three levels.

So Four Parameters and Three Level

No of experiment required = 3*3*3*3 =81.

But by using Taguchi Method of optimization

No of experiment required = 9 only.

References

[1] A. K. Endalew, Y. Kiros, R. Zanzi, Heterogeneous catalysis for biodiesel production from Jatropha curcas oil (JCO). Energy 2011, 36, 2693-2700

[2] A. Dhar, R. Kevin, A. K. Agarwal, Production of biodiesel from high-FFA neem oil and its performance, emission and combustion characterization in a single cylinder DICI engine. Fuel Processing Technology 2012, 97, 118–129

[3] A. Demirbas, Progress and recent trends in biodiesel fuels. Energy Conversion and Management, 2009, 50, 14 -34

[4] C. Martín, A. Moure, G. Martín, E. Carrillo, H. Domínguez, J. C. Parajó, Fractional characterization of jatropha, neem, moringa, trisperma, castor and candlenut seeds as potential feedstocks for biodiesel production in Cuba. Biomass Bioenergy 2010, 34, 533-538

[5] D. Tanwar, Ajayta, Dilip Sharma, Y. P. Mathur, Production and Characterization of Neem Oil Methyl Ester. International Journal of Engineering Research & Technology (IJERT), 2013, 2, 1896-1903

[6] Dennis Y.C. Leung, Xuan Wu, M.K.H. Leung, A review on biodiesel production using catalyzed transesterification, Applied Energy 2010, 87, 1083-1095

[7] E. F. Aransiola, E Betiku, DIO Ikhuomoregbe, TV Ojumu, Production of biodiesel from crude neem oil feedstock and its emissions from internal combustion engines. African Journal of Biotechnology, 2012, 11, 6178-6186

[8] Freedman B, R. Butterfield, E. Pryde, Transesterification kinetics of soybean oil. Journal of the American oil Chemists Society, 1986, 63, 1375-1380

[9] H. Fukuda, A. Kondo, H. Noda, Biodiesel fuel production by transesterification of oils. Journal of Bioscience and Bioengineering, 2001, 92, 405-416

[10] G. T. Jeong, H. S. Yang, D. H. Park, Optimization of transesterification of animal fat ester using response surface methodology. Bioresour. Technol, 2009, 100, 25-30

[11] H. N. Pandey, Development of a New Catalyst for Bio-diesel Production. I[st] International Conference on New Frontiers in Biofuels, DTU, 2010, New Delhi

[12] H Ibrahim, A. S. Ahmed, I. M. Bugaje, Dabo Mohammed, C. D. Ugwumma. Synthesis of Bulk Calcium Oxide (Cao) Catalyst and its Efficacy for Biodiesel Production. Journal of Energy Technologies and Policy, 2013, 3, 14-16

[13] Jon Von Gerpen. Biodiesel processing and production. Fuel Process Technol 2005, 86, 1097–1107

[14] J. M. Marchetti, A. F Errazu, Esterification of free fatty acids using sulfuric acid as catalyst in the presence of triglycerides. Biomass. Bioenerg, 2008, 32, 892–895

[15] Juan Calero, Gema Cumplido, Diego Luna, Enrique D. Sancho, Carlos Luna , Alejandro Posadillo, Felipa M. Bautista , Antonio A. Romero and Cristóbal Verdugo-Escamilla, Production of a Biofuel that Keeps the Glycerol as a Monoglyceride by Using Supported KF as Heterogeneous Catalyst, Energies 2014, 7, 3764-3780

[16] L. C. Meher, D. Vidya Sagar, S.N. Naik. Technical aspects of biodiesel production by transesterification – a review. Renew. Sustain. Energy, 2006, 10, 248-268

[17] M. Agarwal, K. Singh, U. Upadhyaya, S. P. Chaurasia, Potential vegetable oils of Indian origin as biodiesel feedstock – An experimental study. Journal of Scientific & Industrial Research, 2012, 71, 285-289
[18] M. Hassani, G. D Najafpour, M. Mohammadi, M. Rabiee, Preparation, Characterization and Application of Zeolite-based Catalyst for Production of Biodiesel from Waste Cooking Oil. Journal of Scientific & Industrial Research, 2014, 73, 129-133
[19] M A Hanna, Loren Isom, John Campbell, Biodiesel; Current perspectives and future. Journal of Scientific & Industrial Research, 2005, 64, 854-857
[20] Md. H. Alia, Md. Mashud, Md. Rowsonozzaman Rubel, Rakibul Hossain Ahmad, Biodiesel from Neem oil as an alternative fuel for Diesel engine. Procedia Engineering, 2013, 56, 625 – 630
[21] M. A. Fazal, A.S.M.A. Haseeb, H.H. Masjuki. Biodiesel feasibility study: An evaluation of material compatibility; performance; emission and engine durability. Renew. Sustain. Engy Reviews 2011, 15, 1314-1324
[22] Module 5, Lecture 4. Design for Reliability and Quality. IIT, Bombay.
[23] Muthu, V. SathyaSelvabala, T. K. Varathachary, D. Kirupha Selvaraj, J. Nandagopal, S. Subramanian. Synthesis of biodiesel from neem oil using sulfated zirconia via tranesterification. Brazilian Journal of chemical Engineering, 2010, 27, 601-608
[24] N. Satya Sree, V. Madhusudhan Rao, P. Vijetha. Production of Bio-Diesel From Soap Stock of Cotton Seed Oil By Using Ferric Sulphate Catalyst Via A Two Step Heterogeneous Catalysis: Characteristics of Bio-Diesel Produced. International Journal of Scientific & Technology Research, 2014, 3, 141-144
[25] Nielsen P. M., J. Brask, Fjerbaek. Enzymatic biodiesel production: Technical and economical considerations. European Journal of Lipid Science, 2008, 110, 692-700
[26] Olugbenga Olufemi Awolu and Stephen Kolawole Layokun. Optimization of two-step transesterification production of biodiesel from neem (Azadirachta indica) oil. International Journal of Energy and Environmental Engineering, 2013, 4, 1-9
[27] P. Deshpande, Kavita Kulkarni, A. D. Kulkarni, Supercritical Fluid Technology in Biodiesel Production: A Review. Chemistry and Materials Research, 2011, 1, 27-32
[28] Poonam Gera, S. K. Puri, M. K. Jha, Use of Basic Heterogeneous Catalysts for Biodiesel Production: A Review. Ist International Conference on New Frontiers in Biofuels, DTU, 2010
[29] S. Singh, P. K. Omre, K. Gaikwad, Standardization of Process Parameters for Neem Oil & Determination of Properties for Using as a Fuel. International Journal of Engineering Research and General Science, 2014, 2, 1-7
[30] Talebian-Kiakalaieh, N. A. S. Amin, A. Zarei, H. Jaliliannosrati, Biodiesel Production from High Free Fatty Acid Waste Cooking Oil by Solid Acid Catalyst. Proceedings of the 6th International Conference on Process Systems Engineering (PSE ASIA), 2013, Kuala Lumpur
[31] Vivek, A. K. Gupta, Biodiesel production from karanja oil. Journal of Scientific & Industrial Research, 2004, 63, 39-47
[32] V. Manieniyan, R. Senthilkumar, S. Sivaprakasam, Experimental Investigation on Optimized Biodiesel (Based on Various Catalysts) used in a Twin Cylinder Diesel Engine. Ist International Conference on New Frontiers in Biofuels, DTU, 2010

ResearchGate

See discussions, stats, and author profiles for this publication at: http://www.researchgate.net/publication/282763926

Average Bit Error Probability of MRC Combiner in Log Normal Shadowed Fading

CONFERENCE PAPER · APRIL 2015

READS
8

3 AUTHORS, INCLUDING:



Rupender Singh
World Institute of Technology, Gurgaon
3 PUBLICATIONS **0** CITATIONS
SEE PROFILE



P. K. Verma
Delhi Technological University
2 PUBLICATIONS **0** CITATIONS
SEE PROFILE

All in-text references underlined in blue are linked to publications on ResearchGate, letting you access and read them immediately.

Available from: P. K. Verma
Retrieved on: 24 November 2015

Average Bit Error Probability of MRC Combiner in Log Normal Shadowed Fading

Rupender Singh[1], S.K. Soni[2], P. K. Verma[3]
[1, 2, 3]Department of Electronics & Communication Engineering
Delhi Technological University (Formerly Delhi College of Engineering), Delhi
rupendersingh04cs39@gmail.com

Abstract: **In this paper, we provide the average bit error probabilities of MQAM and MPSK in the presence of log normal shadowing using Maximal Ratio Combining technique for L diversity branches. We have derived probability of density function (PDF) of received signal to noise ratio (SNR) for L diversity branches in Log Normal fadingfor Maximal Ratio Combining (MRC). We have used Fenton-Wilkinson method to estimate the parameters for a single log-normal distribution that approximates the sum of log-normal random variables (RVs). The results that we provide in this paper are an important tool for measuring the performance ofcommunication links in a log-normal shadowing.**

Keywords: ***Log normal random variable, FW Method, Maximal Ratio Combining (MRC), Probability of density function(PDF), MQAM, MPSK, Random Variables RVs, ABEP(Average Bit Error Probability).***

1. INTRODUCTION

Wireless communication channels are impaired by detrimental effects such as Multipath Fading and Shadowing[1]. Based on various indoor and outdoor empirical measurements, there is general consensus that shadowing be modeled using Log-normal distribution[8-10]. Fading causesdifficulties in signal recovery. When a receivedsignal experiences fading during transmission, its envelope and phase both fluctuate over time.

One of the methods used to mitigate thesedegradation are diversity techniques, such as spacediversity [1], [2]. Diversity combining has beenconsidered as an efficient way to combat multipathfading and improve the received signal-to-noiseratio (SNR) because the combined SNR comparedwith the SNR of each diversity branch, is beingincreased. In this combining, two or more copies ofthe same information-bearing signal are combiningto increase the overall SNR. The use of log-normal distribution [1], [10] tomodel shadowing which is random variabledoesn't lead to a closed formsolution for integrations involving in sum ofrandom variables at the receiver. Thisdistribution(PDF) can be approximated by another log normal random variable using Fenton-Wilkinson method[3].

This paper presents Maximal-Ratio Combiningprocedure for communication system where thediversity combining is applied over uncorrelated branches ($\rho=0$), which are given as channels with log-normal fading.

Maximal-Ratio Combining (MRC) is one of themost widely used diversity combining schemeswhose SNR is the sum of the SNR's of eachindividual diversity branch. MRC is the optimalcombining scheme, but its price and complexity arehigh, since MRC requires cognition of all fadingparameters of the channel.

The sum of log normal random variables has been considered in [3-6]. Up to now these papers has shown different techniques such as MGF, Type IV Pearson Distribution and recursive approximation. In this paper we have approximated sum (MRC) of log normal random variables using FW method. On the basis of FW approximation, we have given amount of fading (AF), outage probability (P_{out}) and channel capacity (C) for MRC combiner.

In this paper, a simple accurate closed-form using Holtzmanin [14] approximation for the expectation of the function of a normal variant is also employed. Then, simple analytical approximations for the ABEP of M-QAM modulation schemes for MRC combiner output are derived.

2. SYSTEMS AND CHANNEL MODELS

Log-normal Distribution

A RV γ is log-normal, i.e. $\gamma \sim LN(\mu, \sigma^2)$, ifand only if $\ln(\gamma) \sim N(\mu, \sigma^2)$. A log-normal RVhas the PDF

$$p(\gamma) = \frac{\xi}{\sigma\gamma\sqrt{2\pi}} e^{-\frac{(10log_{10}\gamma-\mu)^2}{2\sigma^2}} \quad \text{.....(1)}$$

For any $\sigma^2 > 0$. The expected value of γ is

$$E(\gamma) = e^{(\mu+0.5\,\sigma^2)}$$

And the variance of $\gamma$is

$$Var(\gamma) = e^{(\sigma^2-1)} * e^{(2\mu+\sigma^2)}$$

Where ξ=10/ln 10=4.3429, μ(dB) is the mean of $10log_{10}\gamma$, σ(dB) is standard deviation of $10log_{10}\gamma$.

3. MAXIMAL RATIO COMBINING

The total SNR at the output of the MRC combiner is given by:

$$\gamma_{MRC}=\sum_{i=1}^{L}\gamma_i \quad \text{.....(2)}$$

$$\gamma_{MRC}=\gamma 1+\gamma 2+\gamma 3+\gamma 4 \ldots\ldots\ldots\ldots+\gamma L \quad \text{.....(3)}$$

where$L$ is number of branches.

Since the L lognormal RVs are independentlydistributed, the PDF of the lognormal sum[3]

$$p(\gamma_{MRC})=p(\gamma_1)\otimes p(\gamma_2)\otimes p(\gamma_3)\otimes \ldots\ldots\ldots\otimes p(\gamma_L) \quad \text{.....(4)}$$

where$\otimes$denotes the convolution operation.

The functional form of the log-normal PDF does not permit integration in closed-form. So above convolution can never be possible to present. Fenton (1960) estimate the PDF for a sum of log-normal RVs using another log-normal PDF with the same mean and variance. The Fenton approximation (sometimes referred to as the Fenton-

Wilkinson(FW) method) is simpler to apply for awide range of log-normal parameters.

3.1Consider the sum of *L* uncorrelated log-normal RVs, γ, as specified in (1) where each γ~LN(μ, σ^2) with the expected value and varianceμ and σ respectively. The expected value and variance of γ_{MRC} are

$$E(\gamma_{MRC}) = L\,E(\gamma)$$

And

$$Var(\gamma_{MRC}) = L\,Var(\gamma)$$

The FW approximationis a log-normal PDF with parameters$\mu_M$and σ^2_M such that

$$e^{(\mu_M + 0.5\,\sigma_M{}^2)} = L\,E(\gamma)$$

And

$$e^{(\sigma_M{}^2 - 1)} * e^{(2\mu_M + \sigma_M{}^2)} = L\,Var(\gamma)$$

Solving above equations for $\mu_M$and σ^2_M gives

$$\sigma_M{}^2 = \ln\left(\frac{e^{(\sigma^2-1)}}{L} + 1\right) \ldots\ldots\ldots\ldots\ldots\ldots(5)$$

And

$$\mu_M = \ln(L\,e^{\mu}) + 0.5(\sigma^2 - \sigma_M{}^2) \ldots\ldots (6)$$

So PDF of the sum of L diversity branches using F-W method is given as

$$p(\gamma_{MRC}) = \frac{\xi}{\sigma_M \gamma_{MRC}\sqrt{2\pi}} e^{-\frac{(10log_{10}\gamma_{MRC} - \mu_M)^2}{2\sigma^2_M}} \ldots\ldots\ldots\ldots\ldots\ldots(7)$$

The different μ_M and σ_M have been calculated for different numbers of branches L using above F-W approximationfrom (5) and (6) and shown in table 1.For calculations we have considered γ~LN(0.69,1.07^2).

Table 1 μ_M and σ_M for different number of diversity branches

Number of diversity branches *L*	μ_M	σ_M
2	*2.04*	0.85
4	*2.70*	0.65
6	*3.51*	0.55
8	*4.05*	0.48
10	*4.51*	0.44
15	*5.51*	0.36
20	*6.35*	0.31
25	*7.09*	0.28
30	*7.76*	0.26
50	*10.01*	0.20

In Fig (1) PDF of received SNR using MRC diversity techniques has presented. As we can see from the Fig that as the number of branches increases, PDF of received SNR tends towards Gaussian distribution shape. So we can conclude that FW approximation method also satisfies central limit theorem.

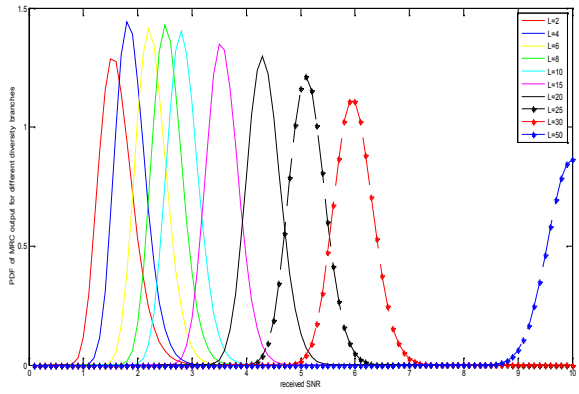


Fig 1. PDF of received SNR of MRC combiner output

3. ABEP of MQAM for MRC Combiner Output

The instantaneous BEP obtained by using maximum likelihood coherent detection for different modulation types employing Gray encoding at high SNR can be written in generic form[15], [16] as

$$P_b(\beta) = \theta.Q(\sqrt{\lambda\beta\gamma_s}) \ldots\ldots.(8)$$

Where

$$\theta = \frac{4}{log_2 M} \;\; and \;\; \lambda = 3.\left(\frac{1}{M-1}\right)$$

$\gamma_s$isreceived SNR in additive white-gaussiannoise, and β is a non-negative random variable depends on the fading type.

ABEP of MQAM for MRC Combiner Output can be written as

$$P_S(E) = \int_0^{\infty} P_b(\beta).\frac{\xi}{\sigma_M \gamma_{MRC}\sqrt{2\pi}} e^{-\frac{(10log_{10}\gamma_{MRC} - \mu_M)^2}{2\sigma^2_M}} d\gamma_{MRC} \ldots(9)$$

It is difficult to calculate the results directly, in this work, weadopt the efficient tool proposed by Holtzmanin[9] to simplifyEg. (5). Taking Eg. (5-7) in [14], we have

Using $10log_{10}\gamma_{MRC} = x$ in (9)

$$P_S(E) = \int_0^{\infty} \psi(x).\frac{\xi}{\sigma_M\sqrt{2\pi}} e^{-\frac{(x-\mu_M)^2}{2\sigma^2_M}} dx$$

Then finally we have ABEP

$$P_S(E) \approx \frac{2}{3}\psi(\mu) + \frac{1}{6}\psi(\mu + \sqrt{3}\sigma) + \frac{1}{6}\psi(\mu - \sqrt{3}\sigma) \ldots.(10)$$

Where

$$\psi(x) = \theta.Q(\sqrt{\lambda \exp(x)\gamma_s})$$

In Fig (3), (4) and (5)ABEP of MQAM has been shown for different numbers of diversity branches from L=2 to 50. We can conclude that as the number of L increases ABEP decreases. We can see that MRC not only improves SNR but also improves performance in sense of ABEP. Also we have concluded that with increasing M=4, 16, 64 ABEP also increases.

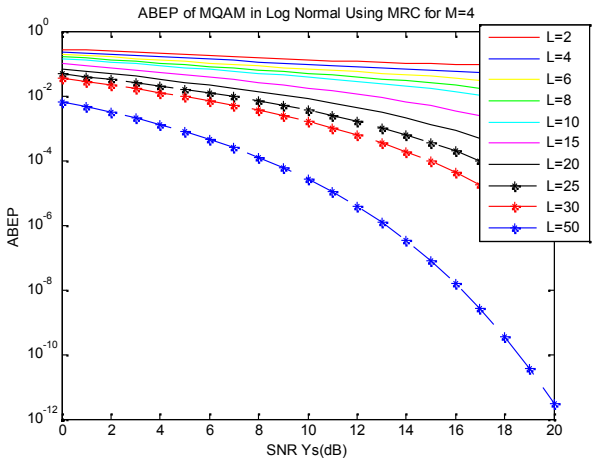


Fig 3. ABEP of MQAM for MRC Combiner Output M=4

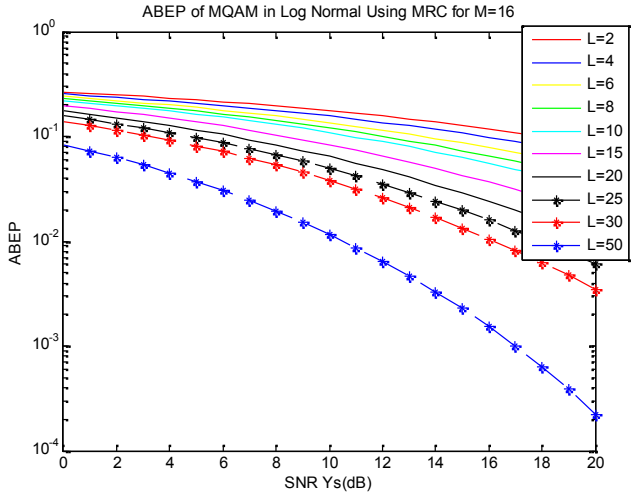


Fig 4. ABEP of MQAM for MRC Combiner Output M=16

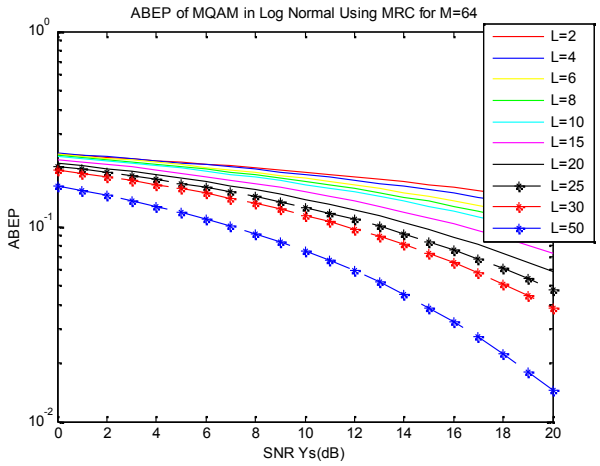


Fig 5. ABEP of MQAM for MRC Combiner Output M=64

4. ABEP OF MPSK FOR MRC COMBINER OUTPUT

The instantaneous BEP obtained by using maximum likelihood coherent detection for different modulation types employing Gray encoding at high SNR can be written in generic form[15], [16] as

$$P_b(\beta) = \theta . Q(\sqrt{\lambda \beta \gamma_s}) \ldots\ldots(11)$$

Where

$$\theta = \frac{2}{log_2 M} \text{ and } \lambda = 3.sin^2\left(\frac{\pi}{M}\right)$$

γ_s isreceived SNR in additive white-gaussiannoise, and β is a non-negative random variable depends on the fading type.

ABEP of MPSK for MRC Combiner Output can be written as

$$P_S(E) = \int_0^{\infty} P_b(\beta).\frac{\xi}{\sigma_M \gamma_{MRC}\sqrt{2\pi}} e^{-\frac{(10log_{10}\gamma_{MRC}-\mu_M)^2}{2\sigma^2 M}} d\gamma_{MRC} \ldots(12)$$

It is difficult to calculate the results directly, in this work, weadopt the efficient tool proposed by Holtzmanin[9] to simplifyEg. (5). Taking Eg. (5-7) in [14], we have

Using $10log_{10}\gamma_{MRC} = x$ in (12)

$$P_S(E) = \int_0^{\infty} \psi(x).\frac{\xi}{\sigma_M\sqrt{2\pi}} e^{-\frac{(x-\mu_M)^2}{2\sigma^2 M}} dx$$

Then finally we have ABEP

$$P_S(E) \approx \frac{2}{3}\psi(\mu) + \frac{1}{6}\psi(\mu + \sqrt{3}\sigma) + \frac{1}{6}\psi(\mu - \sqrt{3}\sigma) \ldots(19)$$

Where

$$\psi(x) = \theta . Q(\sqrt{\lambda \exp(x)\gamma_s})$$

In Fig (6), (7) and (8)ABEP of MPSK has been shown for different numbers of diversity branches from L=2 to 50. We can conclude that as the number of L increases ABEP decreases. We can see that MRC not only improves SNR but also improves performance in sense of ABEP. Also we have concluded that with increasing M=4, 16, 64 ABEP also increases.

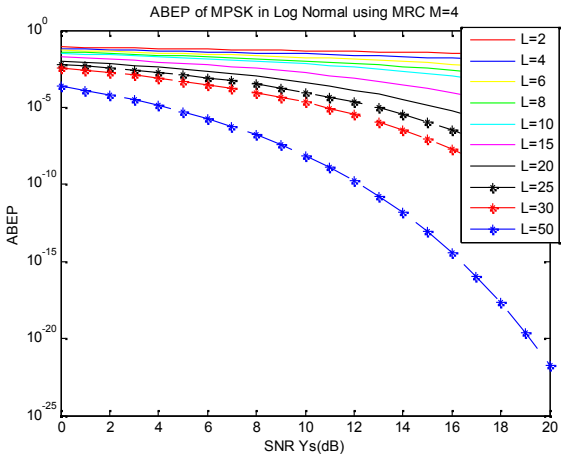


Fig 6. ABEP of MPSK for MRC Combiner Output M=4

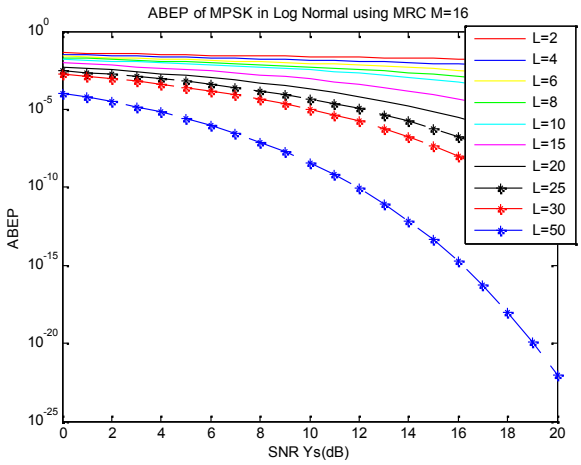


Fig 7. ABEP of MPSK for MRC Combiner Output M=16

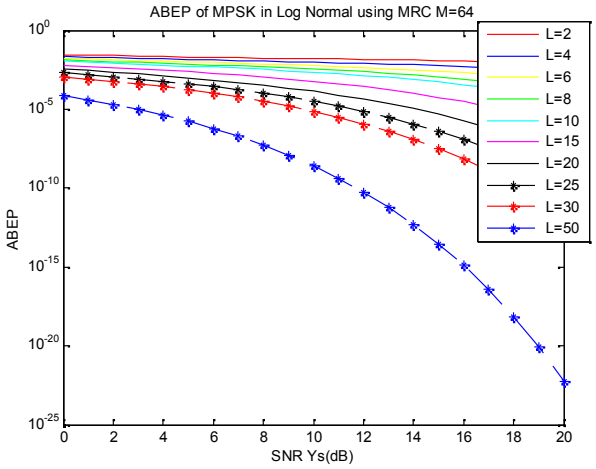


Fig 8. ABEP of MPSK for MRC Combiner Output M=64

5. CONCLUSION

This paper has established a process for estimating the distribution of MRC combiner output for lognormal distributed SNR (a single log-normal RV is a special case). The procedure uses the Fenton- Wilkinson approximation (Fenton, 1960) to estimate the parameters for a single log-normal PDF that approximates the sum (MRC) of log-normal RVs. Fenton Wilkinson (FW) approximation was shown to be general enough to cover the cases of sum of uncorrelated log normal RVs. We have tabulated μ_M and σ_M. ABEP for MQAM and MPSK for MRC combiner output in Log Normal fading channel also plotted from Fig (2) to (8) for different diversity branches L. We can conclude that MRC improves performance as well as ABEP of communication systems in fading environment.

REFERENCES

[1] Marvin K. Simon, Mohamad Slim Alouni*"Digital Communication over Fading Channels"*, Wiley InterScience Publication.

[2] A. Goldsmith, *Wireless Communications*, Cambridge University Press, 2005.

[3] Neelesh B. Mehta, Andreas F. Molisch," Approximating a Sum of Random Variables with a Lognormal", IEEE Trans on wireless communication, vol. 6, No. 7, July 2007.

[4] Rashid Abaspour, MehriMehrjoo, "A recursive approximation approach for non iid lognormal random variables summation in cellular system", IJCIT-2012-Vol.1-No.2 Dec. 2012.

[5] Norman C. Beaulieu, "An Optimal Lognormal Approximation to Lognormal Sum Distributions", IEEE Trans on vehicular technology, vol. 53, No. 2, March 2004.

[6] Hong Nie, "Lognormal Sum Approximation with Type IV Pearson Distribution", IEEE Communication letters, Vol. 11, No. 10, Oct 2007.

[8] H. Suzuki, "A Statistical Model for Urban Radio Propagation", IEEE Trans. Comm., Vol. 25, pp. 673–680,1977.

[9] H. Hashemi, "Impulse response modeling of indoor radio propagation channels," IEEE J. Select. Areas Commun., vol. SAC-11, September 1993, pp. 967–978.

[10] F. Hansen and F.I. Mano, "Mobile Fading-Rayleigh and Lognormal Superimposed", IEEE Trans. Vehic.Tech., Vol. 26, pp. 332–335, 1977.

[11] Mohamed-Slim Alouni, Marvin K.Simon, "Dual Diversity over correlated Log-normal Fading Channels", IEEE Trans. Commun., vol. 50, pp.1946-1959, Dec 2002.

[12] Faissal El Bouanani, Hussain Ben-Azza, MostafaBelkasmi," New results for Shannon capacity over generalized multipath fading channels with MRC diversity", El Bouanani*et al. EURASIP Journal onWireless Communications andNetworking* 2012, 2012:336.

[13]Karmeshu, VineetKhandelwal," On the Applicability of Average Channel Capacityin Log-Normal Fading Environment", Wireless PersCommun (2013) 68:1393–1402 DOI 10.1007/s11277-012-0529-2.

[14] J. M.Holtzman, "A simple, accurate method to calculate spread multipleaccesserror probabilities," IEEE Trans.Commu., vol. 40, no. 3, pp. 461- 464, Mar. 1992.

[15] Y. Khandelwal, Karmeshu, "A new approximation for average symbol error probability over Log-normal channels," IEEE Wireless Commun.Lett., vol.3, pp. 58-61.2014.

Mar. Drugs **2015**, *13*, 6792-6817; doi:10.3390/md13116792

OPEN ACCESS

marine drugs

ISSN 1660-3397

www.mdpi.com/journal/marinedrugs

Review

Biomedical and Clinical Importance of Mussel-Inspired Polymers and Materials

Nagendra Kumar Kaushik [1,†,*], Neha Kaushik [1,†], Sunil Pardeshi [1], Jai Gopal Sharma [2], Seung Hyun Lee [3] and Eun Ha Choi [1,*]

[1] Plasma Bioscience Research Center, Kwangwoon University, Seoul 139701, Korea; E-Mails: neha.bioplasma@gmail.com (N.K.); sunil@datacops.org (S.P.)

[2] Department of Biotechnology, Delhi Technological University, Delhi 110042, India; E-Mail: sharmajaigopal@gmail.com

[3] Graduate School of Information Contents, Kwangwoon University, Seoul 139701, Korea; E-Mail: shlee@kw.ac.kr

† These authors contributed equally in this work.

* Authors to whom correspondence should be addressed; E-Mails: kaushik.nagendra@kw.ac.kr (N.K.K.); ehchoi@kw.ac.kr (E.H.C.); Tel.: +82-2-940-8618 (N.K.K.); +82-2-940-5661 (E.H.C.); Fax: +82-2-940-5664 (N.K.K.); +82-2-940-5664 (E.H.C.).

Academic Editor: Anake Kijjoa

Received: 5 October 2015 / Accepted: 3 November 2015 / Published: 11 November 2015

Abstract: The substance secreted by mussels, also known as nature's glue, is a type of liquid protein that hardens rapidly into a solid water-resistant adhesive material. While in seawater or saline conditions, mussels can adhere to all types of surfaces, sustaining its bonds via mussel adhesive proteins (MAPs), a group of proteins containing 3,4-dihydroxyphenylalanine (DOPA) and catecholic amino acid. Several aspects of this adhesion process have inspired the development of various types of synthetic materials for biomedical applications. Further, there is an urgent need to utilize biologically inspired strategies to develop new biocompatible materials for medical applications. Consequently, many researchers have recently reported bio-inspired techniques and materials that show results similar to or better than those shown by MAPs for a range of medical applications. However, the susceptibility to oxidation of 3,4-dihydroxyphenylalanine poses major challenges with regard to the practical translation of mussel adhesion. In this review, various

strategies are discussed to provide an option for DOPA/metal ion chelation and to compensate for the limitations imposed by facile 3,4-dihydroxyphenylalanine autoxidation. We discuss the anti-proliferative, anti-inflammatory, anti-microbial activity, and adhesive behaviors of mussel bio-products and mussel-inspired materials (MIMs) that make them attractive for synthetic adaptation. The development of biologically inspired adhesive interfaces, bioactive mussel products, MIMs, and arising areas of research leading to biomedical applications are considered in this review.

Keywords: mussels; mussel-inspired biomedical applications; medical adhesive; wound healing; anti-proliferative; anti-inflammatory; stem cell differentiation; surface coating; nano-constructs

1. Introduction

Mussel adhesion is a natural process which involves the secretion of a type of protein glue that hardens rapidly into a solid and turns into a water-resistant adhesive [1]. Many features of this process have inspired the development of synthetic materials for medical applications. The mussel secretes sticky glue that allows it to stick to rocks and solid surfaces. The important factor to its stickiness is a group of proteins called mussel adhesive proteins (MAPs) which contain the catecholic amino acid 3,4-dihydroxyphenylalanine (DOPA) (Figure 1A–C) [2]. "Mussels" are the edible marine bivalves of the family Mytilidae, most of which live on exposed shores in intertidal zones, attached by means of their strong byssal threads to a hard substrate. A byssus refers to a group of strong filaments secreted by mussels when they attach themselves to hard surfaces [2]. Byssal threads, used to attach mussels to substrates, are now known as advanced bonding agents. A number of studies have shown applications of mussel adhesive or glues for industrial and surgical applications [3,4]. Additionally, byssal threads have been investigated in studies about the creation of artificial tendons [5]. Mussel adhesion is mediated by a byssus and by byssal plaques consisting of a complex array of proteins (generally mussel foot proteins, Mfps). The adhesion of Mfps to various surfaces has been widely investigated. For a better understanding of the binding mechanisms of Mfps, researchers explored the force-distance profiles and adhesion energies of three different types of Mfps, termed Mfp-1, Mfp-3, and Mfp-5, on (i) hydrophobic methyl-terminated self-assembled monolayer (CH_3-SAM)—and (ii) hydrophilic alcohol-terminated self-assembled monolayer (OH-SAM) surfaces at various pH levels [6]. At an acidic pH, all of the Mfps samples adhered tightly to the CH_3-SAM surfaces via hydrophobic interactions but only weakly to the OH-SAM surfaces through H-bonding. DOPA (3,4-dihydroxyphenylalanine) residues in Mfps mediate the binding to both SAM surface types, but through different interactions. The typical bidentate H-bonding by DOPA is disturbed by the longer spacing of OH-SAMs; in contrast, on CH_3-SAMs with other nonpolar residues, it partitions to the hydrophobic surface. Asymmetry in the distribution of hydrophobic residues in proteins, the distortion of the bonding on H-bonding surfaces, and the manipulation of physisorbed binding lifetimes are important concepts in the design of adhesives and non-fouling surfaces.

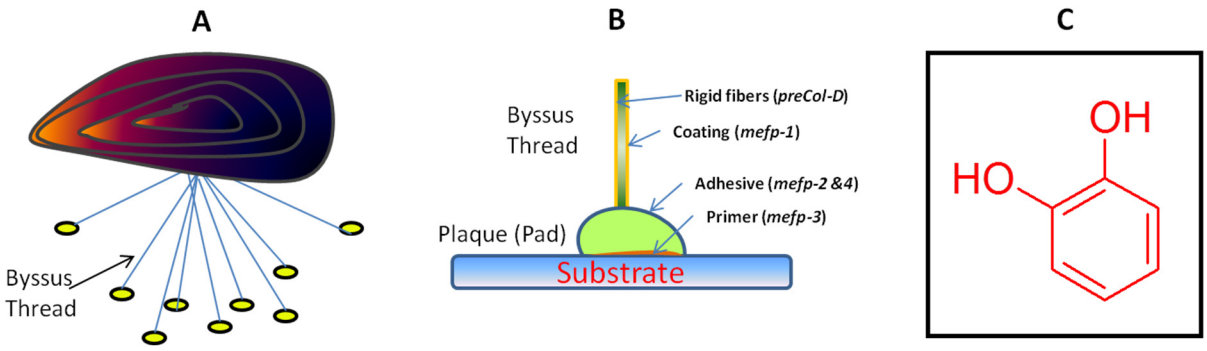


Figure 1. Properties of mussel adhesion: (**A**) biological adhesion; (**B**) bio-inspired adhesion on a substrate; and (**C**) the catechol chemical moiety involved in adhesion.

Researchers have investigated the applications of mussels-inspired materials (MIMs) for the construction of ultra-small magnetic nanoparticles with catechol-derivative anchor groups which possess an irreversible binding affinity to metal oxides and thus can optimally disperse super-paramagnetic nanoparticles under physiological conditions. This not only leads to ultra-stable metal-oxide nanoparticles but also allows close control over the hydrodynamic diameter and interfacial chemistry. The latter is a crucial breakthrough in the assembly of functionalized magnetic nanoparticles [7]. This review demonstrates how an advanced and highly multifunctional material can be engineered and developed using MIMs (mussel-inspired materials). Synthetic adhesives and materials inspired by mussels have been applied extensively, and it is expected that the characterization and adaptation of many other biological adhesive strategies will follow [8]. MIMs play important roles in cancer drug delivery and in the destruction and removal of cancer cells. Recently, a mussel-inspired polymer was designed to form pH-sensitive drug delivery vehicles that are stable in the bloodstream at physiological pH levels, but become activated in acidic tumor environments, thus releasing the drug (Figure 2). A new design involves a modification of the surface of gold nanorods (NRs) with a mussel-inspired polymer coating. The NRs target cancer cells when they are irradiated, thus producing highly localized heating that destroys the cancer cells (Figure 3) [9]. Recent study integrated the chemical structure of the MAP into the design of an injectable synthetic polymer. The novel injectable citrate-based mussel-inspired bioadhesive showed controlled degradability and improved biocompatibility at a low manufacturing cost, with many more advantages in relation to current products such as fibrin glue and cyanoacrylate adhesives, which can induce allergic reactions and toxicity [10]. Injectable citrate-based mussel-inspired bioadhesives are non-toxic and are thus unlikely to cause allergic reactions and side effects. Researchers have also attempted to make the adhesion strength even stronger with no inflammatory responses [10]. In the present review, we discuss the importance of mussel bio-products and MIMs with regard to surface coatings, adhesive properties, medicine, surgery, biomedical science and bio-nanotechnology.

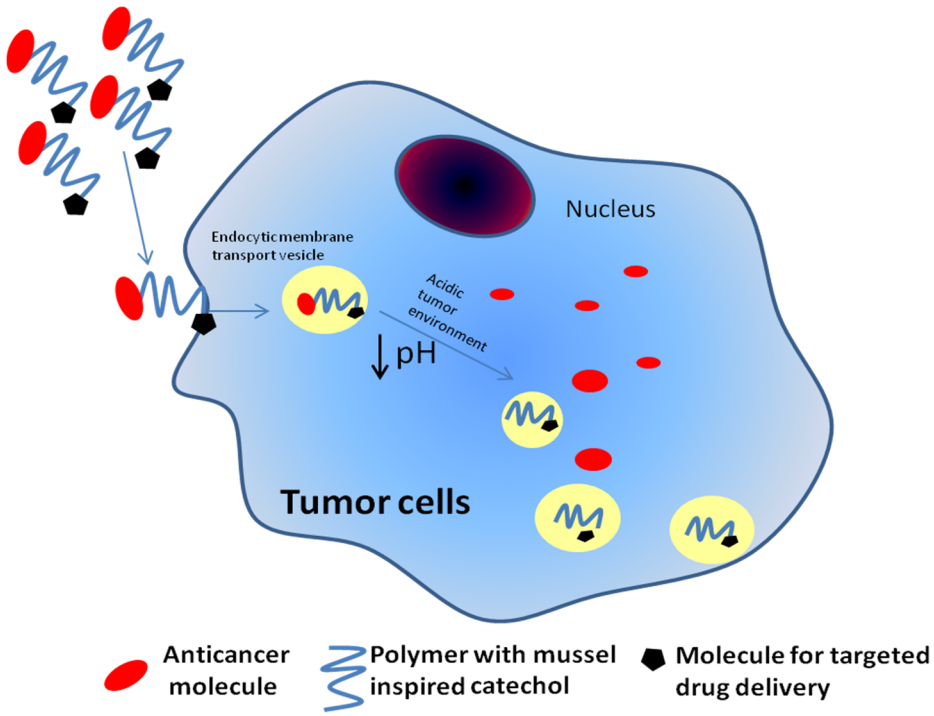


Figure 2. Polymers with a mussel-inspired catechol-anti-proliferative drug conjugate can be up-taken by tumor cells with the help of an endocytic cell membrane transport vesicle and can release drug molecules in the presence of the acidic environment of tumor cells.

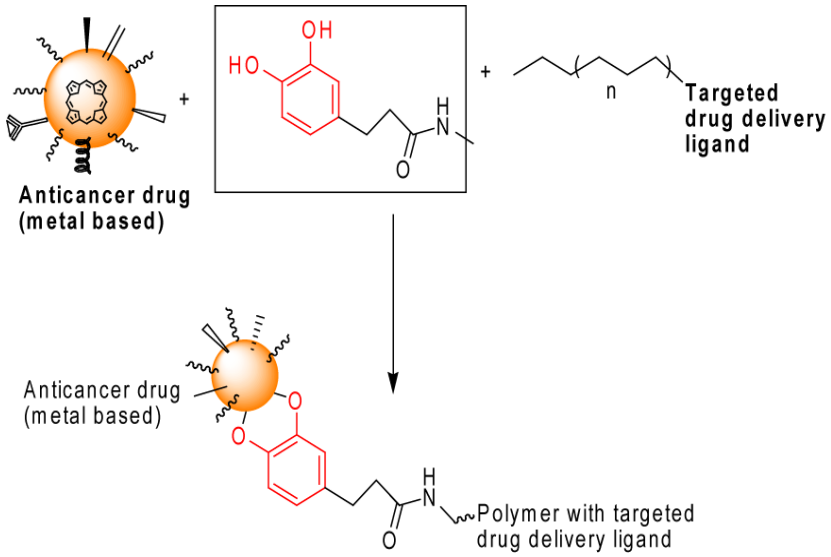


Figure 3. Mussel-inspired targeted drug delivery as an anticancer treatment.

2. Applications of Mussel-Inspired Materials

2.1. Surface Coatings and Adhesive Applications

In the past few years, MIMs have attracted substantial interest for various types of biomedical applications, showed successful applications ranging from coatings for interfacing with cells and tissue, to drug delivery and biosensing [11,12]. Mussel adhesion is mediated by the mfps, abundant in the catecholic amino acid DOPA; however, its trend toward facile auto-oxidation is a drawback which can

lead to unreliable adhesion. Yu *et al.* [13] revealed that mussels limit DOPA oxidation during the formation of adhesive plaque by imposing an acidic reducing system based on thiol-rich mfp, which restores DOPA by coupling the oxidation of thiols to the reduction of dopaquinone. It was also reported that the adhesive proteins secreted by mussels can be used to achieve surface reformation in a broad series of inorganic and organic materials, implying that multifunctional coatings can be fabricated for many applications [14].

Lee *et al.* [15] introduced a simple means of surface modification in which the self-polymerization of dopamine formed an adherent polydopamine (PD) coating on a variety of materials. Coating by PD can serve as a versatile stage for secondary surface-mediated reactions, ultimately leading to metal self-assembled monolayers and grafted polymer coatings. This two-step surface modification method is distinctive in terms of its ease of application, its use of simple ingredients and reaction conditions, its applicability to many types of materials of complex shapes, and its capacity for multiple end uses, especially for antimicrobial and cell adhesive substrates (Figure 4) [15]. It has been shown that DOPA nested in hydrophobic aromatic sequences not only enhances adhesion at a neutral pH (pI or IEP) but also contributes significantly to the cohesive interactions between adhesive proteins [16]. The hydrophobic amino acid residues in the Mfp3 *slow* sequence provide DOPA with a microenvironment that retards oxidation by shielding the amino acids from the solvent, endowing the protein with the ability to maintain adhesion at a neutral to slightly basic pH. More importantly, hydrophobic interactions and inter-residue H-bonding combine to result in strong cohesion within Mfp3 *slow* layers over a relatively wide pH range [16]. This strategy provides an alternative to DOPA/metal ion chelation, and compensates in part for the limitations imposed by facile DOPA-autoxidation. By exploring the adhesive and cohesive mechanisms of bonding by the Mfp3 *slow* sequence, several studies have revealed that the wet adhesion of mussels is more complicated than a simple DOPA-mediated recipe, providing a rationale for engineering DOPA into a new generation of bio-inspired synthetic adhesive polymers. Waite *et al.* [17] reported that DOPA-containing proteins are important with regard to wet adhesion in mussels and possibly in other sessile organisms as well. Bonding depends on DOPA in both reduced and oxidized forms for adhesion and cohesion, respectively. DOPA is highly vulnerable to spontaneous oxidation, and controlling the DOPA redox is a crucial challenge when using it in adhesion applications. Mussels appear to achieve such control in their byssal attachment pad. Understanding the particulars of natural redox control may provide fundamentally important insights into adhesive polymer engineering and antifouling strategies.

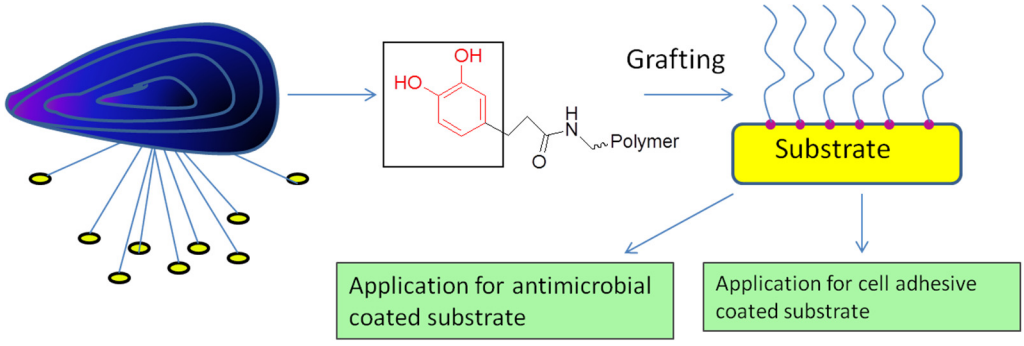


Figure 4. Application of mussel-inspired substrate-coated materials.

Researchers have investigated the composition and formation of byssal plaques and threads with the expectation of discovering technologically relevant innovations in chemistry and materials science. The DOPA residue appears to have double functionality with significant consequences for adsorption and cohesion. Nevertheless, it forms an array of weaker molecular interactions in the form of metal chelates, H-bonds, and pi-cations, which appear to dominate in terms of adsorption. On the other hand, DOPA and its redox couple, dopaquinone, can mediate the formation of covalent cross-links among byssal proteins (cohesion) [18]. Rodgers *et al.* [19] reported that protein-bound DOPA (PB-DOPA) could be formed in mammalian cells by both enzymatic pathways and radical reactions. PB-DOPA has reducing activity and the ability to cause damage to other essential biomolecules (Figure 5). The proposed reaction of PB-DOPA resulting in ring closure and the release of four electrons, was also described by Gieseg *et al.* [20]. This can be mediated through the replenishment of transition metals or from catechol-quinone-catechol redox reactions in the presence of cellular components such as ascorbate or cysteine, resulting in the amplification of radical damaging events. The formation of PB-DOPA confers on protein the capacity to chelate transition metals, generating protein "oxychelates" which may be the one factor among all factors that localize such damage. This investigation on PB-DOPA has mainly focused on detoxification and the proteolysis and excretion [17].

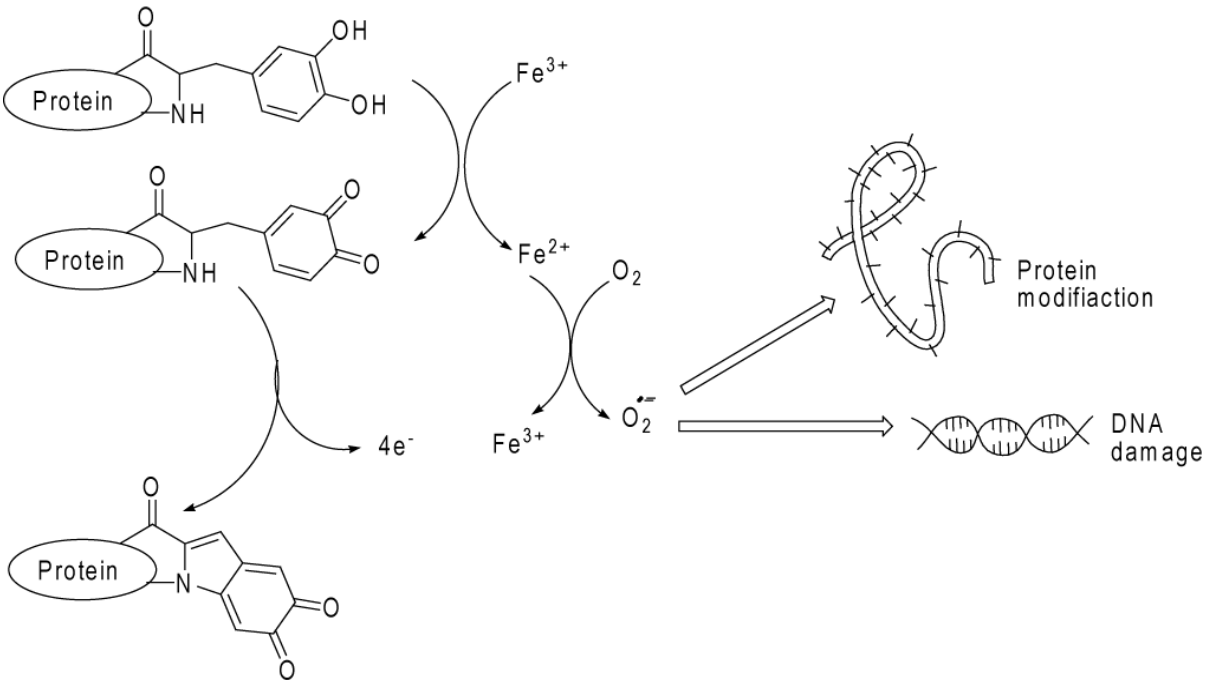


Figure 5. Reaction scheme presenting probable reactions of protein-bound 3,4-dihydroxy-phenylanine (DOPA). Protein-bound DOPA can be further oxidized to dopaquinone, donating two electrons to the higher valency-transition metal ions such as iron or copper present in chelates or metalloproteins. Auto-oxidation of the reduced transition metal can generate radicals such as reactive oxygen species, which can cause oxidative damage to other biomolecules. The proposed reaction of protein-bound (PB)-dopaquinone, resulting in ring closure and the release of four electrons, is described by Rodgers. Adapted the permission from [19]. Copyright © The American Chemical Society, 2000.

Mussel-inspired adhesive hydrogels represent novel candidates for medical sealants or glues. Brubaker and Messersmith [21] described an enzyme-degradable mussel-inspired adhesive hydrogel formulation which was achieved by incorporating the minimal-elastase substrate-peptide Ala-Ala into a branched polyethyleneglycol (PEG) structure. This system takes advantage of the neutrophil elastase expression up-regulation and secretion from neutrophils upon recruitment on wounded tissue. The degradation of the adhesive hydrogel was not observed during short-term trials involving *in vitro* treatments with elastase, though *in vivo* degradation proceeded over several months following implantation in mice. The work of Brubaker and Messersmith [21] represents the first model of an enzymatically degradable mussel-inspired adhesive and expands the potential biomedical applications of these materials. Barrett *et al.* [22] demonstrated a novel bio-inspired approach for designing extremely tough hydrogels. By regulating the pH of the reaction between catechol-terminated branched PEG and Fe^{3+}, a covalently cross-linked network was prepared by the Messersmith research group with a series of coordination bonds which undertake reversible interactions to dissipate energy during the deformation process (Figure 6) [22]. Their findings show the richness of the cross-linking chemical and physical properties accessible in synthetic mussel-inspired biomaterials, which were achieved through the simple manipulation of the pH, composition, and processing method. Cautious administration of these variables provides access to a wide variety of physical properties, reflecting the stability of covalent and coordination cross-linking in the gel network. These biologically inspired hydrogels, with a viscoelastic response and water content reminiscent of hydrated natural soft tissues, represent a new set of biomaterials [22]. Previously developed synthetic polymer hydrogel tissue adhesives and sealants swell greatly under physiologic conditions, which can result in mechanical weakening and adverse medical complications. A recent report described the synthesis and characterization of mechanically hard zero- or negative-swelling mussel-inspired surgical adhesives based on catechol-modified amphiphilic poly(propylene oxide)-poly(ethylene oxide) (PPO-PEO) block copolymers [23]. Catechol oxidation at or less than room temperature resulted in a chemically cross-linked network, with subsequent warming to physiological temperatures inducing a thermal hydrophobic transition in the PPO domains and providing a mechanism for mechanical toughening. This designed approach can be easily adapted for other heat-sensitive copolymers and cross-linking strategies, representing a typical approach that can be used to manage swelling and improve the mechanical properties of hydrogels for new medical applications. Transient network hydrogels, cross-linked through histidine-divalent cation coordination bonds, were studied by Fullenkamp *et al.*, using histidine-modified star PEG polymers [24]. These biomaterials were inspired by the mussel, which utilizes histidine-metal coordination bonds to impart self-healing properties in its byssal threads. Fullenkamp *et al.* calculated pH-dependent speciation curves using equilibrium constants determined by potentiometric titration, providing insight into the pH-dependence of the histidine-metal ion coordination. It was also demonstrated that the new mussel-inspired catecholamine polymer can be used for DNA immobilization via a simple surface modification. One-step immersion of the substrate (noble metals, oxides, and polymer) in a polymer solution forms a substrate that allows the immobilization of DNA strands [25]. This method will be useful for developing DNA microarrays in various types of substrate materials with a simple preparation process. This strategy can be used for the immobilization of various types of other biomolecules, such as probes for cDNA, peptides, aptamers, or direct polymerase chain reaction (PCR) products. This method can also be used in various biomedical assays. Recently, the immobilization of trypsin on a silica and titanium support

was achieved via a mussel-inspired adhesion strategy [26]. The method involves the fabrication of titanium substrates with catechol-containing biomimetic PD followed by the fabrication of trypsin on a PD layer. The immobilized enzyme maintains its catalytic activity after being coated onto PD in a wide variety of monolithic substrates.

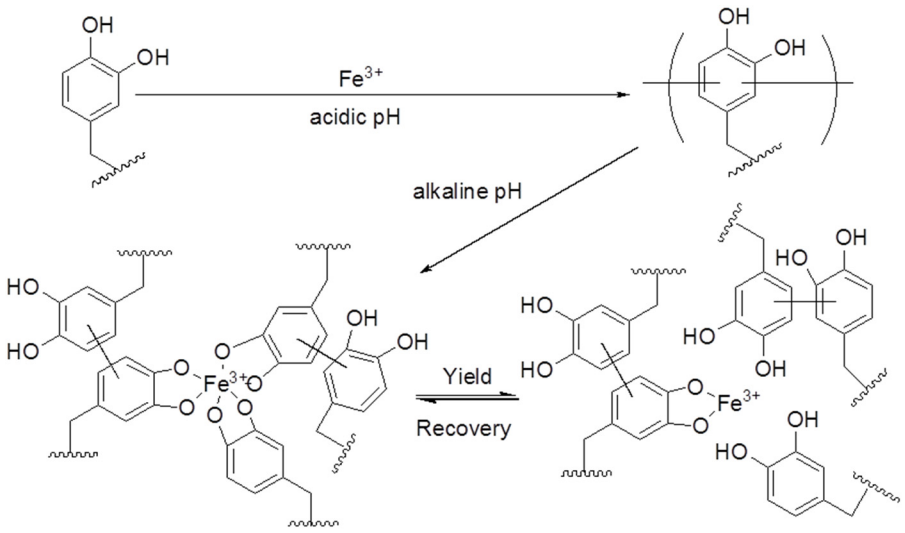


Figure 6. Proposed pH dependence of covalent and coordination-bond formation in catechol-polymer hydrogels containing Fe^{3+}. The reaction of the catechol-terminated branched PEG with Fe^{3+} at an acidic pH results in covalently cross-linked hydrogels. Subsequent equilibration of these gels at a pH of 5, 7, or 9 introduces varying number of Fe^{3+}-catechol coordination bonds that mechanically enhance the covalent network. Under the influence of a mechanical force, these coordination bonds reversibly rupture and re-form, acting as a mechanism for energy dissipation. Both oligomeric and monomeric (unreacted) catechols are believed to participate in the coordination network. Adapted with permission from [22]. Copyright © WILEY-VCH Verlag GmbH and Co. KGaA, Weinheim, 2013.

Recently, researchers verified the reactive encapsulation of individual yeast cells with PD, which is a biocompatible coating material inspired by the adhesive proteins of mussels [27]. This type of individual encapsulation with PD is importantly linked to the realization of artificial spores. The PD coating was found to be stable in comparison with polyelectrolyte multilayers, and effective in protecting living cells and controlling the cell division process. The PD encapsulation strategy is a good starting point for both research and for applications based on artificial spores. This strategy endows living cells with durability against harsh surroundings, provides controllability of cell cycles, and facilitates reactivity for the modification of cell-surfaces (Figure 7). The Messersmith group also introduced a two-step surface modification method in which the self-polymerization of dopamine produced an adherent PD coating on a wide range of inorganic and organic materials, including noble metals, oxides, polymers, semiconductors, and ceramics [15]. Secondary reactions can be used to create a variety of ad-layers, including self-assembled monolayers through the deposition of long-chain molecular building blocks, metal films by electroless metallization, and bioinert and bioactive surfaces via the grafting of macromolecules. In their work, Lee *et al.* [15] engineered PD surfaces for specific biomolecular

interactions by forming an ad-layer of glycosaminoglycan hyaluronic acid (HA). HA/receptor interactions are important in many physiological processes, including angiogenesis, hematopoietic stem-cell commitment and homing, and tumor metastasis. A technique based on MIMs could aid in a number of surgical procedures. Among them are eyelid transplants and the correction of a ruptured fetal membrane or amniotic sac during pregnancy [28].

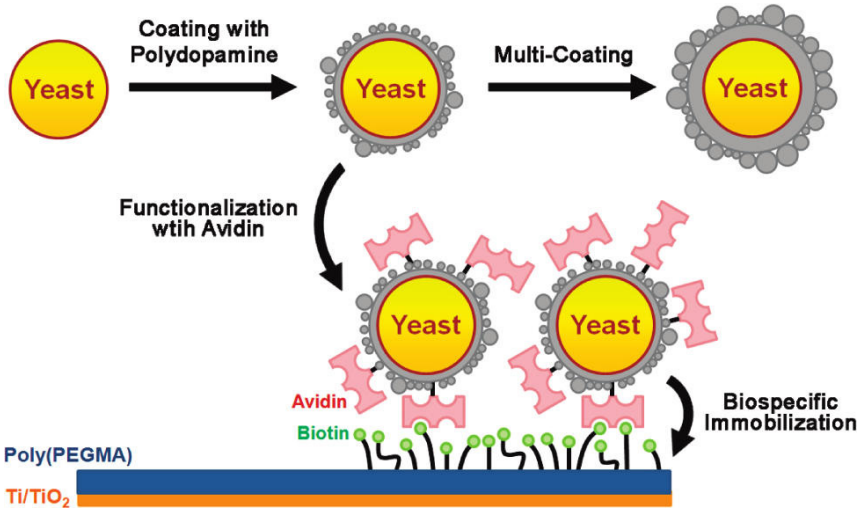


Figure 7. Schematic representation of the polydopamine encapsulation of individual yeast cells and the functionalization of artificial shells. Adapted with permission from [15]. Copyright © The American Chemical Society, 2011.

To create anti-coagulation and anti-hyperplasia cardiovascular devices, the polysaccharide heparin is used. An aqueous solution of DOPA and hexamethylenediamine (PDAM/HD) is used to make adhesive coatings rich in amine groups which are used for covalent heparin immobilization on stainless steel. This technique has been explored to fabricate stainless stents with heparin-retained bioactivity. Hep-PDAM/HD was also found to be a promising microenvironment for the selective enhancement of endothelial cell adhesion, proliferation, migration and the release of nitric oxide (NO), with other favorable properties as compared to control substances. These unique functions qualify the heparinized coating as an attractive alternative for the design of a new generation of stents using bio-inspired dopamine [29].

In another study [30], multifunctional mussel-inspired self-coated membranes with significant blood cell and other cell compatibilities are prepared by a green approach. Heparin-like polymer [HepLP, poly(sodium 4-vinylbenzenesulfonate)-*co*-poly(sodium methacrylate)] and heparin have been studied in relation to mussel-inspired heparin-mimicking coatings. DOPA is grafted onto HepLP or heparin to obtain DOPA-grafted HepLP (DOPA-*g*-HepLP) or DOPA grafted heparin (DOPA-*g*-Hep) using carbodiimide. A Polyethersulfone dialysis membrane is chosen as the substrate for the surface coating of the DOPA-*g*-HepLP and DOPA-*g*-Hep. The coated surface displays augmented hydrophilicity and electronegativity, decreased plasma protein adsorption, and suppressed platelet adhesion compared to a control. Heparin-coated membranes show anticoagulant bioactivities and superior performance in terms of endothelial cell proliferation and morphology differentiation. This kind of construct can have

multi-biomedical applications in hemodialysis, blood purification, organ implantation, and tissue cultures systems [30].

Antifouling surfaces have been studied extensively owing to their significance in medical devices and related industries. Recently, conformal DOPA-melanin (DM) antimicrobial films were formed on various substrates by the simple method of dip-coating in a DOPA solution at a high ionic strength [31]. DM (DOPA-melanin) coatings show high hydrophilicity and the ability to bind and release cations efficiently as compared to PD. These films inhibit the growth of bacteria and demonstrate high antimicrobial activity against *S. aureus* when coated onto polycarbonate materials. Another study also investigated an antifouling system that involves the immobilization of a mussel-inspired catecholamine polypeptoid on TiO_2 thinly coated onto a quartz surface [32]. This surface construct showed improved antifouling property as compared to other conventional antifouling surfaces such as mPEG/quartz surface. These newly developed antifouling surface constructs can be used in research areas such as single-molecule imaging, medical devices, and biosensors.

Achilles tendons (ATs) have a high rate of rupture as compared to other tendons in the human body. AT damage affects a patient's quality of life and requires a long time for recovery. A bioadhesive coating inspired by mussel adhesion was designed and is now in use as a surgical graft material to repair AT damage. The basic mechanism for adhesion is identical to that of mussel catechols, which oxidize to quinones and are cross-linked with other catechols within the adhesive film or with functional groups such as amine and thiol biological surfaces. Polyethylene glycol and polycaprolactone are used with adhesive catechol substances due to their biocompatibility and biodegradable characteristics. The adhesive polymer was solvent-cast onto two scaffolds to determine the practicability of using the adhesive-coated concept in tendon repair. This adhesive coating demonstrated adhesive strength levels that were significantly higher than other medical adhesive materials available on the market. Furthermore, *in vivo* and clinical studies of this type of adhesive construct-augment repair will show many fruitful results in the field of biomaterials for medical applications [33].

Based on mussel-inspired reversible catechol-metal ion chemistry, a hydrogel actuator that combines ionoprinting techniques was developed [34]. Ionoprinting is based on the electrochemical oxidation of iron electrode to deposit ions onto dopamine methacrylamide (DMA) containing hydrogels. The catechol group of DMA formed a tris-complex with the deposited iron metal ion with an increase in the pH and increased cross-linking density. The difference in the cross-linking density between the ionoprinted region and the hydrogel generated enough force for the hydrogel to actuate. Hydrogel films can be changed into different three-dimentional shapes depending on the ionoprinting pattern. The actuation can be customized according to the DMA amount, applied voltage, pH and water content in the hydrogel. The capacity to form a high-stress differential while using a low concentration of catechol offers many opportunities in the design of multifunctional materials due to the focus on other functional groups in the hydrogel. This novel approach will provide a new paradigm in developing novel hydrogel actuators and will be important for the 3D printing of biomaterials for medical purposes. An inexpensive one-pot route to self-healing hydrogels with pH-tunable moduli was also presented. Recently, an advanced responsive mussel-inspired inexpensive and pH-tunable hydrogel was synthesized by reacting tannic acid, trivalent metal ions and polyallylamine in one pot [35]. This synthesized hydrogel behaves as a supramolecule below pH 8 but shows covalent strong cross-linking and can be used for various biomedical applications.

The development of biomaterials to direct the fate of stem cells is essential for the stem-cell-based regeneration of bone tissue. Recently, functionalized electrospun fibers using a mussel-inspired surface coating to regulate the adhesion, growth and differentiation of human mesenchymal stem cells (hMSCs) were developed (Figure 8) [36]. Poly (L-lactide) (PLLA) fibers coated with polydopamine (PD-PLLA) were prepared and incubated in a dopamine solution for 1 h, resulting in the formation of PD with less of an effect on the roughness and hydrophobicity of the fibers. The prepared PD-PLLA fibers modulated the hMSC responses in many ways. Importantly, the adhesion and proliferation of hMSCs cultured on PD-PLLA were significantly enhanced relative to those cultured on PLLA alone. In addition, hMSCs cultured on PD-PLLA demonstrated the up-regulation of genes associated with osteogenic differentiation as well as angiogenesis. These outcomes indicate that the simple bio-inspired surface modification of organic fiber substrates using PD is a very promising means of regulating stem-cell functions, possibly allowing the realization of effective stem-cell delivery carriers for bone tissue engineering applications [36].

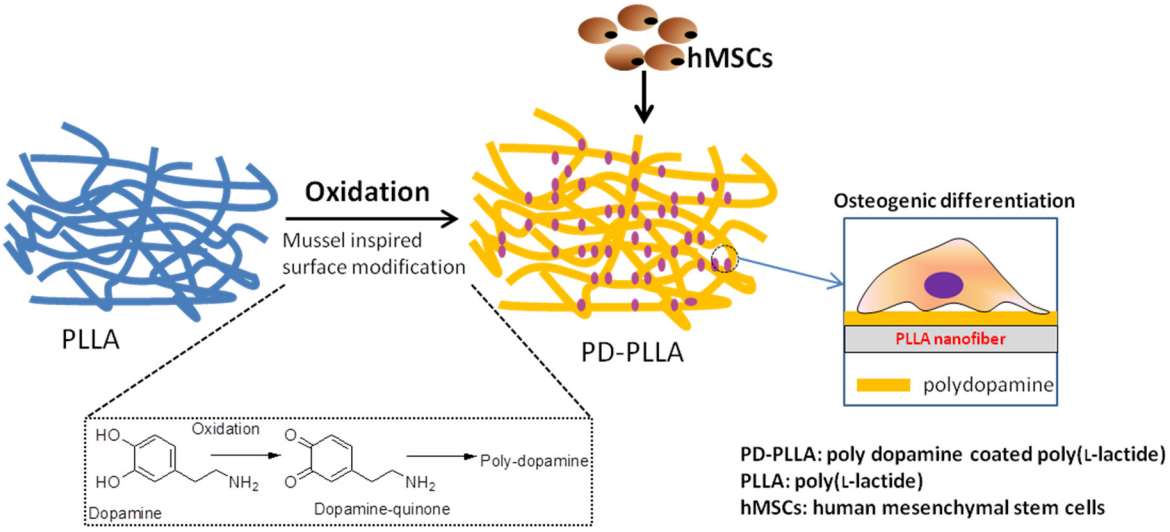


Figure 8. The effect of polydopamine coated Poly (L-lactide) (PLLA) fibers on the adhesion, proliferation and osteogenic differentiation of human mesenchymal stem cells (hMSCs). Adapted with permission from [36]. Copyright © Elsevier, 2012.

2.2. Application of Mussel-Inspired Materials in Medicine and Surgery

The marine microenvironment and the human body have many similarities. Understanding the physics and chemistry of marine bio-products will provide scientists with insight into the design of biomaterials for medical applications.

The conversion of tyrosine to DOPA is an important event in the processing of the adhesive protein in mussels as there are multiple roles played by DOPA at the interfaces in the adhesion process. For inorganic surfaces, unoxidized DOPA forms high-strength but reversible coordination bonds; however, on organic surfaces, it is able to adhere to surfaces via the formation of covalent bonds. This remarkable ability to adhere to both organic and inorganic surfaces is related in part to the equilibrium that exists between DOPA and dopaquinone at marine pH levels, allowing the species to interact with surfaces. It is also notable that the strong bonds between DOPA and organic and inorganic surfaces are formed in the presence of sea water, which is likely a fundamental feature of protein-based

glues which operate in wet oceanic environments. The use of DOPA and related catecholic molecules has recently been considered as part of a potential means of anchoring macromolecules onto oxide surfaces for medical applications [37]. Researchers found that adhesive proteins secreted by mussels serve as a stimulus behind the versatile approach to the surface modification of a wide range of inorganic and organic materials [14]. Recent work has also provided an overview of the recent developments in PD-based materials, including the synthesis of nanoparticles, capsules, and structural mechanisms as well as their physicochemical and biomedical properties [38]. Researchers have synthesized polymers containing DOPA in an effort to create water-resistant adhesives with self-healing and biocompatible properties [39].

Scientists at the Max Planck Institute for Polymer Research in Mainz, Germany, led by Aránzazu del Campo, synthesized an underwater adhesive that bonds strongly to various types of surfaces [39]. In contrast to previous mussel-inspired adhesives, this new glue is reversible, as it degrades and detaches when exposed to light. It is also biocompatible and can repair itself, fusing on its own when cut. This adhesive material can be used for closing wounds and in drug delivery patches, detachable scaffolds for tissue regeneration, and substrates for cell engineering. Campo *et al.* [39] create their waterproof glue with nitrodopamine, a natural molecule that is related to DOPA. They reported that the adhesive properties of nitrodopamine are more stable than those of DOPA (Figure 9). This allows the cross-linking and solidification of the adhesive in a manner similar to the process used by the mussels, but the adhesive degrades when it is exposed to light of a particular wavelength. This synthesized nitrodopamine are identical to the adhesives of mussels, but they can be detached on demand.

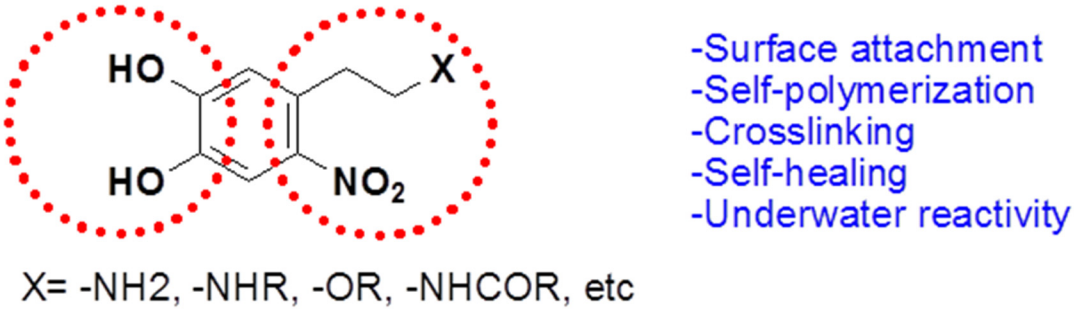


Figure 9. Structure of nitro-dopamine derivatives.

Recently, Bilic *et al.* [40] investigated injectable surgical sealants that are biocompatible with fetal membranes, with the potential to be utilized for the closure of iatrogenic membrane defects. They used dermabond®, Histoacryl®, and Tissucol fibrin glues along with three types of *in situ* formed PEG-based polymer hydrogels in a bonding and acute toxicity study upon direct contact with fetal membranes. They found that biological Tissucol fibrin glue has appealing properties for membrane sealing as compared to other glues. They also developed a new synthetic hydrogel formulation in the form of a mussel-mimetic sealant and the biologic Tissucol fibrin glue with good properties for membrane sealing. Extracts of all adhesives were shown to be non-toxic for cultured cells. Tissucol and one PEG-based hydrogel, which is a type of mussel-mimetic tissue glue, demonstrated efficient, non-disruptive, non-toxic bonding to fetal membranes. Their synthetic hydrogel-type tissue adhesive, which merits further evaluation *in vivo,* has emerged as a potential sealing modality for iatrogenic membrane defects. These results demonstrated

that mussels glue efficiently seals elastomeric membranes under wet or moist conditions with comparable viscoelastic properties [41]. *Ex vivo* studies also showed that proteolytic degradation does not affect mussels or mussel-inspired glues [42]. These materials display good stability in proteolytic environments, which makes them a favorable sealing material for future applications.

Yang *et al.* [10] recently developed injectable citrate-based mussel-inspired bioadhesives in the form of a biodegradable strong wet-tissue adhesive that can effectively close a bleeding wound, thus stopping the bleeding and helping with tissue regeneration without the aid of surgical tools. The injectable citrate-based mussel-inspired bioadhesives can be used for topical and non-topical applications across all disciplines of surgical practice, ranging from a suture/staple replacement; tissue grafts to treat hernias, ulcers, and burns; hemostatic wound dressings for laparoscopic partial nephrectomy; waterproof sealants for vascular anastomoses; and for the treatment of gastrointestinal fistulas, leaks, mucosal oozing or bleeding, and perforations (Figure 10) [10]. Inspired by a mussels byssus secretion through a pH jump, Holten-Andersen *et al.* [43] developed a simple method to control catechol-Fe^{3+} interpolymer cross-linking via changing the pH. The Raman resonance signature of catechol-Fe^{3+} cross-linked polymer gels at high pH levels is similar to that of natural adhesives secreted by mussels. These gels display elastic moduli (G′) that approach those of covalently cross-linked gels as well as self-healing properties [43]. There is an urgent need for medical adhesives that function reliably on wet tissue surfaces with minimal inflammatory responses. To address these performance characteristics, Brubaker *et al.* [44] generated a synthetic adhesive material inspired by mussels. The *in vivo* performance of the material was assessed in a mouse extra-hepatic syngeneic islet transplantation model. They designed the adhesive polymer with a branched PEG core whose end groups were derivatized with catechol, a functional group inspired by mussels adhesive proteins. In an oxidizing environment, the adhesive forms within a minute from catechol-derivatized PEG (cPEG) solutions. The cPEG adhesive elicited minimal inflammatory responses in mice and maintained a bond with supporting tissue for up to one year upon implantation. The synthesized cPEG adhesive was shown to immobilize transplanted islets at epididymal fat pads and external liver surfaces efficiently, permitting normoglycemic recovery and graft revascularization. The findings by Messersmith *et al.* [44] established the use of mussel-inspired adhesives for islet transplantation. Nelson *et al.* [45] developed protein hydroperoxides and protein-bound 3,4-dihydroxyphenylalinine as the key redox-active products during free radical attacks on proteins. Protein-bound 3,4-dihydroxyphenylalinine forms a redox cycle between the catechol and quinone forms and binds transition metals, while hydroperoxides are converted to stable hydroxides. The free amino acid 3,4-dihydroxy phenylalinine, an oxidation product of tyrosine, is a normal metabolite which is involved in the pathways of dopamine and melanin production. On the other hand, the physiological levels of protein-bound 3,4-dihydroxy-phenylalinine are very low, though remarkably elevated levels occur in some pathologic conditions. Unlike free 3,4-dihydroxyphenylalinine, protein-bound 3,4-dihydroxyphenylalinine has been proposed as a signal for the activation of cellular defenses against both oxidative fluxes during oxidative stress and oxidative damage, which occasionally develop. For distinctly free 3,4-dihydroxyphenylalinine, the levels of protein-bound 3,4-dihydroxyphenylalinine can change by five to ten times during oxidative damage *in vivo*, which can serve as an appropriate property for signaling molecules. Several mechanisms by which protein-bound 3,4-dihydroxyphenylalinine may trigger oxidative defenses via NF-κB and other transcription factors have been suggested (Figure 11).

Many effects of 3,4-dihydroxyphenylalinine in these situations may be mediated by the production and actions of protein-bound 3,4-dihydroxyphenylalinine [45].

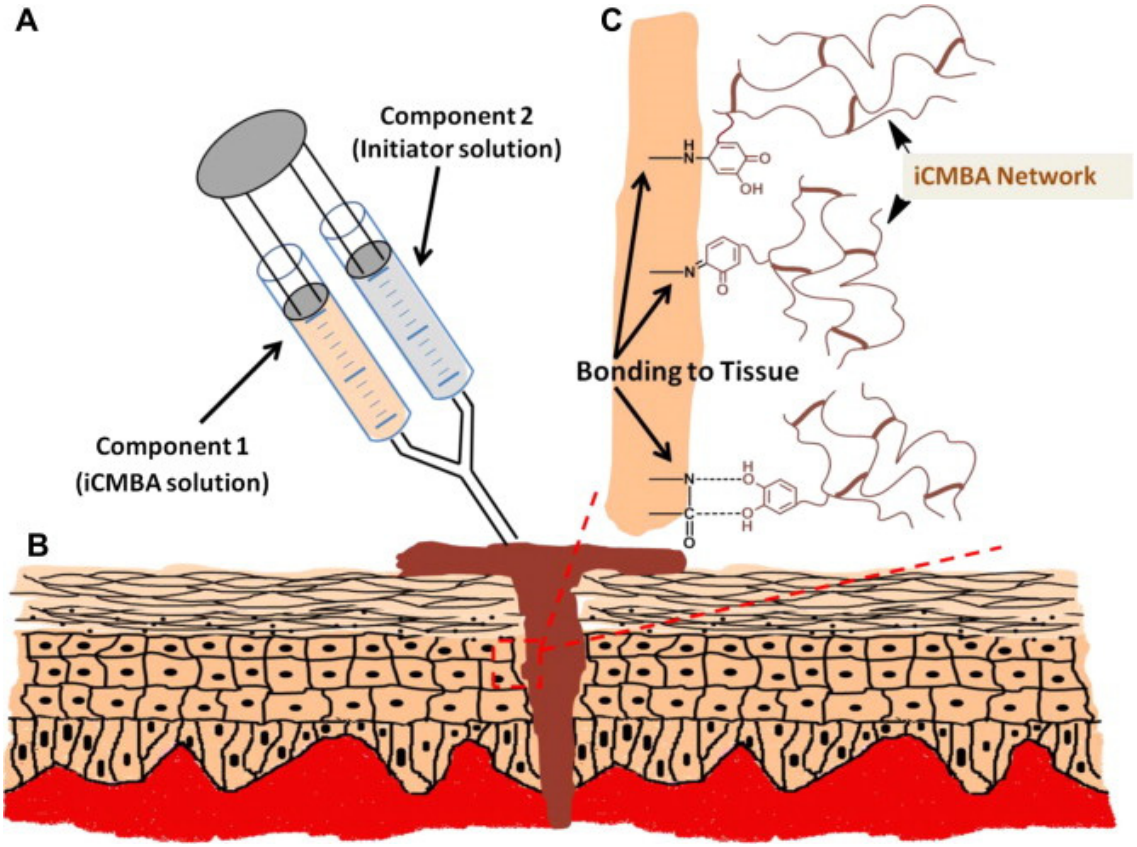


Figure 10. Representation of the injectable citrate-based mussel-inspired bioadhesives (iCMBA) application for wound closure: (**A**) Preparation and application of a two-component adhesive consisting of iCMBA and oxidizing (sodium periodate) solutions; (**B**) Schematic representation of iCMBA utilized for sutureless wound closure; (**C**) Proposed mechanisms of iCMBA adhesion to tissues. Reprinted with permission from [10], Copyright © Elsevier, 2012.

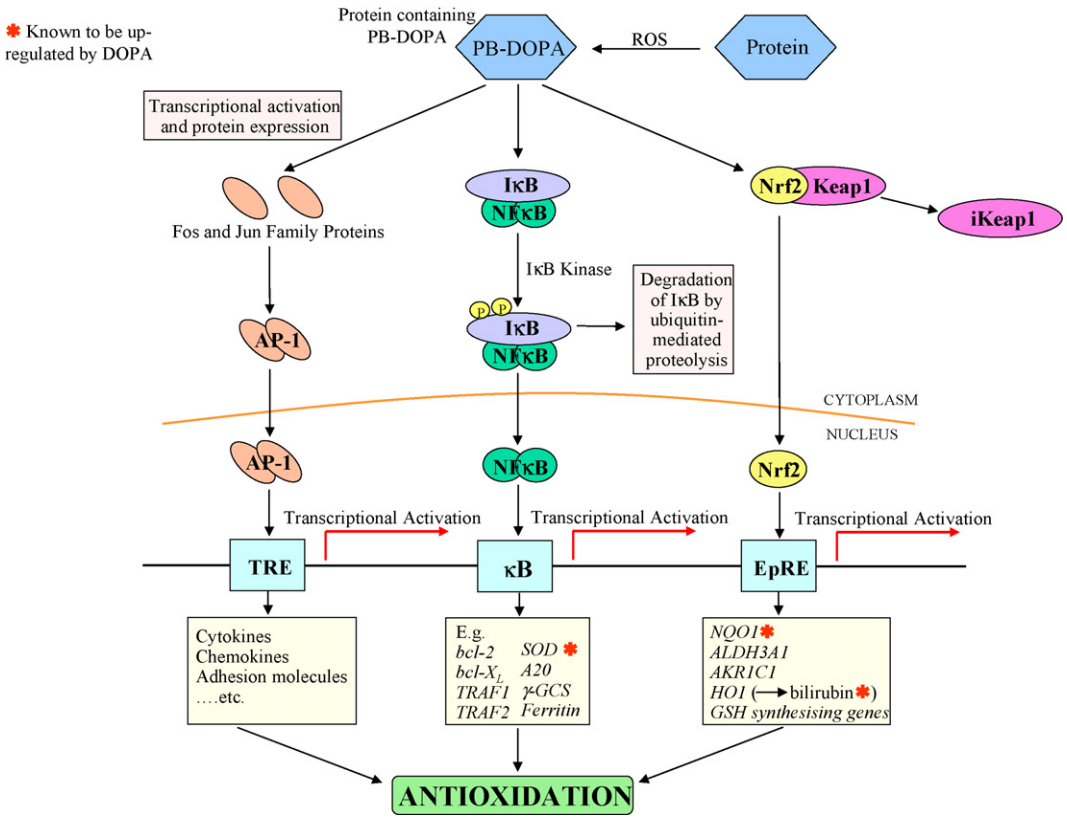
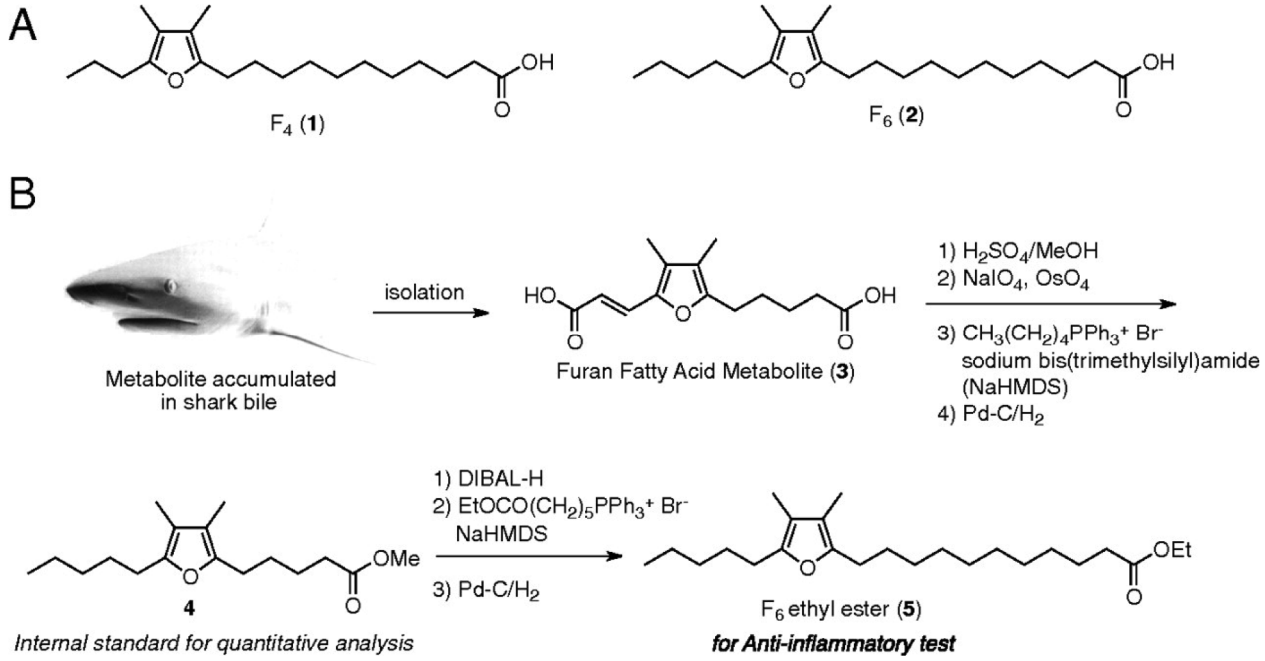


Figure 11. Scheme illustrating the hypothetical induction of antioxidant defenses by PB-DOPA. Reproduced with permission from [45]. Copyright © Elsevier, 2007.

Wakimoto *et al.* [46] demonstrated that furan fatty acids (F-acids) are a minor component of the fatty acids in the lipid extract of the New Zealand green-lipped mussels and partially synthesize furan-6 fatty acid and display more potent anti-inflammatory activities than eicosapentaenoic acid (EPA) (Figure 12). Their study sheds light on F-acids as potential anti-inflammatory agents and paves the way for more thorough examinations of the anti-inflammatory efficacy of the New Zealand green-lipped mussels. They noted that the New Zealand green-lipped mussels may be a preferred food for the efficient intake of F-acids and posited that they can be consumed raw or as stabilized oil extract. Li *et al.* [47] also reported that hard-shelled mussels lipid extract (HMLE) at a dose of 100 mg/kg of body weight possesses similarly strong anti-inflammatory activity compared to New Zealand green-lipped mussels lipid extract (GMLE), diminishing hind paw swelling and arthritis indexes and improving body weight gain in both adjuvant-induced (AIA) and collagen-induced arthritis (CIA) in rats. This strong efficacy may be associated with the down-regulation of inflammatory mediators (LTB4, PGE2, TXB2), pro-inflammatory cytokine (IL-1β, IL-6, IFN-γ, TNF-α) production, MMP (MMP1, MMP13) mRNA expression, and the up-regulation of anti-inflammatory cytokine (IL-4, IL-10) production and TIMP1 mRNA expression in the serum and joint tissues of arthritic rats. They also found no hepatotoxicity in AIA rats that received HMLE and GMLE [47]. Beaulieu *et al.* [48] reported anti-proliferative activities in blue mussels (*Mytilus edulis*) by-products. They tested fractions on four cancerous cell lines: A549 lung adenocarcinoma, BT549 breast tumor, HCT15 human colon tumor and PC3 prostrate cancer. The 50 kDa fraction, enriched in peptides, presented anti-proliferative activity in all cell lines. They claimed that hydrolysates formed due to fractionation from *Mytilus edulis* after enzymatic hydrolysis. At a protein

concentration of 44 µg/mL, the 50 kDa fraction induced mortality rates of 90% for PC3, 89% for A549, 85% for HCT15 and of 81% for the BT549 cell lines. The 50 kDa fraction consists of 56% of proteins, 3% of lipids and 6% of minerals on a dry weight basis and the lowest levels detected of taurine and methionine and the highest levels of threonine, proline and glycine amino acids. Their study suggests that *Mytilus edulis* by-products should be viewed as high-value products with strong potential as anti-proliferative agents.



C

Molecule	Dose (mg/kg)	Anti-inflammatory effect (suppression of paw swelling)
EPA ethyl ester	10	**No significant effect**
F_6 ethyl ester	10	**74% suppression of swelling (*P*=0.015)**

Figure 12. (**A**) Structures of typical F-acids detected in the green-lipped mussels; (**B**) Partial synthesis of furan fatty acid F6, and (**C**) Inhibition of adjuvant-induced arthritis in Wistar rats. The ordinate is the increase in the volume of the rear left paw between the beginning (day 10) and the end of the dosing (day 15) as described by Wakimoto *et al.* [46]. Reprinted with permission from [46]. Copyright © PNAS, 2011.

Polymeric materials that basically heal at damage sites under wet conditions are urgently needed for biomedical applications. Recent research has demonstrated self-repairing in the metal-free water of synthetic polyacrylate and polymethacrylate materials that are surface-modified with mussel-inspired catechols [49]. This construct initiated by H-bonding between catechol functional groups supports other deep physical non-covalent interactions contributed by subsurface moieties. These self-mending

properties of materials can be applied in the medical field in the design of more durable implants in the future.

A mussel-inspired surface functionalization to immobilize bioactive peptides for the enhanced endothelialization of decellularized vein matrixes (DVMs) was developed by Lee *et al.* [50]. These authors were able to transform DVMs with extracellular matrix-derived cell-adhesion peptides by mean of PD coatings. PD-mediated peptide immobilization enhanced the adhesion, metabolic activity, and endothelial differentiation of human endothelial progenitor cells. Their strategy for facilitating enhanced endothelialization would be useful for improving the function of small-diameter tissue-engineered blood vessels which can be used in cases of thrombosis, intimal hyperplasia, and calcification. Decellularized matrices engineered with PD-peptide modifications will be a great invention after further evaluations through long-term cultures of endothelial progenitor cells and by *in vivo* trials. Moreover, Qin and Buehler [3] reported that mussels could help to create artificial tendons. Through a combination of experimentation and a simulation, they demonstrated that the heterogeneous material distribution in byssus threads plays an important role in decreasing the effect of impact loading. They found that a combination of stiff and soft materials at a ratio of 80:20 enables mussels to dissipate impact energy rapidly and effectively. Notably, this facilitates significantly enhanced power under dynamical loading that exceeds 900% of the strength under static loading.

2.3. Application of Mussel-Inspired Materials in Biomedical Nanotechnology

The biological activity of nanoparticles is strongly dependent on the surface properties of the substrate. The present part illustrates the use of mussel-inspired proteins in the fabrication of functionalized bio-inspired nanomaterials leading to the possible realization of important biomedical applications.

Amstad *et al.* [7] developed catechol-derivative anchor groups which possess irreversible binding affinity to iron oxide and can thus optimally disperse super-paramagnetic nanoparticles in a physiologic environment this strategy can provide ultra-stable iron oxide nanoparticles, especially under medically relevant conditions of elevated temperatures and ionic strength levels. It can also control the hydrodynamic diameter and interfacial chemistry. Their work was an important breakthrough in the assembly of functionalized magnetic nanoparticles, e.g., as targeted magnetic resonance-contrast agents. This ideal nanoscale drug delivery vehicle allows control over space-time-released doses. This is achieved by stealth liposomes consisting of self-assembled super-paramagnetic iron-oxide nanoparticles which are individually stabilized with palmityl-nitro DOPA incorporated into the lipid membrane [51]. Alternating magnetic fields were used to control the timing and dose of repeatedly released loads from such vesicles by local heating of the membrane, which changed its permeability without major effects on the environment. Recently, researchers deposited mussel-inspired PD onto gold nanorods, after which antibodies were able to bind to PD-coated nanorods. Anti-epidermal growth factor receptor (EGFR)-PD were stable in media and were specifically bound to EGFR-overexpressing cells. Illumination of the cells targeted with anti-EGFR-PD nanorods enhanced cell death compared to non-irradiated controls and cells treated with antibody-free nanorods. PD facilitated the surface functionalization of gold nanorods with biomolecules, allowing cell targeting and the photo-thermal killing of cancer cells. PD can potentially coat a large variety of nanostructures with targeting ligands as a strategy for the bio-marine environment [52]. Researchers utilized silver nitrate to oxidize the polymer catechol, leading to covalent

cross-linking and hydrogel formation with an immediate reduction and release of Ag (I) [52]. The hydrogels were found to inhibit microbial growth, consistent with the well-known antibacterial properties of silver, while having less toxic effects on mammalian cell viability. One report explains a novel procedure which can be used to immobilize magnetic particles onto whole the *Gluconobacter oxydans* via a synthetic adhesive biomimetic material inspired by the protein adhesive of mussels [53]. Their approach involves the simple coating of a cell-adherent PD film onto magnetic nanoparticles followed by the conjugation of PD-coated nanoparticles to *G. oxydans* and resulting in cell aggregation. Importantly, the *G. oxydan* aggregates showed high specific activity and good reusability. This facile approach offers potential advantages of a low cost, easy cell separation, low diffusion resistance, and high efficiency. Moreover, this approach is a convenient platform technique for the magnetization of cells *in situ* via direct mixing of nanoparticles with a cell suspension. Another study demonstrated that air-plasma-treated electrospun PCL and PLA nanofibers can be used as carriers for the loading and release of charged molecules in a pH-responsive manner [54]. It also demonstrated that a mussel-inspired protein PD coating could finely tailor the pH-responsive loading kinetics and release of charged molecules. These new formulations may have prospective applications in drug delivery to specific targets that are related to variations in the pH level [54].

Recently gold@silver core-shell NRs were prepared using a novel biomimetic method, including deposition of a thin organic PD primer onto gold NRs surfaces, followed by spontaneous electroless silver metallization and the conjugation of antibacterial antibodies and passivating polymers for targeting to Gram-negative and Gram-positive bacteria. These nanorods showed high cytotoxicity on *S. epidermidis* and *E. coli* cells upon exposure to light due to the combined antibacterial effects of plasmonic heating and the release of silver [55]. In another study inspired by biomimetic PD, researchers used PD as a coating of photoluminescent graphene quantum dots (GQDs) through a simple exfoliation and oxidation process to increase the level of stability and efficiency [56]. The PD-coated GQDs show better photoluminescent stability levels than non-coated GQDs, high stability for long time, and can be used as a single-cell imaging agent and for drug and gene delivery [56]. PD-functionalized graphene oxide (GO) also showed increased compatibility compared to unmodified GO on blood cells [57]. GO can be used for many biomedical applications, such as drug delivery, imaging, and photothermal therapy. However, hemolysis in blood cells occurs due to GO amphiphilicity and surfactant-like behavior. In the case of PD, modified GO interacts with the membrane lipid bilayer of blood cells and significantly suppresses toxicity, which also makes it possible to use modified GO for various important biomedical applications. PD-coated carbon materials also show increased compatibility with human cells. The increased compatibility is related to the increased water solubility of carbon nanomaterials, which provides a more suitable environment for cell growth than uncoated carbon materials [58,59].

Recently, chemically cross-linked fracture-resistant nanocomposite hydrogels were prepared using dopamine methacrylamide consisting of a biomimetic side chain, inorganic nano-silicates, and Laponite [60]. The prepared nanocomposite hydrogels showed improved stiffness as well as exceptional energy dissipation capabilities. Nanocomposite hydrogels showed full compressive stress, elastic modulus, toughness, and storage and loss moduli values that were higher than control gels. The catechol side chain of dopamine methacrylamide possibly formed strong physical bonds with Laponite, which can dissipate the fracture energy while minimizing permanent damage to the network architecture and can be used for various biomedical and medical applications.

A human gelatin nano-coating was developed by conjugating dopamine with carbodiimide, the surface modifier, to form bio-adhesive surfaces [61]. Human umbilical endothelial cells were used to check cell attachment and growth on the modified surfaces. The binding strength is significantly enhanced by the recombinant gelatin through the conjugation with dopamine onto a titanium surface. Human umbilical endothelial cell attachment is also enhanced on dopamine conjugated gelatin nano-constructs. This dopamine-conjugated gelatin nanocoated surface is useful for many biomedical purposes, such as a human cell culture system and tissue engineering applications related to the capture and sequestering of growth factors to support cell proliferation.

Enhanced cell adhesion and migration were shown by newly construct monomeric catechols on the surfaces of polymeric nanofibers. The nanofiber (NF) of poly(ε-caprolactone)-polyethylene glycol-amine, fabricated with dihydroxyphenyl propionic acid, displayed catechol moieties on the surface [62]. Catechol on the NFs showed high cell viability, enhanced cell adhesion and good migration as compared to control NFs. These newly developed catecholized NFs can be used in tissue engineering scaffolds with enhanced cell adhesion and migration properties by adding a small amount of catechol. In another study, poly (ε-caprolactone) NFs fabricated with mussel-inspired DM were used for the neuronal differentiation of hMSCs [63]. A mussel-inspired DM coating used for the adsorption of RE-1 silencing transcription factor (REST) onto the scaffold. The mussel-inspired scaffold-mediated sustained release of siRNA promoted the differentiation of stem cells by targeting REST. This construct showed high loading efficiency and reduced burst release of siRNA. DM modification and fiber alignment further enhanced the siRNA loading, release kinetics and REST knockdown efficiency. These newly fabricated scaffolds have many potential applications, such as enhancing MSC neuronal differentiation in non-specific environments. Recently, recombinant mussel adhesive protein (rfp-1), Fe(III)-DOPA complexes and polycaprolactone were used to fabricate mussel-inspired electrospun NFs for applications related to tissue engineering scaffolds [64]. These fabricated NFs are based on recombinant mussel-associated protein rfp-1 and its Fe(III)-DOPA complexation chemistry and their mechanical properties can be modulated by varying the pH.

A three-dimensional (3D), ultralight, mussel-inspired dopamine-fabricated nitrogen-doped graphene aerogel was also developed [65]. Dopamine was self-polymerized on graphene surfaces and embeds nitrogen atoms on pyrolysis. The aerosol showed outstanding electrochemical activity towards the oxidation of biomolecules such as ascorbic acid, dopamine, and uric acid, playing important roles in the physiological functioning of organisms in neutral media based on the 3D open-pore structure and nitrogen doping. The fabricated nitrogen doped graphene aerogel is mechanically stable and fire-resistant and can be used for biomedical applications in the future.

Gold nanorods, fabricated with biomimetic PD, have been recently used for exposing antibodies to target tumor cells as a photothermal therapy [66]. PD was polymerized onto nanorods, and epidermal growth factor receptor antibodies (anti-EGFR) were immobilized on the construct. The anti-EGFR-PD-nanorods specifically and efficiently bind to EGFR-overexpressing cancer cells and show significant anticancer effects compared to negative and positive controls. Dopamine-fabricated magnetic iron oxide nanoparticles are also used recently for the immobilization of lipase proteins [67]. This conjugated magnetic nanoparticle showed a high enzyme loading capacity and strong adhesive interaction between lipase and PD. Enzyme maintained its enhanced stability and activity as compared to control free lipases under various conditions. This new, efficient, facile and economical

strategy for immobilization of enzymes demonstrate high rate of reusability and recovery. Single-nanoparticle@metal-organic framework (MOF) core-shell nanohybrids were constructed using strategy based on mussel-inspired PD [68]. Specifically, nanohybrids with gold nanoparticles sandwiched between the magnetic core and MOF shell through localized reduction by mussel-inspired PD demonstrating flexible, rational functionality integration can be used in the field of nanomedicine. These core-shell nanohybrids also have molecular sieving properties and can be used for controlled drug release, sensing and catalytic applications.

Fe_3O_4@polydopamine nanoparticles are also used in a pH-sensitive manner for the controlled drug release of anticancer drugs (e.g., bortezomib) via reversible bonding between the catechol and boronic acid groups of PD and anticancer drugs [69]. The sustained release of the anticancer drug at a greater concentration was achieved at a lower pH. These core-shell Fe_3O_4 PD nanoparticles can serve as a platform for responsive drug delivery, a recyclable catalyst support and an adsorbent. These constructs of PD onto magnetic nanoparticles have unique features which allow them to act as a versatile platform for multiple biomedical applications. For drug delivery, polymer capsules are also considered to be desirable transport vehicles. A monodisperse PD capsule is prepared by the one-step interfacial polymerization of dopamine on dimethyldiethoxysilane emulsion droplets [70]. The size of the cargo-loaded PD capsule is in the range of 400 nm to 2.4 μm, and it can be tailored by changing the emulsion concentration used with the template or the emulsion condensation time. Stabilized magnetic (Fe_3O_4) nanoparticles, fluorescent quantum dots, and anti-cancer hydrophobic drugs can be preloaded in the emulsion droplets, and these advanced functional materials remain encapsulated in the capsules. This strategy provides a new avenue for PD polymer capsule preparation and encapsulation, and can be used in many biomedical applications. Recently for developing highly efficient nanoconjugates, Fe_2O_3 nanoparticles are functionalized also using an approach involving mussel-inspired dopamine with human serum albumin for the labeling of various types of cell lines, including stem cells [71]. These prepared nano-constructs are nontoxic and can be used for the efficient *in vivo* magnetic resonance imaging with xenograft and focal cerebral ischemia models.

3. Conclusions

DOPA-containing proteins are crucial for wet adhesion in mussels in a microenvironment that retards oxidation by shielding the amino acids from the solvent and endowing the protein with the ability to maintain adhesion at neutral to slightly basic pH levels. More importantly, hydrophobic interactions and inter-residue H-bonding combine to result in strong cohesion within Mfp3 layers over a relatively wide range of pH levels. By exploring the adhesive and cohesive mechanisms of bonding by the adhesive proteins of mussels, recent studies reveal that the adhesion of mussels is more complicated than a simple DOPA-mediated procedure, thus providing the motivation for a new generation of bio-inspired synthetic adhesive polymer materials. Some findings also explained the roles of hydrophobic and hydrophilic interactions in both biological and non-biological instances of mussels and mussel-inspired adhesion. The issues of redox and adhesion may be much broader and not limited solely to mussel DOPA chemistry. Understanding the aspects of natural redox control can provide fundamentally important insight for adhesive polymer engineering, surface modification and antifouling strategies.

Mussel-inspired adhesive exhibit attractive properties for use immediately following tissue injuries, for applications in soft tissues including the gut and the vasculature, and for adhesion in an inflamed environment (*i.e.*, hernia). Research on mussel-inspired medical adhesives has also focused on tissue-specific medical applications, including wound care for diabetic patients, sutures for corneal tissue, and the surgical repair of nerves. MIMs are also capable of repairing defects in human fetal membranes, and they are biocompatible and effective at sealing small holes. The mussels unstable fatty acid components may have potent anti-inflammatory effects, which will be important for various types of autoimmune and inflammatory diseases. Some fractions of peptides from mussels show significant anti-proliferative activities with high nutritive potential as a source of protein, vitamin C, iron, zinc and omega-3. Mussel-inspired controlled drug delivery systems are also a promising emerging area for research. Some advanced types of novel formulations or conjugations with nanomaterials can also lead to the realization of applications in drug delivery to specific targets that are related to variations in pH levels and other physiochemical factors. Using a biodegradable mussel-inspired polymer surface coating also can regulate the adhesion, proliferation and differentiation of human mesenchymal stem cells. Collectively, we can conclude here that MIMs are important for many types of biomedical applications and that many more without immunogenicity issues will be explored by scientific communities and industries in the future.

Acknowledgments

This work was supported by a grant from the National Research Foundation of Korea (NRF) funded by the Korean government (MSIP) (NRF-2010-0027963) and by Kwangwoon University in 2015–16. This research was also supported by the MSIP (Ministry of Science, ICT and Future Planning), Korea, under the ITRC (Information Technology Research Center) support program (IITP-2015-R0992-15-1008) supervised by the IITP (Institute for Information & communications Technology Promotion).

Author Contributions

N.K.K., N.K., S.P., J.G.S. collected and analyzed the data, N.K.K., S.H.L., E.H.C. wrote the manuscript.

Conflicts of Interest

The authors declare no conflict of interest.

References

1. Stewart, R.J.; Ransom, T.C.; Haldy, V. Natural Underwater Adhesives. *J. Polym. Sci. B Polym. Phys.* **2011**, *49*, 757–771.
2. Silverman, H.G.; Roberto, F.F. Understanding Marine Mussel Adhesion. *Mar. Biotechnol. (N. Y.)* **2007**, *9*, 661–681.
3. Mussel-Inspired 'Glue' for Fetal Membrane Repair. Available online: http://esciencenews.com/articles/2010/01/22/mussel.inspired.glue.fetal.membrane.repair (accessed on 10 November 2015).

4. Messersmith, P. Mussel-inspired materials for surgical repair and drug delivery. In *Translation of Mussel Adhesion to Beneficial New Concepts and Materials*, Proceedings of the American Association for the Advancement of Science (AAAS) Annual Meeting, Boston, MA, USA, 14–18 February 2013.
5. Qin, Z.; Buehler, M.J. Impact tolerance in mussel thread networks by heterogeneous material distribution. *Nat. Commun.* **2013**, *4*, 2187.
6. Yu, J.; Kan, Y.; Rapp, M.; Danner, E.; Wei, W.; Das, S.; Miller, D.R.; Chen, Y.; Waite, J.H.; Israelachvili, J.N. Adaptive hydrophobic and hydrophilic interactions of mussel foot proteins with organic thin films. *Proc. Natl. Acad. Sci. USA* **2013**, *110*, 15680–15685.
7. Amstad, E.; Gillich, T.; Bilecka, I.; Textor, M.; Reimhult, E. Ultrastable iron oxide nanoparticle colloidal suspensions using dispersants with catechol-derived anchor groups. *Nano Lett.* **2009**, *9*, 4042–4048.
8. Brubaker, C.E.; Messersmith, P.B. The present and future of biologically inspired adhesive interfaces and materials. *Langmuir* **2012**, *28*, 2200–2205.
9. Su, J.; Chen, F.; Cryns, V.L.; Messersmith, P.B. Catechol polymers for pH-responsive, targeted drug delivery to cancer cells. *J. Am. Chem. Soc.* **2012**, *133*, 11850–11853.
10. Mehdizadeh, M.; Weng, H.; Gyawali, D.; Tang, L.; Yang, J. Injectable citrate-based mussel-inspired tissue bioadhesives with high wet strength for sutureless wound closure. *Biomaterials* **2012**, *33*, 7972–7983.
11. Lynge, M.E.; van der Westen, R.; Postma, A.; Städler, B. Polydopamine—A nature-inspired polymer coating for biomedical science. *Nanoscale* **2011**, *3*, 4916–4928.
12. Lee, H.; Lee, B.P.; Messersmith, P.B. A reversible wet/dry adhesive inspired by mussels and geckos. *Nature* **2007**, *448*, 338–341.
13. Yu, J.; Wei, W.; Danner, E.; Ashley, R.K.; Israelachvili, J.N.; Waite, J.H. Mussel protein adhesion depends on interprotein thiol-mediated redox modulation. *Nat. Chem. Biol.* **2011**, *7*, 588–590.
14. Waite, J.H. Surface chemistry: Mussel power. *Nat. Mater.* **2008**, *7*, 8–9.
15. Lee, H.; Dellatore, S.M.; Miller, W.M.; Messersmith, P.B. Mussel-inspired surface chemistry for multifunctional coatings. *Science* **2007**, *318*, 426–430.
16. Wei, W.; Yu, J.; Broomell, C.; Israelachvili, J.N.; Waite, J.H. Hydrophobic enhancement of Dopa-mediated adhesion in a mussel foot protein. *J. Am. Chem. Soc.* **2013**, *135*, 377–383.
17. Nicklisch, S.C.; Waite, J.H. Mini-review: The role of redox in Dopa-mediated marine adhesion. *Biofouling* **2012**, *28*, 865–877.
18. Waite, J.H. Reverse engineering of bioadhesion in marine mussels. *Ann. N. Y. Acad. Sci. USA* **1991**, *875*, 301–309.
19. Rodgers, K.J.; Dean, R.T. Metabolism of protein-bound DOPA in mammals. *Int. J. Biochem. Cell. Biol.* **2000**, *32*, 945–955.
20. Gieseg, S.P.; Simpson, J.A.; Charlton, T.S.; Duncan, M.W.; Dean, R.T. Protein-bound 3,4-dihydroxyphenylalanine is a major reductant formed during hydroxyl radical damage to proteins. *Biochemistry* **1993**, *32*, 4780–4786.
21. Brubaker; C.E.; Messersmith, P.B. Enzymatically degradable mussel-inspired adhesive hydrogel. *Biomacromolecules* **2011**, *12*, 4326–4334.

22. Barrett, D.G.; Fullenkamp, D.E.; He, L.; Holten-Andersen, N.; Lee, K.Y.C.; Messersmith, P.B. pH-based regulation of hydrogel mechanical properties through mussel-inspired chemistry and processing. *Adv. Funct. Mater.* **2013**, *23*, 1111–1119.
23. Barrett, D.G.; Bushnell, G.G.; Messersmith, P.B. Mechanically robust, negative-swelling, mussel-inspired tissue adhesives. *Adv. Healthc. Mater.* **2013**, *2*, 745–755.
24. Fullenkamp, D.E.; He, L.; Barrett, D.G.; Burghardt, W.R.; Messersmith, P.B. Mussel-Inspired Histidine-Based Transient Network Metal Coordination Hydrogels. *Macromolecules* **2013**, *46*, 1167–1174.
25. Ham, H.O.; Liu, Z.; Lau, K.H.A.; Lee, H.; Messersmith, P.B. Facile DNA Immobilization on Surfaces through a Catecholamine Polymer. *Angew. Chem.* **2011**, *123*, 758–762.
26. Rivera, J.G.; Messersmith, P.B. Polydopamine-assisted immobilization of trypsin onto monolithic structures for protein digestion. *J. Sep. Sci.* **2012**, *35*, 1514–1520.
27. Yang, S.H.; Kang, S.M.; Lee K.B.; Chung T.D.; Lee, H.; Chung, T.D.; Lee, H.; Choi, I.S. Mussel-inspired encapsulation and functionalization of individual yeast cells. *J. Am. Chem. Soc.* **2011**, *133*, 2795–2797.
28. Marder, J. How the Sticking Power of Mussels Can Advance Fetal Surgery. Available online: http://www.pbs.org/newshour/rundown/sticking-power-mussels-advance-fetal-surgery/ (accessed on 18 February 2013).
29. Yang, Y.; Qi, P.; Wen, F.; Li, X.; Xia, Q.; Maitz, M.F.; Yang, Z.; Shen, R.; Tu, Q.; Huang, N. Mussel-inspired one-step adherent coating rich in amine groups for covalent immobilization of heparin: Hemocompatibility, growth behaviors of vascular cells, and tissue response. *ACS Appl. Mater. Interfaces* **2014**, *6*, 14608–14620.
30. Ma, L.; Qin, H.; Cheng, C.; Xia, Y.; He, C.; Nie, C.; Wang, L.; Zhao, C. Mussel-inspired self-coating at macro-interface with improved biocompatibility and bioactivity via dopamine grafted heparin-like polymers and heparin. *J. Mater. Chem. B* **2014**, *2*, 363–375.
31. Kuang, J.; Guo, J.L.; Messersmith, P.B. High Ionic Strength Formation of DOPA-Melanin Coating for Loading and Release of Cationic Antimicrobial Compounds. *Adv. Mater. Interfaces* **2014**, *1*, doi:10.1002/admi.201400145.
32. Ryu, J.Y.; Song, I.T.; Lau, K.H.A.; Messersmith, P.B.; Yoon, T.Y.; Lee, H. New Antifouling Platform Characterized by Single-Molecule Imaging. *ACS Appl. Mater. Interfaces* **2014**, *6*, 3553–3558.
33. Brodie, M.; Vollenweider, L.; Murphy, J.L.; Xu, F.; Lyman, A.; Lew, W.D.; Lee, B.P. Biomechanical properties of Achilles tendon repair augmented with a bioadhesive-coated scaffold. *Biomed. Mater.* **2011**, *6*, doi:10.1088/1748-6041/6/1/015014.
34. Lee, B.P.; Konst, S. Novel Hydrogel Actuator Inspired by Reversible Mussel Adhesive Protein Chemistry. *Adv. Mater.* **2014**, *26*, 3415–3419.
35. Krogsgaard, M.; Andersena, A.; Birkedal, H. Gels and threads: Mussel-inspired one-pot route to advanced responsive materials. *Chem. Commun.* **2014**, *50*, 13278–13281.
36. Rim, N.G.; Kim, S.J.; Shin, Y.M.; Jun, I.; Lim, D.W.; Park, J.H.; Shin, H. Mussel-inspired surface modification of poly (L-lactide) electrospun fibers for modulation of osteogenic differentiation of human mesenchymal stem cells. *Colloids Surf. B* **2012**, *91*,189–197.
37. Lee, H.; Scherer, N.F.; Messersmith, P.B. Single-molecule mechanics of mussel adhesion. *Proc. Natl. Acad. Sci. USA* **2006**, *103*, 12999–13003.

38. Ho, C.C.; Ding, S.J. Structure, properties and applications of mussel-inspired polydopamine. *J. Biomed. Nanotechnol.* **2014**, *10*, 3063–3084.
39. Shafiq, Z.; Cui, J.; Pastor-Pérez, L.; San Miguel, V.; Gropeanu, R.A.; Serrano, C.; del campo, A. Bioinspired underwater bonding and debonding on demand. *Angew. Chem. Int. Ed.* **2012**, *51*, 4332–4335.
40. Bilic, G.; Brubaker, C.; Messersmith, P.B.; Mallik, A.S.; Quinn, T.M.; Haller, C.; Done, E.; Gucciardo, L.; Zeisberger, S.M.; Zimmermann, R.; *et al.* Injectable candidate sealants for fetal membrane repair: Bonding and toxicity *in vitro*. *Am. J. Obstet. Gynecol.* **2010**, *202*, doi:10.1016/j.ajog.2009.07.051.
41. Haller, C.M.; Buerzle, W.; Brubaker, C.E.; Messersmith, P.B.; Mazza, E.; Ochsenbein-Koelble, N.; Zimmermann, R.; Ehrbar, M. Mussel-mimetic tissue adhesive for fetal membrane repair: A standardized *ex vivo* evaluation using elastomeric membranes. *Prenat. Diagn.* **2011**, *31*, 654–660.
42. Haller, C.M.; Buerzle, W.; Kivelio, A.; Perrini, M.; Brubaker, C.E.; Gubeli, R.J.; Mallik, A.S.; Weber, W.; Messersmith, P.B.; Mazza, E.; *et al*. Mussel-mimetic tissue adhesive for fetal membrane repair: An *ex vivo* evaluation. *Acta Biomater.* **2012**, *8*, 4365–4370.
43. Holten-Andersen, N.; Harrington, M.J.; Birkedal, H.; Lee, B.P.; Messersmith, P.B.; Lee, K.Y.C.; Waite, J.H. pH-induced metal-ligand cross-links inspired by mussel yield self-healing polymer networks with near-covalent elastic moduli. *Proc. Natl. Acad. Sci. USA* **2011**, *108*, 2651–2655.
44. Brubaker, C.E.; Kissler, H.; Wang, L.J.; Kaufman, D.B.; Messersmith, P.B. Biological performance of mussel-inspired adhesive in extrahepatic islet transplantation. *Biomaterials* **2010**, *31*, 420–427.
45. Nelson, M.; Foxwell, A.R.; Tyrer, P.; Dean, R.T. Protein-bound 3,4-dihydroxy-phenylanine (DOPA), a redox-active product of protein oxidation, as a trigger for antioxidant defences. *Int. J. Biochem. Cell Biol.* **2007**, *39*, 879–889.
46. Wakimoto, T.; Kondo, H.; Nii, H.; Kimura, K.; Egami, Y.; Oka, Y.; Yoshida, M.; Kida, E.; Ye, Y.; Akahoshi, S.; *et al.* Furan fatty acid as an anti-inflammatory component from the green-lipped mussel Perna canaliculus. *Proc. Natl. Acad. Sci. USA* **2011**, *108*, 17533–17537.
47. Li, G.; Fu, Y.; Zheng, J.; Li, D. Anti-inflammatory activity and mechanism of a lipid extract from hard-shelled mussel (*Mytilus coruscus*) on chronic arthritis in rats. *Mar. Drugs* **2014**, *12*, 568–588.
48. Beaulieu, L.; Thibodeau, J.; Bonnet, C.; Bryl, P.; Carbonneau, M.E. Evidence of anti-proliferative activities in blue mussel (*Mytilus edulis*) by-products. *Mar. Drugs* **2013**, *11*, 975–990.
49. Ahn, B.K.; Lee, D.W.; Israelachvili, J.N.; Waite, J.H. Surface-initiated self-healing of polymers in aqueous media. *Nat. Mater.* **2014**, *13*, 867–872.
50. Lee, J.S.; Lee, K.; Moon, S.H.; Chung, H.M.; Lee, J.H.; Um, S.H.; Kim, D.I.; Cho, S.W. Mussel-inspired cell-adhesion peptide modification for enhanced endothelialization of de-cellularized blood vessels. *Macromol. Biosci.* **2014**, *14*, 1181–1189.
51. Amstad, E.; Kohlbrecher, J.; Müller, E.; Schweizer, T.; Textor, M.; Reimhult, E. Triggered release from liposomes through magnetic actuation of iron oxide nanoparticle containing membranes. *Nano Lett.* **2011**, *11*, 1664–1670.
52. Fullenkamp, D.E.; Rivera, J.G.; Gong, Y.K.; Lau, K.H.; He, L.; Varshney, R.; Messersmith, P.B. Mussel-inspired silver-releasing antibacterial hydrogels. *Biomaterials* **2012**, *33*, 3783–3791.

53. Ni, K.; Lu, H.; Wang, C.; Black, K.C. L.; Wei, D.; Ren, Y.; Messersmith, P.B. A novel technique for *in situ* aggregation of Gluconobacter oxydans using bio-adhesive magnetic nanoparticles. *Biotechnol. Bioeng.* **2012**, *109*, 2970–2977.
54. Jiang, J.; Xie, J.; Ma, B.; Bartlett, D.E.; Xu, A.; Wang, C.H. Mussel-inspired protein-mediated surface functionalization of electrospun nanofibers for pH-responsive drug delivery. *Acta Biomater.* **2014**, *10*, 1324–1332.
55. Black, K.C. L.; Sileika, T.S.; Yi, J.; Zhang, R.; Rivera, J.G.; Messersmith, P.B. Bacterial Killing by Light-Triggered Release of Silver from Biomimetic Metal Nanorods. *Small* **2014**, *10*, 169–178.
56. Nurunnabi, Md.; Khatun, J.; Nafiujjaman, Md.; Lee, D.G.; Lee, Y.K. Surface Coating of Graphene Quantum Dots Using Mussel-Inspired Polydopamine for Biomedical Optical Imaging. *ACS Appl. Mater. Interfaces* **2013**, *5*, 8246–8253.
57. Cheng, C.; Nie, S.; Li, S.; Peng, H.; Yang, H.; Ma, L.; Sun, S.; Zhao, C. Biopolymer functionalized reduced graphene oxide with enhanced biocompatibility *via* mussel inspired coatings/anchors. *J. Mater. Chem. B* **2013**, *1*, 265–275.
58. Yana, P.; Wang, J.; Wang, L.; Liu, B.; Lei, Z.; Yang, S. The *in vitro* biomineralization and cytocompatibility of polydopamine coated carbon nanotubes. *Appl. Surf. Sci.* **2011**, *257*, 4849–4855.
59. Shi, C.; Deng, C.; Zhang, X.; Yang, P. Synthesis of highly water-dispersible polydopamine-modified multiwalled carbon nanotubes for matrix-assisted laser desorption/ionization mass spectrometry analysis. *ACS Appl. Mater. Interfaces* **2013**, *5*, 7770–7776.
60. Skelton, S.; Bostwick, M.; Connor, K.O.; Konst, S.; Casey, S.; Lee, B.P. Biomimetic adhesive containing nanocomposite hydrogel with enhanced materials properties. *Soft Matter* **2013**, *9*, 3825–3833.
61. Yang, X.; Zhu, L.; Tada, S.; Zhou, D.; Kitajima, T.; Isoshima, T.; Yoshida, Y.; Nakamura, M.; Yan, W.; Ito, Y. Mussel-inspired human gelatin nanocoating for creating biologically adhesive surfaces. *Int. J. Nanomed.* **2014**, *9*, 2753–2765.
62. Choi, J.S.; Messersmith, P.B.; Yoo. H.S. Decoration of Electrospun Nanofibers with Monomeric Catechols to Facilitate Cell Adhesion. *Macromol. Biosci.* **2014**, *14*, 270–279.
63. Low, W.C.; Rujitanaroj, P.O.; Lee, D.K.; Kuang, J.; Messersmith, P.B.; Chan, J.K.Y.; Chew, S.Y. Mussel-Inspired Modification of Nanofibers for REST siRNA Delivery: Understanding the Effects of Gene-Silencing and Substrate Topography on Human Mesenchymal Stem Cell Neuronal Commitment. *Macromol. Biosci.* **2015**, *15*, doi:10.1002/mabi.201500101
64. Kim, B.J.; Kim, S.; Oh, D.X.; Masic, A.; Cha, H.J.; Hwang, D.S. Mussel-inspired adhesive protein-based electrospun nanofibers reinforced by Fe(III)-DOPA complexation. *J. Mater. Chem. B* **2015**, *3*, 112–118.
65. Song, X.; Lin, L.; Rong, M.; Wang, Y.; Xie, Z.; Chen, X. Mussel-inspired, ultralight, multifunctional 3D nitrogen-doped graphene aerogel. *Carbon* **2014**, *80*, 174–182.
66. Black, K.C.; Yi, J.; Rivera, J.G.; Zelasko-Leon, D.C.; Messersmith, P.B. Polydopamine-enabled surface functionalization of gold nanorods for cancer cell-targeted imaging and photothermal therapy. *Nanomedicine (London)* **2013**, *8*, 17–28.
67. Ren, Y.; Rivera, J.G.; He, L.; Kulkarni, H.; Lee, D.K.; Messersmith, P.B. Facile, high efficiency immobilization of lipase enzyme on magnetic iron oxide nanoparticles via a biomimetic coating. *BMC Biotechnol.* **2011**, *11*, 63.

68. Zhou, J.; Wang, P.; Wang, C.; Goh, Y.T.; Fang, Z.; Messersmith, P.B.; Duan, H. Versatile Core-Shell Nanoparticle@Metal-Organic Framework Nanohybrids: Exploiting Mussel-Inspired Polydopamine for Tailored Structural Integration. *ACS Nano* **2015**, *9*, 6951–6960.
69. Liu, R.; Guo, Y.; Odusote, G.; Qu, F.; Priestley, R.D. Core-Shell Fe3O4 Polydopamine Nanoparticles Serve Multipurpose as Drug Carrier, Catalyst Support and Carbon Adsorbent. *ACS Appl. Mater. Interfaces* **2013**, *5*, 9167–9171.
70. Cui, J.; Wang, Y.; Postma, A.; Hao, J.; Hosta-Rigau, L.; Caruso, F. Monodisperse Polymer Capsules: Tailoring Size, Shell Thickness, and Hydrophobic Cargo Loading via Emulsion Templating. *Adv. Funct. Mater.* **2010**, *20*, 1625–1631.
71. Xie, J.; Wang, J.; Niu, G.; Huang, J.; Chen, K.; Li, X.; Chen, X. Human serum albumin coated iron oxide nanoparticles for efficient cell labeling. Human serum albumin coated iron oxide nanoparticles for efficient cell labeling. *Chem. Commun.* **2010**, *46*, 433–435.

© 2015 by the authors; licensee MDPI, Basel, Switzerland. This article is an open access article distributed under the terms and conditions of the Creative Commons Attribution license (http://creativecommons.org/licenses/by/4.0/).

EUROPEAN JOURNAL OF PURE AND APPLIED MATHEMATICS
Vol. 8, No. 4, 2015, 469-477
ISSN 1307-5543 – www.ejpam.com

$\mathscr{C}$-cycle Compatible Splitting Signed Graphs $\mathfrak{S}(S)$ and $\Gamma(S)$

Rashmi Jain [1,*], Sangita Kansal[1], Mukti Acharya[2]

[1] *Department of Applied Mathematics, Delhi Technological University, Delhi, India*
[2] *Department of Mathematics, Kalasalingam University, KrishnanKoil, India*

Abstract. A *signed graph* (or, in short, *sigraph*) $S = (S^u, \sigma)$ consists of an underlying graph $S^u := G = (V, E)$ and a function $\sigma : E(S^u) \longrightarrow \{+, -\}$, called the signature of S. A *marking* of S is a function $\mu : V(S) \longrightarrow \{+, -\}$. The *canonical marking* of a signed graph S, denoted μ_σ, is given as

$$\mu_\sigma(v) := \prod_{vw \in E(S)} \sigma(vw).$$

The *splitting signed graph* $\mathfrak{S}(S)$ of a signed graph S is formed as follows:

- Take a copy of S and for each vertex v of S, take a new vertex v'. Join v' to all vertices $u \in N(v)$ by negative edge, if $\mu_\sigma(u) = \mu_\sigma(v) = -$ in S and by positive edge otherwise.

The *splitting signed graph* $\Gamma(S)$ of a signed graph S is formed as follows:

- Take a copy of S and for each vertex v of S, take a new vertex v'. Join v' to all vertices $u \in N(v)$ and assign $\sigma(uv)$ as its sign. Here, $N(v)$ is the set of all adjacent vertices to v.

A signed graph is called *canonically consistent (or $\mathscr{C}$-consistent)* if its every cycle contains even number of negative vertices with respect to its canonical marking. A marked signed graph S is called *cycle-compatible* if for every cycle Z in S, the product of signs of its vertices equals the product of signs of its edges. A signed graph S is *$\mathscr{C}$-cycle compatible* if for every cycle Z in S,

$$\prod_{e \in E(Z)} \sigma(e) = \prod_{v \in V(Z)} \mu_\sigma(v).$$

In this paper, we establish a structural characterization of signed graph S for which $\mathfrak{S}(S)$ and $\Gamma(S)$ are isomorphic and $\mathscr{C}$-cycle compatible.

2010 Mathematics Subject Classifications: 05C22; 05C75

Key Words and Phrases: canonical marking, splitting signed graph, $\mathscr{C}$-consistent, $\mathscr{C}$-cycle compatible, $\mathscr{C}$-sign compatible

*Corresponding author.

Email addresses: rashmi2011f@gmail.com (R. Jain), sangita_kansal15@dce.ac.in (S. Kansal), mukti1948@gmail.com (M. Acharya)

 © 2015 EJPAM All rights reserved.

1. Introduction

A *graph* is an ordered pair $G = (V, E)$, where $V = V(G)$ is a set of *vertices or points* of G and $E = E(G)$ is a collection of pairs of vertices of G, called *edges or lines* of G. For graph theoretical terminology, we refer to [2]. All graphs considered in the paper are finite, simple and connected.

A *signed graph* is an ordered pair $S = (S^u, \sigma)$, where $S^u := G = (V, E)$ is a graph called the underlying graph of S and $\sigma : E(S^u) \longrightarrow \{+, -\}$ is a function, called the *signature* of S. In other terms, we say that the edges are *signed* by σ. In a pictorial representation of a signed graph S, its positive edges are shown as bold line segments ('Jorden curves' drawn on the plane) and negative lines as broken line segments as shown in Figure 1. $E^+(S) = \{e \in E(S^u) : \sigma(e) = +\}$ and $E^-(S) = \{e \in E(S^u) : \sigma(e) = -\}$. The elements of $E^+(S)$ ($E^-(S)$) are called *positive* (*negative*) *edges* of S and the set $E(S) = E^+(S) \cup E^-(S)$ is called the edge set of S.

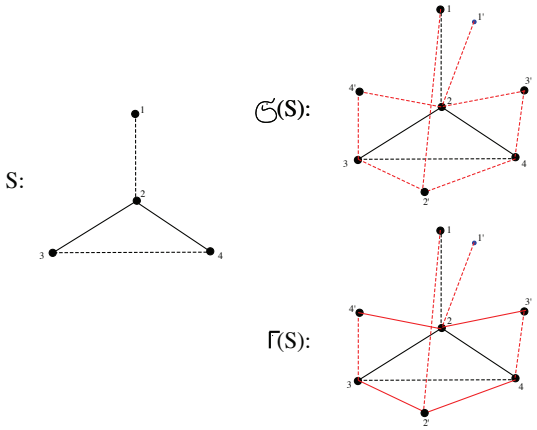


Figure 1: A signed graph S and its splitting signed graphs $\mathfrak{G}(S)$ and $\Gamma(S)$

A signed graph in which all the edges are positive, is called *all-positive signed graph* (*all-negative signed graph* is defined similarly). A signed graph is said to be *homogeneous* if it is either all-positive or all-negative and *heterogeneous* otherwise. By $d(v)$, we denote degree of $v \in V(S)$, $d(v) = d^+(v) + d^-(v)$, here $d^+(v)$ ($d^-(v)$) denotes the positive (negative) degree of v.

A *marking* of S is a function $\mu : V(S) \longrightarrow \{+, -\}$. Sampathkumar in [4] introduced the idea of marking derived from the signs of edges incident to vertices, given as

$$\mu_\sigma(v) := \prod_{vw \in E(S)} \sigma(vw).$$

This marking is called canonical marking. Clearly, $\mu_\sigma(v) = +$ if $d^-(v)$ is even and $\mu_\sigma(v) = -$ if $d^-(v)$ is odd. Thus, in canonical marking of a signed graph, we assign + sign to a vertex if its negative degree is even and - sign if its negative degree is odd. In this paper, a vertex v of $d^-(v) =$ even (odd) is called *positive* (*negative*) *vertex*.

Signed graphs S_1 and S_2 are called *isomorphic*, written as $S_1 \cong S_2$, if there is a graph isomorphism $f : S_1^u \to S_2^u$ that preserves edge signs.

A cycle in a signed graph is said to be *positive (negative) cycle* if the product of the signs of its edges is positive (negative), i.e., its an even (odd) number of edges are negative. A signed graph is said to be *balanced* if every cycle in it is positive (*see* [3]).

A cycle in a marked signed graph is said to be *consistent* if its an even number of vertices are negative and a marked signed graph is called consistent if its all cycles are consistent (*see* [6]). Similarly, a cycle in a signed graph is said to be *canonically consistent (or $\mathscr{C}$-consistent)* if for every cycle in S, the product of signs of its vertices with respect to canonical marking, is positive, i.e., its an even number of vertices are negative and a signed graph is called $\mathscr{C}$-consistent if its all cycles are $\mathscr{C}$-consistent.

A marked signed graph S is called *cycle-compatible* if for every cycle Z in S, the product of signs of its vertices equals the product of signs of its edges. A signed graph S is called *canonically cycle* (or *$\mathscr{C}$-cycle*) *compatible* if for every cycle Z in S,

$$\prod_{e\in E(Z)} \sigma(e) = \prod_{v\in V(Z)} \mu_\sigma(v).$$

A signed graph $S = (S^u, \sigma)$ is said to be *sign-compatible* [6] if it has a vertex marking μ such that every edge $e = uv$ has $\sigma(e) = -$ if and only if $\mu(u) = \mu(v) = -$. If the canonical marking μ_σ has this property, then S is said to be *canonically sign-compatible (or $\mathscr{C}$-sign-compatible)*.

2. Splitting Signed Graphs

Sampathkumar and Walikar introduced the concept of *splitting graph* of a graph in [5]. The splitting graph of a graph G, denoted here $\mathfrak{S}(G)$, is formed as follows:

Take a copy of G and for each vertex v of G, take a new vertex v'. Join v' to all adjacent vertices of v.

There are two notions of *splitting signed graphs* of a signed graph $S = (S^u, \sigma)$ in the literature, viz., $\mathfrak{S}(S)$ and $\Gamma(S)$, both of which have $\mathfrak{S}(S^u)$ as their underlying graph; only the rule to assign signs to the edges of $\mathfrak{S}(S^u)$ differ. An edge uv' in $\mathfrak{S}(S)$ is negative whenever u and v are negative vertices of S and an edge uv' in $\Gamma(S)$ is negative whenever uv is a negative edge of S as reported in [1] and [7] respectively.

A signed graph S is called a $\mathfrak{S}$-splitting (Γ-splitting) signed graph if there exists a signed graph T such that S is isomorphic to $\mathfrak{S}(T)$ ($\Gamma(T)$).

Theorem 1 (Acharya *et al.*[1]). *Following statements hold:*

(i) If $v \in V(S)$ is a positive vertex then $v, v' \in V(\mathfrak{S}(S))$ are positive.

(ii) If $v \in V(S)$ is a negative vertex having an even (odd) number of negative vertices in its neighbourhood then $v \in V(\mathfrak{S}(S))$ is negative (positive) vertex and v' is of opposite sign to v.

Here v' is the vertex as defined above.

Theorem 2 (Acharya *et al.* [1]). *$\mathcal{G}(S)$ is balanced if and only if the following conditions hold in S:*

(i) S is balanced and;

(ii) S does not contain a homogeneous path P_3 of marking +, -, - and the marking of a heterogeneous path P_3 is +, -, - only.

Lemma 1 (Sinha *et al.* [7]). *The following statements hold in $\Gamma(S)$:*

(i) If $v \in V(S)$ is any vertex then $v \in V(\Gamma(S))$ is positive.

(ii) If $v \in V(S)$ is a negative vertex then $v' \in V(\Gamma(S))$ is negative.

Theorem 3 (Sinha *et al.* [7]). *The splitting signed graph $\Gamma(S)$ of a signed graph S is balanced if and only if S is balanced.*

Figure 1 illustrates a signed graph S and its splitting signed graphs $\mathcal{G}(S)$ and $\Gamma(S)$.

3. Main Results

Theorem 4. *For a signed graph S, $\mathcal{G}(S) \cong \Gamma(S)$ if and only if S is any one of the following:*

(i) All-positive or;

(ii) All-negative in which degree of each vertex is odd or;

(iii) Heterogeneous in which end vertices of every negative (positive) edge are (are not) negative.

Proof. Necessity: Let, for a signed graph S, $\mathcal{G}(S) \cong \Gamma(S)$. Since S is a subsignedgraph of $\mathcal{G}(S)$ and $\Gamma(S)$, we concentrate our attention only on the sign of edge uv' in $\mathcal{G}(S)$ and $\Gamma(S)$. By the definition of $\mathcal{G}(S)$, $uv' \in E^-(\mathcal{G}(S))$ if and only if $u, v \in V(S)$ are negative and by the definition of $\Gamma(S)$, $uv' \in E^-(\Gamma(S))$ if and only if $uv \in E^-(S)$. Therefore, we have following three possible cases:

Case I: If $\mathcal{G}(S) \cong \Gamma(S)$ and both $\mathcal{G}(S)$ and $\Gamma(S)$ are all-positive then no edge of S will be negative. Hence, **(i)** follows.

Case II: If $\mathcal{G}(S) \cong \Gamma(S)$ and both are all-negative then every edge and every vertex of S will be negative. Hence, **(ii)** follows.

Case III: If $\mathcal{G}(S) \cong \Gamma(S)$ and both are heterogeneous then S will be heterogeneous and edge uv' in both $\mathcal{G}(S)$ and $\Gamma(S)$ must be of the same sign. This implies that end vertices of every negative (positive) edge of S are (are not) negative. Hence, **(iii)** follows.

Thus, the necessity follows.

Sufficiency: Suppose S is any one of the following:

(i) All-positive or;

(ii) All-negative in which degree of each vertex is odd or;

(iii) Heterogeneous in which end vertices of every negative (positive) edge are (are not) negative.

then by the definitions $\mathcal{S}$ - and Γ- splitting signed graphs, we obtain following results:

Case I: If S is all-positive then $\mathcal{S}(S)$ and $\Gamma(S)$ will be all-positive and $\mathcal{S}(S) \cong \Gamma(S)$.

Case II: If S is all-negative in which degree of each vertex is odd then $\mathcal{S}(S)$ and $\Gamma(S)$ will be all-negative and $\mathcal{S}(S) \cong \Gamma(S)$.

Case III: If S is heterogeneous in which end vertices of every negative (positive) edge are (are not) negative then $\mathcal{S}(S)$ and $\Gamma(S)$ will be heterogeneous as S be a subsignedgraph of $\mathcal{S}(S)$ and $\Gamma(S)$ and edge uv' in both $\mathcal{S}(S)$ and $\Gamma(S)$ will be of the same sign. Hence, $\mathcal{S}(S) \cong \Gamma(S)$.

This completes the proof. □

Corollary 1. *For a signed graph S, $\mathcal{S}(S) \cong \Gamma(S)$ if and only if S is $\mathscr{C}$-sign compatible.*

Theorem 5. *$\mathcal{S}(S)$ is $\mathscr{C}$-cycle compatible if and only if the following conditions hold in S:*

(i) if Z is a positive (negative) cycle then an even (odd) number of negative vertices of cycle Z contain even numbers of negative vertices in their neighbourhoods and;

(ii) for a path $P_3 = (u, v, w)$, any one condition holds:

- *it is homogeneous of marking +, +, +;*
- *it is heterogeneous of marking +, -, +;*
- *it is homogeneous (heterogeneous) of marking -, +, + or -, -, + and $N(u)$ contains an odd (even) number of negative vertices;*
- *it is homogeneous (heterogeneous) of marking -, +, - and vertices u, w are (are not) of same parity (i.e., $N(u)$ and $N(w)$ contain even number of negative vertices or odd number of negative vertices);*
- *it is homogeneous (heterogeneous) of marking -, -, - and vertices u, w are not (are) of the same parity.*

Proof. Necessity: Let $\mathcal{S}(S)$ be $\mathscr{C}$-cycle compatible. Therefore, every cycle in $\mathcal{S}(S)$ is either positive and $\mathscr{C}$-consistent or negative and $\mathscr{C}$-inconsistent. By Theorem 1, every positive vertex of S is positive in $\mathcal{S}(S)$ and every negative vertex of S having an even (odd) number of negative vertices in its neighbourhood is negative (positive) in $\mathcal{S}(S)$. Since S is subsignedgraph of $\mathcal{S}(S)$, if Z is a positive (negative) cycle of S then Z must be $\mathscr{C}$-consistent ($\mathscr{C}$-inconsistent) in $\mathcal{S}(S)$, i.e., an even (odd) number of negative vertices of cycle Z must contain an even numbers of negative vertices in their neighbourhoods. Thus, **(i)** follows.

By the definition of $\mathcal{S}(S)$, a path $P_3 = (u, v, w)$ of S induces a cycle $C_4 = (u, v, w, v')$ in $\mathcal{S}(S)$. The marking of path $P_3 = (u, v, w)$ may be one of the following:

1. +, +, + 2. +, -, + 3. -, +, + 4. -, -, + 5. -, +, - 6. -, -, -

Hence, the following cases arise:

- if marking of path $P_3 = (u, v, w)$ is +, +, + then by Theorem 1, vertices u, v, w, v' have signs +, +, +, + respectively in $\mathfrak{S}(S)$. Thus, path P_3 induces a $\mathscr{C}$-consistent cycle C_4 in $\mathfrak{S}(S)$. By Theorem 2, this cycle C_4 is positive (negative) if and only if P_3 is homogeneous (heterogeneous). Since $\mathfrak{S}(S)$ is $\mathscr{C}$-cycle compatible, P_3 will be homogeneous.

- if marking of path $P_3 = (u, v, w)$ is +, -, + then by Theorem 1, vertices u, v, w, v' have signs +, -, +, + or +, +, +, - respectively in $\mathfrak{S}(S)$. Thus, path P_3 induces a $\mathscr{C}$-inconsistent cycle C_4 in $\mathfrak{S}(S)$. By Theorem 2, this cycle C_4 is positive (negative) if and only if P_3 is homogeneous (heterogeneous). Since $\mathfrak{S}(S)$ is $\mathscr{C}$-cycle compatible, P_3 will be heterogeneous.

- if marking of path $P_3 = (u, v, w)$ is -, +, + and $N(u)$ contains an odd (even) number of negative vertices then by Theorem 1, vertices u, v, w, v' have signs +, +, +, + (-, +, +, +) respectively in $\mathfrak{S}(S)$. Thus, path P_3 induces a $\mathscr{C}$-consistent ($\mathscr{C}$-inconsistent) cycle C_4 in $\mathfrak{S}(S)$. By Theorem 2, this cycle C_4 is positive (negative) if and only if P_3 is homogeneous (heterogeneous). Since $\mathfrak{S}(S)$ is $\mathscr{C}$-cycle compatible, for homogeneous (heterogeneous) P_3, $N(u)$ must contain an odd (even) number of negative vertices.

  Similarly, if marking of path $P_3 = (u, v, w)$ is -, -, + and $N(u)$ contains an even (odd) number of negative vertices then by Theorem 1, vertices u, v, w, v' have signs -, -, +, + or -, +, +, - (+, -, +, + or +, +, +, -) respectively in $\mathfrak{S}(S)$. Thus, path P_3 induces a $\mathscr{C}$-consistent ($\mathscr{C}$-inconsistent) cycle C_4 in $\mathfrak{S}(S)$. By Theorem 2, this cycle C_4 is positive (negative) if and only if P_3 is heterogeneous (homogeneous). Since $\mathfrak{S}(S)$ is $\mathscr{C}$-cycle compatible, for heterogeneous (homogeneous) P_3, $N(u)$ will contain an even (odd) number of negative vertices.

- if marking of path $P_3 = (u, v, w)$ is -, +, - and vertices u and w are (are not) of the same parity, i.e., $N(u)$ and $N(w)$ contain even number of negative vertices or odd number of negative vertices, then by Theorem 1, vertices u, v, w, v' have signs -, +, -, + or +, +, +, + (-, +, +, + or +, +, -, +) respectively in $\mathfrak{S}(S)$. Thus, path P_3 induces a $\mathscr{C}$-consistent ($\mathscr{C}$-inconsistent) cycle C_4 in $\mathfrak{S}(S)$. By Theorem 2, this cycle C_4 is positive (negative) if and only if P_3 is homogeneous (heterogeneous). Since $\mathfrak{S}(S)$ is $\mathscr{C}$-cycle compatible, for homogeneous (heterogeneous) P_3, vertices u and w will (will not) be of the same parity;

- if marking of path $P_3 = (u, v, w)$ is -, -, - and vertices u and w are (are not) of the same parity, i.e., $N(u)$ and $N(w)$ contain even number of negative vertices or odd number of negative vertices, then by Theorem 1, vertices u, v, w, v' have signs -, -, -, +; -, +, -, - or +, -, +, +; +, +, +, - (-, -, +, +; -, +, +, - or +, -, -, +; +, +, -, -) respectively in $\mathfrak{S}(S)$. Thus, path P_3 induces a $\mathscr{C}$-inconsistent ($\mathscr{C}$-consistent) cycle C_4 in $\mathfrak{S}(S)$. By Theorem 2, this cycle C_4 is positive (negative) if and only if P_3 is homogeneous (heterogeneous). Since $\mathfrak{S}(S)$ is $\mathscr{C}$-cycle compatible, for homogeneous (heterogeneous) P_3, vertices u and w will not (will) be of the same parity.

Thus, the necessity follows.

Sufficiency: A cycle in $\mathcal{G}(S)$ is induced due to a cycle or a path P_3 or their combinations in S. If conditions hold then it can be easily seen that every cycle in $\mathcal{G}(S)$ is positive and $\mathscr{C}$-consistent or negative and $\mathscr{C}$-inconsistent, i.e, $\mathcal{G}(S)$ is $\mathscr{C}$-cycle compatible. This completes the proof. □

Signed graph S shown in Figure 2 does not satisfy conditions **(i)** and **(ii)** of Theorem 5, $\mathcal{G}(S)$ is $\mathscr{C}$-cycle incompatible.

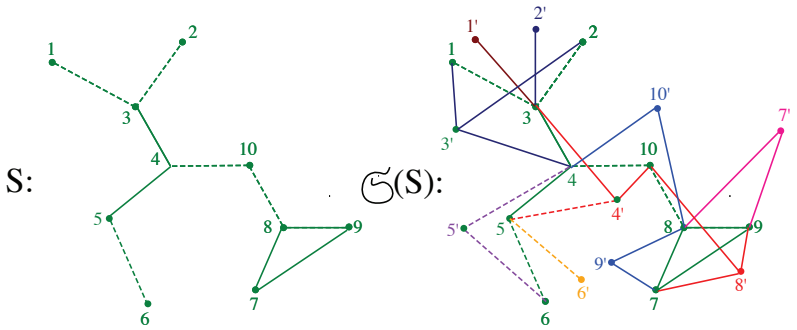


Figure 2: A signed graph S and its $\mathscr{C}$-cycle incompatible $\mathcal{G}(S)$

Signed graph S shown in Figure 3 satisfies conditions **(i)** and **(ii)** of Theorem 5, $\mathcal{G}(S)$ is $\mathscr{C}$-cycle compatible.

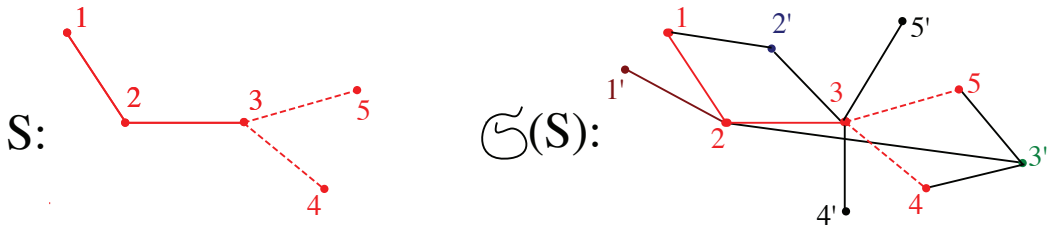


Figure 3: A signed graph S and its $\mathscr{C}$-cycle compatible $\mathcal{G}(S)$

Theorem 6. *For a signed graph S, $\Gamma(S)$ is $\mathscr{C}$-cycle compatible if and only if the following conditions hold in S:*

(i) S is balanced;

(ii) each non-pendant vertex of S is positive.

Proof. Necessity: Let $\Gamma(S)$ be $\mathscr{C}$-cycle-compatible, i.e., every cycle in $\Gamma(S)$ is either positive and $\mathscr{C}$-consistent or negative and $\mathscr{C}$-inconsistent. By Lemma 1, every vertex of S is a positive vertex of $\Gamma(S)$. Hence, every cycle Z of $\Gamma(S)$ that is due to a cycle Z of S is $\mathscr{C}$-consistent. Since $\Gamma(S)$ is $\mathscr{C}$-cycle-compatible, this cycle Z of S must be positive. Therefore, S will be balanced. Thus, **(i)** follows.

By the definition of $\Gamma(S)$, a path $P_3 = (u, v, w)$ of S induces a positive cycle $C_4 = (u, v, w, v')$ in $\Gamma(S)$ and by Lemma 1, vertices u, v, w, v' have signs +, +, +, + or +, +, +, - in $\Gamma(S)$ if v is a positive (negative) vertex of S. Thus, this cycle C_4 is $\mathscr{C}$-consistent if $v \in V(S)$ is a positive vertex. Since $\Gamma(S)$ is $\mathscr{C}$-cycle compatible and cycle C_4 is positive, C_4 must be $\mathscr{C}$-consistent. Hence, every non-pendant vertex of S will be positive. Thus, the necessity follows.

Sufficiency: A cycle in $\Gamma(S)$ is induced due to a cycle or a path P_3 or their combinations in S. If conditions hold then it can be easily seen that every cycle in $\Gamma(S)$ is positive and $\mathscr{C}$-consistent, i.e, $\Gamma(S)$ is $\mathscr{C}$-cycle-compatible. This completes the proof. □

Signed graph S shown in Figure 4 satisfies conditions **(i)** and **(ii)** of Theorem 6, $\Gamma(S)$ is $\mathscr{C}$-cycle compatible.

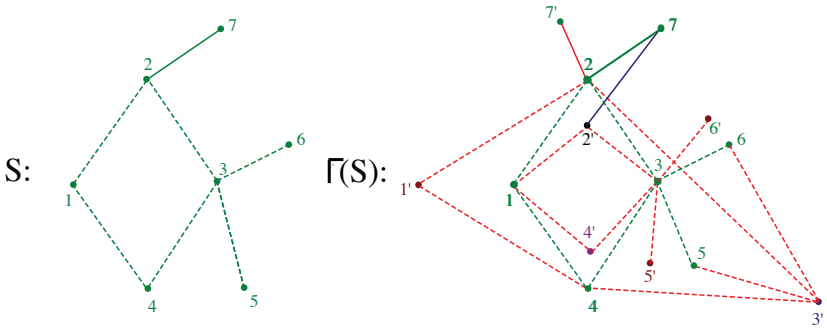


Figure 4: A signed graph S and its $\mathscr{C}$-cycle compatible $\Gamma(S)$

ACKNOWLEDGEMENTS The authors are thankful to Dr B. D. Acharya who always nurtured but could not witness the same. The corresponding author is thankful to the University Grants Commission (UGC), Govt. of India, for granting her research fellowship.

References

[1] M. Acharya, R. Jain, and S. Kansal. *Some results on the splitting signed graphs* $\mathfrak{S}(S)$, Journal of Combinatorics, Information and System Sciences, 39(1-2), 23-32. 2014.

[2] F. Harary. *Graph Theory*, Addison-Wesley Publishing Co., Reading, Massachusetts, 1969.

[3] F. Harary. *On the notion of balance of a signed graph*, Michigan Mathematical Journal, 2, 143-146. 1953.

[4] E. Sampathkumar. *Point-signed and line-signed graphs*, National Academy Science Letters, 7(3), 91-93. 1984.

[5] E. Sampathkumar and H.B. Walikar. *On the splitting graph of a graph*, Karnatak University Journal of Sciences, XXV-XXVI, 13-16. 1980-1981.

[6] D. Sinha. *New frontiers in the theory of signed graphs*, Ph.D. Thesis, University of Delhi, India, 2005.

[7] D. Sinha, P. Garg, and H. Saraswat. *On the splitting signed graphs*, Journal of Combinatorics, Information and System Sciences, 38(1-4), 103-111. 2013.

ResearchGate

See discussions, stats, and author profiles for this publication at: http://www.researchgate.net/publication/281624314

CFD Analysis and Optimization of Geometrical Modifications of Ahmed Body

ARTICLE · SEPTEMBER 2015

DOI: 10.9790/1684-12513749

READS

40

6 AUTHORS, INCLUDING:



M. Zunaid

Delhi Technological University

7 PUBLICATIONS **6** CITATIONS

SEE PROFILE

All in-text references underlined in blue are linked to publications on ResearchGate, letting you access and read them immediately.

Available from: M. Zunaid
Retrieved on: 23 November 2015

IOSR Journal of Mechanical and Civil Engineering (IOSR-JMCE)
e-ISSN: 2278-1684,p-ISSN: 2320-334X, Volume 12, Issue 5 Ver. I (Sep. - Oct. 2015), PP 37-49
www.iosrjournals.org

CFD Analysis and Optimization of Geometrical Modifications of Ahmed Body

Sagar Sharma[1], Saurabh Banga[2], Rohit Singh Dungriyal[3],
Mohammad Zunaid*[4], Naushad Ahmad Ansari[5], Suresh Lal[6]
[1, 2, 3]*U.G Student, Department of Mechanical & Automobile Engineering, Delhi Technological University, Bawana Road, Delhi, India*
[4, 5]*Assistant Professor, Department of Mechanical Engineering, Delhi Technological University, Bawana Road, Delhi, India*
[6]*Dy. Director, CEFEES (DRDO), Delhi, India.*

Abstract: *This project is modeled around reducing the overall drag and lift coefficient by modifying the geometry and comprehending the underlying rootphenomenon for the variation in these drag values. The designing of models used in this project is done through SOLIDWORKS, and CFD simulation in FLUENT (ANSYS) respectively. The purpose of this project is to reduce the inefficiency caused due to aerodynamic factors of drag, lift by presenting development, design and optimization of the geometry modifications of the base model. The improvement of aerodynamic behaviour around the periphery of the model is investigated through numerical simulation. The Ahmed Reference Body having 10 degree rear slant angle has been taken as benchmark model in this paper. Simulation of variants of multifarious modifications and examination of their results is performed to find the best suited variant form (dimension) to boost the aerodynamic efficiency of the model. CFD simulations on Ahmed Body were carried out in order to serve as a benchmark for validating all the simulation results. The steady-state simulations are based on the Reynolds averaged Navier-Stokes equations, with turbulence closure provided through two-equation k-epsilon realizable models.*
Keywords*: Ahmed body, CFD, drag, k-Epsilon realizable model, lift.*

I. Introduction

As the burning of fossil fuels is becoming a more pressing unsustainable issue in lieu of the environmental degradation and increasing energy prices, automobile manufacturers are introducing more fuel efficient cars to the market. One of the main contributors to fuel consumption is the aerodynamic drag since it accounts for more than half of the engine power at highway speeds.

The pressure drag which highly depends on vehicle geometry is because of boundary layer separation from rear trailing end and consequent formation of wake region behind the vehicle. The location of separation determines the size of wake region and consequently it determines the value of aerodynamic drag coefficient.

The drag coefficient quantifies the resistance of an object in a fluid environment. The lower the drag coefficient, the more efficient the car is. The drag coefficient also affects the handling in addition to affecting the top speed of a vehicle. Cars possessing low drag coefficients are desirable, but decreasing the drag drastically can reduce the downforce (increase lift) and lead to loss in road traction and increase in chance of accidents. There are numerous ways to modify a car to optimize its aerodynamics by decreasing the drag coefficient. To streamline the exterior, certain aftermarket accessories such as the roof rack, mud flaps, spoilers, and radio antenna can be removed. Wheel covers, a partial grille block, a properly designed under tray, fender skirts, and a modified front bumper can be utilized to reduce the drag coefficient.

The drag reducing methods are classified into active or passive control methods based upon whether these methods consume energy to control the flow of air or not: Passive flow control strategies such as vortex generators are accompanied by vehicle geometry modifications. Whereas, active control is performed by using actuators that require power, generally extracted from the prime mover of the vehicle. The visible part of these systems includes mobile walls, circular holes or slots distributed over the vehicle surface where the flow must be controlled. Active control methods such as suction, blowing seem constrained to theory and they may not be practical or feasible. In addition, it is yet to be determined how to optimize their control performances. The Ahmed body is a bluff body whose shape is simple enough to model, while maintaining certain important car-like geometry features.The Ahmed body was first proposed by Ahmed(1984) **[1]**. To reduce the computational cost, a symmetry plane is introduced to model half of the model.

For the model, the flow is turbulent, which is based on the Reynolds number determined by the body length and inlet velocity. The simulation solves for the turbulent kinetic energy and dissipation energy in addition to the velocity and pressure fields.

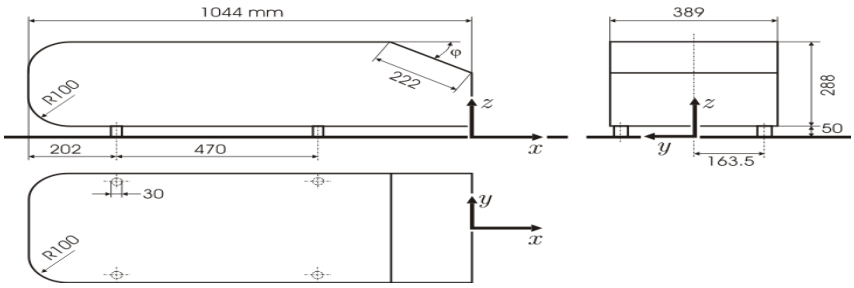


Fig. 1: Geometry of Ahmed model

Manipulation of the rear slant angle of the generic Ahmed body reference model was carried out previously **[2]**, to determine the optimum angle configuration for the least drag coefficient with velocity of air at inlet being 40m/s. The drag coefficient and the corresponding lift coefficient were plotted.The pressure distribution and velocity contours for the various rear slant angles were also investigated to comprehend the aerodynamic behavior around the model.

The Ahmed Body with 10 degree rear slant angle has been chosen as the benchmark model for carrying out computations for studying of the aerodynamic parameters. This paper has the following objectives:

1. To investigate and comprehend the variation of drag and lift coefficient by conducting numerical simulation on the benchmark modeland numerous configurations of 6multifariousgeometrically modified models of the benchmark body. The various configurations are obtained by varying the associated governing geometrical parameter for each modified model.
2. To exhibit the velocity contours foroptimumconfiguration of each geometrically modified model, focusing at the wake region of the body.
3. To portray pressure distribution over the entire body of optimum configuration for a particular geometrical modification of the benchmark model.

II. Literature Review

Han et al. (1992) **[3]** performed aerodynamic shape optimization on Ahmed body with three shape parameters: backlight angle (0º to 30º), boat tail angle (0º to 30º) and ramp angle (0º to 20º). The k-ε turbulence model CFD solver was coupled to an optimization routine. In this study, an analytic approximation function of the objective function (drag coefficient values from CFD analysis) was created in terms of the design variables. The optimization was then performed on this approximation function and optimum parameters were found. The CFD analysis was again performed with this optimum set of parameters and the objective function was updated with new results. This process was continued until the parameters for minimum drag were obtained. The optimization process revealed that the optimum rear body parameters are backlight angle of 17.8^0; boat-tail angle of 18.9^0; and ramp angle of 9.2^0.

Pujals et al. (2001) **[4]** experimentally investigated the potential of separation control strategy based on large-scale coherent streaks. These streaks are generated by means of an array of cylindrical roughness elements on a highly three-dimensional flow subject to an adverse pressure gradient due to geometrical constraints. The geometry chosen was Ahmed body with 25^0 rear slant at Reynolds number Re_L = 1.35 X 10^6. Various configurations of span-wise spacing and stream-wise locations on the roof were investigated and substantial drag reduction was obtained for all sets of wavelength and stream-wise locations. The overall maximum total drag reduction measured was about 10%. PIV as well as static pressure measurements on the slanted surface prove that the drag reduction is due to the suppression to the re-circulation bubble.

Englar and Robert (2001) **[5]** at Georgia Tech implemented pneumatic devices on heavy duty vehicles and conducted wind-tunnel investigations on a generic Heavy Vehicle model with blowing slots on both the leading and trailing edges of the trailer. The trailing edge was provided with a fixed curved surface and a tangential slot ejecting a jet sheet which remained attached to the curved surface by a balance between sub-ambient static pressure on the surface and centrifugal force. Drag coefficient reductions of as much as 50% were produced by blowing with internal pressures of only 1.0 psig; C_D values as low as 0.13 (an 84% drag reduction from the baseline Heavy Vehicle model) were measured at increased blowing rates.

Zunaid et al. (2014) **[6]** designed and implemented the curved boat tail configuration without the AFC device on a generic SUV design. The working principle of the add-on was based on the Coanda effect, causing the airflow over and under the SUV to take a curved path resulting in blowing of air in the immediate wake region. They investigated its effect on various aerodynamic parameters reporting an increase in the average pressure in wake region along with a significant drag reduction of 8.013 %.

Lamond et al. (2009) **[7]** conducted a preliminary investigation into the use of base bleed on a production SUV using CFD analysis.For the geometry studied, a bleed outlet applied to the upper portion was found to be most effective in reducing drag but there may be difficulty in implementation as bleeding air from a high pressure region towards the top would be difficult. It was found that bleed through the sides of the vehicle was also effective and this would allow venting from the sides, underside or roof The paper portrayed that the reduction in drag increased as the mass flow rate of air increased, when the flow was deflected at the outlet; a mass flow rate of under 1.5kg/s could reduce the drag coefficient by 10.7% for an outlet on the upper section of the rear of the vehicle.

Bahram et al. (2001) **[8]** experimented with a square back bluff body using tail and boat plate like add-on for drag reduction. The mean pressure results showed a significant increase in the base pressure with the drag reduction device and it also suppresses large-scale turbulent motions in the wake. The results also showed a reduction of the turbulence intensity as well as a rapid upward deflection of the underbody flow with the device in place and confirmed that the separated flow from the trailing edge of the model reattached on the extended plate (add-on device) which is similar to that of a boat-tail effect using the concept of Coanda effect **[9]** for drag reduction by up to 20%.

Al-Marzooqi et al. (2012) performed an experiment on Ahmed body to improve the aerodynamic efficiency of the SUV model which he used in his paper **[10]**. The add-on device in the form of lateral guide vanes were installed at the rear end of the SUV to direct the air flow into the low pressure wake region at the rear of the vehicle. This would improve the pressure recovery in the wake due to mass addition of the directed air, which in turn would reduce form drag and hence the overall drag of the box. The chord length of the guide vanes was taken as L/8, where L represents the length of the car box. The angle of attack of the lateral guide vanes was also subjected to various manipulations of angles and consequently, significant reduction in the drag coefficient up to 17% was noted.

Gustavsson and Melin (2006) **[11]** at KTH performed the experiments to find the advantages of the VGs when applied to blunt bodies. Wind tunnel was used to perform the simulation of the bluntbody with the VG located at the rear slant angle, behind the shoulder of the body.The dimensions of the main body were given as L=0.95m, W=0.50m and H=0.30m, with rear slant angle of 40 degree. There were two wind tunnel tests conducted by them. In the first test, the main objective was to determine the effectiveness of VGs at redirecting airflow which wassuccessfully confirmed after the test. The second wind tunnel test was conducted with the VGs placed before the rear slant angles in conjunction with a combination of boat tail angles of 20, 40, 60 and 90 degrees and different VG height and length were tested. The least drag coefficient of 0.4540 was obtained in the results.

III. Geometry Modifications Of Ahmed Body

3.1 Benchmark Model

The Ahmed body represents a simplified, ground vehicle geometry of a bluff body type. Its shape is simple enough to allow for accurate flow simulation but retains some important practical features relevant to automobile bodies. Ahmed body with the rear slant angle of 10 degree (as shown in fig-2) is selected as the benchmark model. Different modifications are carried out on this geometry of Ahmed body to obtain best suited configuration for minimum drag coefficient.

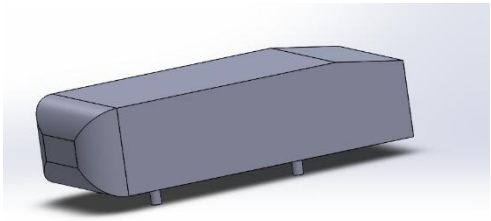


Fig. 2 – Ahmed body with rear slant angle 10 degree

3.2 Roof Panel Cambering

Roof cambering (as shown in fig-3) reduces drag due to air flowing past thesmooth curvature at the top of Ahmed body resulting in increased turbulence and thus, delayed boundary layer separation. Roof camber should not be increased at the expense of enlarging the frontal area as this would be counter-productive and would increase drag coefficient.

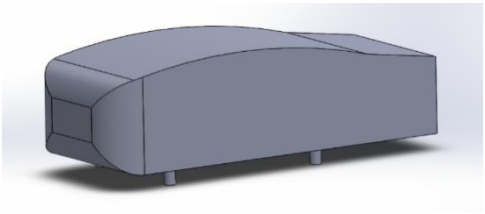


Fig.3 – Roof panel cambering

3.3 Side Panel Cambering

Side panel cambering (as shown in fig-4) results indrag reduction as a consequence of air flowing past the smoothcurvature at the side of Ahmed body, reducing the formation of vortices due to increased turbulence and thus, delayed boundary layer separation. As in case of roof camber, side camber also should not be increased at the expense of enlarging the frontal area as this would be counter-productive and would increase drag coefficient.

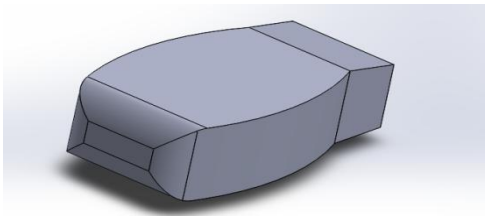


Fig.4– Side panel cambering

3.4 Underbody Rear End Upward Taper

Tilting the underbody rear end upwards (as shown in fig-5) produces a diffuser-like effect which gives a promising scope in reducing drag coefficient. However, it is important to select an optimum angle and ratio of length of taper for best results. Length of taper is taken same as upper body slant length i.e. 222mm.

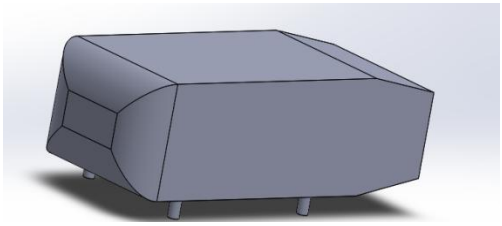


Fig.5– Underbody rear end upward taper

3.5 Rear Side Panel Taper

Tapering the rear side panel inwards (as shown in fig-6) reduces the drag coefficient due to reduced wake area at the rear. Taper is done on both sides equally with different magnitudes.

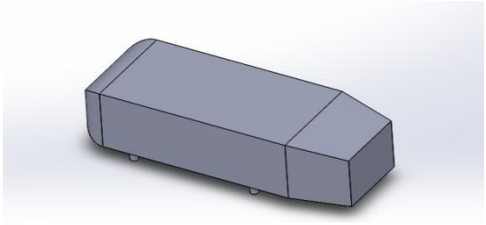


Fig.6– Rear side panel taper

3.6 Rear End Tail Extension

Reduced drag coefficient is obtained with increment in extension of the rear tail (as shown in fig-7) but this shape is inconvenient to accommodate from the perspective ofpractical application and aesthetic design considerations. Conversely, if the rear end tail is cropped at various lengths and curved downwards there is an increase in drag coefficient with each reduction in tail length beyond the rear wheels.

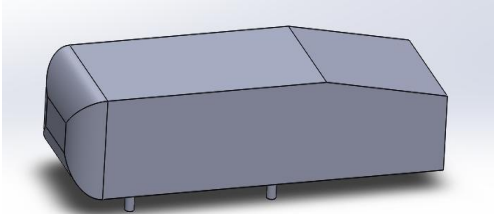


Fig.7– Rear end tail extension

3.7 Chamfered Nose

In this model, instead of using fillet on nose ofthe frontal surface of the Ahmed body, chamfering is done to 100mm (as shown in fig-8). However due to the sharp edges, boundary layer separation occurs and consequently drag coefficient increases.

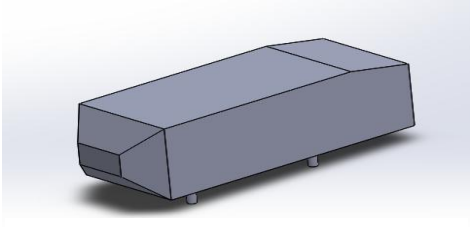


Fig.8– Frontal surface chamfered

IV. Numerical Simulation

The ANSYS Workbench platform is the framework upon which the industry's broadest and deepest suite of advanced engineering simulation technology is built. An innovative project schematic view ties together the entire simulation process, guiding the user through even complex multi-physics analysis with drag-and-drop simplicity. Firstly, Solid works file is attached into ANSYS Workbench. Next, an enclosure is created in which is air surrounding around body having dimensions 5m from front and 7.5m from rear in the 'Design Modeller' in ANSYS. Then, the body is subtracted from air to create single body domain. This subtracted body represent Ahmed body walls around the surrounding air.

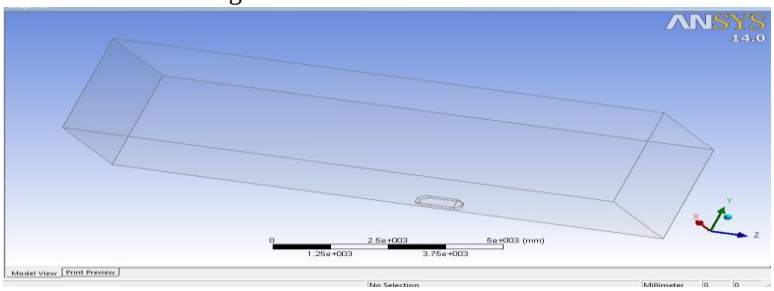


Fig. 9 – Air enclosure in design modeller

4.1 Meshing

The name "Finite Element Method" is meant to suggest the technique we apply to all problems. It means that looking at the geometry, the shape of a region, and immediately imagines it broken down into smaller sub-regions. The idea is that we are going to use a simple approximation method, but the errors in this approximation method become unnoticeable as the size of the sub-region gets smaller. So if we use enough small sub-regions, approximated over each one, and then stitch all the answers back together, we can get as smooth and realizable an answer to our original full size problem, as we want. Meshing was carried out in ANSYS meshing tool and the following specifications were used:

Relevance center: coarse, smoothing: high, Transition: slow, Initisal size seed: Active assembly, Min. size: 1mm, Max. Size: 250mm, Advanced Size functions: Proximity and Curvature.

4.2 Modifications In Meshing

Element size on Ahmed body walls and rollers are still too large but the size of domain air surrounding is good. So, some modifications on Ahmed body were done for getting better result in our analyses, which are explained as follows:

- Roller Sizing- The size of roller meshing is limited to 2mm.
- Face Sizing- The size of faces meshing is limited to 10mm.

4.2.1 Inflation Layer

Often, the velocity and temperature gradients normal to a wall is typically much larger than the gradients parallel to the wall. The inflation layer controlis designed to create thin elements that can capture the normal gradient with minimal elements; use of inflation layers is done to correctly capture the velocity and temperature gradients near no-slip walls.

Program controlled inflation (as shown in fig-10, 11) with First aspect ratio of 5, growth rate of 20% of 5 layers with 10 smoothing iterations was done **[12]**.

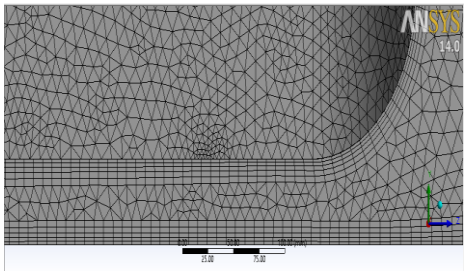


Fig. 10- Prism layer growth front view

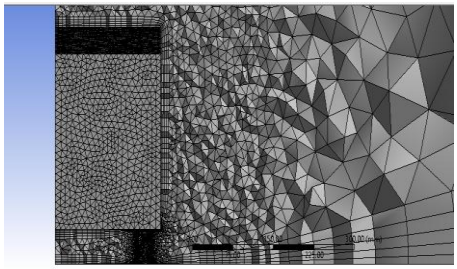


Fig. 11- Prism layer growth sectional view

4.2.2 Limit Size Boxes

3 different volumetric boxes (as shown in fig-12) were created around the model so that the meshing size can be limited there, as it gives better control on the result and analysis.

Size of mesh is about 10mm at 40m/sec.

1. **Car Box:** A box around the body was created and its sizing was limited to 15mm.
2. **Wake Box:** It is done to limit the size at the wake region of the body to 10mm to capture the wake velocity contours more accurately.
3. **Under box:** It is done to limit the size of mesh under the body to 10mm.

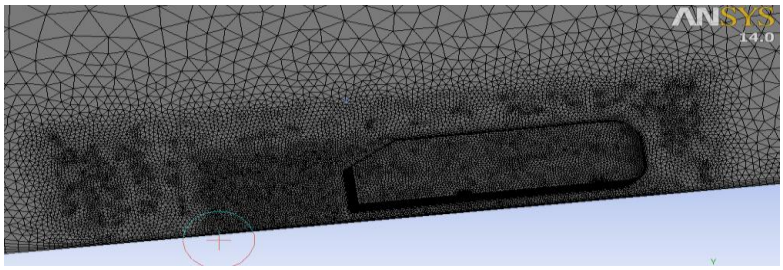


Fig. 12- Meshing of our body

4.3 Steady Flow Numerical Simulation

Computational resources for the steady flow numerical simulations are done on Dell work station (1 CPU 1.8 GHz and 8GB RAM) and Windows 8 OS. Realizable k-epsilon model non-equilibrium wall function is used with Inlet velocity V = 40m/s, turbulence intensity at inlet is about 1% and turbulence viscosity ratio is 10 at inlet,turbulence intensity is about 5% and turbulence viscosity ratio is 10 at outlet. Density of air is 1.225 kg/m^3, temperature is 288.16 K and viscosity is $1.7894e^{-05}$ kg/m^4. Boundary conditions are - uniform velocity at inlet, uniform pressure at outlet, symmetry at lateral and at top wall of the model and moving wall at floor.

Solution method utilizes pressure-velocity coupling scheme as coupled with gradient: least square cell based method, pressure as standard and with momentum. Turbulence kinetic energy, turbulence dissipation rate as first order upwind for the initial 100 iterations and correspondingly as second order upwind for the next 500 iterations. Moreover, turbulence viscosity factor is taken as 0.8 for the initial 100 iterations and consequently taken as 0.95 for the remaining 500 iterations.

Analysis of numerous configurations of multifarious modifications of the benchmark model of Ahmed body with 10 degree rear slant angle iscarried out on ANSYS Workbench. Roof and Side cambering is done at 5 varied H/L ratioseach, ranging from 0.02 to 1.00 with an increment of 0.02 where H is the height of camber and L is the lengthsubjected to cambering. Underbody rear end upward taper is implemented at 4 different taper angles ranging from 5 to 20 degree with an increment of 5 degree. Rear side panel taper is carried out on 3 different lengths of taper of 50, 100 & 150mm. Rear end tail extension are carried out on 3 extensions of 180,360 & 540mm.Chamfered nose is done at 100mm nose length. Therefore, a cumulative total of 22 analyses have been carried out including that of benchmark model of Ahmed body.

V. CFD Simulation Results

5.1 Pressure Distribution

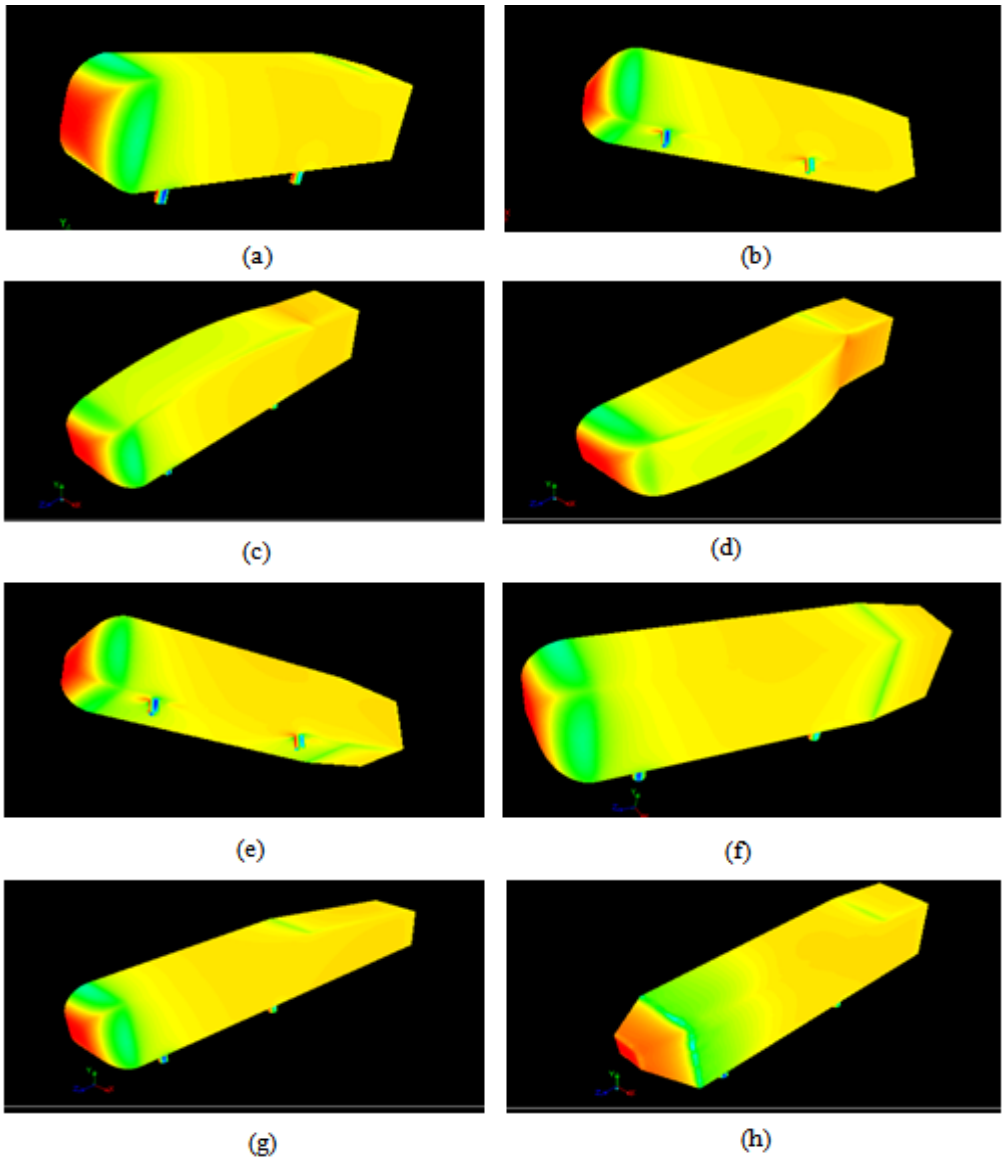


Fig. 13- Pressure distribution: (a) Benchmark model (Frontal view), (b) Benchmark model (Underbody view), (c) Roof panel cambering, (d) Side panel cambering, (e) Underbody read end upward taper, (f) Rear side panel taper, (g) Rear end tail extension, (h) Frontal area chamfered,

The pressure distribution gives us the pressure of air over the various surfaces on the geometry of the model. The red, yellow and green areas depict regions of high, medium and low pressure respectively.The air becomes almost stagnant as it strikes the vehicle which results in air exerting very high pressure on front engine grill of the vehicle represented by the red area. The airflow then gets divided between the upper and lower surface of the vehicle. The higher pressure air on front surface accelerates as it travels over the curved nose surface of Ahmed body, causing the pressure to drop. This lower pressure creates lifts over the roof surface as the air passes over it. As the air continues to flow and make its way to the rear, a notch is created by the rear slant owing to flow separation, leaving a vacuum or low pressure space which the air is not able to fill properly. The resulting lower pressure creates lift which then acts upon the surface of the rear slant.

For the multifarious modifications, the pressure distribution is explained as follows:

- Benchmark model ((Frontal & Underbody view)- As shown in fig-13(a)&(b),the pressure distribution of the benchmark model features high pressure (red) region on the frontal surface, followed by transition to a narrow region of low pressure (green) around the edges of the frontal surface which finally merges into medium pressure (yellow) region which that encompasses the entire surface of the roof, underbody and side panels.
- Roof panel cambering- As shown in fig-13(c), it is observed that the pressure on roof panel decreases as compared to that of the benchmark model on the overall surface of camber with the surface turning comparatively green (from yellow), indicating lower pressure with respect to the benchmark model.
- Side panel cambering- A similar trend is observed with pressure on side panels being lower(even than that on the roof) on the overall surface of camber than that on theside panels of the benchmark model, as exhibited in fig-13(d).
- Underbody read end upward taper-The rear end upward taper model has lower pressure on the onsetoftaper and at the rear end, functioning to reduce the drag at the through pressure recovery, owing to diffuser-like action as is evident in fig-13(e).
- Rear side panel taper-For the case of rear side panel taper, there is slight decrease in pressure at the onset of taper of side panelsas is apparent in fig-13(f), and consequently, at the rear end.
- Rear end tail extension-There is no marked change in pressure distribution of rear tail extension model as shown in fig-13(g), because the modification is in the form of continuation of existing geometry and no alteration in contour.
- Frontal area chamfered-High pressure acts on the entirety of the nose of the Ahmed body as evident by the expanse of red color on theentire frontal surface, as exhibited in fig-13(h).

5.2 Velocity Contours

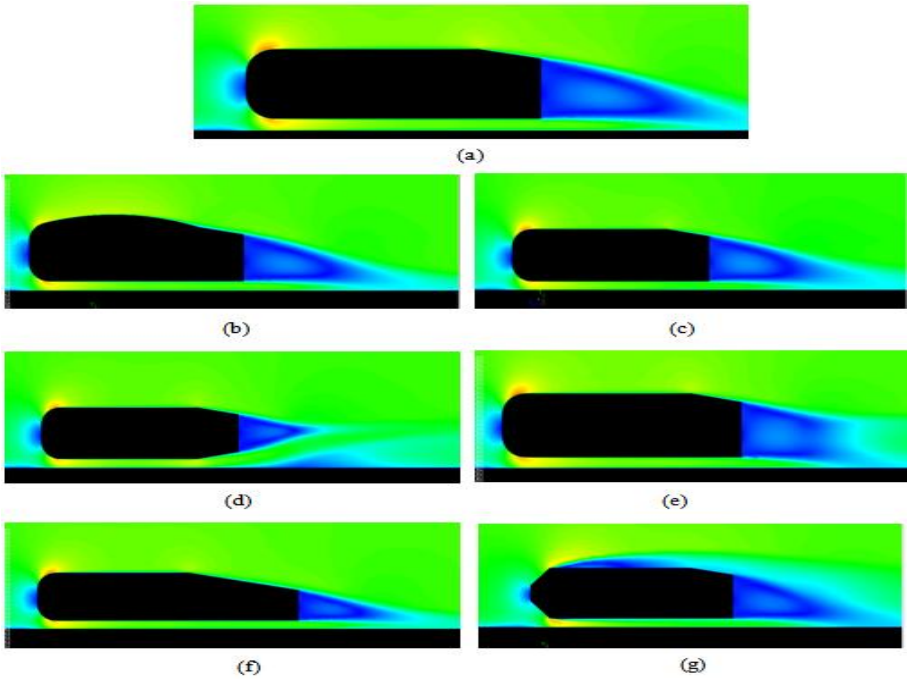


Fig. 14- Velocity contours: (a) Benchmark model (Side view), (b) Roof panel cambering, (c) Side panel cambering, (d) Underbody read end upward taper, (e) Rear side panel taper, (f) Rear end tail extension, (g) Frontal area chamfered

Velocity contours gives us the velocity of air along different geometry sections of the Ahmed body. The green area corresponds to the velocity 40m/sec, while blue area shows low velocity region and red, yellow area gives high velocity region. The velocity contours extending behind the body indicate the low velocity wake region, which causes the form drag. As the wake area is reduced, the drag-causing eddies (vortices), generated due to the pressure difference between the top and bottom of the Ahmed body at the rear trailing end, come closer together. This result in less kinetic energy being dissipated due to these smaller eddies and consequently less compensation power required by the engine to propel the vehicle forward. It additionally results in higher pressure being applied at the rear surface of the body and consequently less form drag.

For the multifarious modifications, the velocity contours are explained as follows:

- Benchmark model- The benchmark model is characterized by a wide tail of low velocity at the rear originating from the trailing edge of the slant - wake region, as can be observed in fig-14(a). Also, low velocity air at the center of the frontal surface, and high velocity of air at the edges of the frontal surface is witnessed in this case.
- Roof panel cambering- In case of roof panel cambering, a lower velocity is exhibited at the onset of camber on the roofas shown in fig-14(b),and no marked departure in the wake region is observed from that of the benchmark model.
- Side panel cambering- For the side cambering model, a similar trend is observed in the wake region but with the difference of lower velocity occurring along the side panels but remaining the same along the roof as in case of the benchmark model, being evident in fig-14(c).
- Underbody read end upward taper-The rear end upward taper has a comparatively narrow (pointed) wake area at the rear as a result of comparatively higher velocity on the underbody, owing to the geometrical modification, as exhibited in fig-14(d).
- Rear side panel taper-For the case of rear side panel taper, there is a similar reduction in wake area but this time along its width accounting for the wake region ending prematurely along the length than that in case of benchmark model, ascan be observed in fig-14(e).
- Rear end tail extension-There is a decrease in rear height for the case of rear tail extension due to modification in the geometry, resulting in decrease of rear wake area as can be seen in fig-14(f).
- Frontal area chamfered- Finally, for the chamfered nose model, low velocity due to boundary layer separation at the edge of the nose on frontal surface of the Ahmed body, continuing throughout the length on the roof of the body and also significantly large wake area is evident in fig-14(g).

VI. Results

The analyses of the 22 multifarious models carried out yield optimum configurations for each geometrical modification of the benchmark model – Ahmed body having 10 degree rear slant angle. The values of the aerodynamic parameters obtained for the benchmark model are- Coefficient of drag (C_d) = 0.238 and the coefficient of lift (C_l) = 0.0848**[2]**. For all the configurations for a particular modification (obtained by varying the associated geometrical parameter),the drag and lift coefficients are plotted and examined to determine the optimum configuration resulting in least drag and lift coefficients. Furthermore, the underlying root causes are also analysed, comprehended and listed.

6.1 Roof Camber

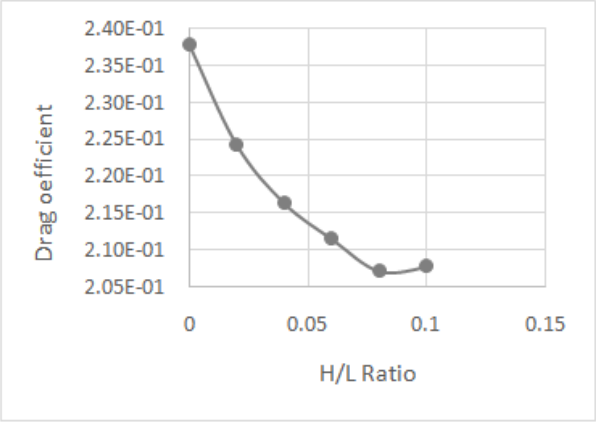


Fig. 15- Roof camber: Drag vs. H/L ratio

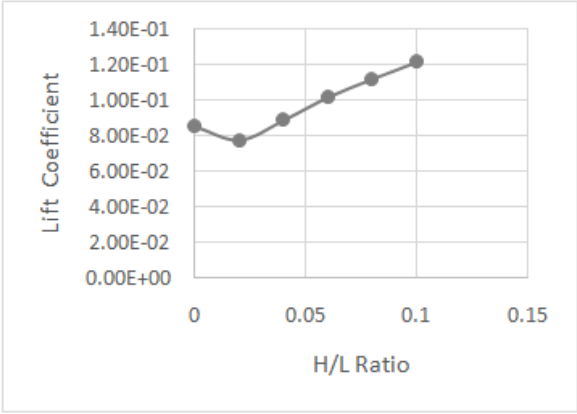


Fig. 16- Roof camber: Lift vs. H/L ratio

- Roof camber having H/L ratio of 0.08 gives least drag configuration (as shown in fig-15) for this modification due to delayed boundary layer separation and thereafter, drag starts to increase again. This increase is due to increase of roof camber at the expense of enlarging the frontal area and this turns out to be counter-productive.
- Roof camber having H/L ratio of 0.02 gives least lift configuration (as shown in fig-16) for this modification and thereafter, it starts to increase continually due to reduction in pressure over the round curvature of roof.

6.2 Side Camber

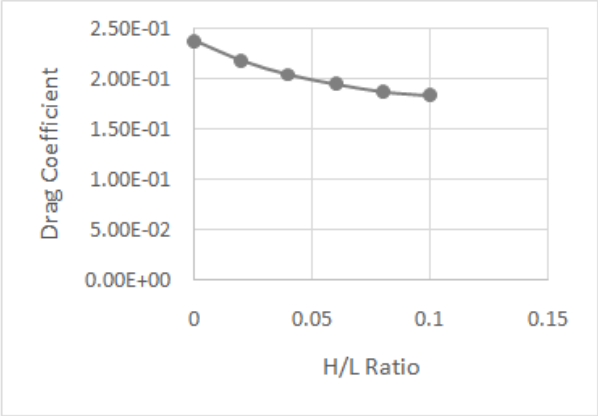


Fig. 17- Side camber: Drag vs. H/L ratio

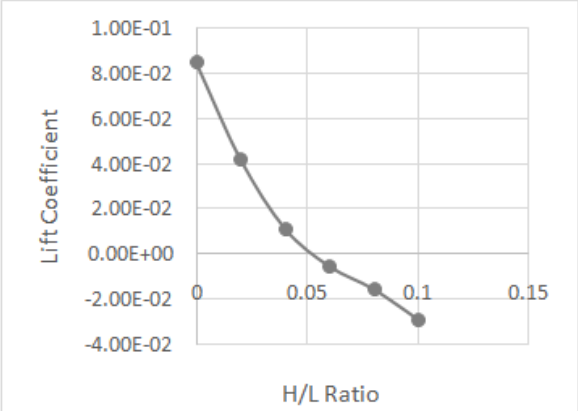


Fig. 18- Side camber: Lift vs. H/L ratio

- Drag coefficient is decreasing with increase in H/L ratio (as exhibited in fig-17) due to delayed boundary layer separation. However, with even further increase in H/L ratio, camber increase occurs at the expense of enlarging the frontal area and this turns out to be counter-productive, same as in the case of roof camber.
- Lift coefficient keeps on continually decreasing with increase in H/L ratio (as exhibited in in fig-18) due to reduction in pressure over the round curvature on the side panels of the Ahmed Body resulting in generation of downforce.

6.3underbody Rear End Upward Taper

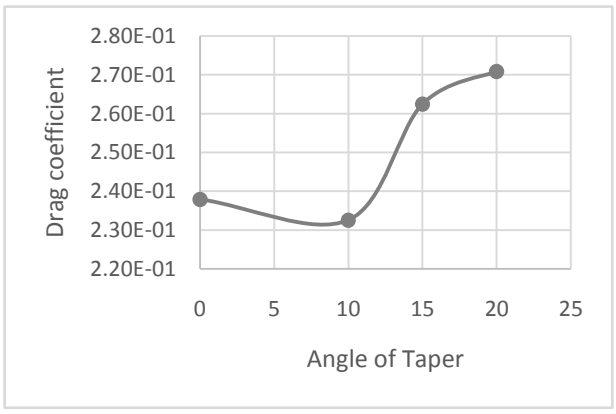


Fig. 19- Underbody Rear End Upward Taper: Drag vs. Angle

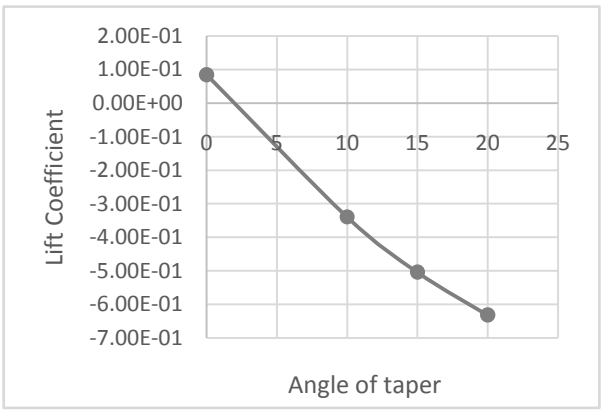


Fig. 20- Underbody Rear End Upward Taper: Lift vs. angle

- Least Drag coefficient obtained at angle of 10 degree (as portrayed in fig-19) for the rear end upward taper due to the smaller wake region formed. However, with further increase in angle, drag coefficient increases as it give rise to boundary layer separation at steep inclined rear underbody taper panel.
- Lift is continually decreasing with increase in angle of taper (as portrayed in fig-20) due to the increase in velocity under the body at rear end which give rise to low pressure formation, consequently resulting generation of downward force.

6.4 Rear Side Panel Taper

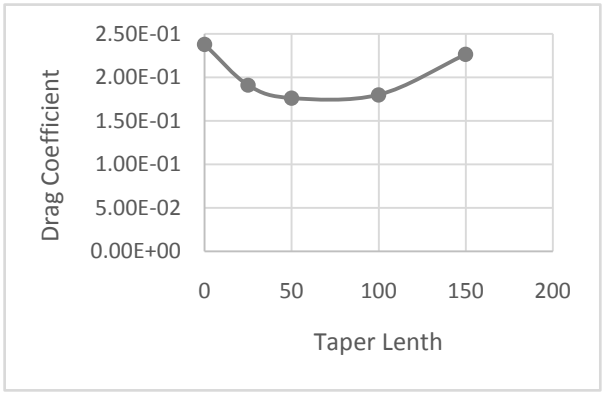


Fig. 21- Rear Side Panel: Drag vs. Taper length

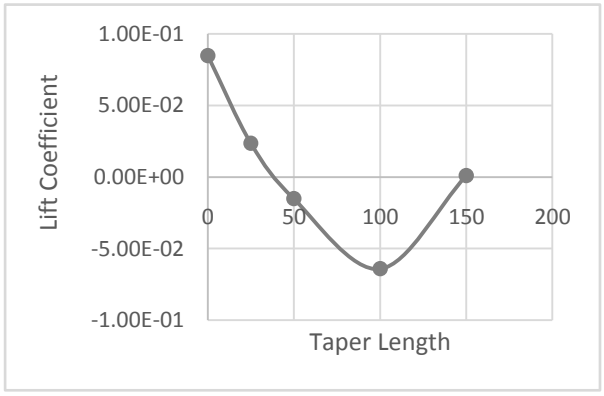


Fig. 22- Rear Side Panel: Lift vs. Taper length

- With rear side panel taper till 50 mm, a marked reduction in drag coefficient is observed (as is evident in fig-21) due to reduction in wake area at the rear end. There is negligible change between taper of 50 - 100mm, and thereafter it starts to increase significantly due to flow separation owing to steep incline of rear panel taper.
- Rear side panel of 100mm gives least lift configuration for this modification (as is evident in fig-22) and thereafter, it starts to increase.

6.5 Rear End Tail Extension

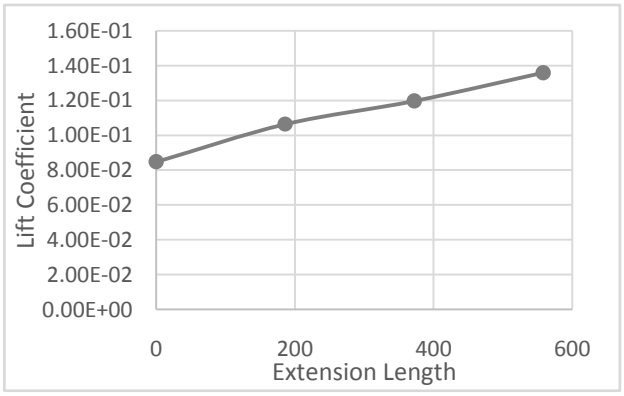


Fig. 23- Rear End Tail Extension: Drag vs. Extension length

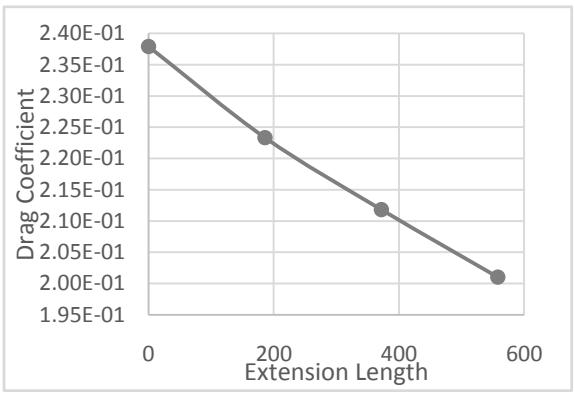


Fig. 24- Rear End Tail Extension: Lift vs. Extension length

- Drag coefficient is decreasing with increasing rear extension (as seen in fig-23) due to reduction in wake region but this shape is practically inconvenient and impractical from design considerations. Conversely if the rear end tail is cropped at various lengths and curved downwards there is an increase in drag coefficient with each reduction in tail length beyond the rear wheels.
- Lift is continually increasing with increasing rear extension (as seen in fig-24) due to increase in velocity and consequent reduction in pressure on the roof owing to larger dimension of surface over which the area flows.

6.6 Chamfered Nose

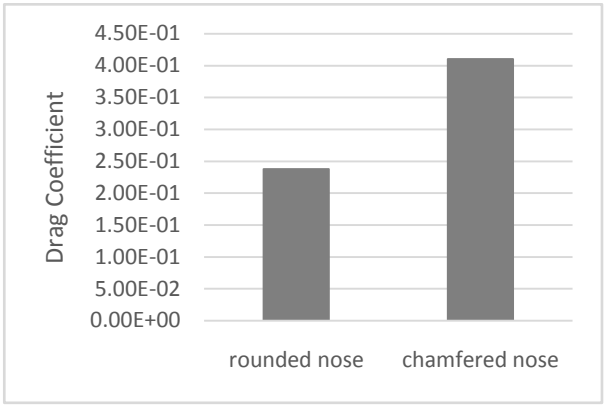


Fig. 25- Chamfered vs. Rounded nose (drag)

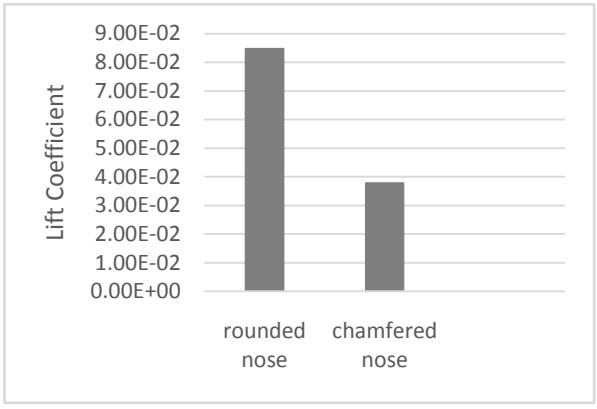


Fig. 26- Chamfered vs. Rounded nose (lift)

- Drag coefficient is increasing in chamfered nose model, as shown in fig-25, as compared to rounded nose (benchmark) model due to boundary layer separation occurring at the sharp edges.
- Lift is decreasing in chamfered nose model as compared to rounded nose(benchmark) model, as shown in fig-26,due to flow of air over the roof at the high velocity which results in low pressure and generation of upward force.

VII. Conclusion

CFD results for multifarious variants of modifications of Ahmed Body with rear slant angle 10 degree are presented after carrying out their design, development and subsequent analysis.Thereafter, comparison and examination of variants of a particular modification is done to establish the effectiveness of each variant. The following conclusions can be drawn from the results:

1. Coefficient of drag (C_d) of **benchmark model** - **Ahmed Body with 10 degree rear slant angle** - is obtained as 0.238 and the coefficient of lift (C_l) as 0.0848.
2. The optimum configuration of **roof camber** modification for least drag is obtained with **H/L ratio of 0.08** resulting in C_d of 0.20705, which implies **reduction of 13%** and resulting in C_l of 0.112.
3. The optimum configuration of **side camber** modification for least drag is obtained with **H/L ratio of 0.10** resulting in C_d of 0.184, which implies **drag reduction of 22.7%** and resulting in C_l of -0.02904, which implies **lift reduction of 134%.**
4. The optimum configuration of **underbody rear end upward taper** modification for least drag is obtained with **angle of 10 degree** resulting in C_d of 0.2326, which implies **drag reduction of 2.27%** and resulting in C_l of -0.339, which implies **lift reduction of 499.7%**.
5. The optimum configuration of **rear side panel taper** modification for least drag is obtained with **taper of 50mm** resulting in C_d of 0.1761, which implies **drag reduction of 26%** and resulting in C_l of -0.0152, which implies **liftreduction of 117.9%**.
6. The feasible configuration of **rear end tail extension** for reducing drag is obtained with **extension of 186mm** resulting in C_d of 0.2233, which implies **drag reduction of 6.18%** and resulting in C_l of 0.1064. The drag goes on continually decreasing with increase in extension dimension but, it becomes practically infeasible to apply.
7. The configuration of **chamfered nose** modification, instead of fillet results in C_d of 0.4102, which implies **drag increase of 72%** and resulting in C_l of 0.03781.

Therefore, the optimum configurations for least drag and lift coefficients, corresponding to each modification of the geometry of the benchmark model are obtained enhancing the aerodynamic behaviour and consequently, the efficiency of the automobile. Future scope for application of these results include coupling of numerous feasible complementarymodifications together or coupling with suitable active and passive drag reducing devices (add-ons) to further boost the efficiency of the automobile.

References

[1] S. R. Ahmed, G. Ramm, G. Faitin, 'Some Salient Features of the Time – Averaged Ground Vehicle Wake', (SAE-TP-840300) Society of Automotive Engineers, Inc., Warrendale, PA, 1984.

[2] Saurabh Banga, Md. Zunaid, Naushad Ahmad Ansari, Sagar Sharma, Rohit Singh Dungriyal, 'CFD Simulation of Flow around External Vehicle: Ahmed Body'DOI: 10.9790/1684-12438794, IOSR Journal of Mechanical and Civil Engineering (IOSR-JMCE).

[3] T. Han, D. C. Hammond, C. J. Sagi, 'Optimization of bluff body for minimum Drag in ground proximity', AIAA Journal, Vol. 30, No. 4, pp. 882-889, doi: 10.2514/3.11005, 1992.

[4] G. Pujals, S. Depardon, C. Cossu,'Drag reduction of a 3D bluff body using coherent stream wise streaks', Springer, Exp Fluids (2010) 49:1085–1094, DOI 10.1007/s00348-010-0857-5, 2010.

[5] Robert J. Englar, 'Advanced Aerodynamic Devices to Improve the Performance, Economics, Handling and Safety of Heavy Vehicles', SAE 2001-01-2072, Georgia Tech Research Institute Aerospace Transportation & Advanced Systems Lab, 2001.

[6] Shubham Singh, M. Zunaid, Naushad Ahmad Ansari, Shikha Bahirani, Sumit Dhall, Sandeep Kumar, 'Numerical Study of the Generic Sports Utility Vehicle Design with a Drag Reduction Add-On Device', Hindawi Publishing Corporation Journal of Computational Engineering Article ID 785294, Volume 2014.

[7] A. Lamond, J. J. Kennedy, M. T. Stickland, 'An investigation into unsteady base bleed for drag reduction in bluff two box SUV's', Proceedings of the 4th European Automotive Simulation Conference (EASC'09), Munich, Germany, 2009.

[8] K. Bahram, S. Zhang, C. Koromilas, 'Experimental and computational study of unsteady wake flow behind a bluff body with a drag reduction device', SAE2001-01B-207, 2001.

[9] M. H. Coanda, "Propelling device," French Patent no. 796843, 1936.

[10] E.M. Wahba., H. Al-Marzooqi, M. Shaath, M. Shahin, T. El-Dhmashawy, 'Aerodynamic Drag Reduction for Ground Vehicles using Lateral Guide Vanes', CFD Letters, vol.4, no.2, pp.68–79, 2012.

[11] T. Gustavsson and T. Melin, 'Application of Vortex generators to a blunt body', Technical Report KTH, Department of Aeronautical and Vehicle Engineering, Royal Institute of Technology, Stockholm,Sweden,2006.

[12] Marco Lanfrit,'Best practice guidelines for handlingAutomotive External Aerodynamics with FLUENT', Version 1.2 (Feb 9th 2005), Fluent Deutschland Gmbh Birkenweg 14a 64295 Darmstadt/Germany.

Clean Development Mechanism in India

Abhishek Pandey, Abhinav Jain
Department of Environmental Engineering
Delhi Technological University

ABSTRACT

Climate change due to global warming is one of the most difficult and important challenges the whole international community is facing. The United Nations responded to this problem by organizing first World Climate Conference in 1979. Subsequently in 1988 Intergovernmental Panel on Climate Change (IPCC) was established. UN Framework of Convention on Climate Change (UNFCC) was signed in 1992 Rio summit making Conference of Parties (COP) Convention's ultimate authority. The Kyoto Protocol was adopted at COP-3 in 1997. The Protocol defines quantified greenhouse gases emissions reduction targets for Annex I Parties in UNFCC. The CDM is one of the market-based solutions for achieving these reduction targets. The CDM endowed developing nations to participate by selling emissions credits, termed as "certified emissions reductions" (CERs), to other nations with obligations to reduce their emissions.

The Clean Development Mechanism was created with three main goals. First, it aims to accomplish the overwhelming goals of the Convention. Second, it aims to promote sustainable development in Non-Annex I nations. Lastly, it intends to reduce the cost of compliance with the Protocol for Annex-1 nations. India is second in using this mechanism just after China. This paper shows how CDM projects are distributed in different sectors and states of India. The analysis shows states like Gujarat and Maharashtra have most number of CDM projects. The analysis also reveals that almost 78% of these projects are in the energy industries. The paper also recommends some future approaches that might increase the efficiency of this technique.

Keywords: Clean development mechanism, Kyoto protocol, Certified emission reductions.

1. INTRODUCTION

The late 1980s saw rising concerns over the changing patterns of climate among environmental scholars. The Intergovernmental Panel on Climate Change (IPCC) reported in 1990 that emissions resulting from humans' household activities contributed largely to the atmospheric concentration of greenhouse gas, which would generally lead to the warming up of the Earth's surface .The Kyoto Protocol of 1997 was the first response by international community to this problem**.** In order to make the targets legally binding, at least 55 countries among 185 signatories to the UN Framework

Convention on Climate Change (UNFCCC) have to ratify the Protocol. In addition, these must include industrialised countries (Annex I Parties to UNFCCC) accounting for 55 per cent of that group's carbon dioxide emissions in 1990. After Russia ratified the Kyoto Protocol, it came into effect in 16th february2005.The Kyoto Protocol set binding targets for the Annex I countries, 37 developed nations and the European community, to reduce their greenhouse gas emissions by around 5.2 percent from the level of 1990 within the time limit of 2012 .

The protocol gave three innovative mechanisms Joint Implementation (JI), the Clean Development Mechanism (CDM) and International Emission Trading , to boost the cost effectiveness of climate change mitigation by opening ways for parties to cut their emission.

2. CLEAN DEVELOPMENT MECHANISM

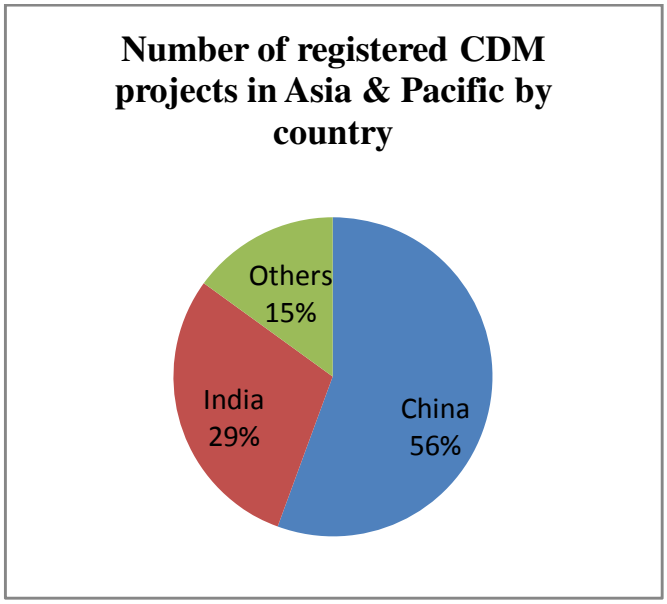
CDM is one of the mechanism stated under the Kyoto Protocol. It has two main purposes first to assist developing countries in achieving sustainable development, thereby contributing to the ultimate objective of the Convention, and secondly to assist developed country Parties in achieving compliance with part of their quantified emission limitation and reduction commitments under Article 3 of Kyoto Protocol.

The major steps in CDM Project Cycle are,

- Submission of the Project Design Document (PDD) to the National CDM Authority (NCDMA);
- Project registration in the host country;
- Project validation and registration by the Executive Board (EB) of the UNFCCC;
- Project monitoring by the host country;
- Verification and certification of the project;
- Issuance of Certified Emission Reductions (CERs)

3. CDM IN INDIA

There are around 8740 CDM projects in the world, of which 7126 are in the Asia and Pacific region. India belong in this Asia and Pacific region. India is one of the world's largest hosts of such clean development projects. India have around one-quarter of the global total – had been registered with India's Designated National Authority for the Clean Development Mechanism. Only China hosts more such projects than India.



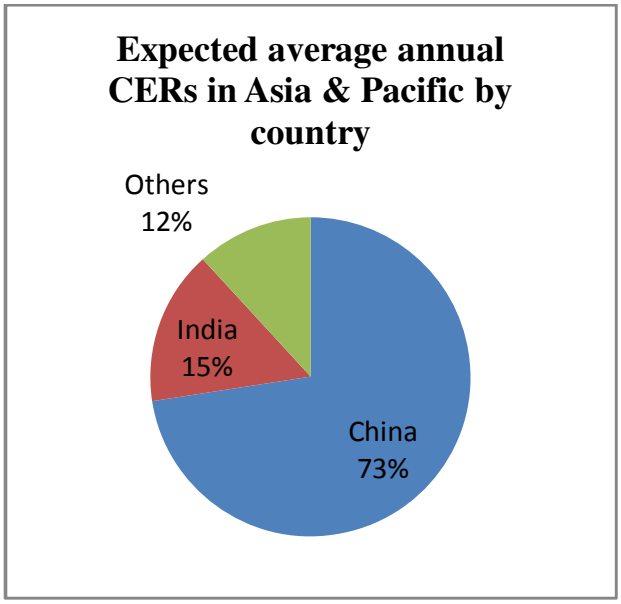


Figure 1 **Figure 2**

Figure 1 shows the percentage of CDM projects India and China have in Asia-Pacific region. India accounts for 29% of the total projects.

Figure 2 shows the number of Certified emission reductions (CERs) issued till 2012 (till first commitment period) in Asia-Pacific region. Around three quarters of CERs were issued to China. India had only 15% share in the total CERs issued.

Total number of CDM projects registered with the National CDM authority till march 2014 are 2857, out of which 676 are large scale projects and 2179 are small scale projects. Table 1 shows the distribution of these projects across different sectors in India.

Table 1

Afforestation and Reforestation	18
Agriculture	3
Chemical Industries	18
Energy Demand	222
Energy Distribution	9
Energy industries(Renewable/Non-renewable sources)	2248
Fugitive emissions from fuel(Solid, Oil and gas)	3
Fugitive emissions from production and consumption of halocarbons and sulphur	6

Manufacturing Industries	237
Metal Production	5
Mining/Mineral Production	4
Solvent use	1
Transport	13
Waste handling and disposal	70
Total (No. of Projects)	**2857**

Currently there are 207 approved methodologies on different sectors with UNFCC which help the people starting their projects.

Some of the CDM projects in operation in India are

- Wind Power based electricity generation in Gujarat, India
- Methane Extraction and fuel Conservation Project, TNPL, Kagitapuram, Tamil Nadu
- Model Project for increasing the efficient use of Energy using a Coke Dry Quenching system at TISCO Jamshedpur, Jharkhand
- Araku Valley Livelihood Project, Andhra Pradesh
- Expansion of Nature and Waste Bhalaswa Composting Plant, Delhi

There are 26 central government projects and 43 state or local government projects in India.

The distribution of these projects between different states of India are shown in Figure 3.

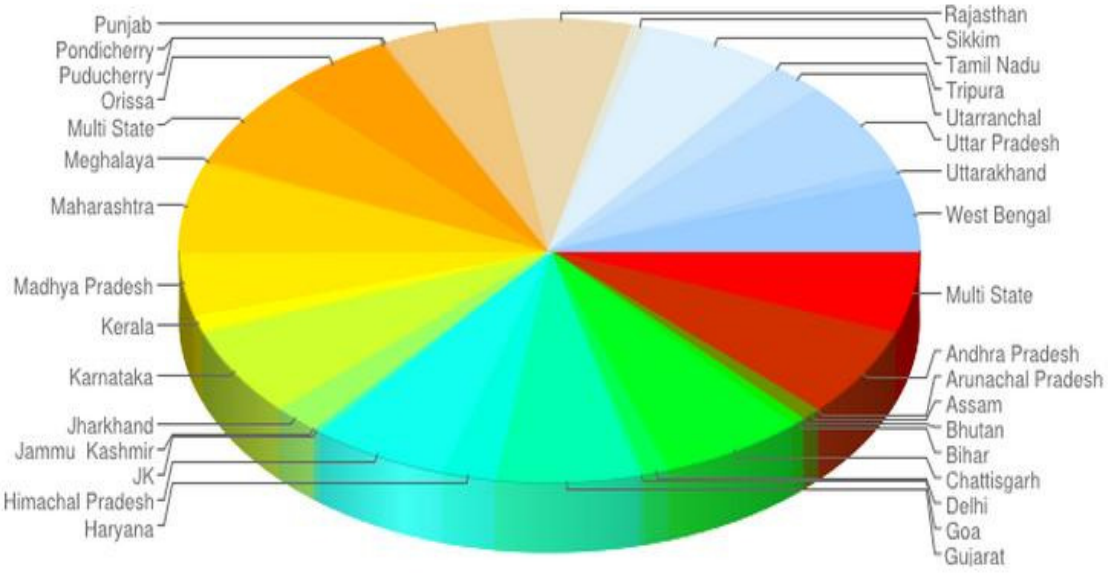


Figure 3

The distribution of CDM projects in India shows the presence of high number of such projects in industrialised states like Maharashtra and Gujarat.

4. INDICATORS OF PROGRESS OF CDM IN INDIA

Total annual reduction expected by the CDM project in India were 229730 Kt CO_2 and the green house gases (GHGs) emission 1523 Mt CO_2.

No. of projects per national carbon emissions in Million tons $C0_2$ for India is 1.37.

Investment capability (No. of CDM projects/GDP) for India is 1.31, which is more than double of the Asia and Pacific region (0.66) and even higher than that of China (0.89).

CDM contribution to the Indian economy (Annual CERs/GDP) is 143.77 tCO_2/ Million US dollars.

The most Important indicator is the actual emission reductions. It is percentage of country emissions covered by estimated CERs. It is 15.1%, which is more than the region average of 8.2 %.

5. HOW TO IMPROVE CURRENT PROCESS?

CDM has proved its worth by surviving after 2012 and has to play a key function in a future international climate regime. But certain area of the process need reforms to make it more effective.

Actions to reduce delays in project registration and certification by streamlining the administrative process and improving the existing methodologies.

Wider implementation of PoAs (Programme of Activities) should be facilitated both by the executive board and potential host countries, as this option potentially enhances the efficiency of the CDM and offers more opportunities for small and low-income developing countries to access the CDM.

The criteria for CDM approval could be expanded to allow for a “policy CDM”, allowing the focus to shift from towards climate mitigation and adaptation actions in developing countries.

We could create a global point system for different types of development aspects of CDM projects. More points could be allotted to the most desirable projects, but all projects would have to reach a minimum number of points for sustainable development benefits to be accepted. Certain parts could be made mandatory if they were considered too important to be left out.

The CDM should be used to encourage developing country engagement under a new proposed financing framework for nationally appropriate mitigation actions. This is likely easier to negotiate in tandem with an expanded CDM than by merely requesting developing countries to take on explicit emissions caps for the short and medium term.[3]

A more vigilant monitoring system should be in place by the host countries to ensure the qualities of CDM projects throughout their crediting period.[4]

One of the disheartening outcomes of CDM has been its low effectiveness. A more radical approach would be to reduce the quantity of CERs issued from projects which have little impact on sustainable development. However identifying such projects could be debatable between different parties.

6. CONCLUSIONS

Analysis clearly show that the share of CDM projects in India in Energy Industries is very high. While in sectors like afforestation and transport are very low. The number projects in Industrialised states like Gujarat and Maharashtra are very high in comparison to less industrialised ones. Reforms are needed to extend this type of projects to less industrialised states. To improve the CDM's contribution to sustainable development in India, the Government of India should consider investing in capacity building in those less developed states that are implementing few CDM projects relative to their population, such as Bihar and Uttar Pradesh.

The CDM in its current form has not realized sustainable development benefits envisaged at the time of its creation. By facilitating investments in the Clean Development Mechanism in the areas that need them the most, the Indian government could reap the double benefit of climate mitigation and economic development. However one should not lose the focus from the actual goal of Kyoto

Protocol, which is not limited to the number of CERs produced but to reduce the emissions through the path of sustainable development.

REFERENCES

[1] Information on cdmindia.gov.in

[2] Report on CDM pipeline overview from cdmpipeline.org

[3] Nguyen, Nhan T.; Minh Ha-Duong; Sandra Greiner et al. 2010: "*Improving the Clean Development Mechanism Post-2012: A Developing Country Perspective*". Carbon & Climate Law Review, Vol. 4, Issue 1, 76.

[4] Emily Boyd; Nate Hultman; J. Timmons Roberts; Esteve Corbera; John Cole; Alex Bozmoski; Johannes Ebeling; Robert Tippman; Philip Mann; Katrina Brown; Diana M. Liverman , *Reforming the CDM for sustainable development: lessons learned and policy futures*, Environmental Science & Policy,2009 vol. 7 issue 7

[5] *National Strategy Study of CDM in India ,* available on www.teriin.org/nss

[6] Johannes Urpelainen ,*The Clean Development Mechanism in India – is it working?*

IOSR Journal of Electrical and Electronics Engineering (IOSR-JEEE)
e-ISSN: 2278-1676,p-ISSN: 2320-3331, Volume 10, Issue 4 Ver. III (July – Aug. 2015), PP 98-104
www.iosrjournals.org

Constant Torque Operation of Wound Rotor Induction Motor using feedback mechanism in a Rectifier Fed Induction Motor Drive

[1]Anmol Aggarwal, [2]JN Rai, [3]Maulik Kandpal
[1,2,3]*Department of Electrical Engineering, Delhi Technological University (Formerly Delhi College of Engineering)*

Abstract: *This paper sets forth a technique to operate wound rotor induction motor in maximum torque region, using a feedback mechanism using rotor speed and slip.Static rotor resistance control has been used to vary the rotor resistance. The AC output voltage of motor is rectified by a diode bridge and is fed to a parallel combination of IGBT and external resistance. Effective value of rotor resistance is varied by varying the duty cycle of IGBT. Simulation models has been prepared in MATLAB in which a constant maximum torque is generated from standstill(s=1) to* $s_{Tmax}(=0.415)$.

Keywords: *Wound rotor induction motor,diode, IGBT, rotor speed, slip, MATLAB*

I. Introduction

Wound rotor induction motor is of pivotal importance when high staring torque is required and when the driven load requires precise speed control. The doubly-fed induction generator (DFIG) used in onshore wind turbines and motor generator set (MG Set) widely employ wound rotor induction motor. In past, liquid resistance starters (LRS) have been used to control the external resistance of rotor circuit for big induction machines but its setup requires large space .This problem can be easily rectified by employing in power electronic devices like chopper circuit and diode bridge which are compact.

In a wound rotor induction motor at the time of starting the entire external resistance is added to the rotor circuit and as the rotor speeds up, the external resistance is varied in steps so that motor torque tends to remain maximum during accelerating period. Finally, under normal operation the external resistance is fully cut off and the slip rings are short circuited.[1, 2, 4]

II. Models

In past pulse generator has been used to achieve varying rotor external resistance. The Wound Rotor Induction Rotor employing pulse generator is shown in Figure 1for such model

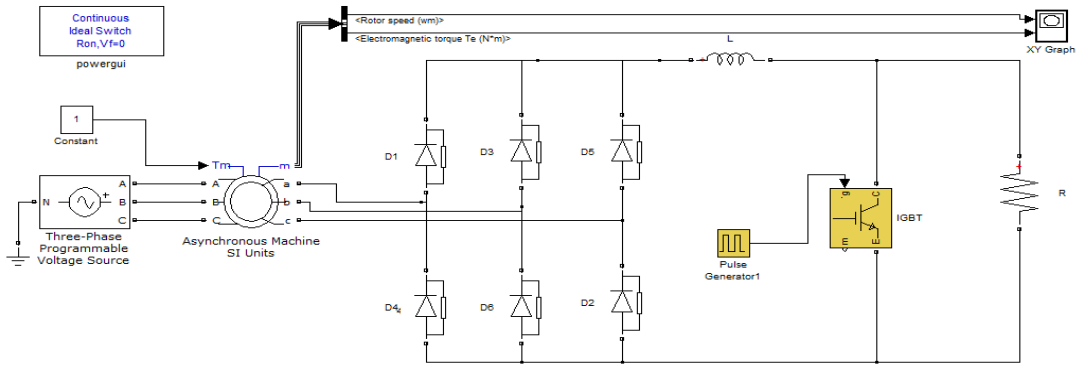


Figure 1: Wound Rotor Induction Motor employing pulse generator

In this model the rectified ac voltage of motor is fed to a parallel combination of resistance R and IGBT. Pulse Generator has been employed to trigger the IGBT.As no feedback mechanism has been employed the duty cycle has to be varied manually to get the desired results thus this model holds very less practical significance.

III. Proposed Models And Implementation

This article discusses about two models which have been simulated in MATLAB to maintain constant maximum torque for motor.

1. Application of feedback mechanism to vary duty ratio using no inductor (Figure 2).

2. Application of feedback mechanism to vary duty ratio using inductor as a filtering device (Figure 3).

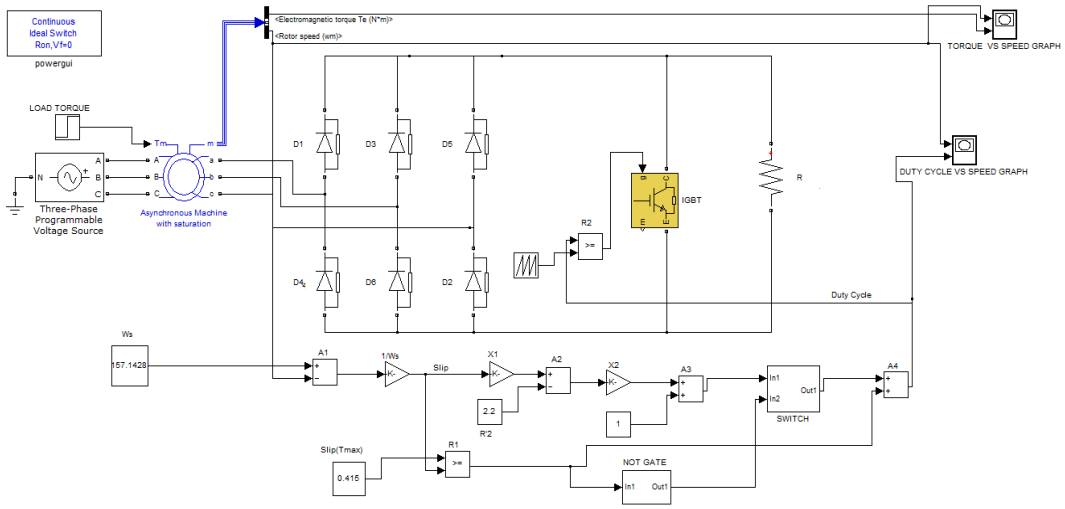


Figure 2:Model 1 for constant torque operation of wound rotor employing feedback control

This method employs in two feedback mechanism of rotor speed and slip to maintain a constant torque upto s_{Tmax} of wound rotor induction motor .The feedback mechanism has been prepared using following equations [1]:

$$s_m = \frac{R_r'}{\sqrt{R_s^2 + (X_s + X_r')^2}} \qquad (1)$$

With an external resistance whose stator referred equivalent resistance is Re

$$s_m = \frac{R_e + R_r'}{\sqrt{R_s^2 + (X_s + X_r')^2}} \qquad (2)$$

$$R_e = 0.5R(1-\delta)a^2 \qquad (3)$$

For maximum torque to occur at standstill i.e. s=1,δ=0 and
$R_e = 0.5Ra^2 (4)$

Where

s_m	Slip	Rr'	Rotor resistance referred to stator side
X_s	Stator Reactance	X_r'	Rotor reactance referred to stator side
R_s	Stator resistance	δ	Duty Cycle
A	Stator to rotor turns ratio	R_e	Stator referred external resistance

In feedback mechanism rotor speed is fed to the negative terminal of add block A1and rotor synchronous speed i.e. 157.14 rad/sec is fed to the positive terminal from constant Ws block toadd block A1.The output of add block A1 gives us the difference of the rotor speed and synchronous speed. The difference in speed is multiplied by a gain which has value same as reciprocal of synchronous speed (1/Ws) which gives us the slip of the motor. The slip value is multiplied by gain of X1 block whose value is $\sqrt{R_s^2 + (X_s + X_r')^2}$ and it gives us the value of effective rotor resistance i.e. $R_e + R_r$'. The output of X1 block is fed to positive terminal of add block A2. R'2 blockcontaining value of Rr' is fed to the negative terminal of add A2 block. The output of add A2 block gives us the value of external rotor resistance referred to stator side i.e. $R_e = 0.5R(1-\delta)a^2$ .R_e is fed to X2 block whose value is equal to negative of reciprocal of $0.5Ra^2$i.e. $(-1*1/0.5Ra^2)$.At this point it's imperative to understand that how the value of R i.e. external resistance introduced into rotor circuit is calculated. We have designed our model in such a way that the breakdown torque is produced from standstill. Hence for maximum torque to occur at standstill when s_m=1 and δ=0 following equation holds .Motor parameters mentioned in appendix have been substituted in the equations:

Using equation (2) we have,

$$1 = \frac{R_e + 2.2}{\sqrt{1.46^2 + (2.56 + 2.55)^2}}$$

R_e =3.11ohms

Using equation (3) we have,

$3.11 = 0.5R1.33^2$

R=3.505ohms

The output of X2 block is fed to positive terminal of add block A3 and a constant value to 1 is fed to another positive terminal of add block A3. The output of add block A3 gives us the value of δ i.e. duty cycle. The output of add block is fed to Inp 1 of SWITCH subsytem.

At this point we would like to re-emphasize that our calculations are valid only for machine running at maximum torque. Thus once the condition of δ=1 has been reached there would be no effect of external rotor resistance . The boundary condition for slip has been calculated using equation (2).

At boundary condition value of external resistance Re is zero as δ=1

$$s_m = \frac{2.2 + 0}{\sqrt{1.46^2 + (2.56 + 2.55)^2}}$$

$s_m = 0.415$

The constant value 0.415 fed to the relational operator R1 which is the value of slip at which value of duty cycle becomes one and there is no effect of external resistance. The relational operator R1 compares the constant value 0.415 with the rotor slip fed to other terminal of relational operator R1. When external resistance is in picture output of relational operator is low because 0.415 would be less than value of calculated slip , but once duty cycle, i.e. δ=1 is reached slip decreases below 0.415 and output of relational operator R1 turns high. The output of relational operator R1 is further fed to In1 of NOT GATEsubsystem.

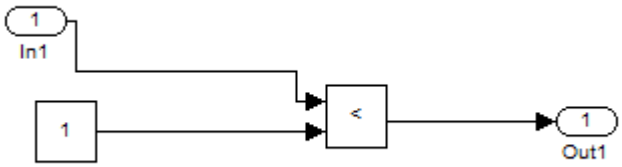


Figure 3:NOT GATE Subsystem

In NOT GATEsubsystem In1 is the output of the relational operator R1. When output of relational operator R1is high output of NOT GATE subsystem becomes 0.The output (Out1) of NOT GATE subsystem is fed to second input terminal In2 of SWITCH block subsystem.

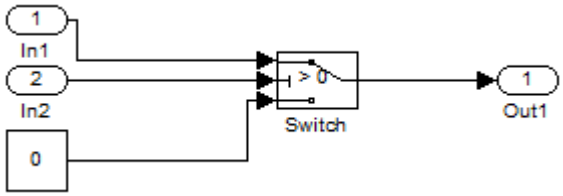


Figure 4:SWITCH block subsystem

If input to second terminal of SWITCH subsystem is high it means that switch would operate with terminal 1 configuration related to In1. The output of switch,which would be duty cycle δ in this case is fed to add block A4. A second input from relational operator R1 is fed to other positive terminal of add block A4. In this particular case the value of input from relational operator would be zero. Thus the output of add block A4 would be duty cycle which is further fed to 1stterminal of Relational Operator R2. The other terminal of relational operator is fed with a saw tooth pulse generated with the help of repeating sequence block which will produce repeated pulses of the duty cycle. Whenever value of terminal 1 would be greater than terminal 2 a gate pulse would be given to IGBT which will turn the power semiconductor device into action.

On the other hand if input to second terminal of SWITCH subsystem is low it means that switch would operate with terminal 3 configuration. The output of switch in this case would be 0 i.e. fed from a constant block .The output of switch is further fed to add block A4. A second input from relational operator R1 is fed in other positive terminal of add block A4. In this particular case the value of this signal would be 1. Thus the output of add block A4 would be 1 which is further fed to 1st terminal of Relational Operator R2. The other terminal of relational operator R2 is fed with a saw tooth pulse generated with the help of repeating sequence block. In this case the output of relational operator would be set at 1.The same is desired because at last we want the value of external rotor resistance being realized by the circuit to reduce to zero so that motor can operate with maximum efficiency for a given load.

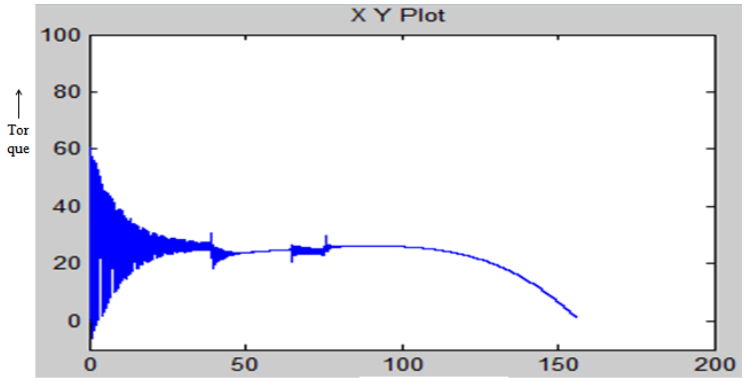


Figure 5:Torque V/S Rotor Speed

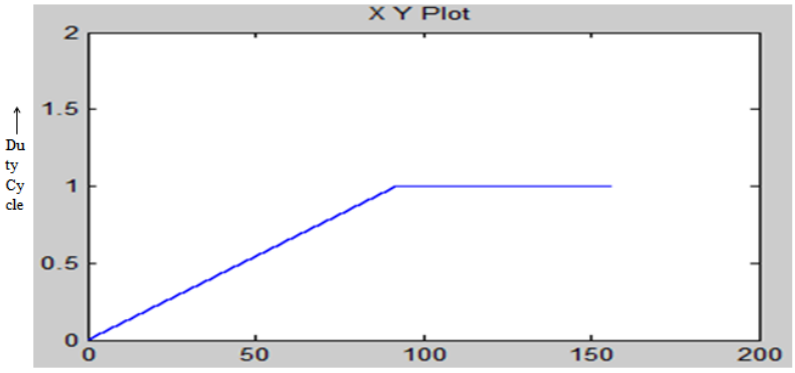


Figure 6: Duty Cycle V/S Speed

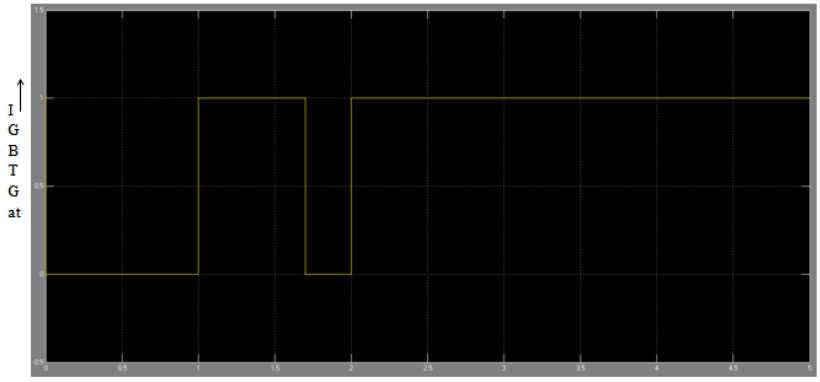


Figure 7:IGBT Gate Pulses

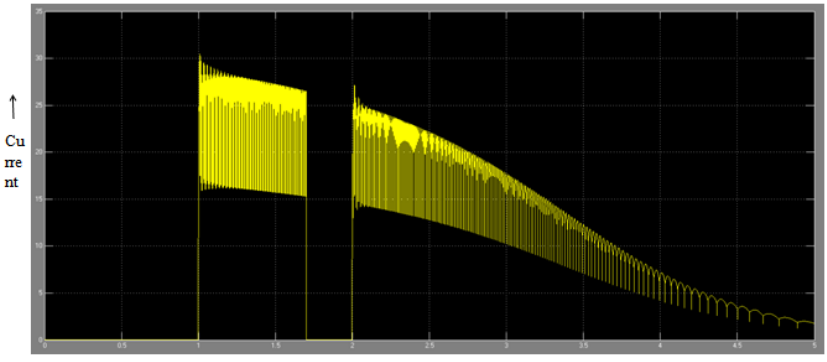


Figure 8:Current flowing in IGBT

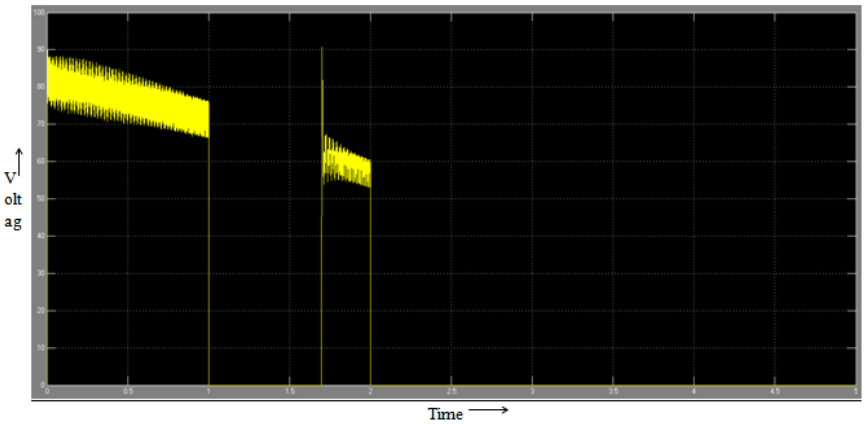


Figure 9:Voltage across IGBT

Model 2:Application of feedback mechanism to vary duty ratio using inductor as a filtering device.

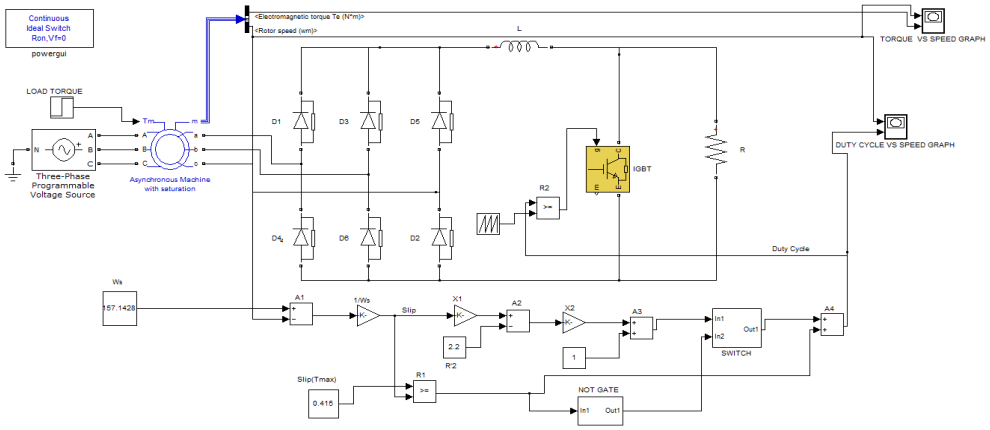


Figure 5: Model 2 for constant torque operationof wound rotor employing feedback control and inductor for rectification

The working of this model is similar to the model discussed above, only difference being that an inductor L has been used in the secondary rotor circuit for filtering purpose.

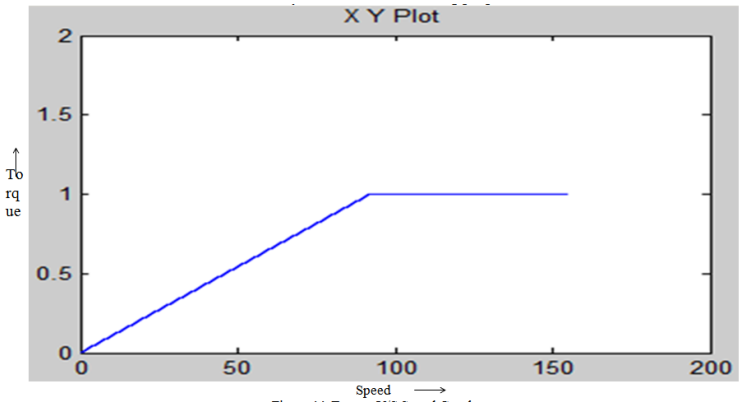


Figure 11:Torque V/S Speed Graph

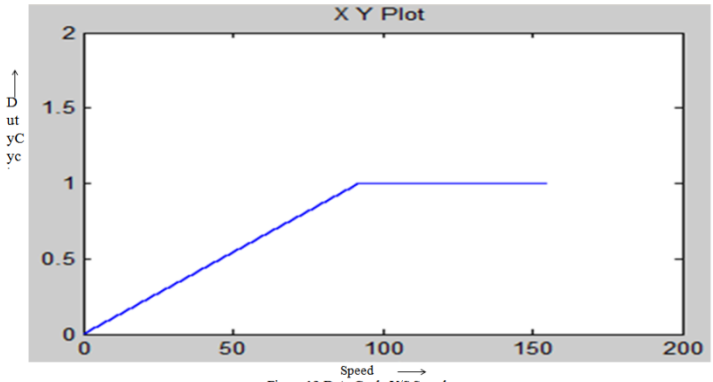


Figure 12:Duty Cycle V/S Speed

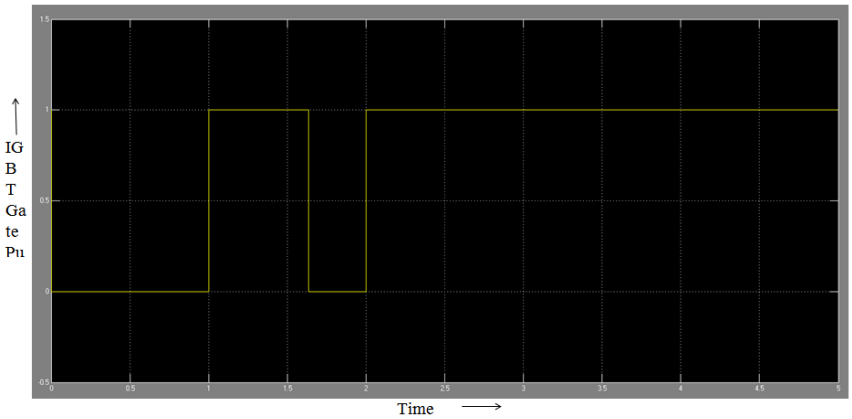


Figure 13: IGBT Gate Pulses

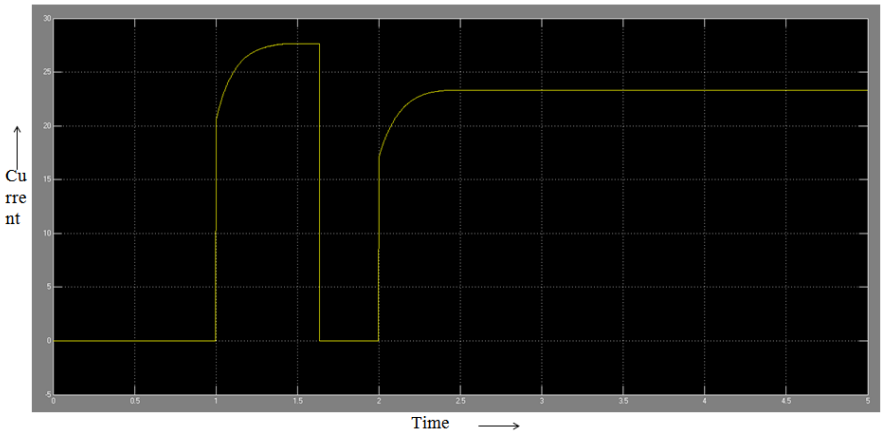


Figure 14: Current flowing through IGBT

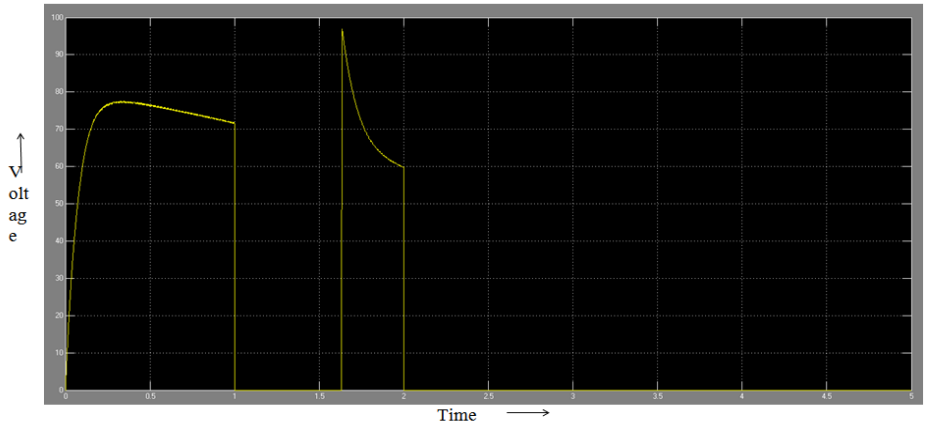


Figure 15: Voltage across IGBT

IV. Conclusion

An automatic controller to run the wound rotor induction motor at maximum torque from standstill slip(s=1) to slip (s_{Tmax}=0.415) has been successfully simulated using two circuits with help of MATLAB.The first model(Figure 2) and second model (Figure 3) employs a feedback mechanism to maintain maximum torque of motor.The second model uses an inductor in the secondary rotor circuit which acts a rectifier and reduces the harmonic distortions in torque curve which were prevalent in the first model.The graph between duty cycle and motor speed has been successfully plotted and observed to be linear which reaffirm that the motor has been operating at maximum torque.

Appendix-A

Specifications of the Wound Rotor Induction Motor [3]
V_L= 240 V
I_L= 5.72 A
Pole pairs= 2
Frequency= 50 Hz
P_{out}= 2.40 HP,Δ-Δ connection
R_s= 1.46 ohms
X_s= 2.56 ohms
X_m= 92 ohms
a=1.33
R_r'= 2.2 ohms
$X_{r'}$= 2.55 ohms

References

[1] Gopal K. Dubey, "Fundamentals of Electrical Drives", Narosa Publishing House Pvt. Ltd., 2001
[2] PS Bimbra, "Electrical Machinery", Khanna Publishers, 2010
[3] Control of Wound Rotor Induction Motor Using Thyristors in the Secondary Circuits,IEEE TRANSACTIONS ON INDUSTRY APPLICATIONS, VOL. 32, NO. 2, MARCWAPRIL 1996
[4] Comparative Study of Speed Control of Induction Motor Using PI and Fuzzy Logic Controller, Anmol Aggarwal, J. N. Rai, Maulik Kandpal, IOSR Journal of Electrical and Electronics Engineering (IOSR-JEEE) e-ISSN: 2278-1676,p-ISSN: 2320-3331, Volume 10, Issue 2 Ver. I (Mar – Apr. 2015), PP 43-52

Journal of Environmental Protection, 2015, 6, 1170-1175
Published Online October 2015 in SciRes. http://www.scirp.org/journal/jep
http://dx.doi.org/10.4236/jep.2015.610104

Detection of *Enterobacter sakazakii* from Commercial Children Dry Milk

Mohammed Mosa Jaffaar[1], Mohammed K. Shebli[1], Abdul Khaliq Abbas Mussa[2], Bayan Hassan Hadi[2], Allaa M. Aenab[3], S. K. Singh[3]

[1]Agricultural Research Directorate, Ministry of Science and Technology, Baghdad, Iraq
[2]Central Public Health Laboratory, Ministry of Health, Baghdad, Iraq
[3]Environmental Engineering Department, Delhi Technological University, Delhi, India
Email: Mohammedmosa1@yahoo.com, allaaaenab@gmail.com

Received 19 August 2015; accepted 25 October 2015; published 28 October 2015

Copyright © 2015 by authors and Scientific Research Publishing Inc.
This work is licensed under the Creative Commons Attribution International License (CC BY).
http://creativecommons.org/licenses/by/4.0/
Open Access

Abstract

This study included isolation and identification of *E. sakazakii* from 51 different samples of powdered infant formula milk involved (Dialak 1 & 2, Celia 1 & 2, Primalac, Biomil 1 & 2, Similac, Nictalia 1 & 2, MAMi, Novolac (AD), Novolac (AR), Novolac (Allernova), S-26 AR, Nursoy, S-26 PDF gold. The results showed that one batch from three of the batches identified of Novolac and Dialak were contaminated and all the types of other infants were non-contaminated. The strains code given as (E1, E2, E3, E4); the bacteria showed resistance to antibiotics used was cephalosporin batch; the third generation showed sensitive to antibiotics life results through inhibition processes such as (Cefotaxime, Sifutetan and Siftadizim), where the diameters of inhibition zone for Siftadizim (18 mm), Sifutetan (22 mm) & Cefotaxime (25 mm) confirmed the bacteria by API and Vitek Compact-2 (biomero).

Keywords

***Enterobacter sakazakii*, Infant Dry Milk, Antibiotic & Vitek Compact-2**

1. Introduction

Enterobacter sakazakii is a gram-negative bacteria, motile, non-spore forming, facultatively anaerobic, bacillus forming yellow pigmented colonies after 24 - 48 hours at 37˚C incubation on a non-selective medium rod that was formerly known as "yellow-pigmented *Enterobacter cloacae*" until 1980 [1]. This bacterium is an emerging opportunistic pathogen predominantly associated with bacterial meningitis in immune compromised neonates [2]. Other clinical presentations of infection include bacteremia and necrotizing enterocolitis [3]. It appears that

How to cite this paper: Jaffaar, M.M., Shebli, M.K., Mussa, A.K.A., Hadi, B.H., Aenab, A.M. and Singh, S.K. (2015) Detection of *Enterobacter sakazakii* from Commercial Children Dry Milk. *Journal of Environmental Protection*, **6**, 1170-1175.
http://dx.doi.org/10.4236/jep.2015.610104

the frequency of *E. sakazakii* infections is low. *Enterobacter sakazakii* has been associated with life-threatening infections in premature low-birth-weight infants. Contaminated infant milk formula (IMF) has been implicated in cases of *E. sakazakii* meningitis. Sensitive and quick methods to reveal low level of pollution sporadically present in IMF preparations would positively contribute towards risk reduction across the infant formula food chain. The bacterium has been cultured from an assortment of food matrices, including meat, grain, cheese, vegetables, spices, bread and herbs [4]. Though the normal habitat of *E. sakazakii* has yet to be specified, infant milk formula (IMF) has been epidemiologically linked to cases of neonatal meningitis. As an oral pathogen reason for systemic infection, *E. sakazakii* must be in possession the instrumentarium to interfere the epithelial cell obstacle in the bowel in order to access the blood circulation and diffusion. Availability of an *in vitro* cell culture model is essential to study the primary steps of entry of *E. sakazakii* into eukaryotic host cells and to identify possibility virulence factors involved in such procedures. We used gentamicin protection examinations and confocal imaging of fluorescently tagged *E. sakazakii* cells to presenting that this bacterium actively invades human epithelial Caco-2 cells. Both f-actin and microtubule structures are needs for infestation. Disruption of cellular tight intersection increased the primary assembly of *E. sakazakii* with Caco-2 cells and significantly enhanced the ability to pervade. Showed that *E. sakazakii* is able to penetrate rat brain endothelial cells and to survive inside macrophages. The locative evidence also implies that *E. sakazakii* has to be able to translocate through the intestinal barrier and establish a systemic infection with symptoms such as bacteremia and meningitis [5]. Invasive bacteria are able to manipulate the host cell cytoskeleton. Doing this either directly by active secretion of bacterium while actin microfilaments are frequently associated with the bacterial invasion process, microtubules can be also involved in breakthrough by microbial pathogens [6].

2. Objectives and Aim of the Study

Study aimed to detection and identification *Enterobacter sakazakii* from different type of infant dry milk by new methods and confirmatory API 20 E and Vitek compact-2.

3. Material and Methods

3.1. Milk Samples

Fifty one samples have been received from public health laboratory of the Central. Samples were collected over a period of nine months between February and December of 2014.

3.2. Isolation of *Enterobacter sakazakii*

Enrichment step dilution in peptone water and transfer (1 gm, 10 gm & 100 gm into (9 ml, 90 ml & 900 ml)) triple cat in EE broth (Enrichment Enterobacter broth) subsequent isolation of pure colonies on violet red bile glucose agar. Several isolated colonies were selected and streaked onto tryptone soy agar (TSA). Typical yellow-pigmented colonies are detected after an overnight incubation for 48 to 72 h at 25˚C.

3.3. The Identification

These presumptive colonies are identified biochemically [7]. This approach provides only a generic test for Enterobacteriaceae and lacks comparison of the effectiveness of antibiotics for the first and third generation cephalosporins within the group against bacteria the necessary capability to specifically identify *E. sakazakii.* Recently, a number of eclectic have become available to assist identification. One of these is the API 20 E biochemical test and vitek confirmatory system. Sakazakii were time and enriched for 6 h at 42˚C. summarizes the findings of these experiments. This method dependably revealed between 1 and 5 CFU *E. sakazakii* in 100 g with higher inocula producing a higher recovery of *E. sakazakii*. Tests were conducted according to the instructions and approach Food and Drug Administration [7]. The limit of detection was determined to be 10 CFU/ml (equivalent to 2.5×10^3 CFU in (250 ml)).Biochemical profiles are frequently used following primary isolation (**Figure 1**), but contradictions in identification may occur in different biochemical kits for the same strain [8].

3.4. Antibiotic Susceptibility Test

Antibiotic was done for each isolate by standard Kirby Bauer method [9]. Muller Hinton agar plates were used

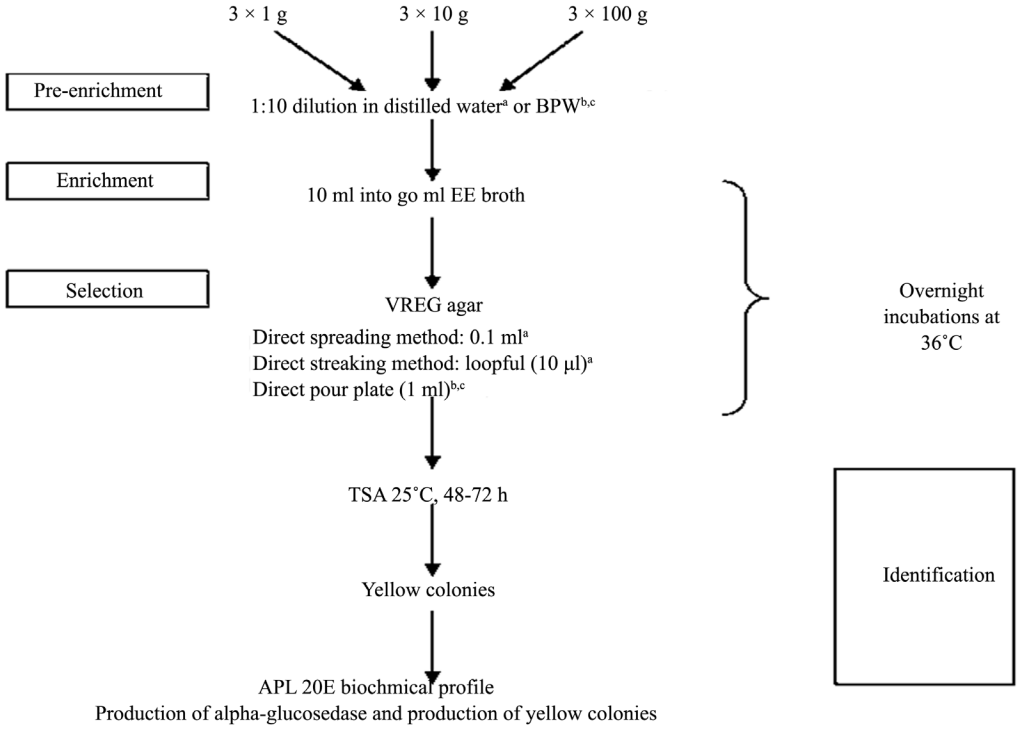


Figure 1. Quantitative *E. sakazakii* isolation procedure.

for bacterial culturing, disc of Cefotaxime, Sifutetan & Siftadizim. Were put over bacterial growth, plates were incubated for 18 hr at 37C, diameter of cleared zones were recorded for results.

3.5. Biochemical Test

Studies have demonstrated that 100% of *Enterobacter sakazakii* are positive for *α*-glucosidase while 100% of other Enterobacter species are negative for this enzyme [10]. On the basis of these observations, the chromogenic substrate 5-bromo-4-chloro-3-indolyl-*α*-D-glucopyranoside (X-*α*-glucoside) has been proposed to differentiate *Enterobacter sakazakii* from other members of the Enterobacteriaceae family [11]. The enzyme *α*-glucosidase hydrolyzes the X-*α* (**Tables 1-3**).

4. Results and Discussion

Enterobacter sakazakii was isolated from four (1.56%) out of the thirty-nine tested infant formula milk. Five strains were isolated and were identified by the FDA method 2002 and API 20 E and Vitek compact-2 (biomero) suggested that the inability to isolate *Enterobacter sakazakii* from powdered formula may have been due to its unequal allocation within the powdered formula or "its existence at such a low concentricity that it escaped disclosure by traditional methods as described by the Food and Agriculture Organization [5] [12]. This study proved that some international global milk powder contaminated with bacteria *Enterobacter sakazakii* and that the children of these bacteria have done a pathogencity represented by diarrhea and severe acute diarrhea. Bacteria were isolated from these four marks: Novolac (AD), Novolac (AR), Novolac (Allernova), Dialak and proven contamination by screening method that recommended by FDA 2002 where the isolation rate (1.56%). Isolates obtained from milk cans indicate resistance to these isolates heating during the manufacturing process and to the inefficiency of the manufacturing process [13]. The results of this study were in line with the results obtained by the researchers [14], as the isolated bacteria from baby milk powder and by (6.80%). The results of the study differed with the study [1]. The researchers have stressed the milk contamination with bacteria *Bacillus cereus* and the reason for their appearance is due to the production of toxins casuals and heat resistance. Tested isolates were resistant to antibiotics where used Cephalosporine group compared to the work of the antibiotic first generation and third. Study showed the first generation (Cephalothin, Safaberden, cefazolin, cephalexin and

Table 1. Biochemical test of *Enterobacter sakazakii* and different bacteria.

Citrate	Positive	Positive	Positive
Glucose	K/A Positive	A/A Positive	A/A Positive
Sucrose	Positive	Positive	Positive
Lactose	Positive	Positive	Positive
α-glucosidase	Positive	Negative	Negative
Urease	Positive	Negative	Negative

Table 2. The proportion of bacteria in milk samples.

Type of samples	Total of samples	Isolated	Percentage
Dialak 1, 2	51	1	1.49
Novolac AD	51	1	1.49
Novolac AR	51	1	1.49
Novolac Allernova	51	1	1.49

Table 3. Isolated bacteria from different types of children dry milk.

Type of Bacteria	Batch No.	Production time	Country of origin	Duplicates	Type of milk
	24 - 25	07.2013			
E. sakazakii	15 - 19	03.2013	Vietnam	3	Dialak 1, 2
	19 - 32	10.2013			
	19 - 27	11.2013			
	11 - 15	08.2013	USA	3	Celia 1, 2
	6 - 64	10.2013			
	15 - 20	04.2013			
	22 - 30	08.2013	Switzerland	3	Primalac
	12 - 45	12.2013			
	8500	10.2013			
	5500	07.2013	Belgium	3	Biomil 1, 2
	2000	04.2013			
	09 - 42	11.2013			
	03 - 26	07.2013	Ireland	3	Nursoy
	02 - 17	03.2013			
	41306	03.2013			
	41308	03.2013	Poland	3	Mami
	41900	11.2013			
	36420	03.2013			
	64222	06.2013	France	3	Nicalia 1, 2
	92391	09.2013			
	02 - 20	03.2013			
	06 - 44	07.2013	Ireland	3	Similac
	02 - 57	09.3013			
	20 - 57	02.2013			
E. sakazakii	16 - 32	07.2013	Germany	3	Novolaclernova
	05 - 46	10.2013			
	08 - 52	02.2013			
E. sakazakii	10 - 58	07.2013	Germany	3	Novolac AD
	03 - 36	10.2013			
	19 - 44	02.2013			
E. sakazakii	08 - 30	03.2013	Germany	3	Novolac AR
	16 - 16	07.2013			
	2A02	10.2012			
	2A27	03.2013	Ireland	3	S-26 AR
	2A34	10.2013			
	2L14	07.2012			
	2L22	03.2013	USA	3	S-26 LF
	2L28	11.2013			

Table 4. Sensitivity of test *Enterobacter sakazakii* for third generation measured in Millimeter (mm) zone of inhibition according to (NCCL).

Antibiotic	E1	E2	E3	E4
Cefotaxime	25	25	25	25
Sifutetan	22	22	22	22
Siftadizim	18	18	18	18

cephradine) did not have any result zone of inhibition. The third generation of the same batch of antibiotic which shows sensitive results through inhibition processes such as (cefotaxime (25 mm), Sifutetan (22 mm), Siftadizim (18 mm)), where the diameters of inhibition zone for Cefotaxime, Sifutetan and Siftadizim. The use of minimum inhibitory concentration Cephalosporine batch shows cefotaxime, Sifutetan and Siftadizim inhibition zone. The major cause is due to the group operates stop the work of the gyrase enzyme is present in prokaryotes and some eukaryotes work by competitive suppression of energy transduction of DNA gyrase by binding to the ATPase active site located on the GyrB subunit. Quinolones bind to these enzymes and prevent them from decatenation replicating DNA. Quinolone-resistant bacteria repeatedly harbor convert topoisomerases that resist quinolone binding 2009 Eukaryotic Cell, 11(8), 1759-1769. Gore J., Bryant Z., Stone M.D., Nollmann M., Cozzarelli N.R. 2006. Used in the study [5], this was identical to the present study in the case reported cephalosporins, such as cefepime, in collection with a second agent. Two studies in [15] and [2], supported the use of cefotaxime for childhood bacterial meningitis. In each of these studies, *Enterobacter sakazakii* meningitis was identified in at least 1 child, and the infection was treated successfully. In another study, [16] described *E. sakazakii* infection in 4 adults that occurred in 1995 and 1996 at the University of Massachusetts Medical Center. Of the 4 adults, 2 presented with pneumonia and 2 with bacteremia. The isolates were uniformly resistant to ampicillin, cefazolin, and extended-spectrum penicillins and were not uniformly susceptible to third-generation cephalosporins or to quinolones. This study proved that the four isolates were sensitive to the third generation cephalosporin group 9, **Table 4**.

References

[1] Forsythe, S. and Iversen, C. (2008) Isolation of *Enterobacter sakazakii* and Other Enterobacteriaceae from Powdered Infant Formula Milk and Related Products. *Food Microbiology*, **21**, 771-773.

[2] Lecour, H., Seara, A., Cordeiro, J. and Miranda, M. (1989) Treatment of Childhood Bacterial Meningitis. *Infection*, **17**, 343-346. http://dx.doi.org/10.1007/BF01650726

[3] Van Acker, J., DeSmet, F., Muyldermans, G., Bougatef, A., Naessens, A. and Lauwers, S. (2001) Outbreak of Necrotizing Enterocolitis Associated with *Enterobacter sakazakii* in Powdered Milk Formula. *Journal of Clinical Microbiology*, **39**, 293-297. http://dx.doi.org/10.1128/JCM.39.1.293-297.2001

[4] Kandhai, M., Reij, W., Gorris, L. and Guillaume, O. (2009) Occurrence of *Enterobacter sakazakii* in Food Production Environments and Households. *Lancet*, 363-369.

[5] Muytjens, H.L. and van der Ros-van de Repe, J. (1986) Comparative *in Vitro* Susceptibilities of Eight Enterobacter Species, with Special Reference to *Enterobacter sakazakii*. *Antimicrobial Agents and Chemotherapy*, **29**, 367-370. http://dx.doi.org/10.1128/AAC.29.2.367

[6] Hoekstra, R.M., Kuehnert, M. and McDonald, L.C. (2007) Invasive *Enterobacter sakazakii* Disease in Infants. *National Center for Infections Disease*, **5**, 885-895.

[7] FDA (2002) Isoilation and Enumeration of *Enterobacter sakazakii* from Dehydrated Infant Formula.

[8] Iversen, C., Druggan, P. and Forsythe, S.J. (2004) A Selective Differential Medium for *Enterobacter sakazakii*. *International Journal of Food Microbiology*, **96**, 133-139. http://dx.doi.org/10.1016/j.ijfoodmicro.2004.01.024

[9] (2002) Performance Standards for Antimicrobial Disk Susceptibility Testing. NCCLSS, Wayne.

[10] Muytjens, H. (1985) *Enterobacter sakazakii*: Identification and Clinical Significance. *Antonie van Leeuwenhoek*, **51**, 618. http://dx.doi.org/10.1007/BF00404602

[11] Iversen, C., Druggan, P. and Forsythe, S. (2004) A Selective Medium for *Enterobacter sakazakii*, a Preliminary Study. *International Journal of Food Microbiology*, **96**, 133-139. http://dx.doi.org/10.1016/j.ijfoodmicro.2004.01.024

[12] FAO (1994) Codex Alimenterius Code of Hygienic Practice for Foods for Infants and Children. CAC/RCP 21-1979.

Food and Agriculture Organization of the United Nations, Rome.

[13] Pagotto, F. (2009) Pathogenesis of Cronobacter Enterotoxin Production, Adherence and Invasion of the Blood-Brain Barrier, Burenu of Microbiol Hazards, Ireland.

[14] Joshua, B., Jeffery, L., Kornacki, B. and Larry, R. (2005) *Enterobacter sakazakii*: Acoliform of Increased Concern to Infant Heath. Center for Food Safety and Technology, Georgia.

[15] Naqvi, S.H., Maxwell, M.A. and Dunkle, L.M. (1985) Cefotaxime Therapy of Neonatal Gram-Negative Bacillary Meningitis. *The Pediatric Infectious Disease Journal*, **4**, 499-502. http://dx.doi.org/10.1097/00006454-198509000-00012

[16] Lai, K.K. (2001) *Enterobacter sakazakii* Infections among Neonates, Infants, Children, and Adults. Case Reports and a Review of the Literature. *Medicine*, **80**, 113-122. http://dx.doi.org/10.1097/00005792-200103000-00004



International Journal of Pavement Engineering

ISSN: 1029-8436 (Print) 1477-268X (Online) Journal homepage: http://www.tandfonline.com/loi/gpav20

Economic assessment of use of pond ash in pavements

Raju Sarkar & A.R. Dawson

To cite this article: Raju Sarkar & A.R. Dawson (2015): Economic assessment of use of pond ash in pavements, International Journal of Pavement Engineering, DOI: 10.1080/10298436.2015.1095915

To link to this article: http://dx.doi.org/10.1080/10298436.2015.1095915

Published online: 29 Oct 2015.

Submit your article to this journal

Article views: 45

View related articles

View Crossmark data

Full Terms & Conditions of access and use can be found at
http://www.tandfonline.com/action/journalInformation?journalCode=gpav20

Download by: [Delhi Technological University] **Date:** 12 November 2015, At: 21:48

INTERNATIONAL JOURNAL OF PAVEMENT ENGINEERING, 2015
http://dx.doi.org/10.1080/10298436.2015.1095915

Taylor & Francis
Taylor & Francis Group

Economic assessment of use of pond ash in pavements

Raju Sarkar[a] and A.R. Dawson[b]

[a]Department of Civil Engineering, Delhi Technological University, Delhi, India; [b]Nottingham Transportation Engineering Centre, University of Nottingham, Nottingham, UK

ABSTRACT

The paper introduces a new type of industrial waste-based subbase material which can replace conventional subbase material (CSM) in pavement construction. Utilisation of this industrial waste, namely pond coal ash produced from a thermal power plant in road construction will help to reduce the disposal problem of this waste and also will help to reduce the problem of scarcity of CSM. Lime and fibre were also added to the pond ash at various percentages to improve the suitability of this type of mix as subbase material. The optimum service life of pavement is studied with the help of numerical modelling and the cost benefit is also presented in the current study. The study reveals that stabilisation of the coal ash with 2% lime may produce an optimal material and, even though a greater thickness may be required to deliver the same pavement performance, direct cost savings of around 10% may be achieved in addition to less easily quantifiable environmental benefits. Design charts are provided to exploit the findings.

ARTICLE HISTORY
Received 7 July 2015
Accepted 23 July 2015

KEYWORDS
Pond ash; geotechnical characterisation; numerical analysis; economic assessment

Downloaded by [Delhi Technological University] at 21:48 12 November 2015

1. Introduction

One of the major challenges facing the manufacturing and processing industries is the disposal of residual waste products. Ash, resulting from the combustion of coal to produce electricity, is a readily available by-product – particularly in India, the focus of this paper. As this availability is becoming more appreciated, demand for economic pavement construction materials, that impose a low environmental impact, is rapidly growing. Therefore, ash is considered in this paper as an alternative subbase material. Though a powdered material, but, due to its pozzolanic properties and when stabilised with cement, it might be made to meet the requirements of cement bound subbase material. Alternatively, lime could be used instead of cement, to give comparable long-term strengths (Sherwood 1995) albeit less rapidly developed (Atkinson *et al.* 1999). Fibre reinforcement is another possible improvement strategy (Kumar and Singh 2008).

Thus, the aim of this paper is to provide means of reliably incorporating ash, as found in disposal ponds at Indian power stations, into viable layers of pavement construction. The paper draws on laboratory test data reported earlier, using this data to numerically compute likely *in situ* behaviour. The aim is ultimately achieved by the production of design charts to guide users to the appropriate material and thickness of pavement layer incorporating that material and by providing an illustrative cost comparison.

2. Pavement layer practice and materials used

In India, in practice, flexible pavements are considered to act as a three-layer structure – subgrade, unbound (so-called) and bound layer. The lowest part of the unbound layers, which is just above the subgrade layer, is commonly known as the subbase layer of the pavement. The higher 'unbound' layer usually comprises a water bound macadam (WBM) or a wet mix macadam that forms the pavement base layer. While no cementing agent is added, compaction and water combine to provide a material held together by physical interlock and suction. It lies just above the subbase layer. The bound layer is usually divided into two parts, viz. the dense bituminous macadam (DBM) that lies above WBM and the top layer, known as bituminous concrete (BC) or wearing course. The subgrade layer is made up of locally available soil. The subbase layer is typically formed of unbound granular materials viz. natural sand, moorum, gravel and or crushed stone based on a combination of availability, economic factors and previous experience. The commonly used materials for the WBM layer are crushed, graded aggregate and granular material, and premixed with water. Crushed stone is also used as coarse aggregate. A DBM is a binder course in which bitumen binds together with a mixture of coarse and fine aggregate. The top bituminous layer (BC) comes directly into contact with the vehicle tyres. It consists of a mixture of aggregates and sufficient bitumen so that it provides an impermeable barrier to water percolation (Chakroborty and Das 2003).

3. Environmental considerations when using conventional materials

The most common materials that are used in road construction are bitumen, aggregate, crushed rock, sand and gravel.

CONTACT Raju Sarkar rajusarkar@dce.ac.in

© 2015 Taylor & Francis

New bitumen is an oil product and, hence, its abstraction from the ground incurs similar issues as those associated with obtaining fossil fuels. However, it is a recyclable material; it can be used repeatedly by reheating it, allowing the asphalt that it binds to be softened, reworked and replaced. But the initial heating and subsequent reheating and recycling requires large amounts of heat energy and thus produces lots of harmful greenhouse gases which pollute the environment. Again in summer, temperature rises and thus bitumen becomes soft. Natural solar heating will also causes softening of the bitumen, resulting in asphalt bleeding, rutting and segregation, and hence leads to failure of the pavement. During winter, if temperature reduces, the bitumen becomes brittle and it can result in cracking, ravelling and unevenness.

The other materials used in pavement construction are the products of mining. While requiring relatively low energy to produce and lay, haul costs (i.e. fuel, labour and maintenance) are the single largest variables in determining the cost of material in road construction. To limit these costs, sand and gravel mines are often opened near to a specific road project and then abandoned once the project is completed (Blodgett 2004), leading to widespread despoliation and degraded air quality at the mining site and its vicinity. Aggregate and sand mines require water to wash some of its product and to control dust on site. To fulfil this demand, many use scarce ground water competing undesirably with the increasing demands of domestic water use.

4. Situation in India

At present, the National Highway network consists of about 71,772 km, comprising only 1.7% of the total length of roads in India, but carries over 40% of the total traffic across the length and breadth of the country (MORT&H 2011). To alleviate congestion and to provide for future development, the Government of India has recently launched an extensive road construction programme under which thousands of kilometres of roads are currently under construction or scheduled for construction in the future. Current methods to be used for the construction of the new roads are not as per international standards. As an example, India is still using very small amounts of recycled aggregate material for road construction. Instead, it mostly depends on conventional materials viz. aggregate, crushed rock, sand and gravel.

As reviewed above, such materials are associated with considerable problems. Thus, to counteract these problems, India needs to focus on recyclable aggregate material or must replace conventional subbase or base materials with alternative materials. These materials could be industrial and domestic waste products since these materials are cheaply available and their use in road construction provides an efficient solution to the associated problems of pollution and disposal of these wastes.

Thermal power is the chief source of energy and produces nearly 70% of total energy production in India. Over 100 million tons per year (Gulhati and Datta 1999) of coal ash is generated by these thermal power plants. Due to high ash content of coal along with a low-percentage utilisation of the fly ash, most of the fly ash is disposed of on land by creating an engineered ash pond to take care of environmental concerns. While many European countries and Japan use more than 50% of fly ashes in an environmentally acceptable manner, India has a modest record of only 5% utilisation (Subbarao *et al.* 2001). The disposal of the fly ash is a serious hazard to the environment and consumes millions of rupees and many hectares of precious land.

Pond ash is the fly ash, as well as the bottom ash, produced by a power plant when it is disposed of in an ash pond in the form of a slurry, typically at a ratio varying between 1 part ash and 6–10 parts of water. Pond ash is a non-crystalline pozzolanic and slightly cementitious material. On the basis of these properties, it might be converted into meaningful wealth as an alternative construction material in civil engineering works (Sarkar *et al.* 2012). Use of pond ash in pavement construction could allow it to be used in large quantities. Therefore, this paper addresses its potential, stabilised both with and without fibres.

5. Opportunities for replacing conventional materials by ash products

There are numerous successful case histories on the utilisation of fly ash either alone or mixed with other material. Typically, fly ash has been used for soil stabilisation in road pavements – Chu *et al.* (1995); as embankment material – Raymond (1961); as structural fill – DiGioia and Nuzzo (1972); for injection grouting – Joshi *et al.*(1981); and as a replacement to cement – Gopalan and Haque (1986). Maser *et al.* (1975) reported successful studies on fly ash–cement mixture for subsidence control. Fawconnier and Korsten (1982) reported that the use of pulverised fly ash filling had effectively stabilised mines, reducing the risk of pillar failure in areas of low safety factor. Galvin and Wagner (1982) observed improved strata control using fly ash fill. Palariski (1993) reported the use of fly ash, mill tailings, rock and binding agents to make consolidated backfill material to improve extraction percentage in coal mines.

Mixing of a predetermined amount of fibre to a soil gives a mesh-like configuration leading to a mechanical means for reinforcement of the matrix, if done at appropriate moisture content (Nataraj and McManis 1997). Tests were carried out on the soils in which fibres were oriented in particular directions by Bauer and Fatani (1991), and Shewbridge and Sitar (1989). Tests were also carried out by Hoover *et al.*(1982), Setty and Rao (1987), Gray and Maher (1989), Maher and Gray (1990), Maher and Ho (1994), Michalowski and Zhao (1996), Consoli *et al.* (1998), and Santoni and Webster (2001) with randomly oriented fibres in soils. There, however, have been very few studies that discussed about fibre-reinforced and stabilised pond ash. Experimental studies have been carried out on some Indian fly ashes mixed with randomly oriented fibres. Chakraborty and Dasgupta (1996) studied the strength characteristics of polymer fibre-reinforced fly ash through triaxial shear tests. Kaniraj and Havanagi (2001) carried out experiments on randomly oriented fibre-reinforced fly ash–soil mixtures.

Dawson and Bullen (1991) investigated the engineering properties and possible use of furnace bottom ash as a subbase material. Index and large-scale pavement facility testing of furnace bottom ash in the laboratory and outdoor were carried out in this and subsequent investigations. Lee and Fishman (1993) studied the resilient and plastic behaviour of classifier tailings and fly ash

Downloaded by [Delhi Technological University] at 21:48 12 November 2015

Downloaded by [Delhi Technological University] at 21:48 12 November 2015

mixtures. Results from cyclic triaxial testing were used to study the resilient and plastic response of fly ash, classifier tailings, and a mixture of the two materials. Gray *et al.* (1994) evaluated a cement-stabilised fly ash base. In their study, the performance of compacted, aggregate-free, cement-stabilised fly ash beneath a highway shoulder was established. A field evaluation of pavement sections containing cement-treated bases with and without fly ash was undertaken by Ksaibati and Conklin (1994). In the study, pavement performance models were developed on the basis of the physical attributes of the sections. Dawson *et al.* (1996) used various combinations of secondary aggregates and binders in pavement foundations. They proposed various methods and procedures for the standard assessment of secondary materials viz. fly ash mixed with gypsum and lime, fly ash mixed with cement kiln dust and granular blast furnace slag and some combination of china clay and coarse aggregate. Ksaibati and Bowen (2001) undertook a wide range of laboratory testing in order to evaluate the feasibility of incorporating bottom ash into a crushed based material. Singh and Kumar (2005) studied the utilisation of fibre-reinforced fly ash in road subbases. Singh and Ramaswamy (2005) investigated the utilisation potential of cement-stabilised fly ash and granulated blast furnace slag mixes in highway construction. Mishra and Karanam (2006) carried out geotechnical characterisation of fly ash composites for backfilling mine voids. Chand and Subbarao (2007) carried out experiments on strength and slake durability of lime-stabilised pond ash. They attempted to check strength and durability aspects of lime-stabilised pond ash to determine its suitability for base and subbase courses of pavements. Titi *et al.* (2009) studied the resilient characteristics of bottom ash. The main aim of their research was to evaluate the characteristics of coal combustion bottom ash for potential utilisation as pavement construction materials.

From the above literature review, it is seen that fly ash can be used as a direct replacement material for unbound layers (subbase or base) of a pavement, with or without admixtures. Very little or no work has been done on the behaviour of the pavement structures incorporating various thicknesses of such ash as candidate layers for a pavement.

Another challenge is to determine the appropriate thicknesses of different layers to get the optimum pavement thickness. This challenge is important as, otherwise, service life or cost of construction of the pavement section may be intolerable. The cost of construction may be less due to the reduction in thickness of a particular layer of pavement, but if the service life is less, then the assumed benefit may, in practice, turn out to be a deterioration.

6. Aim and scope of work

The aim of this work is to determine ways of using coal pond ash as a subbase material in road construction that deliver adequate structural performance and that are economic. To achieve this general aim, an experimental study was carried out to understand the behaviour of pond ash mixed with admixtures, namely fibre and lime. The purpose of mixing these additives with pond ash is to improve the strength, deformability, volume stability (shrinking and swelling), permeability, erodibility, durability, etc. of the mix for their use in the pavement construction. The pond ash was characterised with respect to its physical and geotechnical behaviour. Proctor compaction and triaxial tests were carried out on pond ash alone and also after stabilisation of the pond ash by the addition of different percentages of the above admixtures within practical limits. The optimum percentage of the above admixtures was chosen based on these tests. Important geotechnical properties such as modulus of elasticity, cohesion and an angle of shearing resistance to be used in the numerical analysis were also evaluated from the test results.

Numerical studies on the performance of pavements constructed using these pond ashes, mixed with fibre and lime, were then carried out to evaluate the design life of pavements. A nominal pavement structure was designed considering Delhi silt as the subgrade soil. A stress–strain analysis was then performed, considering that the subbase layer is made up of pond ash stabilised with both admixtures, using the commercially available finite element software 'PLAXIS'. A parametric study was performed by varying the thickness of different layers with respect to a reference structure for each subbase material (pond ash + admixtures). Design charts were produced for different conditions including that of 'equal design life' based on the above parametric study. Finally, cost comparisons of the different pavement structures were carried out.

7. Materials used

7.1. Pond ash

The pond ash samples used in the present research work were obtained from the Badarpur plant site of the National Thermal Power Corporation located in the National Capital Region – Delhi. Pond ash is a pozzolanic material and can be stabilised with fibres and lime. The purpose of mixing these additives with pond ash is to improve the strength, deformability, volume stability (shrinking and swelling), permeability, erodibility, durability, etc. of the mix for its use in pavement construction. The chemical and geotechnical properties of the pond ash sample used in this study are given in Tables 1 and 2, respectively.

7.2. Fibre

A recent technique of soil or pond ash improvement is the mixing of randomly oriented fibres to the soil or pond ash (Chakraborty and Dasgupta 1996). The process is similar to the stabilisation using admixtures, i.e. discrete fibres are simply added and mixed with the pond ash. The compaction characteristics of fibre-reinforced pond ash do not differ significantly from unreinforced specimens (Kumar *et al.* 1996). One of the main advantages of randomly oriented fibres is the maintenance of strength isotropy and the absence of potential plane of weakness, which may develop parallel to oriented reinforcements. The physical and engineering properties of the polypropylene fibres used in this study are listed in Table 3.

Table 1. Chemical properties of Badarpur pond ash.

Constituents in percentage	Badarpur pond ash
SiO_2	49.5
Al_2O_3	25.01
MgO	1.21
Fe_2O_3	9.81
CaO	4.48
Loss on ignition	9.79
Others	0.08

Table 2. Geotechnical properties of Badarpur pond ash.

Properties	Badarpur Pond ash
Fine sand size, 0.475–0.075 mm, %	72
Silt size, 0.075–0.002 mm, %	22
Uniformity coefficient, C_u	4.8
Coefficient of curvature, C_c	1.05
Effective size D_{10}, mm	0.049
D_{30} size, mm	0.11
D_{60} size, mm	0.235
Specific gravity	2.1
LL and PL	Non-plastic
Maximum dry unit weight, kN/m^3	11.7
Optimum moisture content, %	32
Triaxial (CD) Test	
Cohesion intercept (c′), kPa	0
Angle of shearing resistance Φ′, °	28.9

Downloaded by [Delhi Technological University] at 21:48 12 November 2015

7.3. Lime

Calcium oxide (CaO) is a chemical compound, widely used to treat soils in the form of quicklime (CaO), hydrated lime (calcium hydroxide – $Ca(OH)_2$, or as a lime slurry. Quicklime is manufactured by high-temperature transformation of calcium carbonate (limestone – $CaCO_3$) into calcium oxide. Hydrated lime is created when quicklime chemically reacts with water. Hydrated lime reacts with silicates and aluminates in fly ash and clay particles and permanently transforms them into a strong cementitious matrix. The lime used in the present study was procured from the open market in the form of quicklime. This lime was then mixed with pond ash and water in the required proportions, by weight. Since the lime was procured from the open market, it is expected that its chemical composition will be similar to that given in Table 4.

The values of density, shear parameters and modulus of elasticity for different materials are given in Table 7.

8. Experimental investigations

Fibre was added to the pond ash at an increasing percentage of 0.2, 0.3, 0.4 and 0.5. Similarly, the lime was added with the pond ash at an increasing percentage of 2, 3, and 5. The details of the experimental programme are summarised in Table 5. The tests were performed conforming to the specifications given in Table 6.

9. Structural analysis

9.1. Pavement section

First, a typical pavement structure was designed with the selected subgrade material having a CBR equal to 9% and to carry a traffic load of 100 million standard axles (msa) as per IRC: 37-2001. This pavement structure is shown in Figure 1.

9.2. Modelling details

The following assumptions are made in the analysis:

- All layers have finite thickness including the bottom layer (subgrade).
- All layers are of finite extent in the lateral direction (even though infinite in extent in reality).
- Bituminous concrete (BC) and DBM exhibit linear elastic response.
- WBM, subbase and subgrade soils exhibit an elasto-plastic response and failure can be modelled using the Mohr–Coulomb constitutive relationship.

The pavement section was modelled as suggested by Huang (1993) to mechanistically solve the layered pavement response to traffic loading and to investigate the effect of subbase material on flexible pavement design. The pavement section considered for the finite element modelling is shown in Figure 2. A pressure of 575 kPa was applied at the surface distributed over a radius of 150 mm based on specifications of the Indian Road Congress. This uniform pressure is caused by a single wheel load of 40.8 kN. Dimensions of the axisymmetric finite element model employed were selected so that it was sufficiently large and, thus, the constraints imposed at the boundaries will have very little influence on the stress distribution in the system. Based on a small parametric study, this necessitated that the right boundary be placed 1100 mm from the outer edge of loaded area, which is more than seven times the radius of the applied load. The bottom extent of the subgrade was fixed at a subgrade depth of 500 mm, based on usual practice (IRC: 37-2001). Roller supports were provided along the axis of symmetry to achieve the condition that radial

Table 3. Physical and engineering properties of polypropylene fibres (supplier's data).

Properties	Value
Molecular formula	$(CH_2–CH_2)_n$
Young's modulus GN/m^2	7.1
Melting point, °C	89
Tensile strength, N/mm^2	125.28
Unit weight, kN/m^3	9.2
Diameter, mm	0.3
Aspect ratio	90

Table 4. Chemical composition of lime (supplier's data).

Minimum array (acidimetric)	95.00%
Maximum limits of impurities	
Chloride (Cl)	0.10%
Sulphate (SO_4)	0.50%
Iron (Fe)	0.10%
Lead (Pb)	0.02%
Loss on ignition	10%

Table 5. Experimental programme.

Source of pond ash	Details of experiments
Badarpur	Specific gravity Grain size distribution Atterberg limit tests Compaction tests:Light compaction (standard Proctor) test and heavy compaction (modified Proctor) test Consolidated drained triaxial tests under confining pressures of 100, 200 and 300 kPa

Table 6. Standard codes used to perform laboratory tests.

Laboratory tests	Standards/Procedures
Specific gravity	RILEM recommendations (1989)
Grain size analysis	IS: 2720 (Part 4) – 1985
Atterberg limit test	IS: 2720 (Part 5) – 1985
Standard Proctor compaction test	IS: 2720 (Part 7) – 1980
Modified Proctor compaction test	IS: 2720 (Part 8) – 1983
Consolidated drained triaxial shear test	IS: 2720 (Part 19) – 1981

Downloaded by [Delhi Technological University] at 21:48 12 November 2015

displacements are equal to zero. Also, the roller supports were provided along the right boundary which was placed sufficiently away from the centre of loading. At the bottom boundary, roller supports were provided for permitting free movement in the radial direction and a restraint to any movement in the vertical direction.

During the generation of the mesh, clusters were divided into triangular elements. The meshes are composed of 15-noded triangular elements which have a greater ability to model continuously varying stress–strain fields for less computational effort than would be needed using a far greater number of 6-noded triangular elements. Results were found to converge for the adopted mesh as shown in Figure 2.

The finite element analysis of the pavement system was carried out by considering values of resilient modulus, E, and Poisson's ratio, ν, given in Table 7. The pond ash collected from the Badarpur site, as well as the pond ash stabilised with admixtures, was considered as the subbase material in the present study. The adopted properties of these materials are summarised in Table 7.

The resilient modulus of the subgrade has been calculated as per IRC: 37-2001. In India, coarse sand or a mixture of river bed material and crushed stones are commonly used as a conventional subbase material (CSM) for pavement construction (Sinha, 2009). The properties of CSM are derived from the investigations of Lee *et al.* (2001) and Shodhganga (2006). Titi et al. (2009), Kumar and Singh (2008) and Ornebjerg *et al.* (2006) considered the value of resilient modulus of alternative subbase material, bottom ash and fly ash, similar to those being considered in this paper, obtaining values within the range 60–70 MPa. So, in the present study, the value of resilient modulus of pond ash was taken as 70 MPa. Similarly, Kumar and Singh (2008) considered the value of resilient modulus of fly ash mixed with fibre of 0.2 and 0.3% as 102.36 and 142.35 MPa. So in the present study, for simplicity, the values of pond ash mixed with fibre 0.2, 0.3, 0.4 and 0.5% are considered to be 100, 140, 160 and 170 MPa, respectively. Potentially the moduli of the mixes with higher moduli could be underestimated. In the case of pond ash mixed with lime, the resilient modulus is calculated by considering the initial tangent modulus of the triaxial stress–strain graph for 7-day-old material and subject to a confining stress of 100 kPa. The properties of WBM are considered on the basis of studies of Dawson *et al.* (1996) and Theyse (2002). Loulizi *et al.* (2006) tested hot-mix asphalt specimen from −15 °C to a maximum temperature of 40 °C to determine the resilient modulus of hot-mix asphalt. So, a small extrapolation was performed to determine the resilient modulus of hot-mix asphalt for a temperature of 45 °C (assuming

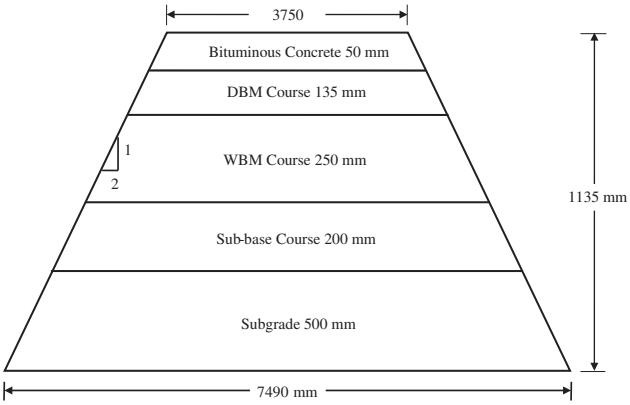


Figure 1. Pavement structure.

Downloaded by [Delhi Technological University] at 21:48 12 November 2015

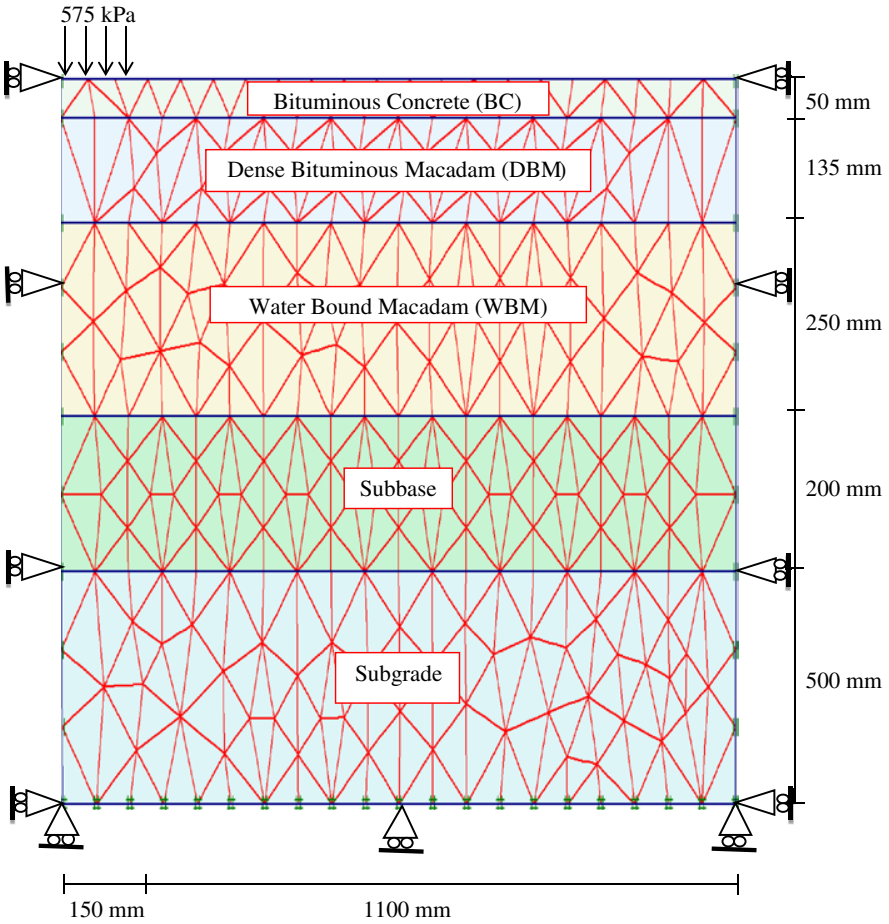


Figure 2. Finite element discretization of pavement section.

the maximum temperature during the summer period). The elastic modulus for bituminous concrete is considered as per IRC: 37-2001.

9.3. Parametric study

To develop design charts which help in decision-making and better utilisation of the technique of pond ash stabilisation by admixtures, a detailed parametric study was carried out by considering the nominal pavement as the reference structure and then varying the thickness of each layer within practical limits with respect to this nominal pavement, as given in Table 8. Other materials considered for subbase layer were as follows: Badarpur pond ash mixed with percentage of fibre and lime as mentioned in Table 7 and CSM. Given the expectation that stabilised ash might not perform so well as a CSM, greater thicknesses of this were considered than that of the CSM in the reference pavement. Also, since the ash-based material is expected to be economic

Table 7. Values of modulus of elasticity, Poisson's ratio and shear parameters for different pavement materials.

Layer	Constitutive model	Material	Maximum dry density (MDD) (kN/m^3)	Specific gravity *G*	Cohesion c′ (kPa)	Angle of repose s Φ′ (°)	Resilient modulus *E* (MPa)	Poisson's ratio (*v*)
BC	Elastic	Bitumen	21				700	0.35
DBM	Elastic	Bitumen Mix	18	2.3	–	–	1400	0.35
WBM	Elasto-plastic (Mohr–Coulomb)	Graded Aggregate	17.6	2.25	40	45	110	0.35
Subbase	Elasto-plastic (Mohr–Coulomb)	CSM[a]	20.4	2.67	14	37	140	0.35
		PA[b]	11.7	2.1	0	28.9	70	
		PA + Fibre						
		0.2%	11.8	2.11	18	30.3	100	
		0.3%	11.9	2.22	21.4	31.6	140	
		0.4%	12	2.25	24.8	33	160	
		0.5%	12	2.26	26.9	34	170	
		PA + Lime						
		2%	12.8	2.22	14	31.5	80	
		3%	13.5	2.25	20	32.2	110	
		5%	13.9	2.31	23.4	33.2	135	
Subgrade	Elasto-plastic (Mohr–Coulomb)	Delhi Silt	18	2.64	20	30	70	0.35

[a]Conventional subbase material.
[b]Pond ash.

Table 8. Variation in thickness considered in pavement study.

Layer	Reference pavement thickness (mm)	Variation in thickness (mm)
Bituminous concrete (BC)	50	None
Dense bituminous macadam (DBM)	135	110, 135, 160, 185
Base course (WBM)	250	150, 200, 250
Subbase course	200	200, 250, 300, 350, 400, 450, 500
Subgrade	300	None

Downloaded by [Delhi Technological University] at 21:48 12 November 2015

compared with the base and asphaltic layers, greater thicknesses of the ash layer might allow thinner layers of the higher pavement layers, introducing the possibility of overall cost savings.

9.4. Design life of pavement

Structural failures in a flexible pavement are of two main types, namely surface cracking and rutting.

9.4.1. Rutting

As per IRC: 37-2001, the occurrence of a rut depth of 20 mm is considered as the failure criterion. The design life or service life of a pavement is defined in terms of the cumulative number of standard axles that can be carried before strengthening of the pavement is necessary. The following equation is proposed in IRC: 37-2001 to calculate the design life on account of rutting failure alone:

$$N_R = 4.1656\ X\ 10^{-8}\left[1/\varepsilon_v\right]^{4.5337} \quad (1)$$

where N_R = Number of cumulative standard axles to produce rutting depth of 20 mm and

ε_v = Maximum vertical compressive strain at the top of subgrade in microns.

A service life ratio (SLR) as given below can be used to compare the effect of subbase material type on service life of a pavement:

$$\mathrm{SLR} = \mathrm{N}_1/\mathrm{N}_2 \quad (2)$$

and using Equation (1),

$$SLR = \left[\varepsilon_{v2}/\varepsilon_{v1}\right]^{4.5337} \quad (3)$$

where N_1, N_2 = Number of passes of a standard axle required to produce allowable rutting in a pavement with subbase material types 1 and 2, respectively, and

ε_{v1}, ε_{v2} = Vertical compressive strain at the top of subgrade layer with subbase material types 1 and 2, respectively

In the following analyses, subbase 1 is taken to be the one comprising CSM, 200-mm thick.

9.4.2. Fatigue

In a similar manner, a SLR can be computed for fatigue failure. The actual relationship will depend on the material that is subject to fatigue. For the purpose of this paper, the fatigue characteristics determined by IRC: 37-2001 for a DBM were adopted:

$$SLR = \left[\varepsilon_{t2}/\varepsilon_{t1}\right]^{3.89} \quad (4)$$

where ε_{t1}, ε_{t2} = Tensile strain at the bottom of the bound DBM course with subbase material types 1 and 2, respectively.

10. Test results and discussion

Figure 3(a–b) plots the maximum vertical compressive strain at the top of the subgrade vs. subbase thickness for the cases when the subbase layer is made up of Badarpur pond ash alone and mixed with fibre and lime, respectively, having the properties as given in Table 8, which vary with stabilisation rate. The magnitude of the maximum subgrade strain decreases with the increase in subbase thickness and with degree of stabilisation. The thicknesses of all layers except the subbase are maintained at their reference values (see Table 8). The magnitude of the vertical strain is simply and positively related to the rutting in the pavement.

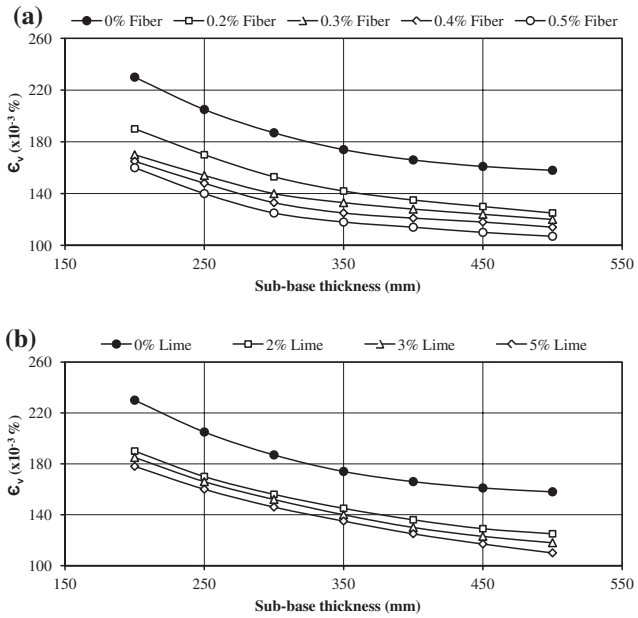


Figure 3. Vertical compressive strain-subbase thickness behaviour of pond ash mixed with (a) fibre and (b) lime.

The lesser the value of the maximum vertical compressive strain in the subgrade, the lesser is the rutting in the pavement and the longer is the life of the pavement.

It can be seen that, for fibre stabilisation, improvement continues until 0.3% fibre has been added but then, adding more fibre, causes little further benefit. In the case of lime, 2% addition achieves significant reductions in strain, whereas additional lime stabilisation achieves little further benefit.

Figure 4(a)–(c) shows the vertical compressive strain at the top of subgrade when the thickness of the subbase and of the bound courses (WBM and DBM) are varied. In each case, the subbase course is made up of pond ash stabilised with the preferred percentages of each admixture as mentioned above. For each arrangement, Figure 4(a–c) shows that the pond ash stabilised with 0.5% fibre gives the minimum strain (i.e. the shortest life). As expected, the maximum strain is obtained when the pond ash is used without any stabiliser.

Figure 5(a–b) shows the plots of the maximum tensile strain at the bottom of the DBM and subbase thickness behaviour for the cases when the subbase layer is made up of Badarpur pond ash mixed with fibre and lime, respectively, in the same percentages as mentioned above. The magnitude of the maximum tensile strain decreases with the increase in subbase thickness. For any particular type of bound material, the magnitude of the tensile strain is simply and positively related to the cracking in the pavement. The lesser the value of the tensile strain at the bottom of the DBM, the lesser is the cracking in the pavement and thus longer is the life of the pavement.

Figure 6 compares the minimum tensile strain at the bottom of the DBM with varying subbase thickness for the cases when the subbase layer is made up of pond ash stabilised with those percentages of each admixture that gave the probable optimal improvement in rutting behaviour (0.5% fibre and 2% lime) as well as for reference cases. As for the vertical subgrade strain, Figure 6 shows that the pond ash stabilised with 0.5% fibre gives the minimum tensile strain. Similarly, as for the case of vertical strain at the top of subgrade, the maximum tensile strain is obtained when the pond ash is used without any stabiliser.

The values of vertical compressive subgrade strain ε_v and tensile strain at the bottom of the bound, DBM, course, ε_t as picked from Figure 3(a–b) and Figure 5(a–b), for the structures including the range of selected subbase, are given in Table 9. The corresponding SLR for different pavement sections was evaluated using Equation (3). The maximum SLR following stabilisation of a 200-mm-thick subbase layer are 1.79 and 0.82 (considering vertical compressive strain), and 1.56 and 0.75 (considering tensile strain), respectively, for 0.5% fibres and 2% lime treatments, respectively. Thus, for the same thickness of ash subbase, treatment by fibres, but not by lime, yields a SLR that is higher than that for the conventional subbase. Vertical strains and tensile strains for pond ash alone and mixed with lime are much higher than that for CSM and so the SLRs are much lower than CSM. For all three alternatives given in Table 9, it is the tensile strain at the bottom of the asphaltic layers which is the limiting condition.

From Figure 7, which plots this SLR data, it is observed that the stiffness ratio (i.e. stiffness of ash compared to stiffness of CSM) increases monotonically with the increase in the SLR when the pond ash is mixed with various percentages of fibre and lime and used as subbase material.

The inverse of the above – the variation in the thickness of different layers of a pavement having a stabilised subbase layer needed to provide the same lifetime of the pavement as the conventional pavement is given in Table 10. As per IRC: 37-2001, the required thickness of the subbase layer for a traffic of 100 msa and for a CBR value of subgrade material of 9% is 200 mm when CSM is used as the subbase material. Thus, it needs to be increased to 315 mm when pond ash alone is used as the subbase material if the service life of the pavement is to remain unaffected (columns 2 and 3 of Table 10). This increased thickness for the same service life is termed as equivalent thickness.

Downloaded by [Delhi Technological University] at 21:48 12 November 2015

Downloaded by [Delhi Technological University] at 21:48 12 November 2015

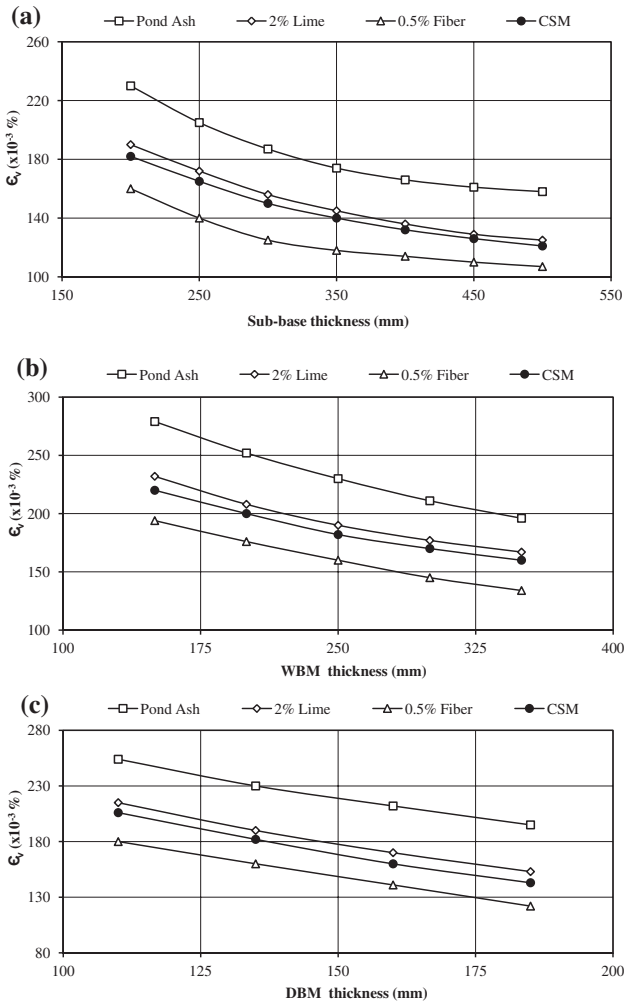


Figure 4. Comparison of variation of vertical compressive strain with (a) subbase, (b) WBM and (c) DBM thickness behaviour of pond ash and its mixes.

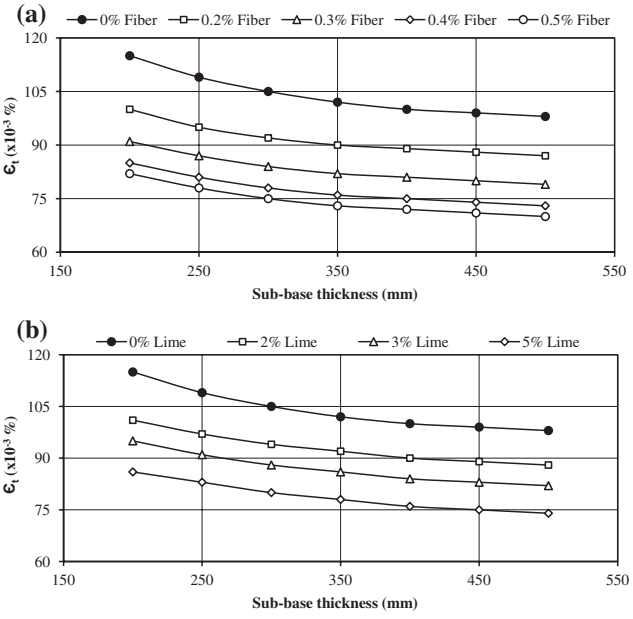


Figure 5. Tensile strain at the bottom of the DBM and subbase thickness behaviour of pond ash mixed with (a) fibre and (b) lime.

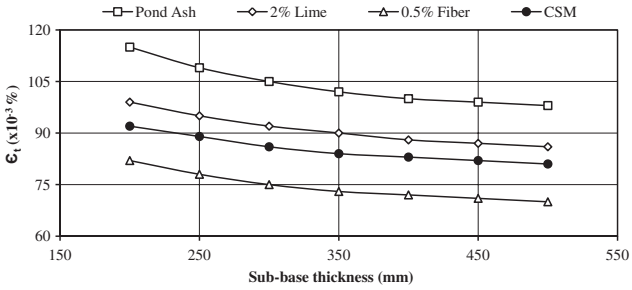


Figure 6. Comparison of variation of tensile strain at the bottom of the DBM as a function of the subbase thickness of pond ash and its mixes.

Table 9. SLR considering vertical compressive strains (VCS) at the top of subgrade and tensile strain (TS) at the bottom of the DBMfor different subbase materials (subbase thickness = 200 mm, WBM = 250 mm).

	Pond ash (PA)	PA + Fibre (0.5%)	PA + Lime (2.0%)	CSM
VCS ($\times 10^{-3}$%)	230	160	190	182
SLR (VCS)	0.35	1.79	0.82	1.00
TS ($\times 10^{-3}$%)	115	82	99	92
SLR (TS)	0.42	1.56	0.75	1.00

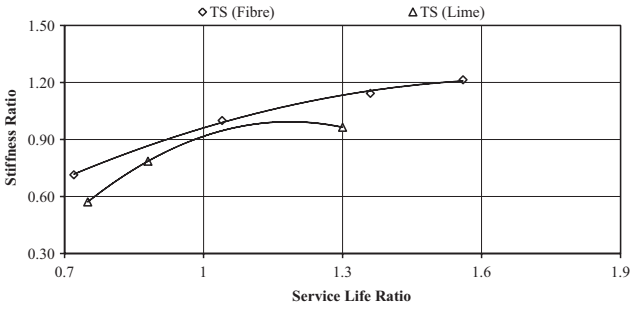


Figure 7. Variation of stiffness ratio (ash:CSM) with SLR of pond ash mixed with fibre and lime.

Table 10. Variation in equivalent thicknesses of different subbase materials for the same life of pavement.

	Subbase		WBM		DBM	
Material	Required thickness (mm)	Increase in thickness (%)	Required thickness (mm)	Increase in thickness (%)	Required thickness (mm)	Increase in thickness (%)
CSM as per IRC (2001)	200	0	250	0	135	0
Pond ash + Fibre (0.5%)	95	−52.5	150	−40.0	97	−28.2
Pond ash + Lime (2.0%)	300	50.0	352	40.8	169	25.2
Pond ash alone	580	190	463	85.2	210	55.6

The problem of a thick pavement section in such cases can be easily overcome by keeping the subbase thickness of 200 mm the same (as per design) but increasing the thickness (usually by a much smaller amount) of either the WBM layer or the DBM layer (as shown in the last 4 columns of Table 10). The decision of such replacement will naturally be guided by economy of construction.

Figure 8 depicts the equivalent thickness of subbase, WBM or DBM layers that will give the same SLR; in each case, the other layers retain their reference thickness. The procedure to pick equivalent thickness is illustrated in Figure 8(b), e.g. when the WBM thickness would be 240 mm over a CSM, its thickness can be reduced to 140 mm if an ash + 0.5% fibre is used as the subbase or must be increased to 445 mm if the ash is used unstabilised (see dashed lines on Figure 8(b)). The results are summarised in Table 10.

11. Economic assessment

In the present study, the pavement is designed for a single subgrade soil. The various layers are considered as shown in Figure 1. Based on assumption made by Central Road Research Institute (CRRI), Delhi (2009), on daily commercial traffic volume of a major part of Delhi, the design data for the cost analysis in the current study are assumed as follows:

Initial traffic in the year of completion of construction	= 100 msa
Design life	= 15 years
CBR value of subgrade (Table 7)	= 9%

Downloaded by [Delhi Technological University] at 21:48 12 November 2015

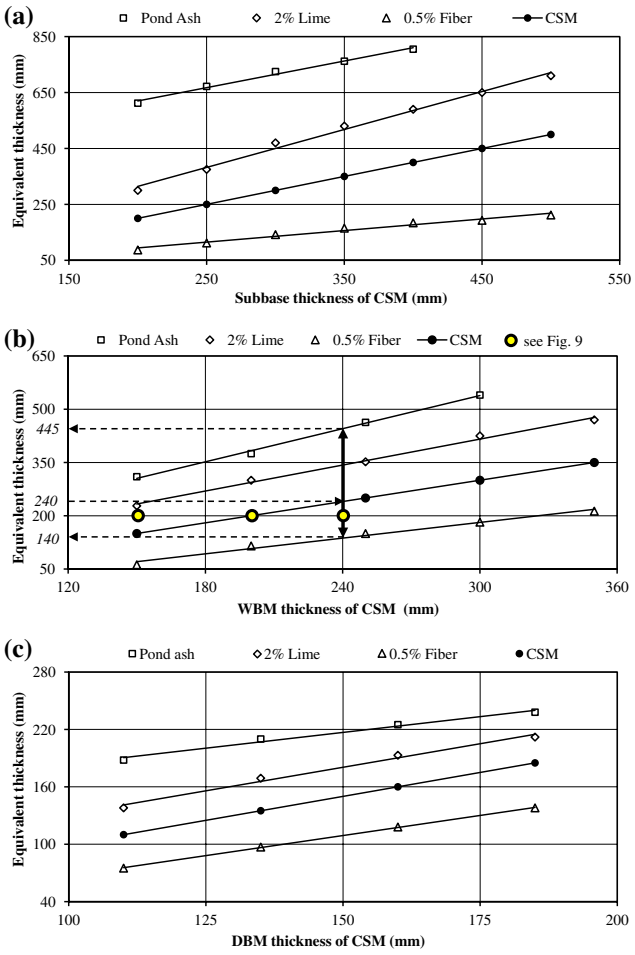


Figure 8. Variation of equivalent thickness of (a) subbase (b) WBM (c) DBM of different materials for same service life when pond ash mixture is used as subbase material.

The pavement was designed as per IRC 37:2001 and a pavement thickness of 635 mm was obtained as shown in Figure 1. Based on IRC 86:1983, the other details were assumed as given below:

Top width of embankment	= 3750 mm
Side slope	= 2H:1 V
Length of embankment	= 1000 m

For simplicity, the cost of the preparation of subgrade, CSM subbase, granular base, DBM and bituminous concrete is considered to be the same in all cases and were taken from Tirumala (2007). However, the cost of the preparation of different subbase layers varies, depending upon the thickness and the material of the subbase. The current schedule of rates for Delhi region is used for the cost analysis of subgrade, subbase, WBM, DBM and BC course.

The details of the cost analysis per $m^3$for subgrade are shown in Table 11.

The cost analysis of subbase constructed by pond ash, pond ash mixed with admixtures and CSM is shown in Table 12. The details of the cost are worked out assuming the plant output per day is 300 m^3. The calculations of admixtures are done as below:

Density of polypropylene fibre	= 920 kg/m^3
Density of lime	= 3350 kg/m^3
The amount of fibre required for the pond ash–fibre mix	= (300 × 0.5% × 920/1000) = 1.38 T
The amount of lime required for the pond ash–lime mix	= (300 × 2% × 3350/1000) = 20.1 T

The details of the cost analysis per $m^3$for base course WBM of Grade-3 are shown in Table 13 on a similar basis.

The cost analysis of DBM as per Ministry of Road Transport & Highways (MORT&H), Government of India, Grade-2 is shown in Table 14, using the same approach. The compositions of the adopted DBM materials are considered as per Sinha (2009):

Coarse aggregate (CA)	= 65%
Fine aggregate (FA)	= 35%
Bitumen content of mix	= 4.5% by wt.
Bulk density of mix	= 2352 kg/m^3
The unit wt. of CA	= 1545 kg/m^3
The unit wt. of FA	= 1650 kg/m^3

The details of the cost are worked out assuming the plant output per day = 147 MT (62.5 m^3)

Finally, the cost analysis of bituminous concrete (BC) is shown in Table 15. The adopted BC materials are as per MORT&H, with the following composition (Sinha, 2009):

Coarse aggregate (CA)	= 62%
Fine aggregate (FA)	= 35%
Filler (lime)	= 3%
Bitumen content of mix	= 5.5% by wt.

Downloaded by [Delhi Technological University] at 21:48 12 November 2015

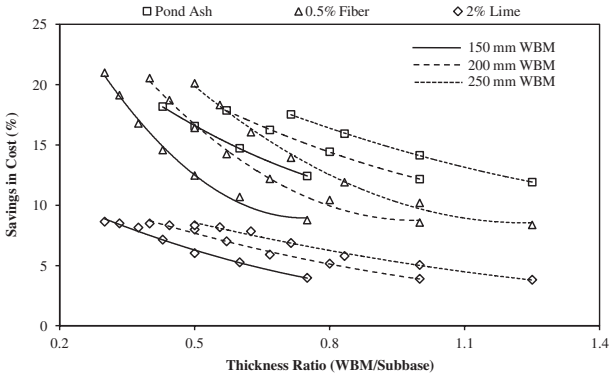


Figure 9. Comparison of percentage saving of cost and thickness ratio considering vertical strain at the top of subgrade.

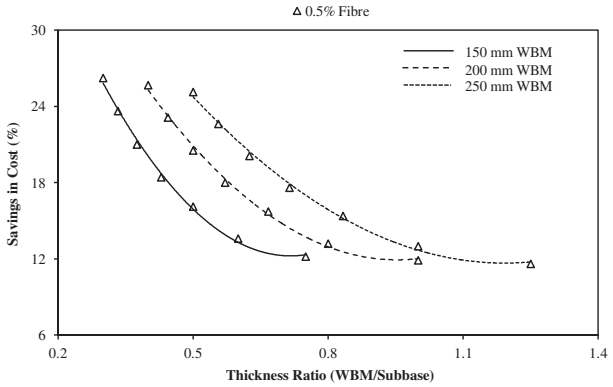


Figure 10. Comparison of percentage saving of cost and thickness ratio considering tensile strain at the bottom of DBM.

Bulk density of mix	= 2376 kg/m^3
The unit wt. of CA	= 1545 kg/m^3
The unit wt. of FA	= 1650 kg/m^3

The details of the cost are worked out assuming the plant output per day = 147 MT (61.9 m^3)

The cost analysis per m^{3}for subgrade, subbase, WBM, DBM and BC is summarised in Table 16. The construction cost of different layers including the subbase layers consisting of pond ash alone and the pond ash stabilised with two different admixtures for the same service life is given in Table 17 for a 1-km-long pavement (using the results summarised earlier in the 'subbase thickness' column of Table 10). Percentage savings in the total cost by direct replacement of CSM by pond ash alone and of ash mixes with admixtures are also shown in Table 17.

As mentioned earlier, for the same pavement life, an increased thickness of subbase made of ash-based material could be used to partially replace a thickness of WBM. A comparison of the savings in the cost of construction with respect to thickness ratio of WBM to subbase for various subbase materials considering maximum vertical compressive strain at the top of subgrade and maximum tensile strain at the bottom of DBM is shown in Figures 9 and 10, respectively. This is based on the thickness data presented in the subbase and WBM thickness columns of Table 10 and on similar computations for other thickness combinations.

Table 11. Cost analysis of subgrade course.

Taking Output: 100 m^3						
(a)	Labour component					
	Sl. No.	Item	Unit	Quantity	Rate (Rs.)	Amount (Rs.)
	1	Mate	Day	0.04	360.49	14.42
	2	Labour (unskilled)	Day	1.50	238.07	357.11
	Total					371.53
	Total per m^3					3.72
(b)	Machinery					
	Sl. No.	Item	Unit	Quantity	Rate (Rs.)	Amount (Rs.)
	1	Grader	Hr	2.00	1800.00	3600.00
	2	Dozer	Hr	0.50	1200.00	600.00
	3	Water tanker	Hr	5.00	350.00	1750.00
	4	Vibratory compactor	Hr	1.25	760.00	950.00
	5	Dumper	Hr	1.25	1400.00	1750.00
	6	Excavator	Hr	1.00	1700.00	1700.00
	7	Soil spreading unit	Hr	0.36	2250.00	810.00
	Total					11160.00
	Total per m^3					111.60

Downloaded by [Delhi Technological University] at 21:48 12 November 2015

Table 12. Cost analysis of subbase constructed by pond ash, pond ash mixed with admixtures and CSM.

Taking Output: 300 m^3						
(a)	Labour component					
	Sl. No.	Item	Unit	Quantity	Rate (Rs.)	Amount (Rs.)
	1	Mate	Day	0.48	360.49	173.04
	2	Labour (Skilled)	Day	2.00	292.45	584.90
	3	Labour (Unskilled)	Day	10.00	238.07	2380.70
	Total					3138.64
	Total per m^3					10.46
(b)	Machinery					
	Sl. No.	Item	Unit	Quantity	Rate (Rs.)	Amount (Rs.)
	1	Grader	Hr	6.00	1800.00	10800.00
	2	Water Tanker	Hr	5.00	350.00	1750.00
	3	Vibratory Compactor	Hr	10.00	760.00	7600.00
	4	Tractor with Rotavator	Hr	10.00	360.00	3600.00
	Total					23750.00
	Total per m^3					79.17
(c)	Material cost					
	Sl. No.	Item	Unit	Quantity	Rate (Rs.)	Amount (Rs.)
	1	Pond Ash (30% extra for loose state)	m^3	390.00	0.00	0.00
	2	Fibre (0.5%)	T	1.38	96000.00	132480.00
	3	Lime (2%)	T	20.1	7000.00	140700.00
	4	CSM*	m^3	384.00	591.10	226982.40
	Combinations		1 (Rs.)	1+2 (Rs.)	1+3 (Rs.)	4 (Rs.)
	Total		0.00	132480.00	140700.00	226982.40
	Total per m^3		0.00	441.60	469.00	756.61
(d)	CP & OC**		11.20	66.40	69.83	105.78
	Grand Total (a + b + c + d)		100.83	597.63	628.46	952.02

*Rate of CSM (75% of RBM @ Rs. 572.20 and 25% of 45–63 Stone Ballast @ Rs.647.80)
**Contractor's Profit and Overhead Charges @12.5% on (a) + (b) + (c).

Table 13. Cost analysis of base course WBM of Grade-3.

Taking Output: 360 m^3						
(a)	Labour component					
	Sl. No.	Item	Unit	Quantity	Rate (Rs.)	Amount (Rs.)
	1	Mate	Day	10.08	360.49	3633.74
	2	Labour(Skilled)	Day	2.00	292.45	584.90
	3	Labour(Unskilled)	Day	200.00	238.07	47614.00
	Total					51832.64
	Total per ^{m3}					143.98
(b)	Machinery					
	Sl. No.	Item	Unit	Quantity	Rate (Rs.)	Amount (Rs.)
	1	Vibratory Compactor	Hr	45.00	760.00	34200.00
	2	Water Tanker	Hr	24.00	350.00	8400.00
	Total					42600.00
	Total per m^3					118.33
(c)	Material cost					
	Sl. No.	Item	Unit	Quantity	Rate (Rs.)	Amount (Rs.)
	1	GSB Material*	m^3	522.00	659.64	344332.08
	Total					344332.08
	Total per m^3					956.48
(d)	Contractor's Profit and Overhead Charges @12.5% on (a) + (b) + (c)					152.35
	Grand Total (a + b + c + d)					1371.14

*Rate of GSB Material (80% of 22–53 Stone Ballast @ Rs. 647.80 and 20% of 10–12.5 Aggregate @ Rs.707.00).

From Figure 9, the saving in the total cost of construction is 11.49, 5.18 and 12.41% when 200-mm-thick subbase layer is made up of pond ash with no addition, 0.5% fibre and 2% lime, respectively, keeping the WBM thickness at 250 mm (thickness ratio = 1.25). The saving in the total cost of construction is 12.13, 5.54 and 12.69% when 200-mm subbase layer is made up of the same materials as mentioned above, keeping the WBM thickness as 200- mm (thickness ratio = 1.0); and savings of 12.39, 5.68 and 12.97% are achieved for a 150-mm WBM thickness and a 200-mm subbase layer (thickness ratio = 0.75).

The saving in the total cost of construction for the equivalent thicknesses of subbase layer made up of pond ash alone and with 2% lime, considering tensile strain at the bottom of DBM, could not be made. This is because, instead of a saving, the cost of construction of the pavement is increased due to the application of these materials (due to the cost of subbase preparation being greater than for the saving in subbase made up of CSM). Only 0.5% fibre treatment produces a cost saving when tensile strain at the bottom of the DBM layer is considered. Figure 10 shows the possible savings as a function of WBM and subbase thickness.

The sensitivity of the percentage saving of the cost of construction of 1-km pavement was checked based on a small parametric study considering maximum vertical compressive strain at the top of subgrade and maximum tensile strain at the bottom of DBM. In the study, the cost of WBM, DBM or BC course was (separately) increased by 10% from the basic price. The thickness

Downloaded by [Delhi Technological University] at 21:48 12 November 2015

Table 14. Cost analysis of DBM of Grade-2.

Taking Output: 62.5 m^3						
(a)	Labour component					
	Sl. No.	Item	Unit	Quantity	Rate (Rs.)	Amount(Rs.)
	1	Labour(Unskilled)	Day	16.50	238.07	3928.16
	Total					3928.16
	Total per m^3					62.85
(b)	Machinery					
	Sl. No.	Item	Unit	Quantity	Rate (Rs.)	Amount(Rs.)
	1	Plant	Day	1.00	10000.00	10000.00
	2	Tipper	Day	3.60	1600.00	5760.00
	3	Loader	Day	1.00	900.00	900.00
	4	Road Roller	Day	3.60	1000.00	3600.00
	Total					20260.00
	Total per m^3					324.16
(c)	Material cost					
	Sl. No.	Item	Unit	Quantity	Rate (Rs.)	Amount(Rs.)
	1	Bitumen	T	6.615	33000.00	218295.00
	2	Coarse Aggregate	m^3	58.90	647.80	38155.42
	3	Fine Aggregate	m^3	29.70	707.00	20997.90
	Total					277448.32
	Total per m^3					4439.17
(d)	Contractor's Profit and Overhead Charges @12.5% on (a)+(b)+(c)					603.27
	Grand Total (a + b + c + d)					5429.45

Table 15. Cost analysis of bituminous concrete (BC).

Taking Output: 61.9 m^3						
(a)	Labour component					
	Sl. No.	Item	Unit	Quantity	Rate (Rs.)	Amount (Rs.)
	1	Labour (Unskilled)	Day	16.50	238.07	3928.16
	Total					3928.16
	Total per m^3					62.85
(b)	Machinery					
	Sl. No.	Item	Unit	Quantity	Rate (Rs.)	Amount (Rs.)
	1	Plant	Day	1.00	10000.00	10000.00
	2	Tipper	Day	3.60	1600.00	5760.00
	3	Loader	Day	1.00	900.00	900.00
	4	Road Roller	Day	3.60	1000.00	3600.00
	Total					20260.00
	Total per m^3					324.16
(c)	Material cost					
	Sl. No.	Item	Unit	Quantity	Rate (Rs.)	Amount (Rs.)
	1	Bitumen	T	8.09	33000.00	266970.00
	2	Coarse Aggregate	m^3	55.78	647.80	36134.28
	3	Fine Aggregate	m^3	29.50	707.00	20856.50
	4	Lime	T	4.20	1800.00	7560.00
	Total					331520.00
	Total per m^3					5304.32
(d)	Contractor's profit and overhead charges @12.5% on (a) + (b) + (c)					711.42
	Grand Total (a + b + c + d)					6402.75

Table 16. Thickness and cost of construction of various layers.

		Subbase course						
Pavement component	Sub-grade	CSM	Pond ash	Pond ash +Fibre (0.5%)	Pond ash +Lime (2%)	WBM course	DBM course	Bituminous concrete
Thickness (mm)	500			200		250	135	50
Cost per m^3 (Rs.)	111.6	952.02	100.83	597.63	628.46	1371.14	5429.45	6402.75

ratio was varied by keeping WBM thickness (=250 mm) constant but increasing the subbase thickness from 200 mm to 500 mm, as mentioned in Table 7.

For these 10% increases in material costs, the parametric study revealed that the saving in the cost of construction reduced by 1.7–2.2% (pond ash alone), 3.1–4.0% (ash + 5% fibre) and 1.3–1.6% (ash + 2% lime); the range being a consequence of the particular material that was 10% more expensive. These figures are based on the change in pavement performance as predicted by the change in vertical compressive strain. The predicted cost saving reduced a little less (by only 1.4–3.9% for the ash + 5% fibre) when the change in tensile strain at the bottom of the DBM was considered. Thus, rutting is expected to be the controlling factor in determining sensitivity to material prices.

12. Design recommendations

From Figure 9, for the thickness ratio of 0.3 (thickness of WBM = 150 mm and subbase = 500 mm) considering vertical strain at the top of subgrade, the percentage saving of the

Downloaded by [Delhi Technological University] at 21:48 12 November 2015

Table 17. Percentage saving in the cost for 1-km-long pavement section with stabilised subbase layer for the same service life.

Sl. No.	Pavement component		Top width (m)	Bottom width (m)	Height* (m)	Volume (m^3)	Rate per m^3 (Rs.)	Total Rate (Rs.)	Total Cost (Rs.) (1+2+3+4+5)	Saving in cost (%)
1	Bituminous Course		3.75	3.95	0.05	192.5	6402.75	1232529	–	–
2	DBM Course		3.95	4.49	0.135	569.7	5429.45	3093158		
3	WBM Course		4.49	5.49	0.250	1247.5	1371.14	1710497		
4	Subbase Course		5.49							
(a)	CSM			6.29	0.200	1178	952.02	1121480		–
(b)	Pond Ash			6.75	0.315	1928	100.83	194380		
(c)	Pond Ash + Fibre (0.5%)			6.07	0.145	838	597.63	500874		
(d)	Pond Ash + Lime (2%)			6.378	0.222	1317	628.46	827901		
5	Subgrade	(a)	6.29	8.29	0.5	3645	111.60	406782	7564446	–
		(b)	6.75	8.75		3875		432450	6663014	11.92
		(c)	6.07	8.07		3535		394506	6931564	8.37
		(d)	6.378	8.378		3689		411692.4	7275777	3.82

*Equivalent height of same SLR.

Downloaded by [Delhi Technological University] at 21:48 12 November 2015

cost of construction of 1-km pavement is maximum (=21.00%) when pond ash mixed with 0.5% fibre is used as subbase material. Similarly, for the thickness ratio of 1.25 (thickness of WBM = 250 mm and subbase = 200 mm), the percentage saving of the cost of construction of 1-km pavement is minimum (=3.82%) when pond ash mixed with 2% lime is used as subbase material. As per IRC: 37-2001, considering a traffic load of 100 msa and CBR of 9% subgrade, the recommended thicknesses of WBM and subbase are 250 mm and 200, respectively, (Figure 1), i.e. thickness ratio = 1.25. For this recommended thickness ratio, the percentage savings of the cost of construction of pavement are minimum than the rest when subbase layer is made up of pond ash alone and mixed with admixtures. However, if we consider the above-recommended thicknesses of WBM and subbase as per IRC: 37-2001, the SLR of the pavement will be reduced by 18% (SLR = 0.82) taking SLR = 1.00 for CSM.

Similarly, from Figure 10, for the thickness ratio of 0.3 (thickness of WBM = 150 mm and subbase = 500 mm) considering tensile strain at the top of WBM, the percentage saving of the cost of construction of 1-km pavement is maximum (=26.23%) when pond ash mixed with 0.5% fibre is used as subbase material. Similarly, for the thickness ratio of 1.25 (thickness of WBM = 250 mm and subbase = 200 mm), the percentage saving of the cost of construction of 1-km pavement is minimum (=11.89%) when same material is used as subbase material.

The main purpose/aim of the present study is to maximise the utilisation of pond ash as subbase material alone or with admixture to replace the CSM, without affecting the service life of the pavement. Again while selecting the subbase material, the cost of construction of the pavement is also to be considered. So keeping both the points in mind and considering Figures 9 and 10, the thickness ratio of 0.3 (thickness of WBM = 150 mm and subbase = 500 mm) when pond ash mixed with 0.5% fibre is used as subbase material is recommended for the construction of pavement keeping other course of pavement section constant.

13. Conclusions

In the present study, induced vertical strain and tensile strain at the top of subgrade and at the top of WBM, respectively, are used to compare the quality and cost of different pavements when the subbase layer is made up of Badarpur pond ash alone and Badarpur pond ash stabilised with different admixtures. A commercially available finite element-based software 'PLAXIS' is used to evaluate the vertical and tensile strain at the top of subgrade and at the top of WBM, respectively, and as well as the distribution of strain inside different layers of pavement. The pavement section was modelled as an axisymmetric problem and standard boundary conditions were used. The extent of the boundaries of the section was then fixed by a small parametric study.

A nominal pavement structure used for the parametric study was first designed as per IRC: 37-2001 considering a traffic load of 100 msa and CBR of 9% corresponding to Delhi silt subgrade at Jamia Millia Islamia. The thickness of subbase layer, WBM layer and DBM layer was then varied with respect to this nominal pavement and the response of the pavement was evaluated.

Designed life and service life of a pavement is defined as the cumulative number of standard axles that can be carried before strengthening of pavement is necessary based on rutting failure criterion. A standard equation is available that uses maximum subgrade vertical strain to evaluate the design life and thus, the quality of the pavement. A SLR is defined as a function of induced subgrade strain in a given pavement vis-à-vis in a conventional pavement structure. Thus, the SLR indicates the lifetime of other pavements vis-à-vis conventional pavement structure.

An equivalent thickness is defined as the modified thickness of a particular layer of a new pavement required that has one of the layers made up of new material such that the lifetime of the new pavement remains the same as that of the conventional pavement. Based on the above parametric study, the equivalent thickness of subbase, WBM and DBM layers are calculated when the subbase layer is made up of Badarpur pond ash mixed with no additive, 0.5% fibre and 2% lime. This was followed by the cost analysis of 1-km-long pavement structure with a top width of 3.75 m based on the schedule of rates for Delhi region. Based on this study, the following conclusions are drawn.

(1) The vertical compressive strain was found to be maximum for pond ash.
(2) i) With the increase in the percentage of fibre (up to 0.5%), the stiffness of pavement increases and the maximum strain decreases.
ii) With the increase in the percentage of lime (up to 5%), the stiffness of pavement increases and the maximum strain decreases. But from simplicity of mixing

point of view, the percentage of lime used was 2% in the test.

(3) For the same SLR, the thickness of subbase layer made up of CSM (=200 mm) varies from 0.145 to 0.315 m. The maximum thickness is obtained from pond ash and minimum from fibre. The corresponding saving in the total cost is 3.82%–11.92%. The maximum cost saving is in pond ash and minimum is in lime.

(4) Keeping the subbase layer made of different admixtures constant (=200 mm), the same service life can be obtained by varying the thickness of WBM. Based on this, the thickness of WBM varies from 0.181 to 0.460 m for 200-mm-thick subbase layer of different admixtures. The maximum WBM thickness was obtained where pond ash used as subbase material and minimum thickness was obtained where fibre-reinforced pond ash used as subbase material. The saving in the total cost of construction is 11.49, 5.18 and 12.41% when 200-mm-thick subbase layer is made up of pond ash with no addition, 0.5% fibre and 2% lime, respectively, considering WBM thickness as 250 mm (thickness ratio = 1.25). Again, the saving in the total cost of construction is 12.13%, 5.54% and 12.69 and 12.39, 5.68 and 12.97% when 200-mm subbase layer is made up of same materials as mentioned above, considering WBM thickness as 200 mm (thickness ratio = 1.0) and 150 mm (thickness ratio = 0.75), respectively.

(5) Keeping the subbase layer made of different admixtures constant (=200 mm), the same service life can be obtained by varying the thickness of DBM. Based on this, the thickness of DBM varies from 0.108 to 0.200 m for 200-mm-thick subbase layer of different admixtures. The maximum DBM thickness was obtained where pond ash was used as subbase material and minimum thickness was obtained where pond ash mixed with 0.5% fibre used as subbase material.

(7) Comparing subbase and WBM, the variation in subbase thickness gives the maximum saving for same SLR.

(8) Based on a parametric study, it is seen that the percentage saving of the cost of construction of the pavement is between 1.3 and 4% for a 10% increase in WBM, DBM or BC costs.

Downloaded by [Delhi Technological University] at 21:48 12 November 2015

Acknowledgements

The first author wishes to thank M/s PDP Steels Limited, Assam, for funding and Delhi Technological University for allowing a short sabbatical visit to the University of Nottingham where most of the research reported here was performed. Both authors thank the Nottingham Transportation Engineering Centre at the University of Nottingham for providing the facilities to host this visit.

Disclosure statement

No potential conflict of interest was reported by the authors.

References

Atkinson, V.M., Chaddock, B.C., and Dawson, A.R., 1999. *Enabling the use of secondary aggregates and binders in pavement foundations*. Crowthorne: Transport Research Laboratory, TRL Report 408.

Bauer, G.E. and Fatani, M.N., 1991. Strength characteristics of sand reinforced with rigid and flexible elements, *Proceedings of ix Asian Regional Conference on soil mechanics and foundation engineering*, Bangkok, 1, 471–474.

Blodgett, S., 2004. *Environmental impacts of aggregate and stone mining-New Mexico case study*. New Mexico, NM: Center for Science in Public Participation.

Bullen, F. and Dawson, A.R., 1991. Furnace bottom ash: its engineering properties and its use as a sub-base material. *ICE Proceedings*. 90, 993–1009.

Central Road Research Institute, 2009. *Pavement engineering and materials – pavement evaluation*. Annual Report 2009–10, 51–76.

Chakraborty, T.K. and Dasgupta, S.P., 1996. Randomly reinforced fly ash foundation material, *Indian Geotechnical Conference*, Madras, India, 1, 231–235.

Chakroborty, P. and Das, A., 2003. Principles of transportation engineering. New Delhi: Prentice Hall of India.

Chand, S.K. and Subbarao, C., 2007. Strength and slake durability of lime stabilized pond ash. *Journal of Materials in Civil Engineering*. ASCE, 19 (7), 601–608.

Chu, T.Y., *et al.*, 1995. Soil stabilization with lime-fly ash mixtures: preliminary studies with silty and clayey soils. *Highway Research Board Bulletin*, 108, 102–112.

Consoli, N.C., Prietto, P.D.M., and Ulbrich, L.A., 1998, Influence of fiber and cement addition on behavior of sandy soil. *Journal of Geotechnical and Geoenvironmental Engineering*. ASCE, 124 (12), 1211–1214.

Dawson, A.R., *et al.*, 1996. Enabling the use of secondary aggregates and binders in pavement foundations, *Results of Phase 2 Study. Link II Project*. UK: University of Nottingham.

DiGioia, A.M. and Nuzzo, W. L., 1972. Fly ash as structural fill. *Journal of Power Division*, ASCE, 98 (1), 77–92.

Fawconnier, C.J. and Korsten, R.W.O., 1982. *Ash fill in pillar design-Increased Underground Extraction of Coal*. The SAIMM Monograph Series, 4, 277–361.

Galvin, J.M. and Wagner, H., 1982. Use of ash to improve strata control in bord and pillar working. *In: Proceedings symposium on strata mechanics*. University of Newcastle-upon-Tyne, 264–270.

Gopalan, M.K. and Haque, M.N., 1986. Strength development of clinically cured plain fly ash concretes, In *Proceedings of Australian Road Research Board*, vol. 13, Pt. 5, 27–33.

Gray, D.H. and Maher, M.H., 1989. Admixture stabilization of sand with discrete randomly distributed fibers. *Proceedings of XII international conference on soil mechanics and foundation engineering, Rio de Janeiro, Brazil*, vol. 2, 1363–1366.

Gray, D.H., Tons, E., and Thiruvengadam, T.R., 1994. Performance evaluation of a cement-stabilized fly ash base. *Transportation Research Record*, 1440, 51–59.

Gulhati, S.K. and Datta, M., 1999. *Geotechnical engineering*. New Delhi: Tata McGraw-Hill.

Hoover, J., *et al.*, 1982. *Performance of randomly oriented fiber-reinforced roadway soils: A laboratory and field investigation*. Iowa DOT Project HR-211, Iowa State University, Department of Civil Engineering, Ames, Iowa.

Huang, Y.H., 1993. *Pavement analysis and design*. Englewood Cliffs: Prentice-Hall.

IRC:37, 2001. *Guidelines for the design of flexible pavement*. New Delhi: Indian Roads Congress.

IRC:86, 1983. *Geometric design standards for urban roads in plains*. New Delhi: Indian Roads Congress.

Joshi, R.C., Natt, G.S., and Wright, P.J., 1981. Soil improvement by lime-fly ash slurry injection, *In:* Proceedings of 10th International Conference on Soil Mechanics & Foundation Engineering, Stockholm, vol. 3, 707–712.

Kaniraj, S.R. and Havanagi, V.G., 2001. Behavior of cement-stabilized fiber-reinforced fly ash-soil mixtures. *Journal of Geotechnical and Geoenvironmental Engineering*, ASCE, 127 (7), 574–584.

Ksaibati, K. and Bowen, M.M., 2001. Utilization of bottom ash in pavement bases, *In*: T.T. Eighmy, ed. *Proceedings of Beneficial Use of Recycled Materials in Transportation Applications*, Edi. , Nov. 13–15, Arlington, Virginia, 875–884.

Ksaibati, K. and Conklin, T.L., 1994. Field performance evaluation of cement-treated bases with and without fly ash. *Transportation Research Record*, 1440, 16–21.

Kumar, P. and Singh, S.P., 2008. Fiber-reinforced fly ash subbases in rural roads. *Journal of Transportation Engineering*. ASCE, 134, 171–180.

Kumar, R., Kanaujia, V.K., and Chandra, D., 1996. Engineering behaviour of fibre-reinforced pond ash and silty sand. *J. Geosynthetics Internationals 1996*, 6 (6), 509–518.

Lee, S.W. and Fishman, K.L., 1993. Resilient and plastic behavior of classifier tailings and fly ash mixtures. *Transportation Research Record*, 1418, 8–15.

Lee, K.W., *et al.*, 2001. *Structural analysis of New England subbase materials and structures*. The New England Transportation Consortium, Report of Project No. 94-1 (NETCR 26). Connecticut, CT.

Loulizi, A., *et al.*, 2006. Comparing resilient modulus and dynamic modulus of hot-mix asphalt as material properties for flexible pavement design, *Transportation Research Record*: Journal of the Transportation Research Board of the National Academies, Washington, DC, 161–170.

Maher, M.H. and Gray, D.H., 1990. Static response of sands reinforced with randomly distributed fibers. *Journal of Geotechnical Engineering, ASCE*, 116 (11), 1661–1667.

Maher, M.H. and Ho, Y.C., 1994. Mechanical-properties of kaolinite fiber soil composite. *Journal of Geotechnical Engineering, ASCE*, 120 (8), 1381–1393.

Maser, K.R., Wallhagen, R.E., and Dieckman, J., 1975. Development of fly ash cement mine sealing system, USBM, Open File Report 26-76, NTIS –PB-250611.

Michalowski, R.L. and Zhao, A., 1996. Failure of fiber-reinforced granular soils. *Journal of Geotechnical Engineering*, ASCE, 122 (3), 226–234

Mishra, M.K. and Karanam, U.M., 2006. Geotechnical characterization of fly ash composites for backfilling mine voids. *Geotechnical and Geological Engineering*, 24 (6), 1749–1765.

MORT&H, 2011. Report of the working group on central roads sector, 12th Five Year Plan (2012–17), Ministry of Road Transport & Highways, Government of India.

Nataraj, M.S. and McManis, K.L., 1997. Strength and deformation properties of soils reinforced with fibrillated fibers. *Geosynthetics International*, 4 (1), 65–79.

Ornebjerg, H., *et al.*, 2006. Management of bottom ash from WTE plants - an overview of management options and treatment methods. *Report of Working Group on Thermal Treatment of Waste*. Kongens Lyngby: International Solid Waste Association.

Palariski, J., 1993. The use of fly ash tailings, rock and binding agents as consolidated backfill for coal mines. *In*: H.W. Gelen, ed. *Proceedings of Mine fill*. Johannesburg: SAIMM, 403–408.

Raymon, S., 1961. Pulverized fuel ash as embankment material. *ICE Proceedings*, 19, 515–536.

Santoni, R.L. and Webster, S.L., 2001. Airfields and roads construction using fiber stabilization of sands. *Journal of Transportation Engineering*, ASCE, 127 (2), 96–104.

Sarkar, R., Abbas, S.M., and Shahu, J.T., 2012. A comparative study of geotechnical behaviour of lime stabilized pond ashes from Delhi region. *International Journal of GEOMATE*, 3 (1), 273–279.

Setty, K.R.N.S. and Rao, S.V.G., 1987. Characteristics of fibre reinforced lateritic soils, *Indian geotechnical conference*. Banglore, India, 1, 329–333.

Sherwood, P., 1995. *Alternative materials in road construction*. London: Thomas Telford Publishing.

Shewbridge, S.E. and Sitar, N., 1989. Deformation characteristics of reinforced sand in direct shear. *Journal of Geotechnical Engineering*, ASCE, 115 (8), 1134–1147.

Shodhganga. 2006. Engineering properties of subgrade soils, moorum and aggregate. Available from: http://shodhganga.inflibnet.ac.in/bitstream/10603/8702/12/12_chapter%204.pdf

Singh, S.P. and Kumar, P., 2005. Utilization of fibre reinforced flyash in road sub-bases, *Fly Ash Utilization Programme (FAUP)*. TIFAC, DST, New Delhi, VIII 17.1–17.8.

Singh, S.P. and Ramaswamy, S.V., 2005. Utilization potential of cement stabilized flyash-gbfs mixes in highway construction, *Fly Ash Utilization Programme (FAUP)*. TIFAC, DST, New Delhi, VIII, 4.36–14.11.

Sinha, A.K., 2009. *Study on subbase materials for rural roads*. Thesis (PhD). Dept. of Civil Engineering, IIT-Roorkee.

Subbarao, C., *et al*., 2001. Fly ash and stabilized fly ash as construction materials, Proceedings of International Conference on Advances in Civil Engineering, 1085–1092.

Theyse, H.L., 2002, *Stiffness, strength, and performance of unbound aggregate material: application of South African HVS and laboratory results to California flexible pavements*. University of California, Report – California Partnered Pavement Research Program.

Tirumala, K.G., 2007. *Geotechnical characteristics of pond ash mixed with randomly oriented Fibres*. MTech thesis. Depatment of Civil Engineering, IIT-Delhi.

Titi, H.H., Coenen, A.R., and Elias, M.B., 2009. Resilient characteristics of bottom ash. *In*: E. Tutumluer and I.L. Al-Qadi, eds. *Bearing Capacity of Roads, Railways and Airfields*, London: Taylor & Francis Group, 117–124. ISBN 978-0415-87199-0.

Downloaded by [Delhi Technological University] at 21:48 12 November 2015

Volume 3, Issue 3 (2015) 503-507 ISSN 2347 - 3258
International Journal of Advance Research and Innovation

Effect of Homogeneous Catalysts on Production of Biodiesel from Crude Neem Oil Feedstock and Cost Analysis of Biodiesel Production

R. S. Mishra, Amit Pal, Anand Prakash Mall
Department of Mechanical Engineering, Delhi Technological University, New Delhi, India

Article Info

Article history:
Received 10 July 2015
Received in revised form
20 July 2015
Accepted 28 August 2015
Available online 15 September 2015

Keywords

Homogeneous Catalysts (KOH and NaOH),
Experimentation,
Acid esterification,
Alkaline transesterification,
Neem Oil (Azadirachta indica),
Neem Oil Methyl Ester (Biodiesel)

Abstract

A two-step transesterification process is developed to convert the high FFA oils to its mono-esters. Using 100 ml of oil, the optimum combination of parameters for pretreatment were found to be 0.45 v/v methanol-oil-ratio, 0.5% v/v H2SO4 acid catalyst, 50˚C and 45 min reaction time. After pretreatment of neem oil, transesterification reaction was carried out with 4.5:1 methanol-to-oil molar ratio, 1% KOH as alkaline catalyst, 75 min reaction time and 50˚C reaction temperature to produce the fatty acid methyl ester. This two step process gave maximum average yield of 70±2%.

1. Introduction

The use of alternative fuels instead of conventional fossil fuels is becoming increasingly significant due to decreasing petroleum reserves and increasing greenhouse gases, all of which lead to global warming, ozone depletion and political and health concerns (Fukuda et al., 2001). Plant oils have been used as alternative fuels for many years, since they are renewable and readily available. However, these oils cannot be used directly as fuel sources in diesel engines due to: (a) high viscosity which leads to poor fuel atomization during the injection process, (b) low volatility and (c) polymerization which results in deposit formation, incompletion combustion and poor emissions (Ma and Hanna, 1999). To overcome these disadvantages, oils can be converted into fatty acid methyl esters (FAME) which are also known as biodiesel. Biodiesel is an alternative fuel that is non-toxic, completely biodegradable and renewable and can be adapted easily without any modification to diesel engines.

Several processes have been developed for biodiesel production, such as pyrolysis, micro emulsification and transesterification. The chemical change of the products from the reactants caused by the thermal energy in the presence of air or nitrogen sparging is called a pyrolytic process. These products are similar to the petroleum-derived fuel. However, during the pyrolysis process, the removal of oxygen leads to reduce the environmental benefits (Ma and Hanna, 1999). The problem of the high viscosity of the substrates has been investigated using microemulsions with solvents (methanol, ethanol and 1-butanol) to meet the international standards of petroleum-derived fuels. However, an increase of lubricating oil viscosity, irregular injector needle sticking, incomplete combustion and heavy carbon deposits were reported in the laboratory screening endurance test. Therefore, transesterification process plays a vital role, in order to overcome these disadvantages.

Corresponding Author,
E-mail address: anandwrites@gmail.com
All rights reserved: http://www.ijari.org

The process of displacing alcohol from an ester to form another ester is called transesterification. Transesterification is the most simple and efficient method to produce biodiesel by using acids, alkalis, or enzymes as catalysts. Triglycerides with high free fatty acid and water contents are not essential for a biodiesel conversion process using an acid catalyst. However, the reaction rates are slower than those of the alkali catalytic process (Freedman et al., 1986). The alkali-catalysis transesterification process has been widely used in the biodiesel industry, because it gives a high yield of conversion of fatty acid methyl esters from triglycerides at low temperatures and pressures in a relatively short reaction time of 4-10 hours. However, it has several drawbacks including product separation, soap formation and negative environmental impacts such as greenhouse gas, CO, hydrocarbons, NOx and particles in exhaust emissions (Nielsen et al., 2008).

Neem is a tree in the family ‘maliaceae’ which grows various parts in Bangladesh. It’s scientific name ‘Azadirachtaindica’. The evergreen tree is large, reaching 12 to 18 meters in height with a girth of up to 1.8 to 2.4 meters. The seeds have 40% oil which has high potential for the production of biodiesel. It has a higher molecular weight, viscosity, density, and flash point than diesel fuel. Neem oil is generally light to dark brown, bitter and has a strong odor that is said to combine the odors of peanut and garlic [M.A. Fazal et al., 2011].

Neem comprises mainly of triglycerides and large amounts of triterpenoid compounds. It contains four significant saturated fatty acids, of which two are palmitic acid and two are stearic acid. It also contains polyunsaturated fatty acids such as oleic acid and linoleic acids [Muthu et al., 2010]

2. Materials and Methodology

2.1. Materials

Crude neem oil was purchased from local market. The magnetic stirrer with hot plate was at DTU laboratory.

Chemicals are used in transesterification process like Pottassium hydroxide pellet (88% purity), Methanol (99% purity), Concentrated sulphuric acid and Sodium hydroxide pellet (88% purity).

2.2. Equipment

A round bottom conical flask is used as reactor for these experimental purposes. A magnetic stirrer with hot plate arrangement is used for heating the mixture in the flask. The mixture is stirred at the same speed for all test runs. The temperature range of 40–60˚C is maintained during this experiment and its monitored by thermometer. The separating funnel is used to separate the methanol-water mixture after acid pretreatment and the glycerol after transesterfication.Three set of trail runs are carried out for each combination of parameter.

2.3. Methodology

The aim of this study is to improve the process for producing biodiesel from crude neem oil.

There are three processes such as
Oil filtration,
Acid esterification
and alkaline transesterification.

2.3.1. Oil filtration

Neem oil has higher moisture content and some other impurities. So, in order to remove the moisture and impurities from the neem oil it should be refined. The purification can be done by boiling oil with about 20% of water. The boiling should continue until no bubbles of water vapor anymore. After one hour the oil then becomes clear. This refined neem oil is taken as raw material for transesterification process.

2.3.2. Acid esterification

100 ml of refined neem oil is poured into the flask and heated up to 60˚C. The 45% v/v methanol is added with the preheated neem oil and stirred for a few minutes. 0.5% of sulphuric acid is added with the mixture. Heating and stirring should continue about 45min at atmospheric pressure. After completion of this reaction, the mixture is poured into a separating funnel for separating the excess alcohol, impurities and sulphuric acid. The excess alcohol, sulphuric acid and impurities move to the top layer and it's discarded. The lower layer is separated for further processing of transesterified into methyl ester. This process reduces the acid value of crude neem oil to less than 1% of FFA.Viscosity reduction increases with increase in methanol-to-oil ratio.

2.3.3. Alkaline Transesterification

After acid pretreatment the esterified oil is taken in flask and heated up to 60˚C. 1% of KOH is dissolved in 30% (6:1 M) methanol. The dissolved solution is poured into flask. The mixture is heated and stirred for 1hr.On completion of reaction, the mixture is poured into separating funnel over 12 hr.The glycerol and impurities are settled in lower layer and it's discarded. The impure biodiesel remain in upper layer. It contains some trace of catalyst, glycerol and methanol. The washing process can be done by the 3/4th of hot distilled water added with methyl ester and gently stirred. The upper layer is pure biodiesel and lower layer is drawn off.

3. Results and Discussion

3.1. Acid esterification

3.1.1. Effect of methanol-to-oil ratio

Two important parameter significantly affected the acid value. These are sulphuric acid concentration and methanol quantities. Molar ratio is defined as the ratio of number of moles of alcohol to number of moles of vegetable oil. Theoretically, transesterification reaction requires 3 moles of alcohol for each mole of oil. However, in practically molar ratio should be higher than stoichiometric ratio. By varying methanol proportion such as 0.35:1, 0.40:1,0.45:1, 0.50:1,0.55:1 methanol-to-oil ratio, among these 0.45:1 gave higher yied. The last two 0.50:1, 0.55:1 have only slight variation. In economic view 0.45:1 proportion is selected for reaction condition. The effect of methanol variation is shown in fig.1. from the figure conversion efficiency is slightly increase up to 0.45:1 methanol-to-oil ratio. After that conversion efficiency is decreased with increase in methanol-to oil ratio because it leads to increasing the acid value. It has been determined that viscosity reduction increases with increase in methanol-to-oil ratio.

Methanol to Oil Ratio (v/v)	0.35	0.40	0.45	0.50	0.55
Conversion Efficiency (%)	77	84	95	90	87

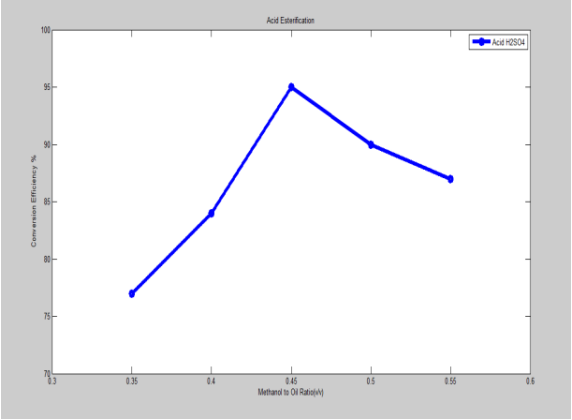


Fig: 1. Effect of Methanol-to-oil ratio on Conversion Efficiency

3.1.2. Effect of acid catalyst amount

Amount of acid catalyst variation is affecting the conversion efficiency. By varying sulphuric acid proportion such as 0.30, 0.40, 0.50, 0.60 and 0.70% v/v. Maximum conversion efficiency 95% is achieved in 0.5 % v/v H2SO4. Effect of acid catalyst variation is shown in fig. 3(i)(b) from the figure more than 0.5% v/v H2SO4, the product color is become black. Lower amount of sulphuric acid addition affects the final product yield.

Acid Catalyst % (v/v)	0.3	0.4	0.5	0.6	0.7
Conversion Efficiency (%)	67	72	95	82	77

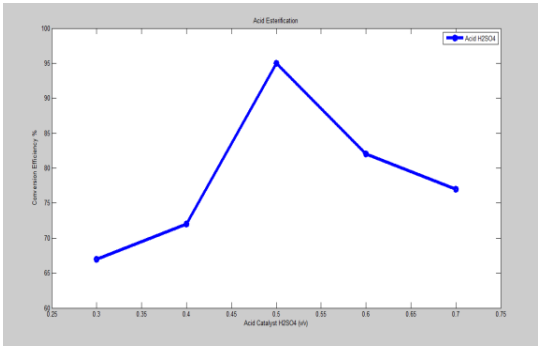


Fig: 2. Effect of acid catalyst amount on Conversion Efficiency

3.1.3. Effect of Reaction Temperature

The conversion efficiency is very low at room temperature even after 2 hr reaction .If increase in temperature the conversion takes place at higher rate. The optimum temperature is achieved at 50˚C.At high reaction temperature; the methanol is lost because melting point of methanol is 65˚C.Above 50˚C product color become black.

3.2. Alkaline Transesterification

3.2.1. Effect of methanol-to-oil ratio

Molar ratio is very important factor for transesterificatin reaction. Theoretically, transesterification reaction requires 3 moles of alcohol for each mole of oil. However, in practically molar ratio should be higher than stoichiometric ratio. The higher molar ratio is required for complete the reaction at higher rate. In lower molar ratio, it takes longer duration for complete the reaction. The effect of methanol-to-oil ratio on conversion efficiency is shown in fig.3(ii) (a) It has been seen that yield is slightly increase up to 4.5:1 methanol-to-oil molar ratio. The maximum methyl ester yield 69% is achieved at 4.5:1methanol to oil molar ratio. With further increase in methanol-to oil molar ratio the conversion efficiency is decreases.

Methanol to Oil Molar Ratio	3	4.5	6	7.5
Conversion Efficiency (%) with 1% NaOH	41	60	51	46
Conversion Efficiency (%) with 1% KOH	50	69	60	55

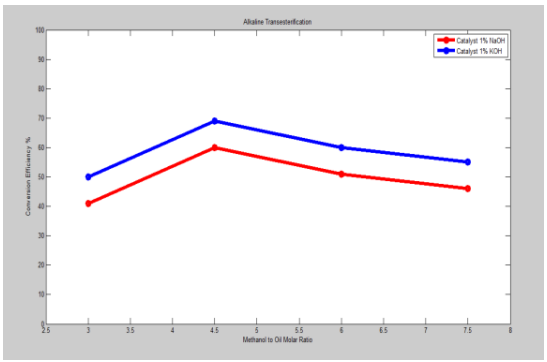


Fig: 3. Effect of methanol on Conversion Efficiency

3.2.2. Effect of Alkaline Catalyst

The amount of catalyst variation is affecting the conversion efficiency. The catalyst proportion is varied from 0.75- 1.50% KOH. The effect of catalyst variation on conversion efficiency is shown in fig.3(ii)(b) From the figure yield is slightly increased up to 1% KOH and after that yield is decreased due to reverse reaction is take place (emulsion formation).The maximum yield is achieved of 70% at 1% KOH.

Alkaline Catalyst %(wt/wt)	0.75	1	1.25	1.5
Conversion Efficiency(%) by NaOH	52	62	55	50
Conversion Efficiency(%) by KOH	62	70	65	60

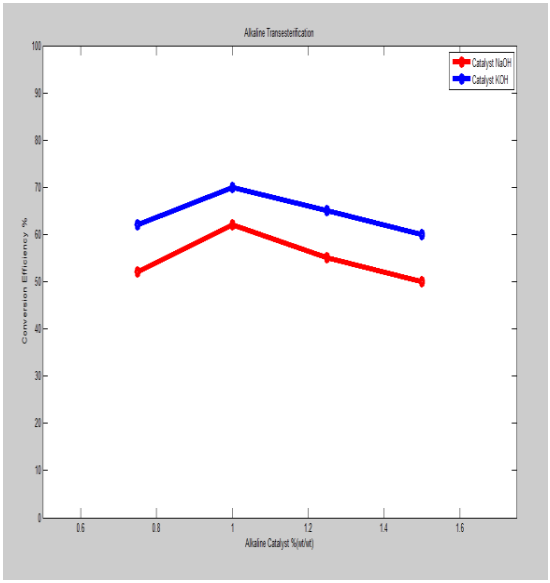


Fig: 4. Effect of Alkaline Catalyst Amount on Conversion Efficiency

3.2.3. Effect of Reaction Temperature

The reaction temperature has important role in alkaline-catalyst transesterification .At room temperature no significant yield is notified for even 2hr reaction. The yield is increased with increase in reaction temperature. The effect of temperature variation on conversion efficiency is shown in fig.3(ii)(c). By varying temperature in four different levels such as 45, 50, 55 and 60˚C among these 50˚C gave maximum methyl ester yield. If greater than 50˚C, chance for loss the methanol. The maximum ester efficiency 72% is achieved at 50˚C.

Reaction Temperature(°C)	45	50	55	60
Conversion Efficiency (%) with 1% NaOH	54	66	64	58
Conversion Efficiency (%) with 1% KOH	64	72	69	62

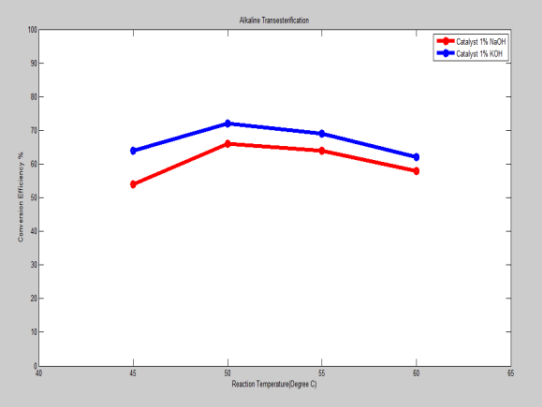


Fig: 5. Effect of Reaction Temperature on Conversion Efficiency

3.2.4. Effect of Reaction Time

The conversion rate is increased with increase in reaction time. In this experiment, reaction time varying from 55-85 min. The effect of reaction time variation on the conversion efficiency is shown fig.3(ii)(d) from the figure yield was slightly increased up to 75min reaction time and after that yield is decreased. The maximum efficiency is achieved of 68% for 75min reaction time. From these experiments the optimum yield is obtained at 75min reaction.

Reaction Time(min)	55	65	75	85
Conversion Efficiency (%) with NaOH	48	52	58	49
Conversion Efficiency (%) with KOH	58	62	68	59

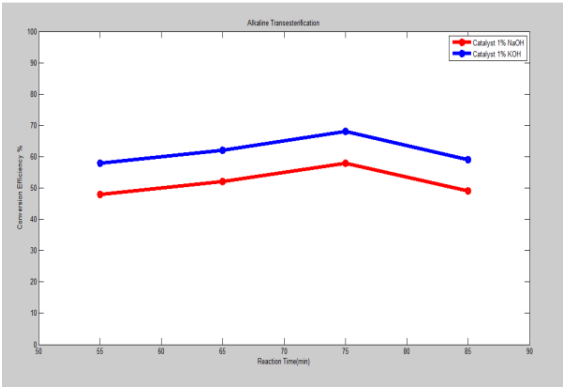


Fig: 6. Effect of Reaction Time on Conversion Efficiency

4. Conclusion

The high FFA (20%) content neem oil has been investigated for the biodiesel production. It has been found that the feedstock with high FFA its could not be transesterified with alkaline catalyst because the alkaline catalyst react with FFA to form soap. So in this study, two step processes was developed to convert FFA to its methyl ester. The first step is acid treatment it reduces the FFA content of oil to less than 1% using acid catalyzed (0.5 % v/v H_2SO_4) reaction with methanol (0.45 v/v) at 50˚C temperature and 45 min reaction time. After acid treatment alkaline transesterfication reaction was carried out at 1% w/w KOH, 4.5 methanols to oil molar ratio, 50˚C and 75 min reaction time. The maximum yield is 70±2%.The effect of molar ratio, catalyst; reaction temperature and reaction time are analyzed in each step process. Excess addition of sulphuric acid darkens the product and it leads to more production cost.

5. Cost Analysis

Sl. No	**Component**	**Cost (Rs.)**
1	Sodium Hydroxide (Catalyst)	23/kg
2	Potassium hydroxide (Catalyst)	36/kg
3	Neem oil (Feedstock)	150/ litre
4	Methanol (Alcohol)	35/ litre
5	Glycerin (By product of Biodiesel)	75/ litre
Sl. No.	**Component**	**Cost (Rs.)**
1	Neem Oil – 100 ml	15
2	Two step transesterification Cost - 65 ml(45 ml + 20 ml) of Methanol [4.5 Methanol/Oil Molar Ratio]	2.275
3	Catalyst KOH 1.0 gm	0.036
4	Recovery (Glycerin 50 ml)	3.75
5	Total Cost (1 + 2 + 3 – 4)	17.311 – 3.75 = 13.561

Biodiesel production from 1 litre Neem Oil=0.70 Litre
So Cost of Biodiesel per litre = [(13.561 /100)*1000] / 0.70 = 193.73 Rs.

The cost of the biodiesel production can be minimized as possible to recover the used methanol. Recycling of methanol again and again in mass production and commercial use, the cost must be come to the lowest amount. Also the by-product such as glycerin and soap play an important role to minimize the cost.

References

[1] A. K. Endalew, Y. Kiros, R. Zanzi, Heterogeneous catalysis for biodiesel production from Jatropha curcas oil (JCO), 2011, 36, 2693-2700

[2] A. Dhar, R. Kevin, A. K. Agarwal, Production of biodiesel from high-FFA neem oil and its performance, emission and combustion characterization in a single cylinder DICI engine. Fuel Processing Technology, 2012, 97, 118–129

[3] A. Demirbas, Progress and recent trends in biodiesel fuels. Energy Conversion and Management, 2009, 50, 14 -34

[4] C. Martín, A. Moure, G. Martín, E. Carrillo, H. Domínguez, J. C. Parajó, Fractional characterization of jatropha, neem, moringa, trisperma, castor and candlenut seeds as potential feedstocks for biodiesel

production in Cuba. Biomass Bioenergy, 2010, 34, 533-538
[5] D. Tanwar, Ajayta, D. Sharma, Y. P. Mathur, Production and Characterization of Neem Oil Methyl Ester. International Journal of Engineering Research & Technology (IJERT), 2, 2013, 1896-1903
[6] Dennis Y.C. Leung, Xuan Wu, M.K.H. Leung, A review on biodiesel production using catalyzed transesterification. Applied Energy, 87, 2010, 1083-1095
[7] E. F. Aransiola, E Betiku, DIO Ikhuomoregbe and TV Ojumu. Production of biodiesel from crude neem oil feedstock and its emissions from internal combustion engines. African Journal of Biotechnology, 2012, 11, 6178-6186
[8] Freedman B, R. Butterfield, E. Pryde, Transesterification kinetics of soybean oil. Journal of the American oil Chemists Society, 1986, 63, 1375-1380
[9] H. Fukuda, A. Kondo, H. Noda, Biodiesel fuel production by transesterification of oils. Journal of Bioscience and Bioengineering, 92, 2001, 405-416
[10] GT Jeong, HS Yang, DH Park, Optimization of transesterification of animal fat ester using response surface methodology. Bioresour. Technol, 100, 2009, 25-30
[11] H.N. Pandey, Development of a New Catalyst for Bio-diesel Production. Ist International Conference on New Frontiers in Biofuels, DTU, New Delhi, 2010
[12] H. Ibrahim, A. S. Ahmed, I.M. Bugaje, Dabo Mohammed, C. D. Ugwumma. Synthesis of Bulk Calcium Oxide (Cao) Catalyst and its Efficacy for Biodiesel Production. Journal of Energy Technologies and Policy, 3, 2013, 14-16
[13] J. V. Gerpen, Biodiesel processing and production, Fuel Process Technol 86, 2005, 1097–1107
[14] J.M. Marchetti, A.F Errazu, Esterification of free fatty acids using sulfuric acid as catalyst in the presence of triglycerides. Biomass. Bioenerg, 2008, 32, 892–895
[15] Juan Calero, Gema Cumplido, Diego Luna, Enrique D. Sancho, Carlos Luna, Alejandro Posadillo, Felipa M. Bautista, Antonio A. Romero, Cristóbal Verdugo-Escamilla, Production of a Biofuel that Keeps the Glycerol as a Monoglyceride by Using Supported KF as Heterogeneous Catalyst, 7, Energies 2014, 3764-3780
[16] L.C. Meher, D. Vidya Sagar, S. N. Naik, Technical aspects of biodiesel production by transesterification – a review. Renew, 10, Sustain. Energy 2006, 248-268
[17] M. Agarwal, K. Singh, U. Upadhyaya, S. P. Chaurasia, Potential vegetable oils of Indian origin as biodiesel feedstock– An experimental study. Journal of Scientific & Industrial Research, 71, 2012, 285-289
[18] M. Hassani, G. D Najafpour, Maedeh Mohammadi and Mahmood Rabiee. Preparation, Characterization and Application of Zeolite-based Catalyst for Production of Biodiesel from Waste Cooking Oil. Journal of Scientific & Industrial Research, 73, 2014, 129-133
[19] M. A. Hanna, Loren Isom, John Campbell, Biodiesel; Current perspectives and future. Journal of Scientific & Industrial Research, 64, 2005, 854-857
[20] F. Ma, M. A. Hanna. Biodiesel production: a review, Bioresour Technol, 70, 1999, 1–15
[21] Md. Hasan Alia, Md. Mashud, Md. Rowsonozzaman Rubel, Rakibul Hossain Ahmad, Biodiesel from Neem oil as an alternative fuel for Diesel engine. Procedia Engineering, 56, 2013, 625 – 630
[22] M. A. Fazal, A.S.M.A. Haseeb, H.H. Masjuki. Biodiesel feasibility study: An evaluation of material compatibility; performance; emission and engine durability. Renew, Sustain. Engy Reviews, 2011, 15, 1314-1324
[23] Module 5, Lecture 4. Design for Reliability and Quality. IIT, Bombay
[24] Muthu, V. Sathya Selvabala, T. K. Varathachary, D. Kirupha Selvaraj, J. Nandagopal, S. Subramanian, Synthesis of biodiesel from neem oil using sulfated zirconia via tranesterification, Brazilian Journal of chemical Engineering, 27, 2010, 601-608
[25] N. Satya Sree, V. Madhusudhan Rao, P. Vijetha, Production of Bio-Diesel From Soap Stock of Cotton Seed Oil By Using Ferric Sulphate Catalyst Via A Two Step Heterogeneous Catalysis: Characteristics of Bio-Diesel Produced. International Journal of Scientific & Technology Research, 3, 2014, 141-144
[26] Nielsen P. M., J. Brask, Fjerbaek, Enzymatic biodiesel production: Technical and economical considerations. European Journal of Lipid Science, 2008, 110, 692-700
[27] Olugbenga Olufemi Awolu, Stephen Kolawole Layokun. Optimization of two-step transesterification production of biodiesel from neem (Azadirachta indica) oil. International Journal of Energy and Environmental Engineering, 4, 2013, 1-9
[28] Padmarag Deshpande, Kavita Kulkarni, A. D. Kulkarni, Supercritical Fluid Technology in Biodiesel Production: A Review. Chemistry and Materials Research, 1, 2011, 27-32
[29] Poonam Gera, S.K. Puri, M. K. Jha, Use of Basic Heterogeneous Catalysts for Biodiesel Production: A Review. Ist International Conference on New Frontiers in Biofuels, DTU, New Delhi, 2010
[30] S. Singh, P.K. Omre, K. Gaikwad, Standardization of Process Parameters for Neem Oil & Determination of Properties for Using as a Fuel, International Journal of Engineering Research and General Science, 2, 2014, 1-7
[31] Talebian-Kiakalaieh, N. A. S. Amin, A. Zarei, H. Jaliliannosrati, Biodiesel Production from High Free Fatty Acid Waste Cooking Oil by Solid Acid Catalyst. Proceedings of the 6th International Conference on Process Systems Engineering (PSE ASIA), 2013, Kuala Lumpur.
[32] Vivek, A. K. Gupta, Biodiesel production from karanja oil. Journal of Scientific & Industrial Research, 63, 2004, 39-47.
[33] V. Manieniyan, R. Senthilkumar, S. Sivaprakasam. Experimental Investigation on Optimized Biodiesel (Based on Various Catalysts) used in a Twin Cylinder Diesel Engine. Ist International Conference on New Frontiers in Biofuels, DTU, New Delhi, 2010

INNOVATIVE ENERGY TECHNOLOGY SYSTEMS AND ENVIRONMENTAL CONCERNS: A SUSTAINABLE APPROACH
ISBN: 978-93-84144-81-4

Efficacy of Heavy Metals in Management of *Fusarium Udum* and *Fusarium Oxysporum F.Sp.Ciceri*

Ankita Shukla[1] and Rajeev Kumar Mishra[2]

[1]*Departmentl of Environmental Science B.B.Ambedkar University, Lucknow, U.P.*
[2]*Department of Environmental Engineering, Delhi Technological University, Delhi*

Abstract

The present study mainly use to evaluate the effect of three heavy metal i.e. Cobalt, Copper and Cadmium against the growth of fusarium udum and fusarium oxysporum f. sp. ciceri causing wilt in arhar and chickpea. Results from the study shows that copper significantly checks the growth of fusarium udum by 100% at 100 ppm conc followed by Cadmium (95.19%) and Cobalt (37.52%) at 100 ppm (at p<0.01) respectively .In case of fusarium oxysporum f. sp. ciceri Cadmium inhibited the growth significantly (100%) at 75 and 100 ppm followed by Copper(89.15%) and Cobalt(48.48%) at 100 ppm conc respectively (at p<0.01). It is shown by findings that copper and cadmium effectively suppressed the growth of both fusarium spp. with increasing concentration. Cobalt shows moderate effect against both the pathogen.

1. Introduction

Heavy metal contamination has been shown to affect the species composition of microbial communities in soil (Doelman, 1985; Duxbury, 1985; Bààth, 1989). Several studies have been done on ecotoxicological impact of heavy metals and metalloids composition and function soil microbial communities (Griller *et al.,* 1998; Kandeler *et al.,* 2000; Renella *et al*., 2005).Some soil-borne diseases *viz. fusarium* wilt of tomato and other vegetable crops have been suppress by micro and macroelements (Engelhard, 1989).Mineral elements also modify the plant root exudates results inhibiting the pathogens along with enhancing the population of plant growth promoting and antagonistic microorganisms (Huber, 1989). With the application of mineral elements in the host plants, enhanced the nutritional status which results in inhibition against fungal pathogens and also alter the physical and chemical properties of the soil and pH of rhizosphere (Schneider *et al*., 1995).Saikia *et al*. (2009) reported the combined activity of *Pseudomonas fluorescens* 4-92(Pf4-92) with zinc, copper and zinc+ copper against *Fusarium oxysporum f.sp.ciceri* causing chickpea wilt. *In vitro* study showed that 20, 30 and 40 g/ml concentration of Zn, Cu and Zn+Cu minerals inhibited the production of fusaric acid and enhanced the production of 2,4 diacetylphloroglucinol(DAPG), Salicylic acid, Pyochelin and Pyoluteorin by Pf4-92. This showed that Zn and Cu with enhancing the biocontrol activity reduced the production of fusaric acid (FA) by pathogen *Fusarium oxysporum f.sp.ciceri.*Application of 400ppm, 800ppm and 1200ppm of different heavy metals alone or in combination was used against *Sclerotium rolfsii sacc*. causing foot-rot in barley. *In vitro* studies indicated that zinc was most effective either alone i.e.1200ppm concentration or in combination wit Cu,Fe and magnesium at all concentrations for control of pathogen in soil,

ISBN: 978-93-84144-81-4

pot culture and field trail(R.K.Singh,1988).Dwivedi (1990) also reported that mercury, cadmium and copper completely (100%) checked the growth of *fusarium oxysporum* f.sp.*psidii* causing wilt disease of guava at 100 µg/ml concentration. Nickel, Cobalt and Stannous reduced the growth at about 60%,42.8% and 33.3% while barium,zinc,calcium, magnese and iron significantly inhibited the growth at higher concentration i.e. 200 µg/ml to 21.4%,21.6%,25.7%,26.6% and 30%.The objective of the present study was to evaluate the effect of three heavy metals viz. Cadmium (Cd), Cobalt (Co) and Copper(Cu) against the growth of *fusarium udum* and *fusarium oxysporum f.sp.ciceri.*

1.1 Materials and Methods

Soil samples and plant parts showing wilt characteristic has been collected from the field of pigeonpea and chickpea. The samples has been taken from Kalli paschim village, District Sarojini nagar, Lucknow . The plant parts are examine under microscope to confirm the presence of respective pathogen .First of all infected plant parts were cut in to pieces (2-3 mm), then it is surface sterilize with 0.1% mercuric chloride solution for 30 seconds. The isolation was made from roots as well as from the foliar parts of wilted pigeonpea and chickpea plants. The plant parts were washed three times with sterilized distilled water and then were transferred aseptically on Potato dextrose Agar (PDA) media. The inoculated plates has been incubated at room temperature (27±2°C) and observations are made daily for emergence of culture. After the development of the fungal colonies stock cultures were prepared using PDA in test tubes and stored in refrigerator at 4°C. Both wilt pathogens viz. *fusarium udum* and *fusarium oxysporum* f. sp.*ciceri* are isolated from infected pigeonpea and chickpea plants and identify as per the monograph and standard procedures.

1000 ppm stock solution of chloride form of heavy metals *viz.*, Cadmium, Chromium and Copper are prepared by adding sterilized distilled water. Toxicity test against both the pathogens has been done by food poisoned technique (Groover and Moore, 1962). Czapek-dox medium is prepare and autoclave at 15lb/in^2 twice for one hour and allow to cool it. After cooling, the desired quantities of heavy metals are mixed with Czapek-Dox agar medium to get final concentration of 50, 75 and 100 ppm. Incorporated medium is pour in petriplates with control one having no phenolic compound. Each experiment has been done in triplicates. 5 mm diameter disks cut from one week old culture of *Fusarium udum* and *Fusarium oxysporum f.sp. ciceri* are transfer at the center of each plate separately. Plates are incubate at 25±2˚C for a week. After 7 days, redial growth is measure and percent growth inhibition is calculate. Data has been analyzed statistically.

ISBN: 978-93-84144-81-4

2. Observations

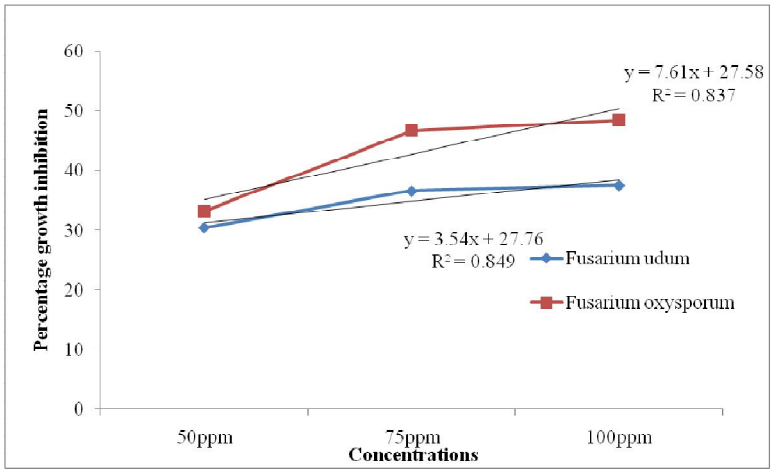


Fig. 1: Effect of cobalt against the growth of Fusarium udum and Fusarium oxysporum f.sp.ciceri

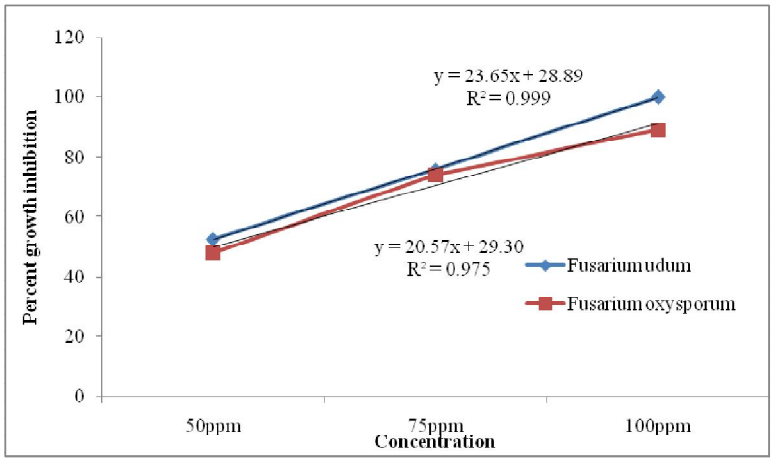


Fig. 2: Effect of copper against the growth of Fusarium udum and Fusarium oxysporum f.sp.ciceri.

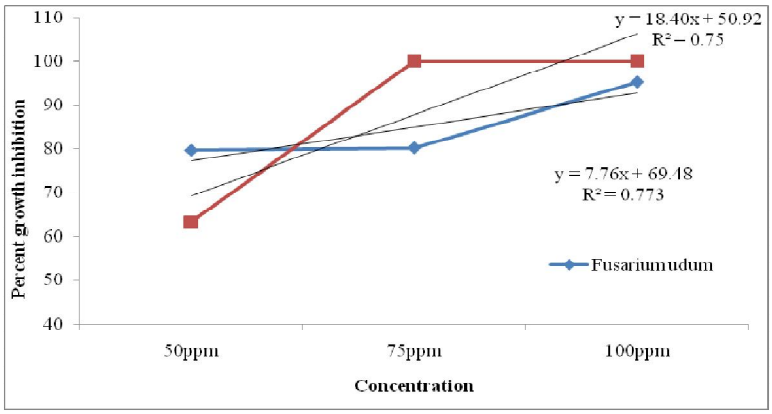


Fig. 3: Effect of cadmium against the growth of Fusarium udum and .Fusarium oxysporum f.sp.ciceri

ISBN: 978-93-84144-81-4

3. Result and Discussion

Findings shows that Cobalt at 50 ppm inhibits the growth of *fusarium udum* upto 30.44%, 36.56% at 75 ppm and 37.52% at 100 ppm with r^2 value 0.849 while in case of *fusarium oxysporum* f.sp.*ciceri* growth is inhibits to 33.26%, 46.67% and 48.48% at 50 ppm, 75 ppm and 100 ppm concentration of cobalt having r^2 value 0.837 respectively(Fig. 1). In case of Copper at 50 ppm inhibits the growth of *fusarium udum* upto 52.70%, 75.89% at 75 ppm and 100% at 100 ppm concentration. The regression coefficient value is 0.999. The radial growth of *fusarium oxysporum* f.sp.*ciceri* inhibits to 48.0% at 50 ppm, 74.22% at 75 ppm and 89.15% at 100 ppm concentration of copper with r^2 value 0.975 (Fig. 2). Cadmium reduce the growth of *fusarium udum* upto 79.67% , 80.15% and 95.19% with increasing concentration 50ppm, 75ppm and 100 ppm concentration having r^2 value 0.773 while radial growth of *fusarium oxysporum* f.sp.*ciceri* is reduce to 63.19% at 50 ppm, 100% at both 75 and 100 ppm concentration with r^2 value 0.75 (Fig 3). It is observe that growth of *fusarium udum* is completely check at 100 ppm of Copper, while 75 and 100ppm of Cadmium completely inhibits the growth of *fusarium oxysporum* f.sp.*ciceri* . There is significant reduction in the growth of *fusarium udum* was significantly reduced at 75 and 100 ppm concentration of cadmium. Cobalt shows the moderate effect against both the pathogen.

It may be conclude from above study that Copper significantly checks the growth of *fusarium udum* by 100% at 100 ppm conc followed by Cadmium (95.19%) and Cobalt (37.52%) at 100 ppm (at $p<0.01$) respectively wherease in case of *fusarium oxysporum* f. sp. *ciceri*, Cadmium inhibited the growth significantly (100%) at 75 and 100 ppm followed by Copper(89.15%) and Cobalt(48.48%) at 100 ppm conc. respectively (at $p<0.01$). In case of heavy metals 100 ppm of copper completely inhibited the growth of *fusarium udum*, while complete inhibition of growth of *fusarium oxysporum* f.sp. *ciceri* has been found at 75 and 100 ppm concentration of cadmium. Dwivedi (1990) also reported that mercury, cadmium and copper completely (100%) checked the growth of *fusarium oxysporum* f.sp.*psidii* causing wilt disease of guava at 100 µg/ml concentration. Nickel, Cobalt and Stannous reduced the growth at about 60%,42.8% and 33.3% while barium , zinc, calcium, magnese and iron significantly inhibited the growth at higher concentration i.e. 200 µg/ml to 21.4%,21.6%,25.7%,26.6% and 30%. The heavy metals and their sensitivity to a fungus vary depending on the types of metals (Ashida,1965; Huisingh,1974). Cadmium and copper were more toxic based on the observation of babich and stotzky(1977). Their tolerance at higher degree may be due to their low permibility to cell memberane as cadmium and copper were toxic at very low level(Babich and Stotzky,1978;Dubey and Dwivedi,1988). The effects of cadmium, cobalt, nickel and zinc on the growth and survival of *Macrophomina phaseolina* has been studied by Dubey and Dwivedi(1988).

Haider(1978) reported that copper fungicide 70% reduced the wilt disease of pigeonpea significantly followed by Brassicol, ceresin dust,sulphur dust and fytola. Ashour *et al.*,1973 reported 100% control of bulb rot of onion caused by *fusarium oxysporum* f. sp. *cepea*.Nickel salts sprayed to crop helps to control mint rust fungus *Puccinia menthae* (Garret, 1970). Preston (1931) studied that *Plasmodiophora brassicae* causing club root disease in cabbages can be control by watering with mercuric chloride. Damping–off peas and tobacco had controlled by soil amended with chlorobromopropene and copper sulphates (Kreutzer *et al.*, 1950 and R.G.Orellana, 1953).Mandal and Sinha (1992) founded that copper chloride, ferric chloride, magnese sulphate controlled *Fusarium oxysporum* f.sp.*lycopersici* by inducing resistance in suspectible tomato plant.

ISBN: 978-93-84144-81-4

4. Conclusion

On the basis of above study, it has been concluded that heavy metal can effectively reduced the growth of both *fusarium udum* and *fusarium oxysporum f.sp.cicer*i. Copper and cadmium at higher concentrations reduced the growth of both the fusarium spp.Hence heavy metals can be used effectively in wilt disease management.

References

[1] Ashida,J.(1965) Adaptation of fungi to metal toxicant. Ann. Rev. Phytopath.,3:154-174.

[2] Ashour,W.A.;.Mursy, A.A; Ali,M.D.H. and Dial,M.M.M.(1973) Agriculture Research Review,52:153-162.

[3] Bàáth(1989) Effect of heavy metals in soil on microbial processes and populations (A review). Water,Air and Soil Pollution,47:335-379.

[4] Babich,H. and Stotzky,G.(1977) Senstivity of various bacteria including actinomycetes and fungi to cadmium and the influence of pH on sentivity. Appl. Environ. Microbiol.,33:681-885.

[5] Babich,H. and Stotzky,G.(1978)Effect of cadmium on biota: Influence of environmental factors. Adv. Appl. Microbiol,23:55-117.

[6] Doelman,P.(1985)Resistance of soil microbial communities to heavy metals. In microbial communities in soil(V.Jensen, A.Kjoller and L.H.Sorensen Eds.):369-384, Elsevier,London.

[7] Duxbury,T.(1985) Ecological aspects of heavy metal responses in microorganisms. In: Advances in Microbial Ecology,Vol.8(K.C.Marshall Eds.):185-236. Plenum Press, New York.

[8] Dwivedi,S.K.(1990) Effect of some heavy metals on growth of *Fusarium oxysporum f. sp. psidii* causing guava wilt disease. In. J. Tropical Pl. Disease,9:127-130.

[9] Engelhard ,A.W.(1989)Soil borne plant pathogens:management of diseases with macro-and microelements.St.Paul,MN: The American Phytopathological Society.

[10] Garrett, S.D. (1970) Pathogenic root-infecting fungi Cambridge University Press, Cambridge, U.K.

[11] Griller,K.E.;Witter,E. and Mc. Grath,S.P.(1988) Toxicity of heavy metals to microorganisms and microbial processes in agricultural soils: A review soil biology and Biochemistry,30:1389-1414.

[12] Grover,R.K. and Moore, J.D. (1962) Toxicometric studies of fungicides against brown rot organisms *Sclerotonia fructicola* and *S. laxa*. *Phytopathology*, 52: 876-880.

[13] Haider, M.G.; Singh, R.K.; Prasad, Harihar; Nath, R.P. and Sharma, R.N. (1978) Effect of some common fungicides on the incidence of pigeon pea wilt. Phytopathological Notes,31:511-512.

[14] Huber,D.M.(1989)The role of nutrition in the take-all disease of wheat and other small grains.In:EngelhardAW,editor.Soilborne plant pathogens:managementof diseases with macro-and microelements.St.Paul, MN: AmericanPhytopathologicalSocietyPress: 46–74.

[15] Huisingh,D.(1974) Heaavy metals: Implications for agriculture. Ann. Rev. Phytopath.,12:375-388.

[16] Kandeler,E.;Tscherko,D.;Bruce,K.D.;Stemmer,M.;Hobbs,P.J.;Bardgett,R.D.and Amlung,W.(2000) Structure and function of soil microbial community in microhabitat of a heavy metal polluted soils. Biology and Fertility of soil,32:390-400.

[17] Mandal,N.C. and Sinha,A.K.(1992) An alternative approaches for the chemical control of *Fusarium* wilt in tomato. Indian Phytopathology,45:194-198.

[18] Preston, N.C. (1931) The prevention of finger and toe (club root) in gardens and allotments. J.Minist. Agric.,38:272-284.

[19] Renella,G.;Mench,M.;Landi,L .and Nannipieri,P.(2005) Microbial diversity and hydrolase synthesis in long term Cd contaminated soil. Soil Biology and Biochemistry,37:133-139.

[20] Saikia, Ratul; Varghese,Saju; Singh, Bhim Pratap and Arora, Dilip K.(2009) Influence of mineral amendment on disease suppressive activity of *Pseudomonas fluorescens* to *Fusarium wilt* of chickpea. Microbiological Research, 164:365-373.

[21] Schnider,U;Keel,C;Blumer,C;Troxler,J;Defago,G.andHass,D.(1995)Amplification of housekeeping factor in *Pseudomonas fluorescens* CHAO enhances antibiotic production and improves biocontrolabilities.JBacteriol.;177:5378–92.

[22] Singh,R.K. (1988) *In vitro* studies on toxicity of heavy metals against *Sclerotium rolfsii* Sacc. and Foot rot pathogen of Barley,Hindustan 30(1&2):40-43.

[23] Kreutzer,W.A. and Montagne,J.T.W.(1950) Chlorobromopropene, a potential fungicideal soil fumigant. Phytopathology,40:16.

[24] Orellana,R.G.(1953) Copper sulphate for the control of damping-off in tobacco seed beds. Phytopathology,43:125-127.

Journal of Material Science and Mechanical Engineering (JMSME)
Print ISSN: 2393-9095; Online ISSN: 2393-9109; Volume 2, Number 7; April-June, 2015 pp. 58-63
© Krishi Sanskriti Publications
http://www.krishisanskriti.org/jmsme.html

Energy and Exergy Analyses of a new Solar Assisted Ejector Cooling and Power Cycle by using Refrigerants R141b, R600, R601 and R601a

Surendra Kumar Agrawal[1], Rajesh Kumar[2]

[1]*Department of Mechanical Engineering,*
Madhav Institute of Technology & Science Gwalior-474005, M.P., India
surendra_srcem@yahoo.com
[2]*Department of Mechanical Engineering, Delhi Technological University,*
Bawana Road, Delhi-110042, India
dr.rajeshmits@gmail.com
** Corresponding author*

Abstract: **In this paper, a solar assisted combined power and ejector refrigeration cycle is proposed and thermodynamically analyzed from the viewpoint of energy and exergy. This cycle combines the Rankine cycle and ejector refrigeration cycle to produce power and refrigeration simultaneously. A simulation is carried out to analyze the cycle performance by using different refrigerants like; R141b, R600, R601 and R601a. The effect of various operating thermodynamic parameters like turbine inlet pressure, turbine back pressure, condenser temperature and evaporator temperature on energy and exergy efficiency of the cycle is observed. It is found that at a common turbine back pressure of 0.4MPa, R141b offers highest energy efficiency (18.37%) and R600 offers highest exergy efficiency (7.65%). At a common evaporator temperature of 270K, R141b offers highest energy efficiency (17.98 %) and R600 offers highest exergy efficiency (6.69%) as compared to other refrigerants is observed. It is clear that, with the increase in turbine inlet pressure from 0.5 MPa to 1.75 MPa of R141b, the energy efficiency increases from 13.8% to 18.69%) and exergy efficiency increases from 3.45% to 8.62%.**

Keywords: **Solar heat, ejector, exergy, refrigerants, power.**

1. INTRODUCTION

Energy is considered as a major agent in the generation of wealth and an important factor in economic developments. With developing technology and the rapid increase in population, the demand for energy and cost of electricity is ever increasing. In view of this, various investigations have been carried out on solar heat and non CFCs operated refrigeration systems like ejector and vapour absorption cooling.

The coefficient of performance of the system increases with an increase in the generator and evaporator temperatures while decreases with an increase in the condenser temperature of the ejector cooling system using the refrigerant R134a [1]. The condenser temperature has more influence than the generator and evaporator temperatures on the area ratio and the entrainment ratio in the ejector refrigeration system by using refrigerants R123 and R141b [2]. The detailed investigation of ejector working characteristics by using R141b, R245fa and R600a as the working fluids shows that different refrigerants perform distinctively different in the ejector refrigeration system [3]. The simulation of solar powered absorption cooling system by using LiBr-H_2O mixture as working fluid is carried out by Atmaca and Yigit [4].

The energy and exergy analyses of single-effect water-lithium bromide absorption cooling system driven by solar heat with cooling capacity of 10 kW is presented by Touaibi [5]. Khaliq et al. [6] presented an industrial waste heat recovery based cogeneration cycle for production of power and refrigeration. They observed the effect of various operating parameters on energy and exergy efficiency. The most of the exergy destruction takes place in the ejector in combined power and ejector refrigeration cycle using R245fa as the working fluid [7]. Dai et al. [8] carried out exergy analysis, parametric analysis and optimization for a novel combined power and ejector refrigeration cycle.

In order to utilize the advantages of the ejector refrigeration cycle and recover solar heat effectively, a new solar assisted combined organic Rankine cycle and ejector refrigeration cycle is proposed and thermodynamically analyzed by using the different refrigerants such as R141b, R 600, R601 and R601a. This combined cycle will produce both power output and refrigeration output simultaneously by using single source of solar heat.

In the present study, exergy method along with energy method is applied to investigate the thermodynamic performance of the proposed cycle. The effect of various operating parameters on energy and exergy efficiency has been observed to find out the optimum operating range.

2. SYSTEM DESCRIPTION

The proposed cogeneration cycle combines the Rankine cycle (RC) and the ejector refrigeration cycle (ERC) as shown in Figure 1. Solar energy falls on the heliostat field and reflected on the aperture area of central receiver which is located at the top of the tower. The concentrated rays which falls on to the central receiver results in higher temperature of the central receiver, is used to heat the oil (Duratherm600). The oil flows through the pipes which transfer the thermal energy from central receiver to the HRVG (1-2). Superheated refrigerant vapour (4) is expanded in a turbine to generate power. The turbine exhaust (5) passes through converging diverging supersonic nozzle of ejector.

The very high velocity refrigerant vapour at the exit of the nozzle creates a very high vacuum at the inlet of the mixing chamber and extract secondary vapour (11) from the evaporator of ERC into the mixing chamber and this causes cooling effect at evaporator-1(E1) of ERC. The primary vapour (5) and secondary vapour (11) are mixed in the mixing chamber. The mixed stream (6) is condensed in the condenser-1(C1). The saturated liquid (7) is divided in to two parts (8, 9), one part (9) is passed through throttling valve-1 (TV1) where pressure is reduced to evaporator (E-1) pressure (10) and feed to evaporator-1 (E1), and second part (8) is pumped by pump-1(P1) to the HRVG of RC cycle. The stream (2) coming out from HRVG enters in to the central receiver.

For the analysis, the specifications of the combinedRC and ERC are given in Table 1.

TABLE 1: Main parameters considered for the analysis

Parameters	R141b	R600	R601	R601a
Environment temperature (^{0}C)	15	15	15	15
Environment pressure (MPa)	0.10135	0.10135	0.10135	0.10135
Turbine inlet pressure range (MPa)	0.5-1.75	1.0-2.5	0.5-1.5	0.5-1.5
Hot oil outlet temperature from CR (^{0}C)	170	170	170	170
Solar radiation received per unit area (Wm^{-2})	850	850	850	850
Apparent Sun temperature (K)	4500	4500	4500	4500
Heliostat aperture area (m^2)	3000	3000	3000	3000
Turbine back pressure range (MPa)	0.2-0.4	0.35-0.65	0.2-0.4	0.35-0.5
Turbine isentropic efficiency (%)	85	85	85	85
Ejector evaporator temperature range (K)	264-272	264-272	264-272	264-270
Condenser temperature range (^{0}C)	20-30	20-30	20-30	26-32
Pump isentropic efficiency (%)	70	70	70	70
HRVG efficiency (%)	100	100	100	100
Pinch point temperature difference (^{0}C)	10.0	10.0	10.0	10.0
Approach point temperature difference (^{0}C)	5.0	5.0	5.0	5.0
Nozzle efficiency (%)	90	90	90	90
Mixing chamber efficiency (%)	85	85	85	85
Diffuser efficiency (%)	85	85	85	85
Energy efficiency of heliostat field (%)	75	75	75	75
Energy efficiency of central receiver (%)	90	90	90	90
Exergy efficiency of heliostat field (%)	75	75	75	75
Exergy efficiency of central receiver (%)	30	30	30	30

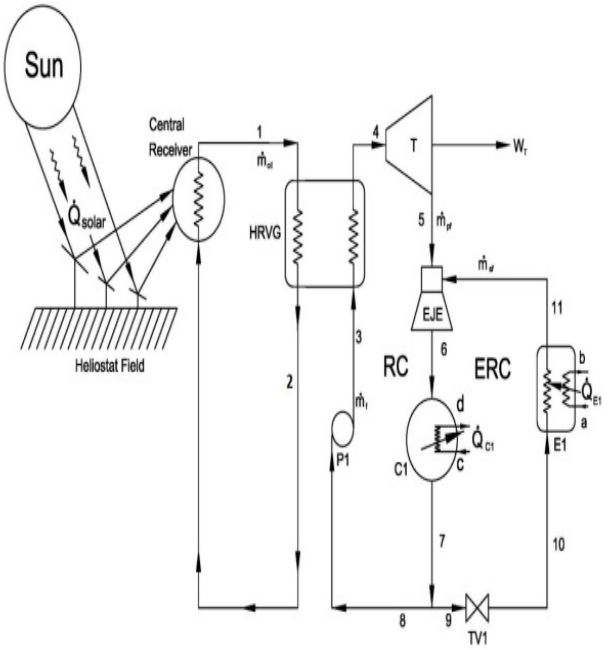


Fig.1. Schematic diagram of solar assisted ejector cooling and power cycle

3. THERMODYNAMIC ANALYSIS

According to the first law of thermodynamics and energy conservation used to determine the overall thermal efficiency, heat and work are equivalent. On the other hand, exergy, based on the second law of thermodynamics, quantifies the difference between heat and work in terms of irreversibility. Exergy is defined as the maximum amount of work which can be produced by a system when it comes to equilibrium with a reference environment, which may be defined mathematically as:

$$\dot{E}_X = \dot{m}[(h-h_0) - T_0(s-s_0)] \tag{1}$$

The entropy generation over a control volume is given by Bejan [9]

$$\dot{S}_{gen} = \frac{dS}{dt} - \sum_{i=o}^{n} \frac{\dot{Q}_i}{T_i} - \sum_{in} \dot{m}\, s + \sum_{out} \dot{m}\, s \geq 0 \tag{2}$$

According to Gouy-Stodola theorem, the exergy destruction and entropy generation are related as

$$\dot{E}_{X,D} = T_0\, \dot{S}_{gen} \tag{3}$$

3.1. Energy Efficiency (η_{energy})

The energy efficiency of the proposed cycle for simultaneous production of cooling and power is given by

$$\eta_{energy} = \frac{\dot{Q}_{E1} + \dot{W}_{NET}}{\dot{Q}_{Solar}} \tag{4}$$

where, $\dot{Q}_{E1}$, $\dot{W}_{NET}$ and $\dot{Q}_{solar}$ are the refrigeration output of ERC, net power output of Rankine cycle and solar heat input respectively.

The basic equations obtained from the law of conservation of energy in the components of RC and ERC are written as follows:

For HRVG: $\dot{m}_{oil}(h_1 - h_2) = \dot{m}_f(h_4 - h_3)$ (5)

For Turbine (T): $\dot{W}_T = \dot{m}_f(h_4 - h_5)$ (6)

For Pump (P1): $\dot{W}_{P1} = \dot{m}_f(h_3 - h_8)$ (7)

Net Work done: $\dot{W}_{NET} = \dot{W}_T - \dot{W}_{P1}$ (8)

For Ejector (EJE):

$$\dot{m}_{pf}\, h_5 + \dot{m}_{sf}\, h_{11} = h_6(\dot{m}_{pf} + \dot{m}_{sf}) \tag{9}$$

For condenser (C1):

$$\dot{Q}_{C1} = \dot{m}_C(h_d - h_c) = (\dot{m}_{pf} + \dot{m}_{sf})(h_6 - h_7) \tag{10}$$

For Throttle Valve (TV1): $h_9 = h_{10}$ (11)

For Evaporator (E1):

$$\dot{Q}_{E1} = \dot{m}_E(h_a - h_b) = \dot{m}_{sf}(h_{11} - h_{10}) \tag{12}$$

3.2. Exergy Efficiency (η_{exergy})

The exergy efficiency for simultaneous production of cooling and power cycle is given by

$$\eta_{exergy} = \frac{\Delta \dot{E}_{X,E1} + \dot{W}_{NET}}{\dot{E}_{X,Solar}} \quad (13)$$

where, $\dot{E}_{X,Solar}$ is incoming exergy associated with solar radiation falling on heliostat, $\Delta \dot{E}_{E1}$ and $\dot{W}_{NET}$ are the change in exergy at ejector evaporator of ERC and exergy associated with net power output of RC respectively.

$$\dot{E}_{X,Solar} = \dot{Q}_{Solar}\left(1 - \frac{T_0}{T_S}\right) \quad (14)$$

where, T_s = Apparent Sun temperature (K)=4500K

$$\Delta \dot{E}_{X,E1} = \dot{m}_{sf}[(h_{10} - h_{11}) - T_0(s_{10} - s_{11})] \quad (15)$$

4. RESULTS AND DISCUSSION

In this paper, parametric analysis is carried out to find out the effect of variation of turbine inlet pressure, turbine back pressure, condenser temperature and evaporator temperature on energy and exergy efficiency of the solar assisted cogeneration cycle for simultaneous production of power and cooling. The thermodynamic properties of refrigerant R141b, R600, R601 and R601a used in the ERC cycle were calculated by NIST Standard Reference Database 23 [10].

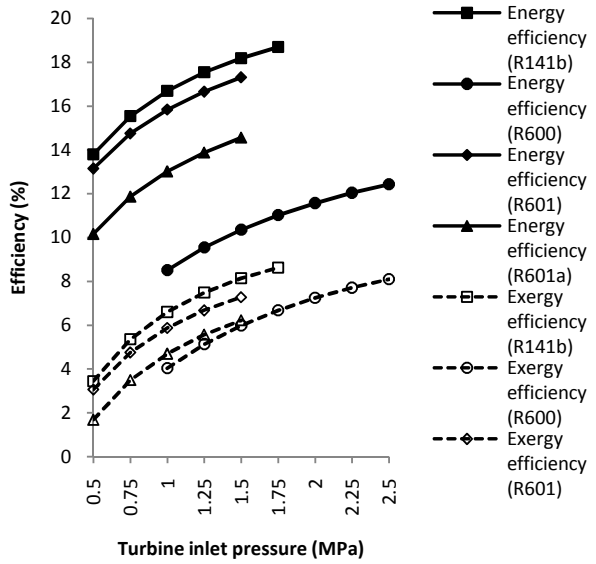


Fig. 2. Effect of turbine inlet pressure on energy and exergy efficiency

Figure 2 shows the effect of turbine inlet pressure on energy and exergy efficiency. With increase in turbine inlet pressure, the enthalpy drop across the turbine increases due to increase in pressure ratio, results in increase in turbine power output. The refrigeration output decreases due to decrease in turbine exhaust temperature which is the primary flow temperature of the ejector. The decreasing primary flow temperature reduces the primary stream velocity leaving the nozzle in the ejector, resulting in the decreasing the entrainment of secondary vapours. Due to combined effect of turbine power and refrigeration output, the energy and exergy efficiency increases with increase in turbine inlet pressure. It is observed that refrigerant R141b offers better energy and exergy efficiency as compared to R600, R601 and R601a. At a common pressure of 1.5 MPa, the refrigerant R141b offers highest energy efficiency (18.18%) and exergy efficiency (8.14%).

Figure 3 shows the effect of turbine back pressure on energy and exergy efficiency. With increase in turbine back pressure, the turbine power decreases because the enthalpy drop across the turbine decreases. It is also clear that the refrigeration output increases with the increase in turbine back pressure because the primary stream velocity leaving the nozzle in the ejector increases. This increase in the nozzle exit velocity contributes to the increasing the entrainment of secondary vapour which leads to the increasing refrigeration output in the evaporator of ERC. Since the rate of increase in refrigeration output is greater than the rate of decrease in turbine power output, the energy efficiency increases with increase in turbine back pressure. It is clear that the exergy output of ERC increases while the exergy of turbine power output decreases with increase in turbine back pressure. Due to combined effect the exergy efficiency decreases with increase in turbine back pressure. At a back pressure of 0.4MPa, R141b offers highest energy efficiency (18.37%) and R600 offers highest exergy efficiency (7.65%).

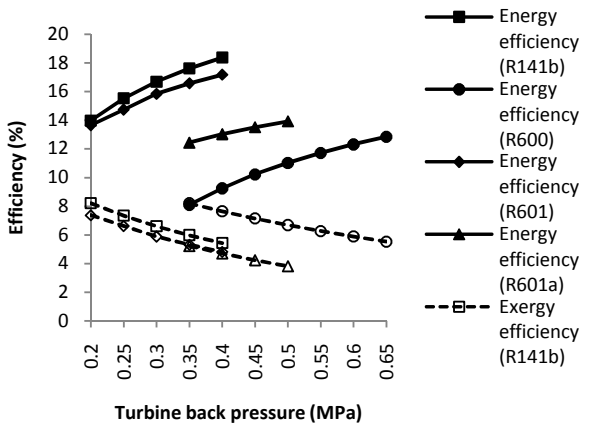


Fig. 3. Effect of turbine back pressure on energy and exergy efficiency

Figure 4 shows the effect of evaporator temperature on energy and exergy efficiency. As the evaporator temperature increases, the refrigeration output increases because the secondary mass flow rate increases in the evaporator. The turbine power output does not vary with the increasing evaporator temperature because the turbine inlet state and outlet state are fixed. The energy and exergy efficiency of combined cycle increases with increase in evaporator temperature. At a common evaporator temperature of 270K, R141b offers highest energy efficiency (17.98 %) and R600 offers highest exergy efficiency (6.69%) compared to other refrigerants.

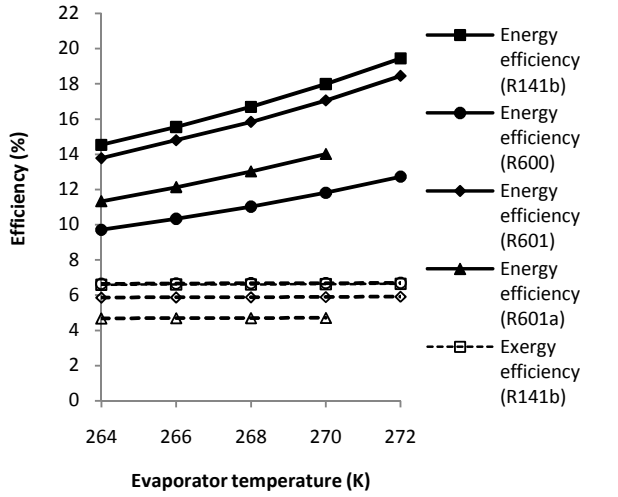


Fig. 4. Effect of evaporator temperature on energy and exergy efficiency

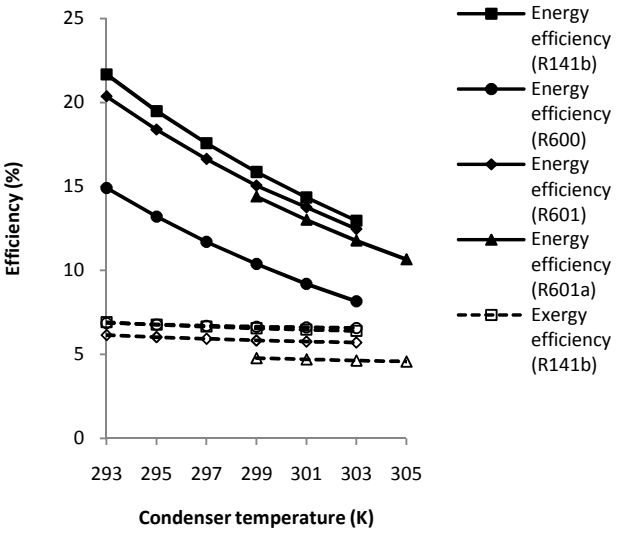


Fig. 5. Effect of condenser temperature on energy and exergy efficiency

The energy and exergy efficiency of combined cycle decreases with increase in condenser temperature as shown in Figure 5. The turbine power output does not vary with the increasing condenser temperature, because the turbine inlet state and outlet state are fixed. As the condenser temperature increases, results in increase in condenser pressure and hence the back pressure on the ejector increases, due to this, refrigeration output and exergy output decreases. At a common condenser temperature of 299K, R141b offers highest energy efficiency (15.86%) and R600 offers highest exergy efficiency (6.65%).

5. CONCLUSION

A combined energy and exergy analyses of a new solar assisted cogeneration cycle for simultaneous production of power and cooling is presented. The effects of key thermodynamic parameters were observed on energy and exergy efficiency of the proposed cycle. The main conclusions of the present study can be summarized as follows:

- with the increase in turbine inlet pressure, the energy efficiency and exergy efficiency increases significantly for all the refrigerants.
- with the increase in turbine inlet pressure from 0.5 MPa to 1.75 MPa of R141b, the energy efficiency increases (13.8% to 18.69%) and exergy efficiency increases (3.45% to 8.62%).
- with the increase in turbine back pressure, the energy efficiency increases and exergy efficiency decreases significantly.
- At a common turbine back pressure of 0.4MPa, R141b offers highest energy efficiency (18.37%) and R600 offers highest exergy efficiency (7.65%).
- with the increase in evaporator temperature, the energy efficiency increases significantly and exergy efficiency increases marginally.
- At a common evaporator temperature of 270K, R141b offers highest energy efficiency (17.98 %) and R600 offers highest exergy efficiency (6.69%) compared to other refrigerants.
- with the increase in condenser temperature, the energy efficiency decreases significantly and exergy efficiency decreases marginally.

REFERENCES

[1] Tirmizi, S.A., Gandhidasan, P. and Zubair, S.M., "Exergetic performance evaluation of ejector cooling system", *International Journal of Exergy,* 9(1), 2011, pp.80-98.

[2] Chen, J., Havtun, H. and Palm, B., "Investgation of Ejectors in Refrigeration System: Optimum Performance Evaluation and Ejector Area Ratio Perspectives", *Applied Thermal Engineering,* 64, 2014a, pp.182-191.

[3] Chen, J., Havtun, H. and Palm, B., "Parametric Analysis of Ejector Working Characteristics in the Refrigeration System", *Applied Thermal Engineering*, 69, 2014b, pp.130-142.

[4] Atmaca, I. and Yigit, A., "Simulation of solar powered absorption cooling system", *Renewable Energy,* 28, 2003, pp. 1277- 1293.

[5] Touaibi, R., Feidt, M., Vasilescu, E.E. and Abbes, M.T., "Parametric study and exergy analysis of solar water-lithium bromide absorption cooling system", *International Journal of Exergy,* 13(3), 2013, pp.409-429.

[6] Khaliq, A., Kumar, R. and Dincer, I., "Exergy analysis of an industrial waste recovery based cogeneration cycle for combined production of power and refrigeration", *Journal of Energy Resources Technology,* 131, 2009, pp.1- 9.

[7] Zheng, B. and Weng, Y.W., "A combined power and ejector refrigeration cycle for low temperature heat sources", *Solar Energy,* 84, 2010, pp.784- 791.

[8] Dai, Y., Wang, J. and Gao, L., "Exergy analysis, parametric analysis and optimization for a novel combined power and ejector refrigeration cycle", *Applied Thermal Engineering,* 29, 2009, pp.1983-1990.

[9] Bejan, A., "Fundamentals of exergy analysis, entropy generation minimization and the generation of flow architecture", *International Journal of Energy Research,* 26, 2002, pp. 545-565.

[10] NIST Standard Reference Database 23, NIST Thermodynamic and Transport Properties of Refrigerants and Refrigerants Mixtures', *REFPROP*, Version 6.01., 1998, USA.

Volume 3, Issue 3 (2015) 471-477 ISSN 2347 - 3258
International Journal of Advance Research and Innovation

Energy-Exergy Performance Comparison of Vapour Compression Refrigeration Systems using Three Nano Materials Mixed in R718 in the Secondry Fluid and Ecofriendly Refrigerants in the Primary Circuit and Direct Mixing of nano Materials in the Refrigerants

R. S. Mishra
Department of Mechanical, Production & Industrial and Automobile Engineering, Delhi Technological University Delhi, India

Article Info

Article history:
Received 03 July 2015
Received in revised form
20 July 2015
Accepted 28 August 2015
Available online 15 September 2015

Keywords

Nano Materials,
Vapour Compression Refrigeration Systems,
Energy and Exergy Analysis,
First and Second Law Analysis,
Irreversibility Analysis

Abstract

This paper describes thermal modelling of vapour compression refrigeration system using (ii) eco-friendly refrigerants in primary circuit with nano particles mixed with R718 in secondary evaporator circuit. This model takes care of the secondary nanoparticles mixed in the fluids as input conditions as geometric characteristics of the system such as size of nanoparticles and the compressor speed to predict the secondary fluids output temperatures, the operating pressures, the compressor power consumption and the system overall energy performance. Such design analysis is conveniently useful to compare the thermal performance of different nanoparticles (Cu, Al_2O_3, TiO_2) based nanofluid as a secondary fluid in a vapour compression refrigeration system. The influence of input variables on the irreversibilities in terms of exergy destruction ratio of the system is presented. Such a model can also be used to design various components viz. evaporator, compressor, condenser and throttle valve for vapour compression refrigeration systems for any desired cooling capacity. This model takes care of use of nanofluids as a secondary fluid in vapour compression refrigeration systems and simulate the non-linear equations of the system. It was observed that for the same geometric characteristics of the system, first and second law performance improved from 8% to 17% by using eco-friendly refrigerants in the primary circuit and nanoparticles mixed with water as a secondary fluid in VCS .and first and second law performance improved from 8% to 32% by mixing nano particles in the eco-friendly refrigerants in the primary circuit

1. Introduction

Now a day's refrigeration based equipment are most important for industrial and domestic applications. Those systems utilize more energy as compared to other appliances. The refrigeration systems have been severely investigated to reduce the energy consumption. The nanoparticle based refrigerant gives a superior thermodynamic properties as compared to the without refrigerant due to increase in the heat transfer performances of base refrigerant in the vapour compression refrigeration systems. There are several methods for improving the thermal performance of vapour compression refrigeration systems. Utility of nano particles mixed in the ecofriendly refrigerants and then used as a refrigerant can significantly enhanced its thermal performance and simanteously decreases exergy destruction ratio. Several authors had defined exergy destruction ratio (EDR) based on its input or based on its output in the vapour compression refrigeration systems.EDR is a ratio of total exergy losses in the system (i.e. which is a sum of total exergy losses in the components in VCR) to the exergy of input (in terms of fuel in terms of compressor work) or a ratio of total exergy losses in the system (i.e. which is a sum of total exergy losses in the components in VCR) to the exergy of input (in terms of product i.e. net exergy due to cooling load). Many types of solid and oxide materials could be used as the nanoparticles to be suspended into the conventional refrigerants. The nano refrigerant/refrigerant could be better working fluid to be used in the refrigeration and air conditioning system to increase the heat transfer performance of that system and overall system performance and save the energy usage. The effect of the suspended copper oxide (CuO), Titanium Oxide (TiO2), Aluminum Oxide (Al_2O_3), into the ecofriendly refrigerants (i.e. R134a, R407c and R404a etc.) eco-friendly refrigerant enhances its first law performance in terms of coefficient of performance. Lots of researches have evaluated the performance of various metallic/ nonmetallic nanoparticle suspended into the conventional fluid to enhance the heat transfer property of base fluid and simple theoretical analysis of suspension of nanoparticle Al_2O_3 in conventional refrigerants. On the other hand the thermodynamic performances of vapour compression system in the primary circuit using nano particles mixed ecofriendly refrigerants yet to be analyzed and also be compared with nano particles (i.e. TiO_2, CuO) mixed with R718 refrigerant and then used in secondary circuit The effect of changing input parameter of VCRS using nano refrigerant is on thermodynamic performance is also investigated.

Corresponding Author,
E-mail address: professor_rsmishra@yahoo.co.in
All rights reserved: http://www.ijari.org

2. Literature Review

Elcock [1] observed by conducting experiments regarding the use of TiO_2 nanoparticles as additives in the refrigeration system to enhance the solubility of the mineral oil with the hydrofluorocarbon (HFC) refrigerant by prepairing a mixture of HFC134a and mineral oil with TiO2 nanoparticles and found the better performance by returning more lubricant oil to the compressor with similar performance to systems using HFC134a. E. Halimic [2] carried out experimental study on the boiling heat transfer characteristics of R22 refrigerant with Al_2O_3 nanoparticles and found the nano particles enhances refrigerant heat transfer characteristics with reduced bubble sizes. Eastman et al.[3] found the pool boiling heat transfer characteristics of R11 refrigerant with TiO2 nanoparticles and observed the heat transfer enhancement to bed reached 20% at a particle loading of 0.01 g/ L. Liu et al. [4] studied the effects of carbon nanotubes (CNTs) on the nucleate boiling heat transfer of R123 and HFC-134a refrigerants and observed that CNTs increases the nucleate boiling heat transfer coefficients for these refrigerants and found a large enhancements up to 36.6% at low heat fluxes of less than 30 kW/m2. Jiang et al. [5] observed experimentally the thermal conductivities of carbon nanotube (CNT) nanorefrigerants are much higher than those of CNT– wate nanofluids spherical nanoparticle–R113 nanorefrigerant and found that the smaller the diameter of CNT larger the thermal conductivity enhancement of CNT nano refrigerant. Hwang et al. [6] had found the thermal conductivity enhancement of nanofluids is greatly influenced by thermal conductivity of nano-particles and base fluid due to the thermal conductivity of water based nanofluid with multiwall carbon nano tube has noticeably higher thermal conductivity as compared to the SiO2 nanoparticles for the same base fluid. Yoo et al. [7] had found the surface to volume ratio of nanoparticles is a dominant factor due to surface to volume ratio is increased with smaller sizes of nanoparticles which influence thermal conductivity of nano fluid rather than nano particles. Choi et al. [8] found 150% thermal conductivity enhancement of poly (a-olefin) oil with the addition of multiwalled carbon nanotubes (MWCNT) at 1% volume fraction. Yang [9] observed 200% thermal conductivity enhancement for poly (a- olefin) oil containing 0.35% (v/v) MWCNT and found that the thermal conductivity enhancement was accompanied by a three order of magnitude due to increase in viscosity. He has also measured the thermal conductivity of a similar copper containing nanofluid, except the base fluid was water and salt was used as a dispersant and found the 70% thermal conductivity enhancement for 0.3% (v/v) copper nanoparticles in water. Eastman et al.[10] had observed 40% thermal conductivity enhancement for ethylene glycol with 0.3% (v/v) copper nano particles (10 nm diameter) by added about 1% (v/v) thioglycolic acid in the dispersion of the nano particles and found a greater thermal conductivity than the same concentration of nanoparticles in the ethylene glycol without the dispersant. Kang et al.[11] had observed the 75% thermal conductivity enhancement for ethylene glycol with 1.2% (v/v) diamond nanoparticles between 30 and 50 nm in diameter by measuring the thermal conductivity of nanofluids and have found no anomalous results Lee et al. [12] observed the thermal conductivity of nanofluids is greatly affected by pH level and addition of surfactant during nanofluids preparation stage due to better dispersion of nanoparticles is achieved with addition of surfactant such as sodium dodecylbenzenesulfonate and found that the optimum combination of pH and surfactant leads to 10.7% thermal conductivity enhancement of 0.1% Cu/H2O nanofluids. Jiang et al. [13] observed the thermal conductivity of nanofluids also depend on the nanoparticles size and temperature. Wu et al. [14] found that the pool boiling heat transfer was enhanced at low nanoparticles concentration of TiO2 in R11 but deteriorated under the condition of high nanoparticles concentration. Trisaksri e.al. [15] had investigated TiO2 in HCFC 141(b) in a cylindrical copper tube and found that the nucleate pool boiling heat transfer deteriorated with increasing nanoparticle concentrations especially at higher heat fluxes. Hao et al. [16] investigated the heat transfer characteristics of refrigerant-based nanofluids flow boiling inside a smooth tube at different nanoparticles concentration, mass fluxes, heat fluxes, and inlet vapor qualities and analyzed the influence of nanoparticles on the heat transfer characteristics of refrigerant-based nanofluid flow boiling inside the smooth tube and also developed correlation for predicting the heat transfer coefficient of refrigerant-based nanofluid and the predicted heat transfer coefficients agree with 93% of the experimental data and found that the heat transfer coefficient of refrigerant-based nanofluid in flow boiling is larger than that of pure refrigerant and the maximum enhancement is about 29.7% when observed with a mass fraction of nanoparticles 0–0.5 wt%. and the reduction of the boundary layer height due to the disturbance of nanoparticles enhances the heat transfer. Hao et al. [17] observed experimentally the nucleate pool boiling heat transfer characteristics of refrigerant/oil mixture with diamond nanoparticles. The refrigerant was R113 and the oil was VG68 and found the nucleate pool boiling heat transfer coefficient of R113/oil mixture with diamond nanoparticles was larger than that of R113/oil mixture by maximum of 63.4% and the enhancement increases with the increase of nanoparticles concentration in the nanoparticles/oil suspension and decreases with the increase of lubricating oil concentration and developed a correlation for predicting the nucleate pool boiling heat transfer coefficient of refrigerant/oil mixture with nanoparticles which agreed well with the experimental data of refrigerant/oil mixture with nanoparticles. Wang et al. [18] had conducted experiments for finding the boiling heat transfer characteristics of R22 refrigerant with Al_2O_3 nanoparticles and observed that the nanoparticles enhanced the refrigerant heat transfer characteristics with reduced bubble sizes that moved quickly near the heat transfer surface. Li et al.[19] studied the pool boiling heat transfer characteristics of R11 refrigerant with TiO2 nanoparticles and found the heat transfer enhancement reached to a 20% at a particle loading of 0.01 g/L. Peng et al. [20] studied the influence of nanoparticles on the heat transfer characteristics of refrigerant-based nano fluid flow boiling inside a horizontal smooth tube, and developed a correlation for predicting heat transfer performance of refrigerant based nanofluids by preparing refrigerant based nanofluids, In his experiment, R113 refrigerant and CuO

nanoparticles were used and found that the heat transfer coefficient of refrigerant-based nanofluids is higher than that of pure refrigerant, and found the maximum enhancement of heat transfer coefficient to be about 29.7%.Kumar et. al. [21] experimentally investigated the effect of concentration of nano Zno ranges in the order of 0.1%,0.3% and 0.5% volume with particle size of 50 nm on various thermodynamic parameters (i.e. COP, suction temperature, input power and pressure raio with ecofriendly R152a as working fluid in the simple vapour compression refrigeration system and found that maximum COP of 3.56 and 21% reduction of power input with 0.5% volume of of zinc oxide (ZnO) and also found that the Pressure ratio decreases with increase in nano Zno concentration. Mahbubul et al. [22] studied the thermo- physical properties, pressure drop and heat transfer performance of Al2O3 nano-particles suspended in the ecofriendly refrigerant (R-134a) and viscosity of ecofriendly R-134arefrigerant was investigated.

Lot of researches have been done and going on based on the performance evaluation of various combinations of different types of refrigerant and also nanoparticle behavior on the nanofluid. On the other hand the performance of VCS using nanofluid (with different nanoparticle) for different types of eco friendly refrigerant is yet to be analyzed. The use nano fluid in VCS (chiller system) is presented in this paper and, the performance evaluation of vapour compression refrigeration system is explored by using new and alternative ecofriendly refrigerants HFO1234yf, HFO1234ze backed by the fact that they are more environments friendly can replaced. R134a, R407c, R404a and R125 in the coming future. This paper presents following research objectives. Thermodynamic first law comparison and % improvement of simple vapour compression system using three ecofriendly alternative refrigerants. Thermodynamic analysis in terms of % improvement in first law efficiency and second law efficiency by using exergetic analysis of simple vapour compression system using Al_2O_3 as nanofluid and comparison of results of performance evaluation in terms of reduction in irreversibility without nanofluid and with nanofluids.

3. Results and Discussions

The computer simulation model was developed using empirical relation of heat transfer equations and energy balance equations using EES software and experimental set up was fabricated. It was observed that our theoretical model matches well with experimental measurement without nano particles for R134a used in the primary VCR circuit. The performances of nano particles mixed with R134a is shown in Table-1 It was observed that as mass flow rate of brine is increases, the the first law efficiency in terms of COP is increases along with increase in second law performance as shown in Table-1(a). Similarly as increase in compressor speed the first lwa efficiency (C O P) and second law performance (exergetic efficiency) in also decreases and exergy destruction ratio in terms of total exergy losses in the system to the exergy of product is also increases as shown in Table-1(b) respectively.

Table: 1a. Variation of mass flow rate of brine in the eveporator on the performance of VCRS for Tbi = 25 ^oC, Twi =25 ^oC, Nano Al_2O_3 ϕ- 0.05 (5 % vol.) mixed with R 134 a in the primary circuit

mb kg/s	C.O.P.	EDR	ɳ effective
0.006	3.688	1.422	0.4129
0.007	3.817	1.341	0.4272
0.008	3.925	1.276	0.4394
0.009	4.018	1.223	0.4497
0.010	4.099	1.18	0.4588

Table: 1b. Variation of compressor speed on the performance of VCRS for T_{bi} = 25 ^{o} C, T_{wi} =25 ^{o}C, Nano Al_2O_3 ϕ- 0.05 (5 % vol.) mixed with R 134 a in the primary circuit

N comp. speed (r.p.m.)	C.O.P.	EDR	ɳ effective
2900	3.688	1.422	0.4129
3025	3.652	1.446	0.4088
3150	3.62	1.468	0.4052
3275	3.592	1.487	0.4021
3400	3.569	1.503	0.3995

Table: 1c. Variation of temperature of water flowing in condenser on the performance of VCRS for T_{bi} = 25 ^{o} C, T_{wi} =25 ^{o}C, Nano Al_2O_3 ϕ- 0.05 (5 % vol.) mixed with R 134 a in the primary circuit

T water in °K	C.O.P.	EDR	ɳ effective
298	3.699	1.415	0.4141
300	3.563	1.507	0.3989
302	3.437	1.599	0.3848
304	3.319	1.691	0.3716
306	3.209	1.784	0.3592

Table: 1d : Variation of temperature of brine flowing in secondary circuit on the performance of VCRS for T_{bi} = 25 ^{o} C, T_{wi} =25 ^{o}C , Nano Al_2O_3 ϕ- 0.05 (5 % vol.)mixed with R 134 a in the primary circuit

T brine in °K	C.O.P.	EDR	ɳ effective
298	3.68	1.428	0.4119
300	3.793	1.355	0.4246
302	3.907	1.286	0.4374
304	4.023	1.221	0.4503
306	4.0994	16.03	0.4634

Similarly the increase in the water flowing in the condender decreases in coefficient of performance and increase in exergy destruction ratio and also decrease in second law performance as shown in Table-1 (c) and the increase in the brine flowing in the evaporator increases in coefficient of performance and decrease in exergy destruction ratio and also increase in second law performance as shown in Table-1 (d) Table-2 shows the % improvement in second law efficiency in terms of exergetic efficiency improvement by using nano particles mixed with R718 in the secondary evaporator circuit. It was also observed that first law efficiency without nano particles using R134a is maximum while by using R1234ze is minimum however second highest is found to be by using. alternate refrigerant R1234yf (GWP=4, and ODP=0) is suitable which can replace R134a in the coming future. It

was also observed that without using nano particles, the first law performance by using R1234yf is better than R1234ze for replacing R134a during 2030 due to higher global warming potential of R134a as compared to R1234yf.

Table: 2a. Performance comparison of first law performance in terms of coefficient of performance and % Improvements in first law efficiency of vapour compression refrigeration system using ecofriendly refrigerant in the primary circuit and water flowing in the condenser in secondary circuit and brine flow in the secondary circuit in the evaporator using Al_2O_3, as nano material of 10 micron size

Refrigerant	COP with Al_2O_3 nano	COP without nano	% Improvement in first law efficiency
R1234ze	3.434	3.15	9.01587
R1234yf	3.604	3.276	10.0122
R134a	3.872	3.555	8.91702

Table: 2b. Performance comparison of first law performance in terms of coefficient of performance and % Improvements in first law efficiency of vapour compression refrigeration system using ecofriendly refrigerant in the primary circuit and water flowing in the condenser in secondary circuit and brine flow in the secondary circuit in the evaporator using copper as nano material of 10 micron size

Refrigerant	COP with copper nano particles	COP without nano	% Improvement in first law efficiency
R1234ze	4.402	3.15	39.746
R1234yf	4.761	3.276	45.32967
R134a	5.923	3.555	66.6104

Table: 2c. Performance comparison of first law performance in terms of coefficient of performance and % Improvements in first law efficiency of vapour compression refrigeration system using ecofriendly refrigerant in the primary circuit and water flowing in the condenser in secondary circuit and brine flow in the secondary circuit in the evaporator TiO_2 as nano material of 10 micron size

Refrigerant	COP with TiO_2 nano	COP without nano	% Improvement in first law efficiency
R1234ze	3.394	3.15	7.810
R1234yf	3.579	3.276	9.24908
R134a	3.823	3.555	7.5387

Table: 2d. Performance comparison of second law performance in terms of coefficient of performance and % Improvements in second law efficiency of vapour compression refrigeration system using ecofriendly refrigerant in the primary circuit and water flowing in the condenser in secondary circuit and brine flow in the secondary circuit in the evaporator Al_2O_3 as nano material of 10 micron size

Refrigerant	Eta_second with nano Al_2O_3	Eta_Second without nano	% improvement in second law efficiency
R1234ze	0.2724	0.2406	13.217
R1234yf	0.2925	0.2548	14.796
R134a	0.3215	0.2860	12.4126

Table: 2e. Performance comparison of second law performance in terms of exergetic efficiency and % Improvements in second law efficiency of vapour compression refrigeration system using ecofriendly refrigerant in the primary circuit and water flowing in the condenser in secondary circuit and brine flow in the secondary circuit in the evaporator copper as nano material of 10 micron size

Refriger Rant	Eta_second with nano copper particles	Eta_second without nano particles	% Improvement in second law efficiency
R1234ze	0.402	0.2406	67.0823
R1234yf	0.421	0.2548	65.22763
R134a	0.4806	0.2860	68.0412

Table: 2f. Performance comparison of second law performance in terms of exergetic efficiency and % Improvements in second law efficiency of vapour compression refrigeration system using ecofriendly refrigerant in the primary circuit and water flowing in the condenser in seconddary circuit and brine flow in the secondary circuit in the evaporator TiO_2 as nano material of 10 micron size

Refrigerant	Eta_second with nano TiO_2	Eta_second without nano	% Improvement in second law efficiency
R1234ze	0.2680	0.2406	11.3882
R1234yf	0.2887	0.2548	13.30455
R134a	0.3160	0.2860	10.4895

Tables: 2. shows the second law efficiency in terms of exergetic efficiency for thee ecofriendly refrigerants and second law performance improvement while by using three nano particles, in terms of exergetic efficiencyand maximum exergetic efficiency is found by using R134a as ecofriendly refrigerant and second highest is also found by using R1234yf as ecofriendly refrigerant in the primary evaporator circuit. It was also observed that second law performance is better due to 39.13% improvement by using R1234yf as compared to 16.52% improvement by using R1234ze in the primary evaporator circuit.

Table: 2g. Performance evaluation (% Improvements) of vapour compression refrigeration system using ecofriendly refrigerant in the primary circuit and water flowing in the condenser in secondary circuit and brine flow in the secondary circuit in the evaporator using Al_2O_3 as nano material of 10 micron size

Refrige EcoFriendly refri-gerants	EDR with Al_2O_3 nano	EDR without nano	% reduction in EDR
R1234ze	2.670	3.155	15.3724
R1234yf	2.430	2.925	16.923
R134a	2.111	2.496	15.4247

Table: 2h. Performance evaluation (% Improvements) of vapour compression refrigeration system using ecofriendly refrigerant in the primary circuit and water flowing in the condenser in secondary circuit and brine flow in the secondary circuit in the evaporator using Copper as nano material of 10 micron size

RefrigeEco Friendlyrefri-gerants	EDR with copper nano	EDR without nano	% reduction in EDR
R1234ze	1.487	3.155	52.8685
R1234yf	1.375	2.925	52.991453
R134a	1.081	2.496	56.6907

Table: 2i. Performance evaluation in terms of EDR (% deprovements) of vapour compression refrigeration system using ecofriendly refrigerant in the primary circuit and water flowing in the condenser in secondary circuit and brine flow in the secondary circuit in the evaporator using TiO2 as nano material of 10 micron size

RefrigeEco Friendlyrefri-gerants	EDR with TiO_2 nano	EDR without nano	% reduction in EDR
R1234ze	2.731	3.155	13.439
R1234yf	2.464	2.925	18.9094
R134a	2.165	2.496	13.2612

Table: 3a. Performance comparison of first law performance in terms of coefficient of performance and % Improvements in first law efficiency of vapour compression refrigeration system using ecofriendly refrigerant in the primary circuit and water flowing in the condenser in secondary circuit and brine flow in the secondary circuit in the evaporator using Al_2O_3, as nano material of 10 micron size

Refrigerant	COP with Al_2O_3 nano	COP without nano	% Improvement in first law efficiency
R1234ze	3.434	3.15	9.01587
R1234yf	3.604	3.276	10.0122
R134a	3.872	3.555	8.91702

Table: 3b. Performance comparison of first law performance in terms of coefficient of performance and % Improvements in first law efficiency of vapour compression refrigeration system using ecofriendly refrigerant in the primary circuit and water flowing in the condenser in secondary circuit and brine flow in the secondary circuit in the evaporator using copper as nano material of 10 micron size

Refrigerant	COP with copper nano particles	COP without nano	% Improvement in first law efficiency
R1234ze	4.402	3.15	39.746
R1234yf	4.761	3.276	45.32967
R134a	5.923	3.555	66.6104

Table: 3c. Performance comparison of first law performance in terms of coefficient of performance and % Improvements in first law efficiency of vapour compression refrigeration system using ecofriendly refrigerant in the primary circuit and water flowing in the condenser in secondary circuit and brine flow in the secondary circuit in the evaporator TiO_2 as nano material of 10 micron size

Refrigerant	COP with TiO_2 nano	COP without nano	% Improvement in first law efficiency
R1234ze	3.394	3.15	7.810
R1234yf	3.579	3.276	9.24908
R134a	3.823	3.555	7.5387

Table: 4a. Performance evaluation (% Improvements in second law effictiveness) of vapour compression refrigeration system using ecofriendly refrigerant in the primary circuit and water flowing in the condenser in secondary circuit and brine flow in the secondary circuit in the evaporator using Al_2O_3 as nano material of 10 micron size

Eco friendly Refrigerants	Second law effectiveness with Al_2O_3 nano particles	Second law effectiveness without nano particles	% improve-Ment in second law efficiency
R1234ze	0.3844	0.3526	9.0187
R1234yf	0.4035	0.3667	10.03545
R134a	0.4334	0.3980	8.89447

Table: 4b. Performance evaluation (% Improvements in second law effictiveness) of vapour compression refrigeration system using ecofriendly refrigerant in the primary circuit and water flowing in the condenser in secondary circuit and brine flow in the secondary circuit in the evaporator using Copper as nano material of 10 micron size

Eco friendly Refrigerants	Second law effectiveness with copper nano particles	Second law effectiveness without nano particles	% improvement in second law efficiency
R1234ze	0.5140	0.3526	45.77425
R1234yf	0.533	0.3667	45.3504
R134a	0.5925	0.3980	48.870

Table: 4c. Performance evaluation (% Improvements in second law effictiveness) of vapour compression refrigeration system using ecofriendly refrigerant in the primary circuit and water flowing in the condenser in secondary circuit and brine flow in the secondary circuit in the evaporator using TiO_2 as nano material of 10 micron size

Eco friendly Refrigerants	Second law effectiveness with TiO_2 nano particles	Second law effectiveness without nano particles	% improvement in second law efficiency
R1234ze	0.380	0.3526	7.7708
R1234yf	0.4006	0.3667	9.2446
R134a	0.4279	0.3980	7.5125

Table: 5a. Reduction in irreversibility in terms of exergy destruction ratio of vapour compression refrigeration system using ecofriendly refrigerant in the primary circuit and water flowing in the condenser in secondary circuit and brine flow in the secondary circuit in the evaporator using Al_2O_3 as nano material of 10 micron size

Refrigerant	EDR with Al_2O_3 nano	EDR without nano	% reduction In EDR
R1234ze	1.602	1.836	12.7451
R1234yf	1.479	1.727	14.360
R134a	1.307	1.513	13.615

Table: 5b. Reduction in irreversibility in terms of exergy destruction ratio of vapour compression refrigeration system using ecofriendly refrigerant in the primary circuit and water flowing in the condenser in secondary circuit and brine flow in the secondary circuit in the evaporator using Al_2O_3 as nano material of 10 micron size

Refrigerant	EDR with copper nano	EDR without nano	% reduction In EDR
R1234ze	0.9457	1.969	51.986
R1234yf	0.8763	2.429	63.9234
R134a	0.6877	1.335	48.4869

Table: 5c. Reduction in irreversibility in terms of exergy destruction ratio of vapour compression refrigeration system using ecofriendly refrigerant in the primary circuit and water flowing in the condenser in secondary circuit and brine flow in the secondary circuit in the evaporator using TiO_2 as nano material of 10 micron size

Refrigerant	EDR with TiO2 nano	EDR without nano	% reduction In EDR
R1234ze	1.632	1.969	17.1153
R1234yf	1.496	2.429	38.41
R134a	1.337	1.335	0.1498

Table: 5(a)-(c). Represents the reduction in the irreversibility in terms of exergy destruction ratio in the system and maximum exergy destruction ratio around 25.294% was observed by using R152a and exergy destruction ratio is 22.79% by using R290 hydrocarbon and 23.403% by using R407c as ecofriendly refrigerant. The Reduction in EDR is 20.09% by using R404a, and 21.37% by using R134a. The R1234ze and R1234yf have slightly less reduction in EDR as compaired by using R134a

4. Conclusions

In this paper, first law and second law analysis of vapour compression refrigeration systems using multiple evaporators and single compressor and single expansion valve with thirteen ecofriendly refrigerants have been presented. The conclusions of the present analysis are summarized below:

1. The First law efficiency (COP) and Second law efficiency (Exergetic efficiency) of vapour compression refrigeration systems using R717 refrigerant is higher but is has toxic nature can be use by using safety measure for industrial applications.
2. COP and exergetic efficiency for R152a and R600 are nearly matching the same values.are better than that for R125 at 313K condenser temperature and showing higher value of COP and exergetic efficiency in comparison to R125.
3. For practical applications R-134a is recommended because it is easily available in the market has second law efficiency slightly lesser than R-152a which was not applicable for commercial applications.
4. The worst component from the viewpoint of irreversibility is expansion valve followed by condenser, compressor and evaporators, respectively. The most efficient component found to be subcooler. The R-152a has least efficiency defects for 313K condenser temperature.
5. Performance evaluation of Vapour compression refrigeration system when calculated nucleate heat transfer coefficient enhancement factor based on Al_2O_3 nanoparticle mixed in the ecofriendly refrigerant and implement into the program results is to be found as 23% using R134a and 18% when using R407c in the primary circuit. Performance evaluation of Vapour compression refrigeration system when calculated nanorefrigerent property implement into the program based on Al_2O_3 nanoparticle mixed in the R134a ecofriendly refrigerant is 13% and Al_2O_3 nanoparticle mixed in the R407c is 9%. Performance evaluation of Vapour compression refrigeration system when nanoparticle into refrigerant oil nanoparticle based on Al_2O_3 nanoparticle mixed in the ecofriendly R134a refrigerant is 11%
6. The performance of vapour compression refrigeration systems using Al_2O_3 particles direct mixed in the R134a gives better first law performance than R407c and improvement in the first law performance is 28% using R134a and Al_2O_3 nano particles mixed with compressor oil and then used is 18.8% and 8% as heat transfer enhancement factor and implement into the refrigerant property and lowest improvement 2.64% when Al_2O_3 directly mixed with R407c, mixed with compressor oil and then used as refrigerant the primary circuit

References

[1] D. Elcock Potential impacts of nanotechnology on energy transmission applications and needs, Environmental Science Division, Argonne National Laboratory, 2007

[2] E. Halimic, D. Ross, B. Agnew, A. Anderson, I. Potts, A comparison of the operating performance of alternative refrigerants, Int J Applied Thermal Engineering, 23, 2003, 1441-1451

[3] JA Eastman, Choi SUS, Li S, Yu W, L J. Thompson, Anomalously increased effective thermal conductivities of ethylene glycol-based nanofluids containing copper nanoparticles, Applied Physics Letters, 78(6), 2001, 718–20

[4] MS Liu, MCC Lin, IT Huang, CC. Wang, Enhancement of thermal conductivity with CuO for Nanofluids". Int. Journal of Chemical Engineering and Technology, 29(1), 2006, 72–77

[5] W. Jiang, G. Ding, H. Peng, Measurement and model on thermal conductivities of carbon nanotube nanorefrigerants, International Journal of Thermal Sciences, 48, 2009, 1108–15
[6] Y. J. Hwang, Y. C. Ahn, HS. Shin, CG. Lee, GT. Kim, HS. Park, et al., Investigation on characteristics of thermal conductivity enhancement of nanofluids, Current Applied Physics, 6(6), 2006, 1068–71
[7] D-H Yoo, KS Hong, H-S. Yang, Study of thermal conductivity of nanofluids for the application of heat transfer fluids, Thermochimica Acta 2007, 455(1–2), 66–9.
[8] Choi SUS, ZG. Zhang, W. Yu, FE. Lockwood, EA. Grulke, Anomalous thermal conductivity enhancement in nanotube suspensions, Applied Physics Letters, 79(14), 2001, 12-20
[9] Y. Yang, Carbon nanofluids for lubricant application, Research journal of University of Kentucky, 2006
[10] JA Eastman, US. Choi, LJ. Thompson, S. Lee, Enhanced thermal conductivity through the development of nanofluids, Mater Res Soc Symp Proc, 1996, 457
[11] Y. Yang, Carbon nanofluids for lubricant application.University of Kentucky, 2006
[12] HU Kang, SH Kim, JM Oh, Estimation of thermal conductivity of nanofluid using experimental effective particle, Experimental Heat Transfer, 19(3), 2006, 181–91
[13] J-H. Lee, KS Hwang, SP Jang, Lee BH, Kim JH, Choi SUS, et al., Effective viscosities and thermal conductivities of aqueous nanofluids containing low volume concentrations of Al_2O_3 nanoparticles, International Journal of Heat and Mass Transfer, 51(11–12), 2008, 2651–2266
[14] W. Jiang, G. Ding, H. Peng, Measurement and model on thermal conductivities of carbon nanotube nanorefrigerants. International Journal of Thermal Sciences, 48, 2009, 1108–15
[15] XM Wu, P. Li, Li, WC. Wang, Investigation of pool boiling heat transfer of R11 with TiO2 nano-particles, Journal of Engineering Thermophysics, 29, 2008, 124–6
[16] V. Trisaksri, S. Wongwises, Nucleate pool boiling heat transfer of TiO2–R141b nanofluids, International Journal of Heat and Mass Transfer, 52(5–6), 2009, 1582–88
[17] P. Hao, D. Guoliang, J. Weiting, H. Haitao, G. Yifeng, Heat transfer characteristics of refrigerant-based nanofluid flow boiling inside a horizontal smooth tube, International Journal of Refrigeration, 32, 2009, 1259–70
[18] P. Hao, D. Guoliang, H. Haitao, J. Weiting, Z. Dawei, W. Kaijiang, Nucleate pool boiling heat transfer characteristics of refrigerant/oil mixture with diamond nanoparticles, International Journal of refrigeration, 33, 2010, 347–58
[19] KJ. Wang, GL Ding, WT. Jiang, Nano-scale thermal transporting and its use in engineering, International Proceedings of the 4th symposium on refrigeration and air condition, 2006, 66–75
[20] P. Li, XM. Wu, H. Li, Pool boiling heat transfer experiments of refrigerants with nanoparticle TiO2, Int: Proceedings of the 12th symposium on engineering thermophysics, 2, 2006, 325–338
[21] H. Peng, G. Ding, W. Jiang, H. Hu, Y. Gao, Heat transfer characteristics of refrigerant-based nanofluid flow boiling inside a horizontal smooth tube, International Journal of Refrigeration, 32, 2009, 1259–1270
[22] D.Sendil Kumar, R. Elansezhian.Zno, Nanorefrigerant in R152a refrigeration system for energy conservation and green environment, Int Journal of Frontior of Mech Engg, 2014, 1-6
[23] I. M. Mahbubul, S. A. Fadhilah, R. Saidur, K. Y. Leong, M. A. Amalina, Thermophysical properties and heat transfer performance of Al2O3/R-134a nano refrigerants, Int. Journal of Heat and Mass Transfer, 57, 2013, 100–108s

Discovery

The International Daily journal
ISSN 2278-5469 EISSN 2278-7550
© 2015 Discovery Publication. All Rights Reserved

High speed neuron implementatio mathematics

Publication History
Received 4 Aug 2015
Accepted 6 Sep 2015
Published 6 Oct 2015

Citation
Yamuna SV, Anshika, N. High speed neuron implementation mathematics, Discovery, 2015, 44(201), 3-22

High speed neuron implementation using Vedic mathematics

Yamuna SV[1], Anshika[2], Nidhi Goel[3], S.Indu[4]
Department of Electronics and Communication Engineering
Delhi Technological University
Delhi, India
[1]yamuna1802@gmail.com, [2]ansh.delhi89@gmail.com, [3]nidhi.iitr@gmail.com, [4]s.indu@rediffmail.com

Abstract— Neural network based systems are said to be much faster than their counterparts. Artificial Neural Network has been considered to speed up processing due to its parallel architecture and the numerous mathematical computations involved for processing any input. In the present work, we have explored the possibility of enhancing the computation speed in a single neuron. This is achieved by performing the neural network computations using Vedic mathematics rather than the conventional addition multiplication process. The multiplier is based on the "Urdhva Tiryagbhyam" sutra, which is one out of sixteen sutras of ancient Vedic mathematics. Here, coding is done in VHDL and synthesis is done in Xilinx ISE series using Modelsim. Several experiments have been conducted to analyze the results. Comparative analysis indicates the improvement in computation speed of neuron designed using Vedic multiplier over the conventional multiplier. This increase in processing speed can be of use in several real time operations where speed is critical.

Keywords— Artificial neural network; Vedic multiplication; Urdhva Tiryagbhyam.

I. INTRODUCTION

The artificial neural networks are used for a number of applications including pattern recognition, classification, identification, GPS systems, speech, vision, and control systems [1-4]. They can also be trained to solve things that are difficult for conventional computers or human beings. Additionally, they have attractive properties like adaptiveness, self-organization, nonlinear network processing and parallel processing. This has lead to the use of neural network in applications involving classification, association, decision-making and reasoning [5]. Artificial neural networks consist of massively parallel network and require parallel architecture for high speed operations in real time applications [6].

Multiplier is a crucial block in designing arithmetic, signal and image processors, such high speed multipliers play an important role in designing efficient architecture [7, 8]. Recently, several high speed multipliers designed using Vedic mathematics have been reported [9, 10]. The use of Vedic mathematics lies in the fact that it reduces the typical calculations in conventional mathematics into very simple one and hence reduces the computation time. This is because the Vedic formulae are claimed to be based on the natural principles on which the human mind works. Vedic mathematics is a collection of arithmetic rules that allow more efficient speed implementation.

In this paper, features of ANN & Vedic multiplier are used to evaluate the performance of a neuron designed with Vedic multiplier against normal multiplier. Also, the hardware implications of both the systems have been done. Section II presents a brief introduction about ANN and an explanation of Vedic multiplier with Urdhva Tiryagbhyam sutra is given in Section III. Section IV explains about the design and hardware implementation of the proposed work. Section V explains the simulation results of the work. The last section VI deals with the conclusion of the proposed work.

II. ARTIFICIAL NEURAL NETWORKS

A. Introduction to Artificial Neural Networks

The work on artificial network has been motivated from the working of human brain in a way that brain is a highly complex nonlinear and parallel computer with a capability to organize its structural constituents known as neurons so as to perform the certain computation many times faster than that of the digital hardware [4]. The computation can be viewed as a system in which the inputs are received from an external stimulus. The recept convert the external stimulus into electrical impulses that convey the information to the neural net and depending on the electrical impulses the neural net conveys or transmits the information to effectors to provide an optimal response to stimulus as shown in "Fig.1". The brain is composed of an integral constituent known as neuron. The brain learns to distinguish different patterns by training these neurons which give the appropriate output [11].

In order to emulate the brain, the concept of artificial neural network has been designed to model the way in which the brain performs a particular task or function of interest.

A neural network is a massively parallel distributed network made up of simple processing units. These processing

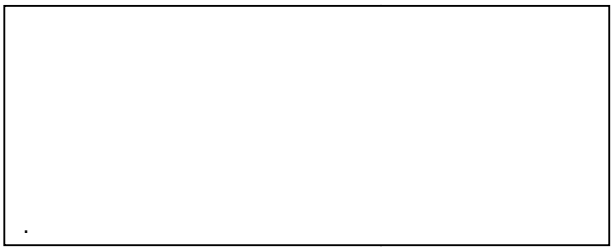


Fig. 1. Block Diagram Representation of Nervous system

units have a natural tendency of storing experiential knowledge and making it available for use [12]. It is analogous to the brain in two aspects:

- The network obtains knowledge from its environment through a learning process.
- Acquired knowledge is stored in interneuron connection strengths known as synaptic weights.

B. Model of Neuron

In 1958, Rosenblatt introduced the mechanics of the single artificial neuron and introduced the ‚Perceptron'. Basic findings from the biological neuron operation enabled early researchers (e.g., McCulloch and Pitts, 1943) to model the operation of simple artificial neurons. An artificial processing neuron receives inputs as stimuli from the environment, combines them in a special way to form a ‚net' input, passes that over through a linear threshold gate, and transmits the signal forward to another neuron [13]. If the sum of all the weighted inputs is above the threshold, the output is fired else not.

The nonlinear (McCulloch) model of neuron is as shown in ‚Fig. 2'.

The neuron may be described in the following way

$$= " \quad (1)$$

$$= " (+) \quad (2)$$

where , ,.. are the input signals.

refers to synaptic weight of neuron

is the output of neuron

The relationship between induced local fields or the activation potential of the neuron depends on whether bias is positive or negative and is given as follows:

$$= + \quad (3)$$

$$= " \quad (4)$$

$$= " ( ) \quad (5)$$

Depending on the application requirement, various activation functions could be used. Usually, three basic type of

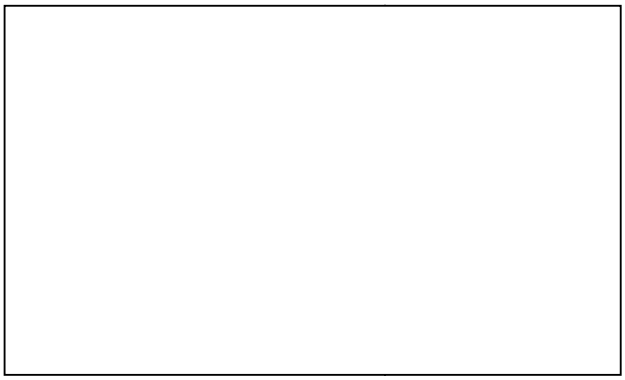


Fig. 2. Nonlinear model of Neuron [4]

activation function i.e. threshold function, piecewise linear function and sigmoid function are used.

C. Hardware Implementation of a Neuron

Though hardware implementation of the artificial neural network has a long history, over 25 years by now [14], still it is the centre of attention for many researchers [15], while its FPGA implantation remains a challenge [16,17,18]. FPGAs are devices which enable the implementation of hardware components in a reconfigurable way. This fact makes that FPGAs are cheaper than ASICs (since FPGAs are reconfigurable so many times, we do not need a new FPGA with each application). Besides the software flexibility, FPGAs present the advantage of the hardware execution speed, with their higher parallelism exploitation. Finally, FPGAs provide a significant improvement in the performance/cost ratio compared with ASICs [19].

The implemented nonlinear model of a single neuron is shown in Fig. 3.

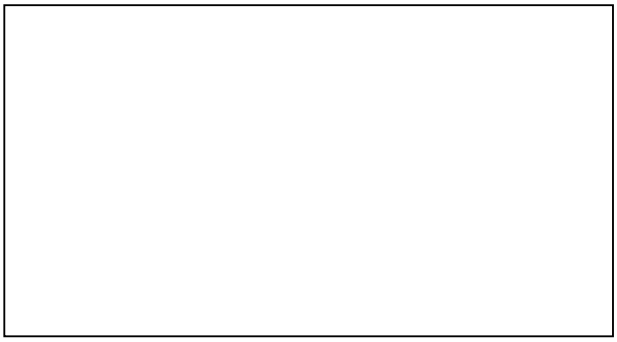


Fig. 3. Block Diagram of a Single Neuron

III. Introduction To Multiplier

Multiplication is an essential and basic function in arithmetic procedures and Vedic mathematics is an ancient methodology developed by Indians, which is capable of faster intellectual computation. Multiplication is one of the most important operations in digital neural network based systems. There are several Multiplication based operations. Frequently used such Computation Intensive Arithmetic Functions are multiply and Accumulate (MAC) and inner product [20]. Further, multipliers play a major role in the overall power consumption of any system. Therefore, reducing their power dissipation satisfies the overall power budget of ANN system.

Higher throughput arithmetic operations are important to achieve the desired performance in many real-time signal and image processing applications [21]. One of the key arithmetic operations in such applications is multiplication and the development of fast multiplier circuit has been a subject of interest over decades. The essential requirements for many applications developed using neural network are reduction of the time delay and power consumption.

A. Vedic Multiplier

The word "Vedic" is a Sanskrit word derived from the word, 'Veda' which means store house of all knowledge. Vedic mathematics is based on 16 Sutras (or aphorisms) that deal with various branches of mathematics like arithmetic, algebra, geometry etc. In Vedic mathematics, methods of basic arithmetic are extremely simple and powerful [22, 23]. In Vedic mathematics, Urdhva Tiryagbhyam sutra is used generally for high speed multiplication. Vedic multiplier is very much advantageous in case of bigger multiplication which would consume more time in a conventional multiplier.

B. Details of Urdhva Tiryagbhyam Method of Multiplication

Urdhva Tiryagbhyam sutra is a sutra for multiplication in the ancient Indian Vedic mathematics. This is based on the generation of all partial products by means of concurrent addition of the partial product. Urdhava Tiryagbhyam obtains parallelism in generation of partial products and their summation.

Vedic mathematics reduces the typical calculations in conventional mathematics into very simple one. This sutra uses Vedic formulae that are based on the natural principles on which the human brain works. Vedic mathematics is a technique of arithmetic rules that allow more efficient speed implementation. Mostly, Urdhva Tiryagbhyam is applicable to all cases of multiplication. 'Urdhva' and 'Tiryagbhyam' words are derived from Sanskrit literature in which 'Urdhva' means 'Vertically' and 'Tiryagbhyam' means 'Crosswise'. Therefore, this algorithm uses the concept of vertical and crosswise multiplication and addition to get the partial products.

C. Algorithm

To illustrate this multiplication scheme, the multiplication of two decimal numbers is chosen. Line diagram for the multiplication is shown in (Fig. 4). The line diagram demonstrates the procedure for multiplication of 2, 3 and 4 bits. In the line diagram, the dots represent bit (0) or (1). From the line diagram of 2 bit multiplication, it is seen that the digits on both sides of the line are multiplied and added with the carry from the previous step [24]. The result generates one of the bits of the result and a carry. In the next step, this carry is added and hence the process goes on. The same procedure is followed for more number of bits. The line diagram shows the methodology adapted for 3 and 4 bits [25].

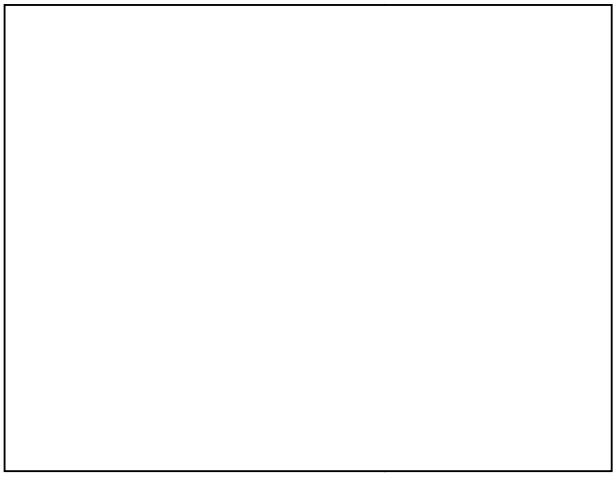


Fig. 4. Line Diagram for Vedic Multiplication of 2, 3 and 4 digits

D. Urdhva Multiplier Hardware Architecture

The 'UrdhvaTiryagbhyam' algorithm can be implemented for binary number system in the same way as decimal number system. As an example, a 4x4 Vedic multiplier hardware implementation is explained.

The 4x4 bit Vedic multiplier module is implemented using four 2x2 bit Vedic multiplier modules. Let's examine 4x4 multiplication say a=a3a2a1a0 and b=b3b2b1b0. The output for the multiplication result is s7s6s5s4 s3s2s1s0. Divide a and b into two parts as a3a2 & a1a0 for a and b3b2 & b1b0 for b using the fundamentals of Vedic multiplication, by taking two bits at a time and using 2 bit multiplier block.

The structure for multiplication will be as shown in (Fig. 5). Each block, as shown is a 2x2 bit Vedic multiplier. The inputs to the first multiplier are a1a0 and b1b0. The last block is a 2x2 bit multiplier with inputs a3a2 and b3b2.

The middle one shows two 2x2 bit multipliers with inputs a3a2 & b1b0 and a1a0 & b3b2. The final result of multiplication is of 8 bits, s7s6s5s4 s3s2s1s0. To get final product (s7s6s5s4 s3s2s1s0) four 2x2 bit Vedic multiplier and three 4-bit Ripple-Carry (RC) adders are required.

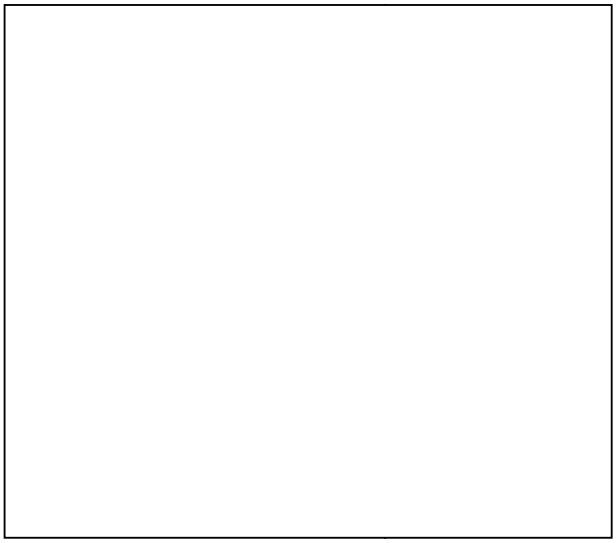


Fig. 5. Block Diagram of 4x4 bit Vedic Multiplier

IV. Proposed Hardware Architecture Of Neuron Implemented Using Vedic Multiplier

The proposed hardware is almost similar to a standard linear neuron (McCulloch Pitts model) except for the multiplier. Here the standard multiplier is replaced with a Vedic multiplier which multiplies the inputs with weights. For evaluation purpose the weights were randomly fixed. Fig. 6, shows the proposed architecture of a single neuron which has been designed using Vedic multiplier instead of standard multiplier to achieve higher speed in designing neural nets.

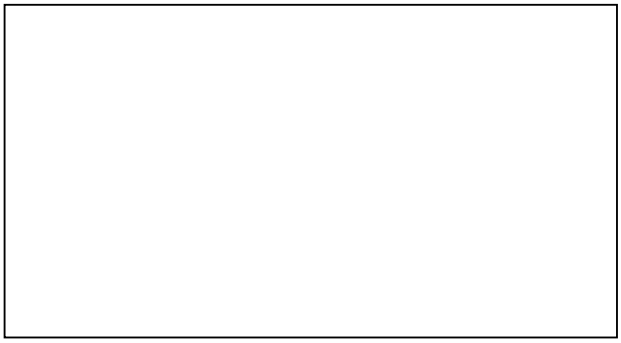


Fig. 6. Proposed Architecture

V. Results

A. Simulation Results

For the purpose of evaluation, performance of a single neuron (with fixed weights) with standard multiplier and Vedic multiplier were compared. The hardware implementation was carried out using VHDL. For implementation, testing and simulation purpose, Xilinx ISE 6.1 with ModelSim simulation tools was used. Spartan II family was chosen as target device. The simulation and synthesis results are as shown:

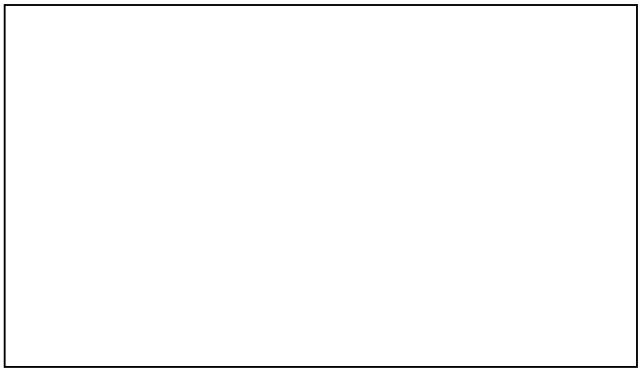


Fig. 7. Simulation results of a neuron using standard multiplier

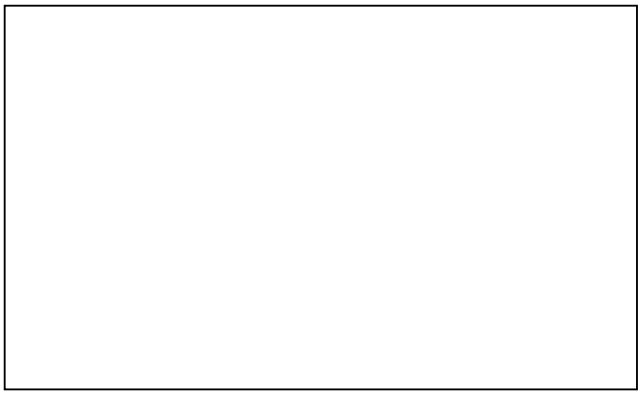


Fig. 8. Simulation results of a neuron using Vedic multiplier

TABLE I. SYNTHESIS RESULT OF NEURON WITH STANDARD MULTIPLIER

Logic Utilization	Used	Available	Utilization
Number of Slices	72	192	37%
Number of 4 input LUTs	125	384	32%
Number of bonded IOBs	25	90	27%

TABLE II. SYNTHESIS RESULT OF NEURON WITH VEDIC MULTIPLIER

Logic Utilization	Used	Available	Utilization
Number of Slices	40	192	20%
Number of 4 input LUTs	70	384	18%
Number of bonded IOBs	25	90	27%

TABLE III. DELAY COMPARISON OF NEURON

FPGA device package : xc2s156-cs144	Delay (ns)	Memory (Kb)
Using standard multiplier	32.969	72772
Using Vedic multiplier	25.675	73668

B. Comparison of Standard Neuron with Vedic Neuron

Table I & II shows the logic utilization of a single neuron realized using standard booth multiplier and Vedic multiplier. From the statistics, it is clear that neuron implemented using Vedic multiplier will utilize less logic compared to the neuron with standard multiplier. Table III compares the result with respect to delay/speed of neural network using standard and Vedic multiplier. The result shows that neuron designed using Vedic multiplier is faster than the one using standard multiplier.

VI. CONCLUSIONS

The technologies like ANN & Vedic mathematics (multiplier) are the two important and promising technologies which can increase the processing speed. In this paper, a novel scheme to combine these two technologies to achieve a high performance neuron or ANN has been proposed. A single neuron is implemented using Vedic mathematics (Vedic neuron) in VHDL. The results of standard neuron and Vedic neuron are compared. Hence, the comparison result indicates that the speed of Vedic neuron is better than standard neuron.

Also, this research can be extended by replacing Vedic adders in place of standard adders in neurons, which would in all means increase the computation speed. Since, neurons are the basic building blocks of Neurocomputers, the speed of Neurocomputers developed using Vedic neurons would be better than the standard Neurocomputers.

References

[1] Girish Kumar Jha, "Artificial neural networks and its applications", Indian Agricultural Research Institute, PUSA, New Delhi, 2007.

[2] Huqqani A. A, Schikuta E, and Mann E, "Parallelized neural networks as a service in neural networks", (IJCNN) International Joint Conference on IEEE, 2014, pp. 2282-2289.

[3] T. Theocharides, G. Link, N. Vijaykrishnan, M. J. Irwin, and V. Srikantam, "A generic reconfigurable neural network architecture implemented as a network on Chip," Proc. of the IEEE International System on Chip Conference, September 2004, pp. 191
[4] Omondi, Amos R., and Jagath Chandana Rajapakse. FPGA implementations of neural networks. Vol. 365. New York, USA, Springer, 2006.
[5] Janusz Starzyk, and Jing Pang, "Evolvable binary artificial neural network for data classification," PDPTA - Parallel and Distributed Processing Techniques and Applications, Distributed Parallel Computing, 1998-2013.
[6] Chun-Hsien Chen and Vasant Honavar, "A Neural Network Architecture for Syntax Analysis," IEEE Transactions on Neural Networks, vol. 10, no. 1, January 1999, pp. 94.
[7] H.Guilt, "Fully iterative fast array for binary multiplication", Electronics Letters, vol. 5, 1996, pp. 263
[8] Ramalatha, M Dayalan, K D Dahiya, and P Priya, "High speed energy efficient ALU design using Vedic multiplication techniques," ICACTEA, 2009., Jul 15-17, 2009, pp. 600-603.
[9] Kunchigi, Vaijyanath, Linganagouda Kulkarni, and Subhash Kulkarni. "High speed and area efficient vedic multiplier," (ICDCS) International Conference on Devices, Circuits and Systems, IEEE, 2012, pp. 360-364.
[10] Y.bansal, C.Madhu, and P.Kaur, "High speed vedic multiplier designs-A review," Proceedings of IEEE, Recent Advances in Engineering and Computational Sciences (RAECS) 2014, 06 March 2014.
[11] Haykin, S. "Neural networks a comprehensive foundation", Prentice Hall Publishing, New Jersey 07458, USA, Vol.1, 1999, 2nd edition, pp 6-7.
[12] Bose, N. K, and Liang P, "Neural network fundamentals with graphs, algorithms, and applications", McGraw Hill, Inc, Hightstown, NJ, USA, 1996.
[13] I.A. Basheer, and M. Hajmeer, "Artificial neural networks: fundamentals, computing, design and application", Elsevier Science B.V, Journal of Microbiological Methods, vol.43, 2000, pp. 3-31.
[14] J. Misra, and I. Saha, "Artificial neural networks in hardware: A survey of two decades of progress", Elsevier, Neurocomputing 74, 2010, pp. 239-255.
[15] A. Tisan, M.N. Cirstea, S. Oniga ,and A. Buchman, " Artificial olfaction system with hardware chip learning neural networks", Proc. of IEEE Int. Conference on Optimisation of Electrical and Electronic Equipment ,2010, pp. 883-884
[16] W. Kurdthongmee, "A novel hardware oriented Kohonen SOM image compression algorithm and its FPGA implementation", Journal of Systems Architecture, vol.54, 2008, pp. 983-994.
[17] A. Gomperts, A. Ukil, and F. Zurfluh, "Development and implementation of parameterized FPGA-based general purpose neural networks for online applications," IEEE Transactions on Industrial Informatics, 2011, pp. 78-89.
[18] Cheng-Jian Lin and Hung-Ming Tsai, "FPGA implementation of a wavelet neural network with particle swarm optimization learning", Elsevier, Mathematical and Computer Modelling vol. 47, 2008, pp 982-996.
[19] J. M. Granado, M. A. Vega, R. P…rez, J. M. S†nchez, and J. A. G‡mez, "Using FPGAs to Implement Artificial Neural Networks", 13th International Conference on Electronics, Circuits and Systems, ICECS '06, IEEE, 2006, pp. 1-4.
[20] Purushottam D. Chidgupkar, and Mangesh T. Karad, "The implementation of Vedic algorithms in digital signal processing", UNESCO International Centre for Engineering Education (UICEE), Australia, vol.8, no.2, 2004.
[21] H. Thapliyal, and H.R Arbania. "Time-Area-Power Efficient Multiplier and Square Architecture Based On Ancient Indian Vedic Mathematics", Proceedings of the 2004 International Conference on VLSI, Las Vegas, Nevada, June 2004, pp. 434.
[22] Harpreet Singh Dhillon, and Abhijit Mitra, "A reduced-bit multiplication algorithm for digital arithmetics," International Journal of Computational and Mathematical Sciences, no.2, 2008.
[23] Shamim Akhter, "VHDL implementation of fast NXN multiplier based on Vedic mathematics", 18th European Conference on Circuit Theory and Design, ECCTD 2007 IEEE, 2007, pp. 472.
[24] Vinay, "Analysis, Verification and FPGA implementation of Vedic multiplier with BIST capability", Phd thesis, Thapar University, 2009.
[25] Anju, and V.K.Agrawal, "FPGA implementation of low power and high speed Vedic multiplier using Vedic mathematics". IOSR Journal of VLSI and Signal Processing (IOSRJVSP), volume 2, issue 5 (May. - Jun. 2013), pp. 55-57

ResearchGate

See discussions, stats, and author profiles for this publication at: http://www.researchgate.net/publication/282854944

Investigation of Surface Morphology in EDM process using Response Surface Methodology

ARTICLE · SEPTEMBER 2015

READS
40

2 AUTHORS, INCLUDING:



Ravinder Kumar
Amity University
10 PUBLICATIONS **11** CITATIONS

SEE PROFILE

All in-text references underlined in blue are linked to publications on ResearchGate, letting you access and read them immediately.

Available from: Ravinder Kumar
Retrieved on: 13 November 2015

OPEN ACCESS

International
Journal
Of Modern Engineering Research (IJMER)

Investigation of Surface Morphology in EDM process using Response Surface Methodology

Ravinder Kumar[1], Surabhi Lata[1], Ramakant Rana[1], Pankaj Kumar[2], Abhinav Kumar[2], Lakshay Kumar[2], Jitender Kumar Verma [2]Roop Lal[3]

[1]*Assistant Professor, Mechanical and Automation Engineering Department, Maharaja Agrasen Institute of Technology, Delhi, India*
[2] *Student, Mechanical and Automation Engineering Department, Maharaja Agrasen Institute of Technology, Delhi, India*
[3]*Assistant Professor, Mechanical Engineering Department, Delhi Technological University, Delhi, India*

ABSTRACT:- *Electric Discharge Machining is used to produce complex and intricate shapes that are difficult-to-machine by the conventional methods. The present research work carries out the investigation of surface roughness trend depending on the process parameters of EDM process. The work material and electrode material selected are Stainless Steel 202 and EN 31 (AISI 52100) respectively. The optimization process of surface roughness (SR) of electrical discharge machining (EDM) is concluded by the Response Surface Methodology. The process control parameters of EDM chosen were current, pulse on time and machining time. RSM method was used to design the experimental model whose adequacy checking was carried out using Minitab software. Experimental results formed the basis of the formulation of the regression equations. The results successfully supported the prediction of surface roughness through the proposed regression equation. It was concluded that the analysis carried out yielded the optimum results of surface roughness within the experimental constraints while varying the EDM process parameters.*

Keywords:- *EDM, RSM, Design of Experiments, Surface Roughness*

I. INTRODUCTION AND LITERATURE REVIEW

Today's technologically advanced world demands materials which are high strength temperature resistant alloys and possess all desired mechanical properties such as high strength, corrosion resistance, toughness, etc. The emerging needs of the automation world led to the development of such difficult-to-machine materials which meets the stringent design requirements and enhance the surface quality. With the advent of these high strength materials, innovation became mandatory in order to search new technologies for machining and processing of the new materials. These materials enhance in terms of thermal, chemical and mechanical properties which are of huge economic benefit to manufacturing industries but defy the traditional machining processes. Therefore, solution is discovered in the advanced machining processes which makes use of different class of energy for material removal using the material properties, like electrical and thermal conductivity, melting temperature, electrochemical equivalent etc. EDM is a non-traditional machining technique which extensively and effectively machines such materials with ease. It machines electrically conductive materials where material is removed due to the thermal energy of the spark. In this process precisely controlled sparks are generated in the presence of a dielectric fluid between the electrode and the workpiece. The sparks or electrical discharge are of short duration and high current density between the tool and the workpiece. It is assertion that after milling, turning and grinding i.e. conventional machining processes, EDM is the fourth most extensively used machining method. Though efficiency of machining is less but the product quality and productivity in terms of surface finish, geometrical dimensions, process accuracy etc. is high [1]. E. Weingärtner et al. [2] reviewed the paper on Modeling and simulation of electrical discharge machining founding a better correlation with experimental results when the latent heats of fusion and evaporation are taken into consideration, as well as temperature-dependent thermo-physical properties of the workpiece. Input parameters used are short discharge durations and high peak currents. Better simulation results were achieved when considering the material properties as temperature-dependent. Z. Qinjian et al. [3] reviewed the paper on electrical discharge and ultrasonic assisted mechanical combined machining of polycrystalline diamond. The metal bonded diamond

grinding wheel was as a tool electrode and the workpiece was supplemented with ultrasonic vibration, electrical discharge and ultrasonic assisted mechanical combined machining achieves efficient precision machining of PCD materials by selecting appropriate combinations of process parameters. The conclusion drawn was that Ultrasonic vibration has chip removal function and it has limited impact on the material removal rate. Karthikeyan et al. [4] used Tungsten carbide/Cobalt (WC–Co) composite and made an attempt to investigate the fracture strength and the reliability of EDMed WC–Co composite using the Weibull distribution analysis. The comparison of results between the machined composites and un-machined composites is carried out and presented in this study. Rajesh et al. [5] optimized the operating parameters for unconventional electric discharge machining through the empirical models developed by conducting a designed experiment based on the Grey Relational Analysis. Genetic Algorithm (GA) based multi-objective optimization for maximization of MRR and minimization of Ra has been done to identify the optimized machining conditions. Jin-Bin et al. [6] analysed the efficiency of traditional cutting processes and found that they are limited by the mechanical properties of the processed material and the complexity of the workpiece geometry, while electrical discharge machining (EDM) being a thermal erosion process, is subject to no such constraints. This paper highlights the development of a comprehensive mathematical model for correlating the interactive and higher order influences of various EDM parameters through RSM, utilizing relevant experimental data as obtained through experimentation. Optimal combination of these parameters was obtained for achieving controlled EDM of the workpieces. Kanlayasiri et al. [7] investigated the following machining variables i.e. pulse-peak current, pulse-on time, pulse-off time, and wire tension. Analysis of variance (ANOVA) technique was used to find out the variables affecting the surface roughness. Results showed that pulse-on time and pulse-peak current are significant variables to the surface roughness of wire-EDMed DC53 die steel. Further, the developed model was validated with a new set of experimental data, and the maximum prediction error of the model was less than 7%. Anand et al. [8] described the selection of machining parameter Discharge current, Pulse on time, Pulse off time in EDM for the machining of AISI 202 Stainless steel material and further using the grey relational analysis for optimizing the machining parameters i.e. material removal rate and surface roughness. Ghoreishi et al. [9] have made a model to optimize process parameters in EDM of tungsten carbide-cobalt composite. Four independent input parameters, viz., discharge current, pulse-on time, duty cycle, and gap voltage were selected to assess the EDM process performance in terms of material removal rate, tool wear rate, and average surface roughness. RSM have been used to plan and analyse the experiments. It has been mainly revealed that all the responses are affected by the rate and extent of discharge energy. The obtained predicted optimal results were also verified experimentally and the values of confirmation errors were computed, all found to be satisfactory, being less than 10%.

The investigation in the non-conventional machining processes is generally related to the effect of Pulse ON time, Pulse OFF time, Spark gap set Voltage, Peak current, Flushing Pressure, Work piece height, wire tension and wire feed on the material removal rate, surface roughness, kerf and gap current. The quality of the surface produced during these processes is of great importance and hence, it is exclusively researched. Surface quality is dependent on the appropriate selection of the machining parameters for any particular material and also on the operator's experience. These papers present the effect of various process parameters extensively on the surface roughness as the response factor in EDM process [10, 11, 12].

II. EXPERIMENTAL SETUP

The effect of various machining parameters was studied by conducting number of experiments on the EDM process. The experiments were conducted to investigate the effects of current, pulse ON time and processing time on surface roughness [13]. The selected workpiece was Stainless Steel 202 while the electrode material were EN 31 (AISI 52100). Table 1 shows the chemical composition of the work material i.e. Stainless Steel 202.

Table I: Composition of SS 202 Steel

Iron (Fe)	Chromium (Cr)	Manganese (Mn)	Nickel (Ni)	Silicon (Si)	Nitrogen (N)	Carbon (C)
68	17- 19	7.50-10	4-6	≤ 1	≤ 0.25	≤ 0.15

This chromium-nickel-manganese alloy was selected as at low temperatures it exhibits excellent toughness. It possess high hardness, strength and good corrosion resistant properties. It was chosen due to its emergent range of applications which includes restaurant equipment, sinks, cooking utensils, automotive trim, architectural structures, railway cars, hose clamps as can be made into plates, sheets and coils.



Figure 1: Photographic view of SS 202

Design of Experiments was carried out in order to study and analyse the effect of various process parameters of EDM on response factor i.e. surface roughness. DOE was used to estimate an unknown function for which only a few values were computed while least square error fitting was used to model the generated relations of the response surface [14]. The weight of work piece is measured using digital weighing machine to maintain the weight uniformity of the workpiece.



Figure 2: EDM Machine and Control Panel

III. SURFACE ROUGHNESS MEASUREMENTS

Surface roughness (Ra) is the measure of the fine surface irregularities on the surface texture of the machined workpiece. It is the arithmetic average deviation of the surface valleys and peaks over the entire cut-off length expressed in micro-meters. Cut-off length is the length that the stylus was dragged across the surface. A longer cut-off length will give a more average value, and a shorter cut-off length gives a less accurate result over a shorter stretch of surface.

Surface roughness measurement was carried out using the Mahr Federal Pocket Surf III (Figure 2). The Pocket Surf is a shop–floor type surface-roughness measuring instrument, which traces the surface of various machine parts and calculates the surface roughness based on roughness standards, and displays the results in µm. The work piece was attached to the detector tracing the minute irregularities of the work piece surface and the vertical stylus displacement during the trace being processed and digitally displayed on the display of the instrument [15, 16]. The surface tester has following measuring range:

R_a = 0.03 µm to 6.35 µm / ***1 µ inch to 250 µ inch***

The roughness values are taken by calculating average of at least three values of measurements per specimen at different locations of specimens.

Surface roughness is an important parameter in the EDM process. The parameters that affect roughness are current, pulse ON time and processing time. Centre-line average 'Ra' SR measurements of machined surfaces were taken to evaluate quantitatively the effect of EDM parameters on surface finish.



Figure 3: Surface Tester

IV. RESPONSE SURFACE METHODOLOGY (RSM)

Response surface methodology, or RSM, is a collection of mathematical and statistical techniques useful for the modeling and analysis of problems in which a response of interest is influenced by several variables and the objective is to optimize this response. The objective is to find the correlation between the variables investigated and the response [17, 18].

Design of Experiments (DOE) was used to estimate an unknown function for which only a few values were computed while least square error fitting was used to model the generated relations of the response surface. A Central Composite Design (CCD) gives a comparatively accurate prediction of all response variable averages related to quantities measured during experimentation, hence it was also used [19]. CCD offers the advantage that certain level adjustments are acceptable and can be applied in the two-step chronological RSM. In these methods, there is a possibility that the experiments will stop with few runs and decide that the prediction model is satisfactory [20]. The current, Pulse ON time and processing time are the machining variables selected for this investigation. The different levels taken for this study are depicted in Table II.

TABLE II: Different Variables Used In The Experiment And Their Level

VARIABLES	UNITS	CODE	LEVELS	
			1	**2**
CURRENT	Ampere (A)	X_1	3	6
PULSE ON TIME	Micro-seconds (µsec)	X_2	8	11
MACHINING TIME	Minutes (min)	X_3	55	65

Machining was carried out by varying the input process parameters each at a time, two replications of surface roughness measurement were taken, and the planning design matrix of the experiments has been shown in Table III.

Table III: PLANNING MATRIX OF THE EXPERIMENTS WITH THE OPTIMAL MODEL DATA

Trial Runs	Current (Amp)	Pulse on Time (µsec)	Machining Time (min)
R1	3	8	55
R2	3	8	65
R3	3	11	55
R4	3	11	65
R5	6	8	55
R6	6	8	65
R7	6	11	55
R8	6	11	65

In this investigation, a second-order model has been utilized. The experimental values are analyzed and the mathematical model is then developed that illustrate the relationship between the process parameters and response factor. The second-order model given below explains the behavior of the system [19, 20, 21].

$$Y = \beta_0 + \sum_{i=1}^{k} \beta_i X_i + \sum_{i=1}^{k} \beta_i i X_i^2 + \sum_{i,j=1, i \neq j}^{k} \beta_{ij} X_i X_j + \epsilon$$

Where Y is the corresponding response, X_i is the input variables, $X_i X_j$ are the interaction terms, respectively, of these input variables. The unknown regression coefficients are β_o, β_i, and β_{ij}.
The equation for calculating the approximate SR is

$$SR = 86.59 - 13.99\ X_1 - 7.286\ X_2 - 1.314\ X_3 + 1.184\ X_1X_2 + 0.1182\ X_2X_3 + 0.2259\ X_3X_1 - 0.01927\ X_1X_2X_3$$

Where X_1 is current in amperes, X_2 is Pulse On time in microseconds and X_3 is Machining Time in minutes

IV. RESULT AND DISCUSSION

Regression analysis developed the correlation between the input process parameters and the response factor i.e. surface roughness (SR) based on the responses obtained from the experiments. In this experimental investigation, a regression equation have been developed by considering three process parameters i.e. current, pulse on time and machining time and surface roughness as the response factor by the MINITAB 16 software. The coefficients of regression model are estimated from the experimental outputs. Main effects of the process parameters were further studied on the response.

SR obtained from the experiment is compared with the predicted value calculated from the regression model and further percentage error is calculated. As all the points on plot come close enough to form a straight line, it implies that the data are normal [22, 23]. Hence, the regression model is reasonably well fitted with the observed values.

Table IV: Plan of Experiments and Output Responses

Trial Runs	Current (X_1)	Pulse on Time (X_2)	Machining Time (X_3)	X_1X_2	X_2X_3	X_1X_3	$X_1X_2X_3$	SR Experimental	SR Theoretical	% Error
R1	3	8	55	24	440	165	1320	4.795	4.7913	0.077
R2	3	8	65	24	520	195	1560	5.562	5.5572	0.086
R3	3	11	55	33	605	165	1815	5.091	5.08545	0.109
R4	3	11	65	33	715	195	2145	5.285	5.28138	0.068
R5	6	8	55	48	440	330	2640	4.075	4.04784	0.666
R6	6	8	65	48	520	390	3120	5.065	5.04048	0.484
R7	6	11	55	66	605	330	3630	4.445	4.41612	0.649
R8	6	11	65	66	715	390	4290	5.210	5.1837	0.504

5.1 Effect of Current on SR:

The Figure 4 shown below indicates that SR is 5.285 µm when the current is 3 amp. It decreases steeply to 4.795 µm when the current is 6 amp. As the current is increased the SR depicts a decrease in the surface roughness though the number of sparks increases. This is due to the low value of current and also due to the low pulse ON time.

5.2 Effect of Pulse ON Time on SR:

The SR increases from 4.86 µm to 5.012 µm when the pulse on time increases from 8 µsec to 11µsec. As the pulse on time increases the intensity of spark is affected as the duration of the spark increases which is directly influencing the amount of material being removed. Increase in number and frequency of sparks leads to increase in SR.

5.3 Effect of Machining Time on SR:

Figure 6 shows an increase in SR value on the increase in the value of machining time. As the machining time is increased from 55 min to 65 min a steep slope is experienced in SR due to the increased duration while all other parameters remaining fixed. SR increases due to the low range of current on which machining process was carried out.

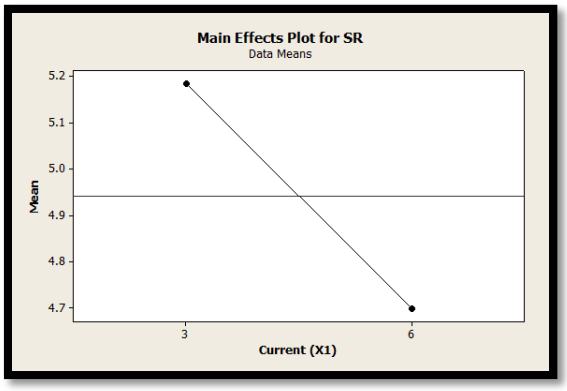


Figure 4: Effect of Current on SR

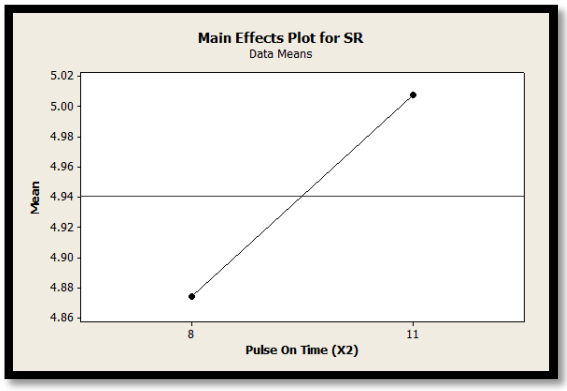


Figure 5: Effect of Pulse ON Time on SR

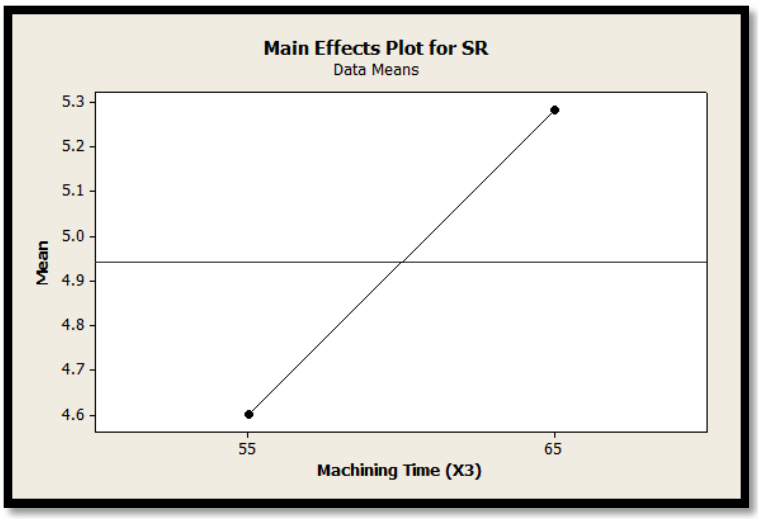
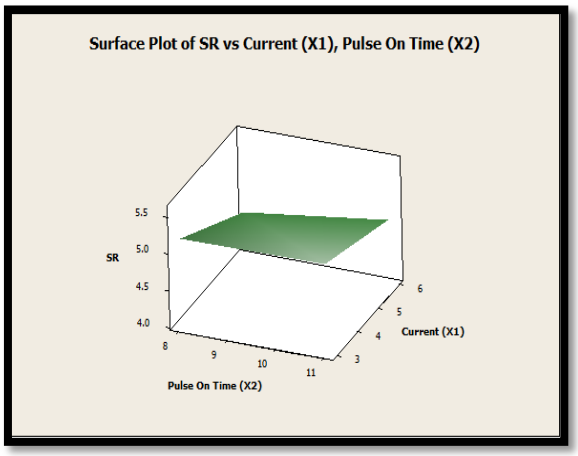


Figure 6: Effect of Machining Time on SR

5.4 Effect of Current and Pulse ON Time on SR:



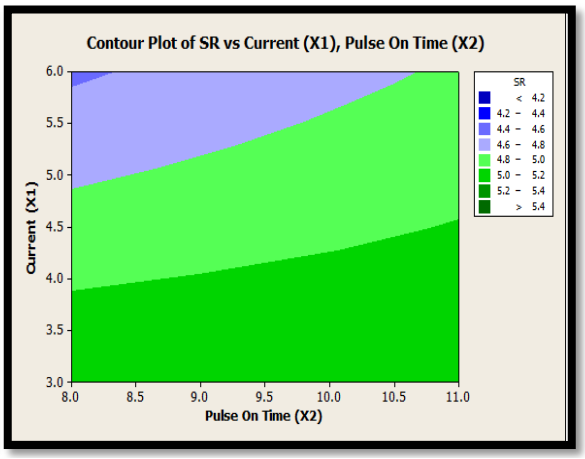
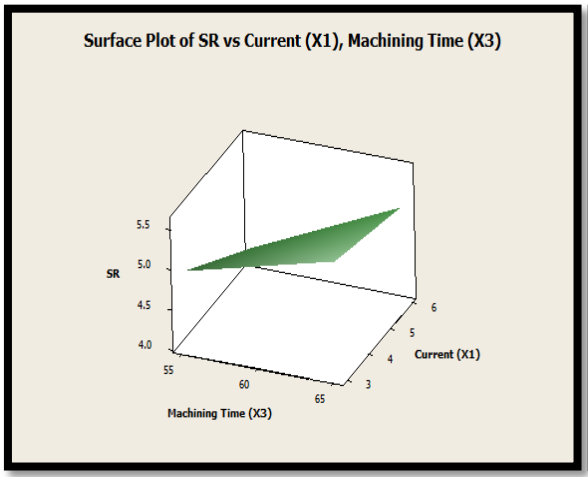


Figure 7: Surface Plot for SR vs X_1 vs X_2 **Figure 8: Contour Plot for SR vs X_1 vs X_2**

Figure 7 and 8 shows the estimated response for SR in relation to the process parameters of current (X_1) and Pulse ON time (X_2) while other parameters remaining constant at their lowest value. It is clear from the above plots that SR significantly decreases with the increase in the value of current for any value of pulse ON time. Though the effect of pulse on value is not prominent in above graphs but at higher values of current SR tends to increase with increase in pulse ON time. This happens due to their individual dominant control over the input energy. As the current increases, the intensity and frequency of the sparks generated increases which develops high temperature and creates crater thereby generating rough surface in the workpiece.

5.5 Effect of Current and Machining Time on SR:

Figure 9 and 10 shows the predicted response for SR in relation to the process parameters of current (X_1) and Machining Time (X_3) while other parameters remaining constant at their lowest value. It is depicted in the above plots that SR decreases parabolically with the increase in the value of current for all values of machining time. The machining time is directly proportional to SR i.e. on low values of machining time smooth surfaces are generated and at high values rough surfaces. Therefore, an optimum surface is generated when current and machining time both are high. This is due to the fact that high and uniform intensity sparks are generated for long duration of time hence, generating smooth surface.



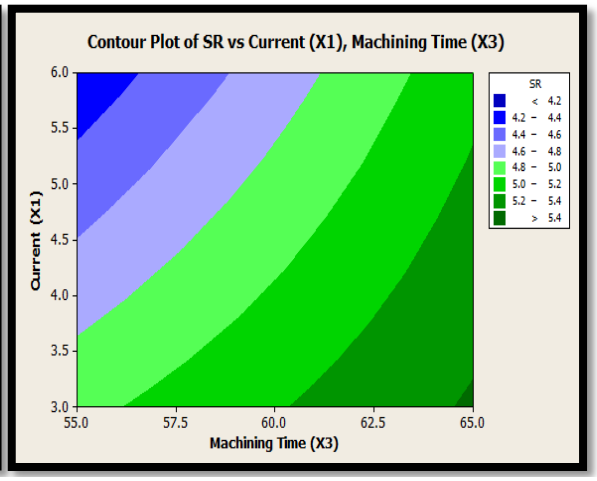
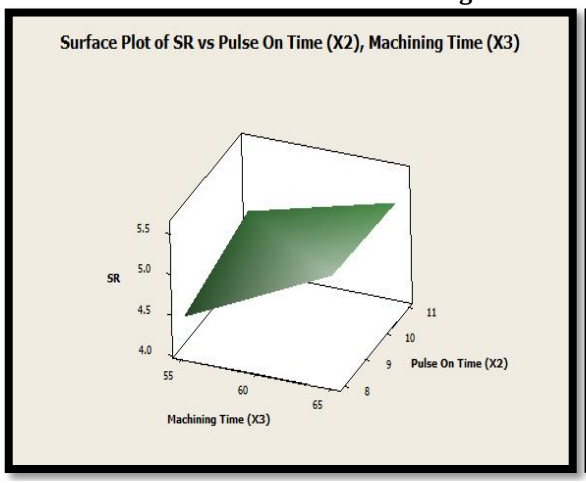


Figure 9: Surface Plot for SR vs X_1 vs X_3 **Figure 10: Contour Plot for SR vs X_1 vs X_3**

5.6 Effect of Pulse ON Time and Machining Time on SR:



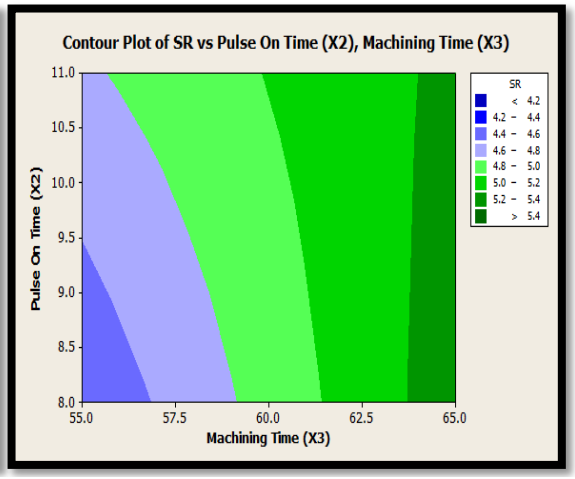


Figure 11: Surface Plot for SR vs X_2 vs X_3 **Figure 12: Contour Plot for SR vs X_2 vs X_3**

Figure 11 and 12 shows the predicted response for SR in relation to the process parameters of pulse ON time (X_2) and Machining Time (X_3) while other parameters remaining constant at their lowest value. It can be seen from the plots that SR increases significantly if pulse ON time and machining time both are kept at high values. As stated earlier, at high machining time high roughness is obtained, this phenomenon is enhanced by high values of the pulse ON time. This is due to high intensity sparks generated per cycle of pulse and for long duration of time.

Therefore, an optimum surface is generated when pulse ON time and machining time are low. This is due to the fact that sparks are generated with uniform frequency and of uniform intensity.

V. CONCLUSION

In this research work, regression analysis of process parameters of EDM machining process was carried out which determined the factors having maximum influence on the surface roughness [24]. A response model of these parameters was developed and found that current, pulse ON time and interaction term of pulse current with other parameters significantly affected the surface roughness. SR is directly proportional to linear effect of current and pulse ON time [25]. The machining of SS 202 workpiece was done with EN 31 electrode and the following conclusion was drawn from the conducted analysis:

1. It has been confirm that the regression technique can be successfully applied to model the input and output variable of electro discharge machining of SS 202 with EN 31.
2. Within the experimental scope, the SR value increases with the increase in the value of pulse-on time.
3. Surface roughness decreases with the increase in current at low values due to predominant increase in intensity of spark generated between tool and workpiece.
4. The proper selection of input parameters can help in achieving a specific output parameter (SR) and a higher efficiency can be determined by theoretical and experimental characteristic diagrams, especially the two dimensional surface and contour plots.

Finally, a research has been conducted to estimate the optimum machining conditions to achieve the best possible outcome of the response factor within the experimental constraints [26, 27]. This study can help automobile and manufacturing industries for developing a robust, reliable knowledge base and early prediction of surface roughness without actual experimenting with EDM process.

REFRENCES

[1]. M. K. Pradhan*, and C. K. Biswas, "Modeling and Analysis of process parameters on Surface Roughness in EDM of AISI D2 tool Steel by RSM Approach".

[2]. E. Weingärtner et al. / Procedia CIRP 2 (2012) 74 – 78

[3]. Z. Qinjian et al. / Procedia CIRP 6 (2013) 589 – 593.

[4]. D. Kanagarajan, K. Palanikumar, R. Karthikeyan, "Effect of Electrical Discharge Machining on strength and reliability of WC–30%Co composite", Materials and Design 39 (2012) 469–474.

[5]. R.Rajesha and M. DevAnandb, "The Optimization of the Electro-Discharge Machining Process Using Response Surface Methodology and Genetic Algorithms", Journal of Procedia Engineering 38 (2012) 3941 – 3950.

[6]. Shih Jing-Shiang, TzengYih-Fong, Yang Jin-Bin. "Study of the parameters in electrical discharge machining through response surface methodology approach".Applied Mathematical Modelling 33 (2009) 4397–4407.

[7]. Yan K. Kanlayasiri, S. Boonmungb. "Effects of wire-EDM machining variables on surface roughness of newly developed DC 53 die steel: Design of experiments and regression model.".Journal of Materials Processing Technology 192–193 (2007) 459–464.

[8]. T.M chenthijegan, M.Devanand and D.ravindran, "Determination of electro discharge machining parameter in AISI 202 stainless steel using grey relation analysis", Mater Procedia engineering 38(2012), 4005-4012.

[9]. S. Assarzadeh, M. Ghoreishi, "Statistical modeling and optimization of process parameters in electro-discharge machining of cobalt-bonded tungsten carbide composite (WC/6%Co)", Procedia CIRP 6 (2013), 463 – 468.

[10]. S.H.Tomadi, M.A.Hassan, Z. Hamedon, R.Daud, and A.G.Khalid, "Analysis of the Influence of EDM Parameters on Surface Quality, Material Removal Rate and Electrode Wear of Tungsten Carbide", Proceedings of the International MultiConference of Engineers and Computer Scientists 2009, Vol II IMECS, March 2009.

[11]. S. H. Lee and X. P. Li, "Study of the effect of machining parameters on the machining characteristics in electrical discharge machining of tungsten carbide", The National University of Singapore, 2009.

[12]. R. Snoeys, F. Staelens, and W. Dekeyser, "Current trends in nonconventional material removal processes," Ann. CIRP, vol. 35(2), p. 467 480, 1986.

[13]. H.S. Payal, R Choudhary and S Singh, "Analysis of electro discharge machined surfaces of EN-31 tool steel", Journal of Scientific & Industrial Research, Vol. 67, p. 1072-1077, 2008.

[14]. A Bhatia, S Kumar, and P Kumar, " A study to achieve minimum roughness in wire EDM" ,International conference on advances in manufacturing and materials engineering, Procedia material science 5 p. 2560-2566, 2014.

[15]. I. Puertas, C. J. Luis, and L. Alvarez, "Analysis of the influence of edm parameters on surface quality, mrr and ew of wc-co," Journal of Materials Processing Technology, vol. 153-154, no. 1-3, pp. 1026–1032, 2004.

[16]. G. Petropoulos, N. Vaxevanidis, and C. Pandazaras, "Modeling of surface finish in electro-discharge machining based upon statistical multi-parameter analysis," vol. 155-156, no. 1-3, p

[17]. Korzynski M., "Experiment methodology", WNT Warszawa, 2006.

[18]. Md. A R Khan, and M. M. Rahman, "Development of Regression Equation for Surface Finish and Analysis of Surface Integrity in EDM", International Journal of Mechanical, Aerospace, Industrial and Mechatronics Engineering Vol 7, No. 3, 2013.
[19]. SingaramLakshmanan, and M Kumar, "Optimization of EDM parameters using Response Surface Methodology for EN31 Tool Steel Machining", International Journal of Engineering Science and Innovative Technology (IJESIT), Volume 2, Issue 5, September 2013.
[20]. S. S. Baraskar, S. S. Banwait, and S. C. Laroiya, "Mathematical Modeling of Electrical Discharge Machining Process through Response Surface Methodology", International Journal of Scientific & Engineering Research, Volume 2, Issue 11, November-2011.
[21]. Mohd B. Ndaliman*, Ahsan A. Khan, and Zakaria M. Zain," Performance of PM Compacted Cu-TaC Electrodes during EDM",Kulliyyah of Engineering International Islamic University Malaysia, 2013.
[22]. Mohammed Yakub Ali, "Development in EDM process variables", International Islamic University Malaysia, 2013.
[23]. Aligiri E., Yeo S.H., and Tan P.C., "A new tool wear compensation method based on real-time estimation of material removal volume in micro-EDM", Journal of Materials Processing Technology 210, p. 2292–2303, 2010.
[24]. Uhlmann E, Roehner M., "Investigations on reduction of tool electrode wear in micro-EDM using novel electrode materials", CIRP Journal of Manufacturing Science and Technology 1, p. 92–96, 2008.
[25]. Uhlmann E., Piltz S., Röhner M., "Influence of Diamond Coatings on Electrode Wear in Mirco-EDM", Proceedings of the 7th Euspen International Conference – Bremen, 2007.
[26]. O. H. Erzurumlu, T., "Comparison of response surface model with neural network in determining the surface quality of moulded parts," Materials and Design, vol. 28, no. 2, pp. 459–465, 2007.
[27]. M. K. Pradhan, R. Das, and C. K. Biswas, "Comparisons of neural network models on surface roughness in electrical discharge machining," Proceedings of the Institution of Mechanical Engineers, Part B: Journal of Engineering Manufacture, vol. 223, p. (In Press), 2009.

ResearchGate

See discussions, stats, and author profiles for this publication at: http://www.researchgate.net/publication/281097857

INVESTIGATIONS ON EFFECT OF INCORPORATION OF PHOTOVOLTAIC SYSTEM WITH COMBINED CYCLE GAS TURBINEPLANT

ARTICLE · JULY 2014

READS
14

3 AUTHORS, INCLUDING:



B B Arora
Delhi Technological University
26 PUBLICATIONS **19** CITATIONS
SEE PROFILE



Jitendra Nath Rai
Delhi Technological University
30 PUBLICATIONS **4** CITATIONS
SEE PROFILE

All in-text references underlined in blue are linked to publications on ResearchGate, letting you access and read them immediately.

Available from: Jitendra Nath Rai
Retrieved on: 09 November 2015

INVESTIGATIONS ON EFFECT OF INCORPORATION OF PHOTOVOLTAIC SYSTEM WITH COMBINED CYCLE GAS TURBINEPLANT

Naimul Hasan[1] , B.B .Arora[2], J.N. Rai[3]

[1]Department of Electrical Engineering, Jamia Millia Islamia .New Delhi

[2]Department of Mechanical Engineering, Delhi Technological University,Delhi, India

[3] Research Scholar, Dept. Of Elec. Engg, Jamia Miliia Islamia, N.Delhi

ABSTRACT

India is witnessing a huge demand in power requirement. Economic development has led to development in Industries and demand for housing has increased. To meet this ever-rising power demand, efforts have been made to increase the efficiency at the generating end. One of such efforts is the CCGT plant in which the exhaust of Gas Turbine is used to run the Steam Turbine; hence giving an overall efficiency upto 60%. But, the recent trends in electrical engineering has been shifted to renewable forms of energy via solar, wind et,.keeping in mind the emphasis is on importance ofsustainable development. This paper is a preliminary study of how solar energy can be used through photovoltaic panels for the excitation of GT and auxiliary purposes in CCGT plant. The results of the same have been plotted and the future developments of this research have been discussed in detail.

Keywords: Solar, PV, CCGT, Power, Photovoltaic

I INTRODUCTION

In power systems, various methods are employed to overcome the ever-rising electricity demand. In India, most Power Plants are driven by fossil fuels. A Combined Cycle Gas Turbine Plant(Fig. 1)is one themeans so as to make the efficiency of a plant to reach the 60% mark.[1][4].

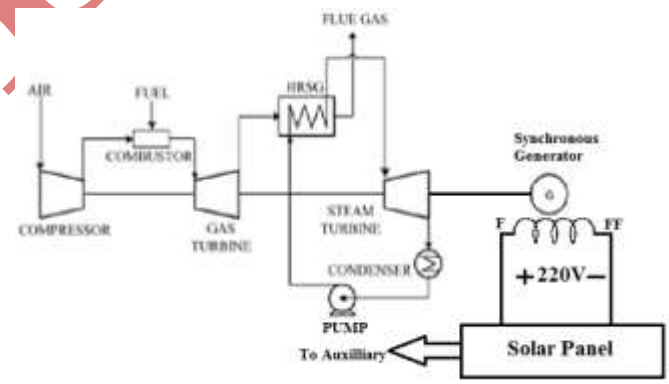


Fig 1. Combined Cycle Gas Turbine with Solar Panel

In a CCGT plant, the input temperature to a steam turbine is about 540°C and the exhaust can be maintained at the atmospheric pressure, due to design consideration the input temperature is limited and the efficiency of the about 45%. Theinput temperature of the gas turbine can be as high as 1100°C but the exhaust temperature can be lowered to about 550-650°C, the efficiency of a gas turbine is about 35%. It can be seen that to obtain higher efficiencies the exhaust of the gas turbine can used to drive the steam turbine giving efficiency up to 62%.The plant consists of a compressor, combustor, gas turbine, waste heat recovery boiler, steam turbine, and generator(s) associated with solar voltaic. [7][8]

Similarly, the emerging form of energy (Renewable Energy) is a socially and politically defined category of energy sources. Solar energy being one of them.Hence, we can employ solar panelswith the CCGT plant to make it less dependent on fossil fuels. The tariff for the consumers would also go down, since solar energy is at its peak in summer season, the time the electricity utilization is maximum in a year.

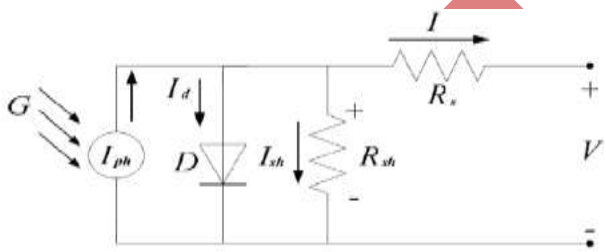


Fig 2. Equivalent Circuit of a PV cell

A simplest equivalent circuit(Fig. 2) of a solar cell is a current source in parallel with a diode. The output of the current source is directly proportional to the solar energy (photons) that hits on the solar cell (photocurrent I_{ph}). During darkness, the solar cell is not an active device; it works as a diode, i.e. a p-n junction. It produces neither a current nor a voltage. However, if it is allowed to connect to an external source (large voltage) it generates a current *Id*, called diode (D) current or dark current. [15]

Hence the combination of solar energy with CCGT plant could make a possible difference.

II THEORETICAL BACKGROUND

Equations which define the model of a CCGT Plant:The airflow (W) in the gas turbine is given as

$$W = W_a \frac{P_a}{P_{ao}} \frac{T_{io}}{T_i} \qquad (1)$$

Where Ti is ambient temperature and P_a denotes the atmospheric pressure.

$$\eta_{cc} = \eta_{gt} + \eta_{st}(1 - \eta_{gt}) \qquad (2)$$

The Where η_{cc} is the efficiency of the combined cycle, η_{gt} is the efficiency of Gas Turbine and η_{st} is the efficiency of Steam Turbine.thermal efficiency of the simple gas turbine cycle is given as [6]

$$\eta = \frac{(1 - \frac{1}{p_p})(a - p_p)}{\eta_c(k_1 - 1) - p_p + 1} \qquad (3)$$

Where, $a = \eta_c \eta_t k_1$ [10][11][12]Equations which define the model of a PV cell:

$$V_t = \frac{kT_{op}}{q} \quad (4)$$

$$V_{oc} = V_t \ln\left(\frac{I_{ph}}{I_S}\right) \quad (5)$$

$$I_d = \left[e^{\frac{(V+IR_s)}{(nV_tCN_s)}} - 1\right] I_s N_p \quad (6)$$

$$I_S = I_{rs}\left(\frac{T_{op}}{T_{ref}}\right)^3 e^{\left[\frac{qE_g}{nk}\left(\frac{1}{T_{op}} - \frac{1}{T_{ref}}\right)\right]} \quad (7)$$

$$I_{rs} = \frac{I_{sc}}{\left[e^{\left(\frac{V_{oc}q}{kCT_{op}n}\right)} - 1\right]} \quad (8)$$

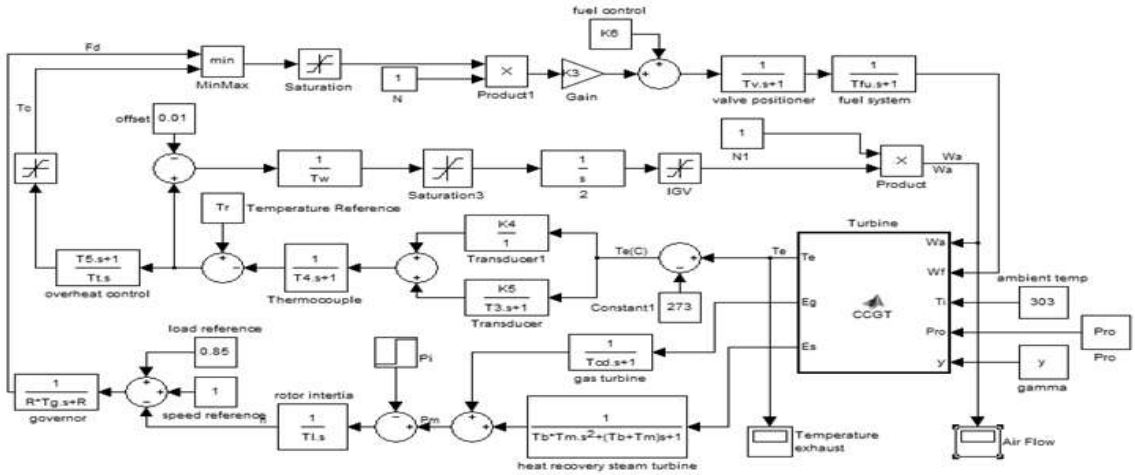


Fig 3. CCGT Simulink Model

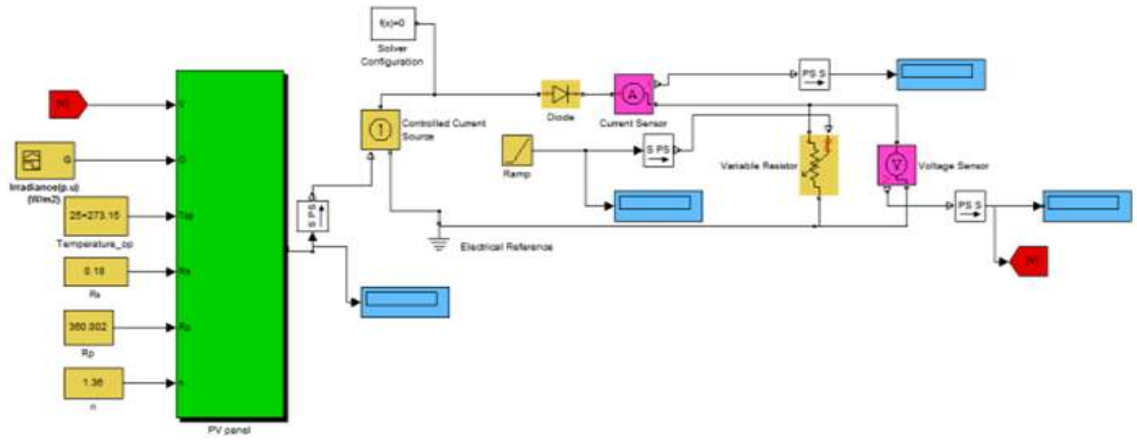


Fig 4. Simulink Model of Photovoltaic Panel

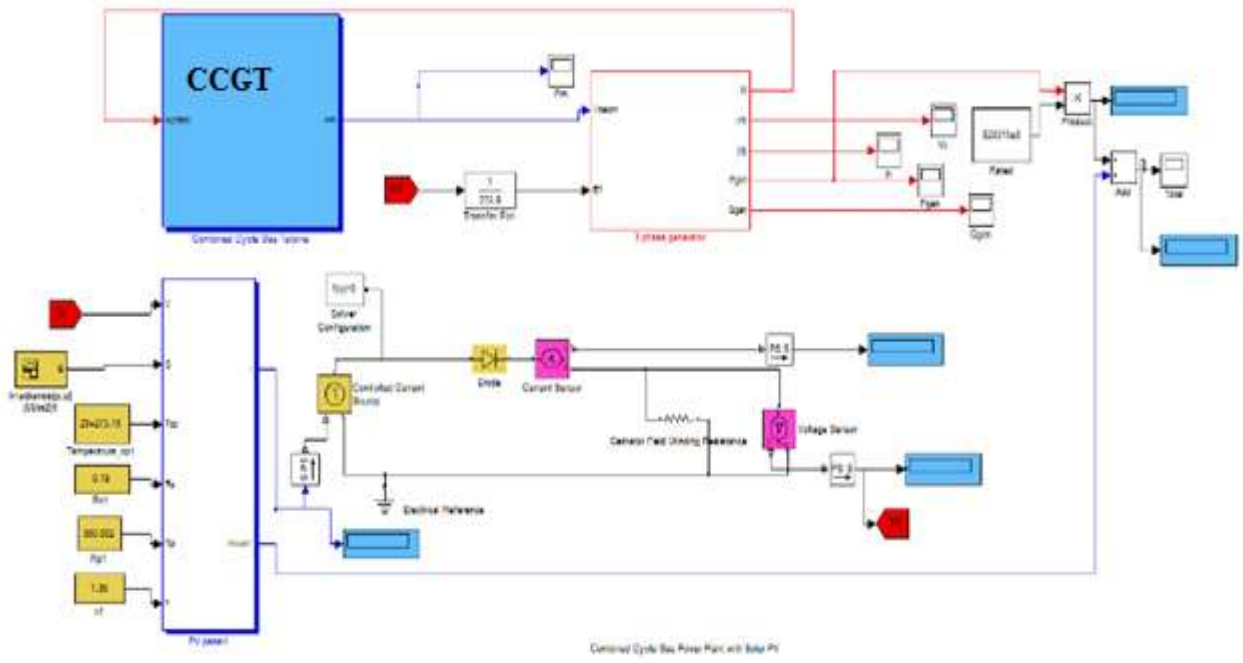


Fig 5. Simulink Model of Integrated Photovoltaic in CCGT

$$I_{sh} = \frac{V + IR_s}{R_p} \quad (9)$$

$$I_{ph} = G_k \left[I_{sc} + K_I (T_{op} - T_{ref}) \right] \quad (10)$$

$$I = I_{ph} N_p - I_d - I_{sh} \quad (11)$$

where, G_k is solar insolation in W/m^2,

T_{ref} is reference temperature(298 K),

T_{op} is operating temperature of cell,

R_s is series resistance,

R_{sh} is shunt resistance,

k is Boltzmann constant,K is temperature coefficient,

N is data points used,

n is diode emission factor,

I_{ph} is photon current & I_d is dark current,

I_{sh} is short circuit current at reference state.

III DESCRIPTION OF SIMULINK MODEL AND RESULTS

The CCGT model (J. N. Rai. et.al. 2013)consists of various blocksdescribing various parameters whose variations have already been studied in order to optimize the performance of combined cycle. There are blocks related with speed/load, temperature control, fuel control, air control and other blocks for gas turbine, waste heat

recovery boiler/steam turbine, rotor shaft, and temperature transducer. All the parameters used in the model are given in Table I& II. [2] [3][5]

A circuit based simulation model for a PV cell for estimating the IV characteristic (temperature and irradiance) and cell parameters (parasitic resistance and idealty factor)has been discussed. The simulation model is used for analysing the behaviour of PV Panel by varying various parameters of the cell in accordance with the given equations. Using a Shockley diode equationan accurate *simulink* PV panel model was developed.The model is based on the equivalent diagram of the solar panel described in the theoretical background. [12] [13] [14]

Further with above Simulink model the response of CCGT. has been investigated which shows the variation of current with respect to the timeFigure 6.

Figure. 7 shows the Variation of Generated Electrical Power. It depicts the variation is almost constant. The output is stable. It can also be seen that the generator output falls which is also controllable with reactive power control as shown in Figure.8.

Further the effect of varying input condition of CCGT as Variation of CCGT parameter i.e Exhaust Temperature of Gas Turbine (^{o}C), Air Flow (p.u.) and Fuel Flow (p.u) (Figure. 9) has been investigated.

Turbine Output (input of generator) is constant for a while (Figure 10). As the system is uncontrollable, the output falls which can be brought to the near to its rated value by controlling the CCGT parameters. The Field Excitation for synchronous generator is accompanied with solar voltaic which shows the positive impact on the performance. It can also be seen that now the start-up time is higher than the normal plant model (J. N. Rai et.al. 2013) with increased power output.

IV CONCLUSION

The parameters considered above cannot be varied simultaneously due to complexity of system. Some parameters are located and the other parameters will be the function of critical parameters in one way or the other. Interrelations amongst the various parameters are balanced by superimposing some constraints on the parameters.The level of benefits achieved as a result of system optimization has included the following:

- Increased output-3 to 5%
- Reduced fuel consumption-3 to 5%
- Reduced power consumption-3 to 5%

Both, the CCGT and PV panel models are combined. PV panel is used to give the excitation to the CCGT Plant Generator and also the remaining energy developed can be used for driving the auxiliaries in the Plant. Since the solar output is DC itself, the conversion losses from AC to DC as was the earlier case in CCGT plant have been taken care of. Start-up Time would be high as compared to Normal Combined Cycle Gas Power Plant.

This paper provides a path for further research work in future by integrating solar plant to increase the clean energy generation and to enhance the existing plant capacity in India.

IJEE

Table 1 : System Parameters

Symbol	Description	Value
T_i	Compressor inlet temperature	$30\,^{\circ}C$
T_{do}	Compressor discharge temperature	$390\,^{\circ}C$
T_{fo}	Gas turbine inlet temperature	$1085\,^{\circ}C$
T_{eo}	Gas turbine exhaust temperature	$535\,^{\circ}C$
P_{ro}	Compressor pressure ratio	11.5
γ	Ratio of specific heat	1.4
η_c	Compressor efficiency	0.85
η_t	Turbine efficiency	0.85
R	Speed Regulation	0.04
T_t	Temperature control integration rate	0.469
$T_{c\max}$	Temperature control upper limit	1.1
$T_{c\min}$	Temperature control lower limit	0
$F_{d\max}$	Fuel control upper limit	1.5
$F_{d\min}$	Fuel control lower limit	0
T_v	Valve positioner time constant	0.05
T_{fu}	Fuel system time constant	0.4
T_w	Air control time constant	0.4669
T_{cd}	Compressor volume time constant	0.2
K_0	Gas turbine output coefficient	0.0033
K_1	Steam turbine output coefficient	0.00043
T_g	Governor time constant	0.05
K_4	Gain of radiation shield	0.8
K_5	Gain of radiation shield	0.2
T_3	Radiation shield time constant	15
T_4	Thermocouple time constant	2.5
T_5	Temperature control time constant	3.3
K_3	Ratio of fuel adjustment	0.77
K_6	Fuel valve lower limit	0.23
T_m	Tube metal heat capacitance time constant of waste heat recovery boiler	5
T_b	Boiler storage time constant of waste heat recovery boiler	20
T_i	Turbine rotor time constant	18.5

IJEEE

Table II. Parameters of Three-Phase Synchronous Machine

Symbol	Description	Value
Fr	Rated Frequency	50
Poles	Number of poles of the generator	4
Pf	Rated Power Factor	0.9
V_R	Rated Voltage	11Kv
Pr	Rated output Power in Watt	82.831Mw
Rs	Synchronous Resistance	0.0048
X_d	Direct-Axis Reactance	1.790
Xq	Quadrature-Axis Reactance	1.660
X_{ls}	Leakage Reactance	0.215
H	Interia Constant	3.77
K_A	Gain Constant	50
T_A	Amplifier Time Constant	.06
V_{Rmax}	Maximum Voltage	1
V_{Rmin}	Minimum Voltage	-1
T_E	Exciter Time Constant	0.052
K_E	Exciter Gain	-0.0465
T_F	Field Time Constant	1.0
K_F	Field Gain	0.0832

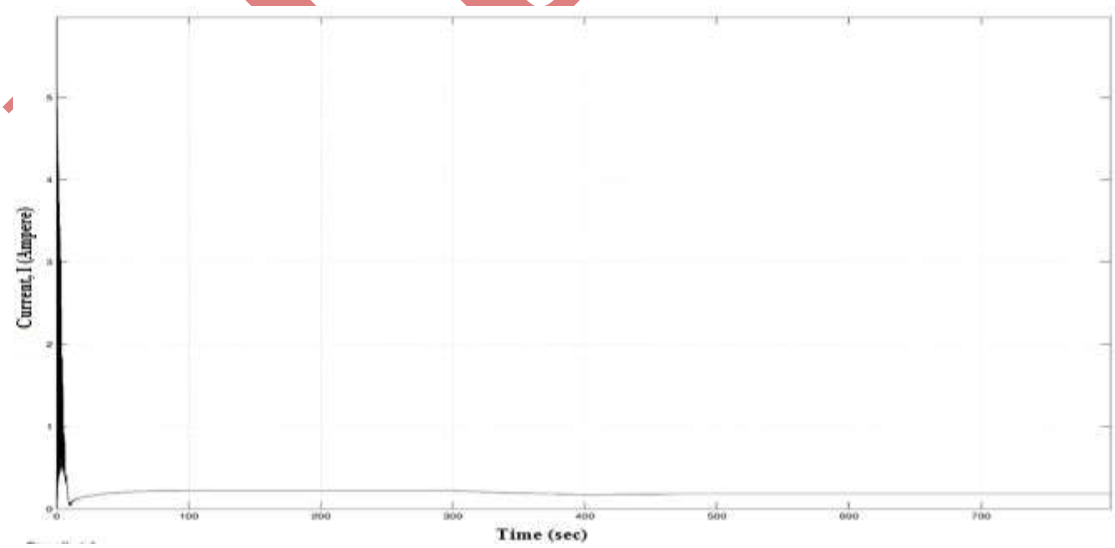


Fig 6. Variation of Current with Time

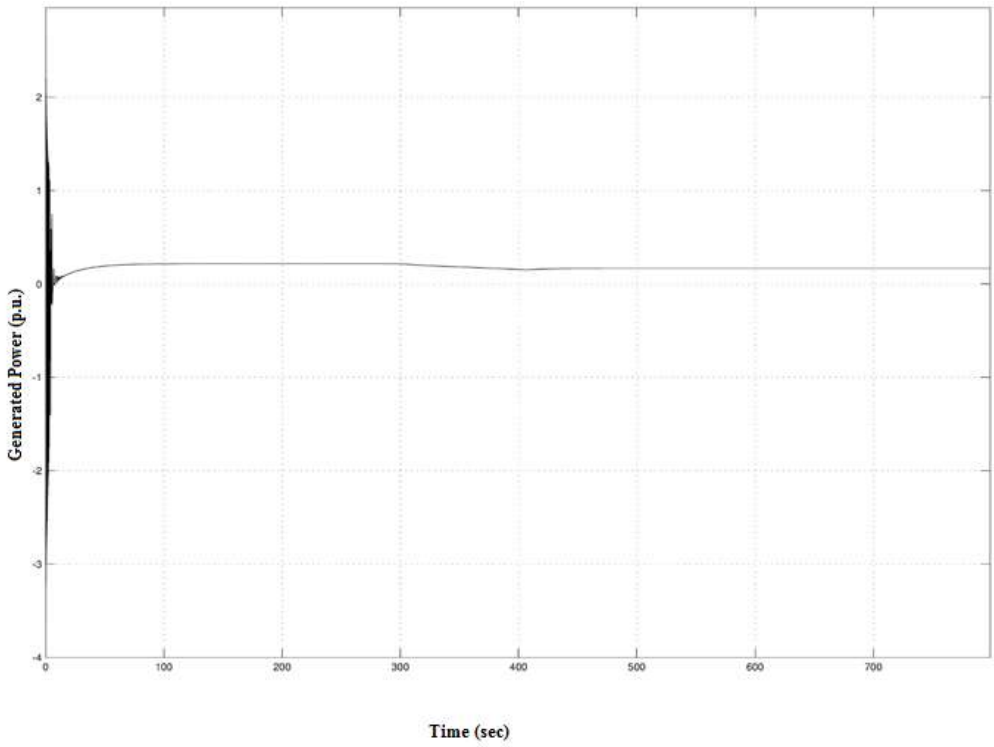


Fig 7. Variation of Generated Power with Time

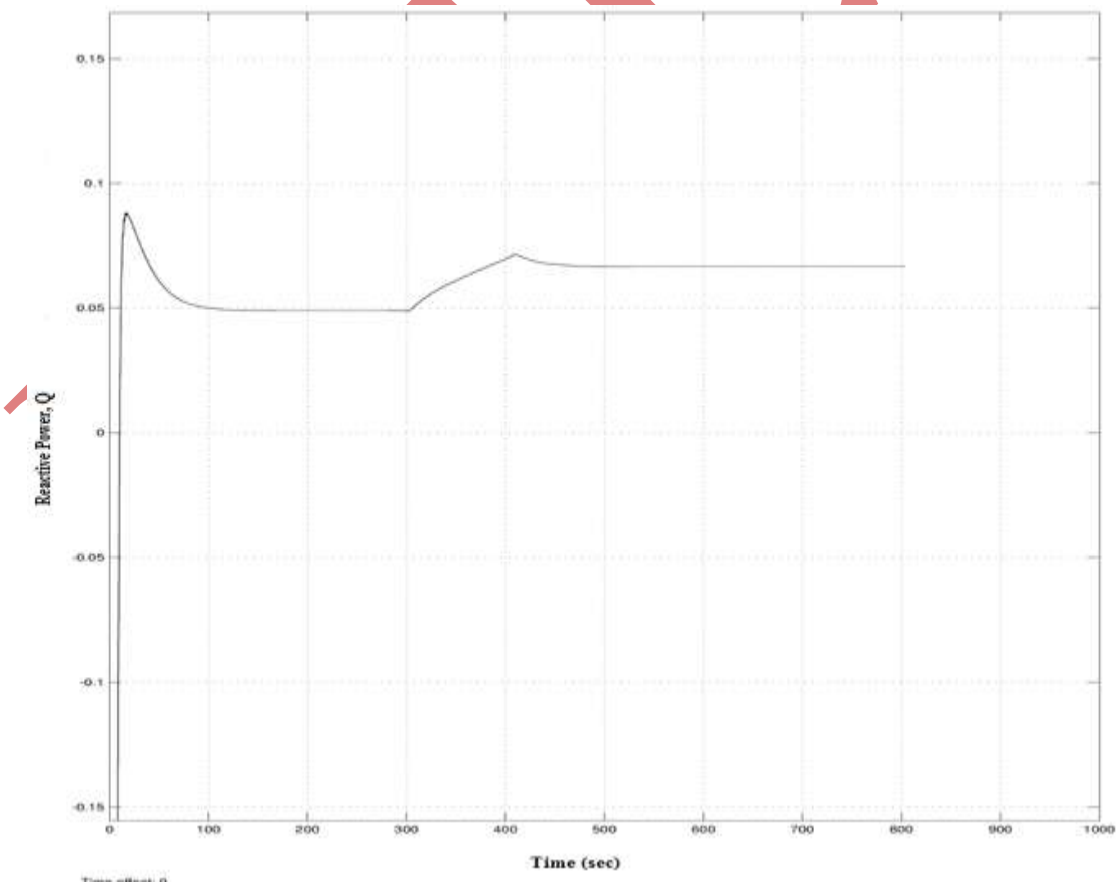


Fig 8. Variation of Reactive Power with Time

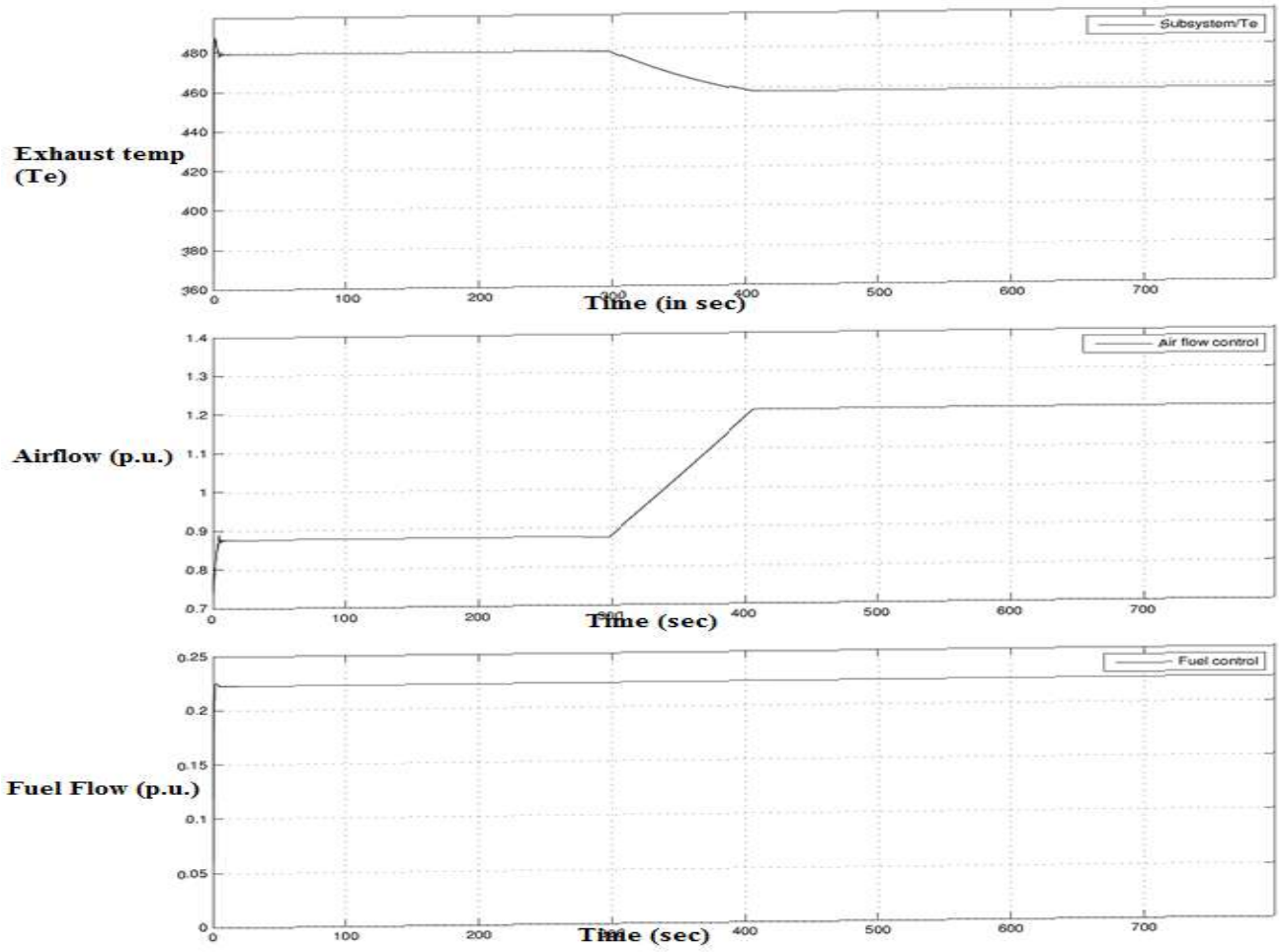


Fig 9. Variation of various System parameters with time

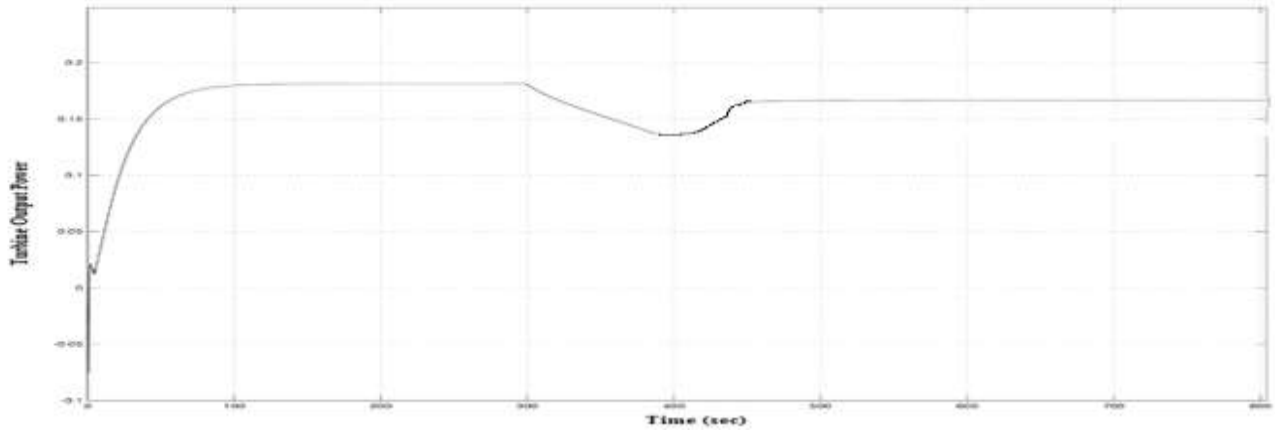


Fig 10. Variation of Turbine Output Power with Time

REFERENCES

[1]N. Kakimoto, K. Baba, , "Performance of gas turbine-based plants during frequency drops," IEEE Transactions on Power Systems,vol.18, pp. 1110- 1115, Aug. 2003.

[2]S. Al-Zubaidy, F.S. Bhinder, "Towards optimizing the efficiency of electrical power generation," Energy Conversion Engineering Conference, vol.3, pp. 1857-1862, Aug. 1996.

[3]K. Kunitomi, A. Kurita, H. Okamoto, Y. Tada, S. Ihara, P. Pourbeik, W. W. Price, A. B. Leirbukt, and J. J. Sanchez-Gasca, "Modeling frequency dependency of gas turbine output," Proc. IEEE/Power Eng. Soc. Winter Meeting, Jan. 2001.

[4]W. I. Rowen, "Simplified mathematical representations of heavy-duty gas turbines," Trans. Amer. Soc. Mech. Eng., vol. 105, pp. 865–869, Oct. 1983.

[5]F. P. de Mello and D. J. Ahner, "Dynamic models for combined cycle plants in power system studies," IEEE Trans. Power Syst., vol. 9, pp. 1698–1708, Aug. 1994.

[6]John H Horlock, "Advanced gas turbine cycles," Pergamon Press, 2003.

[7]Rolf Kehlhofer, Rukes Bert, Hannemann Frank, and Stirnimann Franz. "Combined-cycle gas & steam turbine power plants," PennWell, 2009.

[8]F. Drbal Lawrence, G. Boston Patricia, L. Westra Kayla, Black& Veatch. Power Plant Engineering. p. 241 Springer. 1996.

[9]Rai, J. N., Hasan, N., Arora, B. B., Garai, R., Gupta, R. K., & Kapoor, R. (2013). "Study the Effect of Temperature Control on the Performance of the Output of Combined Cycle Gas Turbine". International Journal of Theoretical and Applied Mechanics, 8(1), 15-23.

[10]J. N. Rai, NaimulHasan, B. B. Arora, Rajesh Garai, Rahul Kapoor, Ibraheem(2013) "Performance Analysis of CCGT Power Plant using MATLAB/Simulink Based Simulation" International Journal of Advancements in Research & Technology, Vol. 2(5), pp. 285-290

[11]Mantzaris, J., &Vournas, C. (2007). Modelling and Stability of a Single-Shaft Combined Cycle Power Plant. International Journal of Thermodynamics, 10(2).

[12]Patel, H., & Agarwal, V. (2008). MATLAB-based modeling to study the effects of partial shading on PV array characteristics. Energy Conversion, IEEE Transactions on, 23(1), 302-310.

[13]González-Longatt, F. M. (2005). Model of photovoltaic module in Matlab. II CIBELEC, 2005, 1-5.

[14]Tsai, H. L., Tu, C. S., & Su, Y. J. (2008, October). Development of generalized photovoltaic model using MATLAB/SIMULINK. In Proceedings of the world congress on Engineering and computer science (Vol. 2008, pp. 1-6).

[15]Rahim, N. A., Saidur, R., Solangi, K. H., Othman, M., & Amin, N. (2012). Survey of grid-connected photovoltaic inverters and related systems. Clean Technologies and Environmental Policy, 14(4), 521-533.

IJEEE

DOI : 10.18843/rwjasc/v6i4/03
DOI URL : http://dx.doi.org/10.18843/rwjasc/v6i4/03

INVESTMENT BEHAVIOR OF ENGINEERS: AN EMPIRICAL STUDY

Priya Kansal,
Research Scholar
Delhi Technological University, India.

Dr. Seema Singh,
Head of the Department
Department of Humanities
Delhi Technological University, India.

ABSTRACT

The study investigated the behavioral biases of individual investors and their impact on the investment behavior in context of Indian Stock Market. A structured questionnaire were developed and distributed among 196 individual investors who are engineering graduate. The respondents are selected based on convenience sampling. Multi-criteria technique of AHP is used to define the relative contribution of each of the behavioral bias in shaping the investor behavior. Most of the investors over-rate their loss aversion tendency and are found to have fear of loss. Herd behavior among the investors is also observed and they are found to follow the advice of their advisor, relative and friend while buying and selling the in familiar stocks. Results revealed that behavioral biases significantly influence investment behavior that may lead them towards less than optimal investments.

Keywords: Investment Behavior, Behavioral biases, AHP, Loss Aversion, Herding, Mental Accounting.

INTRODUCTION:

Traditional models of finance assume that the investors are totally rational. They take their investment decision to maximize their expected utilities. Efficient Market Hypothesis, proposed by Eugene Fama (1970) suggests that all the markets are fully efficient. In efficient markets investors demonstrate the self-control on their decisions. They react on each and every piece of information and that to rationally. There is no role of emotions feelings and other behavioral factors. But this assumption no longer works as the number of researchers have found the evidence that the emotional and behavioral factors also play an important role in investment decision making. And, that the investors not always react as rational creature when comes to investment as the feeling of loss, winner's pride, mental accounting, framing of investments, herding etc also effect the decision making.

Behavioral Finance is an emerging field which deals with the irrational nature of investors. Efficient Market Hypotheses suggest that all the market information are immediately incorporated in security prices and that security prices are the best estimated and accurate prices all the time. But Behavioral Finance denies this assumption and suggest that there are number of evidence such as January Effect, Weekend effect, Seasonality etc. through which it has proved that markets are not efficient all the time and investors often travel from rationality to irrationality in perhaps a predictable manner. To some extent, our emotions, feelings and perceptions influence the investment decisions and these are known as mental biases. Behavior finance makes an attempt to study the irrational behavior of investors in the market based on the said mental bias. It also explains the factors responsible for such behavior. The established finance seeks to understand stock markets using models in which investors are "rational". Rationality for that purpose means when investors receive new information, they update their viewpoint on any financial action efficiently. This traditional framework is theoretically simple, but **Shiller (2000)** advocates that stock market are strongly governed by the market information, which directly influence the investment behavior of the investor. It can be concluded that individual trading behavior cannot be understood in established traditional finance structure. **Clark (1918)** rightly mentioned that the economist may attempt to ignore psychology, but it is sheer impossibility for him to ignore human nature. Emergence of the concept of Behavioral finance in 1980s was the response to the anomalies detected in the standard finance models which are blamed for the lack of realism in the assumptions on human behavior. It examines financial phenomenon of investment through the dual lenses of finance and of psychology. In behavioral finance, all stock market anomalies are explained by psychological theories. **Lintner (1998)** defines behavioral finance as being "the study of how humans interpret and act on information to make informed investment decisions". **Olsen (1996)** asserts that this field of psychological finance tries to understand the complexity of standard finance through of psychological decision making process of market. It may be argued here that some stock market phenomenon can be better understood using such models in which some investors are not fully rational. Behavioral finance is expected to look into the following possible behavioral patterns in financial markets:

- Reaction of an investor to a price change
- Reaction of an investor to a news
- Extrapolation of past trends into the future
- Focus on some popular stocks and lack of attention to fundamentals
- Seasonal price cycles etc.

On theoretical level, if exploitable pricing anomalies exist in the market, the credibility of the Efficient Market Hypothesis (proposed by Fama, 1970) is diluted. When new information is quickly reflected into the price, market is known to be efficient. According to Efficient Market Hypothesis, the current market price reflects all available information and the current market price in any market could be the true estimate of the value of the security.

The theories of behavioral finance are not denying the established theories rather these are making them more realistic by examining their relaxed behavioral assumptions. Behavioral finance does this by adding the aspect of individual investment patterns in financial markets. Without this contributions the anomalies exist in financial markets cannot be explained.

BACKGROUND OF THE STUDY:

Individual investment pattern is influenced by number of demographic and socioeconomic factors. For example the age of investor plays a key role in the process of decision making. With the sample of more than 75000 US investors, Korniotis and Kumar (2008) in their study concluded that although with the age trading experience and knowledge increases due to positive effect of learning but declines with age due to the adverse effects of cognitive aging. This is usually thought that small investors are more prone to behavioral biases than professionals, who are better trained (Malmendier and Shanthikumar, 2004). Yet some empirical work suggests that professionals exhibit some behavioral biases to a greater extent than non-professionals (Haigh and List, 2005). Family size, marital status, numbers of children impact the asset allocation and stock market participation (Love, 2010). The present study investigates the effect of these factors on the mental biases of engineers. Specially engineers are taken because engineers are supposed to be more inclined towards the rationalistic thoughts and therefore may have more logistic decision making power. They may tend to believe that the world is more deterministic than it is and this gives them more confidence in statistics. Engineers are supposed to be more hostile to the idea that emotions have utility in the workplace, believing instead that this profession must be based on logic, reason, inference, deduction and the hard cold facts of observable reality (Bessler et al., 2010). Except this, engineers now a separate group of professionals in the society. The number of engineering graduates is increasing every year. As per UGC Reports of different years, the ratio of total graduates awarded an engineering degree is now 17% compared to 5% in 2001-02. Engineering is a degree which proves to be most employable without the requirement of higher education or the postgraduate. This is the only decision of the engineers what to opt as a career after getting engineering degree. This research attempts to identify the determinants of investment behavior of individual investors (who possess engineering degree) and their relative importance in investment behavior. The impact of investment behavior on investment decision would also be covered. In our study investor behavior would be studied in terms of nine biases which are anchoring, cognitive dissonance, herding, loss aversion, mental accounting, overconfidence, optimism, regret, self-attribution. We would identify the relative importance of each bias in shaping investment behavior.

LITERATURE REVIEW:

Oslen (1998) suggested behavioral finance is a new dimension of finance theory, which seeks to understand and predict standard financial market implications of psychological decision-making. Behavioral finance is not the replacement of modern finance but it seeks to supplement them by explaining the irrationality and anomalies exist in the financial markets. Behavioral finance exerts that by understanding the psychological mechanism of decision making, the modern and standard finance models may be extended to better understand and reflect the true picture in today's evolving markets.
Since the role of emotions and psychology has been considered relevant in investment, number of economists, psychologists, investment professionals have worked upon on this topic. The literature review is divided in two sections. First section deals with the journey from the rational thoughts to the irrational thoughts with the introduction of Behavioral Finance. Second section deals with the patterns of irrational behaviors and discusses the biases found in rational behavior.

Depart from rationality to irrationality:

According to Eugene Fama (1970) "Efficient market hypothesis states that financial prices incorporate all available information and prices can be regarded as optimal estimates of true investment value at all times". This hypothesis is based on the assumption that investors behave rationally, always try to maximize expected utility and consider all available information (Shiller, 1997). Traditional theories are based on the preposition of Efficient Market Hypothesis. However, common investors tend to be irrational as they are many of times mislead by their moods, emotions and beliefs. According to Simon (1956) people have limited capacity of processing information in solving complex problems. Moreover, "people have limitations in their attention capabilities and they do take into account social considerations (e.g. by deciding not to invest in tobacco companies)", (Kahneman, 1973). Kahneman and Tversky, (1973, 1979) pointed out that, "people fail to update beliefs correctly and have preferences that differ from rational agents". In addition, "rational traders are bounded in their possibilities such that markets will not always correct non-rational behavior", (Barberis and Thaler, 2003). Hence, traditional theories

may give an unreal and deceptive description of financial behavior. Theories based on the prepositions of modern finance do not match with the current global financial scenario.

Behavioral finance introduces the behavioral aspects and focuses on the application of psychological and economic principles for the improvement of individual investment decision-making process. In his book titled "Beyond Greed and Fear", Shefrin (2000) states that people are "imperfect processors" of information and are usually biased, commit mistakes and have perceptual problems.

***Understanding investment patterns and behavioral biases**:*

The study of investment psychology provides confirmation of a variety of psychological effects that help better understand the behavior of investors in context of stock markets. Individual investors appear to invest in a manner that is inconsistent with the standard finance. Specifically, they are undiversified (Benartzi and Thaler (2001); Bhatnagar (2012)), loss averse (Kahneman and Tversky, 1979), overconfident (Gervais and Odean, 2001; Barber and Odean, 2001), prone to over reaction (DeBondt and Thaler, 1985, 1987), and shows mental accounting (Tversky and Kahneman, 1981). Barber and Odean (2000) concluded investors are reluctant to realize the losses and show hurry in selling their profitable stocks. Grinblatt and Keloharju (2000) also confirm the findings of Barber and Odean (2000) and also documented that investors have tendency to stick on a reference. Hirshleifer and Shumway (2003) find that moods of investors at the time of trading, also influenced by cloud cover or number of hours of daylight .According to Kahneman, 1973 "People are limited in their capacity for processing information, since they possess a limited working memory and limited computational capabilities and are limited in their attention capacity and hence ability to perform multiple tasks simultaneously",. Similarly, Miller (1956) states that investor can process only seven piece of information at a time. People generally adopt simplifying rules-of-thumb, or heuristics, to deal with the complexity of investment decisions which may result in behavior that is not fully rational (Gabaix and Laibson, 2000). Similarly, people also have the tendency to follow the judgment and behavior of others while making an investment decision (Asch, 1956) and this herding behavior cause the endogenous fluctuations (bubbles and crashes) in financial markets (Topol, 1991). Shiller (1990) has documented the importance of the role of conversation in diffusion of admired ideas in context of financial markets. Shiller and Pound (1989) surveyed individual investors and observed that most of the investors are influenced by interpersonal communication while investing in a particular stock. Further, many studies, for example, Tversky and Kahneman (1971, 1974), DeBondt and Thaler (1985), Barberis, Shleifer and Vishny (1998), Odean (1998, 1999) find that individuals judge the event on the basis of hoe they have recently occurred and not on the basis of all past statistics also. Also, if people are taking steps to averse losses in the stock market, then it is very important to study regret aversion (Bell, 1982). The phenomena of "mental accounting" (Thaler, 1980, 1999) which explains that the people tend to take decisions in a narrow fashion instead of taking into consideration a broader frame, (Tversky and Kahneman, 1981, and Kahneman and Lovallo, 1993). Mental accounting is a tendency of investors when they put different types of gambles into separate mental accounts by ignoring the likely connection between the accounts and make use of simple "prospect theoretic decisions rules" to each account separately. Such mental accounts are mostly isolated on the basis of content and time (Goldberg, von Nitsch, 2001). North Craft and Neale (1987) have disclosed that when the agents were told to estimate the price of property, where they were pre provided by the proposed list of prices, one group was provided with lower price list as compared to the other group. The influence of Anchoring Bias could be very clearly seen in the results as the group provided with higher price list, estimated the property at a higher price. Cognitive Dissonance is the feeling of discomfort felt by investors, if they come across with some idea, which is against their view point. James Montier (2002), the author of Book "Insights into Irrational Minds and Markets", elaborates the Conservatism Bias, because of which investors tend to cling to the forecasts they have made and they find it difficult to move away from that forecast. Gervais and Odean (2001) discussed Self Attribution Bias in their paper "Learning to be overconfident", in which they have discussed that traders in stock market also show the susceptibility of self-enhancing bias which finally leads to Overconfident Bias.

OBJECTIVE:

Following are the major objectives of the study:

- To study the investment behavior of individual.

- To identify the biases reflect in the investment behavior of engineers.
- To study the relative importance of each biases in shaping investment behavior.

RESEARCH METHODOLOGY:

For the purpose of study, we have used primary data. A structured questionnaire with 29 predefined variables of 9 construct (biases) is used to collect the data. The questionnaire has been circulated to those individuals who invest in equity market and resides in Delhi NCR. Total sample size is 196.
Analytical Hierarchical Process (AHP) proposed by Tomas L. Saaty (2008) is used to identify the relative importance of each bias in shaping investment behavior. Along with AHP, regression analysis is used to study the contribution of each bias in shaping investment behavior.

FINDINGS AND ANALYSIS:

Biases of Individual Investment Behavior:

The literature review helped us to identify 9 biases which influenced the investment behavior. These biases are loss aversion, herding, mental accounting, cognitive dissonance, overconfidence, anchoring, regret aversion, optimism and self-attribution. They are divided into different subfactor. AHP, with the help of pair wise comparison of the investors' responses, defined priorities for the behavioral dimensions in terms of their relative contribution in the formation of investor behavior. AHP determined loss aversion as the most important bias among all followed by mental accounting, herding, cognitive dissonance and over confidence (Figure:1) The most important factor which shows that investors are loss averse is the tendency of the investors to immediately realize their gains to avoid the losses. Also, investors are reluctant to realize the losses. They hold the securities if they are incurring the loss on them. The have fear of loss and that's why they hold their investments in volatile stock market environment. These all factors lead them to be loss averse which shapes their investment behavior. Second most important bias that shapes the investment behavior is herding in term of the tendency of investors to follow the opinion of advisors, friend and relative in both buying and selling the stocks which are not familiar to them. After herding, the bias which comes third in priority is mental accounting which suggests that investors generally use the funds in the stock market that they earn from the stock market only.

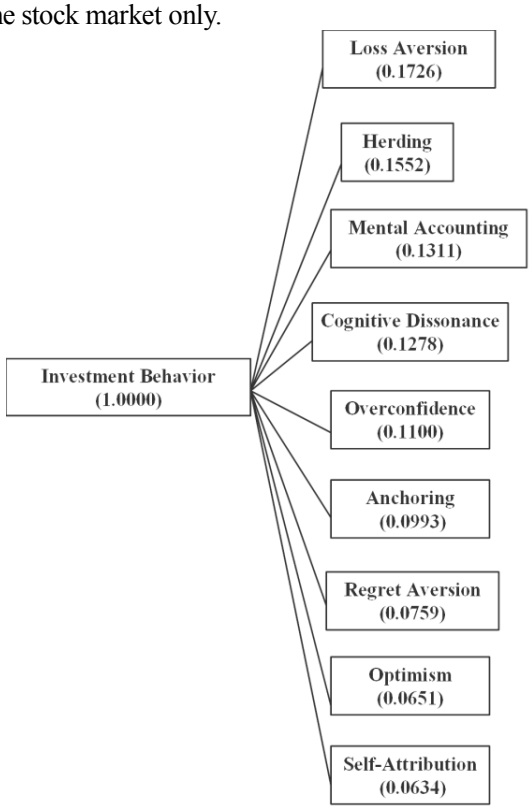


Figure :1 Biases of Individual Investment behavior and their relative weights according to AHP

The cognitive dissonance is at fourth place as suggested by AHP which suggest that investors usually do not remain with their portfolio when they think that they have mistaken in portfolio construction. Overconfidence gets fifth ranking in investment decision making as investor are confident enough in their stock picking abilities. The next bias which contributes in decision making process is anchoring in terms of the investor's tendency to fix the last lowest price to buying price and the last highest price to selling price. The behavioral bias regret aversion is at seventh rank, depicting that investors regret their decisions when the prices of the securities which they bought immediately go down. Optimism is at eighth rank. Findings reveal that investors usually buy the stocks which are rising with the expectation of further price rise. The last bias which is important in shaping investment behavior is self - attribution which is the tendency of investors to attribute themselves for their successes and attribute the bad luck or others for their losses.

IMPACT OF BEHAVIORAL BIASES ON INVESTMENT BEHAVIOR:

Regression analysis helped to identify the impact of behavioral biases on overall investment behavior. It reveals that which bias affects the most the investment behavior. Findings are summarized in Table:1

Table 1: Results of Regression Analysis : Impact of behavioral biases on investment behavior

Independent Variable	Coefficient	Std. Error	t-statistics	sig
Anchoring	0.196	0.156	0.318	0.004*
Cognitive Dissonance	0.218	0.161	3.206	0.001*
Herding	0.283	0.157	0.986	0.008*
Loss Aversion	0.356	0.112	1.508	0.000*
Mental Accounting	0.267	0.16	0.401	0.018*
Overconfidence	0.214	0.157	1.367	0.014*
Optimism	0.168	0.157	2.131	0.003*
Regret Aversion	0.173	0.156	1.775	0.006*
Self - Attribution	0.163	0.153	1.976	0.003*
	R-square	0.298	**F-Statistics**	2.148
	Durbin Watson	1.865	**Probability**	0.015

*significant at 5%

Findings of Regression analysis revealed that investment behavior is significantly affected by all the broad behavioral biases. All the biases, anchoring, cognitive dissonance, herding, loss aversion, mental accounting, overconfidence, optimism, regret aversion and self attribution have significant impact on investment behavior (p value is less than 0.05 for all), that supports the argument made earlier that behavioral biases has an impact on investment behavior. Moreover, R- square value of 29.8 % also suggest that behavioral biases cast high impact on overall investment behavior.

CONCLUSION:

The study investigated the behavioral biases of individual investors and their impact on the overall investment behavior in context of Indian Stock Market. The empirical findings from the analysis propose that individual investors tend to be irrational somehow when considered from a standard finance perspective. Results revealed that investor behavioral traits and biases significantly influence the investment decision making process. The investors are found to have high level of loss aversion and herding, mental accounting, cognitive dissonance and overconfidence while they are not much anchored, regret averse, optimistic and self –attributed. But these biases also have a significant impact on overall investment behavior. The bottom line is that individual investors do not behave in accordance with the tenets of standard finance theory and behavioral biases lead them to take investment decisions that may be less than optimal.

REFERENCES:

[1] Asch, S. (1956). Studies of independence and conformity: A minority of one against a unanimous majority. *Psychological Monographs*. 70.

[2] Barber, B. and Odean, T. (2001). Boys Will be Boys: Gender, Overconfidence and Common Stock Investment. *Quarterly Journal of Economics.* Vol. 116(1), 261-292.

[3] Barber, B. M. and T. Odean, (2000). Trading is Hazardous to your Wealth: The Common Stock Investment Performance of Individual Investors. *The Journal of Finance*. Vol. 55(2), 773-806.

[4] Barberis, N., A. Shleifer, and R. Vishny (1998). A Model of Investor Sentiment. *Journal of Finance* .vol.49, 307–345.

[5] Barberis, Nicholas &Thaler, Richard (2003). A survey of Behavioral Finance, Handbook of the Economics of Finance, in G.M. Constantinides & M. Harris & R. M. Stulz (ed.*). Handbook of the Economics of Finance*, ed. 1(1), chapter 18, 1053-1128 Elsevier.

[6] Bell, D. (1982). Regret in Decision Making under Uncertainty. *Operations Research.* Vol.30, 961-981.

[7] Benartzi, S. and Thaler, R.H. (2001). Naïve Diversification Strategies in Retirement Saving Plans. *American Economic Review.* Vol. 91(1), 9-98.

[8] Bessler W., Drobetz W. and Grüninger M.C. (2010). International Tests of the Pecking Order Theory, *Working Paper, Midwest Finance Association (MFA).* 1-47.

[9] Bhatnagar, K. V. (2012). Do Indian pensioners hold diversified portfolio? http://www.igidr.ac.in/money/mfc_5/kavim.pdf. Retrieved on 23/01/2013 at 03:49 PM, from www.igidr.ac.in

[10] Clark, J. M. (1918). Economics and Modern Psychology. *Journal of Political Economy.* Vol.26, 1-30

[11] De Bondt, W. and Thaler R. H. (1987). Further evidence on investor overreaction and stock market seasonality. *Journal of Finance*. Vol.42, 557−581.

[12] De Bondt, W., and Thaler R. H. (1985). Does the stock market overreact? *Journal of Finance*. Vol.40, 793−808.

[13] Fama, Eugene (1970). Efficient Capital Markets: A Review of Theory and Empirical Work. *Journal of Finance*. Vol.25 (2), 383–417.

[14] Gabaix, X., and D. Laibson, (2000). A Boundedly Rational Decision Algorithm. *American Economic Review.* Vol. 90, 433-438

[15] Gervais, S., and T. Odean (2001). Learning to be Overconfident. *Review of Financial Studies*, Vol. 14, 1−27

[16] Goldberg J. and R. V. Nitzsch. (2001). Behavioral Finance. John Wiley and Sons Ltd.

[17] Haigh, Michael, and John List (2005). Do Professional Traders Exhibit Myopic Loss Aversion? An Experimental Analysis. *The Journal of Finance*, Vol. 60, 523-34

[18] Hirshleifer, D. and T. Shumway (2003). Good Day Sunshine: Stock Returns and the Weather. *The Journal of Finance*, Vol.58 (3), 1009-1032.

[19] Kahneman, D. (1973). Attention and Effort. Englewood Cliffs, New Jersy: Prentice-Hall

[20] Kahneman, D. and D. Lovallo (1993). Timid choices and bold forecasts: A Cognitive perspective on Risk taking. *Management Science.* Vol. 39(1), 17-31.

[21] Kahneman, D. and Tversky A. (1973). On the Psychology of Prediction. *Psychological Review.* Vol.80, 237–51.

[22] Kahneman, D. and Tversky, A. (1979). Prospect Theory: An Analysis of Decision under Risk. *Econometrica*. Vol. 47, 263-291

[23] Korniotis, George M., and Kumar Alok (2008). Do Portfolio Distortions Reflect Superior Information or Psychological Biases? *Working Paper, University of Texas at Austin.*

[24] Lintner, G. (1998). Behavioral finance: Why investors make bad decisions. *The Planner*. Vol. 13(1), 7-8.

[25] Love, D. A. (2010). The effects of marital status and children on savings and portfolio choice. *The Review of Financial Studies*. Vol. 23(1), 385-431.

[26] Malmendier, Ulrike and Devin Shanthi Kumar (2004), Do Security Analysts Speak in Two Tongues? *Quarterly Journal of Economics*. Vol.112, 631-45

[27] Miller, G. A., (1956). The magical number seven plus or minus two: Some limits on our capacity for processing information. *Psychological Review*. Vol. 63, 81-97.
[28] Montier James (2002). Behavioral Finance: Insight into Irrational Minds and Markets. West Sussex, England: John Wiley & Sons.
[29] Northeraft G.B. and M.A. Neale (1987). Experts, Amateurs, and Real Estate: An Anchoring-and-Adjustment Perspective on Property Pricing Decisions, *Organizational Behavior and Human Decision Processes*. Vol. 39, 228-241.
[30] Olsen, R. (1996). Implications of herding behavior for earnings estimation, risk assessment, and stock returns. *Financial Analysts Journal*. Vol. 52(4), 37-44
[31] Olsen, R. (1998). Behavioral Finance and its Implications for stock price Volatility, *Financial Analysts Journal*. Vol.54 (2), 10-18.
[32] Saaty, T. L. (2008). Decision Making with the Analytical Hierarchy Process. *International Journal of Services Sciences*. Vol.1 (1), 83-98.
[33] Shefrin, H, (2000). Beyond Greed and Fear: Understanding behavioral finance and the psychology of investing. Boston, USA: Harvard Business School Press
[34] Shiller R. J. (1997). Human Behavior and Efficiency of the Financial System, Conference Proceedings of the Recent Developments in Macroeconomics Conference held in New York, conducted by the Federal Reverse Bank of New York, Federal Reserve Bank and New York.
[35] Shiller Robert J (2000). Irrational Exuberance. Princeton University Press
[36] Shiller, R. J. and J. Pound. (1989). Survey evidence on diffusion of interest and information among institutional investors. *Journal of Economic Behavior and Organization*. Vol.12 (1), 47-66.
[37] Thaler, R. H. (1980). Toward a positive theory of consumer choice. *Journal of Economic Behavior & Organization*. Vol.1 (1), 39-60.
[38] Thaler, R. H. (1999). Mental accounting matters. *Journal of Behavioral Decision Making*, Vol.12 (3), 183-206.
[39] Topol, R. (1991). Bubbles and volatility of stock prices: Effect of mimetic contagion. *The Economic Journal*. Vol. 101(4), 786-800.
[40] Tversky, A. and Kahneman, D. (1971). Belief in the Law of Small Numbers, *Psychological Bulletin*. Vol.76, 105-110.
[41] Tversky, A. and Kahneman, D., (1981). The Framing of Decisions and the Psychology of Choice. *Science*. Vol. 211(4), 453-458.

International Journal of Advancement in Engineering Technology, Management & Applied Science

Volume 2, Issue 9 September 2015 ISSN No: 2349-3224

Isolation and Characterization of Potential Phosphate Solubilizing Bacteria from the rhizoplane of Kukrail forest, Lucknow

Faria Fatima[1], Neelam Pathak[2], Smita Rastogi Verma[3]

[1]Integral Institute of Agriculture, Science and Technology, Integral University, Lucknow-226026, India

[2]Department of Biosciences, Integral University, Lucknow-226026, India

[3]Department of Biotechnology, Delhi Technological University, Delhi-110042

Abstract

Phosphorus is an important element for seed formation, disease resistance, improvement in fruit and crops quality. The inoculation of P-solubilizing bacteria is found as a promising technique as it helps in increase of P availability in soils fertilized with insoluble form of phosphates. A study has been conducted to isolate and characterize several phosphate solubilizing bacteria form rhizospheric soil at morphological and biochemical level. Five bacteria having highest solubilization index, pH reduction and acid phosphatase were isolated which can be used as biofertilizer in agricultural area.

Introduction

Soil is a dynamic, living matrix that is an important part of the terrestrial ecosystem as it is a crucial resource for agricultural production, food security and maintenance of a large amount of life processes. Soil is considered as a depot of microbial activity, though only 5% of living micro-organisms is estimated. The functions of soil microorganisms are central to the decomposition processes and cycling of nutrient. They play an important role in soil process that determines plant growth. For successful functioning of introduced microbial bioinoculants and their influence on soil health, efforts have been made to investigate soil microbial diversity.

Rhizospheric bacteria are one of the major groups of microbes, which are plentiful in rhizosphere soil ranging between 10^{-6} to 10^{-8} colony-forming units (cfu) per gram, and some of them have shown great potential for plant health promotion and as biocontrol agents of nematodes (Siddiqui and Mahmood, 1999). These plant growth promoting rhizobacteria (PGPRs) are currently being exploited towards these ends. Antoun and Prevost (2006) gave evidence in the literature indicating that PGPRs can be a true success story in sustainable agriculture.

Phosphate solubilizing bacteria (PSBs) are important categories of PGPRs which are used in the form of biofertilizers in various agricultural countries, as significant areas of cultivated soils are deficient in nutrients, for *e.g.* phosphorus (P) (Xie, 1996). Phosphorous is the major essential macronutrient for plant growth and development and hence is commonly added as fertilizer to optimize yield. PSBs have been used to convert insoluble phosphate into soluble forms available for plant growth (Nahas *et al.*, 1990). It has been shown that PSBs increased P availability in soils and increase mineral content in the plant (Sheng *et al.*, 2002).

A combination of application of rock phosphate and bacteria that solubilize them might provide a faster and permanent supply of phosphorous for optimal plant productivity. This conversion occurs through acidification, chelation and exchange reactions and results in the production of organic acids, which have become indicators for routine isolation and selection procedures of PSBs (Illmer *et al.*, 1995). Collection of soil, isolation and screening of the phosphate solubilizing bacteria and their morphological and biochemical characterization was done in present study.

Materials and Methods

Collection of soil sample

The soil samples were collected from different locations of the Kukrail forest, Lucknow, Lawns of Integral University, Lucknow and Central Institute of Medicinal, and Aromatic Plants

(CIMAP), Lucknow. The soil samples were taken from two zones *viz*., upper zone, which is 10-15 cm deep and lower zone, which is 20-25 cm in depth.

Isolation and screening of phosphate solubilizing bacteria

The soil rhizospheric samples were screened for the presence of phosphate solubilizing bacteria. The bacteria were grown on nutrient agar media. For this nutrient agar medium comprising of yeast extract 0.3 %; peptone 0.5 %; $CuSO_4$ 100 µg/ml was prepared and pH adjusted to 7.0. This medium was complemented with agar 1.5 % and autoclaved at 15 psi for 15 min. Autoclaved medium was poured in sterile petriplates (25 ml/plate) under laminar flow hood and allowed to solidify. Soil rhizospheric samples from various locations were taken and serial dilutions were made. For this 1 g sample was taken and added in tube containing distilled water and mixed thoroughly. This represented 10^{-1} dilution. Under aseptic conditions, 10^{-2} to 10^{-9} dilutions of samples were prepared.

Screening of phosphate solubilizing bacteria

The isolates were screened on the basis of plate assay. Two media *viz.,* Pikovskaya's media (Pikovskaya, 1948) and bromophenol blue media were used for screening. The Pikovskaya's medium consisted of yeast extract 0.50 (g/l), dextrose 10.00 (g/l), calcium phosphate 5.00 (g/l), ammonium sulphate 0.50 (g/l), potassium chloride 0.20 (g/l), magnesium sulphate 0.10 (g/l), manganese sulphate 0.0001 (g/l), ferrous sulphate 0.0001(g/l). Bromophenol media consist of yeast extract 0.50 (g/l), dextrose 10.00 (g/l), calcium phosphate 5.00 (g/l), ammonium sulphate 0.50 (g/l), potassium chloride 0.20 (g/l), magnesium sulphate 0.10 (g/l), manganese sulphate 0.0001(g/l), ferrous sulphate 0.0001 (g/l) and 0.5 % of bromophenol blue dye. Both the media were prepared and pH adjusted to 7.0. This medium was complemented with agar 1.5 % and autoclaved at 15 psi for 15 min. Autoclaved medium was poured in sterile petriplates (25 ml/plate) under laminar flow hood and allowed to solidify. Bacterial colonies were inoculated on petriplates containing medium for plate assay and the plates were incubated in inverted position in incubator for up to 24 h at 37° C. Positive cultures were screened by observing transparent

halo zones in Pikovskaya's medium and yellow halo zone on bromophenol blue medium.

Pure cultures of phosphate solubilizing bacterial species

Positive bacterial colonies were subculture on fresh petriplates containing medium for plate assay. Axenic cultures were isolated by incubating the plates in inverted position in incubator for up to 24 h at 37° C. Positive cultures were screened by observing transparent halo zones in Pikovskaya's medium which is due to the solubilization of insoluble tricalcium phosphate into the soluble form and yellow halo zones appears on bromophenol blue medium which is due to the production of organic acids leading to lowering of pH in the medium.

Morphological characterization of bacterial isolates by Gram staining procedure

The purity and tentative identification of the isolated phosphate solubilizing bacteria was done by Gram's staining procedure. The cell shape and Gram's property of bacteria were examined after staining with standard Gram staining procedure. A thin smear of bacterial isolate was prepared on the glass slide, air-dried and heat-fixed. It was stained in the following sequential order: covered with crystal violet for 30 s, washed with distilled water, covered with Gram's iodine solution for 60 s, washed with 95 % ethyl alcohol, washed with distilled water, counter-stained with safranin for 30 s and finally washed with distilled water. The stained and air-dried slides were examined under microscope using oil-immersion objective technique. Gram-positive bacteria retains the color of crystal violet and stain in purple color, while the Gram-negative takes the color of counter stain safranin appear pink in color.

Biochemical characterization of phosphate solubilizing bacteria

Solubilization index based on colony diameter and halo zone for each PSB indicate the efficiency of solubilization of insoluble phosphate into the soluble one thus forming a transparent halo zone around the colony. Catalase production, oxidase production, urease production and nitrate reduction are valuable criteria for differentiating and identifying various types of bacteria. Hence, the positive bacterial isolates were also analyzed qualitatively for their nitrate reducing,

urease, oxidase and catalase producing capabilities.

Solubilization index (SI)

0.1 ml of each PSB culture preserved in sterile distilled water was placed on Pikovskaya's agar (Pikovskaya, 1948) plates and incubated for seven days. Solubilization Index was measured using following formula (Edi-Premono *et al*., 1996).

$$SI = \frac{\text{Colony diameter + halo zone diameter}}{\text{Colony diameter}}$$

pH change

1 ml of three days old culture of bacteria in sterile distilled water was added to sterile 100 mL Pikovskaya's broth (PB) medium and kept on shaker for seven days. Sterile uninoculated medium served as control. Initial pH and change in pH was recorded on 3rd, 5th and 7th day by digital pH meter.

Nitrate reduction test

Certain bacteria reduce nitrate to nitrite while others are capable of further reducing nitrite to form nitrogen or ammonia. The isolates were incubated at 37° C overnight followed by addition of 0.5 ml each of sulphanilic acid (0.8 % in 5 N acetic acid) and α-naphthylamine (0.5 % in 5 N acetic acid). The appearance of red or pink color indicated the positive test for nitrate reduction.

Urease test

The overnight cultures were inoculated to the test tubes containing sterilized urea broth and incubated for 24-48 hours at 20ºC ±8ºC. The development of pink color was taken as positive for the test.

Catalase test

Catalase test was performed by growing bacteria in nutrient broth overnight at 37° C followed by addition of a drop of 3 % H_2O_2. The production of effervescence due to catalase-catalyzed breakdown of H_2O_2 to molecular oxygen indicated positive reaction.

Oxidase test

To the Trypticase Soy Agar (Himedia) plates, overnight cultures of the test isolates were spotted and plates were incubated for 24 h at 20ºC ± 8º C. After incubation, two to three drops of tetramethyl-phenylenediamine dihydrochloride was added to the surface of the growth of each test organism. The color change to puple or maroon was taken as oxidase positive.

Analysis of acid phosphatase enzyme activity from various isolates

All the bacterial isolates tested positive in plate assay were subjected to analyses of activity of acid phosphatase enzyme. Bacterial colonies tested positive in plate assay were inoculated in Pikovskaya's broth, poured in test tubes (10 ml/tube) and autoclaved at 15 psi for 15 min. The tubes were incubated in incubator shaker at 120 rpm, 37° C for overnight. 10 ml of above grown bacterial culture was taken and filtered through Whatman no. 1 filter paper. This was considered as enzyme or protein sample. The enzyme acid phosphatase was assayed using para nitrophenyl phosphate (PNP-P) as a substrate. The reaction mixture contained 2.5 ml (0.1 M) sodium acetate buffer (pH 5.8), 1 ml (1 mM) magnesium chloride, 0.5 ml 1 % PNP-P and 0.5 ml of a suitable dilution of enzyme preparation. One ml of the reaction mixture was transferred to 2 ml of 0.2 M sodium hydroxide before and after 15 min incubation at 37° C to stop the reaction. The sodium hydroxide solution added before incubation acts as a control sample for each analysis. The amount of para nitro phenol (PNP) liberated was measured by recording the absorbance at 420 nm using an appropriate calibration curve. Activity is expressed as μmol PNP liberated min^{-1}. The blank was run in a similar manner using distilled water.

Determination of protein content by Lowry's method

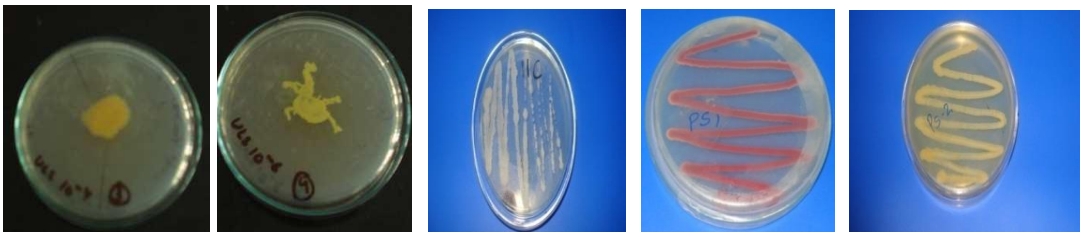
500 µl of bacterial culture was taken in microfuge tube and protein was precipitated with equal volume of ice-cold 20 % trichloroacetic acid (TCA) and kept at 4° C overnight. The pellet was recovered by centrifuging at 12,000 rpm for 5 min at room temperature and decanting the supernatant. The pellet was washed with 0.1 ml ice-cold 10 % TCA and ice-cold acetone. Depending on the pellet size, it was dissolved in 0.5-1.0 ml of 0.1 N NaOH. The solution was subjected to heating for 5 min in boiling water bath and vortexed vigorously. The protein content was determined by Lowry's method (Lowry *et al.,* 1951). For protein content determination, 0.5 ml of protein solution was taken in test tube and 2.5 ml of alkaline solution [prepared by mixing 2 % Na_2CO_3 solution (in NaOH), 2 % sodium potassium tartrate and 1 % $CuSO_4.5H_2O$ in 100:1:1] was added. The contents were mixed well and the tubes were incubated at room temperature for 10 min. This was followed by addition of 0.25 ml of 1.0 N Folin's reagent. The contents in the tube were mixed thoroughly and after 10 min, absorbance at 660 nm against reagent blank was determined spectrophotometrically using bovine serum albumin fraction V as standard.

Results and Discussion

Isolation and screening of phosphate solubilizing bacteria

Different types of soil samples, *viz.,* Normal soil, Usar soil and Sandy soil were collected from various locations. Based on serial dilution 10 bacterial isolates from different soil samples were isolated, from which 5 bacterial isolates having potential phosphate solubilizing ability were observed by plate assay. Various bacteria, which were isolated from soil, were preserved on the nutrient agar media (Fig.1). The shape, color and type of colony were estimated on the nutrient media and further the Gram's staining was performed.

International Journal of Advancement in Engineering Technology, Management & Applied Science
Volume 2, Issue 9 September 2015 ISSN No: 2349-3224



1 2 3 4 5

Figure1. Bacterial isolates having phosphate solubilizing potential growing on nutrient agar media

The tricalcium phosphate present in Pikovskaya's medium in insoluble form was converted into the soluble form by the phosphate solubilizing bacteria (phosphate solubilizers), thereby giving a clear zone around a positive colony (Fig.2a).



Figure 2. (a)Bacteria showing phosphate solubilization leading to formation of clear zone in Pikovskaya's medium (b) Bacteria showing yellowing of bromophenol blue medium

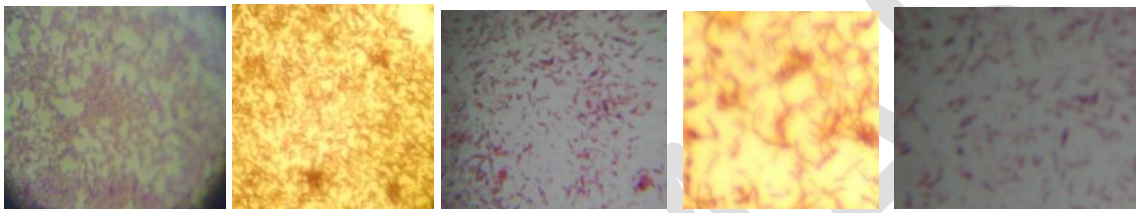
In bromophenol blue medium (Fig.2b) all the positive bacterial isolates were capable of producing organic acids, which led to change in pH and thereby color change from blue to yellow.

Bacterial isolates were characterized by analyzing their shape, presence of catalase, oxidase, urease and nitrate reduction abilities. The isolates were examined and the results are given in

International Journal of Advancement in Engineering Technology, Management & Applied Science
Volume 2, Issue 9 September 2015 ISSN No: 2349-3224

Morphological characterization of PSBs by microscopic examination

All the 5 isolates were studied for their Gram reaction property, cell morphology using standard Gram's staining procedure. The isolates, as shown (Fig.3) were found to be purple and pink colored, Gram-positive and Gram-negative respectively, of varying size under microscope using oil immersion technique.



1 2 3 4 5

Figure 3. Gram's staining slides of bacterial isolates

Biochemical characterization of isolates

Solubilization index (SI)

All the 5 isolates were able to solubilize tricalcium phosphate (TCP) in Pikovskaya's agar medium and the diameter of the zones of solubilization indicated wide variations among the isolates (2.5 to 3.4).

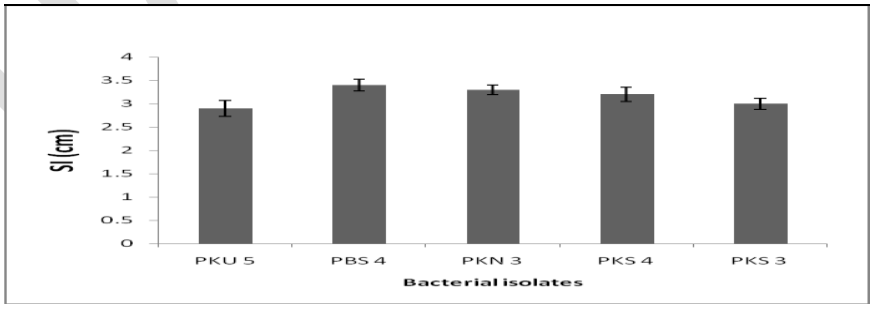


Figure 4 Histogram showing solubilization indices of bacterial isolates

International Journal of Advancement in Engineering Technology, Management & Applied Science
Volume 2, Issue 9 September 2015 ISSN No: 2349-3224

pH change

All the 5 isolates were allowed to grow on Pikovskaya's broth (PB) supplemented with TCP (0.5 % w/v). These bacterial isolates showed decrease in pH with time. Minimum pH was observed after 7th day. The pH lowered down due to the liberation of the organic acids in liquid media (Nahas, *et al.*, 1996). The minimum pH of 3.2 was shown by isolate PKN 3 after 7th day. The bacterial isolates, PKS 4, PBS 4, PKS 3 and PKU 5 significantly decreased the pH of media up to 3.3, 3.6, 3.8, 3.6 and 3.4 respectively after 7th day of growth (Fig.5). Therefore, these bacterial isolates were considered of exhibiting high phosphate solubilizing efficiency.

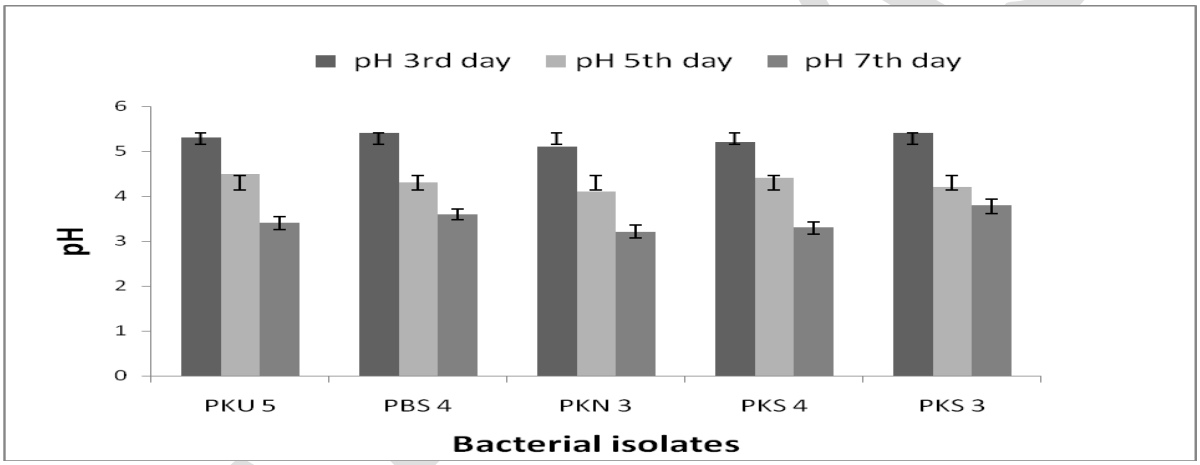


Figure 5 Histogram showing comparative analysis of bacterial isolates on the pH on different days of growth

Nitrate reductase test

Nitrate, present in the broth, is reduced to nitrite, which may then be reduced to nitric oxide, nitrous oxide, or nitrogen. The nitrate reduction test is based on the detection of nitrite and its ability to form a red compound when it reacts with sulfanilic acid to form a complex (nitrite-sulfanilic acid) which then reacts with α-naphthylamine to give a red precipitate (prontosil). The isolates, which reduce nitrate into nitrite and further reduce nitrite into ammonia, indicates the presence of pink color, showing positive results (table 1).

Urease test

Microorganism, which can produce a urease enzyme, attacks the carbon and nitrogen bond amide compound with the liberation of ammonia gas. Phenol red acts as an indicator dye. Due to the production of ammonia, the yellow media turns deep pink in color indicating hydrolysis of urea (table 1).

Catalase and oxidase test

The production of catalase enzyme breaks the hydrogen peroxide into water and oxygen, which comes in the form of effervescence, indicating positive catalase reaction (Fig.6). The oxidase test is a test which helps in determining if bacteria can produce certain cytochrome c oxidases which reduces N,N,N′,N′-tetramethyl-p-phenylenediamine (TMPD) or N,N-dimethyl-p-phenylenediamine (DMPD) results in dark-blue to maroon color when oxidized, and colorless when reduced. Oxidase-positive bacteria possess cytochrome oxidase or indophenol oxidase (an iron-containing hemoprotein) (Fig. 7) (table 1).



Figure 6 Positive catalase test

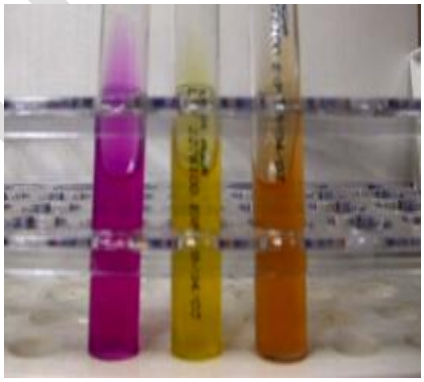


Figure 7 Positive oxidase test

Table 1. Tentative identification of bacterial isolates

Bacterial isolates	Gram positive or negative	Shape	Nitrate reduction test	Urease test	Catalase production test	Oxidase test	Tentative identification
PKU 5	Negative	Rod	Positive	Positive	Positive	Positive	*Pseudomonas brassicacearum*
PBS 4	Negative	Rod	Positive	Negative	Positive	Negative	*Pantoea agglomerans*
PKN 3	Positive	Rod	Positive	Positive	Positive	Negative	*Bacillus cereus*
PKS 4	Positive	Rod	Positive	Positive	Positive	Positive	*Bacillus anthracis*
PKS 3	Positive	Spherical	Positive	Positive	Positive	Negative	*Staphylococcus succinus*

Quantitative analysis of acid phosphatase enzyme activities

The tentative PSBs were grown on Pikovskaya's broth containing 0.5 % TCP and their phosphatase activities were measured. The phosphatase activity was estimated in the supernatant of broth taken after centrifugation at 10,000 X g at 4° C. The main mechanism for the solubilization of insoluble organic and inorganic phosphate was due to production of an enzyme acid phosphatase, which catalyzes hydrolysis of phosphate to liberate inorganic phosphorus (Pi). Thus, the isolates were evaluated for their acid phosphatase producing ability by measuring Pi ability. Among all the positive isolates, six bacteria exhibited significantly higher amount of acid phosphatase enzyme activity, including bacteria **PKN 3, PKU 5, PKS 4, PBS 4,** and **PKS 3** (Fig. 8). Moreover, these isolates also showed relatively higher solubilization index. Thus, the

solubilization index and the acid phosphatase enzyme activity are directly proportional to each other indicating that high enzymatic activity results in the formation of large halo zone.

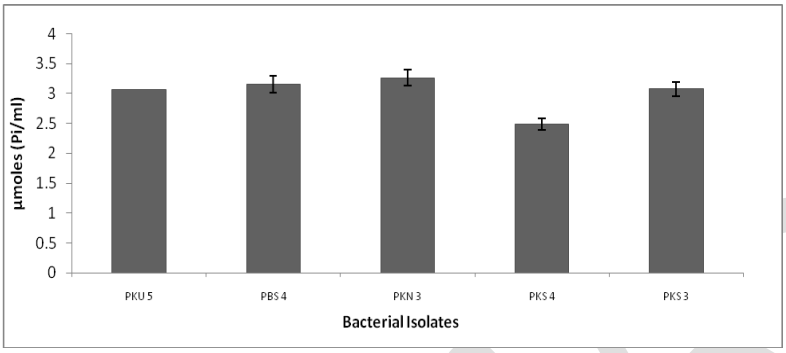


Figure 8 Histogram showing acid phosphatase activity of bacterial isolates

Conclusion

The results indicated existence of variation among the isolated PSBs at morphological and biochemical levels. Some of the isolates showed white colored pigmented colonies while others formed light green and light orange colonies. The variation in colony color could be due to the production of different types of pigments. Several bacterial species are known to produce various kinds of pigments, the allocation of these pigments in the genus is uncertain (Palleroni et al., 1970). In addition to this, these isolates also showed diversity in shape from round to irregular shaped colonies. Furthermore, the round shaped colonies were non-spreading where as the irregular shaped colonies were spreading type. PSBs also exhibited diversification in cell shape, Gram property, nitrate reductase, urease oxidase, and catalase activities.

Prominent halo zones were found in case of positive PSB isolates on Pikovskaya's agar. Based on transparent halo zone the isolates that exhibited higher SI also exhibited higher acid phosphatase activity. However, on the basis of morphological and biochemical characterization of isolates these PSBs were tentively identified as *Pseudomonas brassicacearum*, *Pantoea agglomerans*, *Bacillus cereus*, *Bacillus anthracis*, *Staphylococcus succinus.*

Acknowledgements

The authors are highly thankful to Vice Chancellor, Integral University for his support and encouragement. The grant of Uttar Pradesh Biodiversity Board is gratefully acknowledged.

References

1. SIDDIQUI, ZA, MAHMOOD I, (1999), ***Role of bacteria in the management of plant parasitic nematodes: a review***, Bioresource Technol 69, 167–179.
2. ANTOUN H, PRÉVOST D, (2006), ***Ecology of plant growth promoting rhizobacteria. In: PGPR: Biocontrol and Biofertilization***, Siddiqui, Z.A. (ed.), Springer, pp.1–38.
3. XIE, H, PASTERNAK J. J, GLICK B. R, (1996), ***Isolation and characterization of mutants of the plant growth promoting rhizobacterium Pseudomonas putida GR12-2 that overproduce indoleacetic acid***, Curr. Microbiol, 32, 67-71.
4. NAHAS E, BANZATTO D.A, ASSIS L.C, (1990), **Fluorapatite *solubilization by Aspergillus niger in vinasse medium.*** Soil Biol. Biochem, 22, 1097–1101.NAHAS, E, (1996**), *Factors Determining Rock Phosphate Solubilization by Microorganisms,*** World Journal of Microbiology and Biotechnology, Vol. 12, No. 6, (November 1996), pp. 567-572.
5. SHENG X.F, HUANG W.Y, (2002), ***Mechanism of potassium release from feldspar affected by the strain NBT of silicate bacterium,*** Acta Pedol. Sin, 39, 863–871.
6. ILLMER P, BARBATO A, SCHINNER F, (1995), ***Solubilization of hardly-soluble $AlPO_4$ with P-solubilizing microorganism***, Soil Biol. Biochem, 27, 265–270.
7. EDI PREMONO M, MOAWAD A. M, AND VLEK P. L. G, (1996), ***Effect of phosphate-solubilizing Pseudomonas putida on the growth of maize and its survival in the rhizosphere***, Indones. J. Crop Sci, 11, 13Ð23.
8. LOWRY O.H, N.J. ROSEBROUGH, A.L. FARR, R.J. RANDALL, (1951), ***Protein Measurement with the Folin Phenol Reagent***., J. Biol. Chem. 193, 265-275.

9. NAHAS, E, (1996**),** ***Factors Determining Rock Phosphate Solubilization by Microorganisms,*** World Journal of Microbiology and Biotechnology, Vol. 12, No. 6, (November 1996), pp. 567-572.

IJAETMAS

ResearchGate

See discussions, stats, and author profiles for this publication at: http://www.researchgate.net/publication/281650413

White Light Emission and Color Tunability of Dysprosium doped Barium Silicate Glasses

ARTICLE *in* JOURNAL OF LUMINESCENCE · SEPTEMBER 2015

Impact Factor: 2.72 · DOI: 10.1016/j.jlumin.2015.08.063

READS

54

9 AUTHORS, INCLUDING:



Amit Kr Vishwakarma

Delhi Technological University

3 PUBLICATIONS **6** CITATIONS

SEE PROFILE



Kaushal Jha

Delhi Technological University

4 PUBLICATIONS **6** CITATIONS

SEE PROFILE



Jayasimhadri

38 PUBLICATIONS **453** CITATIONS

SEE PROFILE



Ravindra Sinha

Delhi Technological University

236 PUBLICATIONS **532** CITATIONS

SEE PROFILE

Available from: Kaushal Jha

Retrieved on: 24 November 2015

CrossMark
click for updates

View Article Online
View Journal

Dalton Transactions

Accepted Manuscript

This article can be cited before page numbers have been issued, to do this please use: A. K. Vishwakarma, K. Jha, J. Mula, S. Bathula, B. Gahtori and D. Haranath, *Dalton Trans.*, 2015, DOI: 10.1039/C5DT02436F.



This is an *Accepted Manuscript*, which has been through the Royal Society of Chemistry peer review process and has been accepted for publication.

Accepted Manuscripts are published online shortly after acceptance, before technical editing, formatting and proof reading. Using this free service, authors can make their results available to the community, in citable form, before we publish the edited article. We will replace this *Accepted Manuscript* with the edited and formatted *Advance Article* as soon as it is available.

You can find more information about *Accepted Manuscripts* in the Information for Authors.

Please note that technical editing may introduce minor changes to the text and/or graphics, which may alter content. The journal's standard Terms & Conditions and the Ethical guidelines still apply. In no event shall the Royal Society of Chemistry be held responsible for any errors or omissions in this *Accepted Manuscript* or any consequences arising from the use of any information it contains.

ROYAL SOCIETY OF CHEMISTRY

www.rsc.org/dalton

Please do not adjust margins

ROYAL SOCIETY OF CHEMISTRY View Article Online
DOI: 10.1039/C5DT02436F

Journal Name

ARTICLE

Published on 27 August 2015. Downloaded by University of California - Santa Barbara on 27/08/2015 11:31:03.

Emerging Cool White Light Emission from Dy^{3+} doped Single Phase Alkaline Earth Niobate Phosphors for Indoor Lighting Applications

Received 00th January 20xx,
Accepted 00th January 20xx

DOI: 10.1039/x0xx00000x

www.rsc.org/

Amit K. Vishwakarma,[a] Kaushal Jha,[a] M. Jayasimhadri,*[,a] B. Sivaiah,[a,b] Bhasker Gahtori,[a,b] D. Haranath[b]

Single-phase cool white-light emitting $BaNb_2O_6:Dy^{3+}$ phosphors have been synthesized via conventional solid-state reaction method and characterized using X-ray diffraction (XRD), scanning electron microscopy (SEM) observations and spectrofluorophotometric measurements. XRD and Rietveld strucutural refinement studies confirms that all the samples exhibit pure orthorhombic [space group- $C222_1(20)$]. SEM observations reveals the dense particle packaging with irregular morphology in micron range. The as-prepared phosphors exhibit blue (482 nm) and yellow (574 nm) emissions under 349, 364, 386 and 399 nm excitations corresponding to $^4F_{9/2} \rightarrow {}^6H_J$ (J= 15/2, 13/2) transitions of Dy^{3+} ions. The energy transfer mechanism between Dy^{3+} ions has been studied in detail and the luminescence decay lifetime for $^4F_{9/2}$ level was found to be around 146.07 µs for the optimized phosphor composition. The calculated Commission Internationale de L'Eclairage (CIE) chromaticity coordinates for the optimized phosphor is (x=0.322, y=0.339), which is close to the National Television Standard Committee (NTSC) (x=0.310, y=0.316) coordinates. The values of CIE chromaticity coordinates and correlated color temperature (CCT) of 5907 K endorses cool white-light emission from the phosphor. The study reveals that $BaNb_2O_6:Dy^{3+}$ phosphor could be a potential candidate for near ultra-violet (NUV) excited white-LEDs applications.

1. Introduction

In recent years, rare earth ion doped inorganic luminescent materials have been extensively studied in the fields of materials science, physics, chemistry and life sciences due to various potential applications in display devices (e.g., cathode ray tubes, vacuum fluorescent displays, and field emission display), lighting gadgets (e.g., fluorescent tubes and white-light emitting diodes), solid-state lasers, biological labelling, X-ray, medical devices, ionization radiation and so on.[1-2] Among them, white light emitting diodes (w-LEDs) have been considered to be the next generation illumination sources in the field of solid-state lighting instead of traditional incandescent and currently implemented fluorescent lamps due to their numerous advantages such as small size, high energy efficiency, energy-saving, robustness, high brightness, fast switching, longer life time (>100 000 h) and environmental friendliness.[3-5] Currently, two approaches have been implementing to achieve white light through solid-state lighting (SSL). The first one is phosphor-free SSL approach employing RGB-LEDs, which consist of red, green and blue monochromatic LEDs to obtain white-light. The main drawback of this approach is that every LED must be adjusted by individual power supply to balance the emission intensity of each color. However, the second approach involves phosphor integrated to the SSL device. The phosphor-converted (pc) LED uses an ultra-violet (UV)/near ultra-violet (NUV) light in combination with single/multiple phosphors that convert a part of the light emitted by the UV/NUV LED into white-light.[6,7] At present, most of the commercially available w-LEDs are based on the second approach because of the simplicity in operation. The combination of blue LED (InGaN) coated with yellow-emitting ($Y_3Al_5O_{12}$: Ce^{3+}) phosphor is one of the widely used approach currently to produce w-LEDs. However, this approach encounters some serious issues such as halo effect of blue/yellow color separation, color dependence on chromaticity, and poor color-rendering index (<65) due to the lack of green and red-emitting phosphor components at long wavelength region, which limits the LED applications further.[8] On the other hand, UV/NUV LED coated with multicolor-emitting phosphors is an alternative approach to obtain white-light emission with an excellent color-rendering index (>90) as the luminous efficiency of NUV/UV chip pumped w-LEDs is higher than the blue chip[9]. However, UV/NUV excitable multiple color-emitting phosphors have some disadvantages such as low luminous efficiency due to blending together of blue, green and red-emitting phosphors and different degradation schedules of each phosphor.[9,10] Therefore, single phase phosphor has become a necessary pre-requisite for the fabrication of w-LEDs using UV/NUV LED chips to overcome the problems mentioned above. There are different methodologies to obtain white light emission from single phase host lattice by (i) doping single rare earth (RE) ion, (ii) doping of two or more RE ions, which are excited simultaneously, (iii) co-doping of different ions and controlling the emission via energy transfer processes, and (iv) controlling the concentration of the defect and reaction conditions of defect related luminescent materials.[11]

Alkaline earth niobates have emerged as novel materials with huge technological and scientific importance due to their excellent non-linear optical, photocatalytic, piezoelectric, ionic

[a] Luminescent Materials Research Lab, Department of Applied Physics, Delhi Technological University, Delhi 110 042, India
[b] CSIR-National Physical Laboratory, Dr. K.S. Krishnan Road, New Delhi 110 012, India

Please do not adjust margins

View Article Online
DOI: 10.1039/C5DT03003J

Published on 27 August 2015. Downloaded by University of California - Santa Barbara on 27/08/2015 11:31:03.

conductive and photorefractive properties for the applications involving acoustic transducers, delay lines in filters, optical modulators, beam deflectors etc.[12,13] Among all inorganic phosphors, oxide based phosphors are preferred choice for display and SSL applications due to their exceptional chemical stability, inertness and moisture resistance. Moreover, rare-earth doped alkaline earth niobate phosphors have attracted much attention and have been applied for light emitting diodes (LEDs) and plasma display panel (PDP) applications.[14] The metaniobate ceramic, with the general formula $M^{2+}Nb_2O_6$ (M^{2+}=divalent alkaline earth or transition metals) are sub-component of the complex perovskite family, $A(M_{1/3}Nb_{2/3})O_3$ and they are mostly exist in an isostructural form of orthorhombic structure with columbite mineral group with the exception of the M=Sr, Ba and Pb analogues, which crystallize in different orthorhombic structures.[15-17] In this quest, barium metaniobate ($BaNb_2O_6$) has been selected as host lattice due to its smaller band gap and exhibits higher charge generation under UV light irradiation compared to other binary niobates. Moreover, $BaNb_2O_6$ has been widely used as a high quality refractory material for photocatalytic and microwave dielectric applications in recent years.[18] The luminescent properties of various rare-earth ions doped niobate phosphors have been investigated and reported elsewhere.[19-21,14] However, to the best of our knowledge, luminescent properties of Dy^{3+} ions doped $BaNb_2O_6$ phosphors has never been reported in the literature. Hence, in the current study, the said phosphor has been chosen to synthesize and investigate thoroughly for the first time. In addition, it is well-known that Dy^{3+} ions with $4f^9$ electronic configuration has complex energy levels and various possible transitions between f-f levels that are highly selective and exhibit sharp line spectra.[22] It gives emission in blue and yellow band and the intensity ratio of these two emission bands depends on the host crystal structure.[23,24]

In the current work, a series of Dy^{3+} ions doped single-phase $BaNb_2O_6$ phosphors have been prepared by solid-state reaction method to explore its possibility as potential phosphor for white-LEDs by investigating photoluminescence and colorimetric properties in detail.

2. Experimental procedure

$Ba_{(1-x)}Nb_2O_6:xDy^{3+}$ (where x = 0.01, 0.1, 0.5, 1.0, 1.5, 2.0 and 2.5 mol %) were synthesized by conventional solid-state reaction method. The precursor chemicals namely, $BaCO_3$ (Fisher scientific, 99%), Nb_2O_5 (Fisher scientific, 99.9%) and Dy_2O_3 (Sigma Aldrich, 99.9%) all of AR grade were taken as starting materials. A stoichiometric amount of precursor materials were thoroughly mixed using an agate mortar and pestle for an hour with acetone as dispersing medium. Raw powder sample was kept in an alumina crucible and then heated in a programmable muffle furnace at 625°C for an hour to remove CO_2 and then sintered at 1200°C at heating rate 6 °C min^{-1} for 5 hour in air atmosphere. Finally, the sample was naturally cooled to room temperature (~25°C) in the furnace itself.

The structure of the prepared sample was determined through XRD. The crystalline phases were identified by X-ray diffractometer (Rigaku make, model-Mini flex-II), using nickel-filtered Cu K_α radiation (λ= 1.54056 Å) in the range of 20°≤ 2θ ≤ 60° and the accelerating voltage was kept at 30.0 kV and tube current at 15 mA. The FullProf suite programme was used to reveal the structural refinement. The morphological observations were carried out by SEM (Hitachi, Model- S-3700N). The photoluminescence excitation (PLE) and photoluminescence (PL) spectra were recorded using Shimadzu spectrofluorophotometer (model: RF-5301PC) fitted with a Xenon flash lamp. The lifetime measurement was carried out using a time-resolved luminescence spectrometer (model- F900 Edinburgh), equipped with a time correlated single photon counting system and microsecond xenon flash lamp as the source of excitation.

3. Colorimetric theory

The color of any object (self luminous or reflecting) can be conveniently specified via Commission International de L' Eclairage (CIE) chromaticity coordinates marked on a chromaticity diagram.[25] These color coordinates are calculated from the PL emission spectra using $\bar{x}(\lambda), \bar{y}(\lambda)$ and $\bar{z}(\lambda)$ color matching functions defined in the CIE 1931. For a specified power spectral density P(λ), the degree of stimulation required to match the color of P(λ) is given by three equations:

$$X = \int_\lambda \bar{x}(\lambda)P(\lambda)d\lambda$$

$$Y = \int_\lambda \bar{y}(\lambda)P(\lambda)d\lambda$$

$$Z = \int_\lambda \bar{z}(\lambda)P(\lambda)d\lambda$$

where *X, Y*, and *Z* are the tristimulus values. The tristimulus value provides stimulation (i.e. power) value for each of three primary (red, green, blue) colors to match the color of P(λ).

The tristimulus values specifying the color is stored in the ratio of the primary colors and not in the specific amounts of each individual primary color, the number of dimensions used to match the color of P(λ). This was done for the CIE 1931 *XYZ* space, and the resultant CIE 1931 *x-y* chromatic diagram is the most commonly used tool, to describe color, in spectroscopy today. From *(X, Y, Z)*, the *(x, y)* chromaticity coordinates are calculated as:

$$x = \frac{X}{X+Y+Z}$$

$$y = \frac{Y}{X+Y+Z}$$

Further, the quality of white light is evaluated from the chromaticity coordinates using McCamy's relation,[26] by first evaluating ratio between inverse slope line and chromaticity epicentre as:

$$n = \frac{(x - x_e)}{(y - y_e)}$$

where x_e= 0.3320 and y_e =0.1858. Then the Correlated Color Temperature (CCT) was evaluated as:

$$CCT = -449n^3 + 3525\,n^2 - 6823.3n + 5520.33$$

The color purity or color saturation of a light source is the distance in the chromaticity diagram between the *(x, y)* color-coordinate point of the test source and the coordinate of the equal-energy point divided by the distance between the equal-energy point and the dominant wavelength point. The color purity is thus given by:

This journal is © The Royal Society of Chemistry 20xx

View Article Online
DOI: 10.1039/C5DT02436F

Published on 27 August 2015. Downloaded by University of California - Santa Barbara on 27/08/2015 11:31:03.

$$\text{Color purity} = \frac{\sqrt{(x-x_{ee})^2+(y-y_{ee})^2}}{\sqrt{(x_d-x_{ee})^2+(y_d-y_{ee})^2}}$$

where, *(x, y)*, *(x_{ee}, y_{ee})* and *(x_d, y_d)* represent the chromaticity coordinates of the light source under test, equal-energy reference illuminant and dominant-wavelength point, respectively.[27]

4. Results and discussion

4.1 Structural and morphological analysis

The crystal structure of $BaNb_2O_6$ compound was reported for the first time by Sirotinkin *et al*. in 1990, and has orthorhombic [space group $C222_1$ (20)] structure with cell parameters a = 7.880 Å, b = 12.215 Å, c =10.292 Å and Z = 8.[28] The phase purity of the as-prepared phosphors was characterized using XRD. Fig. 1 illustrates the XRD patterns of undoped and Dy^{3+} ions doped $BaNb_2O_6$ phosphors that are in agreement with the PDF-4+(ICDD) standard card no. 04-012-8861. It was found that there is no change in peak positions among all XRD patterns, which indicate pure phase formation for undoped and doped $BaNb_2O_6$ phosphors with respect to their corresponding (hkl) planes. This fact could be due to large ionic radius of Ba^{2+} (1.24 Å) than Dy^{3+}(0.95 Å) and Dy^{3+} ions may occupy Ba^{2+} sites when they enter into $BaNb_2O_6$ host lattice. Hence, no additional peaks were found up to 2 mol% doping of Dy_2O_3, which means that Dy^{3+} ions were successfully substituted for Ba^{2+} ions without changing crystal structure of the host lattice.

The average crystallite size (D) and strain (ε) of the samples were calculated using most reliable Williamson–Hall (W-H) equation[29, 30] $[\beta\, Cos\,\theta = \left(\frac{K\lambda}{D}\right) + 4\varepsilon\, Sin\theta]$, where K = shape factor (0.94), D is average crystallite size, λ is wavelength of CuKα radiation, θ is Bragg's diffraction angle of the planes and β is the corrected full width at half maximum (FWHM). The average crystallite size of $Ba_{(1-x)}Nb_2O_6$: xDy^{3+} (x = 0.0, 0.1, 0.5, 1.0 and 2.0 mol%) samples was found to be in the range 44 and 55 nm. The strain present in lattice was calculated and the values for x = 0.0, 0.1, 0.5, 1.0 and 2.0 mol% Dy^{3+} ions doped $BaNb_2O_6$ sintered at 1200°C were found to be 0.081, 0.114, 0.113, 0.061 and 0.091, respectively. Further the average crystallite size calculated by Debye - Scherer's formula[31] $[D = K\lambda/\beta Cos\theta]$ was found to be in the range 40 and 89 nm and is in good agreement with the calculations performed using W-H method.[32] The Rietveld refinement of undoped $BaNb_2O_6$ was carried out using FullProf software shown in Fig. 2 (a) and the resulting parameters are summarized in Table 1. The results indicate a good agreement between the observed and calculated diffraction patterns of orthorhombic phase [space group $C222_1$ (20)] without any anonymous peak.[33] The unit cell parameters were determined and are found to be a =7.8707 Å , b = 12.2096 Å, c =10.2881 Å and cell volume (V) = 988.680 $Å^3$, which are close to those reported by Sirotinkin *et al* [27]. The refinement finally converging to goodness-of fit parameter (χ^2) = 4.2%, R_{wp} = 31.0% and R_p = 25.6%. Fig. 2(b) shows the orthorhombic structure of $BaNb_2O_6$ lattice projected onto b-c plane.

Fig. 3(a) & (b) represents SEM micrograph of 0.5 mol% Dy^{3+} ions doped $BaNb_2O_6$ phosphor. The micrograph reveals inhomogeneous and uneven dense morphology in micrometer range. The typical crystalline particle size is the range of 4-6 micrometer in dimension. It is obvious that, micrometer sized crystalline powder would be very much suitable to produce an efficient white light for solid-state lighting applications.[34]

4.2 Photoluminescence studies

The Fig. 4 illustrates the PLE spectrum of the $Ba_{(1-x)}Nb_2O_6$:xDy^{3+} (x=0.5 mol%) phosphor by monitoring the emission wavelength at 574 nm. The PLE spectrum consists of seven sharp peaks due to intra 4f-4f transitions located at 326, 349, 364, 386, 427, 454 and 474 nm, which are attributed from ground state $^6H_{15/2}$ to the different excited states ($^6P_{3/2}$,$^4M_{17/2}$), $^6P_{7/2}$, ($^4I_{11/2}$,$^6P_{5/2}$), ($^4F_{7/2}$,$^4I_{13/2}$), $^4G_{11/2}$, $^4I_{15/2}$ and $^4F_{9/2}$, respectively.[35, 36]

Fig. 5(a) shows the PL emission spectra of $Ba_{(1-x)}Nb_2O_6$:xDy^{3+} (x= 0.01, 0.1, 0.5, 1.0, 1.5, 2.0, 2.5 mol%) phosphors with different doping concentration of Dy^{3+} ions at 386 nm excitation wavelength. Emission spectra exhibit two intense peaks at 482 and 574 nm and a very weak peak at 664 nm corresponding to the $^4F_{9/2} \rightarrow {}^6H_{15/2}$, $^4F_{9/2} \rightarrow {}^6H_{13/2}$, and $^4F_{9/2} \rightarrow {}^6H_{11/2}$ transitions, respectively.[35] The $^4F_{9/2} \rightarrow {}^6H_{15/2}$ transition belongs to the magnetic dipole allowed and its intensity does not depend on crystal field of the host.[38] On the other hand, the intensity of the hypersensitive transitions (ΔL=2; ΔJ=2) correspond to $^4F_{9/2} \rightarrow {}^6H_{13/2}$ belongs to a forced electric dipole transition, which is allowed in case that Dy^{3+} ions are located at the local sites with non-inversion center symmetry.[38-40] In Dy^{3+} doped $BaNb_2O_6$ phosphor, the intensity of yellow emission ($^4F_{9/2} \rightarrow {}^6H_{13/2}$) is stronger than blue ($^4F_{9/2} \rightarrow {}^6H_{15/2}$) that confirms the location of the active ions (Dy^{3+}) in low symmetry environment without the inversion centre in the host. As the radius of Dy^{3+} ions is less than Ba^{2+}, Dy^{3+} ions can easily enter into Ba^{2+} sites having low symmetry. This is in good agreement with the results obtained from XRD analysis.[41] Moreover, the emission spectra of the sample $Ba_{(1-x)}Nb_2O_6$:xDy^{3+} measured at 349, 364, 386 and 399 nm excitations as shown in inset of Fig 5(b). The similar profile of emission lines has been observed with different intensities for each excitation. The emission intensity at 386 nm excitation is considered as optimum as its intensity is higher than the emission intensity observed for other excitation wavelengths. This may be due to relatively higher absorption at that wavelength.

The branching ratio (β) is a critical parameter to calculate the relative intensities of emission lines originating from $^4F_{9/2}$ excited state. The branching ratios for yellow and blue transitions originating from $^4F_{9/2}$ were calculated by taking the integrals under respective emission bands. For all Dy^{3+} ion concentrations, the sum of the branching ratios for the corresponding emission bands $^4F_{9/2} \rightarrow {}^6H_{15/2}$ and $^4F_{9/2} \rightarrow {}^6H_{13/2}$ were found to be unity ($\beta_{482} + \beta_{574}$) suggesting that both the transitions have wide possibility of attaining stimulated emission with higher efficiency.[42] Moreover, it could be noticed that the emission band $^4F_{9/2} \rightarrow {}^6H_{15/2}$ is broadened and also observed that this transition splits into a maximum number of J + ½ Stark components in the blue emission region (450-500 nm), where J is the total angular momentum of electrons.[43, 44]

In Fig. 5(a), the emission intensity increases initially with an increase in concentration of Dy^{3+} ions and reaches to a maximum at x= 0.5 mol% and then gradually decreases beyond 0.5 mol% due to concentration quenching phenomenon. As the doping concentration of Dy^{3+} ions increases, the distance between luminescent centres decreases that increases the possibility of non-radiative energy transfer.[45] The concentration quenching phenomenon resulted mainly by the non-radiative energy transfer among Dy^{3+} ions. In the present system, energy transfer

View Article Online
DOI: 10.1039/C5DT02436F

Published on 27 August 2015. Downloaded by University of California - Santa Barbara on 27/08/2015 11:31:03.

mechanism from one Dy^{3+} ions to another depends on critical distance between Dy^{3+}-Dy^{3+} ions. Hence, the critical distance (R_c) between the adjacent Dy^{3+} ions could be necessary to calculate. According to Blasse[46, 47, 45] the critical distance could be expressed as:

$$Rc \approx 2\left[\frac{3V}{4\pi X_c N}\right]^{\frac{1}{3}}$$

where, V is the volume of unit cell, X_c is the critical/optimised concentration (mole) of the activator ions and N is the number of cations per unit cell. By analyzing the experimental data, the values are found to be V=988.68 Å^3, N =8 and X_c = 0.005. The calculated critical energy transfer distance is 36 Å for the current system. Van Uitert[48] has pointed out energy transfer generally associated with exchange interaction, radiation re-absorption, or multipolar interactions. The exchange interaction is usually accountable for the energy transfer for the forbidden transition and the critical distance of about 5 Å.[47] Since, the distance between adjacent Dy^{3+} ions is larger than 5 Å, as a result the exchange interaction becomes ineffective and multipolar interaction will become important in this case. According to Dexter's theory, when the doping amount of the activator is large enough, the luminescence intensity I and the mole fraction of activator ions x could be related as follows[49, 50]:

$$log(I/x) = -\frac{Q}{3} log\, x + A$$

where, A is a constant and Q represents interaction type between rare-earth ions. If Q=6, 8 and 10, the interaction may be corresponding to the electric dipole-dipole (d-d), dipole-quadrupole (d-q) and quadrupole-quadrupole (q-q) interactions, respectively.[51] Depending on the emission spectra of $Ba_{(1-x)}Nb_2O_6$:xDy^{3+} excited at 386 nm, the correlation between *log(I/x)* and *log(x)* is shown in Fig. 6. The calculated value of Q is 4.95, which is close to 6 discloses that the concentration quenching mechanism in the $BaNb_2O_6$:Dy^{3+} phosphor occurs due to electric dipole-dipole (d-d) interaction.[52, 45]

The radiative emission process explained as that the radiation excites the Dy^{3+} ions to the higher excited levels and then quickly relaxed to the $^4F_{9/2}$ level by non-radiative and radiative transfer from $^4F_{9/2}$ excited level as shown in schematic energy level diagram in Fig. 7. The upward and downward arrows indicate in this figure represent excitation and emission, respectively. The possible non-radiative channels explained in Fig. 7 could be : (i) the possible resonant energy transfer (RET): ($^4F_{9/2}$+$^6H_{15/2}$ → $^6H_{15/2}$+$^4F_{9/2}$) by considering the energy match rule, and (ii) cross relaxation channels (CRC1, CRC2 and CRC3) among Dy^{3+} ions are responsible for de-population of $^4F_{9/2}$ energy level by non-radiative such as ($^4F_{9/2}$+$^6H_{15/2}$→$^6F_{11/2,}$ $^6H_{9/2}$+$^6F_{5/2}$), ($^4F_{9/2}$+$^6H_{15/2}$→$^6F_{9/2}$, $^6H_{7/2}$+$^6F_{5/2}$) and ($^4F_{9/2}$+$^6H_{15/2}$→ $^6F_{1/2}$+$^6F_{11/2}$, $^6H_{9/2}$) for as prepared phosphors.[53, 41, 45]

Further, the luminescence intensity ratio of yellow to blue (*Y/B*) is essential for white-light emission. The calculated *(Y/B)* ratio for the optimized excitation wavelength of 386 nm was found to be close to unity for all doping concentrations. There has been slight variation in the value of the ratio near to unity for other three excitations wavelengths namely, 349, 364 and 399 nm, which confirms excellent stability of the color coordinates against different excitations and concentrations. The intensity ratio being almost constant was attributed to the local environment around Dy^{3+} ions and is invariant with the varying concentration of Dy^{3+} ions.[39]

4.3 CIE chromaticity coordinates

The Fig. 8 shows the CIE chromaticity coordinates for the optimised sample calculated from the emission spectra measured under different excitations. The CIE chromaticity coordinates for optimized phosphor were found to be (0.312, 0.343), (0.319, 0.364), (0.322, 0.339) and (0.312, 0.342) for corresponding excitations 349, 364, 386, 399 nm, respectively and are indicated in Fig. 8. An excellent white-light chromaticity coordinates (0.322, 0.339) were observed for 386 nm excitation and is very close to the standard equal energy white-light point (0.333, 0.333). The CIE chromaticity coordinates under optimized excitation (λ_{ex}=386 nm) for different Dy^{3+} ions concentration is given Table.2. It is interesting to note that the optimized $Ba_{(1-x)}Nb_2O_6$:xDy^{3+} (x=0.5 mol%) phosphor sample exhibited superior white luminescence coordinates compared to different Dy^{3+} doped phosphor hosts such as CaMoO4:Dy^{3+} (0.28, 0.27)[41], $Sr_3Gd(PO_4)_3$:Dy^{3+} (0.25, 0.29)[45], YPO_4:Dy^{3+} (0.36, 0.42)[22] and found to be extremely close to commercial pc-LED (Blue LED+YAG:Ce^{3+}) and National Television System Committee (NTSC) white-light emission having (0.32, 0.32) and (0.310, 0.316), respectively.

The calculated CCT values for Dy^{3+} ions doped $BaNb_2O_6$ phosphors were found to vary between 5689-6373 K and falls in cool-white region. The calculated CCT was 5907 K for optimized concentration (x=0.5 mol%) of $BaNb_2O_6$:Dy^{3+} phosphor, which represents cool-white emission and is very close to "ideal white" region of the chromaticity diagram. The higher value of CCT indicates better visual acuity and greater brightness perception as compared to lower values.[54] The CCT values lie in the cool white-light region signifying the possibility of the phosphor for application in w-LEDs for outdoor illumination.

Using the chromaticity coordinates given in Fig. 8 for optimized concentration of as-prepared phosphor, the color purity was calculated and found to be around 7.89×10^{-2}, 5.39 × 10^{-2}, 5.39 × 10^{-2} and 7.89 × 10^{-2} corresponding to 349, 364, 386, 399 nm excitations wavelengths, respectively. The low value of the color purity indicates the purity for white-light emission.[53, 27] The above-mentioned results indicate that the as-prepared phosphor can be considered as a potential candidate for fabrication w-LEDs based on NUV chips as excitation source.

4.4 Luminescence decay curve analysis

The room-temperature luminescence decay curve has been plotted for $Ba_{(1-x)}Nb_2O_6$:xDy^{3+} (x=0.5 mol %) phosphor and is shown in Fig. 9. It represents the decay curve of $^4F_{9/2}$→ $^6H_{13/2}$ emission for phosphor when excited under 386 nm wavelength. To understand the behaviour of luminescent decay, the decay curve was fitted with different equations and the best fit was observed for bi-exponential equation[55, 56]:

$$I = A_1\, e^{-t/\tau_1} + A_2\, e^{-t/\tau_2}$$

where, I is the luminescence intensity; t is time; τ_1 and τ_2 are the decay time for the exponential component and A_1 and A_2 are the fitting parameter constants, respectively. Thus, the average lifetime in case of bi-exponential fitting can be determined by using equation:[41]

This journal is © The Royal Society of Chemistry 20xx

$$\tau_{avg} = \frac{A_1\tau_1^2 + A_2\tau_2^2}{A_1\tau_1 + A_2\tau_2}$$

The fluorescent lifetime τ_{avg} for $^4F_{9/2}$ level for optimized phosphor sample was found to be ~146.07 µs. Generally, the PL decay curves can be influenced by energy transfer between Dy^{3+} ions. If there is no interaction between the rare-earth ions, the decay curves are usually fitted to a single exponential function. The bi-exponential fitting behaviour shows the possibility of interaction between Dy^{3+} ions in $BaNb_2O_6$ lattice as discussed in the previous sections.

5. Conclusions

Single-phase $BaNb_2O_6:Dy^{3+}$ white-light emitting phosphors were successfully synthesized using solid-state reaction method. The crystallinity and pure phase of the as-prepared phosphors were examined by XRD and Rietveld refinement studies. All the prepared samples exhibited single-phase with orthorhombic structure. The excitation spectra indicate that the phosphors could be effectively excited by NUV LED chips having excitation wavelength of 386 nm. In order to determine the optimized doping concentration of $BaNb_2O_6:Dy^{3+}$ phosphors, the luminescent measurements were carried out. 0.5 mol% of Dy^{3+} has been found to be the optimum doping concentration under different excitation wavelengths. The blue (482 nm) and yellow (574 nm) emission bands corresponding to $^4F_{9/2} \rightarrow {}^6H_J$ (J= 15/2, 13/2) transitions and the value of Y/B ratio close to unity has been successfully achieved. The combination of these emission bands emit white-light and the CIE chromaticity coordinates for the optimized phosphor is (x=0.322, y= 0.339) with CCT value of 5907 K, which is close to the standard white-lamp calorimetric point in cool white region. All the above-mentioned results indicate that the Dy^{3+} ions doped $BaNb_2O_6$ phosphor could be used as a practical potential luminescent material for NUV based w-LED applications.

Acknowledgements

The author (M. Jayasimhadri) is grateful to DST-SERB, Govt. of India for the sanction of a research project (No. SB/FTP/PS-082/2014, dt. 02/03/2015).

References

1. M. Zhang, Y. Liang, R. Tang, D. Yu, M. Tong, Q. Wang, Y. Zhu, X. Wu, G. Li, *RSC Adv.*, 2014, **4**, 40626-40637.
2. H. Qian, J. Zhang, L. Yin, *RSC Adv.*, 2013, **3**, 9029-9034.
3. S. H. Park, K. H. Lee, S. Unithrattil, H. S. Yoon, H. G. Jang, W. B. Im, *J. Phys. Chem. C*, 2012, **116**, 26850-26856.
4. Y. Uchida, T. Taguchi, *Opt. Eng.*, 2005, **44** (12), 124003-9.
5. H. S. Jang, W. Im Bin, D. C. Lee, D.Y. Jeon, S. S. Kim, *J. Lumin*., 2007, **126** (2), 371−377.
6. S. Nakamura, S. Pearton, G. Fasol. *The Blue Laser Diode- the complete story*, 1997, Springer- Verlag Berlin Heidelberg GmbH, pp. 230-231.
7. J. K. Sheu, S. J. Chang, C. H. Kuo, Y. K. Su, L. W. Wu, Y. C. Lin, W. C. Lai, J. M. Tsai, G. C. Chi, R. K. Wu, *IEEE Photon. Technol. Lett.*, 2003, **15**, 18-20.
8. K. Li, X. Liu, Y. Zhang, X. Li, H. Lian, J. Lin, *Inorg. Chem.*, 2015, **54,** 323-333.
9. T. Jia, Z. Ci, Q. Wu, G. Zhu, C. Wang, Y. Wang, *ECS J. Solid State Sci. Technol.*, 2015, **4**(5), R78-82.
10. J. McKittrick, L. E. Shea-Rohwer, *J. Am. Ceram. Soc*., 2014, **97**, 1-26.
11. M. Shang, C. Li, J. Li, *Chem. Soc. Rev.***,** 2014, **43**, 1372-1386.
12. H. Zhu,Z. Zheng, X. Gao, Y. Huang, Z. Yan, J. Zou, H. Yin, Q. Zou, S. H. Kable, J. Zhao, Y. Xi, W. N. Martens, R. L. Frost, *J. Am. Chem. Soc.*, 2006, **128**, 2373-2384.
13. P. W. C. Sarvezuk, E. J. Kinast, C. V. Colin, M. A. Gusmao, J. B. M. da Cunha, O. Isnard, *J. Appl. Phys.*, 2011, **109**, 07E160-3.
14. D. V. D. Voort, J. M. E. De Rijk, G. Blasse, *Phys. Stat. Sol.*, 1993, **135**, 621-626.
15. F. Huang, Q. Zhou, C. Ma, L. Li, X. Huang, F. Li, Q. Cui, D. Xu, W. Wang, T. Cui, G. Zou. *RSC Adv.*, 2013, **3**, 13210-13213.
16. S. Lei, D. Guo, C. Wang, D. Cheng, X. Gao, S. Zeng, Y. Xiao, B. Cheng, *Cryst. Engg. Comm.*, 2014, **16**, 7949-7955.
17. R. C. Pullar, J. D. Breeze, N. M. Alford, *J. Am. Ceram. Soc.*, 2005, **88** (9), 2466-2471.
18. A. K. Vishwakarma, K. Jha, M. Jayasimhadri, A. S. Rao, K. Jang, B. Sivaiah, D. Haranath, *J. Alloys Compd.*, 2015, **622**, 97-101.
19. Y. Zhou, Z. Qui, M. Lu, Q. Ma, A. Zhang, G. Zhou, H. Zhang, Z. Yang, *J. Phys. Chem. C*, 2007, **111,** 10190-10193.
20. M. K. Ekmekci, M. Erdem, A. S. Basak, *Dalton Trans.***,** 2015, **44**, 5379-5385.
21. M. K. Ekmekci, M. Erdem, A. Mergen, G. Ozen, B.D. Bartolo, *J. Alloys. Compd.***,** 2014, **591**, 230-233.
22. **A.**K. Parchur, A. I. Prasad, S. B. Rai and R. S. Ningthoujam, *Dalton Trans.*, 2012, **41**, 13810-13814.
23. M. Jayasimhadri, B. V.Ratnam, K. Jang, H. S. Lee, *Int. J. Appl. Ceram. Technol.*, 2011, **8**, 709-717.
24. K. Mishra, S. K. Singh, A. K. Singh, S. B. Rai, *Mater. Res. Bull.*, 2012, **47**, 1339-1344.
25. S. Dutta, S. Som, S. K. Sharma, *Dalton Trans.*, 2013, **42**, 9654-9661.
26. C. S. McCamy, Color Res. Appl., 1992, **17**, 142-144.
27. E. F. Schubert, *Light emitting Diodes 2nd Ed*., Cambridge University Press Newyork, 2006, pp. 292.
28. V. P. Sirotinkin, S. P. Sirotinkin, *Russ. J. Inorg. Chem.*, 1990, **35**, 1246-1248.
29. B. D. Cullity, *Elements of X-Ray Diffraction*, Addison-Wesley, Massachusetts, 1956, pp. 312.
30. S. Bathula, B. Gahtori, M. Jayasimhadri, S. K. Tripathy, K. Tyagi, A. K. Srivastava, A. Dhar, *Appl. Phys. Lett.,* 2014, **105**, 061902-4.
31. B. P. Singh, A. K. Parchur, R. K. Singh, A. A. Ansari, P.Singh, S. B. Rai, *Phys. Chem. Chem. Phys.*, 2013, **15**, 3480-3489.
32. A. K. Parchur, R. S. Ningthoujam, *Dalton Trans.*, 2011, **40**, 7590-7594.
33. H. M. Rietveld, *J. Appl. Cryst.*, 1968, **2**, 65-71.
34. Y. Zhou, Q. Ma, M. Lu, Z. Qiu, A. Zhang, *J. Phys. Chem. C.*, 2008, **112**, 199901-19907.
35. D. L. Monika, H. Nagabhushana, R. H. Krishna, B. M Nagabhushana, S. C. Sharma, T. Thomas, *RSC Adv.*, 2014, **4**, 38655-38662.
36. E. Pavitra, G. S. R. Raju, W. Park, J. S. Yu, *New J. Chem.*, 2014, **38**, 163-169.
37. B. V. Ratnam, M. Jayasimhadri, K. Jang, H. S. Lee, *J. Am. Ceram. Soc.*, 2010, **93**, 3857-3861.
38. Z. Ci, Q. Sun, S. Qin, M. Sun, X. Jiang, X. Zhang, Y. Wang, *Phys. Chem. Chem. Phys.***,** 2014, **16**, 11597-11602.
39. Q. Su, Z. Pei, L. Chi, H. Zhang, Z. Zhang, F. Zou, *J. Alloys Compd.*, 1993, **192**, 25-27.
40. J. L. Fry, H. H. Caspers, H. E. Rast, S. A. Miller, *J. Chem. Phys.*, 1968, **48**, 2342-2348.

View Article Online
DOI: 10.1039/C5DT02436F
Published on 27 August 2015. Downloaded by University of California - Santa Barbara on 27/08/2015 11:31:03.

View Online
DOI: 10.1039/C5DT02436B

41. S. Dutta, S. Som, S. K. Sharma, *Dalton Trans.*, 2013, **42**, 9654-9661.
42. M. Jayasimhadri, K. Jang, H. S. Lee, B. Chen, S. S. Yi, J. H. Jeong, *J. Appl. Phys.*, 2009, **106**, 013105-4.
43. G. H. Dieke, S. Singh, *J. Opt. Soc. Am.*, 1956, **46** (7), 495-499.
44. B. Liu, C. Shi, *Appl. Phys. Lett.*, 2005, **86**, 191111-3.
45. Q. Liu, Y. Liu, Z. Yang, Y Han, X. Li, G. Fu, *J. Alloys Compd.*, 2012, **515**,16-19.
46. G. Blasse, *Philips Res. Rep.*, 1969, **24** (2), 131-144.
47. Q. Xu, J. Sun, D. Cui, Q. Di, J. Zeng, *J. Lumin.*, 2015, **158**, 301-305.
48. L. G. Van Uitert, *J. Electrochem. Soc.* 1967, **114**, 1048-1053.
49. D. L. Dexter, *J. Chem. Phys.*, 1953, **21**, 836-850.
50. D. L. Dexter, J. H. Schulman, *J. Chem. Phys.*, 1954, **22**, 1063-1070.
51. H. Li, R. Zhao, Y. Jia, W. Sun, J. Fu, L. Jiang, Su. Zhang, R. Pang, C. Li, *Appl. Mater. Interfaces,* 2014, **6**, 3163-3169.
52. L. Zhang, H. Zhong, X. Li, L. Cheng, Li. Yao, J. Sun, J. Zhang, R. Hua, B. Chen, *Physica B*, 2012, **407**, 68-72.
53. J. S. Kumar, K. Pavani, A. M. Babu, N. K. Giri, S. B. Rai, L. R. Moorthy, *J. Lumin.*, 2010, **130**, 1916-1923.
54. M. R. N. Soares, M. J. Soares, A. J. S. Fernandes, L. Rino, F. M. Costa, T. Monteiro, *J. Mater. Chem.*, 2011, **21**, 15262-15265.
55. B. C. Jamalaiah, J. S. Kumar, A. M. Babu, L R. Moorthy, K. Jang, H. S. Lee, M. Jayasimhadri, J. H. Jeong, H. Choi, *J. Lumin.*, 2009, **129**, 1023-1028.
56. M. Jayasimhadri, L. R. Moorthy, R. V. S. S. N. Ravikumar, *Opt. Mater.*, 2007, **29**, 1321-1326.

Tables

Table 1. Calculated crystallographic data of $BaNb_2O_6$ by Rietveld refinement method.

Formula	$BaNb_2O_6$
Radiation	Cu Kα
2 θ (°)	20-60
Symmetry	Orthorhombic
Space group	$C222_1$ (20)
a(Å)	7.8707
b(Å)	12.2096
c(Å)	10.2881
α (°)	90
β (°)	90
γ (°)	90
Z	8
R_p	25.6
R_{wp}	31.0
X^2	4.2
V($Å^3$)	988.680
Density (mg/m^3)	5.62

Table 2. Y/B ratio, CIE chromaticity coordinates and CCT for $BaNb_2O_6:Dy^{3+}$ phosphors at various doping concentrations.

λ_{ex}=386 nm			
X (Dy^{3+} concentration in mol%)	**Y/B ratio**	**(*x*, *y*)**	**CCT (K)**
0.01	1.11	(0.329, 0.339)	5689
0.10	1.06	(0.322, 0.338)	6000
0.50	1.01	(0.322, 0.339)	5907
1.00	1.05	(0.314, 0.341)	6373
1.50	1.06	(0.320, 0.340)	6056
2.00	1.11	(0.331, 0.332)	5623
2.50	1.07	(0.312, 0.319)	6652

Figures

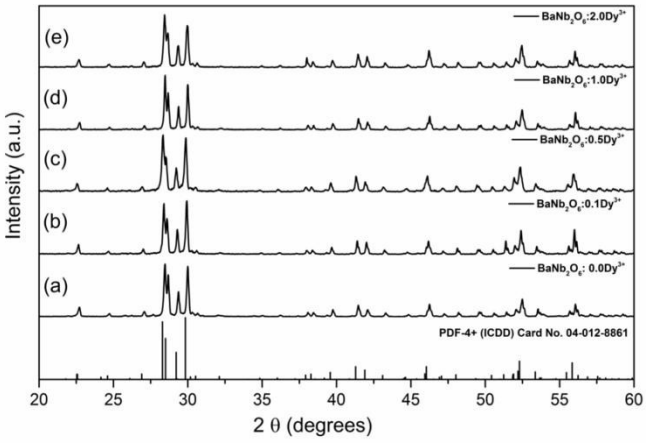


Fig. 1: Powder XRD patterns of $Ba_{(1-x)}Nb_2O_6:xDy^{3+}$ (x=0.0, 0.1, 0.5, 1.0, 2.0 mol%) phosphors.

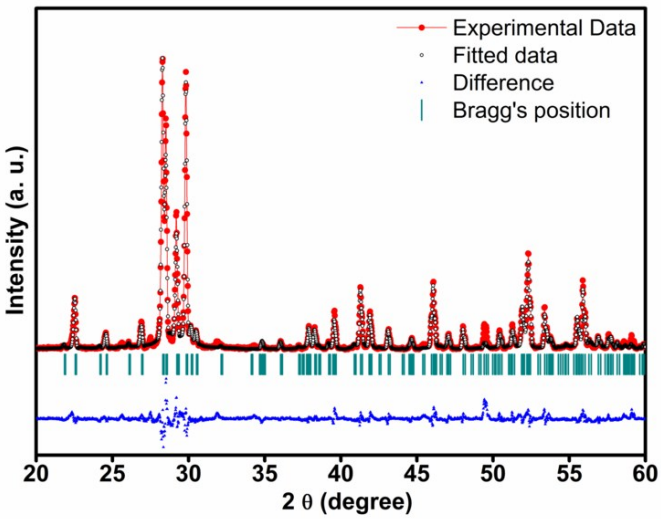


Fig. 2(a): Experimental, calculated and difference in X-ray diffraction pattern of $BaNb_2O_6$ powder.

Published on 27 August 2015. Downloaded by University of California - Santa Barbara on 27/08/2015 11:31:03.

This journal is © The Royal Society of Chemistry 20xx

View Article Online
DOI: 10.1039/C5DT02436F

Published on 27 August 2015. Downloaded by University of California - Santa Barbara on 27/08/2015 11:31:03.

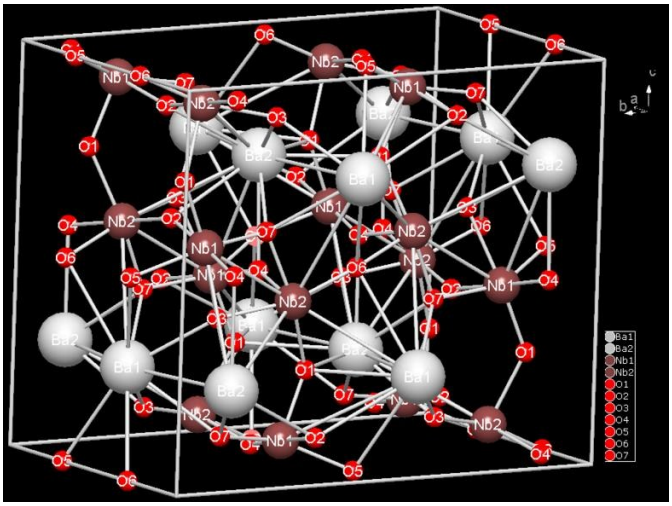


Fig. 2(b): Crystal structure of $BaNb_2O_6$ in b-c plane.

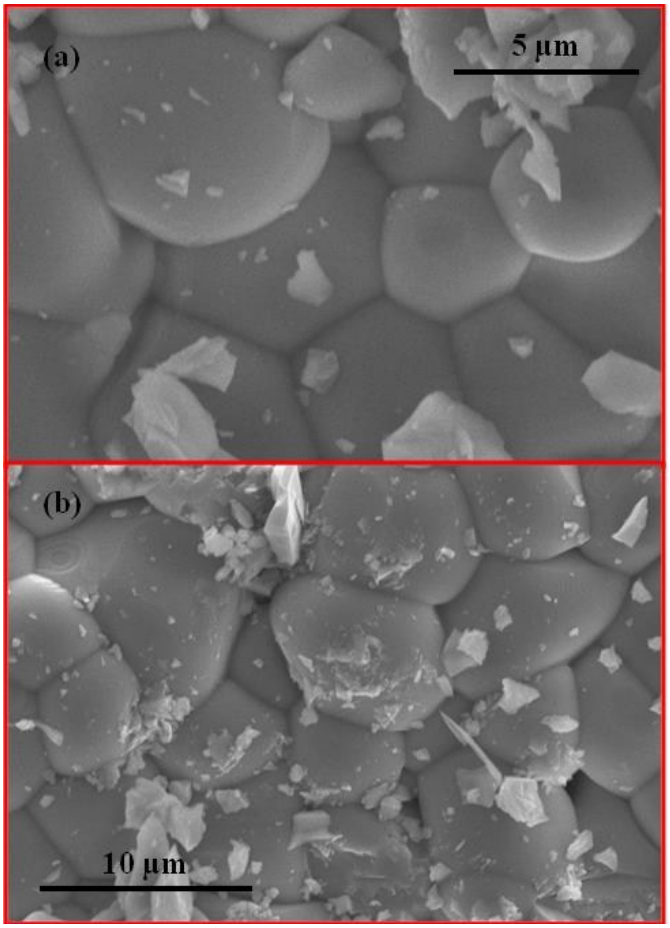


Fig. 3: (a & b). SEM micrographs of $Ba_{(1-x)}Nb_2O_6:xDy^{3+}$ (x=0.5 mol%) phosphor sintered at 1200°C.

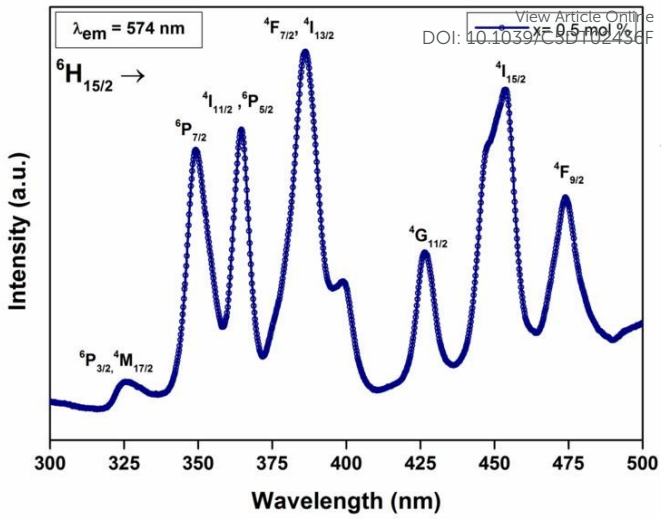


Fig. 4: Photoluminescence excitation spectra (λ_{em}=574 nm) of $Ba_{(1-x)}Nb_2O_6:xDy^{3+}$ (x=0.5 mol%) phosphor.

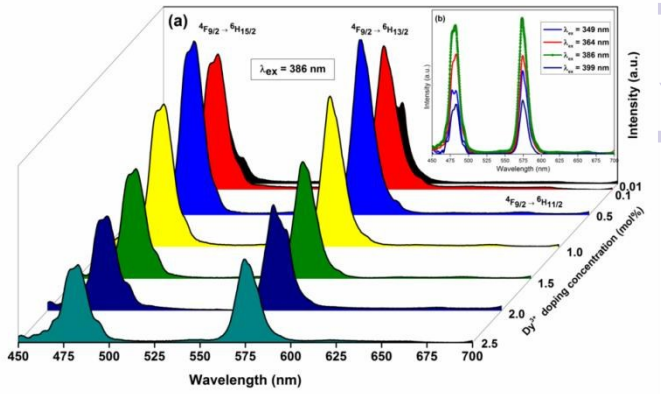


Fig. 5: (a) Emission spectra (λ_{ex}=386 nm) of $BaNb_2O_6:Dy^{3+}$ phosphor at different mol% concentration of Dy^{3+} ions. **(b)** emission spectra of $Ba_{(1-x)}Nb_2O_6:xDy^{3+}$ (x=0.5 mol%) phosphor at different excitations (λ_{ex}=349, 364, 386, 399 nm) (in inset).

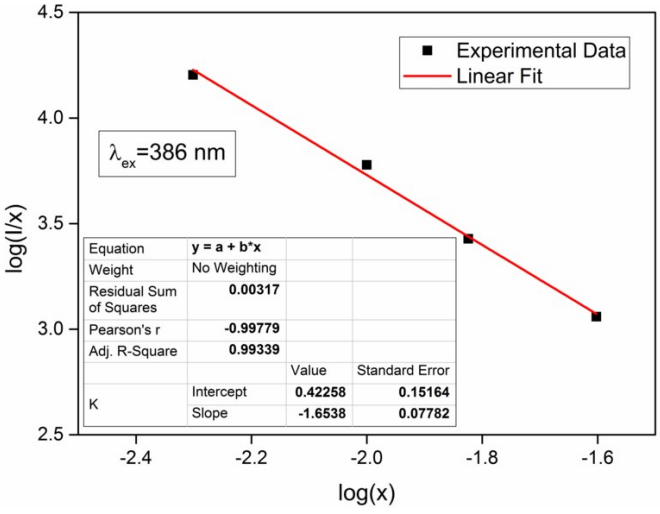


Fig. 6: Relationship of log(I/x) with log(x) in $BaNb_2O_6:Dy^{3+}$ phosphor under 386 nm excitation

View Article Online
DOI: 10.1039/C5DT02484H

Published on 27 August 2015. Downloaded by University of California - Santa Barbara on 27/08/2015 11:31:03.

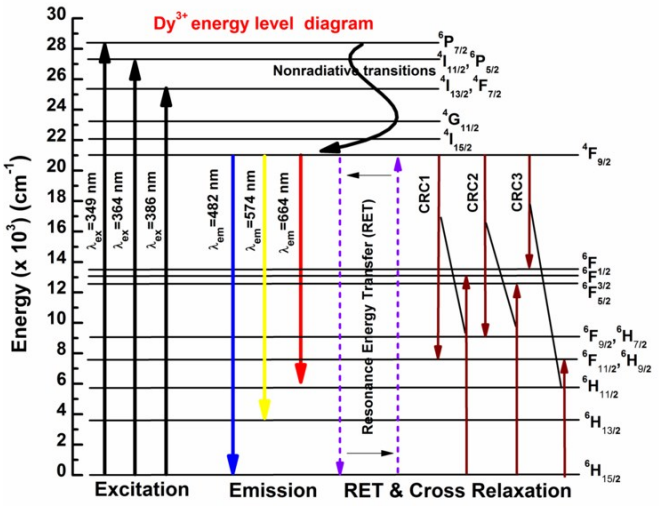


Fig. 7: Partial energy level diagram illustrating excitation, emission and energy transfer mechanisms of Dy^{3+} ions in $BaNb_2O_6$ phosphors.

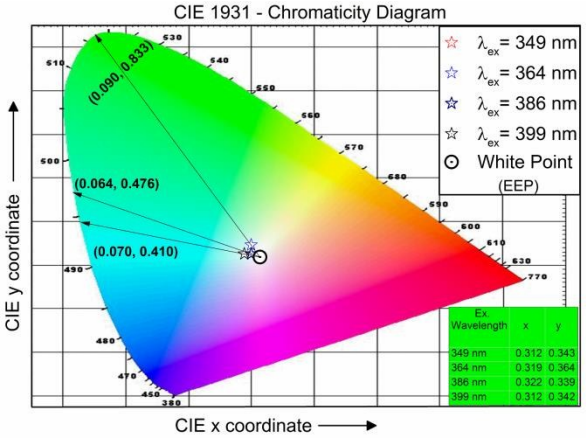


Fig. 8: CIE chromaticity diagram for Dy^{3+} ions doped $BaNb_2O_6$ phosphor.

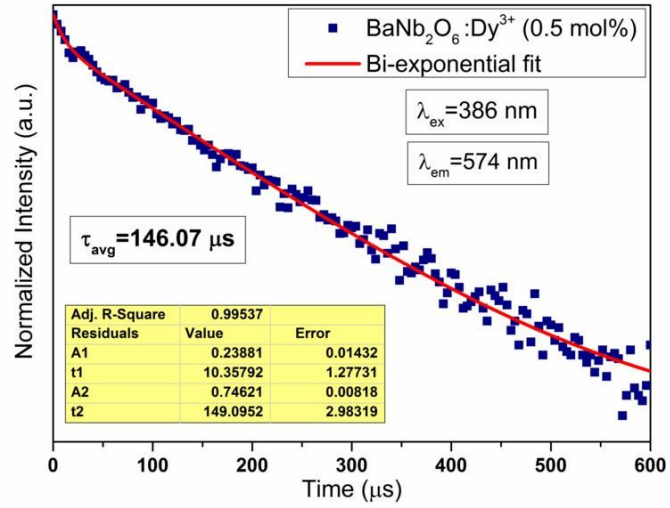


Fig. 9: Luminescence decay curve (λ_{em}=574 nm) of $Ba_{(1-x)}Nb_2O_6$:xDy^{3+} (x=0.5 mol%) phosphor under 386 nm excitation.

This journal is © The Royal Society of Chemistry 20xx

ResearchGate

See discussions, stats, and author profiles for this publication at: http://www.researchgate.net/publication/280383466

Magnetic adsorbents for the treatment of water/wastewater—A review

ARTICLE *in* JOURNAL OF WATER PROCESS ENGINEERING · JULY 2015

DOI: 10.1016/j.jwpe.2015.07.001

CITATIONS
2

READS
121

3 AUTHORS, INCLUDING:



S. K. Singh
Delhi Technological University
79 PUBLICATIONS **91** CITATIONS

SEE PROFILE

Available from: S. K. Singh
Retrieved on: 13 November 2015

Journal of Water Process Engineering 7 (2015) 244–265

Contents lists available at ScienceDirect

Journal of Water Process Engineering

journal homepage: www.elsevier.com/locate/jwpe

Magnetic adsorbents for the treatment of water/wastewater—A review

Dhruv Mehta[a,*], Siddharth Mazumdar[b], S.K. Singh[a]

[a] Department of Environmental Engineering, Delhi Technological University, New Delhi 110042, India
[b] Depart of Civil Engineering, Birla Institute of Technology and Science, Rajasthan 333031, India

ARTICLE INFO

Article history:
Received 27 January 2015
Received in revised form 3 July 2015
Accepted 6 July 2015

Keywords:
Adsorption
Magnetic Adsorbents
Review
Water
Wastewater

ABSTRACT

In recent years, adsorption has displayed promising and effective results as a treatment technology for water and wastewater by industries. In the process, a number of adsorbents have been synthesized and applied for the treatment of pollutants such as metals, dyes, pharmaceutical products in solutions. However, for adsorption to be unconditionally adopted by industries, a few obstacles such as high capital cost, difficult segregation of adsorbent from solution, and complex synthesis processes need to be addressed. The removal of suspend adsorbents in wastewater from a continuous flow system is a challenge which if addressed properly would enable us to recover the spent adsorbent efficiently. The spent adsorbents can then be regenerated and used again by the industries thereby leading to reduced capital investment. Therefore, studies have been carried out aiming at the incorporation of magnetism in such adsorbents to aid their removal from wastewater. This review aims to comprehensively list and discuss adsorbents which exhibit magnetic properties and their adsorption behaviour under diverse conditions. The literature survey presented in this paper renders evidence to the good potential of magnetic adsorbents to remove various pollutants from wastewater. However, the practical utility of such adsorbents needs to be explored before they can be commercially applied.

© 2015 Elsevier Ltd. All rights reserved.

Contents

1. Introduction 245
2. Magnetic adsorbents 245
 2.1. Sorption of Anions 245
  2.1.1. Arsenic 245
  2.1.2. Chromium 247
  2.1.3. Phosphorous 248
  2.1.4. Different anionic species 248
 2.2. Sorption of cations 248
  2.2.1. Cadmium 248
  2.2.2. Copper 251
  2.2.3. Fluoride 252
  2.2.4. Lead 253
  2.2.5. Mercury 254
  2.2.6. Different cationic species 254
 2.3. Sorption of dyes 255
  2.3.1. Same type of dye 255
  2.3.2. Different type of dyes 257

* Corresponding author.
E-mail address: dhruv.meh19@gmail.com (D. Mehta).

http://dx.doi.org/10.1016/j.jwpe.2015.07.001
2214-7144/© 2015 Elsevier Ltd. All rights reserved.

2.4. Sorption of organic pollutants 261
3. Conclusion 262
References 262

1. Introduction

Water is an essential source for maintaining life on this planet. Even though it is available in abundance, the chemical composition varies across the strata, thus affecting its suitability for domestic as well as industrial purposes. Groundwater accounts for only 0.6 % of the total available water resources [1]. It is this 0.6% which caters to the global water needs. However, with the onset of rapid industrialization, the quality of drinking water has reduced significantly. Discharge of industrial effluent, solid waste from households and industries etc., are responsible for the increasing levels of groundwater pollution. Hence to treat water, several techniques such as membrane separation process [2–4], coagulation and flocculation [5–6], filtration [7–10], adsorption [11–16], chemical treatment [17–18] have been developed.

Adsorption is a surface boundary phenomenon of accumulation of species onto a liquid or solid phase from a bulk phase. It is a phenomenon which has been observed since ancient times. Current available literature dates it back to 1773 when Scheele carried out adsorption experiments of the uptake of gases by charcoal and clay [19]. Since then, the field of adsorption has witnessed a lot of research. Some significant contributions to this field were the development of isotherm models by Langmuir [20] and Freundlich [21] and the kinetic models developed by Lagregren [22] and Ho [23]. Today, adsorption plays an important role in the industrial processes. Higher efficiency and insensitivity to toxic substances compared to the other conventional methods of water purification has made it much more popular.

Some adsorbents which have been widely used for water purification are activated carbon [24–31], silica gel [32–36], zeolite [37–43], clay minerals [44–47]. However due to their high generation costs, researchers shifted their focus to the use of dead biomass and waste such as peanut shell [48], garden grass [49], ground coffee [50], saw dust [51–52], sunflower leaves [53], egg shells [54], almond shell [55] sugarcane bagasse [56], Anabaena sphaerica [57], Bacillus laterosporus [58], green algae [59], orange peel [60], pine cone [61], guava leaf [62] for the removal of dyes, metals and organic pollutants from wastewater. Agricultural waste as adsorbents presents us with an attractive option due to their low cost and high abundance. Numerous studies have been conducted to develop cheaper effective adsorbents containing natural biopolymers. Even though these adsorbents have proved to be very effective in the removal of pollutants from wastewater, they suffer one inherent disadvantage. It is difficult to separate them from wastewater in a continuous flow system. Hence, studies have been conducted to explore the use of magnetism as an effective means of separating these suspended adsorbents from water.

The use of magnetism for water purification is an age old concept. Available texts predate the use of magnetism for water treatment to as early as 1873 [63]. Since then magnetism has been employed in various water treatment methods such as anti scaling technique in boilers, pipelines in factories [64–67], coagulation [68], biological processes [69–70]. The use of magnetism in an adsorption process is a relatively newer concept; one which is gathering increasing attention from the researchers day by day. Magnetic adsorbents are a new class of adsorbents where a base adsorbent is embedded with magnetic particles which are oxides of metals such as Fe, Co, Ni and Cu [71]. On application of an external magnetic field, the magnetic adsorbent can be rapidly and easily separated from water due to the presence of the metal component in the adsorbent. Magnetic ion exchange resins (MIEX) were first used for the removal of natural organic matter in 1995 [72]. Since then magnetic particles modified with polymer [73–74], carbon nanotubes [75] etc., have been used commercially.

This review focuses on the use of various magnetic adsorbents for the removal of pollutants from wastewater. A summary of the data published pertinent to the topic is presented and the results of these findings have been discussed. At the end, the results (relating to pH, adsorption capacity, isotherms, and kinetics) have been compiled in the form of a table. For more information, the readers are advised to refer to the full articles that are listed in the References

2. Magnetic adsorbents

2.1. Sorption of Anions

2.1.1. Arsenic

Arsenic is a toxic carcinogen present in drinking water predominantly as As (III) (H_3AsO_3, $H_2AsO_3^-$, and $HAsO_3^{2-}$) and As (V) (H_3AsO_4, $H_2AsO_4^-$, and $HAsO_3^{2-}$) [76]. These oxides are difficult to destroy and can be only transformed into insoluble compounds. Chronic exposure to arsenic contaminated water can cause serious medical complications such as loss of appetite, cancer of skin, lungs and bladder [77]. Hence in order to minimize the health risk, the World Health Organization (WHO) has set 10 μg/L as the maximum limit of arsenic that can be present in drinking water. Removal of arsenic from industrial wastewater has recently gained a lot of attention. Numerous investigations have been performed on the study of magnetically treated adsorbents and their capability to remove arsenic from water.

Shan and Tong [78] fabricated Mag–Fe–Mn containing 46.1% Fe and 9.2% Mn by weight .Batch experiments were carried out and the adsorption isotherms of Mag-Fe-Mn, Mag-Mn, Mag-Fe, Mag-core were examined and it was found that the four adsorbents followed freundlich model better which was possible due to the irreversible adsorption and heterogeneous nature of adsorbents. Langmuir adsorption capacity of Mag-Fe-Mn was nearly twice that of the other adsorbents. The authors studied the effect of pH on the removal efficiency of the adsorbent. Removal percentage of As(III) remained above 95% in the pH range of 4–8. At pH > 8, enhanced electrostatic repulsion due to deprotonation of arsenic species, negative zeta potential of Mag–Fe–Mn particles and the potential competition from the hydroxyl ion were responsible for the decreased removal of arsenic.

Kilianová et al. [79] used ultrafine Fe_2O_3 particles as an adsorbent for removal of arsenate ions from an aqueous solution. The authors found all As(V) was removed when the pH was in acidic range. This corresponded well with the zeta potential of the adsorbent which was equal to 7.6. 100% efficiency was achieved between pH of 5 and 7.6, and Fe/As ≈ 20/1. Arsenic removal at equilibrium was found to be 45 mg/g. Binary oxides of chitosan were synthesized by template method for removal of arsenite from water [80]. No effect of pH was observed in the range of 3–9 and reduced thereafter. The adsorption capacity obtained from the Langmuir model was 16.94 mg/g. Presence of Ca^{2+} and Mg^{2+} significantly affected the performance of the adsorbent. Field trials reduced the initial As(III) concentration from 983.71 μg/l to7.44 μg/l. Luo et al. [81] studied the interaction of arsenic ions with Fe_3O_4–RGO–MnO_2 nanoparticles where RGO is Reduced Graphite Oxide, over the entire pH range; with initial arsenic concentration ranging from

0.01 to 10 mg/L. The authors noted that the adsorption capacity decreased slightly in the pH range of 2–10 and rapidly after pH of 10. Adsorption of As(V) at low pH was due to electrostatic attraction of positive sites on Fe_2O_3–RGO–MnO_2 and the negative charge due to As(V). As(III) ions were converted to As(V) by MnO_2 before their adsorption. Adsorption experiments revealed that the data obtained fitted the Langmuir isotherm model accurately. It was seen that the maximum adsorption capacity of Fe_3O_4–RGO–MnO_2 (3:8) was 14.04 mg/g for As(III) and 12.22 mg/g for As(V) which was higher than adsorption capacities of Fe_3O_4–RGO–MnO_2 (3:4) and Fe_3O_4–RGO–MnO_2 (3:12). Groundwater samples with initial arsenic concentration of 1 mg/L were treated by Fe_3O_4–RGO–MnO_2 nanocomposites with a dosage of 0.5 mg/L. The residual concentration was noted to be 3 μg/l for both As(III) and As(V).

The adsorption capability of γ-Fe_2O_3 was combined with the photocatalytic ability of TiO_2 to form a superparamagnetic binary oxide γ-Fe_2O_3–TiO_2 by Yu et al. [82]. The adsorbent was able to achieve 99.82% removal efficiency with initial As(III) of 1.01 mg/L, contact time 3 h, and pH 3 under the presence of UV light. Under the same conditions 35.56% removal efficiency was achieved by γ-Fe_2O_3.Maximum arsenic removal capability of 33.33 mg/g was observed at solution pH of 7. The authors stated that γ-Fe_2O_3 has higher adsorption capacity for As(V) than As(III). In case of γ-Fe_2O_3–TiO_2 under the presence of UV light, TiO_2 was able to oxidise As(III) into As(V) which was then adsorbed on the available sites of γ-Fe_2O_3. While in case of γ-Fe_2O_3, little As(III) was oxidized to As(V) and hence low removal efficiency of As(III) was observed. Phosphate ions were the greatest competitor with arsenic for active sites on the adsorbent's surface. Sikder et al. [83] impregnated iron onto a chitosan-carbxymethyl β-cyclodextrin complex to form beads having a high affinity for arsenic. The pore size distribution was 3.5–8.7 μm and was responsible for mass transfer between adsorbent and wastewater. The removal rates of As(III) and As(IV) increased with increasing iron loading on the adsorbent surface. Fe^0 oxidized to Fe(III), over a wide range of pH, making the adsorbent surface positively charged and establishing electrostatic attraction between the adsorbent and the adsorbate. The Langmuir capacities of As(III) and As(V) at room temperature were 18.51 mg/g and 13.51 mg/g, respectively.

Boron nitride nanotubes (BNNTs) [84] functionalized with Fe_3O_4 particles had an optimal removal capacity of 0.96 mg/g at pH 9. Strong adsorption at pH > pH_{pzc} suggested adsorption was through surface complexation. Adsorption of As(V) occurred via ligand exchange, where the arsenate oxyanion replaced the hydroxyl ions in the iron lattice without disturbing the crystal structure of the compound. Fe_3O_4 modified with cetyltrimethylammonium bromide (CTAB) enhanced the adsorption capacity of Fe_3O_4@CTAB from 7.59 mg/g to 23.07 mg/g [85]. Two site Langmuir model and the Freundlich model captured the trend of the experimental results. The authors concluded that two types of adsorption sites were present; one was Fe_3O_4 particles and the other was CTAB anchored on the magnetic surface. The influence of pH was studied in the range of 3–11 and maximum adsorption rate of 95% was observed at pH < 6. This is because the zeta potential of Fe_3O_4@CTAB was 6.4 Therefore at pH < 6, the positively charged adsorbent could attract the negatively charged arsenic specie $H_2AsO_4^-$. Above pH 6, the adsorbent surface became negatively charged thereby decreasing the adsorbent rate till 90% at pH. With further increase in pH due to the strong repulsion between the similarly charged adsorbent surface and As(V) specie in the solution, the adsorption rate decreased till 27%.

Fe_3O_4 modified with ascorbic acid exhibited higher surface area (178.48 m^2/g) compared to Fe_3O_4 particles (15.63 m^2/g) [86]. The arsenic removal rate decreased from 45% to less than 15% as pH increased above 7. The zeta potential changed from positive to negative as the pH rose above 7, thus decreasing the adsorption of negatively charged arsenic species. Zhang et al. [87] investigated the potential of biochar as a magnetic adsorbent by embedding γ-Fe_2O_3 particles into the biochar matrix. Studies of the hysteresis loop showed that the sample exhibited ferromagnetic properties. Adsorption isotherms of As(V) to biochar/γ-Fe_2O_3 were determined by mixing 0.1 g biochar/γ-Fe_2O_3 with 50 mL arsenic solutions of different concentrations ranging from 5 to 200 mg/L in the digestion vessels. The isotherm data was better described by the Langmuir model. The Langmuir maximum adsorption capacity of the biochar/γ- Fe_2O_3composite to As(V) is 3147 mg/kg.

Akin et al. [88] synthesized magnetic Fe_3O_4-NPs nanoparticles using red mud and studied the effect of the nanoparticles for arsenate As(V) removal. The adsorption experiments were carried out on aqueous solutions with As(V) concentrations ranging between 10 and 1000 μg/l. As(V) removal was noted to be pH dependent and the maximum removal occurred at pH of 2.5. The adsorption mechanism was better explained by the Freundlich model. Furthermore the authors noted that in other similar studies, adsorption capacity was found to be more due to a higher adsorbent particle size and initial As(V) concentration. The prepared adsorbent was used to test the removal of arsenic from natural groundwater samples which contained 1570 μg/l of As(V) and 280 μg/l of As(III). Maximum adsorption efficiency for As(V) at optimum conditions was noted to be 99.2%. The residual As(V) concentration was found to be 12.56 μg/l. The authors proposed a use of two stage adsorption process for use in drinking water treatment. Magnesium was doped into α-Fe_2O_3 crystals by Tang et al. [89] to form cubic spinel magnesium ferrite. The ultrafine $Mg_{0.27}Fe_{2.5}O_4$nanoadsorbent had a large BET specific surface area of 438.2 m^2/g, and demonstrated a superior arsenic adsorption performance on both As(III) and As(V). The adsorption capacities on As(III) and As(V) were found to be more than 127 mg/g and 83 mg/g, respectively.The arsenic adsorption on the ultrafine $Mg_{0.27}Fe_{2.5}O_4$nanoadsorbent followed the inner sphere complex mechanism, and abundant surface hydroxyl groups played the major role in its superior arsenic adsorption performance. 98 % arsenic removal was observed from natural water samples having initial As(III) and As(V) concentration of 0.044 mg/L and 0.071 mg/L, respectively.

Copper ferrite manufactured from sludge of printed circuit board (PCB) industry was tested for arsenic removal [90]. The authors concluded that arsenic removal decreased with increasing pH and the maximum adsorption capacity was 45.66 mg/g at pH 3.7 and decreased to zero at pH of 11.2. The variation in removal capacity at different pH was attributed to the protonation of the adsorbent surface at acidic pH and formation of negatively charged surface at alkaline pH. The pH_{zc} was found to be 7.3. The adsorbent could be recovered in 20 s using a magnet. In the field trials, arsenic concentration was brought down to 4.2 μg/l from concentration range 31.6–89.3 μg/l. Liu et al. [91] produced a Fe_3O_4 loaded activated carbon using pinewood sawdust. The maximum adsorption occurred at pH of 8 and the maximum Langmuir adsorption capacity was 204.2 mg/g. Adsorption increased with rising pH, however beyond pH of 8, with further increase, adsorption decreased. This was due to the electronic repulsion between the adsorbent and arsenate species above the pH_{zc} which was 7.05. The author concluded that the chemical interaction between the adsorbent and arsenate species dominated the effects of high surface area of the adsorbent.

Fe_3O_4 particles were grown on the surface of wheat straw by Tian et al. [92] and investigated for the removal of arsenic from water. Wheat straw provided the necessary surface for iron loading and itself had no impact on the adsorption mechanism. Adsorption capacity increased with increasing iron content on the wheat straw and the experimental data followed the Langmuir model. Adsorption capacity for As(III) was found to be highest between pH 7–9 which was explained by the surface complexa-

tion model. The adsorbent could be regenerated after 10 cycles of adsorption.

2.1.2. Chromium

Water pollution by Chromium is an increasing problem due to the heavy metals' use in various industries like chrome plating, dyes, battery, leather tanning etc. The more toxic form of Chromium is the hexavalent form, Cr(VI), which can lead to diseases like cancer, epigastric pain and nausea upon strong exposure [93]. The US Environmental Protection Agency (EPA) has capped Cr (VI) discharge into wastewater at 0.5 mg/L and total Cr at 2 mg/L [94]. Therefore, Cr(VI) should be removed efficiently from industrial effluent before it is discharged into the soil and water so that groundwater isn't contaminated.

Magnetic beads constituting Rhizopuscohniialginate were able to remove 100% Cr(VI) from wastewater at pH 1 and 4 h of contact time [93]. Adsorption increased with rising temperature and the Langmuir adsorption capacity at room temperature was 5.79 mg/g. Groups of $-NH_3^+$, $-NH_2^+$and —NH— were the preponderant sorption sites in the Cr(VI) biosorption. Li et al. [95] synthesized a magnetic cyclodextrin- chitosan/graphene oxide (CCGO) to study the adsorption behaviour of Cr (VI) in an aqueous solution. The TEM images showed that the magnetic β-cyclodextrin -chitosan spheres were anchored on the surface of GO layers. Adsorption was favourable at pH lower than 6.8 due to the existence of dominant $HCrO_4^-$ specie which was attracted to the positively charged adsorbent surface. At pH more than 6.8, the higher concentration of OH^- ions competed with Cr(VI) for active sites on the adsorbent surface. The adsorption isotherms fitted the Langmuir model with maximum adsorption capacity of 67.66 mg/g. CCGO kept its structure intact after 5 adsorption–desorption cycles and a 5% decrease in adsorption was observed. The decrease was because (1) Cr(VI)-adsorbed CCGO could not completely be desorbedfrom cavities of cyclodextrin. With the increase of adsorbed Cr (VI) remaining on cavity of cyclodextrin, the adsorption capacity decreased. (2) Cr(VI) was partially reduced into Cr(III) by the surface hydroxyl group on CCGO. At lower pH, some Cr(III) was precipitated on the surface of the CCGO in the form of Cr_2O_3. With the increase of Cr_2O_3 remaining on CCGO, the active sites decreased, causing less Cr (VI) adsorbed by the used CCGO.

Graphene oxide used as a base to impregnate Fe_3O_4 particles could remove 85% Cr(VI) at neutral pH, in 5 min [96]. Magnetic chitosan particles were prepared by Thinh et al. [97]. Optimal conditions for Cr(VI) removal were found to be at pH of 3 and contact time of 100 min. The maximum adsorption capacity was 55.8 mg/g. The Langmuir model was found to fit well with the experimental data. Nanocomposites (MCNC) of chitosan and $MnFe_2O_4$ could remove Cr(VI) from low concentration aqueous solutions (0.6–1 mg/L) [98]. Ram spectra indicated the presence of chitosan and $MnFe_2O_4$ in MCNC. Chitosan was chelated to the metal ions. Maximum removal efficiency was achieved at pH 5, agitation time 12 h, temperature 300 K. MCNC showed high Cr(VI) removal capacity of 35.2 mg/g and the process obeyed Freundlich isotherm model.

A study was carried out to investigate the applicability of magnetically modified PS-EDTA resin for removal of chromium from water [99]. Highest uptake capacities of the resin were observed in the pH range of 3–4. The effect of pH was due to protonation of the NH_2 group and the Fe_3O_4 nanoparticles. The maximum uptake of 99.3% was achieved within 8 h while equilibrium was achieved in 5 h. The shorter time period to attain equilibrium and higher uptake suggests high affinity for Cr(VI). The adsorption capacity of the resin increased rapidly initially and slowly after the concentration of Cr was more than 100 mg/L. The maximum adsorption capacity was found out to be 240.2 mg/g compared to 123.3 mg/g of raw resin. The experimental data fitted the Langmuir isotherm model. The efficiency of the resin was more than 91% after the tenth adsorption–desorption cycle. Regeneration of magnetic PSEDTA obtained was achieved by using 0.5 M NaOH. Gupta et al. [100] combined the magnetic properties of iron oxide with the adsorptive properties of carbon nanotubes to produce a magnetic adsorbent (MWCNT/nano iron oxide). Compared to activated carbon, the prepared composite showed a greater adsorption capability. The composite was effective in removing Cr(III) in pH range of 3–7. The adsorption of Cr(III) increased with the agitation speed. With an increase in thickness of layer of resin, 90% removal of Cr(III) was observed. Luo et al. [101] further enhanced the adsorption capabilities of the adsorbent by modifying it with MnO_2. The TEM images showed that MnO_2 formed a thin, uniform and a continuous layer on Fe_3O_4/o-MWCNTs. Adsorption was favourable at low pH due to existence of predominant $HCrO_4^-$ ions having low adsorption free energy. The Langmuir adsorption capacity was dependent upon temperature suggesting that the adsorption process was endothermic.

Li et al. [102] fabricated a nitrogen-doped porous carbon containing magnetic nanoparticles (RHC-mag-CN) and investigated the potential of the sorbent for Cr(VI) removal from water during the batch process. The specific area of the porous composite was measured as 1136 m^2/g and the particles were superparamagnetic. The high surface area benefits the removal of Cr(VI) ions. Maximum Cr(VI) removal was observed at pH of 3 with adsorption capacity of 16 mg/g, which is nearly twice the adsorption capacity of RHC. The Langmuir isotherm was found to be favourable for the adsorption study of Cr(VI).

Chen et al. [103] synthesized magnetic MCM-41 nanosorbents and studied its effect on removal of chromium (VI) oxyanions from distilled, tap and natural waters. Adsorption of chromium oxyanions was observed at low pH ($\leq$2.8). Maximum adsorption capacity of 105 mg/g was observed at pH of 2. The adsorption decreased as pH increased and became zero at pH of 7. The adsorption of chromium oxyanions could be adequately described by the Freundlich equation. Simulated polluted waters from tap, river and mountain run offs were tested, and it was found that the magnetic nanosorbents had high affinity for chromium oxyanions. Calcium in treated hard water led to a decrease in adsorption capacity. Maximum chromium removal was found to be 97%, however, this decreased in the presence of copper cation. Yao et al. [104] prepared a magnetic polymer (TEPA-NMPs) for chromium removal. The maximum chromium removal observed was 99.4 % for pH value of 5.5 and initial Cr concentration of 100 μg/l. The maximum adsorption capacity was noted to be 370.4 mg/g and hence no influence of coexisting anions was observed on determination of Cr(VI) removal.

Yarrowialipolytica, a yeast found on pomegranate leaves, when modified with Fe^0/Fe_3O_4particles was found to be three times more effective than unmodified yeast in removing Cr(VI) ions from water [105]. Under optimal conditions (pH 2.0, temperature 30 and 40 °C for NCIM 3589 and 3590, respectively, 1 h at 100 rpm), the maximum specific uptake was found to be 186.32 and 137.31 mg/g, respectively, when 1000 mg/L concentration of Cr(VI) ions were used. According to the authors, the yeast – Fe^0/Fe_3O_4 composites integrated chemical reactions (involving Fe^0/Fe_3O_4 composites) and biological processes (via surface functional groups) in metal removal.

Carbon encapsulated Fe_3O_4 magnetic particles could remove 92.4% Cr(VI) from water at room temperature and neutral pH [106]. This was due to the abundance of hydroxyl groups on the adsorbents surface which attracted the chromium ions. Selective adsorption of Cr(VI) from wastewater by magnetic iron-nickel oxide was investigated by Wei et al. [107]. The maximum adsorption capacity was 30 mg/g found at pH 5 and reduced with increasing TDS levels in the water. Adsorption energies obtained by DKR equation in different TDS conditions were between 10.31

and 21.321 kJ/mol. Presence of phosphate ions had a deleterious effect on the adsorption of chromium. Batch experiments were performed on contaminated wastewater using mesoporous γ-Fe_2O_3 as an adsorbent [108]. Initial Cr(VI) concentration was between 5 and 100 mg/L and adsorbent dose was 0.05 g. The adsorption capacity increased from 4.5 to 15.6 mg/g as pH decreased from 7 to 2.5. The adsorption capacity was comparable to more popular 10 nm nonporous γ-Fe_2O_3 but could be much easily separated using magnetic field. The adsorption mechanism was only due to electrostatic attraction which was confirmed by FTIR analysis. The mesopores had no influence on the adsorption capacity.

Maghemite nanoparticles synthesized by Jian et al. [109] were efficient in removing Cr(VI) at mildly acidic and neutral pH. pH_{zpc} for the adsorbent was 6.6. For initial maghemite concentrations ≥6, adsorption was rapid for the first 5 min, but decreased as the contact time increased. Adsorption of chromium fitted the L-F isotherm better The presence of low concentrations of humic acid did not have a significant impact on the adsorption of Cr(VI) however at relatively high humic acid concentration (20 ppm) the adsorption of Cr(VI) was partially inhibited. A magnetic poly-(MA-DVB) microsphere with surface dendrimer containing amino groups was obtained through stepwise reaction between methyl acrylate (MA) and ethylenediamine (EDA) [110]. Maximum adsorption capacity of 212.6 mg/g was obtained at pH 3. The adsorption equilibrium of Cr(VI) was obtained inabout 12 min, and more than 98% of adsorbed Cr(VI) was desorbed from the magnetic microspheres in about 30 min using Na_2SO_4 solution.

Hybrid materials constituting MMT (montmorillonite), PEI (800 g/mol or 25,000 g/mol), and large Fe_3O_4 NPs were prepared (Fe_3O_4-PEI800-MMT and Fe_3O_4-PEI25000-MMT) to test their efficiency for Cr(VI) removal from aqueous solutions [111]. pH had little effect on the removal of chromium from 1 to 9. The removal efficiency increased from 2 to 6 with maximum efficiency occurring at pH of 6. With further increase in pH, the efficiency decreased. The adsorption capacity of Fe_3O_4-PEI800-MMT and Fe_3O_4-PEI25000-MMT calculated from plot of Ce/qe vs Ce were 8.77 and 7.69 mg/g, respectively. Montomorillonite was also combined with chitosan to form a magnetically separable adsorbent CTS/MMT-Fe_3O_4 [112]. Batch experiments were performed revealed that the Cr(VI) removal efficiency increased from 22.63% to 99.65% as adsorbent dose increased from 10 mg to 70 mg. Optimum pH vale for adsorption was pH 2. Adsorption capacity was dependent on the MMT content and decreased from 56.68 to 34.49 mg/g as wt% increased from 0% to 110 %. The decrease in adsorption capacity was due to decreasing —NH_2 content, which was responsible for the adsorption process, as increasing MMT content occupied more surface on the adsorbent. The presence of —NH_2 groups was confirmed by IR spectra.

Microstructured Fe^{2+}/TiO_2 tubes having a hierarchical structure could remove Cr(VI) from water under the presence of UV light [112]. TiO_2 nanosheets stood vertical on the tubular surface with random distribution. The hierarchical structure served not only as a catalyst for reduction of Cr(VI) to Cr(III) under the presence of UV light but as an effective adsorbent for the removal of Cr(III). The removal effectiveness of 99.3% could be reached with initial Cr(VI) concentration of 10 mg/L. PEI was grafted on the surface of PGMA microspheres to form m-PGMA-PEI microspheres by Sun et al. [114]. The adsorption process was favourable under acidic conditions and the maximum adsorption capacity was 362.7 mg/g at pH 2. The microspheres had a higher adsorption capacity than pure Fe_3O_4 particles due to the presence of amino groups which played an important role in adsorption. Isotherm experiments were carried out by changing initial Cr(VI) concentration from 25 to 500 mg/L and the experimental data was found to fit the Langmuir model. SO_4^{2-} concentrations of 300 mg/L resulted in a 23.7% adsorption efficiency loss of Cr(VI). No remarkable loss in efficiency was noticed after 5 adsorption–desorption cycles. Fe3O4@gly-PPy NCs were synthesized via in situ chemical oxidative polymerization of glycine doped polypyrrole encapsulated by Fe_3O_4 particles [115]. TEM images bolstered the fact that the Fe_3O_4 particles were trapped inside the gly—PPy moiety. The adsorption capacity was temperature dependent and found to increase from 238 to 303 mg/g as temperature increased from 25 to 35C. The structure of Fe_3O_4 remained intact after adsorption since no change was observed in the peak of nanocomposite in X ray diffraction pattern. Decreasing negative values of gibbs free energy ΔG suggested that the adsorption process was spontaneous with high affinity.

2.1.3. Phosphorous

Magnetic polymer particles (PAM/oleic acid/Fe_3O_4) were synthesized using acrylamide (AA) as a functional monomer, and ethylene glycol di methacrylate (EDGMA) as a cross linking agent [116]. Optimum pH conditions for phosphate removal in a batch system were found to be 3.0 ± 0.1. Experimental data was in good agreement with the Langmuir isotherm model and the maximum monolayer phosphate uptake was 37.82 mg/g. Adsorption capacity decreased with increasing pH, and the authors noted that maximum desorption efficiency with 0.5 M NaOH. The recycled capacity of adsorbent decreased by 21 % after 5 adsorption–desorption cycles possibly due to the detachment of polyacrylamide from the magnetite surface during the recycling processes.

Zircomium ferrite was used for adsorption of phosphorous from wastewater of wastewater treatment plants by Ishiwata et al. [117]. Powered form of the adsorbent was found to be more effective than the particle form. Powered zirconium ferrite was able to remove 99.1% phosphorous from sewage water with a dose of 500 mg/L in 15 min. A maximum of 83.8% recovery ratio of phosphorous was achieved with a 7% sodium hydroxide solution.

2.1.4. Different anionic species

Phosphonium-silane was ionically attached to the surface of Fe_3O_4 particles to synthesize a super-paramagnetic adsorbent (PPhSi-MNPs) capable of removing arsenic and chromium pollutants from water [118]. Adsorption of both the ions was favourable at low pH range i.e. pH 3–4. The maximum removal percentage of As(V) and Cr(VI) was 97% and 67.8%, respectively, at pH 3. However at pH 9, this percentage drastically reduced for As (7.9%) and significantly for Cr (41.3%). The adsorption equilibrium data for both anions were well fitted by the Langmuir isotherm model. The maximum adsorbed quantities for As(V) and Cr(VI) were found to be 50.5 mg/g and 35.2 mg/g, respectively. XPS and EDX results indicated that a synergy of electrostatic interaction and ion-exchange between positive ligand and negative pollutant anions played a significant role in enabling high adsorption. Maximum desorption efficiency for As(V) i.e., 89.4% could be achieved using 0.1 M NaOH, however desorption efficiency for Cr(VI) was low (51.6%).

A summary of the adsorption capacity and other parameters for the removal of anions from wastewater using magnetic adsorbents has been presented in Table 1. Table 2 represents the applicable isotherm and kinetic models for each of the magnetic adsorbents discussed. In most cases Pseudo Second order kinetic data and Langmuir Isotherm were found to fit well with the experimental data.

2.2. Sorption of cations

2.2.1. Cadmium

Cadmium ion (Cd(II)) is one of the most toxic heavy metal ion found in industrial wastewater. Owing to its difficult separation from contaminated water, it tends to be propagated in the food chains and hence poses a serious threat to human health. It has been classified as a group B1 carcinogen by the US Environment-

Table 1
Adsorption capacity and other parameters for adsorption of anions by magnetic adsorbents.

S. no.	Adsorbent Name	Contact time	Optimal pH	Temperature °C	Concentration Range	Adsorbent Capacity	Saturation Magnetization (emu/g)	Pollutant	Reference
1	MNP modified with Fe-Mn binary oxide	90 min	04-Aug	25	200 μg/L	As (III)- Langmuir -39 mg/g Two Site Langmuir- 47.76 mg/g	23.2	As(III)	[78]
2	γ- Fe_2O_3	1 h	5-7.6	-	100 mg/L	As (V)- 45mg/g	-	As(V)	[79]
3	Magnetic binary oxide particles	14 h	7	30 ± 2	1 mg/L	As (III) -16.94 mg/g	18.78	As(III)	[80]
4	Fe_3O_4 and MnO_2 modified Graphene oxide nanocomposite (3:8)	24 h	7	25.5 ± 0.2	0.01-10 mg/L	As (III)- 14.04 mg/g As (V) - 12.22 mg/g	48.57	As(III), As(V)	[81]
5	γ-Fe_2O_3–TiO_2	10-720 min	7	-	0.1-50 mg/L	As (III) -33.03 mg/g	46.28	As(III)	[82]
6	Iron impregnated chitosan-caboxymethyl-β cyclodextrin	12 h	05-Jul	25-60	1-20 mg/L	As (III)- 18.51 mg/g As (V) - 13.51 mg/g	-	As(III), As(V)	[83]
7	Fe_3O_4 nanoparticle-coated boron nitride	24 h	9	25 ± 0.2	1-40 mg/L	As (V)- 32.2 mg/g	-	As(V)	[84]
8	Cetyltrimethylammonium bromide modified Fe_3O_4 particles	2 h	6	25	100 μg/L-7 mg/L	As (V) -23.07 mg/g	67.2	As(V)	[85]
9	Ascorbic acid coated Fe_3O_4 nanoparticles	24 h	02-Jul	Room temperature	0.1 mg/L	As (III) -46.06 mg/g As (V)- 16.56 mg/g	40	As(III), As(V)	[86]
10	Magnetic Biochar	24 h	-	22 ± 0.5	5-200 mg/L	As (V) - 3147 mg/kg	69.2	As(V)	[87]
11	Magnetic nanoparticles from waste red mud	120 min	2.5	25 ± 1	10-1000 μg/L	As (V) - 400 μg/g	55.3	As(V)	[88]
12	Magnesium Ferrite	-	7	25	-	As (III)- 127.4 mg/g As (V) - 83.2 mg/g	32.9	As(III), As(V)	[89]
13	Copper Ferrite from PCB Sludge	300 min	3.7	27 ± 1	10 mg/L	As (V) - 45.66 mg/g	62.52	As(V)	[90]
14	Fe_3O_4-loaded activated carbon from waste biomass	24 h	8	30	20-100 mg/L	As (V) - 204.2 mg/g	47.67	As(V)	[91]
15	Magnetic Wheat Straw- MWS1 MWS2 MWS5	12 h	-	30	1-28 mg/L	As (III) As (V) 0.760 mg/g 4.018 mg/g 2.313 mg/g 6.683 mg/g 3.898 mg/g 8.062 mg/g	MWS1-6.18 MWS2-9.12 MWS3- 11.87	As(III), As(V)	[92]
16	Bio-functional magnetic beads made from Rhizopuscohnii	8 h	1	28	5–200 mg/L	6.73 mg/g	-	Cr(VI)	[93]
17	Graphene Oxide functionalized with Magnetic Cyclodextrin–Chitosan	-	3	-	5–50 mg/L	67.66 mg/g	22.15	Cr(VI)	[95]
18	RGO-Fe_3O_4 hybrid composites M1, M2, M3	5 min	<7	-	500 μg/L	-	M1-41.12 M2-32.07 M3-29.68	Cr(VI)	[96]
19	Magnetic Chitosan nanoparticles	100 min	3	25–45	60–180 mg/L	55.8 mg/g @ 25°C 46.71 mg/g @ 35°C 43.29 mg/g @ 45°C	-	Cr(VI)	[97]
20	Magnetic $MnFe_2O_4$/Chitosan nanocomposites	12 h	5	27	0.5–1 mg/L	Cr (VI) 35.2 mg/g	35.2	Cr(VI)	[98]
21	Magnetic PS-EDTA resin	5 h	4	30	5-1000 mg/L	250 mg/g	2.07	Cr(VI)	[99]
22	Iron Oxide / Carbon Nanotubes composite	60 min	05-Jun	25 ± 2	20 mg/L	90% removal	-	Cr(III)	[100]

Table 1 (*Continued*)

S. no.	Adsorbent Name	Contact time	Optimal pH	Temperature °C	Concentration Range	Adsorbent Capacity	Saturation Magnetization (emu/g)	Pollutant	Reference
23	Carbon Nanotubes modified with Magnetite and Manganese Oxide	150 min	2	2-62	50–300 mg/L	150.8 mg/g @ 2°C 170.4 mg/g @ 22°C 186.9 mg/g @ 62°C	10.21	Cr(VI)	[101]
24	N-doped porous carbon with magnetic nanoparticles	2 h	3 ± 0.02	25	10–130 mg/L	16 mg/g	-	Cr(VI)	[102]
25	MCM-41	-	2	25 ± 2	-	2 mmol/g	8.3	Cr(VI)	[103]
26	Tetraethylenepentamine-functional Fe_3O_4 polymer	120 min	5.5	30	1-100 μg/L	370.4 mg/g	-	Cr(VI)	[104]
27	YarrowiaLipolytica cells modified with Fe^0/Fe_3O_4 particles	1 h	2	30 for NCIM 3589 40 for NCIM 3590	100–1000 mg/L	NCIM 3589 −186.32 mg/g NCIM 3590-137.31 mg/g	70.58	Cr(VI)	[105]
28	Carbon encapsulated Fe_3O_4 particles	150 min	7.6	28	507 μg/mL	92.4% removal	-	Cr(VI)	[106]
29	Iron–Nickel Oxide from waste Nickel Liquid	1 h	5	23-25	10–50 mg/L	30 mg/g	-	Cr(VI)	[107]
30	Mesoporous γ-Fe_2O_3	120 min	2.5	22 ± 2	5–100 mg/L	15.6 mg/g	-	Cr(VI)	[108]
31	Maghemite nanoparticles	2 h	4	25	50–500 ppb	1.62 mg/g	-	Cr(VI)	[109]
32	Polymer microspheres with surface dendric modification	12 min	3	20	150 mg/L	231.8 mg/g	10.1	Cr(VI)	[110]
33	Magnetite–Polyethylenimine–Montmorillonite	120 min	0-11	25 ± 2	10–25 mg/L	Fe_3O_4-PEI800-MMT- 8.77 mg/g Fe_3O_4-PEI25000-MMT- 7.69 mg/g	4.2	Cr(VI)	[111]
34	Chitosan/Montmorillonite microspheres	150 min	2	35	6–80 mg/L	74.2 mg/g	-	Cr(VI)	[112]
35	Micro/nanostructured Fe^{2+}/TiO_2 tubes	1 h	3.5–3.8	-	10 mg/L	99.3% removal	-	Cr(VI)	[113]
36	PGMA microspheres with amino groups	5 h	2	25	25–500 mg/L	492.61 mg/g	8.6	Cr(VI)	[114]
37	Fe_3O_4 coated glycine doped polypyrrole magnetic nanocomposite	24 h	2	25–45	-	238 mg/g @ 25°C 270 mg/g @ 35°C 303 mg/g @ 45 °C	2.2	Cr(VI)	[115]
38	Magnetite modified with Polyacrylamide and Oleic acid	24 h	4.5	25	500–900 mg/L	37.82 mg/g	41.2	P	[116]
39	Ferromagnetic zirconium ferrite	45 min and 30 min	-	-	3.19 mg/L	Particle form-91 % removal Powder form-96 % removal	18.6	P	[117]
40	Phosphonium-silane coated iron oxide nanoparticles	50 min for As (V) 70 min for Cr (VI)	3	25	10-200 mg/L	As (V)- 50.5 mg/g Cr (VI)- 35.2 mg/g	68.2	As (V), Cr (VI)	[118]

Protection Agency and is responsible for the itai–itai disease [119]. Therefore, it is inevitable to develop methods which are both efficient and economically feasible in order to remove Cd from water systems.

Yang et al. [120] used simple co condensation process followed by a redox process to synthesize a chitosan modified with α-ketoglutaric acid and then combined with Fe_3O_4 nanoparticles. From the TEM images, the authors observed that the presence of α-ketoglutarate acid enlarged the effective surface area of the adsorbent (α-KA-Fe_3O_4/CS) and made the magnetic nanoparticles more uniformly distributed. pH studies were carried out up to pH 8 and the maximum removal efficiency of 93% was observed at pH 6 and initial Cd(II) concentration of 100 mg/L. The adsorption behaviour could be explained by surface charge and proton-competitive adsorption. The Cd(II) removal capacity increased with the initial Cd(II) concentration, and the maximum Cd(II) adsorption capacity reached 201.2 mg/g with the initial Cd(II) concentration of 1000 mg/L. Batch experiments were carried out to demonstrate the Cd removal efficiency using magnetic nanoparticles recycled from sludge in printed circuit board (PCB) industry [121]. When initial Cd solution of 1000 mg/L was taken, removal efficiency of more than 85% was observed under controlled pH between 5 and 6. Positive value of ΔH suggested the adsorption process was endothermic. The Cd (II) adsorption capacity increased from 13.87 to 17.54 mg/g when temperature increased from 298 to 318 K.

Shellac polymer is rich in carboxyl and hydroxyl groups. This property was utilized by Gong et al. [122] to synthesize shellac coated iron oxide particles (SCMN). During IR spectrum analysis,

Table 2
Isotherm and Kinetic models for adsorption of anions by magnetic adsorbents.

S. no.	Adsorbent Name	Applicable Isotherm Model	Applicable Kinetics Model	Pollutant	Reference
1	MNP modified with Fe-Mn binary oxide	Freundlich,Sips,Two Site Langmuir Model	Pseudo-Second order	As(III)	[78]
2	$\gamma - Fe_2O_3$	Freundlich	-	As(V)	[79]
3	Magnetic binary oxide particles	Langmuir	Pseudo-First-Order	As(III)	[80]
4	Fe_3O_4 and MnO_2 modified Graphene oxide nanocomposite	Langmuir	Pseudo-Second-Order	As(III), As(V)	[81]
5	γ-Fe_2O_3–TiO_2	-	Pseudo-Second-Order	As(III)	[82]
6	Iron impregnated chitosan-caboxymethyl-β cyclodextrin	Langmuir	Pseudo-Second-Order	As(III), As(V)	[83]
7	Fe_3O_4 nanoparticle-coated boron nitride	Dubinin-Radushkevich	Pseudo-Second-Order	As(V)	[84]
8	Cetyltrimethylammonium bromide modified Fe_3O_4 particles	Two-site Langmuir	Pseudo-Second-Order	As(V)	[85]
9	Fe_3O_4	Langmuir	-	As(III), As(V)	[86]
10	Magnetic Biochar	Langmuir	Pseudo-First-Order	As(V)	[87]
11	Magnetic nanoparticles from waste red mud	Freundlich	Pseudo-Second-Order	As(V)	[88]
12	Magnesium Ferrite	As (III)- Freundlich As (V) - Langmuir	Pseudo-Second-Order	As(III), As(V)	[89]
13	Copper Ferrite from PCB Sludge	Langmuir	Pseudo-Second-Order	As(V)	[90]
14	Fe_3O_4-loaded activated carbon from waste biomass	Freundlich	Pseudo-second-order	As(V)	[91]
15	Magnetic Wheat Straw	Langmuir	-	As(III), As(V)	[92]
16	Bio-functional magnetic beads made from Rhizopuscohnii	Langmuir	Pseudo-First-Order	Cr(VI)	[93]
17	Graphene Oxide functionalized with magnetic Cyclodextrin–Chitosan	Langmuir	Pseudo-Second-Order	Cr(VI)	[95]
18	RGO-Fe_3O_4		Pseudo-Second-Order	Cr(VI)	[96]
19	Magnetic Chitosan nanoparticles	Langmuir	Pseudo-Second-Order	Cr(VI)	[97]
20	$MnFe_2O_4$/chitosan nanocomposites	Freundlich	Pseudo-Second-Order	Cr(VI)	[98]
21	Magnetic PS-EDTA resin	Langmuir	Pseudo-Second-Order	Cr(VI)	[99]
22	Carbon Nanotubes modified with Magnetite and Manganese Oxide	Langmuir	Pseudo-Second-Order	Cr(VI)	[101]
23	N-doped porous carbon with magnetic nanoparticles	Langmuir	-	Cr(VI)	[102]
24	MCM-41	Freundlich, LeVan–Vermeulen	-	Cr(VI)	[103]
25	Tetraethylenepentamine-functional Fe_3O_4 polymer	-	Pseudo-Second-order	Cr(VI)	[104]
26	YarrowiaLipolytica cells modified with Fe^0/Fe_3O_4 particles	Scatchard, Langmuir, Freundlich	-	Cr(VI)	[105]
27	Iron–Nickel Oxide from waste Nickel liquid	Langmuir, Freundlich	-	Cr(VI)	[106]
28	Maghemite nanoparticles	Langmuir, Langmuir-Freundlich	Pseudo-Second-Order	Cr(VI)	[109]
29	Polymer microspheres with surface dendric modification	Langmuir	-	Cr(VI)	[110]
30	Magnetite–Polyethylenimine–Montmorillonite	Langmuir	-	Cr(VI)	[111]
31	Chitosan/Montmorillonite microspheres	Langmuir	Pseudo-Second-Order	Cr(VI)	[112]
32	Micro/nanostructured Fe^{2+}/TiO_2 tubes	-	Pseudo-First Order	Cr(VI)	[113]
33	PGMA microspheres with amino groups	Langmuir	Pseudo-Second-Order	Cr(VI)	[114]
34	Fe_3O_4 coated glycine doped polypyrrole magnetic nanocomposite	Langmuir	Pseudo-Second-Order	Cr(VI)	[115]
35	Magnetite modified with Polyacrylamide and Oleic acid	Langmuir, Freundlich	Pseudo-Second-Order	P	[116]
36	Phosphonium-silane coated iron oxide nanoparticles	Langmuir	Pseudo-Second-Order	As(V), Cr (VI)	[118]

shifting of vibration peaks of OH^- from 3394 cm^{-1} to 3371 cm^{-1}, 1716 cm^{-1} to 1712 cm^{-1}, and 1415 cm^{-1} to 1408 cm^{-1} suggested the interaction of carboxyl groups with SCMN and Cd(II). XPS experiments further supported the fact that Cd(II) was chemically adsorbed onto the adsorbent surface. Maximum Langmuir adsorption capacity observed was 18.8 mg/g. The authors compared the effect of initial pH between SCMN and bare magnetic nanoparticles (BMN). The amount of Cd(II) adsorbed increased slowly for both SCMN and BMN for pH < 7. For pH between 7 and 8, SCMN was observed to have a higher adsorption capacity. This was due to a higher surface charge on SCMN than BCM, and chemisorptions due to the carboxyl groups on SCMN's surface.

2.2.2. Copper

Contamination of water resources by heavy metals is a grave issue due to the toxic and detrimental impact it has on humans, plants and animals. Copper, an abundant element in various industries like mining, electroplating, paints, fertilizers, pigments etc., is discharged into the municipal wastewater. In the human body it gets deposited in the liver, brain, pancreas and consequently results

in vomit, convulsion and even death [123]. Therefore efficient and effective methods need to be explored in order to remove Copper from water systems before it is discharged into the environment.

Lin et al. [124] synthesized a magnetic adsorbent by modifying the surface of Fe_3O_4 with SiO_2 and *N*-[3-(trimethoxysilyl)propyl]-ethylenediamine (TPED). The adsorbent was found to have an increased surface area as compared to the Fe_3O_4 core. Maximum Langmuir monolayer uptake was 10.41 mg/g at pH 5.5 and adsorbent dose 0.5 g/50 mL. Initially, adsorption process was rapid but gradually became slower due to decrease in active sites. The optimum conditions to desorb the adsorbent were found to be with 0.1 mol/l HNO_3. Regeneration studies resulted in a loss 13.6% in the adsorption capacity which might be due to the detachment of silica coating from the magnetite core during the process of recycling.

Mei et al. [125] also modified the surface of Fe_3O_4 particles with 1,6-hexadiamine to synthesize MNP-NH_2 nanoparticles. Effect of pH on the removal efficiency of Cu(II) was studied by the authors. The removal efficiency increased from 53% to 100% as the pH was increased from 2 to 6.At low pH, NH_2 group of the adsorbent protonated to form NH_3^+ cations, leading to an electrostatic repulsion with Cu^{2+}. The tendency to form NH_3^+ cations decreased with increase in pH. Compared to MNP-NH_2 particles, Fe_3O_4 (MNP) particles had a lesser tendency to attract Cu(II) ions. Increasing adsorbentdose in a 10 mg/L Cu solution, resulted in maximum copper removal of 74%, but a decreasing adsorbent capacity. This was possible due to interference between binding sites and higher adsorbed dose; insufficiency of metal ions solution with respect to available binding sites; aggregation resulting from higher adsorbent dose leading to a decrease in surface area. It was found that the sorption of Cu(II) ions was well fitted to the Langmuir equation with maximum monolayer adsorption capacity of 25.77–26.58 mg/g at 298–333 K. No difference was observed in the desorption capacity of the adsorbent during 15 sorption–desorption cycles indicating that the nano adsorbent had good reusability. River waters polluted with industrial wastewater and tap water were tested. In both the cases 98% removal of Cu(II) was observed and was hardly influenced by the coexisting ions in the river water and tap water.

Fe_3O_4 particles coated with pectin have also been used as an adsorbent (PIOMN) for copper removal [126]. SEM images revealed that PIOMN was spherical in shape and had a tendency to agglomerate into large aggregates resulting in rough surface. Maximum adsorption capacity was observed for adsorbent with 1% pectin content. Increasing the pectin content decreased the surface area leading to lower adsorption capacity. $pH_{zpc}$for copper was at 2.5, thus copper removal was suppressed at lower pH. The adsorption mechanism of Cu(II) uptake in PIOMN adsorbent was based on ionexchange between hydrogen ions of free carboxylic acid in PIOMN adsorbent and copper ions in solution, and electrostatic force between Cu(II) and PIOMN adsorbent. Cu(II) binding efficiency on PIOMN adsorbent decreased when salt concentrations increased in the presence of Cu(II), which was attributed to the competition between Cu(II) and cations involving Na(I) and Ca(II) for available sites during sorption process.

Carboxyl groups of Gum Arabic interacted with the hydroxyl group of Fe_3O_4 to form a magnetic adsorbent (GA-MNP) for the removal of copper ions [127]. The authors determined the amount of gum Arabic in final product using TGA analysis to be 5.1%. Two gum Arabic molecules were bound to one molecule of Fe_3O_4. The adsorption capacity of GA-MNP was more than twice that of MNP particles. A shift of isoelectric point from 6.78 to 3.6 was observed on modification, authors predicted different adsorption mechanisms for GA-MNP and MNP. Saccharomyces cerevisiae was immobilised onto the surface of magnetic chitosan particles by Peng et al. [128] to form an adsorbent SICCM which was very effective in removing copper from aqueous solution. Removal efficiency increased till pH 4.5 and remarkably decreased thereafter. Adsorption isotherm experiments were conducted with different initial Cu concentration solutions.The removal efficiency increased till 98.6 % with increase in initial Cu(II) concentration from 40 to 60 mg/L. However a decrease in 45.4 % removal efficiency was observed on further increase of initial Cu(II) concentration till 400 mg/L. The authors suggested that the high concentrations of Cu(II) inhibited the biological activity of SICCM. The adsorption behaviour obeyed the Langmuir adsorption isotherm model with a maximum adsorption capacity of 144.9 mg/g. FTIR analysis confirmed that the hydroxyl and amino groups on the adsorbent surface which were involved in the copper adsorption. Carboxymethyl-β-cyclodextrin (CM-β-CD) was grafted onto the magnetite surface via carbodiimide method to produce spherical or ellipsodial nanoparticles [129]. Adsorption capacity increased till pH 4 and then remained constant till pH 6 for low Cu(II) concentrations. However for high Cu(II) concentrations, adsorption capacity continued to increase till pH 6. The maximum adsorption capacity was determined to be 47.2 mg/g. Both FTIR and XPS analyses revealed that the oxygen atoms on CMCD-MNPs are the main binding sites for Cu(II) to form surface complexes.

Researchers have also investigated the potential of EDTA functionalized magnetic nanoparticles (MNPs-EDTA) and for removal of copper from aqueous solutions [130]. No adsorption was observed at pH 2. Adsorption capacity increased at pH increased to 6. Langmuir model was found to be the best fit with adsorption capacity of 46.27 mg/g at pH 6. Over 98.3% Cu(II) was removed from polluted river water with little impact of coexisting ions. Sulphonated magnetic graphene oxide was prepared by researchers for testing its potential for copper removal from water [131]. Optimum Cu(II) uptake of 62.73 mg/g was achieved at pH 4.68 and temperature 50 °C. The experimental data of isotherm followed the Langmuir isotherm model. Lan et al. [132] synthesized magnetic hyaluronic acid (Fe_3O_4@SiO_2-HA) microspheres through immobilization of hyaluronic (HA) acid on magnetic silica microspheres. Adsorption capacity increased from 6 to 12.2 mg/g as pH increased from 2 to 6.8 and slowly decreased to 11.6 at pH 8. The adsorption capacity of Cu(II) with Fe_3O_4@SiO_2-HA microspheres decreased with increasing the concentration of alkaline earth metal ions in the range of 10–50 mg/L. The reduction in Cu(II) adsorption capacity reached as high as 10% for 50 mg/L Mg(II) and 9.1% for50 mg/L Ca(II). It was observed that the adsorption capacity for Cu2+ ions also decreased in the presence of coexisting heavymetal ions at all concentrations. The adsorption equilibrium studyexhibited that the Cu (II) adsorption of HA-supported magneticsilica microspheres fit the Freundlich isotherm.

Waste fungal mycelium was used to prepare a composite (Cu (II) – MICA) capable of removing copper from water [133]. FTIR analysis indicated that the adsorbent contained amido and hydroxide groups which could chelate Cu(II) ions. Optimum pH was found to be 5.5 and the experiment data fit well the Langmuir isotherm model with adsorption capacity 71.36 mg/g. Cu (II) – MICA had high selectivity sorption for Cu(II). The metal ion affinity was in the order Cu(II) > Zn(II) > Co(II) > Ni(II).

2.2.3. Fluoride

Fluoride contamination in drinking water is a problem of paramount importance worldwide. Ingestion of high concentrations of Fluoride can have adverse effects on human health. Long term exposure to such contaminated water can lead to Fluorosis which affects the teeth and bones and causes neurological damage in severe cases [134]. According to the World Health Organization, the optimum range of Fluoride in water should be 0.5–1.5 mg/L. Therefore removal of Fluoride from water is something which should be looked at seriously.

Zhao et al. [134] synthesized Fe_3O_4@Al $(OH)_3$ NPs and investigated the adsorption feasibility of this nanomaterial for fluoride.

Amount of fluoride adsorbed increased with mass ratio of $Al(OH)_3$ and did not change considerably after it reached 2.5. Adsorption was strong between pH 5 and 7. The authors used XPS spectra to confirm that the adsorption was driven by both electrostatic attraction and surface complexation. The equilibrium adsorption data could be described both by the Langmuir and Fruendlich model. Maximum adsorption capacity achieved was 88.49 mg/g at 25 °C. Surface texture was not altered significantly after fluoride adsorption. Residual concentration of fluoride was 0.3 mg/L with an initial fluoride concentration of 20 mg/L. Adsorption was competitive in the presence of another anions in the order $PO_4^{3-} > SO_4^{2-} > Br^- \approx NO_3^- \approx Cl^-$. Two types of adsorbents of bayerite/SiO_2/Fe_3O_4 were prepared via the adsorption gel method (MASG) and the homogeneous precipitation method (MAHP) by Chang et al. [135]. Both the adsorbents possessed superparamagnetic properties. The adsorption capacities of MASG and MAPH at pH of 6 were 38 g/kg and 8 g/kg, respectively, while SiO_2/Fe_3O_4 had an adsorption capacity of zero, leading the authors to believe that Fe_3O_4 particles were well enclosed by SiO_2 film, preventing any interaction between the magnetic component and the fluoride ions. The reduction in fluoride ion concentration due to MASG and MAPH was attributed to the functional groups on the adsorbent surfaces.

Researchers have also synthesized PPy/Fe_3O_4 nanocomposites with magnetic behaviour for the removal of fluoride from water [136]. PPy/Fe_3O_4 exhibited biphasic kinetic profile of sorption with an initial rapid uptake followed by a slow gradual phase. The authors explained the above mechanism based on reduction in diffusion path and increased exposed surface area. XRD results indicated that the dominant mechanism of fluoride removal appeared to be ion-exchange. ATR-FTIR spectra further confirmed that the fluoride ions adsorbed on the surface of adsorbent by replacing doped chloride ions. Fluoride interaction with PPy/Fe_3O_4 nanocomposites was endothermic in nature and found within the range 17.63–22.31 mg/g. Consistent removal efficiency of 70% was achieved on using sulphate doped Fe_3O_4/Al_2O_3 particles over a wide pH range of 4–10 [137] for fluoride removal. Adsorption isotherm at pH 7 could be well described by two-site Langmuir model which suggested that there were two types of active sites with different binding energy out of which 57.5% were high energy binding sites. Maximum adsorption capacity calculated was 70.4 mg/g. Ion exchange and inner-sphere complex formation were important mechanisms for fluoride removal by the Fe_3O_4/Al_2O_3 particles.

2.2.4. Lead

The environmental release of Lead (Pb) can mainly be attributed to industrial wastewater containing Lead-acid battery wastewater [138]. It is known to cause problems like nausea, convulsions, cancer, coma etc. upon long term drinking [139]. The World Health Organization [138] has set an upper limit of 0.05 mg/L for Lead in drinking water. However, Lead can be directly recovered from waste and therefore there is a demand of innovative and economical methods that can reduce contamination and regenerate Pb.

Han and Wei [140] fabricated Fe_3O_4microroses and explored the possibility of Pb(II) removal during water treatment. The BET surface area of Fe_3O_4microroses was calculated to be 43 m^2/g. This surface area is higher than many of the commercially available adsorbents .Experiments were carried out at pH of 5.5 and initial Pb(II) concentration of 80 mg/L. The maximum adsorption capacity was dependent on temperature and varied from 46.5 to 47.1 mg/g. Peng et al. [141] combined the advantages of magnetic Fe_3O_4 and Xanthan Gum (XG) to fabricate a hybrid adsorbent Fe_3O_4 @ silica–XG, with high affinity towards Pb(II) and good magnetic separability. The adsorbent exhibited strong adsorption of fluoride when the pH was between 5 and 6, attaining 100% Pb(II) removal from the aqueous solution. The maximum adsorption capacity calculated by Langmuir isotherm was 21.32 mg/g. Pb(II) removal in the presence of other cations decreased in the order Pb(II) > Cu(II) > Zn(II) > Cd(II). Fe_3O_4 @ silica–XG composite was able to treat a battery industry effluent with 97% efficiency up to 21 adsorption–desorption cycles, and could be efficiently generated with 0.05 mol/l HCl solution. Ferrofluids based maghemite particles were incorporated by Idris et al. [142] on sodium alginate to form superparamagnetic beads. Maximum Pb (II) removal efficiency achieved after 2 h of contact time was 92.5%, at neutral pH, due to less competition available to Pb(II) from H^+ ions for binding sites on the adsorbent surface. It was observed that the equilibrium amount of Pb(II) adsorbed on beads reaches a constant value with increasing initial concentrations which suggested that the uptake of lead obeyed the Langmuir type adsorption equation. The maximum adsorption capacity obtained was 50 mg/g.

To utilize the advantage of alginate, having a large surface area, Bée et al. [143] encapsulated maghemite functionalized nanoparticles in calcium-alginate beads to provide it with magnetic properties. Batch experiments performed with Pb(II) solution having concentration of 2.94 g/l, had the maximum uptake in 4 h of contact time with the adsorbent dose of 0.15 g. Maximum adsorption capacity was found to be 97 ± 6 mg/L. The equilibrium adsorption isotherm, analysed using the Langmuir model, showed that an efficient adsorption of Pb(II) ions was thus achieved due to the carboxylate groups of both the polymer matrix and the functionalized magnetic nanoparticles. The results revealed that the adsorption capacity of magsorbent could be effectively enhanced when the initial pH was above 2.3 and below 6, which could be explained by the increased electrostatic attraction between Pb(II) and the magsorbent. A high desorption efficiency was achieved by using 2 mol/L nitric acid to remove the sorbed Pb(II) ions. The adsorption efficiency of magsorbent did not deteriorate in 5 adsorption/ desorption cycles.Sodium alginate gel beads (Fe_3O_4@SA-Zr) were prepared using zirconium(IV) as crosslinking ions, for the removal of Pb(II) from water [144]. Carboxyl groups of SA and hydroxyl groups binding to Fe species were involved in Pb(II) adsorption through the formation of carboxyl-metal and M–O–metal complexes. Removal efficiency of Pb(II) ions decreased from 100% to 72.5% as initial Pb(II) concentration was increased above 200 mg/L. Adsorption capacity of Fe_3O_4@SA-Zr decreased with temperature and had a maximum value of 333.33 mg/g at 293 K. K_d values of Fe_3O_4@SA-Zr for Pb(II) were greater than that for Cu(II), Cd(II), Hg(II) and Zn(II) suggesting higher affinity of Pb(II) towards the adsorbent.

A novel adsorbent triethylene-tetramine grafted magnetic chitosan was prepared by Kuang et al. [145] to study its effects on Pb(II) in an aqueous solution. The maximum adsorption capacity was 370.63 mg/g at a pH of 6, $T = 298$ K, contact time $t = 1.5$ h, Pb(II) dose = 200 mg/L, and adsorbent dose = 500 mg/L. The adsorbent achieved a maximum of 97.89% removal of Pb(II). Value of correlation coefficient suggested that pseudo second order kinetic equation was appropriate model for the experimental data. Intraparticle diffusion model indicated that chemisorption was the rate determining step. Langmuir model was in good agreement with the given experimental data.Fe_3O_4-TETA-CMS could be easily separated by the magnetic field. Chitosan was also used to fabricate magnetic chitosan/grapheme oxide particles (MCGO) [146]. It proved to be an effective adsorbent for removal of lead. Optimum pH was found to be 5. Maximum adsorption capacity was calculated to be 76.94 mg/g. The authors concluded presence of inclusions in GO, —OH and —NH_2 groups in chitosan molecules as possible sites for adsorption.

Magnetic chitosan coated yeast biomass modified with ethylenediamine (EYMC), yeast biomass coated with magnetic chitosan microparticles (YMC), ethylenediamine-modified magnetic chitosan microparticles (EMC), magnetic chitosan microparticles

(MC) were taken as test adsorbents for the removal of Pb(II) from aqueous solutions [147]. Preliminary investigations showed that EYMC had high lead removal efficiency compared to the other three adsorbents. The percentage of lead removal onto EMYC was found to increase rapidly with pH up 4, and then increased very gently with further increase in pH. Pb(II) adsorption could be accomplished through the ion exchange reactions with hydroxyl and carboxyl groups and through the complexation with $-NH_2$ groups. The adsorption process was observed to be endothermic,as the adsorption efficiencies increased with increase oftemperature.

2.2.5. Mercury

Mercury (Hg), a toxic pollutant under section 307 (a) of the Clean Water Act (CWA), remains a challenge in water treatment due to its ability to bio accumulate due to very low regulatory concentrations [148]. Main sources of contamination of Hg are batteries, paper & pulp industries, oil refineries etc [149]. Adsorption can be used as an effective tool to achieve lower wastewater effluent concentrations.

Faluconer et al. [148] impregnated magnetite (Fe_3O_4) particles onto the activated carbon surface to for magnetic powdered activated carbon (MPAC). A 3:1C: Fe MPAC was able to adsorb 84 % of Hg(II) ions from a solution with initial concentration of 100 μg/l. Hg(II) was removed from polluted water using modified magnetic iron oxide nanoparticleswith 2-mercaptobenzothiazole [149]. Removal of Hg ions remains constant in a wide pH range from 2.5 to 11. Complete adsorption of Hg(II) could be achieved in 4 min for initial Hg(II) concentration less than 200 μg/l.Magnetic removal of Hg(II) was assessed by Girginova et al. [150] using silica coated magnetite particles (Fe_3O_4/SiO_2). These particles were then later modified by grafting dithiocarbamate groups on its surface ($Fe_3O_4/SiO_2/NH/CS_2^-$). Magnetic measurements performed indicated that Fe_3O_4/SiO_2 had a lower value of magnetic saturation compared to Fe_3O_4. This was because the silica shells surrounded the magnetite particles, thus preventing the interaction between magnetic cores. The authors found $Fe_3O_4/SiO_2/NH/CS_2$ to be more efficient compared to Fe_3O_4/SiO_2 for Hg(II) removal, attaining an adsorption capacity of 25 μg/g, compared to 8 μg/g which was achieved by Fe_3O_4/SiO_2. The corresponding Hg(II) uptake percentages were 74% and 24%, respectively. The authors suggested that the higher efficiency of $Fe_3O_4/SiO_2/NH/CS_2$ could be due to a high stability of chelates formed between DTC group and Hg (II).

A reversible solid sensor (Fe_3O_4-R6G) for Hg (II) based on magnetic $Fe_3O_4$was developed by Wang et al. [151] in which the signal was transduced through opening the rhodamine spirolactamring upon Hg (II) binding. It showed a high selectivity for Hg (II) sensingin comparison to other cations, and could adsorb 91% of Hg(II) ions in aqueous solution. Thiol-functionalized magnetic silica nanocomposite could achieve maximum Hg(II) adsorption of 19.79 mg/g [152]. Thiol groups present played an important role in Hg adsorption and their presence was further confirmed by AFM images. Further investigations were carried out by Hakami et al. [153]. The adsorption data fitted the Freundlich isotherm and the maximum capacity for Hg(II) was calculated to be 207.7 mg/g when 4 mg/L of the adsorbent was used. Removal of Hg(II) was independent of pH at concentrations lower than 200 μg/l. For Hg(II) concentrations greater than 200 μg/l, reduction in removal efficiency was observed at pH less than 2 and more than 7. This was due to the change in zeta potential of nanoparticle-mercury complex from negative to positive at higher Hg(II) concentrations. Batch experiments were carried out by with dithiocarbamate functionalized Fe_3O_4 particles to study the effect of sorbent for Hg(II) removal from water [154]. 6 mg/L of magnetic particles was sufficient enough to produce a residual Hg(II) concentration lower than 1 μg/l for initial metal concentration equal to 50 μg/l. The Sips model provided a good description of the equilibrium data, predicting a maximum sorption capacity of 206 mg/g at 21 ± 1 °C.

2.2.6. Different cationic species

Huang et al. [155] studied the effect of magnetic properties of nZVI for heavy metal removal of different concentrations of Cd(II), Cr (IV) and Pb (II). Results showed that the magnetic removal efficiencies of heavy metals varied with the metal species, nZVI loading, reaction and magnetic separation time. In most cases, use of 1.5 mg/mL E-nZVI or NE-nZVI resulted in removal efficiencies of more than 80% for Pb(II), Cd(II), and Cr(IV). Increasing the magnetic treatment time from 1 to 20 min was shown to lead to 20% increase in Pb(II) removal efficiency, but no improvements for Cd(II) and Cr(IV). In contrast, increasing the reaction time decreased the Pb(II) removal efficiency, yet no effects observed for Cd(II) and Cr(IV). In general, 1 min reaction and 5 min magnetic treatment were found sufficient to achieve considerable heavy metal removals.

Magnetically modified sugarcane bagasse with high adsorption capacity was prepared by Yu et al. [156]. Adsorption of Cd(II) and Pb(II) in single solute system increased from pH 2 to 5. Isoelectric point was found to be 2.4 and therefore responsible for an increased uptake of Cd(II) and Pb(II) by the adsorbent. Pb(II) exerted an inhibitory effect on Cd(II) adsorption in a binary system. Inhibitory effect increased with increased in initial concentration ratio of Pb(II) and Cd(II). Removal percentages of Cd(II) decreased greatly with the increasing of Pb(II) concentration from 45.02% to 7.55% when ratio changed from 1:4 to 3:2 at initial total concentration 0.5 mmol/L.Magnetic hydroxyapatite nanoparticles (MNHAP) were synthesized and explore the possibility of using MNHAP as adsorbents for the removal of Cd(II) and Zn(II) from aqueous solution [157]. MNHAP had higher affinity for Cadmium than Zinc in a binary system while maximum adsorption capacities were found to be 1.964 and 2.151 mmol/g, respectively.

A magnetic resin was prepared with micro-suspension polymerization and subsequent surface modification with amino groups [158]. Ion concentrations of Cu(II), Ni(II), and Co(II) reduced to 0.537, 1, 0.1 mg/L respectively for various initial concentration solutions. Recovery of metals in pure form was above 99 percent for all the three metals. The authors concluded that each amino group interacted with one metal ion, rather than forming a complex. Thus the interaction was weak and bound metal ion could be easily recovered from the magnetic resin. Pang et al. [159] grafted PEI on a magnetic powder composed of SiO_2 and Fe_3O_4 to form a magnetic adsorbent for the removal of Cu(II), Zn(II) and Cd(II) from aqueous phase. Maximum removal was observed at pH 6.5 with the adsorbent showing preferential adsorption in the order Cu(II) > Zn(II) > Cd(II). The Langmuir model described the equilibrium data well. Acid treatment of the adsorbent produced an irrevocable decrease in Zn(II) removal efficiency, while an increase in removal efficiency was observed on alkali treatment.It was possible that first the PEI-grafted adsorbent was protonated and some H^+ occupied the surface binding sites in the process of acid treatment and second a few weak grafted PEI released to the solution due to the acid soaking, inducing to the decrease of amino groups. Similarly, after treated by alkali, the surface of the adsorbent was deprotonated, and some functional groups especially hydroxyl might form on the adsorbent surface to chelatemetal ions. The adsorbent retained an 84 percent efficiency up to four adsorption desorption cycles on treatment with 0.02 mol/L EDTA solution.

A study was conducted by Zhang et al. [160] in which, $CoFe_2O_4$-rGO was prepared by the stated method and used to test its efficacy in removal of Pb(II) and Hg(II). Highest adsorption equilibrium for Pb was 299.4 mg/g at pH 5.3; while for Hg was 157.9 mg/g at pH 4.6.Super paramagnetic magnetite (Fe_3O_4) nanoparticles coated with CM-β-CD polymer were synthesized, which could be usedas an efficient adsorbent for the removal of heavy metal

ions from wastewater [161]. Surface modification with CM-β-CD increased the maximum uptake capacity of magnetite particles from 28.01, 17.01, 8.83 mg/g for Pb (II), Cd (II) and Ni (II) to 64.5, 27.7 and 13.20 mg/g. Presence of carboxyl and hydroxyl groups in the CM-β-CD polymer generated strong affinity for the metal ions. The equilibrium data could be described by the Langmuir model. Adsorption of Pb (II) was preferential to that of Cd (II) and Ni (II) in multi metal solutions. Competitive adsorption of Pb (II) was described using the Pearson theory while the suppressive effect of Pb (II) over Cd (II) and Ni (II) was attributed to Pb metal coordination, stereochemical and redox characteristics. Urban wastewater when treated with the adsorbent showed Pb (II) removal of 99.99 percent at pH 7 despite the presence of Cd (II) and Ni (II).

A summary of the adsorption capacity and other parameters for the removal of cations from wastewater using magnetic adsorbents has been presented in Table 3. Table 4 represents the applicable isotherm and kinetic models for each of the magnetic adsorbents discussed. In most cases Pseudo Second order kinetic data and Langmuir Isotherm were found to fit well with the experimental data.

2.3. Sorption of dyes

Dyes are colouring agents used to impart value to the final product. These dyes released as effluent from industries such as textile, clothing, and printing process are disposed off into the municipal waste stream [162]. Besides making the water odious, dyes are also known to have carcinogenic and mutagenic effects on humans and aquatic organisms [163]. Hence from environment point of view, their removal is of utmost significance.

2.3.1. Same type of dye

2.3.1.1. Acid Orange. Magnetic chitosan nanoparticles were prepared and then modified with ethylene diamine to increase the $-NH_2$ active groups to enhance the adsorption capacity (EMCN) for acid dyes [164]. The adsorption behaviour towards Acid Orange 7 (AO7) and Acid Orange 10 (AO10) was studied. Maximum adsorption capacity occurred at pH 4 for AO7 and pH 3 for AO10. The EMCN showed higher adsorption capacity for AO7 than AO10 due to smaller particle size and presence of monovalent sulfonated acid group. The monovalent nature of AO7 dye makes more protonated amino groups on the chitosan particle available for adsorption of dye molecules. Langmuir adsorption capacity for AO7 was 3.47 mmol/g and 2.25 mmol/g at 298 K. In another case, $CuFe_2O_4$/activated carbon with mass ratios 1:1, 1:1.5 and 1:2 was synthesized by Zhang et al.[165] for the removal of AO7 from wastewater. Saturation magnetization was found to decrease for low $CuFe_2O_4$ content in the composite. Removal of AO7 remained constant till pH 7and was above 60 percent on further increasing pH till 10. The authors concluded that the activated carbon in the composite was mainly responsible for AO7 removal. The experimental data was satisfied by the Freundlich model suggesting that copper ferrite particles made the surface of activated carbon homogeneous. Adsorption capacity of the 1:1.5 composite was 654 mg/g compared to 404 mg/g of the original activated carbon.

2.3.1.2. Acid Red B. Four magnetic powder MnO–Fe2O3 composites of different Mn:Fe mole rates were prepared and their performance was evaluated for azo dye- acid red B (ARB) from water [166]. Both the surface and inner cavities of the composite were found to be readily accessible for ARB adsorption. Acidic range of pH i.e. <5 was found to be favourable for the removal of ARB. The order of adsorption capacity at the pH range studied was Mn1Fe3+Fe > Mn1Fe3 > Mn1Fe2 > Mn2Fe3. The sequence of uptake of ARB was observed to be in the same order. The maximum adsorption capacity was for Mn1Fe3+Fe equal to 105.3 mg/g. Sulphate ions of concentration 0.05 mol/L decreased the removal of ARB by Mn1Fe3+Fe from 98 percent to 10.7 percent.

2.3.1.3. Methylene Blue. A lot of studies have been carried out to on removing methylene blue (MB). Zhang et al. [167] studied the adsorption of methylene blue onto humic acid-coated Fe_3O_4 nanoparticles (HA-Fe_3O_4) with a saturation magnetization of 77 emu/g. The HA-Fe_3O_4 nanoparticles were found to possess much higher adsorbed amount of MB than the bare Fe_3O_4 nanoparticles and HA powders with the maximum adsorbed amount of MB as 0.291 mmol/g. Also, the amount of MB adsorbed was directly proportional to the pH of the MB solution. Senapati et al. [168] synthesized a $CoFe_2O_4$–Cr_2O_3–SiO_2 fluorescent magnetic nanocomposite (FMNC) for degradation of methylene blue in aqueous solution under UV irradiation. The composite is a suitable photocatalyst for degradation of organic pollutants due to photoluminescence property and high band gap energy. Through experiments, the saturation magnetization (M_s), coercivity(H_c) and retentivity (M_r) were found to be 5.10 emu g^{-1}, 482 Oe and 1.79 emu g^{-1}, respectively. Chen et al. [169] fabricated magnetic manganese oxide nanostructures by mixing $KMnO_4$with Fe_3O_4 particles capped by oleic acid. The various MnO_x composites were observed to have large adsorption capabilities attributed to the large surface area and pore volume. The N2 adsorption–desorption isotherms can be categorized as type IV indicating the presence of mesopores. The compounds also showed strong binding of methylene blue due to a combination of electrostatic attraction and hydrogen bonding. Fan et al. [170] prepared a magnetic adsorbent toward methylene blue which constituted magnetic chitosan and graphene oxide (MCGO). The adsorption process doesn't fit to the first order rate equation and follows a pseudo second order model. The maximum adsorption capacity was found to be 180.83 mg/g. Ai et al. [171] produced a Graphene nanosheet (GNS)/magnetite (Fe_3O_4) composite with an extraordinary adsorption capacity and fast adsorption rate of methylene blue (MB) in water. The composite was found to possess a saturation magnetization of 42.9 emu g^{-1}. Moreover, it showed a faster rate for MB adsorption when compared with other magnetic carbonaceous composite, i.e., AC/Fe_3O_4 compositeand MWCNTs/Fe_3O_4 composite. In the experiments that were performed, the adsorption capacity was found to be directly proportional to the pH of the solution.

2.3.1.4. Methyl Orange. Zhu et al. [172] utilized the miroemulsion process to produce Mγ-Fe_2O_3/CSCs with weight ratio of γ-$Fe_2O_3$to chitosan of 1:10 and 2:5 for the investigation of adsorption of methyl orange (MO). The adsorption capacities for the two composites were found to be 29.50 mg/g and 29.37 mg/g, respectively. The saturated magnetization (σ_s) was found to vary with the additive dosage of γ-Fe_2O_3.To quantify the effect of adsorbent amount, it was observed that removal of MO increased from 15.35% to 98.25% with increasing adsorbent dosage from 0.1 g L^{-1} to 1.0 g L^{-1}. The Lagergren pseudo-second-order kinetics fit the adsorption isotherms best. Fe_3O_4/ZnCr-layered double hydroxide adsorbent is effective in removing heavy metal ions like Fe^{2+}, Fe^{3+}, Cr^{3+}, and Zn^{2+} into precipitates via two-step microwave hydrothermal method [173]. The maximum adsorption capacity for methyl orange was found to be 240.16 mg/g.

Yu et al. [174] fabricated magnetic carbon nanotubes (CNTs) by Fenton's reagent method. These serve as adsorbents for removal of methyl orange (MO) dye from aqueous solutions with an adsorption capacity of28 mg/g and the mean energy of adsorption as 3.72 kJ/mol.The Freundlich isotherm model fitted the experiment data better than the Langmuir isothermmode.

Table 3
Adsorption capacity and other parameters for adsorption of cations by magnetic adsorbents.

S. no.	Adsorbent Name	Contact time	Optimal pH	Temperature °C	Concentration Range	Adsorbent Capacity	Saturation Magnetization (emu/g)	Pollutant	Reference
1	α-ketoglutaric acid modified magnetic chitosan	90 min	6	25 ± 1	10-1000 mg/L	201.2 mg/g	20.26	Cd(II)	[120]
2	$CuFe_2O_4$ from PCB sludge	180 min	6	25 ± 1	-	13.87 mg/g @ 25°C 15.63 mg/g @ 35 °C 17.54 mg/g @ 45 °C	62.52	Cd(II)	[121]
3	Shellac-coated Iron Oxide	24 h	8	25	0.469–82.8 mg/L	18.8 mg/g	39.1	Cd(II)	[122]
4	Amine-functionalized Silica Magnetite	24 h	5.5 ± 0.1	25	50-150 mg/L	10.41 mg/g	57.2	Cu(II)	[124]
5	Amine functionalized Fe_3O_4	5 min	6	25	0.1-5 mg/L	25.77 mg/g	-	Cu(II)	[125]
6	Pectin coated Iron Oxide	24 h	5.5 ± 0.1	25 ± 1	10-1000 mg/L	48.99 mg/g	59.2	Cu(II)	[126]
7	Gum Arabic treated Fe_3O_4	5 min	5.1	27	200 mg/L	38.5 mg/g	-		[127]
8	S. cerevisiae immobilised on chitosan-coated magnetic nanoparticles	2 h	4.5	28	40-500 mg/L	144.9 mg/g	-	Cu(II)	[128]
9	Carboxymethyl-β-cyclodextrin modified Fe_3O_4	4 h	6	25-55	50-400 mg/L	47.2 mg/g @ 25 °C 42.01 mg/g @ 35°C 38.75 mg/g @ 45 °C	-	Cu(II)	[129]
10	EDTA functionalized Fe_3O_4	5 min	6	25	1-6 mg/L	46.27 mg/g	81.42	Cu(II)	[120]
11	Sulfonated Graphene Oxide	6 h	5	50	20-60 mg/L	62.73 mg/g	-	Cu(II)	[131]
12	Hyaluronic acid microspheres	7 h	6.8	25	10-50 mg/L	29.42 mg/g	44.59	Cu(II)	[132]
13	Composite using waste fungal mycelium and Fe_3O_4	8 h	5.5	25	0-300 mg/L	71.36 mg/g	4.2	Cu(II)	[133]
14	Hydrous Aluminium oxide embedded Fe_3O_4 (2:5)	1 h	6.5	25 ± 1	0-160 mg/L	88.49 mg/g	17.9	F	[134]
15	Aluminum-type superparamagnetic adsorbents	MASG- 8 h MASP – 9 h	6	25	-	MASG- 15 g/kg MASP – 5.5 g/kg	MASG- 8.7 MASP – 8.7	F	[135]
16	Polypyrrole& Fe_3O_4 composite	24 h	6.5	25-45	5-100 mg/L	17.63-22.31 mg/g	-	F	[136]
17	Sulfate-doped Fe_3O_4/Al_2O_3	7 h	7	25	2-160 mg/L	70.4 mg/g	16	F	[137]
18	Fe_3O_4 microroses	100 min	5.5	20-33	80 mg/L	46.5- 47.1 mg/g	-	Pb(II)	[140]
19	Fe_3O_4& Silica-Xanthan gum composite	240 min	6	20	10-100 mg/L	21.32 mg/g	-	Pb(II)	[141]
20	Magnetic alginate beads from sodium alginate	12 h	7	30	100-400 mg/L	50 mg/g	47.9	Pb(II)	[142]
21	Maghemite functionalized with citrate ions encapsulated into calcium alginate beads	4 h	2.3-6	-	0.25-4 mmol/L	100 mg/g	32.2	Pb(II)	[143]
22	Sodium Alginate gel beads crosslinked by Zirconium	24 h	5	30	50-800 mg/L	333.3 mg/g	7.88	Pb(II)	[144]
23	Triethylene-Tetramine grafted magnetic chitosan	1.5 h	6	25	200 mg/L	369 mg/g	-	Pb(II)	[145]
24	Chitosan/Graphene Oxide composite	60 min	5	30 ± 0.2	-	76.94 mg/g	58.5	Pb(II)	[146]

Table 3 (*Continued*)

S. no.	Adsorbent Name	Contact time	Optimal pH	Temperature °C	Concentration Range	Adsorbent Capacity	Saturation Magnetization (emu/g)	Pollutant	Reference
25	Ethylenediamine-modified yeast biomass coated with magnetic chitosan microparticles	1 h	5.5	20-40	10-500 mg/L	121.26 mg/g @ 20 °C 127.37 mg/g @ 30 °C 134.9 mg/g @ 40°C	-	Pb(II)	[147]
26	Magnetic powdered activated carbon	120 min	4.5	-	100 μg/L	91% removal	-	Hg(II)	[148]
27	Iron oxide modified with 2-mercaptobenzothiazole	4 min	9	25	2-4000 ng/mL	590 μg/g	-	Hg(II)	[149]
28	Silica coated magnetite	2 d	-	25 ± 1	50 μg/L	25 μg/g	62	Hg(II)	[150]
29	Rhodamine hydrazide modifying Fe_3O_4 microspheres	30 min	-	-	0.01-0.2 mM	34.7 μ mol/g	74.2	Hg(II)	[151]
30	Thiol-functionalized magnetic silica	60 min	-	-	-	19.79 mg/g	-	Hg(II)	[152]
31	Thiol-functionalised silicacoated magnetite nanoparticles	1 h	6	22.5	40-1000 μg/L	207.7 mg/g	0.25	Hg(II)	[153]
32	Dithiocarbamate functionalized magnetite	-	7	22 ± 1	50 μg/L	112 ± 3 mg/g	-	Hg(II)	[154]
33	Nanoscale zero valent iron particles	5 min	Neutral	-	100 μg/mL	100% removal for Pb (II) 100% removal for Cr (VI) 80% removal for Cd (II)	-	Pb(II), Cr(VI), Cd(II)	[155]
34	Magnetic modified sugarcane bagasse	-	5	-	0.05–1.2 mmol/L	1.2 mmol/g for Pb (II) 1.1 mmol/g for Cd (II)	-	Pb(II), Cd(II)	[156]
35	Magnetic Hydroxyapatite nanoparticles	24 h	5 ± 0.1	25 ± 1	10^{-4}–10^{-2} mol/L	1.964 mmol/g for Cd (II) 2.151 mmol/g for Zn (II)	59.4	Cd(II), Zn(II)	[157]
36	Amine modified magnetic beads	-	3-5	Room temperature	-	Co (II)- 50.3 mg/g Ni (II)- 49.6 mg/g Cu (II)- 51.7 mg/g	20.3	Co(II), Cu(II), Ni (II)	[158]
37	Polyethylenimine grafted magnetic adsorbent	10 min	6.5	Room temperature	100–600 mg//L	Cu(II)- 157.81 mg/g Zn(II)- 138.84 mg/g Cd(II) – 105.26 mg/g	-	Cu(II), Zn(II), Cd(II)	[159]
38	Cobalt ferrite reduced Graphene oxide	-	Pb(II) – 5.3 Hg(II) – 4.6	25	-	Pb(II) – 299.4 mg/g Hg(II) – 157.9 mg/g		Pb(II), Hg (II)	[160]
39	Carboxymethyl-β-cyclodextrin polymer grafted on Fe_3O_4	45 min	5.5	25	50–400 mg/L	Pb(II) – 64.5 mg/g Cd(II) - 27.7 mg/g Ni(II) – 13.2 mg/g	-	Pb(II), Cd(II), Ni (II)	[161]

2.3.1.5. Methyl Violet. Duan et al. [175] used the chemical precipitation method to prepare a magnetic composite of Fe_3O_4-halloysite nanotube (HNT) with a high adsorption capacity for methyl violet (MV). The composite fits suitable to the role of removing cationic dyes from waste water. An increase in removal efficiency from 52.97% to 99.94% was observed with the increase in dosage of adsorbent from0.05 to 0.40 g. However it declined from 77.05 to 18.20 mg/g as the adsorbent dose increased from 0.05 to0.40 g. Thus, the optimum amount arrived at was 0.10 g.

2.3.2. Different type of dyes

Zhang et al. [176] modified Fe_3O_4 magnetic nanoparticles(MNPs) with 3-glycidoxypropyltrimethoxysilane (GPTMS) and glycine (Gly) to form excellent adsorbents for both anionic and

Table 4
Isotherm and Kinetic Models for adsorption of cations by magnetic adsorbents.

Sno.	Adsorbent Name	Applicable Isotherm Model	Applicable Kinetics Model	Pollutant	Reference
1	α-ketoglutaric acid modified magnetic chitosan	Langmuir	Pseudo-Second-Order	Cd(II)	[120]
2	$CuFe_2O_4$ from PCB sludge	Langmuir	Pseudo-Second-Order	Cd(II)	[121]
3	Shellac-coated Iron Oxide	Langmuir, Freundlich	Pseudo-Second-Order	Cd(II)	[122]
4	Amine-functionalized Silica Magnetite	Langmuir	Pseudo-Second-Order	Cu(II)	[124]
5	Amine functionalized Fe_3O_4	Langmuir	Pseudo-Second-Order	Cu(II)	[125]
6	Pectin coated Iron Oxide	Langmuir, Freundlich	Pseudo-Second-Order	Cu(II)	[126]
7	Gum Arabic treated Fe_3O_4	Langmuir	-	Cu(II)	[127]
8	S. cerevisiae immobilised on chitosan-coated magnetic nanoparticles	Langmuir		Cu(II)	[128]
9	Carboxymethyl-β-cyclodextrin modified Fe_3O_4	Langmuir	Pseudo-Second-Order	Cu(II)	[129]
10	EDTA functionalized Fe_3O_4	Langmuir	Pseudo-Second-Order	Cu(II)	[130]
11	Sulfonated Graphene Oxide	Langmuir	Pseudo-Second-Order	Cu(II)	[131]
12	Hyaluronic acid microspheres	Freundlich	Pseudo-Second-Order	Cu(II)	[132]
13	Composite using waste fungal mycelium and Fe_3O_4	Langmuir	Pseudo-Second-Order	Cu(II)	[133]
14	Hydrous Aluminium oxide embedded Fe_3O_4 (2:5)	Langmuir, Freundlich	Pseudo-Second-Order	F	[134]
15	Aluminum-type adsorbents	Langmuir	-	F	[135]
16	Polypyrrole and Fe_3O_4 composite	Freundlich, Langmuir-Freundlich	Pseudo-Second-Order	F	[136]
17	Sulfate-doped Fe_3O_4/Al_2O_3	Two-site Langmuir	Elovich	F	[137]
18	Fe_3O_4& Silica-Xanthan gum composite	Langmuir	Pseudo-Second-Order	Pb(II)	[141]
19	Magnetic alginate beads from sodium alginate	Langmuir	Pseudo-Second-Order	Pb(II)	[142]
20	Maghemite functionalized with citrate ions encapsulated into calcium alginate beads	Langmuir	Pseudo-Second-Order	Pb(II)	[143]
21	Sodium Alginate gel beads crosslinked by Zirconium	Langmuir	Pseudo-Second-Order	Pb(II)	[144]
22	Triethylene-Tetramine grafted magnetic chitosan	Langmuir	Pseudo-Second-Order	Pb(II)	[145]
23	Chitosan/Graphene Oxide composite	Langmuir	Pseudo-Second-Order	Pb(II)	[146]
24	Ethylenediamine-modified yeast biomass coated with magnetic chitosan microparticles	Langmuir, Freundlich	Pseudo-Second-Order	Pb(II)	[147]
25	Iron oxide modified with 2-mercaptobenzothiazole	Langmuir	-	Hg(II)	[149]
26	Thiol-functionalised silicacoated magnetite nanoparticles	Langmuir, Freundlich	-	Hg(II)	[153]
27	Dithiocarbamate functionalized magnetite	Langmuir, Freundlich	Pseudo-Second-Order	Hg(II)	[154]
28	Magnetic modified sugarcane bagasse	Langmuir	Pseudo-First-Order, Pseudo-Second-Order	Pb(II), Cd(II)	[156]
29	Magnetic Hydroxyapatite nanoparticles	Langmuir	Pseudo-Second-Order	Cd(II), Zn(II)	[157]
30	Amine modified magnetic beads	Langmuir	Pseudo-Second-Order	Co(II), Cu(II), Ni(II)	[158]
31	Polyethylenimine grafted magnetic adsorbent	Langmuir	Pseudo-Second-Order	Cu(II), Zn(II), Cd(II)	[159]
32	Cobalt ferrite reduced Graphene oxide	Langmuir	Pseudo-Second-Order	Pb(II), Hg(II)	[160]
	Carboxymethyl- β-cyclodextrin polymer grafted on Fe_3O_4	Langmuir	Pseudo-Second-Order	Pb(II), Cd(II), Ni(II)	[161]

cationic dyes (Only in this case MB refers to methyl blue and MEB refers to methylene blue, OR is orange I, AZ is azure I, AR is acid red 18). After studying the effect of pH it was concluded that the adsorption quantity for anionic dyes (MB, AR and OR) increased with the initial pH of the solution decreasing from 6.0 to2.0.Moreover, the adsorption quantity for two cationic dyes(MEB and AZ) increased with the pH from 8.0 to 12.5. In addition to this, the experiments revealed that the equilibrium adsorption capacity (q_e) of the dye increases with the initial dye concentration increasing. The maximum adsorption capacity (q_m) of the five dyes: MB, OR, AR, MEB and AZ was calculated by the Langmuir equation and is 158,49, 45, 123 and 357 mg g^{-1}, respectively.

Table 5
Adsorption capacity and other parameters for adsorption of dyes and organic pollutants by magnetic adsorbents.

S. no.	Adsorbent Name	Contact time	Optimal pH	Temperature °C	Concentration Range	Adsorbent Capacity	Saturation Magnetization (emu/g)	Pollutant	Reference
1	Ethylenediamine modified chitosan	1.5 h	AO7-4 AO10-3	25	0.5-6 mmol/L	AO7 -3.47 mmol/g AO10 – 2.25 mmol/g	25.6	Acid Orange 7 Acid Orange 10	[164]
2	$CuFe_2O_4$/activated carbon composite	30 min	5.2 ± 0.1	25 ± 1	Up to 1200 mg/L	392 mg/g	-	Acid Orange 7	[165]
3	MnO–Fe_2O_3 composites	2 h	3.5	20	100-400 mg/L	Mn1Fe3+Fe -105.3 mg/g Mn1Fe3 – 85.5 mg/g Mn1Fe2 – 77.5 mg/g Mn2Fe3 – 71.4 mg/g	36.7-45.6	Acid Red B	[166]
4	Humic acid-coated Fe_3O_4 nanoparticles	2 h	8.4	20	0.2-5 mmol/L	0.291 mmol/g	77	Methylene Blue	[167]
5	Cobalt Ferrite- Silica dioxide composite	40 min	-	-	-	51 % during first 15 min	5.1	Methylene Blue	[168]
6	Manganese Oxide S1-Dried product S2- S1 after calcification	-	7.6	Room Temperature	100 mg/L	S1- 35.4 mg/g S2 – 70 mg/g	S1-11 S2-5	Methylene Blue	[169]
7	Chitosan & Graphene Oxide composite	-	10	30 ± 0.2	-	180.83 mg/g	-	Methylene Blue	[170]
8	Graphene & Magnetite composite	20 min	Basic pH	25	10-25 mg/L	43.82 mg/g	42.9	Methylene Blue	[171]
9	Fe_2O_3crosslinked chitosan composite (1:10)	120 min	4	27 ± 0.2	-	29.5 mg/g	-	Methyl Orange	[172]
10	Fe_3O_4/ZnCr-layered double hydroxide	24 h	6.4-7.3	25	-	240.16 mg/g	23.6	Methyl Orange	[173]
11	Carbon nanotubes	3 h	-	25	20-80 mg/L	28.8 mg/g	12.4	Methyl Orange	[174]
12	Fe_3O_4 impregnated on Halloysite nanotube	8 h	Natural	25	150 mg/L	90.09 mg/g	8.47	Methyl Violet	[175]
13	Fe_3O_4 modified with 3-glycidoxypropyltrimethoxysilane and glycine	120 min	MB,OR,AR- 2.5 MEB,AZ-12	25	20-400 mg/L	MB*- 158 mg/g OR- 49 mg/g AR- 45 mg/g MEB- 123 mg/g AZ- 357 mg/g	37	Methyl Blue, Methylene Blue, Orange I, Azure I, Acid Red 18	[176]
14	Sodium Dodecyl Sulfate modified Maghemite	5 min	6	Room Temperature	1-400 mg/L	BCB-166.7 mg/g Th-200 mg/g JG- 172.4 mg/g	-	Brilliant Cresyl Blue, Thionine, Janus Green B	[177]
15	Carbon nanotubes, polyether, ferroferric oxide polymer	6 h	6.2	35	5-25 mg/L	Orange II – 67.57 mg/g Sunset Yello FCF- 85.47 mg/g Amarnth- 47.39 mg/g	-	Orange II, Sunset Yellow FCF, Amarnth	[178]
16	Carbon nanotubes and iron oxide composed nanocomposite	24 h	7	25 ± 2	1.4-37.4 mg/L	MB- 15.74 mg/g NR- 20.33 mg/g BCB- 23.55 mg/g	-	Methylene Blue, Neutral Red, Brilliant Cresyl Blue	[179]
17	Carbon nanotube modified with magnetic nanoparticle	15 min	7	Room temperature	-	CV- 227.7 mg/g JG- 250 mg/g Th – 36.4 mg/g MB – 48.1 mg/g	-	Crystal Violet, Thionine, Janus Green B, Methylene Blue	[180]

Table 5 (*Continued*)

S. no.	Adsorbent Name	Contact time	Optimal pH	Temperature °C	Concentration Range	Adsorbent Capacity	Saturation Magnetization (emu/g)	Pollutant	Reference
18	Magnetic Alginate Beads	48 h	6.7 ± 0.2	-	0.4-20 mmol/L	MO- $2 * 10^{-3}$ mmol/g MB- $5.9 * 10^{-2}$ mmol/g	-	Methyl Orange, Methylene Blue	[181]
19	Magnetic alginate beads crosslinked with epichlorohydrin	48 h	MO- 8.0 ± 0.2 MB- 7.5 ± 0.3	-	-	MO- 0.02 mmol/g MB- 0.7 mmol/g	-	Methyl Orange, Methylene Blue	[182]
20	Magnetically modified spent grain	3 h	-	Room temperature	-	Aniline Blue – 44.7 mg/g Bismarck Brown Y – 72.4 mg/g Crystal Violet -40.2 mg/g Nile Blue A – 64.1 mg/g	-	Aniline Blue, Bismarck Brown Y, Crystal Violet, Nile Blue A	[183]
21	Aminated β-cyclodextrin functionalized Fe_3O_4	4 h	7	25	5-20 mg/L	CBZ- 1.304 mg/g NAP- 1.074 mg/g BPA- 0.899 mg/g	57.1	Carbamazepine, Naproxen, Bisphenol A	[184]
22	Activated Carbon from almond shells treated with Fe^{3+}/Fe^{2+} solution	72 h	2	25-45	23-227 mg/L	73.96 mg/g @ 25°C 84.07 mg/g @ 35 °C 87.15 mg/g @45 °C	4.47	Tri Nitro Phenol	[178]
23	Montmorillonite combined with Cu(II)/Fe(III) oxides	3 h	5	20	4.4 mg/L	96% removal	3.9	Humic Acid	[179]
24	Cationic Hydrogel	-	7	23 ± 1	-	100% removal	-	Natural Organic Matter	[180]
25	Magnetized ragweed pollen grains	24 h	DI water – 6.3-6.5 Stormwater- 7.09	-	1 mg/L	(% removal) DI Stormwater 72.4 100 67.9 80 94.1 98.6 39.4 100 55.6 84.6	-	Natural Organic Mateer	[181]

Afkhami et al. [177] modified Maghemite nanoparticles with sodium dodecyl sulfate (SDS) to form an adsorbent SDS–γ-Fe_2O_3 for removal of cationic dyes brilliant cresyl blue (BCB), thionine (Th) and janus green b (JG) with maximum predicted adsorption capacities as 200.0, 166.7 and 172.4 mg g^{-1}, respectively. The adsorption efficiencies initially increased with adsorbent dose and decreased after a certain dosage. Increasing the amount of surfactant up to 3.0 mL, the efficiency of removal of dyes was nearly constant. But at higher volumes, clearly the equilibrium sorption decreased as the SDS volume increased.

Gao et al. [178] combined multi-wall carbon nanotubes, poly (1-glycidyl-3-methylimidazolium chloride) (ionic liquid-based polyether) and ferroferric oxide to prepare a magnetic polymer multi-wall carbon nanotube (MPMWCNT) nanocomposite. The model adsorbents used were anionicazo dyes of orange II, sunset yellow FCF and amaranth. The adsorption of the dyes was favoured by low pH values due to ionization/dissociation of the adsorbate molecules. Ranking of the anionic azo dyes in terms of adsorption capacity of MPMWCNT was the following order: sunset yellow FCF > orangeII > amaranth. Gong et al. [179] prepared a magnetic multi-wall carbon nanotube (MMWCNT) nanocomposite for removal of cationic dyes like methylene blue, neutral red (NR) and brilliant cresyl blue from aqueous solutions. The adsorption capacity which initially increased declined as the MMWCNT dosage crossed 0.5 g L^{-1}. The q_m values for the adsorption of MB, NR and BCB were 15.74 mg g^{-1}, 20.33 mg g^{-1} and 23.55mg g^{-1}, respectively. The experiments also showed that the adsorption of the dyes was directly proportional to the pH of the solution.

Madrakian et al. [180] used magnetic-modified multi-walled carbon nanotubes as an adsorbent for removal of cationic dyes crystal violet (CV), thionine (Th), janus green B (JG), and methylene blue (MB) from water samples with maximum adsorption capacities to the tune of 227.7, 250.0, 36.4 and 48.1 mg/g, respectively. After various investigations, 7.0 was found to be the optimum pH for removing the dyes. On increasing the pH from 4 to 7, the adsorption quantity increased. Thereafter, it remained constant. Following a sustainable production procedure for a magnetic adsorbent, Rocher et al. [181] prepared magnetic beads with a biopolymer extracted from algae, sodium alginate. The beads were tested for the removal of methyl orange and methylene blue. The absorption of the pollutants on the adsorbent follows pseudo-second-order kinetics. The amount of dye absorbed was found to increase with an increase

Table 6
Isotherm and Kinetic models for adsorption of dyes and organic pollutants by magnetic adsorbents.

Sno.	Adsorbent Name	Applicable Isotherm Model	Applicable Kinetics Model	Pollutant	Reference
1	Ethylenediamine modified chitosan	Langmuir	-	Acid Orange 7 Acid Orange 10	[164]
2	$CuFe_2O_4$/activated carbon composite	Freundlich	-	Acid Orange 7	[165]
3	MnO–Fe_2O_3 composite	Langmuir	Pseudo-Second-Order	Acid Red B	[166]
4	Humic acid-coated Fe_3O_4 nanoparticles	Langmuir	Pseudo-Second-Order	Methylene Blue	[167]
5	Cobalt Ferrite- Silica dioxide composite	-	Pseudo-First-Order	Methylene Blue	[168]
6	Chitosan & Graphene Oxide composite	Langmuir	Pseudo-Second-Order	Methylene Blue	[170]
7	Graphene & Magnetite composite	Langmuir	Pseudo-Second-Order	Methylene Blue	[171]
8	Fe_2O_3crosslinked chitosan composite	-	Pseudo-First-Order	Methyl Orange	[172]
9	Fe_3O_4/ZnCr-layered double hydroxide	-	Pseudo-Second-Order	Methyl Orange	[173]
10	Carbon nanotubes	Freundlich, Dubinin-Radushkevich	Pseudo-Second-Order	Methyl Orange	[174]
11	Fe_3O_4 impregnated on Halloysite nanotube	Langmuir	Pseudo-Second-Order	Methyl Violet	[175]
12	Fe_3O_4 modified with 3-glycidoxypropyltrimethoxysilane and glycine	Langmuir	Pseudo-Second-Order	Methyl Blue, Methylene Blue, Orange I, Azure I, Acid Red 18	[176]
13	Sodium Dodecyl Sulfate modified Maghemite	Langmuir	-	Cresyl Blue, Thionine, Janus Green B	[177]
14	Carbon nanutube, polyether, ferroferric oxide polymer	Langmuir	Pseudo-Second-Order	Orange II, Sunset Yellow FCF, Amarnth	[178]
15	Carbon nanotubes and iron oxide composed nanocomposite	Freundlich	Pseudo-Second-Order	Methylene Blue, Neutral Red, Brilliant Cresyl Blue	[179]
16	Carbon nanotube modified with magnetic nanoparticle	Langmuir	-	Crystal Violet, Thionine, Janus Green B, Methylene Blue	[180]
17	Magnetic Alginate Beads	Langmuir	Pseudo-Second-Order	Methyl Orange, Methylene Blue	[181]
18	Magnetic alginate beads crosslinked with epichlorohydrin	Langmuir	Pseudo-Second-Order	Methyl Orange, Methylene Blue	[182]
19	Magnetically modified spent grain	Langmuir	-	Aniline Blue, Bismarck Brown Y, Crystal Violet, Nile Blue A	[183]
20	Aminated β-cyclodextrin functionalized Fe_3O_4	Freundlich	Pseudo-Second-Order	Carbamazepine,Naproxen, Bisphenol A	[184]
21	Activated Carbon from almond shells treated with Fe^{3+}/Fe^{2+} solution	Sips	Pseudo-Second-Order	Tri Nitro Phenol	[185]
22	Montmorillonite combined with Cu(II)/Fe(III) oxides	Langmuir	-	Humic Acid	[186]
23	Cationic Hydrogel	-	Pseudo-Second-Order	Natural Organic Matter	[187]
24	Magnetized ragweed pollen grains	Freundlich	-	Natural Organic Matter	[188]

in the concentration of the dye. The adsorption is mainly due to the encapsulated activated carbon which is not pH-sensitive. Therefore pH was not found to have a profound effect on the adsorption process. The maximum adsorption capacities were found to be 0.02 mmol/g and 0.059 mmol/g for MO and MB, respectively. The same authors' cross linked epicholorhydrin with the magnetic beads prepared before [182]. The maximum adsorption capacities were found to be 0.02 mmol/g and 0.7 mmol/g for MO and MB respectively. The adsorption of MB is accompanied by both electrostatic and hydrophobic interactions as opposed to only hydrophobic interactions in the case of the negatively charged MO.

Safarik et al. [183] magnetically altered spent grain by contact with water-based magnetic fluid to form an adsorbent for the removal of water-soluble dyes. The maximum adsorption capacity attained was 72.4 mg of due (Bismarck brown Y) per g of spent grain.

2.4. Sorption of organic pollutants

Disposal of organic pollutants such as pharmaceutically active compounds, humic acid, trinitrophenol is a public concern. Most of these chemicals are not completely removed from municipal wastewaters by sewage treatment plants [184]. Not only are these

compounds difficult to remove from the environment, they also have adverse effects on plant and animal life. Hence due to this fact, their removal from the environment is of great importance.

The ability of β-CDen to adsorb organic pollutants was combined with Fe_3O_4 particles to form magnetic nanospheres capable of removing PhACs – carbamazepine (CBZ), naproxen (NAP) and EDCs- Bisphenol A (BPA) from wastewater [184]. For CBZ the adsorption capacity was not affected by the solution pH. This was attributed to non-electrostatic interactions involving hydrogen bonds, hydrophobic and Van der Waals interactions. Adsorption capacity of NAP reduced greatly on increasing the pH from 3 to 11. The interactions were favourably hydrophobic. Adsorption capacity of BPA remained unaffected till pH 9 and reduced thereafter. This was explained on the basis of its pK_a value which lies between 9.6 and 10.2. Maximum adsorption capacities were found to be 1.304, 1.074 and 0.899 mg/g for CBZ, NAP and BPA respectively. These values were more than twice that of TGA coated magnetite particles indicating β-CDen enhanced the adsorption properties. Its presence in the nanospheres was further confirmed by results from FTIR and TGA. Activated carbon made from almond shells was treated with a solution containing Fe^{3+}/Fe^{2+} ions to give it magnetic properties [185]. This magnetic adsorbent (MASAC) was used to study the removal of trinitrophenol (TNP) from water. TNP adsorption decreased as pH rose. The dominant interactions of TNP were donor–acceptor complexation with aromatic rings of the carbon basal planes, hydrogen bonding interactions between –COOH and–OH surface functions with the nitro groups' oxygens and the acidic —OH and dipole interaction. The experimental data was well described by Sips model. In a multicomponent system containing Dinitrophenol (DNP) and TNP, $Q_{mix}/Q_o < 1$ suggested that DNP had a suppressive effect on TNP adsorption.

Magnetically modified Montmorillonite has also been used as a magnetic adsorbent for the removal of humic acid by Peng et al. [186]. 96 percent removal was observed at pH 6.1 from a 4.4 mg/L humic acid solution containing 0.02 M NaCl. Adsorption was both pH and ionic dependent. The adsorption mechanism of humic acid to the magnetic material was suggested to be the ligand exchange reaction between carboxylic groups of humic acid molecules and the magnetic material. The dependence of adsorption on pH values was due to the effect of pH on the surface charge of the magnetic material and the ionization of humic acid and the minimization of humic acid molecules at lower pH values. The increase of adsorption with the increase of ionic strength was due to the compression of the diffuse double layer and charge neutralization, the compression of the molecular volume of humic acid and the screening of the surface charge of both adsorbent and adsorbate by salt. Maximum adsorption capacity exceeded 98 mg/g.

Rao et al. [187] conducted removal of natural organic matter (NOM) using a cationic hydrogel (MCH). MCH exhibited preferential removal of higher molecular weight fraction of Aldrich Humic Acid (AHA). Maximum adsorption amount of AHA on MCH was reached at pH 7. Electrostatic precipitation was considered to be the main mechanism of removal of NOM. Pollen grains have also been used to remove HOC's from contaminated water [188]. Ragweed pollen grains were magnetized through treatment with Ferric Chloride solution and then tested in two different water samples: deionized water (DI) and natural storm water. More sorption was noticed in case of storm water than DI water. This was attributed to the fact that natural water contained more organic matter, hence more TOC. HOC and TOC formed complexes through hydrogen bonding, van der waals forces or hydrophobic association. After that the presence of cations promoted flocculation, which reduced the electrostatic repulsion and lead to sorption of the complexes on the adsorbents surface.

A summary of the adsorption capacity and other parameters for the removal of dyes and organic pollutants from wastewater using magnetic adsorbents has been presented in Table 5. Table 6 represents the applicable isotherm and kinetic models for each of the magnetic adsorbents discussed. In most cases Pseudo Second order kinetic data and Langmuir Isotherm were found to fit well with the experimental data.

3. Conclusion

The review article attempts to identify and inspect a wide range of magnetic adsorbents for the removal of diverse type of pollutants such as heavy metals, non metals, dyes and organic pollutants from water. The use of magnetic adsorbents offers a significant advantage over other adsorbents which is the ability to separate them from an aqueous solution on application of a magnetic field. From the published literature it was observed that the mechanism and kinetics of the adsorption processes depended on the chemical nature of the adsorbent surface as well as the experimental conditions such as pH, adsorbent dosage, contact time, temperature and initial pollutant concentration. Further it was noticed that most of the adsorbents followed either of the Langmuir and Freundlich isotherm and these models could be used to determine the adsorption capacities of different adsorbents. Amongst the kinetic models, pseudo second order model was followed by the most number of adsorbents. Even though a significant amount of literature regarding magnetic adsorbents is available and is increasing at an immense pace every day, there still exists several gaps that need to be addressed. These include

1. Economic studies of magnetic adsorbents to evaluate their feasibility on a commercial scale.
2. Detailed assessment of magnetic adsorbents in case of multi pollutant solutions such as 1. Heavy metals and Dyes, 2. Heavy metals and Organic pollutants 3. Organic pollutants and Dyes.
3. Investigations of the adsorption capability of different magnetic adsorbents with real industrial effluents.
4. Investigation of the removal capability of the adsorbents in a fixed bed column.

References

[1] A. Bhatnagar, E. Kumar, M. Sillanpää, Fluoride removal from water by adsorption—a review, Chem. Eng. J. (2011) 811–840.
[2] G.M. Geise, H.-S. Lee, D.J. Miller, B.D. Freeman, J.E. McGrath, D.R. Paul, Water purification by membranes: the role of polymer science, J. Polym. Sci. B: Polym. Phys. (2010) 1685–1718.
[3] B.V. Bruggen, C. Vandecasteele, T.V. Gestel, W. Doyen, R. Leysen, A review of pressure-driven membrane processes in wastewater treatment and drinking water production, Environ. Prog. (2003) 46–56.
[4] H.T. Madsen, Membrane filtration in water treatment – removal of micropollutants, in: E.G. Sogaard (Ed.), Chemistry of Advanced Environmental Chemistry of Advanced Environmental Purification Processes of Water, Elsevier, 2014, pp. 199–248.
[5] J. Gregory, Coagulation and flocculation with an emphasis on water and wastewater treatment, Chemical Engineering Journal (1981) 80.
[6] J. Bratby, Coagulation and Flocculation in Water and Wastewater Treatment, IWA Publishing, London, 2006.
[7] D.D. Ratnayaka, M.J. Brandt, K.M. Johnson, Water filtration granular media filtration, in: D.D. Ratnayaka, M.J. Brandt, K.M. Johnson (Eds.), Water Supply, Elsevier, 2009, pp. 315–350.
[8] M. Scholz, Rapid filtration, in: M. Scholz (Ed.), Wetland Systems to Control Urban Runoff, Elsevier, 2006, pp. 73–79.
[9] S. Aslan, H. Cakici, Biological denitrification of drinking water in a slow sand filter, J. Hazard. Mater. (2007) 253–258.
[10] N.P. Cheremisinoff, What sand filtration is all about, in: N.P. Cheremisinoff (Ed.), Handbook of Water and Wastewater Treatment Technologies, Elsevier, 2002, pp. 235–267.
[11] V. Gupta, I. Ali, Water treatment for inorganic pollutants by adsorption technology, in: V. Gupta, I. Ali (Eds.), Environmental Water: Advances in Treatment, Remediation and Recycling, Elsevier, 2013, pp. 29–91.
[12] V. Gupta, I. Ali, Water treatment for organic pollutants by adsorption technology, in: V. Gupta, I. Ali (Eds.), Environmental Water:Advances in Treatment, Remediation and Recycling, Elsevier, 2013, pp. 93–116.
[13] T. Karanfil, Activated carbon adsorption in drinking water treatment, Int. Sci. Technol. (2006) 345–373.

[14] G. Newcombe, Adsorption from aqueous solutions: water purification, in: Adsorption by Carbons, Elsevier, 2008, pp. 679–709.
[15] M.S. Onyango, H. Matsuda, Fluoride removal from water using adsorption technique, in: Advances in Fluorine Science, Elsevier, 2006, pp. 1–48.
[16] R. Martin, K. Iwugo, Recovery of water from wastewater by the activated carbon adsorption process, Stud. Environ. Sci. (1982) 265–283.
[17] V. Yargeau, Water and wastewater treatment: chemical processes, in: F. Zeman (Ed.), Metropolitan Sustainability: Understanding and Improving the Urban Environment, Elsevier, 2012, pp. 390–405.
[18] T. Tebbutt, Chemical treatment, in: T. Tebbutt (Ed.), Principles of Water Quality Control (Third Edition), Elsevier, 1983, pp. 175–185.
[19] A. Dabrowski, Adsorption from theory to practice, Adv. Colloid Interface Sci. (2001) 135–224.
[20] I. Langmuir, Constitution and fundamental properties of solids and liquids, J. Am. Chem. Soc. (1916) 2221–2295.
[21] Freundlich, H.M.F, Uber die adsorption in losungen, Zeitschrift für Physikalische Chemie (1906) 385–470.
[22] S. Lagergren, K. Sven, Zur theorie der sogenannten adsorption gelöster stoffe, Vetenskapsakad. Handl (1898) 1–39.
[23] Y. Ho, D. Wase, C. Forster, Kinetic studies of competitive heavy metal adsorption by spaghnum moss peat, Environ. Technol. (1966) 71–77.
[24] F.D. Natale, A. Erto, A. Lancia, Desorption of arsenic from exhaust activated carbons used for water purification, J. Hazard. Mater. (2013) 451–458.
[25] N. Spahis, A. Addoun, H. Mahmoudi, N. Ghaffour, Desorption of arsenic from exhaust activated carbons used for water purification, Desalination (2008) 519–527.
[26] M. Razvigorova, T. Budinova, N. Petrov, V. Minkova, Purification of water by activated carbons from apricot stones, lignites and anthracite, Water Res. (1998) 2135–2139.
[27] S. Pollard, F. Thompson, G. McConnachie, Microporous carbons from Moringa oleifera husks for water purification in less developed countries, Water Res. (1995) 337–347.
[28] W.-G. Li, X.-J. Gong, K. Wang, X.-R. Zhang, W.-B. Fan, Adsorption characteristics of arsenic from micro-polluted water by an innovative coal-based mesoporous activated carbon, Bioresour. Technol. (2014) 166–173.
[29] D. Mohan, C.U. Pittman Jr., Activated carbons and low cost adsorbents for remediation of tri- and hexavalent chromium from water, J. Hazard. Mater. (2006) 762–811.
[30] A.M. Warhurst, G.L. McConnachie, S.J. Pollard, The production of activated carbon for water treatment in Malawi from the waste seed husks of Moringa oleifera, Water Sci. Technol. (1996) 177–184.
[31] A. Wolborska, Adsorption on activated carbon of p-nitrophenol from aqueous solution, Water Res. (1989) 85–91.
[32] F. Cao, P. Yin, X. Liu, C. Liu, R. Qu, Mercury adsorption from fuel ethanol onto phosphonated silica gel prepared by heterogenous method, Renew. Energ. (2014) 61–68.
[33] Y. Zhang, R. Qu, C. Sun, C. Wang, C. Ji, H. Chen, et al., Chemical modification of silica-gel with diethylenetriamine via an end-group protection approach for adsorption to Hg(II), Appl. Surf. Sci. (2009) 5818–5826.
[34] P. Yin, Q. Xu, R. Qu, G. Zhao, Removal of transition metal ions from aqueous solutions by adsorption onto a novel silica gel matrix composite adsorbent, J. Hazard. Mater. (2009) 228–232.
[35] G.P. Kumar, P.A. Kumar, S. Chakraborty, M. Ray, Uptake and desorption of copper ion using functionalized polymer coated silica gel in aqueous environment, Sep. Purif. Technol. (2007) 47–56.
[36] P.A. Kumar, M. Ray, S. Chakraborty, Hexavalent chromium removal from wastewater using aniline formaldehyde condensate coated silica gel, J. Hazard. Mater. (2007) 24–32.
[37] K. Rida, S. Bouraoui, S. Hadnine, Adsorption of methylene blue from aqueous solution by kaolin and zeolite, Appl. Clay Sci. (2013) 99–105.
[38] N. Chaouati, A. Soualah, M. Chater, Adsorption of phenol from aqueous solution onto zeolites Y modified by silylation, Comptes Rendus Chimie (2013) 222–228.
[39] J. Yang, X. Dong, Y. Zhou, M.B. Yue, C.F. Zhou, F. Wei, et al., Selective adsorption of zeolite towards nitrosamine in organic solution, Microporous Mesoporous Mater. (2009) 381–388.
[40] V. Badillo-Almaraz, P. Trocellier, I. Dávila-Rangel, Adsorption of aqueous Zn(II) species on synthetic zeolites, Nuclear Instruments Methods Phys. Res. Sec. B Beam Int, Mater, Atoms (2003) 424–428.
[41] X. Jin, B. Yu, Z. Chen, J.M. Arocena, R.W. Thring, Adsorption of Orange II dye in aqueous solution onto surfactant-coated zeolite: characterization, kinetic and thermodynamic studies, J. Colloid Interface Sci. (2014) 15–20.
[42] M. Yang, J. Lin, Y. Zhan, H. Zhang, Adsorption of phosphate from water on lake sediments amended with zirconium-modified zeolites in batch mode, Ecol. Eng. (2014) 223–233.
[43] S. Kong, Y. Wang, H. Zhan, M. Liu, L. Liang, Q. Hu, Competitive adsorption of humic acid and arsenate on nanoscale iron–manganese binary oxide-loaded zeolite in groundwater, J. Geochem. Explor. (2014) 220–225.
[44] U.C. Ugochukwu, M.D. Jones, I.M. Head, D.A. Manning, C.I. Fialips, Biodegradation and adsorption of crude oil hydrocarbons supported on homoionic montmorillonite clay minerals, Appl. Clay Sci. (2014) 81–86.
[45] L. Zhang, L. Luo, S. Zhang, Adsorption of phenanthrene and 1,3-dinitrobenzene on cation-modified clay minerals, Colloids Surf A Physicochem. Eng. Aspects (2011) 278–283.
[46] Y.E. Mouzdahir, A. Elmchaouri, R. Mahboub, A. Gil, S. Korili, Equilibrium modeling for the adsorption of methylene blue from aqueous solutions on activated clay minerals, Desalination (2010) 335–338.
[47] C. Blachier, L. Michot, I. Bihannic, O. Barrès, A. Jacquet, M. Mosquet, Adsorption of polyamine on clay minerals, J. Colloid Interface Sci. (2009) 599–606.
[48] A. Witek-Krowiak, R.G. Szafran, S. Modelski, Biosorption of heavy metals from aqueous solutions onto peanut shell as a low-cost adsorbent, Desalination (2011) 126–134.
[49] M. Hossain, H. Ngo, W. Guo, T. Setiadi, Adsorption and desorption of copper(II) ions onto garden grass, Bioresour. Technol. (2012) 386–395.
[50] N. Azouaou, Z. Sadaoui, A. Djaafri, H. Mokaddem, Adsorption of cadmium from aqueous solution onto untreated coffee grounds: equilibrium, kinetics and thermodynamics, J. Hazard. Mater. (2010) 126–134.
[51] M.H. Kalavathy, L.R. Miranda, Comparison of copper adsorption from aqueous solution using modified and unmodified Hevea brasiliensis saw dust, Desalination (2010) 165–174.
[52] L. SI, M. A-HI, Removal of Copper from aqueous solution by Agricultural by-products-sawdust, Energy Procedia (2012) 915–923.
[53] H. Benaïssa, M. Elouchdi, Removal of copper ions from aqueous solutions by dried sunflower leaves, Chem. Eng. Process. (2007) 614–622.
[54] D. Podstawczyk, A. Witek-Krowiak, K. Chojnacka, Z. Sadowski, Biosorption of malachite green by eggshells: mechanism identification and process optimization, Bioresour. Technol. (2014) 161–165.
[55] A. Ronda, M. Martin-Lara, E. Dionisio, G. Blázquez, M. Calero, Effect of lead in biosorption of copper by almond shell, J. Taiwan Inst. Chem. Eng. (2013) 466–473.
[56] E. Khoramzadeh, B. Nasernejad, R. Halladj, Mercury biosorption from aqueous solutions by Sugarcane Bagasse, J. Taiwan Inst. Chem. Eng. (2013) 266–269.
[57] A.M. Abdel-Aty, N.S. Ammar, H.H. Ghafar, R.K. Ali, Biosorption of cadmium and lead from aqueous solution by fresh water alga Anabaena sphaerica biomass, J. Adv. Res. (2013) 367–374.
[58] R.M. Kulkarni, K.V. Shetty, G. Srinikethan, Cadmium(II) and nickel(II) biosorption by Bacillus laterosporus (MTCC 1628), J. Taiwan Inst. Chem. Eng. (2014) 1628–1635.
[59] E. Bakatula, E. Cukrowska, I. Weiersbye, L. Mihaly-Cozmuta, A. Peter, H. Tutu, Biosorption of trace elements from aqueous systems in gold mining sites by the filamentous green algae (Oedogonium sp.), J. Geochem. Explor. (2014) 492–503.
[60] R. Sivaraj, C. Namasivayam, K. Kadirvelu, Orange peel as an adsorbent in the removal of Acid violet 17 (acid dye) from aqueous solutions, Waste Manage. (2001) 105–110.
[61] N.M. Mahmoodi, B. Hayati, M. Arami, C. Lan, Adsorption of textile dyes on Pine Cone from colored wastewater: kinetic, equilibrium and thermodynamic studies, Desalination (2011) 117–125.
[62] V. Ponnusami, S. Vikram, S. Srivastava, Guava (Psidium guajava) leaf powder: novel adsorbent for removal of methylene blue from aqueous solutions, J. Hazard. Mater. (2008) 276–286.
[63] A. Hay. (1873). Patent No. 140. USA.
[64] C. Gabrielli, R. Jaouhari, G. Maurin, M. Keddam, Magnetic water treatment for scale prevention, Water Res. (2001) 3249–3259.
[65] J. Coey, S. Cass, Magnetic water treatment, J. Magn. Magn. Mater. (2000) 71–74.
[66] S.A. Parsons, B.-L. Wang, S.J. Judd, T. Stephenson, Magnetic treatment of calcium carbonate scale- effect of pH control, Water Res. (1997) 339–342.
[67] F. Alimi, M. Tlili, M.B. Amor, G. Maurin, C. Gabrielli, Effect of magnetic water treatment on calcium carbonate precipitation: Influene of the pipe material, Chem. Eng. Proces. Process Intens. (2009) 1327–1332.
[68] P.C. Singer, K. Bilyk, Enhanced coagulation using a magnetic ion exchange resin, Water Res. (2002) 4009–4022.
[69] Y. Ji, Y. Wang, J. Sun, T. Yan, J. Li, T. Zhao, et al., Enhancement of biological treatment of wastewater by magnetic field, Bioresour. Technol. (2010) 8535–8540.
[70] S.-Q. Ni, J. Ni, N. Yang, J. Wang, Effect of magnetic nanoparticles on the performance of activated sludge treatment system, Bioresour. Technol. (2013) 555–561.
[71] O. Philippova, A. Barabanova, V. Molchanov, A. Khokhlov, Magnetic polymer beads: recent trends and developments in synthetic design and applications, Eur. Polym. J. (2011) 542–559.
[72] R.D. Ambashta, M. Sillanpää, Water purification using magnetic assistance: a review, J. Hazard. Mater. (2010) 38–49.
[73] C. Albornoz, E.E. Sileo, S.E. Jacobo, Magnetic polymers of maghemite (gamma-Fe2O3) and polyvinyl alcohol, Phys. B Condens. Matter (2004) 149–153.
[74] O. Philippova, A. Barabanova, V. Molchanov, A. Khokhlov, Magnetic polymer beads: recent trends and developments in synthetic, Eur. Polym. J. (2011) 542–559.
[75] J. Hu, D. Shao, C. Chen, G. Sheng, J. Li, X. Wang, et al., Plasma-induced grafting of cyclodextrin onto multiwall carbon nanotube/iron oxides for adsorbent application, J. Phys. Chem. B (2010) 6779–6785.
[76] D. Mohan, C.U. Pittman Jr., Arsenic removal from water/wastewater using adsorbents—a critical review, J. Hazard. Mater. (2007) 1–53.
[77] B.K. Mandal, K.T. Suzuki, Arsenic round the world: a review, Talanta (2002) 201–235.

[78] C. Shan, M. Tong, Efficient removal of trace arsenite through oxidation and adsorption by magnetic nanoparticles modified with Fe–Mn binary oxide, Water Res. (2013) 3411–3421.
[79] M. Kilianová, R. Prucek, J. Filip, J. Kolařík, L. Kvítek, A. Panacek, et al., Remarkable efficiency of ultrafine superparamagnetic iron(III) oxide nanoparticles toward arsenate removal from aqueous environment, Chemosphere (2013) 2690–2697.
[80] R.M. Dhoble, S. Lunge, A.G. Bhole, S. Rayalu, Magnetic binary oxide particles (MBOP): a promising adsorbent for removal of As(III) in water, Water Res. (2011) 4769–4781.
[81] X. Luo, C. Wang, S. Luo, R. Dong, X. Tu, Z. Guisheng, Adsorption of As(III) and As(V) from water using magnetite Fe3O4-reduced graphite oxide–MnO2 nanocomposites, Chem. Eng. J. (2012) 45–52.
[82] L. Yu, X. Peng, F. Ni, J. Li, D. Wang, Z. Luan, Arsenite removal from aqueous solutions by γ-Fe_2O_3–TiO_2 magnetic nanoparticles through simultaneous photocatalytic oxidation and adsorption, J. Hazard. Mater. (2013) 10–17.
[83] M.T. Sikder, S. Tanaka, T. Saito, M. Kurasaki, Application of zerovalent iron impregnated chitosan-caboxymethyl-β-cyclodextrin composite beads as arsenic sorbent, J. Environ. Chem. Eng. (2014) 370–376.
[84] R. Chen, C. Zhi, H. Yang, Y. Bando, Z. Zhang, N. Sugiur, et al., Arsenic(V) adsorption on Fe3O4 nanoparticle-coated boron nitride nanotubes, J. Colloid Interface Sci. (2011) 261–268.
[85] Y. Jin, M. Tong, Y. Hou, Removal of arsenate by cetyltrimethylammonium bromide modified magnetic nanoparticles, J. Hazard. Mater. (2012) 461–468.
[86] L. Feng, M. Cao, X. Ma, Y. Zhu, C. Hu, Superparamagnetic high-surface-area Fe3O4 nanoparticles as adsorbents for arsenic removal, J. Hazard. Mater. (2012) 439–446.
[87] M. Zhang, B. Gao, S. Varnoosfaderani, A. Hebard, Y. Yao, M. Inyang, Preparation and characterization of a novel magnetic biochar for arsenic removal, Bioresour. Technol. (2013) 457–462.
[88] I. Akin, G. Arslan, A. Tor, M. Ersoz, Y. Cengeloglu, Arsenic(V) removal from underground water by magnetic nanoparticles synthesized from waste red mud, J. Hazard. Mater. (2012) 62–68.
[89] W. Tang, Y. Su, Q. Li, S. Gao, J.K. Shang, Superparamagnetic magnesium ferrite nanoadsorbent for effective arsenic (III, V) removal and easy magnetic separation, Water Res. (2013) 3624–3634.
[90] Y.-J. Tu, C.-F. You, C.-K. Chang, S.-L. Wang, T.-S. Chan, Arsenate adsorption from water using a novel fabricated copper ferrite, Chem. Eng. J. (2012) 440–448.
[91] Z. Liu, F.-S. Zhang, R. Sasai, Arsenate removal from water using Fe_3O_4-loaded activated carbon prepared from waste biomass, Chem. Eng. J. (2010) 57–62.
[92] Y. Tian, M. Wu, X. Lin, P. Huan, Y. Huang, Synthesis of magnetic wheat straw for arsenic adsorption, J. Hazard. Mater. (2011) 10–16.
[93] H. Li, Z. Li, T. Liu, X. Xiao, Z. Peng, L. Deng, A novel technology for biosorption and recovery hexavalent chromium in wastewater by bio-functional magnetic beads, Bioresour. Technol. (2008) 6271–6279.
[94] A. Barai, R.D. Engelken, Chromium-based regulations and greening in metal finishing industries in the USA, Environ. Sci. Policy (2002) 121–133.
[95] L. Li, L. Fan, M. Sun, H. Qiu, X. Li, H. Duan, et al., Adsorbent for chromium removal based on graphene oxide functionalized with magnetic cyclodextrin?chitosan, Colloids Surf. B: Biointerfaces (2013) 76–83.
[96] L. Zhou, H. Deng, J. Wan, J. Shi, T. Su, A solvothermal method to produce RGO-Fe3O4 hybrid composite for fast chromium removal from aqueous solution, Appl. Surf. Sci. (2013) 1024–1031.
[97] N.N. Thinh, P.T. Hanh, L.T. Ha, L.N. Anh, T.V. Hoang, V.D. Hoang, et al., Magnetic chitosan nanoparticles for removal of Cr(VI) from aqueous solution, Mater. Sci. Eng. C (2013) 1214–1218.
[98] Y. Xiao, H. Liang, Z. Wang, MnFe2O4/chitosan nanocomposites as a recyclable adsorbent for the removal of hexavalent chromium, Mater. Res. Bull. (2013) 3910–3915.
[99] N. Mao, L. Yang, G. Zhao, X. Li, Y. Li, Adsorption performance and mechanism of Cr(VI) using magnetic PS-EDTA resin from micro-polluted waters, Chem. Eng. J. (2012) 480–490.
[100] V. Gupta, S. Agarwal, T.A. Saleh, Chromium removal by combining the magnetic properties of iron oxide with adsorption properties of carbon nanotubes, Water Res. (2011) 2207–2212.
[101] C. Luo, Z. Tian, B. Yang, L. Zhang, S. Yan, Manganese dioxide/iron oxide/acid oxidized multi-walled carbon nanotube magnetic nanocomposite for enhanced hexavalent chromium removal, Chem. Eng. J. (2013) 256–265.
[102] Y. Li, S. Zhu, Q. Liu, Z. Chen, J. Gu, C. Zhu, et al., N-doped porous carbon with magnetic particles formed in situ for enhanced Cr(VI) removal, Water Res. (2013) 4188–4197.
[103] X. Chen, K.F. Lam, K.L. Yeung, Selective removal of chromium from different aqueous systems using magnetic MCM-41 nanosorbents, Chem. Eng. J. (2011) 728–734.
[104] X.-P. Yao, Z.-J. Fu, Y.-G. Zhao, L. Wang, L.-Y. Fang, H.-Y. Shen, Use of tetraethylenepentamine-functional Fe_3O_4 magnetic polymers for matrix solid phase dispersion extraction and preconcentration of Cr(VI) in water samples at ultratrace levels, Talanta (2012) 124–130.
[105] A. Rao, A. Bankar, A.R. Kumar, S. Gosavi, S. Zinjarde, Removal of hexavalent chromium ions by Yarrowia lipolytica cells modified with phyto-inspired Fe0/Fe3O4 nanoparticles, J. Contam. Hydrol. (2013) 63–73.
[106] H. Zhang, D.-L. Liu, L.-L. Zeng, M. Li, β-Cyclodextrin assisted one-pot synthesis of mesoporous magnetic Fe_3O_4@C and their excellent performance for the removal of Cr (VI) from aqueous solutions, Chin. Chem. Lett. (2013) 341–343.
[107] L. Wei, G. Yang, R. Wang, W. Ma, Selective adsorption and separation of chromium (VI) on the magnetic iron–nickel oxide from waste nickel liquid, J. Hazard. Mater. (2009) 1159–1163.
[108] P. Wang, I.M. Lo, Synthesis of mesoporous magnetic γ-Fe2O3 and its application to Cr(VI) removal from contaminated water, Water Res. (2009) 3727–3734.
[109] W. Jiang, M. Pelaez, D.D. Dionysiou, M.H. Entezari, D. Tsoutsou, K.O. Shea, Chromium(VI) removal by maghemite nanoparticles, Chem. Eng. J. (2013) 527–533.
[110] Q. Wang, Y. Guan, X. Liu, X. Ren, M. Yang, High-capacity adsorption of hexavalent chromium from aqueous solution using magnetic microspheres by surface dendrimer graft modification, J. Colloid Interface Sci. (2012) 160–166.
[111] I. Larraza, M. López-Gónzalez, T. Corrales, G. Marcelo, Hybrid materials: magnetite-polyethylenimine-montmorillonite, as magnetic adsorbents for Cr(VI) water treatment, J. Colloid Interface Sci. (2012) 24–33.
[112] D. Chen, W. Li, Y. Wu, Q. Zhu, Z. Lu, G. Du, Preparation and characterization of chitosan/montmorillonite magnetic microspheres and its application for the removal of Cr (VI), Chem. Eng. J. (2013) 8–15.
[113] S. Xu, Y. Zhang, S. Pan, H. Ding, G. Li, Recyclable magnetic photocatalysts of Fe^{2+}/TiO_2 hierarchical architecture with effective removal of Cr(VI) under UV light from water, J. Hazard. Mater. (2011) 29–35.
[114] X. Sun, L. Yang, H. Xing, J. Zhao, X. Li, Y. Huang, et al., Synthesis of polyethylenimine-functionalized poly(glycidyl methacrylate) magnetic microspheres and their excellent Cr(VI) ion removal properties, Chem. Eng. J. (2013) 338–345.
[115] N. Ballav, H. Choi, S. Mishra, A. Maity, Synthesis, characterization of Fe3O4@glycine doped polypyrrole magnetic nanocomposites and their potential performance to remove toxic Cr(VI), J. Ind. Eng. Chem. (2014), http://dx.doi.org/10.1016/j.jiec.2014.01.007
[116] Y.-F. Lin, H.-W. Chen, Y.-C. Chen, C.-S. Chiou, Application of magnetite modified with polyacrylamide to adsorb phosphate in in aqueous solution, J. Taiwan Inst. Chem. Eng. (2013) 45–51.
[117] T. Ishiwata, O. Miura, K. Hosomi, K. Shimizu, D. Ito, Y. Yoda, Removal and recovery of phosphorus in wastewater by superconducting high gradient magnetic separation with ferromagnetic adsorbent, Phys. C. (2010) 1818–1821.
[118] A.Z. Badruddoza, Z.B. Shawon, M.T. Rahman, K.W. Hao, K. Hidajat, M.S. Uddin, Ionically modified magnetic nanomaterials for arsenic and chromium removal from water, Chem. Eng. J. (2013) 607–615.
[119] T. Inaba, E. Kobayashi, Y. Suwazono, M. Uetani, M. Oishi, H. Nakagawa, et al., Estimation of cumulative cadmium intake causing Itai–itai disease, Toxicol. Lett. (2005) 192–201.
[120] G. Yang, L. Tang, G. Zeng, Y. Cai, X. Wei, Y. Zhou, et al., Cd(II) removal from aqueous solution by adsorption on -ketoglutaricacid-modified magnetic chitosan, Appl. Surf. Sci. (2014) 710–716.
[121] Y.-J. Tu, C.-F. You, C.-K. Chang, Kinetics and thermodynamics of adsorption for Cd on green manufactured nano-particles, J. Hazard. Mater. (2012) 116–122.
[122] J. Gong, L. Chen, G. Zeng, F. Long, J. Deng, Q. Niu, et al., Shellac-coated iron oxide nanoparticles for removal of cadmium(II) ions from aqueous solution, J. Environ. Sci. (2012) 1165–1173.
[123] Y.T. Zhou, H.L. Nie, C.B. White, Z.Y. He, L.M. Zhu, Removal of Cu^{2+} from aqueous solution by chitosan-coated magnetic nanoparticles modified with α-ketoglutaric acid, J. Colloid Interface Sci. (2009) 29–37.
[124] Y. Lin, H. Chen, K. Lin, B. Chen, C. Chiou, Application of magnetic particles modified with amino groups to adsorb copper ions in aqueous solution, J. Environ. Sci. (2011) 44–50.
[125] H.Y. Mei, C. Man, H.Z. Bo, Effective removal of Cu(II) ions from aqueous solution by amino-functionalized magnetic nanoparticles, J. Hazard. Mater. (2010) 392–399.
[126] J.-L. Gong, X.-Y. Wang, G.-M. Zeng, L. Chen, J.-H. Deng, X.-R. Zhang, et al., Copper(II) removal by pectin–iron oxide magnetic nanocomposite adsorbent, Chem. Eng. J. (2012) 100–107.
[127] S.S. Banerjee, D.H. Chen, Fast removal of copper ions by gum arabic magnetic modified nano-adsorbent, J. Hazard. Mater. (2007) 792–799.
[128] Q. Peng, Y. Liu, G. Zeng, W. Xu, C. Yang, J. Zhang, Biosorption of copper(II) by immobilizing Saccharomyces cerevisiae on the surface of chitosan-coated magnetic nanoparticles from aqueous solution, J. Hazard. Mater. (2010) 676–682.
[129] A. Badruddoza, A. Tay, P. Tan, K. Hidajat, M. Uddin, Carboxymethyl-β-cyclodextrin conjugated magnetic nanoparticles as nano-adsorbents for removal of copper ions: synthesis and adsorption studies, J. Hazard. Mater. (2011) 1177–1186.
[130] Y. Liu, M. Chen, Y. Hao, Study on the adsorption of Cu(II) by EDTA functionalized Fe_3O_4 magnetic nanoparticles, Chem. Eng. J. (2013) 46–54.
[131] X.-J. Hu, Y.-g. Liu, H. Wang, A.-w. Chen, G. Zeng, S.-m. Liu, et al., Removal of Cu(II) ions from aqueous solution using sulfonated magnetic graphene oxide composite, Sep. Purif. Technol. (2013) 189–195.
[132] S. Lan, X. Wu, L. Li, F. Guo, S. Gan, Synthesis and characterization of hyaluronic acid-supported magnetic microspheres for copper ions removal, Colloids Surf. A: Phys. Eng. Aspects (2013) 42–50.
[133] Y. Ren, M. Zhang, D. Zhao, Synthesis and properties of magnetic Cu(II) ion imprinted composite adsorbent for selective removal of copper, Desalination (2008) 135–149.

[134] X. Zhao, J. Wang, F. Wu, T. Wang, Y. Cai, Y. Shi, et al., Removal of fluoride from aqueous media by Fe_3O_4@$Al(OH)_3$ magnetic nanoparticles, J. Hazard. Mater. (2010) 102–109.
[135] C.-F. Chang, P.-H. Lin, W. Holl, Aluminum-type superparamagnetic adsorbents: synthesis and application on fluoride removal, Colloids Surf. A Physicochem. Eng. Aspects (2006) 194–202.
[136] M. Bhaumik, T.Y. Leswifi, A. Maity, V. Srinivasu, M.S. Onyango, Removal of fluoride from aqueous solution by polypyrrole/Fe3O4 magnetic nanocomposite, J. Hazard. Mater. (2011) 150–159.
[137] L. Chai, Y. Wan, N. Zhao, W. Yang, X. You, Sulfate-doped Fe3O4/Al2O3 nanoparticles as a novel adsorbent for fluoride removal from drinking water, Water Res. (2013) 4040–4049.
[138] B. Markert, K. Friese, Trace Elements—Their Distribution and Effects in the Environment, 4th ed., Elsevier, Holland, 2000.
[139] Y.H. Li, Z. Di, J. Ding, D. Wu, Z. Luan, Y. Zhu, Adsorption thermodynamic, kinetic and desorption studies of Pb2+ on carbon nanotubes, Water Res. (2005) 605–609.
[140] L. Han, Y. Wei, Low-temperature synthesis of Fe_3O_4 microroses and their application in water treatment, Mater. Lett. (2012) 1–3.
[141] X. Peng, F. Xu, W. Zhang, J. Wang, C. Zeng, M. Niu, et al., Magnetic Fe_3O_4@silica?xanthan gum composites for aqueous removal and recovery of Pb^{2+}, Colloids Surf. A Physicochem. Eng. Aspects (2014) 27–36.
[142] A. Idris, N.S. Ismail, N. Hassan, E. Misran, A.-F. Ngomsik, Synthesis of magnetic alginate beads based on maghemite nanoparticles for Pb(II) removal in aqueous solution, J. Ind. Eng. Chem. (2012) 1582–1589.
[143] A. Beé, D. Talbot, S. Abramson, V. Dupuis, Magnetic alginate beads for Pb(II) ions removal from wastewater, J. Colloid Interface Sci. (2011) 486–492.
[144] X. Li, Y. Qi, Y. Li, Y. Zhang, X. He, Y. Wang, Novel magnetic beads based on sodium alginate gel crosslinked by zirconium(IV) and their effective removal for Pb2+ in aqueous solutions by using a batch and continuous systems, Bioresour. Technol. (2013) 611–619.
[145] S.-P. Kuang, Z.-Z. Wang, J. Liu, Z.-C. Wu, Preparation of triethylene-tetramine grafted magnetic chitosan for adsorption of Pb(II) ion from aqueous solutions, J. Hazard. Mater. (2013) 210–219.
[146] L. Fan, C. Luo, M. Sun, X. Li, H. Qiu, Highly selective adsorption of lead ions by water-dispersible magnetic chitosan/graphene oxide composites, Colloids Surf. B Biointerfaces (2013) 523–529.
[147] T.-t. Li, Y.-g. Liu, Q.-q. Peng, X.-j. Hu, T. Liao, H. Wang, et al., Removal of lead(II) from aqueous solution with ethylenediamine-modified yeast biomass coated with magnetic chitosan microparticles: Kinetic and equilibrium modeling, Chem. Eng. J. (2013) 189–197.
[148] E.K. Faulconer, N.V. Hoogesteijn von Reitzenstein, D.W. Mazyck, Optimization of magnetic powdered activated carbon for aqueous Hg(II) removal and magnetic recovery, J. Hazard. Mater. (2012) 9–14.
[149] H. Parham, B. Zargar, R. Shiralipour, Fast and efficient removal of mercury from water samples using magnetic iron oxide nanoparticles modified with 2-mercaptobenzothiazole, J. Hazard. Mater. (2012) 94–100.
[150] P.I. Girginova, A.L. Daniel-da-Silva, C.B. Lopes, P. Figueira, M. Otero, V.S. Amaral, et al., Silica coated magnetite particles for magnetic removal of Hg2+ from water, J. Colloid Interface Sci. (2010) 234–240.
[151] Z. Wang, D. Wu, G. Wu, N. Yang, A. Wu, Modifying Fe3O4 microspheres with rhodamine hydrazide for selective detection and removal of Hg2+ ion in water, J. Hazard. Mater. (2013) 621–627.
[152] B.Y. Song, Y. Eom, T.G. Lee, Removal and recovery of mercury from aqueous solution using magnetic silica nanocomposites, Appl. Surf. Sci. (2011) 4754–4759.
[153] O. Hakami, Y. Zhang, C.J. Banks, Thiol-functionalised mesoporous silica-coated magnetite nanoparticles for high efficiency removal and recovery of Hg from water, Water Res. (2012) 3913–3922.
[154] P. Figueira, C. Lopes, A. Daniel-da-Silva, E. Pereira, A. Duarte, T. Trindade, Removal of mercury (II) by dithiocarbamate surface functionalized magnetite particles: application to synthetic and natural spiked waters, Water Res. (2011) 5773–5784.
[155] P. Huang, Z. Ye, W. Xie, Q. Chen, J. Li, Z. Xu, et al., Rapid magnetic removal of aqueous heavy metals and their relevant mechanisms using nanoscale zero valent iron (nZVI) particles, Water Res. (2013) 4050–4058.
[156] J.-X. Yu, L.-Y. Wang, R.-A. Chi, Y.-F. Zhang, Z.-G. Xu, J. Guo, Competitive adsorption of Pb^{2+} and Cd^{2+} on magnetic modified sugarcane bagasse prepared by two simple steps, Appl. Surf. Sci. (2013) 163–170.
[157] Y. Feng, J.-L. Gong, G.-M. Zeng, Q.-Y. Niu, H.-Y. Zhang, C.-G. Niu, et al., Adsorption of Cd (II) and Zn (II) from aqueous solutions using magnetic hydroxyapatite nanoparticles as adsorbents, Chem. Eng. J. (2010) 487–494.
[158] Z.Y. Lin, Y.X. Zhang, Y.L. Chen, H. Qian, Extraction and recycling utilization of metal ions (Cu^{2+}, Co^{2+} and Ni^{2+}) with magnetic polymer beads, Chem. Eng. J. (2012) 104–112.
[159] Y. Pang, G. Zeng, L. Tang, Y. Zhang, Y. Liu, X. Lei, et al., PEI-grafted magnetic porous powder for highly effective adsorption of heavy metal ions, Desalination (2011) 278–284.
[160] Y. Zhang, L. Yan, W. Xu, X. Guo, L. Cui, L. Gao, et al., Adsorption of Pb(II) and Hg(II) from aqueous solution using magnetic $CoFe_2O_4$-reduced graphene oxide, J. Mol. Liq. (2014) 177–182.
[161] A.Z. Badruddoza, Z.B. Shawon, T.W. Daniel, K. Hidajat, M.S. Uddin, Fe3O4/cyclodextrin polymer nanocomposites for selective heavy metals removal from industrial wastewater, Carbohydr. Polym. (2013) 322–332.
[162] M. Doğan, Y. Özdemir, M. Alkan, Adsorption kinetics and mechanism of cationic methyl violet and methylene blue dyes onto sepiolite, Dyes Pigments (2007) 701–713.
[163] L.S. Silva, L.C. Lima, F.C. Silva, J.M. Matos, M.R. Santos, L.S. Júnior, et al., Dye anionic sorption in aqueous solution onto a cellulose surface chemically modified with aminoethanethiol, Chem. Eng. J. (2013) 89–98.
[164] L. Zhou, J. Jin, Z. Liu, X. Liang, C. Shang, Adsorption of acid dyes from aqueous solutions by the ethylenediamine-modified magnetic chitosan nanoparticles, J. Hazard. Mater. (2011) 1045–1052.
[165] G. Zhang, J. Qu, H. Liu, A.T. Cooper, R. Wu, CuFe2O4/activated carbon composite: a novel magnetic adsorbent for the removal of acid orange II and catalytic regeneration, Chemosphere (2007) 1058–1066.
[166] R. Wu, J. Qu, Y. Chen, Magnetic powder $MnO–Fe_2O_3$ composite—a novel material for the removal of azo-dye from water, Water Res. (2005) 630–638.
[167] X. Zhang, P. Zhang, Z. Wu, L. Zhang, G. Zeng, C. Zhou, Adsorption of methylene blue onto humic acid-coated Fe3O4 nanoparticles, Colloids Surf. A Physicochem. Eng. Aspects (2013) 85–90.
[168] K.K. Senapati, C. Borgohain, K.C. Sarma, P. Phukan, Photocatalytic degradation of methylene blue in water using $CoFe_2O_4–Cr_2O_3–SiO_2$ fluorescent magnetic nanocomposite, J. Mol. Catal. A Chem. (2011) 111–116.
[169] H. Chen, P.K. Chu, J. He, T. Hu, M. Yang, Porous magnetic manganese oxide nanostructures: Synthesis and their application in water treatment, J. Colloid Interface Sci. (2011) 68–74.
[170] L. Fan, C. Luo, M. Sun, X. Li, F. Lu, H. Qiu, Preparation of novel magnetic chitosan/graphene oxide composite as effective adsorbents toward methylene blue, Bioresour. Technol. (2012) 703–706.
[171] L. Ai, C. Zhang, Z. Chen, Removal of methylene blue from aqueous solution by a solvothermal-synthesized graphene/magnetite composite, J. Hazard. Mater. (2011) 1515–1524.
[172] H.-Y. Zhu, R. Jiang, L. Xiao, W. Li, A novel magnetically separable-Fe_2O_3/crosslinked chitosan adsorbent: Preparation, characterization and adsorption application for removal of hazardous azo dye, J. Hazard. Mater. (2010) 251–257.
[173] D. Chen, Y. Li, J. Zhang, W. Li, J. Zhou, L. Shao, et al., Efficient removal of dyes by a novel magnetic Fe3O4/ZnCr-layered double hydroxide adsorbent from heavy metal wastewater, J. Hazard. Mater. (2012) 152–160.
[174] F. Yu, J. Chen, L. Chen, J. Huai, W. Gong, Z. Yuan, et al., Magnetic carbon nanotubes synthesis by Fenton's reagent method and their potential application for removal of azo dye from aqueous solution, J. Colloid Interface Sci. (2012) 175–183.
[175] J. Duan, R. Liu, T. Chen, B. Zhang, J. Liu, Halloysite nanotube-Fe3O4 composite for removal of methyl violet from aqueous solutions, Desalination (2012) 46–52.
[176] Y.-R. Zhang, S.-Q. Wang, S.-L. Shen, B.-X. Zhao, A novel water treatment magnetic nanomaterial for removal of anionic and cationic dyes under severe condition, Chem. Eng. J. (2013) 258–264.
[177] A. Afkhami, M.S. Tehrani, H. Bagheri, Modified maghemite nanoparticles as an efficient adsorbent for removing some cationic dyes from aqueous solution, Desalination (2010) 240–248.
[178] H. Gao, S. Zhao, X. Cheng, X. Wang, L. Zheng, Removal of anionic azo dyes from aqueous solution using magnetic polymer multi-wall carbon nanotube nanocomposite as adsorbent, Chem. Eng. J. (2013) 84–90.
[179] J.-L. Gong, B. Wang, G.-M. Zeng, C.-P. Yang, C.-G. Niu, Q.-Y. Niu, et al., Removal of cationic dyes from aqueous solution using magnetic multi-wall carbon nanotube nanocomposite as adsorbent, J. Hazard. Mater. (2009) 1517–1522.
[180] T. Madrakian, A. Afkhami, M. Ahmadi, H. Bagheri, Removal of some cationic dyes from aqueous solutions using magnetic-modified multi-walled carbon nanotubes, J. Hazard. Mater. (2011) 109–114.
[181] V. Rocher, J.-M. Siaugue, V. Cabuil, A. Bee, Removal of organic dyes by magnetic alginate beads, Water Res. (2008) 1290–1298.
[182] V. Rocher, A. Bee, J.-M. Siaugue, V. Cabuil, Dye removal from aqueous solution by magnetic alginate beads crosslinked with epichlorohydrin, J. Hazard. Mater. (2010) 434–439.
[183] I. Safarik, K. Horska, M. Safarikova, Magnetically modified spent grain for dye removal, J. Cereal Sci. (2011) 78–80.
[184] S. Ghosh, A.Z. Badruddoza, K. Hidajat, M.S. Uddin, Adsorptive removal of emerging contaminants from water using superparamagnetic Fe_3O_4 nanoparticles bearing aminated β-cyclodextrin, J. Environ. Chem. Eng. (2013) 122–130.
[185] D. Mohan, A. Sarswat, V.K. Singh, M. Alexandre-Franco, C.U. Pittman Jr., Development of magnetic activated carbon from almond shells for trinitrophenol removal from water, Chem. Eng. J. (2011) 1111–1125.
[186] X. Peng, Z. Luan, H. Zhang, Montmorillonite–Cu(II)/Fe(III) oxides magnetic material as adsorbent for removal of humic acid and its thermal regeneration, Chemosphere (2006) 300–306.
[187] P. Rao, I.M. Lo, K. Yin, S.C. Tang, Removal of natural organic matter by cationic hydrogel with magnetic properties, J. Environ. Manage. (2011) 1690–1695.
[188] B.J. Thio, K.K. Clark, A.A. Keller, Magnetic pollen grains as sorbents for facile removal of organic pollutants in aqueous media, J. Hazard. Mater. (2011) 53–61.

ResearchGate

See discussions, stats, and author profiles for this publication at: http://www.researchgate.net/publication/282603447

Literature review of multi-aspect research works carried out on the concept and implementation of GSCM

RESEARCH · OCTOBER 2015

DOI: 10.13140/RG.2.1.2996.8085

READS

50

3 AUTHORS, INCLUDING:



Sheetal Soda

National Institute of Technology Jalandhar

3 PUBLICATIONS **0** CITATIONS

SEE PROFILE

All in-text references underlined in blue are linked to publications on ResearchGate, letting you access and read them immediately.

Available from: Sheetal Soda
Retrieved on: 12 November 2015

Literature review of multi-aspect research works carried out on the concept and implementation of GSCM

Sheetal Soda*, Anish Sachdeva and Rajiv Kumar Garg

Department of Industrial and Production Engineering,
National Institute of Technology,
Jalandhar, India
Email: sheetugrey@gmail.com
Email: asachdeva@nitj.ac.in
Email: gargrk@nitj.ac.in
*Corresponding author

Abstract: Recent research advances in green supply chain management (GSCM) have thrown exciting opportunities for new dimensions of the subject to evolve. Individual findings, when pooled together, raise possibilities of further research yielding altogether new management practices with potential affirmative ramifications for environment and industry. This paper strives to scrutinise a sizable quantum of literature on GSCM to identify techniques for critically analysing various aspects of GSCM implementation and their prospective categorisation, implications and complications. Substantial literature on GSCM is prominently identified with application of techniques like AHP/ANP, ISM, TOPSIS, DEMATEL etc. to evaluate performance of the GSCM measures adopted, selection of suppliers, undertaking barrier analysis, mechanism formulation/implementation, inter-relationships between factors and generic/standard exploration of the intricacies of GSCM. Categorising the literature, on the basis of these six categories and their further investigation to assess prospects and deficiencies, extend an opportunity to the furtherance of our knowledge on GSCM practices.

Keywords: multi-criteria decision-making techniques; MCDM techniques; literature review; green supply chain management; GSCM; performance evaluation; barrier analysis, mechanism formulation.

Reference to this paper should be made as follows: Soda, S., Sachdeva, A. and Garg, R.K. (xxxx) 'Literature review of multi-aspect research works carried out on the concept and implementation of GSCM', *Int. J. Industrial and Systems Engineering*, Vol. X, No. Y, pp.xxx–xxx.

Biographical notes: Sheetal Soda is a Research Scholar with Department of Industrial and Production Engineering, Dr. B.R. Ambedkar National Institute of Technology, Jalandhar (India). She obtained her BTech in Mechanical and Automation Engineering from Guru Gobind Singh Indraprashtha University New Delhi (India) and ME in Production Engineering from Delhi Technical University (formerly Delhi College of Engineering), Delhi (India). She has to her credit, experience of more than seven years of industrial and teaching domains. She is life time member of Indian Society for Technical Education (ISTE).

Copyright © 20XX Inderscience Enterprises Ltd.

Anish Sachdeva is working as an Associate Professor in the Department of Industrial and Production Engineering at National Institute of Technology, Jalandhar, and Punjab, India. He obtained his Bachelor in Industrial Engineering from National Institute of Technology (erstwhile Regional Engineering College), Jalandhar, India. Subsequently, he obtained his Masters in Industrial Engineering from Punjab Technical University, Jalandhar and PhD from Mechanical and Industrial Engineering Department at Indian Institute of Technology (IIT), Roorkee, India. He has more than 16 years of experience in teaching and industry. His areas of interest are reliability and maintenance engineering, supply chain management, modelling and simulation.

Rajiv Kumar Garg is Professor in Industrial and Production Engineering Department at Dr. B.R. Ambedkar National Institute of Technology Jalandhar, India. He holds a BSc Engg (hons.) in Mechanical Engineering from Regional Engineering College Kurukshetra, and ME (hons.) in Industrial Engineering and a PhD from Thapar Institute of Engineering and Technology Patiala (India). He has over 26 years of industry and teaching experience. He has guided 37 MTech and 11 PhD candidates for pursuing their PhD degree. He has over 129 publications in international and national journals to his credit. He is a reviewer of eight international journals and also Chief Editor of *International Journal of Machining and Machinability of Materials* (*IJMMM*). He has been designated as a member of International and National Advisory Committees of various international and national conferences organised by various international and national organisations/institutions.

1 Introduction

Recent times have witnessed an increased consideration for environmental concerns on the part of industrial and manufacturing units, thereby giving a push to green technologies and other environment-friendly measures, to curtail the polluting effect inherent in the processes involved. This has led to the development of the discipline of green supply chain management (GSCM), which aims at developing such methodologies and process, concerning industrial production and distribution that have minimal or no hazardous impact on the environment, along with financial incentives for the adopting concern. According to Zhu and Sarkis (2004), GSCM encompasses a set of environmental management (EM) practices which are useful for logistics management and are designed to incorporate environmental considerations into the forward and reverse logistics (RL). Examples of GSCM practices include reducing packaging and waste, assessing suppliers based on environmental performance, developing more eco-friendly products, and reducing carbon emissions associated with the transport of goods (Walker et al., 2008).

GSCM has sparked of immense interest in industry and academic domain, with huge prospects of growth and development in coming times. Extensive research has been carried on the various aspects of the subject, which has led to emergence of a substantial quantum of literature on GSCM (Sarkis et al., 2011). Analysis of the researches carried out provide scholars with an opportunity to identify hidden and indirect facets of the subject, and find new leads that could unravel the potential of GSCM in elevating itself to be one of the most relevant tools on the part of industry to align their operations with an environmental-friendly approach and maximise their gains in the process. Advancement

of knowledge in the field of GSCM can be ensured by examining the studies already undertaken and building further knowledge-base, on the basis of the former (Srivastava, 2007).

Adoption of GSCM practices are adopted voluntarily, for the sake of only environmental is rare. In general, the adoption of GSCM measures is not necessarily a voluntary decision on the part of the manufacturer, rather it may be a result of various push and pull factors, as well as inputs by other stake holders in the supply chain. For example, the physical infrastructure associated with any enterprise also contributes to environmental degradation, which can be countered substantially by reusing and recycling of components in the construction supply chain. Besides that, the role of environment-centric innovations by the manufacturer plays a significant role in augmenting GSCM in an enterprise (Zhu et al., 2012). Activities influenced by GSCM have a tendency to affect the efficiencies of the entire supply chain (Pishdar et al., 2014). Thereby, companies are waking up to the benefits of GSCM, thereby making optimal use of their resources and securing competitive advantages (Farzianpour et al., 2014). GSCM affects major determinants of profitability such as quality, customer satisfaction and efficiency (Olugu et al., 2011). Interestingly, the consumers are also indirectly contributing to the espousal of GSCM measures, by raising their demands and showing their preference for eco-friendly products (Chang et al., 2013).

Companies are recognising that EM is a key strategic issue with the potential for a lasting impact on organisational performance. For example, more than 40,000 companies have implemented ISO14001, the EM system standard (Zhu and Sarkis, 2006). Greening the supply chain is increasingly a concern for many business enterprises and a challenge for logistics management in 21st century. Of particular concern is how to raise organisational environmental awareness and incorporate EM practices into the logistics activities (Zhu et al., 2008a, 2008b, 2008c).

Hitherto, adoption of environmental friendly measures was limited as a responsibility to individual departments of the manufacturing units; and not across the board of the organisation. For example, environmental excellence in product development, process design, operations, logistics, marketing, regulatory compliance and waste management are responsibilities of the respective departments only, and there was a conspicuous absence of an integrated approach in making the concern's undertaking green on a holistic basis. But slowly and steadily, the business units and manufacturing concerns across the world are waking to the economic gains that are associated with deployment of green practices.

The quality revolution of the 1980s and the supply chain management revolution of 1990s, has opened new vistas for industrial establishments to adopt eco-friendly practices that save money and augment brand image of the products before the customers. This coupled with strict government regulations apropos conservation of environment have pushed industrial units to join the GSCM bandwagon. Though even today, GSCM has not penetrated into the industrial establishments, the way it should have been; nevertheless the recent years have witnessed phenomenal rise in the popularity and espousal of the concept in a practical way across the globe (Diabata and Govindan, 2011).

2 Research methodology

Recent work on GSCM has led to emergence of extensive literature about its various aspects and facets. Comprehensive reviews on seminal work on GSCM such as green design (Zhang et al., 1997), production planning and control for remanufacturing (Bras and McIntosh, 1999; Daniel and Guide, 2000), issues in green manufacturing and product recovery (Daniel et al., 1996; Gungor and Gupta, 1999), RL (Carter and Ellram, 1998; Fleischmann et al., 1997) and logistics network design (Fleischmann et al., 2000; 2001; Jayaraman et al., 2003) have been published, and added to the repository of research work carried out on the subject. Though, there is plethora of literature on GSCM, yet it can be said with certainty that a substantially large part of the research work revolves around the theoretical aspects of the GSCM nature and falls short on extending practical models and methodologies that can be ascribed to the concept. This paper makes an attempt at presenting an across-the-board view of the available literature on various facets of GSCM, so that further addition can be made to the existing pool of knowledge compiled on the subject.

The objective of this paper is to gather a comprehensive understanding of the extent of evolution of GSCM, and the scope of its practical implementation by identifying major research works carried on the subject, which is identified with environmental thinking and its integration with existing models of supply-chain management. The study promises, to a considerable extent, the identification of gaps, issues and opportunities for further study and research on the subject. A literature review seems to be a valid approach, as it is a necessary step in structuring a research field and forms an integral part of any research conducted (Smith et al., 2002). This helps to identify the conceptual content of the field (Meredith, 1993) and guides towards theory development.

In this paper, in-depth study of the research papers is presented, to ensure that not only the essence of various studies undertaken is fully understood; but also the finer details enshrined in the literature are effectively captured. This has helped in correlating the commonalities as well as the disparities amongst the available literature on the subject. Efforts were made to see how the concept of GSCM, manifests itself in different form in diverse settings, yet aspiring to chase common goals. The existing literature studied on the subject can be grouped into various sets in accordance with main aspect of GSCM studied, therein. Resultantly, six major categories have been identified, i.e.,

1 identification of performance evaluation of the measures adopted

2 selection of suppliers

3 undertaking barrier analysis

4 mechanism formulation/implementation

5 inter-relationships between factors

6 generic/standard exploration.

Categorising the literature, on the basis of these six, and their further investigation to assess the prospects and deficiencies, extend an opportunity to the furtherance of our knowledge on GSCM practices. The tools/techniques deployed in various studies were also reviewed and their classification was also undertaken. The selection of methodology of choosing and subsequent analysis of the papers required careful consideration, so that

a comprehensive view of the work done on diverse aspects of GSCM may be ensured. This entailed that the papers should be chosen from different regional, organisational and industrial domains.

It is worth noting that the particular tool/technique used depends on a host of factors, such as the nature of the problem, the nature and availability of data, familiarity with the technique, compatibility between the analysis and solution tools/techniques envisaged, previous related works and the wish to use new emergent tools/techniques in operations research/decision science (OR/DS).

2.1 Research techniques deployed by researchers in studying/analysing various aspects of GSCM

The decision to adopt GSCM strategies that could lead to optimum gains for the manufacturer in terms of trade-off between the benefits and cost involved is of considerable significance. Making such a decision, however, is never an easy task as there are many factors concerned with the decision-making process. This is a typical multi-criteria decision-making (MCDM) problem. MCDM problems often feature themselves as research tasks, and are addressed by deploying an array of techniques to find an optimal solution to them. Green manufacturing and remanufacturing have used mathematical models, tools and techniques to a much larger extent. GSCM seems a promising area for trying out new operations research techniques and for using traditional techniques for overall GSCM Design. The problem is complex and challenging, as a very large number of parameters, decision variables and constraints are involved along with a large number of estimation requirements such as those of expected demands and returns and cost criteria associated with each decision. Perhaps, a combination of various tools and techniques (both traditional and new) may be combined for the purpose of formulation, approximation, analysis and solution of such complex problems.

Different approaches/techniques have been proposed by researchers to such problems, the most prominent being the 'analytic hierarchy process' (AHP) (Saaty, 1980) and 'technique for order preference by similarity to ideal solution' (TOPSIS) (Hwang and Yoon, 1981). AHP is the most widely used technique for multiple criteria analyses. TOPSIS is also widely used to solve many complicated decision-making problems because of its effectiveness in solving MCDM problems and computational simplicity (Wang and Chan, 2013). Other techniques that relate with MCDM problems involve fuzzy logic, DEMATEL method, analytic hierarchy processes, network analysis [analytic network process (ANP)], interpretive structural modelling (ISM) and grey relational analysis (GRA). Since the problems relating with application of GSCM techniques in real world situation are characterised by a multitude of factors, the assessment of the quantum and intensity of their respective effects acquires the proposition of MCDM problems, and hence call for the deployment of various techniques as mentioned above.

All the deployed techniques are associated with empirical studies carried on the part of the researchers, and are identified with logical results, reached therein. All the techniques are bracketed under the broad heading of MCDM techniques, and aim at factoring in various elements that form a part of a complex system, and are difficult to ascertain from their correlation point of view. This is pertinent to mention that many researchers have employed more than one technique in their research work, but the fact

that the objectives so chased were similar. Speaking in general, all the techniques corresponded to MCDM framework.

3 Literature review of GSCM

As the preliminary exercise of the research undertaken, an extensive and in-depth study of the existing research works in the field of GSCM was carried out to study the nature of work and deductions precipitated on the subject so far. Environmental sustainability has moved from the fringes of supply chain management research to an area of significant research activity (Pagell and Shevchenko, 2014). It needs to be stated that as a research subject, GSCM has caught the fancy of scholars in an extensive way, only recently. Nevertheless, a tremendous progress has been achieved in understanding the intricacies of GSCM, which has the potential of unleashing further research work that can have far reaching ramifications in the shape of new or more effective practical applications.

The literature apropos the research work undertaken on GSCM, which has been studied as part of this project, address diverse issues of the subject viz. Factors affecting the implementation and output of GSCM measures, prospective changes that can be introduced in the existing supply chain, the factors that act as de-motivators for producers/manufacturers to adopt GSCM practices and generic studies carried out on the management tool in focus. On the basis of same, the literature of research works has been categorised as addressing the following broad aspects.

3.1 Performance evaluation

There are a number of factors that play simultaneous respective roles, whenever a GSCM measure is put into practice. The factors however differ in their contribution towards achieving the desired objectives for which the management tool has been deployed. Conversely, there are also some factors that play detrimental roles in realising the objectives sought by GSCM measures. Such factors have also been studied and assessed by the researchers, so that they can be countered effectively. In nutshell, many of the research papers deal with the 'performance evaluation' of various factors that are identified with set up in which GSCM is introduced; or are part of the GSCM mechanism enforced.

Fuzzy alpha cut analysis has been deployed for the purpose of performance evaluation and supplier selection in manufacturing industry by Arunkumar et al. (2011). The Suppliers have been evaluated by undertaking usability evaluation of the AHP-based model of the problem, by making use of triangular fuzzy number to express their subjective preferences. Diabata and Govindan (2011) highlighted the 11 types of drivers, an ISM model was developed and the interaction between these drivers were analysed for the firm under study using the ISM model and MICMAC analysis by classifying the drivers into four sectors as autonomous, dependent, linkage, and driver/independent. Lin et al. (2011) in their study explored the criteria that influence the performance of the automobile manufacturing industry and evaluated its performance to find key factors in improving the manufacturers' green performance using the fuzzy set theory and decision making trial and evaluation laboratory (DEMATEL). The results provided directions to automobile manufacturers in determining the key criteria and seeking the best guidance for improving environmental image and competitive advantage. Wang and Zhang (2005)

introduced a performance assessment index system, thereby establishing a performance assessment model of GSCM using fuzzy assessment method with the help of case study. The assessment model of green supply chain performance was established according to the characteristics of green supply chain performance assessment. Muralidhar et al. (2012) presented a new decision making approach for group multi-criteria evaluation for GSCM strategies, which clubbed green procurement, manufacturing, green service to customer and EM process with order allocation for dynamic supply chains to cope market variations by using fuzzy-AHP method fuzzy TOPSIS method. Both these models gave highest rank to green manufacturing, followed by green purchasing. Muralidhar et al. (2013) proposed new strategies for evaluating the GSCM for according priority to environmental factors, in cement manufacturing life cycle analysis, thereby reducing the carbon foot prints. Then GRA was combined with TOPSIS methodology to obtain priority for measurement indicators. It was strongly recommended that if fly ash is used as primary raw material in cement manufacturing system, it will significantly reduce carbon foot prints and load on the environment. Lin (2013) deployed fuzzy set theory and DEMATEL method to form a structural model to find out the cause and effect relationships among criteria by dividing set of complex factors. The proposed method successfully extended the DEMATEL method by applying both linguistic variables and a fuzzy aggregation method; hence it can effectively avoid vague and imprecise judgments. Najjar and Alsyouf (2003) assessed the most popular maintenance approaches, i.e., strategies, policies or philosophies, using a fuzzy multiple criteria decision making (MCDM) evaluation methodology. By using the suggested fuzzy evaluation methodology they were able to identify and select, in advance, the most informative (efficient) maintenance approach that was the most cost-effective and suited the technical system in its operating context. Kenneth et al. (2012) worked to theorise and empirically assess a comprehensive GSCM practices and performance model using a structural equation modelling (SEM) methodology. The model incorporated green supply chain practices that link manufacturers with supply chain partners (both suppliers and customers) to support environmental sustainability throughout the supply chain. The results of this investigation supported the proposition that GSCM practices are both environmentally necessary and good business. Hu and Hsu (2006) developed and validated a set of critical factors of GSCM practices that could be used by managers in implementing and adopting their own GSCM practices by using statistical tests. Zhu and Sarkis (2006) compared drivers and practices of GSCM in a developing country (China), focusing on three typical sectors, the automobile industry, the thermal power plants and the electronic/electrical industry with the help of ANOVA technique. They sought to determine where the differences occur and which industries are further along. This study indicated that Chinese companies in different industries have differing drivers and practices. They tend to confirm that globalisation and China's entry into the world trade organisation have helped promote GSCM practices in manufacturing enterprises. Eltayeb et al. (2011) tried to assess the actual environmental, economic and intangible outcomes resulting from the adoption of green supply chain initiatives, using factor analysis with the help of a structured questionnaire. Through designing environmentally friendly products and taking back products and packaging, business organisations can generate benefits to the environment, in the form of reduced waste and better resource utilisation, in addition to economic benefits and cost reductions to the organisations. Zhu et al. (2012) developed and empirically tested a theoretical model on different types of institutional pressures

motivating manufacturing enterprises to pursue GSCM practices and commensurate performance outcomes. The statistic results showed that institutional pressures have driven the manufacturer adoption of internal GSCM practices which in turn related to their external GSCM practices adoption. The statistic results also suggested that GSCM practices do not directly affect economic performance, but can improve it indirectly. Francesco and Fabio (2010) assessed the determinants and motivations for the implementation of GSCM by using statistical tools. Drawing upon a database of over 4,000 manufacturing facilities in seven OECD countries this paper assessed the determinants and motivations for the implementation of GSCM.

While ascertaining the performance evaluation, researchers have tried various innovative methods in treating the underlying performance drivers. Some have focused their studies in identifying the most potent factors affecting GSCM, some have bracketed various factors into groups and then subjected them to analysis; some tried to observe the interactions between them; some put forward models on the basis of some case study conducted. A study has been carried our setting forth the cause and effect relationship between the various criteria that affect performance. Attempts have also been made to propose strategies capable of evaluating GSCM measures. The subject of motivations and determinants on part of the manufacturer to go for GSCM has also been studied by a substantial number of researchers. Majority of researchers have deployed a multitude of techniques used for analysing MCDM problems like ISM, MICMAC, DEMATEL, fuzzy logic, ANOVA, factor analysis, SEM methodology and hybrid models like fuzzy-AHP method and fuzzy TOPSIS method, GRA and TOPSIS.

With the evolution of GSCM studies in the last two decades, tremendous headway has been made in understanding the measures that help in making industrial operations and activities ‘green’. But have we been able to identify all such measures? Have we been able to extract the maximum from the measures that have already been identified? Have we tried to prune the undesirable components (such as cost, operational complexities, etc.) associated with such measures? It is in this context that the relevance of performance evaluation of GSCM measures and models assumes significance from research point of view.

3.2 Supplier selection

Supplier selection is an important criterion in GSCM practices. In a green supply chain, firms need to have extensive supplier selection and performance evaluation processes (Kainuma and Tawara, 2006) since the supplier plays an important role in GSCM implementation. Supplier selection is a process of selecting key suppliers based on a pre-established set of criteria; it plays an important role in deciding the right members in supply chain management, especially in GSCM because the environmental performance and sustainability of a company depends on these members (Tseng and Chiu 2013). Suitability of a supplier may be attributed to a number of criteria such as adoption of green practices at its end, cutting down of transportation/logistics cost at the end of manufacturer owing to locational attributes associated with the supplier, smart/tech-oriented endeavours on the part of the supplier that lead to slashing of environmentally hazardous procedures in the existing supply chain.

Table 1 Performance evaluation

S. no.	*Year*	*Title/author*	*Findings*	*Tool/technique used*
1	2011	'An analysis of the drivers affecting the implementation of green supply chain management', Diabata and Govindan	Develop a model of the drivers affecting the implementation of GSCM.	ISM
2	2011	'GSCM performance in automobile manufacturing industry under uncertainty', Lin et al.	Explores the criteria that influence the performance of the automobile manufacturing industry.	Fuzzy DEMATEL
3	2005	'Study on the performance assessment of green supply chain', Wang and Zhang	Performance assessment model of GSC is established using the fuzzy assessment method.	Fuzzy
4	2012	'Evaluation of green supply chain management strategies using fuzzy AHP and TOPSIS', Muralidhar et al.	Presents a new decision making approach for group multi-criteria evaluation for GSCM strategies.	Fuzzy AHP and TOPSIS
5	2013	'The influence of GRA and TOPSIS for assortment of GSCM strategies in cement industry', Muralidhar et al.	Proposed new strategies for evaluating the GSCM for enhancing the priority to environmental factors in cement manufacturing.	GRA and TOPSIS
6	2011	'GSCM performance in automobile manufacturing industry under uncertainty', Lin et al.	Explores the criteria that influence the performance of the automobile manufacturing industry.	Fuzzy DEMATEL
7	2011	'Using fuzzy DEMATEL to evaluate the GSCM practices', Lin	Examine the influential factors and to form a structural model to find out the cause and effect relationships among criteria.	Fuzzy DEMATEL

Note: Summary of the previous studies of GSCM according to mathematical tools/technique used.

Table 1 Performance evaluation (continued)

S. no.	*Year*	*Title/author*	*Findings*	*Tool/technique used*
8	2003	'Selecting the most efficient maintenance approach using fuzzy multiple criteria decision making', Najjar and Alsyouf	Assess the maintenance approaches, i.e., strategies, policies, or philosophies, using a fuzzy multiple criteria decision making (MCDM) evaluation methodology.	Fuzzy
9	2012	'Green supply chain management practices: impact on performance', Kenneth et al.	Theorise and empirically assess a comprehensive GSCM practices and performance model.	SEM
10	2006	'Empirical study in the critical factors of (GSCM) practice in Taiwanese electrical and electronics industries', Allen and Chia	Develop and validate a set of critical factors of green supply chain management (GSCM) practices that could be used by managers in implementing and adopting their own GSCM practices.	SEM
11	2006	An inter-sectoral comparison of GSCM in China: drivers and practices (Zhu and Sarkis)	Compares drivers and practices of GSCM in one developing country, China, focusing on three typical sectors, the automobile industry, the thermal power plants and the electronic/electrical industry.	ANOVA
12	2011	'Green supply chain initiatives among certified companies in Malaysia and environmental sustainability: investigating the outcomes', Tarig et al.	Assess the actual environmental, economic and intangible outcomes resulting from the adoption of green supply chain initiatives.	FA
13	2012	'Institutional-based antecedents and performance outcomes of internal and external GSCM practices', Zhu et al.	Develops and empirically tests a theoretical model on the different types of institutional pressures motivating manufacturing enterprises to pursue GSCM practices and commensurate performance out comes.	SEM
14	2010	'Shadows and lights of GSCM: determinants and effects of these practices based on a multi-national study', Francesco and Fabio	Assesses the determinants and motivations for the implementation of GSCM.	SEM
15	2011	'Multi-criteria supplier evaluation and selection using fuzzy AHP', Arunkumar et al.	Fuzzy alpha cut analysis has been deployed for the purpose of performance evaluation and supplier selection in manufacturing industry.	Fuzzy AHP

Note: Summary of the previous studies of GSCM according to mathematical tools/technique used.

Table 2 Supplier selection

S. no.	*Year*	*Title/author*	*Findings*	*Tool/technique used*
1	2011	'Evaluation the drivers of GSCM practices in uncertainty', Wu et al.	Find influential factors in selecting GSCM criteria and evaluated the supplier performance.	Fuzzy DEMATEL
2	2012	'Using FAHP to determine the criteria for partner's selection within a green supply chain – the case of hand tool industry in Taiwan', Lee et al.	FAHP approach is proposed to select the most important criteria for green supplier selection in the Taiwanese hand tool industry.	Fuzzy AHP
3	2012	'A novel hybrid MCDM approach based on fuzzy DEMATEL, fuzzy ANP and fuzzy TOPSIS to evaluate green suppliers', Buyukozkan and Cifci	Propose an evaluation framework for green suppliers.	Fuzzy DEMATEL, fuzzy ANP and fuzzy TOPSIS
4	2008	'A fuzzy goal programming approach for GSC optimization under activity-based costing and performance evaluation with a value-chain structure', Tsai and Hung	Integrates activity-based costing (ABC) and performance evaluation in a value-chain structure for optimal GSC supplier selection and flow allocation.	Fuzzy goal programming
5	2012	'Sustainable supplier selection: a ranking model based on fuzzy inference system', Amindoust et al.	A new ranking method on the basis of fuzzy inference system (FIS) is proposed for supplier selection problem.	Fuzzy
6	2010	'A multi-criteria decision making approach for location planning for urban distribution centers under uncertainty', Awasthi et al.	Presented a fuzzy multi criteria approach for evaluating environmental performance of suppliers.	Fuzzy TOPSIS
7	2008	'A decision support system for supplier selection based on a strategy-aligned fuzzy SMART approach', Chou and Chang	Assess different suppliers that make use of SCM strategy	SCM strategy
8	2007	'Global supplier development considering risk factors using fuzzy extended AHP-based approach', Chan and Kumar	Developed an efficient system for supplier selection at global basis.	SCM strategy

Note: Summary of the previous studies of GSCM according to mathematical tools/technique used.

Table 2 Supplier selection (continued)

S. no.	*Year*	*Title/author*	*Findings*	*Tool/technique used*
9	2009	'Selection of optimal supplier in supply chain management strategy with analytic network process and choquet integral', Tseng et al.	Selection of appropriate supplier using ANP.	ANP
10	2006	'A fuzzy approach for supplier evaluation and selection in supply chain management', Chen et al.	Grade appropriate suppliers based on a number of factors.	TOPSIS
11	2006	'Employing dynamic fuzzy membership functions to assess environmental performance in the supplier selection process', Humphreys et al.	Enable inclusion of environmental criteria in supplier selection.	Fuzzy
12	2007	'Environmental principles applicable to green supplier evaluation by using multi-objective decision analysis', Lu et al.	Proposed an MCDM process for performance evaluation of suppliers.	AHP
13	2007	'Supplier selection with multiple criteria in volume discount environments', Xia and Wu	Determine the number of suppliers to employ and the order quantity allocated to these suppliers in the case of multiple sourcing and multiple products.	AHP
14	2007	'An integrated model for supplier selection decisions in configuration changes', Wang and Che	Showed the integration of different criteria that allows the supplier selection of a specific commercial product to be explored and modelled.	Fuzzy
15	2008	'Analysis and selection of green suppliers using interpretative structural modeling and analytic hierarchy process', Kannan et al.	Applied an integrated model which analysed and selected green suppliers.	ISM and AHP
16	2006	'The impact of supply chain management practices on competitive advantage and organizational performance', Li et al.	Presented another way of supplier selection using grey-based approach.	Fuzzy
17	2009	'Contractor selection with multi criteria decision support tools', Baykasoglu et al.	Deployed techniques for understanding of relative performance, advantages and disadvantages of various contractors of construction projects.	AHP and ANP

Note: Summary of the previous studies of GSCM according to mathematical tools/technique used.

Baykasoglu et al. (2009) deployed MCDM techniques like AHP and ANP for understanding of relative performance, advantages and disadvantages of various contractors of construction projects while analysing them on the front of green operations. Wu et al. (2011) used fuzzy DEMATEL method to find influential factors out of 15 evaluation factors in selecting GSCM criteria. This study was designed to compare the importance of each criterion to represent the degree of significance. The DEMATEL method evaluated supplier performance to find key factor criteria to improve performance and provided a novel approach of decision-making information in GSCM implementation. Lee et al. (2012) proposed integrating fuzzy logic and analytical hierarchy process (AHP) approach to select the most important criteria for green supplier selection in the context of Taiwanese hand tool industry. A list of criteria, along with their priority levels, is presented. According the finding results, pollution control; green image, environment-related certificates, environmental purchasing managing systems, employment practices and purchase price are the most important criteria for Taiwan hand tool companies to select green suppliers. Buyukozkan and Cifci (2012) proposed an evaluation framework for green suppliers. The identified components were integrated into a novel hybrid fuzzy MCDM model by combining the fuzzy DEMATEL model, the analytical network process (ANP) and technique for order performance by similarity to ideal solution (TOPSIS) in a fuzzy context. The proposed model was implemented in Ford Otosan, one of the pioneering companies about environmental subjects in Turkey. The combined fuzzy ANP and fuzzy DEMATEL approaches used in this study offered a more precise and accurate analysis by integrating interdependent relationships within and among a set of criteria. Tsai and Hung (2008) propose a fuzzy goal programming (FGP) approach that integrates activity-based costing (ABC) and performance evaluation in a value-chain structure for optimal GSC supplier selection and flow allocation. The paper provides a new approach to assess and control a complex GSC based on value-chain activities, and obtain a more precise solution. The establishment of this GSC model not only helps decision-makers to monitor GSC comprehensive performance but also can facilitate further improvement and development of GSC management. Amindoust et al. (2012) applied fuzzy logic to handle the subjectivity of decision makers' assessments and a new ranking method on the basis of fuzzy inference system (FIS) was proposed for supplier selection problem. In the evaluation process, decision makers' opinions on the importance of deciding the criteria and sub-criteria, in addition to their preference of the suppliers' performance with respect to sub-criteria were considered in linguistic terms. Awasthi et al. (2010) presented a fuzzy multicriteria approach for evaluating environmental performance of suppliers by using fuzzy TOPSIS. Chou and Chang (2008) proposed a system to evaluate alternative suppliers that utilises SCM strategy to identify supplier qualified criteria and the resulting model allowed decision-maker to incorporate the supply risks of individual supplier into final decision making. Chan and Kumar (2007) identified some of the important and critical criteria including risk factors for the development of an efficient system for global supplier selection. Tseng et al. (2009b) studied the selection of appropriate suppliers using ANP and choquet integral, given a specific SCM strategy considering a set of requirements and evaluation criteria. Chen et al. (2006) used TOPSIS to rank suitable suppliers based on quantitative and qualitative factors such as quality, price, and flexibility and delivery performance. Recent studies in multi-criteria supplier selection problems such as one by Humphreys et al. (2006), proposed a hierarchical fuzzy system with scalable fuzzy membership functions

to facilitate incorporation of environmental criteria in the selection process. Lu et al. (2007) constructed an MCDM process for GSCM to help managers in measuring and evaluating performance of suppliers using fuzzy AHP. Xia and Wu (2007) developed an integrated approach of AHP improved by rough sets theory and multi-objective mixed integer programming to simultaneously determine the number of suppliers to employ and the order quantity allocated to these suppliers in the case of multiple sourcing and multiple products with multiple criteria and supplier capacity constraints. Furthermore, Wang and Che (2007) presented a model using fuzzy performance indicators, and showed the integration of different criteria that allows the supplier selection of a specific commercial product to be explored and modelled. Li et al. (2007) presented another way of supplier selection using grey-based approach, but the computation process seem to be insufficient, showing unreasonable approach for the fuzzy number. Kannan et al. (2008) applied an integrated model which analysed and selected green suppliers based on their environmental performance using the ISM and AHP.

A variety of techniques have been deployed for researchers to select the best of the suppliers, with an aim to make the supply chain greener. Some researchers have used fuzzy DEMATEL, while others fuzzy TOPSIS to evaluate performance evaluation of suppliers. Yet others have blended fuzzy logic and AHP for the same. A group of researchers have been tried deploying a hybrid technique featuring DEMATEL, ANP and TOPSIS using fuzzy as a base element. A FGP method which considers ABC while focusing on performance evaluation has also been tried. A ranking method based on FIS has also been proposed, as has been one in which ISM and AHP have been used simultaneously. Some researchers have undertaken. There is another group of researchers who have preferred to work on lesser technical method and adopted a more generalised approach in evaluating the suppliers. A hierarchical fuzzy system with scalable functions forms the basis of another research work. Apart from these, various models have been thrown by various research works which are characterised by integration of various criteria.

GSCM is a supply chain-oriented concept, and hence the importance of suppliers in the implementation and augmentation of the same cannot be discounted. Prudent selection of suppliers, with due consideration of green operations, multiply the effectiveness of the supply chain in achieving the objective of environmental conservation. If each link, in the supply chain associates itself with environment-conscious inputs, it snowballs into a massive green endeavour and manifests itself in the shape of an effective GSCM-based initiative, on a holistic basis. Therefore, the selection of supplier is of utmost importance, when embarking upon an operation that is intended to be ‘green’ in its nature and effects.

3.3 Functional barriers

GSCM measures are yet to reach the level of their desired adoption by industries/manufacturers throughout the world, most notably being in third world and developing countries. The reason is that there are many factors associated with implementation of GSCM, which demotivate many industries/manufacturers to incorporate the same in their scheme of things. Mostly cost escalation or inconvenience in implementation is cited as major barriers in the espousing GSCM practices. Various researches are carried out to figure out the factors that retard the growth of GSCM

propagation in industrial sectors, and methods have been suggested to counter them effectively.

The barriers in implementation of GSCM in a particular business establishment are inter-related, as they cast their influence on each other. They are classified as driving barriers if they support other barriers; and dependent barriers if they are influenced by other barriers. Singh et al. (2014) find the relationship between the barriers by ISM. Mathiyazhagan et al. (2012) deployed ISM qualitative analysis to understand the mutual influences amongst the 26 barriers by survey to identify which barrier was acting as the most influencing one and the result was helpful for industries to make easier the adoption of green concept in their supply chain by removing the dominant barrier. It indicated that different Indian auto component manufacturing industries have differing barriers for the implementation of GSCM. Luthra et al. (2011) put forward a structural model of 11 barriers to implement GSCM in Indian automobile industry using ISM and prioritise them. The structured model developed will help to understand interdependence of the barriers. Dashore and Sohani (2013) presented a hierarchical sustainable framework for evaluating the barriers to the implementation of the GSCM in an organisation, driving and dependence power analysis (DDPA) was used to classify and identify critical barriers. Balasubramanian (2012) presented a hierarchical sustainability framework for evaluating the barriers to the adoption of GSCM in the United Arab Emirates (UAE) construction sector by using ISM and DDPA Technique. Wooi and Zailani (2010) investigated the barriers that hinder the SMEs in Malaysia from implementing green supply chain and found that resources barrier is the key barrier that impedes the adoption of GSCM initiative and the technical barrier is expected to be the key barrier for the SMEs in the manufacturing sectors in Malaysia. A questionnaire-based survey was conducted to rank these enablers and they found contextual relationships among the enablers and developed a hierarchy-based model for the enablers by using ISM (Mudgal et al., 2009).

Researchers have been carried out by deploying various modelling techniques to rank the barriers in the way of implementing GSCM, or to gauge their effect in a particular scenario. Generally, ISM and DDPA has been used for the purpose. Some models have also been formulated to study the interdependence of barriers on each other.

GSCM has been an exciting concept theoretically, and gets more exciting when it is put into practice. It is a matter of concern, that so far the concept has not taken a practical shape with relation to its potential. There are number of barriers that impede the practical espousal of GSCM across the spectrum of industries. The first step in quashing these barriers understands them fully and then develops strategies to counter them effectively. Hence, the identification and study of GSCM barriers is of paramount importance, and the same needs to be carried out in general, as well as specifically for diverse industrial sectors.

Table 3 Functional barriers

S. no.	*Year*	*Title/author*	*Findings*	*Tool/technique used*
1	2012	'An ISM approach for the barrier analysis in Implementing GSCM', Mathiyazhagan et al.	Interpretive structural modelling (ISM) qualitative analysis was used to understand the mutual influences amongst the 26 barriers by survey.	ISM
2	2011	'Barriers to implement GSCM in automobile industry using interpretive structural modeling technique – an Indian perspective', Luthra et al.	Identify the barriers to implement GSCM in Indian automobile industry and to prioritise them.	ISM
3	2013	'Green supply chain management: a hierarchical framework for barriers', Dashore and Sohani	Presented a hierarchical sustainable framework for evaluating the barriers to the implementation of the green supply chain management (GSCM) in an organisation.	ISM
4	2012	'A hierarchical framework of barriers to green supply chain management in the construction sector', Balasubramanian	Presented a hierarchical sustainability framework for evaluating the barriers to the adoption of green supply chain management (GSCM) in construction sector.	ISM
5	2010	'Green supply chain initiatives: investigation on the barriers in the context of SMEs in Malaysia', Wooi and Zailani	Investigated the barriers that hinder the SMEs in Malaysia from implementing green supply chain.	Hypothesis testing
6	2009	'Greening the supply chain practices: an Indian perspective of enablers relationship', Mudgal et al.	Rank the enablers and found contextual relationships among the enablers and developed a hierarchy-based model.	ISM
7	2014	'An interpretive structural modelling approach for analysing barriers in total productive maintenance implementation', Singh et al.	Developed the relationships among the identified TPM barriers.	ISM

Note: Summary of the previous studies of GSCM according to mathematical tools/technique used.

3.4 Mechanism formulation/implementation

Various researchers have devised an assortment of models and mechanism for implementing GSCM in industry-specific, location-based or generic settings. Others have deduced findings pertaining to implications and inferences of implementing green measures in a supply chain. Certain models were proposed keeping in view specific limitations faced by a particular type of industry, or one which is faced with a particular set of situational factors. Mechanism formulation or implementation of GSCM in specific settings, present an interesting reading for scholars and help them to assess the limits that are generally attributed to the growth and proliferation of the management practices.

Chen et al. (2012) used ANP model to solve complex GSCM strategy-selection problems and evaluated the most important activity in each business functions viz, design, purchasing, manufacturing, and marketing and service – and associated their related activities with 'greenness'. A detailed procedure solved complex GSCM strategy-selection problems and evaluated the most important activity in each business function with the help of taking a case study on leading Taiwanese Electronics Company to identify the proposed procedure's stability. Xiangru and Jingang (2008) designed an evaluation index system on GSCM and the evaluation model was structured by AHP-Fuzzy comprehensive evaluation. The evaluation index system and evaluation model not only gave the results of comprehensive evaluation green degree to enterprise GSCM, but could also be carried out single-factor evaluation. RL may translate into GSCM practices if suitable policies and strategies may be made by a business establishments by using a dynamic simulation model. In this context, Mutingi (2014) carried simulation and analysis of various key variables by using system dynamics (SD) principles, to understand their influences. Jiance and Liying (2012) determined seven factors that affected implementation of GSCM in Chinese enterprises and an index system including 32 indexes (nodes) about these factors had been set up. They ranked these factors and indexes by ANP and found that the key factor of GSCM is government and laws especially regional laws and regulations. Sarkis (2003) modelled a decision framework which was solved as an ANP for decision making within the green supply chain. The focus of the paper was on the components and elements of GSCM and how they served as a foundation for the decision framework. Wang and Chan (2013) proposed a fuzzy hierarchical TOPSIS approach along with AHP in order to achieve sustainable economic and environmental performance. It provided a novel approach to examine various challenges that firms might be faced with when implementing GSCM initiatives and it also enabled organisations to identify improvement areas required for adopting these green initiatives. Luthra et al. (2012) used the ISM methodology for finding relationships among the various interrelated factors vital for implementing GSCM relevant to Indian manufacturing, for which MICMAC Analysis has been carried out. The model suggested how these factors were interrelated. An organisation may be benefited in analysing which factors they have to improve upon to implement GSCM in Indian manufacturing industry. Tseng and Chiu (2013) presented quantitative evaluation measures in uncertainty using fuzzy set theory. They proposed a hybrid MCDM approach to deal with the alternatives problem in linguistic preferences and ranked alternative suppliers using a GRA. The study illustrated the case of a printed circuit board manufacturer in Taiwan that seeks to implement GSCM and selected a green supplier to meet its requirements. Lee et al. (2012) in their research, explored the effect of GSCM

efforts and other organisational factors on firm performance of small and medium enterprises (SMEs) by using SEM. They developed a research model relating GSCM practice and business performance through three organisational variables (employee satisfaction, operational efficiency, and relational efficiency) as moderators. Their result indicated that business performance would be improved when GSCM enhanced operational efficiency. Gavronski et al. (2011) provided a model for development of GSM capabilities. Using the resource-based view (RBV) of the firm as the theoretical background, they postulated that plant resources are positively related to green manufacturing capabilities, which in turn are positively related to GSM capabilities. The data from a survey of a sample of manufacturing plants indicated that a managerial philosophy that included external knowledge exchange directly supported both greener process management and environmental collaboration with suppliers. Chan et al. (2012) proposed and empirically tested a model delineating the relationship among environmental orientation, GSCM activities (green purchase, customer cooperation and investment recovery) and corporate performance. The findings explicated the importance for firms, in particular those operating in a highly competitive market condition, to nurture a pro-environmental corporate culture and improve their sensitivity to salient external stakeholders' environmental demands so as to pursue greener supply chain management.

Various mechanisms have been proposed by different research scholars, which on implementation will push GSCM practices to greater heights. Mechanism formulation is a complex activity which calls for careful deployment of MCDM techniques. Some have proposed an evaluation index system, while others have focused on the inter relationship between the inherent factors that propel GSCM practices, while others tend to delineating the relationship among the same. Some researchers have based their studies by making use of SEM by taking in consideration various variables that are integral to the concept of GSCM, while others have focused on the resources at the disposal of the firm.

Mechanism formulation with intent to promote GSCM practices is research in the real and practical sense of the word, as it throws open new and innovative methods by which GSCM can be put into practice. Model formulation should rather be considered as extension of the domain of the concept. It helps in bringing forth new ideas and notions by which GSCM can be practically accomplished; and at the same time provides an opportunity to other scholars to build upon the model so formulated. The study of new models of GSCM implementation help a researcher to get informed about the latest practice-based aspects of subject.

3.5 Inter-relationships between factors

The factors that identify themselves with the implementation of a GSCM measure are interrelated with each other, and the quantum of their effect invariably depends upon the extent and mode of interaction between them. The correlation amongst the factors is of utmost importance to understand the manifestation of a GSCM measure in real-world settings, and to further improve upon the efficacy of the same, under a given set of conditions. The relations are invariably represented in the shape of mathematical equations featuring the variables, which signify the underlying factors affecting the outcome a GSCM measure.

Table 4 Mechanism formulation/implementation

S. no.	*Year*	*Title/author*	*Findings*	*Tool/technique used*
1	2012	'A business strategy selection of green supply chain management via an analytic network process', Chen et al.	Proposes a network to clarify managerial levels and firm-related content and to solve complex GSCM strategy-selection problems.	ANP
2	2008	'Research of evaluation model on enterprise's green degree of GSCM', Xiangru and Zhang	Designed an evaluation index system on GSCM and the evaluation model.	Fuzzy AHP
3	2012	'Study on the determining and importance sequence of factors affecting GSCM', Jiance and Liying	Determined 7 factors that affected implementation of GSCM in Chinese enterprises and an index system.	ANP
4	2002	'A strategic decision framework for green supply chain management', Joseph Sarkis	Modelled a decision framework for decision making within the green supply chain.	AHP
5	2012	'A hierarchical fuzzy TOPSIS approach to assess improvement areas when implementing green supply chain initiatives', Wang and Chan	Proposed a fuzzy TOPSIS approach along with AHP in order to achieve sustainable economic and environmental performance.	Fuzzy TOPSIS
6	2012	'Implementation of the GSCM In manufacturing industry in India using interpretive structural modeling technique', Luthra et al.	Finds the relationships among various interrelated factors vital for implementing GSCM relevant to Indian manufacturing.	ISM
7	2013	'Evaluating firms green supply chain management in linguistic preferences', Tseng and Chiu	Presented quantitative evaluation measures in uncertainty using fuzzy set theory	Fuzzy
8	2012	'Green supply chain management and organizational performance', Lee et al.	Developed a research model relating GSCM practice and business performance.	SEM
9	2011	'A resource-based view of green supply management', Gavronski et al.	Provide a model for development of GSCM capabilities.	Hypothesis testing
10	2012	'Environmental orientation and corporate performance: the mediation mechanism of green supply chain management and moderating effect of competitive intensity', Chan et al.	Proposed and empirically tested a model delineating the relationship among environmental orientation, (GSCM) activities.	SEM
11	2014	'The impact of reverse logistics in green supply chain management: a system dynamics analysis', Mutingi	Carried simulation and analysis of various key variables by using system dynamics (SD) principles, for reverse logistics.	SD

Note: Summary of the previous studies of GSCM according to mathematical tools/technique used.

Zhu and Sarkis (2004) examined the relationships between GSCM practice and environmental and economic performance. Using moderated hierarchical regression analysis they evaluated the general relationships between specific GSCM practices and performance. They also investigated how two primary types of management operations philosophies, quality management and just-in-time (or lean manufacturing) principles, influence the relationship between GSCM practices and performance. Zhu et al. (2008) investigated the correlation of two major factors, organisational learning and management support, with the extent of adoption of GSCM practices in Chinese manufacturing firms, where their inbound and outbound logistics activities were potential polluters to the environment. The hypotheses were tested using standard hierarchical multiple regression models employing ordinary least square (OLS) estimation. Their findings showed significant positive relationships between organisational learning mechanisms, organisational support and the adoption of GSCM practices, after controlling for a number of other influences including regulations, marketing, supplier, cost pressures, industry levels of the relevant practice and organisational size. Giovanni and Vinzi (2012) used SEM for testing the research hypotheses on a large sample of Italian firms, and estimated the structural paths between constructs by means of both covariance – and component-based approaches. They investigated the relationships between EM and performance to verify whether the implementation of an effective internal environmental is a firm's precondition to subscribe to a green supply chain.

Relationships between various aspects of GSCM are studied in various research works, using moderated hierarchical regression analysis, OLS estimation, SEM, etc. Relationship between GSCM practices and performances, cost and environmental gains, between adoption of GSCM measures and management support/organisational learning, inputs and results, internal initiatives on the part of the organisation and its subscription to GSCM on a desirable scale, etc. have been studied. The deductions of the studies on the inter-relationships of factors have led to establish the factors that are more effective in reaching the desired results on environmental and economic front, when GSCM initiatives are undertaken; subject to the peculiarity of the conditions in which the latter are enforced.

Though researchers have been able to pin point majority of factors that are individually relevant from the view point of understanding and proliferating GSCM; the interrelationships between them still remains an unexplored area. Surprisingly, the inter-relations between factors hold a key to massive potential gains the scale of which is still unknown to us. They will surely be as good as individual, perhaps more profound in their effect. It is in this background that their study assumes much significance.

3.6 Generic/standard exploration

Many studies are comparatively more theoretical in nature, limited to assess and ascertain the fundamental aspects of the subject. Such research works tend to address objectives of general nature, in context of adoption and implementation of GSCM by a particular industry, geographical domain or a specific firm. Some researches falling under this category tend to re-ascertain the existing attributes of the management practice in particular settings.

Table 5 Inter-relationships between factors

S. no.	*Year*	*Title/author*	*Findings*	*Tool/technique used*
1	2004	'Relationships between operational practices and performance among early adopters of GSCM practices in Chinese manufacturing enterprises', Zhu and Sarkis	Examined the relationships between GSCM practice and environmental and economic performance.	Regression analysis
2	2008	'Firm level correlates of emergent GSCM practices in the Chinese context', Zhu et al.	Investigates the correlation of two major factors, organisational learning and management support, with the extent of adoption of green supply chain management.	Regression analysis
3	2012	'Covariance versus component-based estimations of performance in GSCM', Giovanni and Vincenzo	Used SEM for testing the research hypotheses and estimated the structural paths between constructs by means of both covariance - and component-based approaches.	SEM

Note: Summary of the previous studies of GSCM according to mathematical tools/technique used.

Table 6 Generic/standard exploration

S. no.	*Year*	*Title/author*	*Findings*	*Tool/technique used*
1	2012	'An empirical study of green supply chain management in Indian perspective', Toke et al.	Recognise and select appropriate strategy for implementing GSCM.	AHP
2	2012	'Green supply chain management: a case study from Indian electrical and electronics industry', Kumar et al.	Investigated the GSCM practices likely to be adopted by the manufacturing industry.	Mean score
3	2007	'An empirical study of the implementation of GSCM practices in the electrical and electronic industry and their relation to organizational performances', Chien and Shih	Investigated the GSCM practices likely to be adopted by the electrical and electronic industry in Taiwan.	SEM
4	2012	'Why do firms adopt/implement green practices? – An institutional theory perspective', Lin and Sheu	Examined how institutional theory influenced GSCM practices and supply chain performance.	SEM
5	2006	'Extending green practices across the supply chain – the impact of upstream and downstream integration', Vachon and Klassen	Conceptualise and empirically test GSCP, and consider both and separately upstream and downstream interactions in the supply chain.	Hypothesis testing
6	2012	'A planning optimization framework for construction and demolition waste management', Xanthopoulos et al.	Deployed optimised-frameworks of disassembly processes of an end-of-life building.	SEM

Note: Summary of the previous studies of GSCM according to mathematical tools/technique used.

Toke et al. (2012) strived to rank interactions and weightage of critical success factors of GSCM in Indian manufacturing sector. They recognised and selected appropriate strategy for implementing GSCM and AHP, which was applied for determining relative importance and selecting appropriate approach in GSCM practice. The purpose of this study was to establish the consistency and priority approaches for implementing GSCM in response to critical success factors. Kumar, et al. (2012) investigated the GSCM practices likely to be adopted by the manufacturing industry of electrical and electronics products in India by analysing the data using 'mean score'. Study also focused on the impact of environmental collaboration in the supply chain on manufacturing and environmental performance. Lin and Sheu (2012) in their study examined how institutional theory influenced GSCM practices and supply chain performance by examining whether firms submit to institutional pressures in their adoption of green practices in addition to seeking economic efficiency. Based on the data collected from the USA and Taiwan manufacturing plants in the electric and electronics industry using survey method, SEM was performed to examine theoretical relationships among various institutional variables, green supply chain practices, and manufacturing performance. The findings proved that pressures from institutional actors have a significantly positive impact on GSCM practices adoption, which in turns improve organisational performance. Construction activities are considered to cause much of eco-destruction, coupled with resource depletion and wastage. Xanthopoulos et al. (2012) deployed optimised-frameworks of disassembly processes of an end-of-life building, by taking in consideration 'bill of materials', as an input; recycling and reusage can be encouraged in the supply chain of construction business. Chien and Shih (2007) investigated the GSCM practices likely to be adopted by the electrical and electronic industry in Taiwan. The data was then analysed using statistical package for the social sciences, and SEM was used as a path analysis model to verify the hypothetical construction of the study. The results indicated that the original equipment manufacturing and original designing and manufacturing manufacturers in Taiwan's electrical and electronic industry have adopted green procurement and green manufacturing practices in response to the current wave of international green issues and had generated favourable environmental and financial performances for the respective companies. Vachon and Klassen (2006) brought forth green practices along two dimensions viz. environmental collaboration and monitoring. Validity and reliability of scales for new and existing constructs were assessed through factor analysis. Hierarchical linear regression was used to test the hypotheses for the antecedents of GSCP. Technological integration with primary suppliers and major customers was positively linked to environmental monitoring and collaboration. For logistical integration, a linkage was found only with environmental monitoring of suppliers. Finally, as the supply base was reduced, the extent of environmental collaboration with primary suppliers increased.

Diverse studies on the extent of GSCM adoption, their attributive factors, their fall outs and concerned issues have been undertaken in a number of research studies. Efforts have been made to rank interactions and weightage of critical success factors of GSCM implementation. Certain studies focus on environmental collaboration and the subsequent monitoring of the initiatives taken. Management practices most likely to be adopted in future, impact of institutional pressures on GSCM adoption; relationships among various institutional variables, green supply chain practices, and manufacturing performance. The suitability of the factors taken into consideration have been of extreme significance, as

well as the hypotheses deliberated upon. Techniques like AHP, SEM, 'mean score', factor analysis, hierarchical linear regression have been deployed by the researchers while undertaking their studies.

Generic/standard explorations consolidate the validity of the existing knowledge base of the subject, and help in testing the same in diverse and specific industrial/geographical settings. They form the base of further studies, and act as a launch pad for more complex explorations. A researcher, who intends to carry out a new study, cannot afford to overlook the generic/standard explorations, for they form the foundations on which more challenging undertakings are based.

4 Gaps in literature

The literature that has been reviewed, presents interesting observations that hold a promise of providing possibilities for new researches and adoption of a fresh perspective on the concept of GSCM by researchers, on many counts. Various gaps have also been identified that point to the missing links that could be bridged to attain more insights on how GSCM can be more effectively implemented to get the desired benefits on front of environment friendly and cost effective operations. For example, apropos the research works conducted on the barriers in the implementation of GSCM practices, the factors are considered individually, as well as their inter-linkages are also taken into consideration. Nevertheless, some of the interrelations between the barriers can be reduced to mathematical equations. Though it will require hefty inputs, yet the results will help in a tremendous way to consolidate our understanding about the barriers in implementing GSCM. Some barriers are location-specific or sector specific in nature, and there is an element of ambivalence regarding their applicability in a universal manner. Similarly, studies conducted on one specific firm, always carry an uncertainty that whether the results achieved, can be generalised in the context of the subject studies, i.e., GSCM whatever is applicable to a part, may not be applicable to the whole. In fact, what is applicable for one firm, may not apply to a similar firm operating in a different geographical/industrial set up. In context of model formulation, researchers have worked upon creating models that are more effective to implement GSCM practically. But they themselves states that all the underlying factors have not been considered for the sake of convenience and computation. This points that though there is a scope for further improvisation of the deductions, the same was not carried out because of complexities involved in working them out. This is a gap, which has been purposely introduced; and it is hoped that with better management/computational tools one day the researchers will be able to fine tune their findings by making their deductions more inclusive in nature. In some research papers, among other things, factors such as green image, environment-related certificates, environmental purchasing are cited. But in most of the developing countries, where the need of deploying GSCM practices is felt more intensely, the availability of certificates/management systems at the end of the supplier may not reflect the real picture at his end. The reason being, that many of the mentioned 'criteria', can be secured easily; but the spirit underlying the same may generally be missing. Furthermore, some models are tested on only one firm; which casts aspersion on the validity of the model across the horizon of firms from different sectors and with a diverse spatial distribution. Last but not the least, the deductions of the many studies carried out, hinges upon the beliefs and opinions of the respondents to whom the

questionnaires were sent or responses were invited. This introduces an element of subjectivity in the results deduced. The lack of quantifiable information as well as numerical data, affects the objectivity of the results.

Nevertheless, the findings deduced by various researchers has helped in bringing forth new ideas and notions by which GSCM can be practically accomplished; and at the same time provides an opportunity to other scholars to build upon the findings so achieved. The study of research literature of GSCM implementation will help aspiring researchers to get informed about various aspects of subject. Their findings will form the base of further studies, and will act as a launch pad for more complex explorations. A researcher, who intends to carry out a new study, cannot afford to overlook the existing research works done, for they form the foundations on which more challenging undertakings are based.

5 Conclusions

The study carried out on the diverse type of literature on GSCM, extended by various researchers of the subject have led to the conclusion that though the mentioned management tool has gained wide popularity and acceptance on the academic front, still a lot needs to be done on ground (industrial front) level. It has been observed that much of work done on literary front is of subjective interest, and confines itself to the domain of describing the facets of GSCM or aspires to evaluate the performance of various factors that are identified with the application of the same. This, in the most practical terms, can be referred as highlighting the basics of the management concept with respect to a particular industry, industrial set up or geographical domain. Limited research literature has been generated corresponding to identifying hitherto unexplored aspects of GSCM, having the potential for large scale transformation in the implementation and adoption of the scale, across spatial or sectoral horizons. Though on one hand, this presents a monotonous view of the work done so far on the subject; at the same time, it offers bright optimism that there is still a lot to be explored and new discoveries can be made with regard to green practices that of can have far reaching positive ramifications for environment and economic/industrial progress of mankind. Integration of findings hitherto reached by researchers, throw exciting opportunities in developing a holistic approach of understanding the concept of GSCM and meditating on what new can be determined apropos the subject. The analysis of literature resulting from various research works gives a clear picture of the gaps and unattended aspects of GSCM. Extensive research can be carried out on such attributes that have so far not been worked upon. Gradual addition to the knowledge base of subject matter will help the concept to evolve and find new dimensions, which at later stage will help in rapid extension GSCM, both qualitatively and in magnitude.

5.1 Limitations of the study

The findings of this study are substantially helpful in understanding the conceptual and practical aspects of GSCM implementation; nevertheless the study has been characterised by a number of limitations. The most prominent is the scope and applicability of the models studied. Most of the studies undertaken limit themselves to particular

settings – industrial, geographical, etc.; and the validity of the models on a universal scale is debatable. Furthermore, many elements that constitute the green supply chain have subjective traits, which are non-quantifiable. Such elements, are either not featured in the models altogether; or are not optimally represented therein. This study is also limited by the lack of practical testing of the models studied. The study is theoretical in nature and the validity of the models/theories extended by the literature reviewed needs to be tested in peculiar spatial and operational settings. Though a large number of studies were reviewed while undertaking this study, the possibility of existence of hitherto unknown variable, and their interplay with others in a given supply chain cannot be ruled out. Furthermore, the nature of operational domain varies from case to case. A model which is workable in a developed country, say Germany may not be as effective in an underdeveloped country, say Sudan. This limits the validity of the findings only to those particular settings, where the original study was carried out and not necessarily in conditions opposite to it. There are many models in the study, which are theoretically derived and may not have been tested in real time conditions in diverse operational settings. Thus, there are a number of limitations attached with this study; nevertheless care and caution have been taken to make the finding comprehensive and inclusive to maximum possible extent.

References

Amindoust, A., Ahmeda, A., Saghafinia, A. and Bahreininejada, A. (2012) 'Sustainable supplier selection: a ranking model based on fuzzy inference system', *Applied Soft Computing*, Vol. 12, No. 6, pp.1668–1677.

Arunkumar, N., Karunamoorthy, L. and Muthukumar, S. (2011) 'Multi-criteria supplier evaluation and selection using fuzzy AHP (alpha cut analysis): a case study', *Int. J. Industrial and Systems Engineering*, Vol. 8, No. 4, pp.449–471.

Balasubramanian, S. (2012) 'A hierarchical framework of barriers to green supply chain management in the construction sector', *Journal of Sustainable Development*, Vol. 5, No. 10, pp.15–27.

Baykasoglu, A., Ozbay, E., Gogus, T.T. and Oztay, A. (2009) 'Contractor selection with multicriteria decision support tools', *Int. J. Industrial and Systems Engineering*, Vol. 4, No. 2, p p.174–197.

Bras, B. and McIntosh M.W. (1999) 'Product, process, and organizational design for remanufacture – an overview of research', *Robotics and Computer-Integrated Manufacturing*, Vol. 15, No. 3, pp.167–178.

Buyukozkan, G. and Cifci, G. (2012) 'A novel hybrid MCDM approach based on fuzzy DEMATEL, fuzzy ANP and fuzzy TOPSIS to evaluate green suppliers', *Expert Systems with Applications*, Vol. 39, No. 3, pp.3000–3011.

Carter, C.R. and Ellram, L.M. (1998) 'Reverse logistics: a review of the literature and framework for future investigation', *Journal of Business Logistics*, Vol. 19, No. 1, pp.85–102.

Chan, F.T.S. and Kumar, N. (2007) 'Global supplier development considering risk factors usingfuzzy extended AHP-based approach', *The International Journal of Management Science*, Vol. 35, No. 4, pp.417–31.

Chan, R.Y.K., He, H., Chan, H.K. and Wang, W.Y.C. (2012) 'Environmental orientation and corporate performance: The mediation mechanism of green supply chain management and moderating effect of competitive intensity', *Industrial Marketing Management*, Vol. 41, No. 4, pp.621–630.

Chang, B.Y., Kenzhekhanuly, Y. and Park, B. (2013) 'A study on determinants of green supply chain management practice', *International Journal of Control and Automation*, Vol. 6, No. 3, pp.199–208.

Chen, C., Shih, H.S., Shyur, H.J. and Wu, K.S. (2012) 'A business strategy selection of green supply chain management via an analytic network process', *Computers and Mathematics with Applications*, Vol. 64, No. 8, pp.2544–2557.

Chen, C.T., Lin, C.T. and Huang, S.F. (2006) 'A fuzzy approach for supplier evaluation and selection in supply chain management', *International Journal of Production Economics*, Vol. 102, No. 2, pp.289–301.

Chien, M.K. and Shih, L.H. (2007)'An empirical study of the implementation of green supply chain management practices in the electrical and electronic industry and their relation to organizational performances', *International Journal of Environment Science & Technology*, Vol. 4, No. 3, pp.383–394.

Chou, S.Y. and Chang, Y.H. (2008) 'A decision support system for supplier selection based on a strategy-aligned fuzzy SMART approach', *Expert Systems with Applications*, Vol. 34, No. 4, pp.2241–2253.

Daniel, V. and Guide Jr., R. (1998) 'Scheduling with priority dispatching rules and drum-buffer rope in a recoverable manufacturing system', *International Journal of Production Economics*, Vol. 53, No. 1, pp.101–116.

Daniel, V. and Guide Jr., R. (2000). 'Production planning and control for remanufacturing: industry practice and research needs', *Journal of Operations Management*, Vol. 18, No. 4, pp.467–483.

Daniel, V., Guide Jr., R., Srivastava, R. and Michael S. (1996) 'Are production systems ready for the green revolution?', *Production and Inventory Management Journal*, Vol. 37, No. 4, pp.70–78.

Dashore, K. and Sohani, N. (2013) 'Green supply chain management: a hierarchical framework for barriers', *International Journal of Engineering Trends and Technology, Vol.* 4, No. 5, pp.2172–2182.

Diabata, A. and Govindan.K. (2011) 'An analysis of the drivers affecting the implementation of green supply chain management', *Resources, Conservation and Recycling.*, Vol. 55, No. 6, pp.659–667.

Eltayeb, T.K., Zailani, S. and Ramayah, T. (2011) 'Green supply chain initiatives among certified companies in Malaysia and environmental sustainability: investigating the outcomes', *Resources, Conservation and Recycling*, Vol. 55, No. 5, pp.495–506.

Farzianpour, F., Pishdar, M., Shakib, M.D., Hashemi, S. and Toloun, M.R. (2014) 'Consumers perceived risk and its effect on adoption of online banking services management' *American Journal of Agricultural and Biological Sciences*, Vol. 11. No. 1, pp.47–56.

Fleischmann, M., Beullens, P., Ruwaard, J.M.B. and Wassenhove, L.N.V. (2001) 'The impact of product recovery on logistics network design', *Production & Operations Management*, Vol. 10, No. 2, pp.156–173.

Fleischmann, M., Krikke, H.S., Dekker, R. and Flapper, P.S.D. (2000) 'A characterization of logistics networks for product recovery', *Omega*, Vol. 28, No. 6, pp.653–666.

Fleischmann, M., Ruwaard, J.M.B., Dekker, R., Laan. E.V., Nunen J.A.E.E. and Wassenhove, L.N.V. (1997) 'Quantitative models for reverse logistics: a review', *European Journal of Operational Research*, Vol. 103, No. 1, pp.1–17.

Francesco, T. and Fabio, I. (2010) 'Shadows and lights of GSCM (green supply chain management): determinants and effects of these practices based on a multi-national study', *Journal of Cleaner Production*, Vol. 18, Nos. 10–11, pp.953–962.

Gavronski, I., Klassen, D.R., Vachon, S. and Nascimento, L.F.M. (2011) 'A resource-based view of green supply management', *Transportation Research Part E*, Vol. 47, No. 6, pp.872–885.

Giovanni, P.D. and Vinzi, V.E. (2012) 'Covariance versus component-based estimations of performance in green supply chain management', *International Journal of Production Economics, Vol.* 135, No. 2, pp.907–916.

Gungor, A. and Gupta, S.M. (1999) 'Issues in environmentally conscious manufacturing and product recovery: a survey', *Computers & Industrial Engineering*, Vol. 36, No. 4, pp.811–853.

Hu, A.H. and Hsu, C.W. (2006) 'Empirical study in the critical factors of green supply chain management (GSCM) practice in the Taiwanese electrical and electronics industries', *IEEE International Conference on Management of Innovation and Technology*, Vol. 2, No. 1, pp.854–857.

Humphreys, P., McCloskey, A., McIvora, R., Maguire, L. and Glackina, C. (2006) 'Employing dynamic fuzzy membership functions to assess environmental performance in the supplier selection process', *International Journal of Production Research*, Vol. 44, No. 12, pp.2379–2419.

Jayaraman, V. (2003) 'The design of reverse distribution networks: models and solution procedures', *European Journal of Operational Research*, Vol. 150, No. 1, pp.128–149.

Jiance, Z. and Liying, Y. (2012) 'Study on the determining and importance sequence of factors affecting GSCM', *9th International Conference on Service Systems and Service Management* IEEE, China.

Kainuma, Y. and Tawara, N. (2006) 'A multiple attribute utility theory approach to lean and green supply chain management', *International Journal of Production Economics*, Vol. 101, No. 1, pp.99 –108.

Kannan, G., NoorulHaq, A., Sasikumar, P. and Arunachalam, S. (2008)'Analysis and selection of green suppliers using interpretative structural modeling and analytic hierarchy process', *International Journal of Management and Decision Making*, Vol. 9, No. 2, pp.163–82.

Kenneth, W. G., Pamela J. Z., Meacham, J. and Bhadauria, V.S. (2012) 'Green supply chain management practices: impact on performance', *Supply Chain Management: An International Journal, Vol.* 17, No. 3, pp.290–305.

Kumar, S., Chattopadhyaya, S. and Sharma, V. (2012)' Green supply chain management: a case study from Indian electrical and electronics industry', *International Journal of Soft Computing and Engineering*, Vol. 1, No. 6, pp.275–281.

Lee, S.M., Kim, S.T. and Choi, D. (2012) 'Green supply chain management and organizational performance', *Industrial Management & Data Systems*, Vol. 112, No. 8, pp.1148–1180.

Lee, T.R., Le, T.P.H., Genovese, A. and Koh, S.C. (2012) 'Using FAHP to determine the criteria for partner's selection within a green supply chain The case of hand tool industry in Taiwan', *Journal of Manufacturing Technology Management*, Vol. 23, No. 1, pp.25–55.

Li, S., Nathan, B.R., RaguNathan, T.S. and SubbaRao, S. (2006) 'The impact of supply chain management practices on competitive advantage and organizational performance', *Omega*, Vol. 34, No. 2, pp.107–124.

Lin, R.J. (2013) 'Using fuzzy DEMATEL to evaluate the green supply chain management practices', *Journal of Cleaner Production*, Vol. 40, Special Volume: Sustainable Consumption and Production for Asia: Sustainability Through Green Design and Practice, pp.32–39.

Lin, R.J. and Sheu, C. (2012) 'Why do firms adopt/implement green practices? – an institutional theory perspective', *Procedia – Social and Behavioral Sciences*, Vol. 57, No. 9, pp.533–540.

Lin, R.J., Chen, R.H. and Nguyen, T.H. (2011) 'Green supply chain management performance in automobile manufacturing industry under uncertainty', *Procedia – Social and Behavioral Sciences*, Vol. 25, No. 1, pp.233–245.

Lu, Y.Y., Wu, C.H. and Kuo, T.C. (2007) 'Environmental principles applicable to green supplier evaluation by using multi-objective decision analysis', *International Journal of Production Research*, Vol. 45, Nos. 18–19, pp.4317–4331.

Luthra, S., Garg, D., Kumar, S. and Haleem A. (2012) 'implementation of the green supply chain management in manufacturing industry in india using interpretive structural modeling technique', *BPR Technologia : A Journal of Science, Technology & Management*, Vol. 1, No. 1, pp.1–17, ISSN: 2278–8387.

Luthra, S., Kumar, V., Kumar, S. and Haleem, A. (2011) 'Barriers to implement green supply chain management in automobile industry using interpretive structural modeling technique – an Indian perspective', *Journal of Industrial Engineering and Management*, Vol. 4, No. 2, pp.231–257.

Mathiyazhagan, K., Govindan, K., Noorulhaq, A. and Geng, Y. (2013) 'An ISM approach for the barrier analysis in implementing green supply chain management', *Journal of Cleaner Production, Vol.* 47, No. 1, pp.283–297.

Meredith, J. (1993) 'Theory building through conceptual methods', *International Journal of Operations & Production Management*, Vol. 13, No. 5, pp.3–11.

Mudgal, R.K., Shankar, R., Talib, P. and Raj, T. (2009) 'Greening the supply chain practices: an Indian perspective of enablers relationship', *International Journal of Advanced Operations Management*, Vol. 1, Nos. 2–3, pp.151–176.

Muralidhar, P., Ravindranath, K. and Srihari, V. (2012) 'Evaluation of green supply chain management strategies using fuzzy AHP and TOPSIS', *IOSR Journal of Engineering*, Vol. 2, No. 4, pp.824–830.

Muralidhar, P., Ravindranath, K. and Srihari, V. (2013) 'The influence of GRA and TOPSIS for assortment of GSCM strategies in cement industry', *International Journal of Supply Chain Management*, Vol. 2, No. 1, pp.49–54.

Mutingi, M. (2014) 'The impact of reverse logistics in green supply chain management: a system dynamics analysis' *International Journal of Industrial and Systems Engineering, Vol.* 17, No. 2, pp.186–201.

Najjar, B.A. and Alsyouf, I. (2003) 'Selecting the most efficient maintenance approach using fuzzy multiple criteria decision making', *International Journal of Production Economics*, Vol. 84, No. 1, pp.85–100.

Olugu, E.U., Wong, K. Y. and Shaharun, A. M. (2011) 'Development of key performance measures for the automobile green supply chain' *Resources, Conservation and Recycling*., Vol. 55, No. 1, pp.567–579.

Pagell, M. and Schevchenko, A. (2014) 'Why research in sustainable supply chain management should have no future', *Journal of Supply Chain Management*, Vol. 50, No. 1, pp.1–32.

Pishdar, M., Toloun, M.R.S.H., Zamani, S. and Farzianpour, F. (2014) 'Development of factors effective in the success of green supply chain management', *American Journal of Agricultural and Biological Sciences*, Vol. 9, No. 1, pp.33–43.

Sarkis, J. (2003) 'A strategic decision framework for green supply chain management', *Journal of Cleaner Production*, Vol. 11, No. 4, pp.397–409.

Sarkis, J., Zhu, Q. and Lai, K.H. (2011) 'An organizational theoretic review of green supply chain management literature', *International Journal of Production Economics*, Vol. 130, No. 1, pp.1–15.

Singh, M., Sachdeva, A. and Bhardwaj, A. (2014) 'An interpretive structural modelling approach for analysing barriers in total productive maintenance implementation', *International Journal of Industrial and Systems Engineering, Vol.* 16, No. 4, pp.433–450.

Smith, M.E., Richard. T. and Paul, J. (2002) *Management Research – An Introduction*, Sage Publications, London.

Srivastava, S. (2007) 'Green supply-chain management: a state-of the-art literature review', *International Journal of Management Reviews*, Vol. 9, No. 1, pp.53–80.

Toke, L.K., Gupta, R.C. and Dandekar, M. (2012) 'An empirical study of green supply chain management in Indian perspective', *International Journal of Applied Science & Engineering Research*, Vol. 1, No. 2, pp.372– 383.

Tsai, W.H. and Hung, S.J. (2008) 'A fuzzy goal programming approach for green supply chain optimization under activity-based costing and performance evaluation with a value-chain structure', *International Journal of Production Research*, Vol. 47, No. 18, pp.4991–5017.

Tseng, M.L. and Chiu, A.S.F. (2013) 'Evaluating firms green supply chain management in linguistic preferences', *Journal of Cleaner Production*, Vol. 40, Special Volume: Sustainable Consumption and Production for Asia: Sustainability Through Green Design and Practice, pp.22–31.

Tseng, M.L. and Lin, R.J. (2013)'Determine the driving criteria in firm's GSCM practices with dependence and uncertainty', *Journal of Cleaner Production*, Vol. 40, No. 1, pp.22–31.

Tseng, M.L., Chiang, J.H. and Lan, L.W. (2009b) 'Selection of optimal supplier in supply chain management strategy with analytic network process and choquet integral', *Computers & Industrial Engineering*, Vol. 57, No. 1, pp.330–340.

Vachon, S. and Klassen, R.D. (2006) 'Extending green practices across the supply chain: the impact of upstream and downstream integration', *International Journal of Operations &Production Management*, Vol. 25, No. 9, pp.898–916.

Walker, H., Sisto, L.D. and Mcbain, D. (2008) 'Drivers and barriers to environmental supply chain management practices: lessons from the public and private sectors', *Journal of Purchasing and Supply Management, Vol.* 14, No. 1, pp.69–85.

Wang, H.S. and Che, Z.H. (2007) 'An integrated model for supplier selection decisions in configuration changes', *Expert Systems with Applications*, Vol. 32, No. 4, pp.1132–1140.

Wang, S.Z. and Zhang, H.C. (2005) 'Study on the performance assessment of green supply chain', *IEEE International Conference on Systems, Man and Cybernetics,* , Vol. 1, pp.942–947.

Wang, X. and Chan, H.K. (2013) 'A hierarchical fuzzy TOPSIS approach to assess improvement areas when implementing green supply chain initiatives', *International Journal of Production Research*, Vol. 51, No. 10, pp.3117–3130.

Wooi, G.C. and Zailani, S. (2010) 'Green supply chain initiatives: investigation on the barriers in the context of SMEs in Malaysia', *International Business Management*, Vol. 4, No. 1, pp.20–27.

Wu, K.J., Liao, C.J., Tan, K.H., Chiu, S.F. and Tseng, M.L. (2012) 'Exploring decisive factors effecting green supply chain practices under uncertainty', *Proceedings of the Asia Pacific Industrial Engineering & Management Systems Conference*, pp.89–102.

Wu, K.J., Tseng, M.L. and Vy, T. (2011)'Evaluation the drivers of green supply chain management practices in uncertainty', *Procedia – Social and Behavioral Sciences, Vol.* 25, pp.384 – 397.

Xanthopoulos, A., Aidonis, D., Vlachos, D. and Lakovou, E. (2012) 'A planning optimisation framework for construction and demolition waste management', *International Journal of Industrial and Systems Engineering*, Vol. 10, No. 3, pp.257–276.

Xia, W. and Wu, Z. (2007) 'Supplier selection with multiple criteria in volume discount environments', *Omega*, Vol. 35, No. 5, pp.494–504.

Xiangru, M. and Jingang, Z. (2008) 'Research of evaluation model on enterprise's green degree of GSCM', *International Seminar on Business and Information Management.*

Zhang, H.C., Kuo, T.C., Huang, S.H. and Lu, H. (1997) 'Environmentally conscious design and manufacturing: a state-of-the-art survey', *Journal of Manufacturing Systems*, Vol. 16, No. 5, pp.352–371.

Zhu, Q. and Sarkis, J. (2004) 'Relationships between operational practices and performance among early adopters of green supply chain management practices in Chinese manufacturing enterprises', *Journal of Operations Management*, Vol. 22, No. 3, pp.265–289.

Zhu, Q. and Sarkis, J. (2006) 'An inter-sectoral comparison of green supply chain management in China: drivers and practices', *Journal of Cleaner Production*, Vol. 14, No. 5, pp.472–86.

Zhu, Q. and Sarkis, J. (2007) 'The moderating effects of institutional pressures on emergent green supply chain practices and performance' *International Journal of Production Research*, Vol. 45, No. 18, pp.4333–4355.

Zhu, Q., Sarkis, J. and Lai, K.H. (2008a) 'Green supply chain management implications for closing the loop', *Transportation Research Part E: Logistics and Transportation Review*, Vol. 44, No. 1, pp.1–18.

Zhu, Q., Sarkis, J. and Lai, K.H. (2008c) 'Confirmation of a measurement model for green supply chain management practices implementation', *International Journal of Production Economics*, Vol. 111, No. 2, pp.261–73.

Zhu, Q., Sarkis, J. and Lai, K.H. (2012) 'Green supply chain management innovation diffusion and its relationship to organizational improvement: an ecological modernization perspective', *Journal of Engineering and Technology Management*, Vol. 29, No. 1, pp.168–185.

Zhu, Q., Sarkis, J. and Lai, K.H. (2013) 'Institutional-based antecedents and performance outcomes of internal and external green supply chain management practices', *Journal of Purchasing and Supply Management*, Vol. 19, No. 2, pp.106–117, http://dx.doi.org/10.1016/j.pursup.2012.12.001.

Zhu, Q., Sarkis, J., Cordeiro, J.J. and Lai, K.H. (2008a) 'Firm-level correlates of emergent green supply chain management practices in the Chinese context', *Omega*, Vol. 36, No. 4, pp.577–591.

Zhu, Q., Sarkis, J., Cordeiro, J.J. and Lai, K.H. (2008b) 'Firm-level correlates of emergent green supply chain management practices in the Chinese context', *Omega*, Vol. 36, No. 1, pp.577–91.

ResearchGate

See discussions, stats, and author profiles for this publication at: http://www.researchgate.net/publication/280978653

Material Flow and Microstructural Studies in Friction Stir Welding / Processing of Aluminium: A Literature Review

ARTICLE · JUNE 2015

READS
38

3 AUTHORS, INCLUDING:



Radhey SHYAM Mishra
Delhi Technological University
20 PUBLICATIONS **25** CITATIONS
SEE PROFILE



Ranganath M Singari
Delhi Technological University, Formerly Del…
45 PUBLICATIONS **83** CITATIONS
SEE PROFILE

All in-text references underlined in blue are linked to publications on ResearchGate, letting you access and read them immediately.

Available from: Ranganath M Singari
Retrieved on: 07 November 2015

Volume 3, Issue 2 (2015) 500-511 ISSN 2347 - 3258
International Journal of Advance Research and Innovation

Material Flow and Microstructural Studies in Friction Stir Welding / Processing of Aluminium: A Literature Review

V. Jeganathan Arulmoni, R.S. Mishra, Ranganath M. S
Department of Mechanical and Production & Industrial Engineering, Delhi Technological University, Delhi, India

Article Info
Article history:
Received 8 April 2015
Received in revised form
15 April 2015
Accepted 22 May 2015
Available online 15 June 2015

Keywords
Friction Stir Welding,
Processing,
Aluminium,
Alloys,
Wear,
Properties

Abstract
Material flow in friction stir welding / processing under different process parameters with aluminium has been studied by many scientists. All such studies have been considered and a detailed review is presented in this paper. Results indicated friction stir welding / processing with aluminium and alloys may successfully utilised, because of the significantly improved strength in the material and at the same time the ductility also retained, along with the substantiallyimproved hardness. FSP was found to be beneficial also in improving wear resistance.

1. Introduction

Friction stir welding is a solid state joining process that provides many advantages compared with conventional fusion welding methods such as lower residual stresses, especially high joint strength and low distortion because of lower welding temperature and also elimination of porosities and solidification cracking because of no melting occurrence. This welding method was invented in TWI in Cambridge, England in 1991 firstly for joining aluminium alloys. It also has made low cost welded joints because of much lower power consuming, no needs of joint edge preparations before welding application and also no gas shielding required compared with conventional welding methods. Friction stir processing (FSP) was developed for micro structural modification of metallic materials. Welding/processing parameters, tool geometry, and joint design exert significant effect on the material flow pattern and temperature distribution, thereby influencing the micro structural evolution of material. In FSP, a rotating tool is inserted into a material and high plastic deformation is produced. FSP is used to enhance ductility, induces super plasticity and improve corrosion resistance properties. FSP has been successfully applied to various cast aluminium and magnesium and copper alloys to eliminate casting defects and thereby improve their mechanical properties.

An FSW/FSP tool consists of a shoulder and a pin. The tool is plunged till the shoulder touches the work piece. The friction between the shoulder and work piece results in the biggest component of heating. The main function of the tool is to 'stir' and 'move' the material. Tool rotational speed depends upon the hardness of the material. Processing speed is nothing but traverse speed. An increase in traverse speed and decrease in rotation of the FSP tool may cause reduction in the grain size of the stir zone for the specimen friction stir processed without any metal particles. The main objective of this paper is to discuss the study of friction stir welding / processing of aluminum and its alloys. The investigations made by various scientists and authors regarding the effect of FSP parameters such as tool rotational speed, processing speed, groove width and depth on microstructure and micro hardness have been taken into consideration of this review study.

Corresponding Author,
E-mail address: ranganathdce@gmail.com
All rights reserved: http://www.ijari.org

2. Literature Review

An exhaustive review of published data on the effect of process parameters on friction stir welding / processing works on aluminium and its alloys has been discussed. The review has been presented in a tabular form. Nearly 53 papers related to study of friction stir welding / processingof aluminium and aluminium alloys have been considered. The review table given below explains the details of parameters considered by earlier authors.

Serial No	Author and Year	Materials Used	Tool Utilised	Processing Parameters	Reteach Conducted
1.	A. Bastiera et al., [2008]	7050 aluminim alloy	Tool with Cylindrical pin radius is equal to 5 mm, shoulder radius is equal to 15 mm and pin height is equal to 9 mm.	The material behaviour for temperatures between 20 and 500 ◦C. Welding and rotational speeds are set respectively to 1.7 mms^{-1} and 260 rpm. The pin is tilted by 2◦ from the vertical axis and a cone angle of 7◦ under the shoulder is adopted.	A parametric study about the influence of welding and rotational speeds is carried out. Computational Fluid Dynamics package is used to establish the material flow and the temperature field during the process and to estimate the residual state induced by the process. The steady-state assumption and the original elastoviscoplastic constitutive law.
2.	A. Orozco-Caballero et al., [2013]	Al-Zn-Mg-Cu alloy commercial 3 mm Al 7075-T6 (nominal composition in wtpct 5.68Zn-2.51Mg-1.59Cu-0.19Cr-bal Al) rolled plates	Concentric threaded pin with flutes 3mm in diameter and 2 mm in length.	FSP using a rotation rate of 1000 rpm and a traverse speed of 500 mm min^{-1} along the rolling direction.	A finer grain size, 0.3 vs 0.5 mm, was obtained by processing at the highest cooling rate. Materials showed super plastic behaviour with a maximum elongation to fracture of about 510%. Grain boundary sliding was the operative deformation mechanism
3.	A. Yazdipoura et al., [2009]	Al 5083 non-heat treatable alloy (4.2mg, 0.60mn, 0.25S, 0.15Fe, 0.09zn, 0.09cr, 0.06cu, 0.02Ti bal AL) Mix of sic & mos2 50 mm x 100 mm	H-13 steel SD-15mm PD-4mm, PL-1mm, penetration depth was selected at 1mm, rapid cooling applied (mixture of methanol & dry ice)	560-900 rpm, traverse speed 16-57mm/min	Modeling, Microstructure, on cooling rate on the nano grains forming, grain refining mechanism
4.	A.G. Rao et al., [2009]	AL-30Si base alloy, permanent mould cast plates (Al, 30Si, 0.2mg, 0.1Fe)	A tool made of H13 steel having flat shoulder diameter of 25 mm and pin of 6 mm diameter.	1000 rpm, 16mm/min, single/two pass, 100% overlap, cooling for 2nd pass	This paper demonstrates the effect of two pass overlap friction stir processing on microstructural refinement of Al–30Si alloy, which delineates significant reduction in size and aspect ratio of silicon particles from average 200 to 2 µm and 4.93 to 1.75 µm respectively. The stir zone of two pass overlap FSP exhibits relatively homogeneous Si particle distribution.
5.	Adem Kurt et al., [2011]	1050 AL (0.4Fe, 0.12Si, 0.03cu, 0.02mg, 0.02mn, bal Al) , monolithic cold rolled plates Sic-10µm, SiC mixed with methanol applied to surface of the plates, 50 mm x 100 mm x 5 mm, no binder	AISI 1050 steel, cylindrical shoulder, no pin, SD-12mm	1050 AL (0.4Fe, 0.12Si, 0.03cu, 0.02mg, 0.02mn, bal Al) , monolithic cold rolled plates Sic-10µm, SiC mixed with methanol applied to surface of the plates, 50mmx100mmx5mm, no binder	Microstructural observations were carried out by employing optical microscopy of the modified surfaces. Mechanical properties like hardness and plate bending were also evaluated. The results showed that increasing rotating and traverse rate caused a more uniform distribution of SiC particles.
6.	B. Zahmatkesh et al., [2010]	AL2024 hot rolled T4 plates 76mm x 6.4mm x 305mm (0.058Si, 0.18Fe, 4.64cu,	The pin generally has cylindrical plain, frustum tapered, threaded and flat surfaces. In this study, threaded pin profile was used. The pin was 2.5 mm	tool rotating rate of 800 rpm, and travel speed of 25 mm/min with a tool tilt angle 3^{o}	Microstructural evolution and tribologicalbehavior of friction stir processed (FSP) Al2024-T4 were investigated. Microstructural characteristics of the samples were investigated by optical microscopy

		0.69mn, 1.57mg, 0.02cr, 0.18zn, 0.04Ti)	in diameter and 2.5 mm in length.		(OM) and scanning electron microscopy (SEM).
7.	Chung-Wei Yang et al., [2012]	AA 4032 Al cast alloy homogenized at 413oC for 3h, furnace cooled and machined at 85mmx30mmx4 mm	PD-6mm, PL-2mm, SD-17mm	1400rpm, pressure 43.4mpa, 2 deg angle	FSP and artificial peak aging on erosion resistance test, micro hardness
8.	Devinder Yadav and RanjitBauri, [2012]	Pure aluminum 99.2% 12mm plate	M2 steel, SD-12mm, PD-3mm, PL-2.1mm, cylindrical tool	a tool rotation speed of 640rpm and traverse speed of 150mm/min with a downward force of 5 kN.	Friction stir processing refined the grain size to 3μm in a single pass from the starting coarse grain size of 84μm. Electron backscattered diffraction (EBSD) results showed occurrence of dynamic recrystallization and also revealed existence of different orientations within the stir zone and across the transition zone. Transmission electron microscopy (TEM) revealed fine grains with well defined boundaries.
9.	Douglas C. Hofman n and Kenneth S. Vecchio, [2005]	AA6061-T6 3.2 mm thick FSP, SFSP(submerge d FSP) with water	Tool Steel SD-12,7mm, 19.1mm, PD-3.18mm, PL-2.79mm	2 HP mill, 1000 rpm, 0.42-1.69mm/s	This research demonstrates the use of submerged friction stir processing (SFSP) as an alternative and improved method for creating ultrafine-grained bulk materials through severe plastic deformation. SFSP is compared with friction stir processing (FSP) done in air, through the use of thermocouples and transmission electron microscopy.
10.	F.Y. Tsai and P.W. Kao, [2012]	Cast AL-Si base alloy,AC8A (11.8Si, 1.12Ni, 1.15cu, 1.06mg, 0.28Fe) solution heat treated at 883k for 4 hrs	Tool for FSP has a shoulder of 16 mm diameter and the tool pin has a 6 mm diameter and a 1.2 mm pitch height.	1400 rpm, 45mm/min	This study demonstrated that friction stir processing (FSP) could result in a significant improvement in tensile properties of AC8A, particularly in ductility. Both tool rotation rate and traversing speed could affect the strength of FSPed specimens, which was related to the characteristics of coarsening, dissolution and reprecipitation of the strengthening particles.
11.	G. Madhus udhan Reddy and K. Srinivas a Rao, [2010]	Cast A356 Al castings	A straight cylindrical friction stir tool (pin length 3 mm, pin diameter 6mm, shoulder diameter 15mm) made of high carbon steel was used in the present study.	A tool rotational speed of 2000 rpm, a transitional speed of 20 mm/minute, and plunging speed 30 mm/minute were employed.	The friction stir processed zone was characterized by metallography, electron micro probe analysis, hardness, dry sliding wear and potentio dynamic polarization testing. Hardness mapping showed that stir zones experienced increase of 40% compared to the as-cast metal. Further uniform micro-hardness was observed in the friction stir processed zone, which was not the case with as-cast A356 aluminum alloy.
12.	GhaderFaraji and ParvizAsadi, [2011]	Commercially available nano-sized (30 nm) Al2O3 particles with the purity of 99.9% were	The circular and square tools were used in this work. Tools were made of hardened H13 tool steel. Tools consisted of a pin with 5mm in diameter, 3mm in height, and a	The FSP tool was rotated in 900 and 1200rpm in the clock-wise direction. The traverse speed was changed from 40 to 80 mm/min. The tilted angle was 3◦.	The microstructures, wear property and micro-hardness of AZ91 Mg alloy/alumina particle reinforced nano-composite produced by friction stir processing (FSP) were investigated.

		used in volume fraction of 8% to produce nano-composite layer on the surface of AZ91. AZ91 composition (in wt.%) was Al, 9.1; Zn, 0.68; Mn, 0.21; Si, 0.085; Cu, 0.0097; Ni, 0.001; Fe, 0.0029 and Mg, bal.	shoulder with 15mm in diameter.		
13.	H.J. Liu and X.L. Feng, [2012]	2219-T6 aluminum alloy plates	The tool was made of tool steel, and consisted of only a shoulder with a diameter of 22 mm.	The tool rotating speed (ω) was 1000 rpm, and the traverse speed (*v*) was 200–400 mm/min. The displacement control was used and the plunge depth was kept constant at 0.5 mm. The tilted angle was 2.5^0	The microstructure was characterized using optical microscopy, scanning electron microscopy, and transmission electron microscopy. Two types of heat treatments, aging treatment and solutionizing followed by water quenching and aging treatment, were applied to the processed samples.
14.	H.W. Zhang et al., [2007]	The material of the plate is Al 6061-T6 and is modeled as a rate-independent elastic–plastic material.	The radii of the pin and the shoulder are 3 and 7.5 mm, respectively.	To accelerate the convergence, the rotational and the translational speeds are both increased 1000 times in the analysis	Material flow in friction stir welding (FSW) under different process parameters is simulated by using the finite element technique based on the nonlinear continuum mechanics. Results indicate that the distribution of the equivalent plastic strain correlates well with the distribution of the microstructure zones in the weld.
15.	I. Charit and R.S. Mishra, [2003]	AL2024 hot rolled T4 plates solution heat treated, quench, natural aging, transverse direction and polished, 76mmx6.4mmx 305mm (0.07Si, 0.17Fe, 4.6cu, 0.64mn, 1.5mg, 0.01cr, 0.15zn, 0.03Ti)	High strength cobalt alloy	300 rpm, 25.4mm/min	The present study demonstrates that superplasticity at higher strain rates can be achieved in a commercial 2024 Al alloy via friction stir processing. Ductility values for the FSP alloy are substantially higher than that of the parent alloy (non-superplastic) at comparable temperature and strain rate ranges.
16.	K. Elangovan and V. Balasubramanian, [2008]	AA6061-T6 (1.1mg,0.12mn, 0.35Fe, 0.58Si, 0.22cu, bal Al) Heat treatable wrought, normal to rolling direction, 300mmx 150mmx6mm	High carbon steels. Different shapes , straight cylindrical, taper cylindrical, threaded cylindrical, square, triangular, different SD of each pin profile, SD-15mm, 18mm& 21mm,PD-6mm, PL-5.5mm, D/d ratio 2.5, 3.0 & 3.5	Axial loads 7kn, 1200 rpm, 1.25 mm/sec	In this investigation, an attempt has been made to understand the effect of welding speed and tool pin profile on FSP zone formation in AA2219 aluminium alloy.
17.	K. Elangovan and V. Balasubramanian, [2008]	AA6061-T6 (1.1mg,0.12mn, 0.35Fe, 0.58Si, 0.22cu, bal Al) Heat treatable wrought, normal to	High carbon steels. Different shapes refer fig, straight cylindrical, taper cylindrical, threaded cylindrical, square, triangular. SD-18mm,Pd-6mm, PL-5.5mm, D/d ratio	Axial loads 6kn, 7kn, 8kn, 1200 rpm, and 1.25 mm/sec.	Tool pin profile, axial force, mechanical properties

		rolling direction	3.0		
18.	K. Surekha and A. Els-Botes, [2011]	AA2219-T87 (6.1cu, 0.25mn,, 0.04Zn, 0.05Ti, 0.13Fe, 0.16Zr, 0.09V) 250mmx150mmx5mm	a non-consumable non-threaded tool made up of high-speed tool steel whose shoulder diameter is 12 mm and pin diameter and length are 5 and 2.8 mm respectively.	800, 1200,1600 rpm, speed 0.37mm/s, 0.76mm/s, three passes	Micro structure, corrosion behavior, multipass
19.	K. Surekha et al., [2008]	The material used in this work is AA2219-T87 alloy with the nominal composition in wt.% of Cu–6.1, Mn–0.25, Zr–0.16,V–0.09, Ti–0.05 and rest Al. The AA2219-T87 plates	a non-consumable threaded tool made up of high-speed tool steel.	Up to three passes were given at three rotation speeds of 800 (slow – S), 1200 (medium– M), 1600 (fast – F) rpmand two welding speeds (0.37 (slow – S) and 0.76 (fast – F) mm/s). The depth of the processed region was 2 mm in a 5 mm thick plate.	Anodic polarization and electrochemical impedance tests in 3.5% NaCl showed an improved corrosion resistance of the processed alloy, which increased with the number of passes. Salt spray and immersion tests also showed improved resistance to corrosion. The increased resistance to corrosion is attributed to the dissolution of CuAl2 particles, which was established by XRD and DSC studies.
20.	K.N. Ramesh et al., [2012]	Al-5086-O alloy 150x110mm2 6 mm plate	Hot die steel tool SD-24mm, PD-6 mm, PL-3mm, cylindrical pin, processing parallel to rolling direction	1025 rpm, fixed, traverse speed 30mm/min, 50mm/min, 110mm/min 150mm/min, mild steel backing plate 12 passes	Imp method material is cooling after each pass. CMP FSP performed for 12 passes without allowing any cooling, mech properties, one rotational speed, different combination feeds.
21.	L. Karthikeyan et al., [2010]	A 319 sand cast 200x50x10mm (Al, 5.2Si,2.51cu, 0.35Fe, 0.26mn, 0.15mg, 0.04Ni, 0.29Zn, 0.09Ti, 0.03Pb, 0.01Sn)	High carbon steel, cylindrical threaded, right handed 1 mm pitch, SD-18mm, PD-6mm, PL-5.7mm,	800, 1000,1200,1400,1600 rpm, 40.2, 75mm/min. single pass. For one feed-four speeds	Yield strength, tensile strength, ductility, microhardness
22.	L. Karthikeyan and V.S. Senthil Kumar, [2011]	AA6063-T6 (cu-0.01, mg0.5mg, 0.43Si, 0.02Fe, 0.06mn, 0.05Ni, 0.005Zn, 0.01Ti, 0.01Sn) 100x50x10mm	SD-18mm, PD-6mm, PL-5.7mm,pitch 1 mm threaded	Maximum power – 30 hp, maximum axial force – 25 kN and a maximum spindle speed – 3000 rpm.	In this investigation the surfaces of AA6063-T6 aluminum alloy were friction sir processed and the effects of process variables such as axial force, tool feed and rotational speed were studied.
23.	L. Karthikeyan et al., [2009]	2285 cast al alloy 4cu, 1.5mg, 0.6si, 0.6Fe, 0.6mn, 2Ni, 0.1Zn, 0.2Ti, 0.05Pb, 0.5Sn, bal Al, 200 mm x 50 mm x 10 mm	HSS SD-16mm, PD-5mm, PL-4.7mm, cylindrical	1400 rpm,1800rpm, 10,12,15mm/min, single pass	Micro, Mechanical properties, tensile, hardness, k type thermocouple
24.	L.B. Johannes et al., [2007]	Al 5083 non-heat treatable alloy (4.7mg, 0.51mn, 0.51Fe, 0.10cr, 0.11cu, bal AL) 8mm , countinous cast	MP159 high strength cobalt alloy PD&PL-6.4mm,SD-25mm, threaded right hand screw, counter clockwise	600 rpm, 25.4mm/min, single pass for optimum level, then 8 passes	Super plasticity, mechanical properties
25.	LivanFratini et al., [2009]	The FSW between 3.2 mmthick AA2139-T8 blanks were considered for the three joint	The utilized tools were made of H13 steel quenched at 1020 ^{0}C, characterized by a 52 HRc hardness. FSW process used three types:Butt joint, Lap joint, T-joint, Tool shoulder [mm] : 12 ,	The material was furnished in the T8 condition, namely after a solubilization at 530 ^{0}C for 4 h, a cooling in water and an artificial aging at 175 ^{0}C for 8 h, the blanks were cold stretched .	In the paper the microstructural phenomena in terms of average grain size occurring in friction stir welding (FSW) processes are focused. A neural network was linked to a finite element model (FEM) of the process to predict the average grain size values. The utilized net was trained

		configurations proposed	20, 20 Pin cone angle: 0^0 , 15^0 , 15^0 Pin major diameter [mm]: 4, 5.8, 6 Pin height [mm]: 2.7, 4.9, 5.5		starting from experimental data and numerical results of butt joints and then tested on further butt, lap and T-joints. The obtained results show the capability of the AI technique in conjunction with the FE tool to predict the final microstructure in the FSW joints.
26.	M. Chiumenti et al., [2013]	This rocess is primarily used on aluminum alloys, and most often on large pieces which cannot be easily heat treated to recover temper characteristics.	The movement of the pin is split into advancing speed (assigned to the work-piece in the opposite direction) and rotation (assigned to the pin).	During the welding process, the pin is rotating at a very high speed (e.g. 50–1500 rpm, depending on the work-piece material), a fully Lagrangian approach (which follows the material particles of the continuum in their motion) is unaffordable.	This work presents the strategy adopted for the numerical simulation of the FSW process. A coupled thermo-mechanical solution of both the momentum and energy balance equations is presented. A very general kinematic framework has been used to deal with the specific description of motion in the FSW problem.
27.	M.A. Garcı´a-Bernal et al., [2009]	Al 5083 cast alloy with mn contents as CC(continous strip casting) (4.72mg, 0.49mn, 0.19cr, 0.16Fe, 0.09Si) different mn contents 0.49, 0.74, 1.00	MP 159 alloy SD-16mm, conical threaded pin bottom 7mm, minor diameter 4.8 mm, PL-5mm, right hand screw .	400 rpm, 0.42 mm/s(1 ipm) , plunge depth 5.4mm, tilt angle 2.5o.	High strain rate , super plasticity
28.	M.A. García-Bernal et al., [2012]	Al 5083 cast alloy with mn contents as CC(continous strip casting) (4.72mg, 0.49mn, 0.19cr, 0.16Fe, 0.09Si) different mn contents 0.49, 0.74, 1.00	MP 159 alloy SD-16mm, conical threaded pin bottom 7mm, minor diameter 4.8 mm, PL-5mm, right hand screw, plunge depth 5.4mm, tilt angle 2.5o.	400 rpm, 0.42 mm/s(1 ipm)	Hot deformation behavior, strain rate, elongation
29.	M.L. Santella et al., [2005]	A 319, A356 200x50x16mm (A356-Al-7Si, 0.3mg, A319-Al, 6Si, 3.5Cu)	H-13 steel SD-13mm, pin cylindrical, hemispherical, PD-5.2mm, PL-3.4 mm	1000 rpm, 1.7mm/s fixed, 5-6 passes	Mechanical properties
30.	M.P. Miles et al., [2005]	6061 Al alloy 25mm thick and 7075 50 mm thick	SD-25mm, concave shoulder 8mm cylindrical pin, 2.8 degree, tool translation 3.3mm per pass	600 rpm, 100mm/min, processing depth 3mm for 25mm thick 6061, 350 rpm and 127mm/min processing depth 6mm for 50mm thick 7075 AL	FSP and mechanical properties
31.	Magdy M. El-Rayesa and Ehab A. El-Danaf, [2012]	AA6082-T651 (1.2Si, 0.75mg,0.79mn bal AL) 129mmx100mmx6mm	Mo-W tool steel SD-15mm, concentric square pin, edge length 6mm, 5mm long	850 rpm, traverse speed 90, 140,224 mm/min. no of passes-overlapping	Microstructure, mechanical properties, multi pass
32.	Mehdi Zohoor et al., [2012]	The specimen used in this work was a 5 mm Al5083 sheet with 130 mmlength, 60 mmwidth.	The material of tool used in this work was H13 steel with shoulder diameter of 16 mm. The tool pin used in FSP is a standard M6 1 (pitch height of 1 mm, diameter of 6 mm and	The FSP parameters were 750 and 1900 rpm in tool rotational speed, 25 mm/min in traverse speed and tilted angle of 3^0. In order to fix the specimens, they were clamped onto	Results showed that the specimens with micro and nano-sized particles present fine grains and higher level of hardness. Tensile properties of specimens friction stir processed with and without Cu particles were also evaluated. According to the results,

		Then, the Cu particles were embedded and compressed into the groove	counterclockwise) with pin height of 3.2 mm.	the thick St37 steel by the bolts.	the composite with nano-sized particles exhibited enhanced tensile strength and ductility rather than AA5083 Aluminum alloy. X-ray diffraction (XRD) studies were carried out on the specimens FSPed with Cu particles in order to identify the phases present in the stir zone (SZ) of the specimens.
33.	Nhon Q. Vo et al., [2012]	A 3.75 mm thick sheet of twin-roll-cast (TRC) Al–Mg–Sc alloy with a nominal composition of Al–4.1Mg–0.47Sc–0.022Zr–0.041Ti–0.15Fe–0.043Si, wt.% (Al–4.5 Mg–0.28Sc–0.007Zr–.02Ti–0.07Fe–0.04Si, at.%) produced at CSIRO, Australia,	FSP tool is made of a step-spiral tool steel. The shoulder diameter and pin height are 12.0 and 2.20 mm, respectively. The pin diameter at the tip and the shoulder end (root) are 3.75 and 6.00 mm, respectively.	Two different tool rotational rates – 325 and 400 rpm – were utilized and the resulting samples are labeled F325 and F400. The tool traverse speed was 3.4 mm s^{-1} (8 inch min^{-1}) and the tilt angle of the tool, 2.5^0, was constant during FSP processing.	In the stir zone of the sample processed at 400 rpm rotational rate, the microhardness increase is mainly due to grain refinement, rather than precipitate strengthening, because the Al3Sc precipitates, with spherical lobed cuboids and platelet-like morphology, grow and coarsen to a 10–20 nm radius. The Scsupersaturation across the stir-processed zone has a concentration gradient, which is higher on the retreating side and lower on the advancing side of the friction-stir tool.
34.	Olivier Lorrain et al., [2010]	The workpiece material was 4mm thick aluminium alloy 7020-T6 rolled plates.	Two tools, made of high carbon steel, were used to produce the joints.The tools differ from their pin profile: the first tool has a straight cylindrical pin (SC) whereas the second tool has a tapered cylindrical pin (TC3F) with three flats. The two tools have unthreaded pin. Their shoulder was concave and they were tilted by 2.5◦ to provide compressive force to the stirred weld zone.	Rotational and feed speeds ranged, respectively, from 300 to 1620rpm and 100 to 900mm/min	FSW experiments were performed using two different pin profiles. Both pins are unthreaded but have or do not have flat faces. The primary goal is to analyse the flow when unthreaded pins are used to weld thin plates. Cross-sections and longitudinal sections of welds were observed with and without the use of material marker (MM) to investigate the material flow. Material flow with unthreaded pin was found to have the same features as material flow using classical threaded pins: material is deposited in the advancing side (AS) in the upper part of the weld and in the retreating side (RS) in the lower part of the weld; a rotating layer appears around the tool.
35.	Peng Dong et al., [2014]	The base material used in this study was a 3 mm-thick 6005AT6 aluminium alloy plate, with the nominal chemical composition of Al–0.46 Mg–0.63Si–0.17Cu–0.2Mn–0.24Fe wt.%.	The shoulder diameter and the pin length of the tool were 10 mm and 2.8 mm, respectively.	The selected FSW parameters were 1200 rpm, 300 mm/min and 0.1 mmfor rotation speed, welding speed and plunge depth, respectively.	Microstructure, microhardness and corrosion susceptibility of friction stir welded joint in an AlMgSiCu alloy were investigated. It was found that the joint exhibits different corrosion susceptibility among the microstructural zones.
36.	Q. Zhang et al., [2012]	The starting materials used in this study were Al powder (99.9% purity, 13 μm), Ti powder (99% purity, 45 μm) and Cu powders	A steel tool with a concave shoulder 20 mm in diameter and a threaded conical pin 8 mm in root diameter, 5.5 mm in tip diameter and 4 mm in length was used for FSP both in air and water.	The forged plates were subjected to 4-pass FSP with 100% overlapping in air at a rotation rate of 1000 rpm and a traverse speed of 25 mm min^{-1} (defined as FSP-air). Some FSP-air samples were subjected to additional 2-	The forged sample exhibited lower strength and ductility due to the presence of coarse Al3Ti clusters with a size range of 50–100 m and coarse matrix grains. Four-pass FSP in air resulted in the refinement and redistribution of the Al3Ti clusters, and the generation of micron matrix grains, thereby increasing the strength

		(99% purity, 75 µm)		pass FSP, with 100% overlap in flowing water at a rotation rate of 1000 rpm and a traverse speed of 200 mm min^{-1} (defined as FSP-water).	and ductility of the composites. Furthermore, coarse Al2Cu particles dissolved and re-precipitated due to a relatively long duration of thermal exposure.
37.	R.S. Mishra et al., [2003]	Commercial available SiC powder (99.5% purity and 0.7 mm average particle size) and 5083Al alloy (Al/Mg/ Mn) rolled plate were used in this study.	A tacking tool with a pin height of 1.0 mm was used.	A constant tool rotating rate of 300 rpm was adopted and traverse rate and depth of shoulder was varied. The tool spindle angle (angle between spindle and workpiece normal) of 2.58 was used,	A novel surface modifying technique, friction stir processing (FSP), has been developed for fabrication of surface composite. Al/SiC surface composites with different volume fractions of particles were successfully fabricated.
38.	R.S. Mishra et al., [2000]	7075-T651 (5.6Zn, 2.5mg, 1.6cu,0.23cr) 6.5mm	FSP Tool	Single pass 0.3 mm length. Weld processing parameters are proprietary, but it can be noted that the traverse speed was 15 cm/min.	Tensile strength, strain rate
39.	S. Janaa et al., [2010]	Cast AL alloy (6.8Si, 0.063Fe, 0.016Cu, 0.571mg, 0.178Ti)	Concave shoulder and conical pin with stepped spiral feature, SD-12mm, PL-2mm, PD-4mm	2236 rpm, 0.42, 0.98, 2.33 & 3.67 mm/s, tool rotation counter clock wise, ref fig-no of passes, 1-6 passes and overlapping	Process parameters on grain growth(abnormal grain growth)
40.	S. Jerome et al., [2012]	Friction Stir Processing was used for the development of surface composite of aluminium 5083 alloy reinforced with TiC particles.	Pin Ø 6 mm, pin length: 2 mm, left handed thread	These tests were performed for base metal, single pass and double pass FSP with TiC particles. The size of the samples used was 20mm x20 mm and the sand particle size was 80µm. The slurry concentration of 25% and 50% was prepared and erosion rates were performed at 500 and 900 r.p.m.	The aim of the present study is to develop defect free surface composite of Al 5083 alloy reinforced with TiC particles and investigate the particle distribution in the matrix, mechanical properties and wear behavior of the composites. Microstructural observations were carried out by using optical and scanning electron microscopy (SEM). The microstructural studies revealed that distribution of particles were more uniform in samples subjected to double pass than the single pass FSP. The microhardness profiles along top surface and across the cross section of the processed samples were evaluated.
41.	S. Soleymani et al.,[2012]	Commercially Al5083 rolled plates of 3 mm thickness with a nominal composition of 4.3Mg–0.68Mn–0.15Si–bal. Al (in wtpct) were used as the base material. A mixture of SiC and MoS2 powders at weight ratio of 2 to 1 were used as the reinforcement.	A tool made of H-13 steel with a shoulder of 20 mm diameter and a pin of 6 mm diagonal length and 2.8 mm height	A single pass friction stir process with rotation speed of 1250 rpm and travel speed of 50 mm/min was subjected in room temperature to all samples with a tilt angle of 3◦ was used to perform the FSP.	Microstructure, hardness and dry sliding wear behavior of the hybrid composite have been investigated and compared with those of base metal and Al/SiC and Al/MoS2 composites. Microstructural analyses of the hybrid composite showed a uniform distribution of reinforcing particles inside the processed zone and a good bonding between surface processed layer and base material.
42.	Sima Ahmad Alidokht	A 356 Al alloy with backing plate (Al, 7.18Si,	H-13, SD-20mm, PD-6mm, PL-3.7mm, threaded pin, pitch distance 1mm, ref fig	500-1250 rpm, 50mm/min, tilt angle 3o	Wear behavior SEM, disc material AISI D3 material

	et al., [2012]	0.4mg,0.Fe)			
43.	T. Dieguez et al., [2012]	7075-T651 Al alloy 4mm thickness	H13 tool steel, Concave shoulder 12.5mm, square side pin of 2.5mm	514rpm, 51mm/min	Tensile properties
44.	T.S. Mahmoudn and S.S.Mohamed, [2012]	A413 cast Al alloy ingot machined into 400mmx100mmx10mm thickness	H-13 SD-26mm, PD-10mm,Pl-9mm, R4 curved shape	900, 1120 and 1400 rpm, 20,40,63mm/min, 3 deg	Triboloigical, microstructure, mechanical , tensile specimen-fig in longitudinal and tranverse
45.	Telmo G. Santosa et al., [2014]	Butt joints were produced in cold rolled plates of AA6082-T6alloy with 4 mm thickness.	An FSW tool was developed in order to meet the following design criteria:- conduct the current without interfering with the machine electrical circuit;- confine the electric current to the layer below the probe, avoiding the current to flow through the tool main body and shoulder;- continuous adjustment of the probe length and facility of replacement;- guarantee the mechanical robustness of the tool body.	The overall system comprises the FSW machine, the electric current supply which consists of a 12 V battery with 720 A nominal current intensity and a data acquisition system.	This paper presents a variant of Friction Stir Welding (FSW) aiming to minimize or eliminate the rootdefects that still constitute a major constrain to a wider dissemination of FSW into industrial applications.The concept is based on the use of an external electrical energy source, delivering a high intensity current,passing through a thin layer of material between the back plate and the lower tip of the tool probe. Heatgenerated by Joule effect improves material viscoplasticity in this region, minimizing the root defects
46.	V. Balasubramanian, [2008]	Rolled plates of five different grades of aluminium alloys, namely, AA1050, AA6061, AA2024, AA7039 and AA7075 were used as the base materials in this investigation.	Threaded cylindrical pin profiled, non-consumable tool made of high carbon steel was used to fabricate the joints. Shoulder diameter 18mm, pin diameter 6mm, pin length 5.7mm, thread pitch 1mm,	An indigenously designed and developed machine (15 HP; 3000 rpm; 25 kN) was used to fabricate the joints.	an attempt has been made to establish relationship between the base material properties and FSW process parameters. FSW joints have been made using five different grades of aluminium alloys (AA1050, AA6061, AA2024, AA7039 and AA7075) using different combinations of process parameters. Macrostructural analysis has been done to check the weld quality (defective or defect free). Empirical relationships have been established between base metal properties and tool rotational speed and welding speed, respectively. The developed empirical relationships can be effectively used to predict the FSW process parameters to fabricate defect free welds.
47.	VahidFirouzdor and Sindo Kou, [2011]	6061 Al was welded to commercially pure Cu by FSW.	tools prepared from a H13 tool steel. The tool shoulder was 10 mm in diameter and concave. The pin was 4 mm in diameter and threaded, and the pin length was 1.6 mm. The tool was rotated counterclockwise when viewed from above and tilted 3 deg forward.	The travel speed varied from 38 mm/min (1.5 ipm) to 203 mm/min (8 ipm). The rotation speed was 1400 rpm.	Modified lap FSW significantly improved the weld quality in Al-to-Cu lap FSW.
48.	W. Woo et al.,[2012]	6061-T6 Al plate The nominal chemical composition was 1.0Mg, 0.6Si, 0.3Cu, and balanceAlwt%).	The hard steel tool has the diameter of the pin and the tool shoulder of 6.35 and 25.4 mm, respectively.	The Al plate sample continuously traverses at a constant traveling speed of 0.42 mm/s as the tool is rotating (156 revolutions/min). The measurement positions were predetermined at 5, 8 and 10 mm (underneath tool), and 15, 20, 30, 70	Significant neutron peak broadening was observed in situ underneath the tool of friction stir processing (FSP) in 6061-T6 aluminum alloy.

				and 100 mm (outside) from the tool center.	
49.	Wanchuck Woo et al., [2007]	AA6061-T6 solution heat treated and aged for 6 hrs at 185oc, 306x306x6.5mm, (1.0 mg, 0,6si, 0.3cu, bal al) ref fig for material size	H-13 Tool Steel SD-19.05mm, PD-6.35mm, PL-6.23mm. case 2. Without tool pin	1250 rpm, 4.7mm/s, 12.4 mpa compressed pr	Tool pin, shoulder, natural aging, micro
50.	Xiuli Feng, Huijie Liu and Sudarsanam Suresh Babu, [2011]	AA2219-T6 al-cu alloy plates fixed with tank filled with tank filled with water at 298k, 2.5mm thick	Pinless tool SD-22mm	1000 rpm, 200-400 mm/min plunge depth 0.5mm, angle 2.5o	Grain refinement, precipitation reactions
51.	Y. Tozaki et al., [2010]	The material used is aluminium alloy 6061-T4 plate with the thickness of 2mm whose chemical composition (wt.%) is Mg: 0.6, Si: 1, Cu: <0.01, Fe: <0.2, Mn: 0.05, Cr: <0.05, Zn: 0.3, Ti: <0.05, Al: bal.	It should be noted that the tool has no probe, but a scroll groove of 0.5mm depth on its shoulder surface, which is referred to as the scroll tool. For comparison with the scroll tool, two tools with different geometries were employed. One is a conventional probe tool with a standard metric M3 left-hand threaded probe whose length is 3.7mm, hereafter denoted as the probe tool. All tools have a concave shoulder of 10mm diameter with the angle of concavity of 11.5◦ and are made of high-speed steel	For the scroll tool and the plain tool, the tool rotational speeds of 2000 and 3000 rpm, the tool holding times of 1–7 s and the shoulder plunge depths of 0.5, 0.7 and 0.9mm were used. In all cases, the plunge rate was 10 mm/min. For the probe tool, the tool rotational speeds of 2000 and 3000rpm and the tool holding times of 0.2, 1, 2 and 3 s were employed, where the plunge rate and the shoulder plunge depth were 20mm/min and 0.2mm, respectively.	The experimental observations showed that the scroll tool had comparable or superior performance to a conventional probe tool. It was confirmed that sound welding could be achieved without a probe hole, in which the scroll groove played significant roles in the stirring of the material and the shoulder plunge depth was the important processing variable.
52.	Yong X. Gan et al., [2010]	The main focus of FSP was on aluminum based alloys and composites.	Review Paper		The objective of this article is to provide a review of friction stir processing (FSP) technology and its application for microstructure modification of particle reinforced composite materials.
53.	Z.Y. Ma et al., [2006]	A 356 T6 treatment, solution treated 540oC for 4 hr, 25oC water quenched and aged 155oC for 4h (Al, 7Si, 0.3mg,)	FSP Tool	Tool rotation rate (rpm) 300, 500, 700, 900 rpm	Friction stir processing (FSP)was applied to cast A356 Al to modify the as-cast microstructure. FSP homogenizes and refines the cast microstructure, completely eliminates porosity, and creates a microstructure with fine Si particles (0.25–0.42 _m) distributed in a fine grain aluminum matrix (3–4_m).

3. Summary

The effect of friction stir processed aluminium along with parameters such as tool rotational speed, processing speed, groove width and depth on microstructure and micro hardness investigated and explained by many researchers have been discussed. The strength of the friction stir processed material improved significantly and at the same time the ductility was also retained, the hardness also improved substantially. FSP was found to be beneficial in improving wear resistance. The high wear behavior in the stir zone is attributed to a lower coefficient of friction and the improved micro-hardness in this region.

References

[1] A. Bastiera, M. H. Maitournama, F. Rogerb, K. Dang Vana, Modelling of the residual state of friction stir welded plates,Journal of materials processing technology, 200, 2008, 25–37

[2] A. Orozco-Caballero, C. M. Cepeda-Jiménez, P. Hidalgo-Manrique, P. Rey, D. Gesto, D. Verdera, O.A. Ruano, F. Carreno, Lowering the temperature for high strain rate superplasticity in an AleMgeZneCu alloy via cooled friction stir processing,Materials Chemistry and Physics, 142, 2013, 182-185

[3] A. Yazdipoura, A. Shafiei M, K. Dehghani, Modeling the microstructural evolution and effect of cooling rate on the nanograins formed during the friction stir processing of Al5083,Materials Science and Engineering A, 527, 2009, 192–197

[4] A. G. Rao, B. R. K. Rao, V. P. Deshmukh, A. K. Shah, B. P. Kashyap, Microstructural refinement of a cast hypereutectic Al–30Si alloy by friction stir processing, Materials Letters, 63, 2009, 2628–2630

[5] Adem Kurt, Ilyas Uygur, ErenCete, Surface modification of aluminium by friction stir processing, Journal of Materials Processing Technology, 211, 2011, 313–317

[6] B. Zahmatkesh, M. H. Enayati, F. Karimzadeh, Tribological and microstructural evaluation of friction stir processed Al2024 alloy,Materials and Design , 31, 2010, 4891–4896

[7] Chung-Wei Yang, Yun-Han Chang, Truan-Sheng Lui, Li-Hui Chen, Effects of friction stir processing and artificial peak aging on erosion resistance of Al–11Si–4Cu–2Ni–0.7Mg cast alloy,Materials and Design, 40, 2012, 163–170

[8] D. Yadav, R. Bauri, Effect of friction stir processing on microstructure and mechanical properties of aluminium, Materials Science and Engineering A, 539, 2012, 85–92

[9] Douglas C. Hofmann, Kenneth S. Vecchio, Submerged friction stir processing (SFSP): An improved method for creating ultra-fine-grained bulk materials,Materials Science and Engineering A, 402, 2005, 234–241

[10] F. Y. Tsai, P. W. Kao, Improvement of mechanical properties of a cast Al–Si base alloy by friction stir processing, Materials Letters, 80, 2012, 40–42

[11] G. Madhusudhan Reddy, K. Srinivasa Rao, Enhancement of wear and corrosion resistance of cast A356 aluminium alloy using friction stir processing,Transactions of The Indian Institute of Metals, 63 (5), 2010, 793 - 798

[12] Ghader Faraji, Parviz Asadi, Characterization of AZ91/alumina nanocomposite produced by FSP,Materials Science and Engineering A, 528, 2011, 2431–2440

[13] H. J. Liu, X. L. Feng, Effect of post-processing heat treatment on microstructure and microhardness of water-submerged friction stir processed 2219-T6 aluminum alloy, Materials and Design, 2012

[14] H. W. Zhang, Z. Zhang, J. T. Chen, 3D modeling of material flow in friction stir welding under different process parameters, Journal of Materials Processing Technology, 183, 2007, 62–70

[15] I. Charit, R. S. Mishra, High strain rate super plasticity in a commercial 2024 Al alloy via friction stir processing,Materials and Engineering A, 359, 2003, 290-296

[16] K. Elangovan, V. Balasubramanian, Influences of tool pin profile and welding speed on the formation of friction stir processing zone in AA2219 aluminiumalloy, journal of materials processing technology, 200, 2008, 163–175

[17] K. Elangovan, V. Balasubramanian, Influences of tool pin profile and tool shoulder diameter on the formation of friction stir processing zone in AA6061 aluminiumalloy,Materials and Design, 29, 2008, 362–373

[18] K. Surekha, A. Els-Botes, Development of high strength, high conductivity copper by friction stir processing,Materials and Design, 32, 2011, 911–916

[19] K. Surekha, B. S. Murty, K. Prasad Rao, Microstructural characterization and corrosion behavior of multipass friction stir processed AA2219 aluminium alloy, Surface & Coatings Technology, 202, 2008, 4057–4068

[20] K. N. Ramesh, S. Pradeep, Vivek Pancholi, Multipass Friction-Stir Processing and its Effect on Mechanical Properties of Aluminum Alloy 5086, Metals & Materials Society and ASM International, 2012

[21] L. Karthikeyan, V. S. Senthilkumar, K. A. Padmanabhan, On the role of process variables in the friction stir processing of cast aluminum A319 alloy,Materials and Design, 31, 2010, 761–771

[22] L. Karthikeyan, V. S. Senthil Kumar, Relationship between process parameters and mechanical properties of friction stir processed AA6063-T6 aluminum alloy,Materials and Design, 32, 2011, 3085–3091

[23] L. Karthikeyan, V. S. Senthilkumar, V. Balasubramanian, S. Natarajan, Mechanical property and microstructural changes during friction stir processing of cast aluminum 2285 alloy, Materials and Design, 30, 2009, 2237–2242

[24] L. B. Johannes, R. S. Mishra, Multiple passes of friction stir processing for the creation of superplastic 7075 aluminum,Materials Science and Engineering A, 464, 2007, 255–260

[25] LivanFratini, Gianluca Buffa, Dina Palmeri, Using a neural network for predicting the average grain size in friction stir welding processes, Computers and Structures, 87, 2009, 1166–1174

[26] M. Chiumenti, M. Cervera, C. Agelet de Saracibar, N. Dialami, Numerical modeling of friction stir welding processes, Comput. Methods Appl. Mech. Engrg., 254, 2013, 353–369

[27] M. A. Garcı´a-Bernal, R.S. Mishra, R. Verma, D. Herna´ndez-Silva, High strain rate superplasticity in continuous cast Al–Mg alloys prepared via friction stir processing, Scripta Materialia, 60, 2009, 850–853

[28] M. A. García-Bernal, R. S. Mishra, R. Verma, D. Hernández-Silva, Hot deformation behavior of friction-stir processed strip-cast 5083 aluminum alloys with different Mncontents, Materials Science and Engineering A, 534, 2012, 186– 192

[29] M. L. Santella, T. Engstrom, D. Storjohann, T.-Y. Pan, Effects of friction stir processing on mechanical

properties of the cast aluminum alloys A319 and A356,Scripta Materialia, 53, 2005, 201–206
[30] M. P. Miles, M. W. Mahoney, C. B. Fuller, Prediction of Bending Limits in Friction-Stir-Processed Thick Plate Aluminum, Metallurgical and Materials Transactions A, 2005
[31] Magdy M. El-Rayesa, Ehab A. El-Danaf, The influence of multi-pass friction stir processing on the microstructural and mechanical properties of Aluminum Alloy 6082,Journal of Materials Processing Technology, 212, 2012, 1157–1168
[32] Mehdi Zohoor, M. K. Besharati Givi, P. Salami, Effect of processing parameters on fabrication of Al–Mg/Cu composites via friction stir processing, Materials and Design, 39, 2012, 358–365
[33] Nhon Q. Vo, David C. Dunand, David N. Seidman, Atom probe tomographic study of a friction-stir-processed Al–Mg–Scalloy, ActaMaterialia, 60, 2012, 7078–7089
[34] Olivier Lorrain, Véronique Favier, Hamid Zahrouni, Didier Lawrjaniec, Understanding the material flow path of friction stir welding process using unthreaded tools,Journal of Materials Processing Technology, 210, 2010, 603–609
[35] Peng Dong, Daqian Sun, Bing Wang, Yueying Zhang, Hongmei Li, Microstructure, microhardness and corrosion susceptibility of friction stir welded AlMgSiCualloy, Materials and Design, 54, 2014, 760–765
[36] Q. Zhang, B.L. Xiao, P. Xue, Z.Y. Ma, Microstructural evolution and mechanical properties of ultrafine grained Al3Ti/Al–5.5Cu composites produced via hot pressing and subsequent friction stir processing, Materials Chemistry and Physics, 134, 2012, 294– 301
[37] R. S. Mishra , Z.Y. Ma, I. Charit, Friction stir processing: a novel technique for fabrication of surface composite, Materials Science and Engineering A, 341, 2003, 307-310
[38] R. S. Mishra, M. W. Mahoney, S.X. McFadden, N.A. Mara, A. K. Mukherjee, High Strain Rate Superplasticity in A Friction Stir Processed 7075 Al Alloy,Scripta mater, 42, 2000, 163–168
[39] S. Janaa, R.S. Mishra, J.A. Baumann, G. Grant, Effect of process parameters on abnormal grain growth during friction stir processing of a cast Al alloy, Materials Science and Engineering A, 528, 189–199
[40] S. Jerome, S. Govind Bhalchandra, S.P. Kumaresh Babu, B. Ravisankar, Influence of Microstructure and Experimental Parameters on Mechanical and Wear Properties of Al-TiC Surface Composite by FSP Route, Journal of Minerals & Materials Characterization & Engineering, 11(5), 2012, 493-507
[41] S. Soleymani, A. Abdollah-zadeh, S.A. Alidokht, Microstructural and tribological properties of Al5083 based surface hybrid composite produced by friction stir processing, Wear, 278– 279, 2012, 41– 47
[42] Sima Ahmad Alidokht, Amir Abdollah-zadeh, SoheilSoleymani, TohidSaeid, Hamid Assadi, Evaluation of microstructure and wear behavior of friction stir processed cast aluminum alloy,Materials Characterization, 63, 2012, 90–9 7
[43] T. Dieguez, A. Burgueno, H. Svobod, Superplasticity of a Friction Stir Processed 7075-T651 aluminum alloy, Procedia Materials Science, 1, 2012, 110 – 117
[44] T. S. Mahmoudn, S. S. Mohamed, Improvement of microstructural, mechanical and tribological characteristics of A413 cast Al alloys using friction stir processing, Materials Science & Engineering A, 558, 2012, 502–509
[45] Telmo G. Santosa, R. M. Miranda, Pedro Vilac¸, Friction Stir Welding assisted by electrical Joule effect, Journal of Materials Processing Technology, 2014
[46] V. Balasubramanian, Relationship between base metal properties and friction stir welding process parameters, Materials Science and Engineering A, 480, 2008, 397–403
[47] Vahid Firouzdor, Sindo Kou, Al-to-Cu Friction Stir Lap Welding,The Minerals, Metals & Materials Society and ASM International, 2011
[48] W. Woo, Z. Feng, X.-L.Wang, K.An, B.Clausen, T. A. Sisneros, J. S. Jeong, In situ neutron diffraction analysis of grain structure during friction stir processing of an aluminum alloy, Materials Letters, 85, 2012, 29–32
[49] Wanchuck Woo, Hahn Choo, Donald W. Brown, and Zhili Feng, Influence of the Tool Pin and Shoulder on Microstructure and Natural Aging Kinetics in a Friction-Stir-Processed 6061–T6 Aluminum Alloy, The Minerals, Metals & Materials Society and ASM International, 2007
[50] Xiuli Feng, Huijie Liu, Sudarsanam Suresh Babu, Effect of grain size refinement and precipitation reactions on strengthening in friction stir processed Al–Cu alloys, Scripta Materialia, 2011
[51] Y. Tozaki, Y. Uematsu, K. Tokaji, A newly developed tool without probe for friction stir spot welding and its performance, Journal of Materials Processing Technology, 210, 2010, 844–851
[52] Yong X. Gan, Daniel Solomon, Michael Reinbolt, [2010] Friction Stir Processing of Particle Reinforced Composite Materials, Materials, 3, 2010, 329-350
[53] Z. Y. Ma, S. R. Sharma, R. S. Mishra, Effect of friction stir processing on the microstructure of cast A356 aluminum, Materials Science and Engineering A, 433, 2006, 269–278

Fish Physiol Biochem
DOI 10.1007/s10695-015-0168-0

Oxygen stress: impact on innate immune system, antioxidant defence system and expression of HIF-1α and ATPase 6 genes in *Catla catla*

Samar Pal Singh · JaiGopal Sharma · Tauqueer Ahmad · Rina Chakrabarti

Received: 12 December 2014 / Accepted: 13 November 2015
© Springer Science+Business Media Dordrecht 2015

Abstract *Catla catla* catla (2.28 ± 0.1 g) were exposed to six different levels of dissolved oxygen: 1 (DO-1), 3 (DO-3), 5 (DO-5), 7 (DO-7), 9 (DO-9) and 11 (DO-11) mg/L. DO-5 served as control. In DO-1 and DO-3, the number of red blood cells (RBC), lysozyme, respiratory burst activity and nitric oxide synthase were significantly ($p < 0.05$) lower compared to the control one. In DO-7 and DO-9, RBC and lysozyme were significantly ($p < 0.05$) higher compared to the control one. Thiobarbituric acid reactive substances was significantly ($p < 0.05$) higher in catla exposed at low (1 and 3 mg/L) and high (9 and 11 mg/L) dissolved oxygen compared to others. In muscles and hepatopancreas, reduced glutathione was significantly ($p < 0.05$) higher in DO-5 and DO-7 and in gills of DO-5 compared to others after 1 h. In muscles, glutathione *S*-transferase (GST) was significantly ($p < 0.05$) lower in DO-5 and DO-7 compared to others. In hepatopancreas, GST and glutathione peroxidise (GPx) were significantly ($p < 0.05$) higher in DO-1 and DO-3 compared to others. In gills, GPx was higher in DO-9 and DO-11 after 48 h. In brain, hypoxia-inducible factor (HIF)-1α mRNA level was induced in DO-1 and DO-3 compared to others after 1 h of exposure. In gills and hepatopancreas, HIF-1α mRNA level was significantly ($p < 0.05$) higher in DO-1 compared to others after 1 h. The ATPase 6 mRNA level was significantly ($p < 0.05$) higher in brain and hepatopancreas of DO-1 after 1 h and in gills and hepatopancreas of DO-3 and DO-9, respectively, after 48 h compared to others.

Keywords *Catla catla* · Lysozyme · Nitric oxide synthase · Antioxidant enzymes · Hypoxia-inducible factor (HIF)-1α · ATPase 6

S. P. Singh · T. Ahmad · R. Chakrabarti (✉)
Aqua Research Lab, Department of Zoology, University of Delhi, Delhi 110007, India
e-mail: aquaresearchlab@yahoo.co.in

J. Sharma
Department of Biotechnology, Delhi Technological University, Delhi 110042, India

Introduction

The availability of ambient dissolved oxygen has been considered as one of the most important parameters for survival and growth of aquatic organisms. In the aquatic environment, dissolved oxygen level varies considerably because of the photoperiod and respiration cycles. Fish may be exposed to transient hyperoxia in their natural habitats during the daylight hours of summer as a result of the production of oxygen by algae under intensive solar irradiation (Halliwell and Gutteridge 1989). Hyperoxic condition is also encountered during transportation of live fish under an oxygen atmosphere. The diel-cycling hypoxia often found in high biomass aquatic ecosystems during the dark

cycle when the oxygen consumption rate of organisms exceeds oxygen production (D'Avanzo and Kremer 1994; Graham 1990). This phenomenon is particularly obvious during the summer months in shallow water bodies (Grecay and Stierhoff 2002; Stierhoff et al. 2003). Moreover, global climate change especially rise in summer water temperature possesses threat to the aquatic organisms that leads to decrease in dissolved oxygen level in the aquatic system. Environmental hypoxia may have negative effect on fish, even leading to death (Secor and Gunderson 1998). Within a physiological temperature range, oxygen consumption of fish increases more than twofold with every 10 °C increase in temperature (Hochachka and Somero 2002). The recommended minimum dissolved oxygen requirements for cold water, tropical freshwater and tropical marine fishes are 6, 5 and 5 mg/L, respectively (Mallya 2007). Most fish species will tolerate a drop below these minimum values for a short period of time, probably the cold water species are likely to tolerate a lower level than tropical fish.

Many studies show that transitions between hypoxia/anoxia and normoxia and/or between normoxia and hyperoxia may result in oxidative stress (Hermes-Lima 2004; Sies 1991; Storey 1996). Oxidative stress is a situation when steady-state reactive oxygen species (ROS) concentration is transiently or chronically enhanced, disturbing cellular metabolism and its regulation and damaging cellular constituents (Janssens et al. 2000; Lushchak 2011). It directly influences physiology, welfare and behaviour of the organisms. The deleterious effects of free radicals may be controlled by specific antioxidant systems. Many freshwater animals appear to be well-adapted to deal with such periodic fluctuations in oxygen levels. Some species maintain high antioxidant defences at all times, whereas others use an anticipatory strategy. In this process, the organism enhances antioxidant capacity during the hypoxic/anoxic state in order to prepare for oxidative stress that will occur when oxygen levels rise again (Hermes-Lima and Zenteno-Savin 2002; Lushchak et al. 2001). This latter phenomenon has been found in goldfish *Carassius auratus* (Lushchak et al. 2001) and in common carp *Cyprinus carpio* (Vig and Nemcsok 1989). Hypoxia induces primary, secondary and tertiary stress responses in fish. Kvamme et al. (2013) studied the effect of hypoxia on innate immune responses in Atlantic salmon (*Salmo salar*). But the appearance of immune parameters and defensive competence varies greatly from species to species (Schrøder et al. 1998).

Hypoxia also induced the expression of genes. Gene expression analyses in gonads of mature zebrafish (*Danio rerio*) maintained under normoxia (3 mg/L) and hypoxia (1 mg/L) following short-term (4 days) and long-term (14 days) exposures showed differential expression of genes associated with initial adaptive response and a suite of genes belonging to different ontology categories related with lipid metabolism, steroid synthesis and immune response which could lead to reproductive impairment (Martinovic et al. 2009). Zebrafish embryos were able to survive in absence of oxygen and their embryonic development ceased and the embryos entered a state of suspended animation (Padilla and Roth 2001). However, the molecular basis of the zebrafish response to hypoxic stress has not been clarified. The over expressions of CYP 1A (cytochrome P450 gene family 1) were found in liver of Amur sturgeon *Acipenser schrenckii* in hypoxia stress (Ni et al. 2014). Understanding how hypoxia alters gene expression will likely contribute to our knowledge of how vertebrates in general respond to hypoxia and will illustrate the dynamic interactions between genes and environment.

India is the second largest inland fish producing country in the world. Aquaculture has been playing significant role in the economy of the country. Carps contributed around 82 % of the aquaculture production. In pond culture, low dissolved oxygen availability resulted in respiratory stress of carps leading to poor growth. Carp gulping for air at the surface is found particularly in the early morning is a sign of oxygen deficiency in the culture pond. Mass mortality may occur due to prolonged oxygen deficiency of water (ICAR 2013). Being a tropical country, climate change will influence the aquaculture production in India. There is a wide scientific consensus that changes in the composition of the atmosphere will lead to significant changes in global climate (IPCC 2007; Brander 2010). The most important changes caused by climate change are the shortening of winter period and a rise in summer water temperatures (Magnuson et al. 1979; Huttula et al. 1992). This will influence the dissolved oxygen level of aquatic environment.

Catla catla is an economically important, surface dwelling carp species and extensively used in composite culture. The aim of the present investigation was to study the effect of both hypoxia and hyperoxia on the immune system, lipid peroxidation and enzymatic and non-enzymatic antioxidant systems of catla exposed to various concentrations of dissolved oxygen. The mRNA level of hypoxia-inducible factor (HIF)-1α and mitochondrial (MT) ATPase genes were also quantified. Serum lysozyme is a cationic enzyme that attacks the β-1, 4 glycosidic bond between *N*-acetylmuramic acid and *N*-acetylglucosamine in the peptidoglycan of bacterial cell walls. This enables lysozyme to lyse certain gram-positive bacteria and gram-negative bacteria (Alexander and Ingram 1992). Reduced glutathione (GSH) is low molecular mass tripeptide (Glu-Cys-Gly) described as non-enzymatic antioxidant. They are usually known as free radical scavengers (Pamplona and Costantini 2011). High molecular mass antioxidant group consists of enzymatic antioxidants like superoxide dismutases (SOD), catalases, Se-dependent glutathione peroxidases (GPx) and glutathione *S*-transferase (GST).

One of the pivotal mediators of the cellular response to hypoxia is hypoxia-inducible factor (HIF), a transcription factor (Benita et al. 2009). HIF-1α is a master regulator of hypoxia-induced gene responses that allows rapid adaptation to oxygen availability. This effect is mediated through key regulators of bioenergetics and growth. The mitochondrial (MT) ATP 6 gene provides information for making a protein that is essential for normal mitochondrial function. The MT-ATP 6 protein forms one part of a large enzyme called ATP synthase (F_0F_1-ATPase). This enzyme is responsible for the final step of oxidative phosphorylation. Specifically, one segment of ATP synthase allows positively charged particles, called protons, to flow across a specialized membrane inside mitochondria. Another segment of the enzyme uses the energy created by this proton flow to convert a molecule called adenosine diphosphate (ADP) to ATP. Present investigation is the first study with this freshwater carp challenged with various dissolved oxygen levels. The information related to the physiological responses to hypoxia and hyperoxia induced stresses is most essential for the assessment of the health status of the cultivable organisms. This will help in the development of proper husbandry for this economically important species.

Materials and methods

Fish maintenance

Catla catla catla (2.28 ± 0.12 g) were collected from local fish farm and transported to the wet laboratory facility. Fish were randomly distributed in eighteen aquaria (50 L each). Each aquarium was connected with one filtration unit (Sera fil bioactive 130, Germany). This helped to maintain the water quality in the aquarium. Each aquarium was covered with transparent fibreglass sheet having two holes at two ends for the connection of filtration unit and gas pipes. These pipes were fitted tightly. This arrangement helped to maintain the desirable dissolved oxygen level in the aquarium. Prior to the start of the experiment, fish were acclimated to experimental conditions under 12:12 h light/dark photoperiod for 21 days. Water temperature was maintained at 25 ± 0.50 °C, and the dissolved oxygen was kept at 5 ± 0.15 mg/L. During the acclimation and experimental period, pelleted feed (containing 40 % of crude protein) was provided two times (9.00 a.m. and 5.00 p.m.) daily at a feeding rate of 5 % of body weight per day.

Experimental design

Fish were exposed to six different levels of dissolved oxygen: 1 (DO-1), 3 (DO-3), 5 (DO-5), 7 (DO-7), 9 (DO-9) and 11 (DO-11) mg/L. Each level had three replicates. The oxygen tension in DO-1 and DO-3 treatments was regulated through the pumping of nitrogen (Laser Gases, India), whereas in DO-9 and DO-11 through the pumping of oxygen gas (Laser Gases, India). The bubbling rate of gas was adjusted by mechanical controller to keep the dissolved oxygen concentration stable. The dissolved oxygen levels of 5 and 7 mg/L treatments were maintained using continuous aeration (Rocker 320 aerator, Taiwan). The exact time of reaching desirable dissolved oxygen concentration in each aquarium was recorded. It required 45 min to 3 h to reach the desirable oxygen concentration of water from the acclimation dissolved oxygen condition (5 mg/L). Water temperature was continuously monitored in individual aquarium. pH, and oxygen concentrations were measured using digital oximeter (HACH 40 D, USA). Dissolved oxygen concentration in each aquarium was measured thrice

daily during the exposure of fish, and variations between the desirable and actual dissolved oxygen concentrations for individual aquarium were recorded (Table 1). During the experimental period, the water temperature of experimental aquarium was 25 ± 0.50 °C and pH ranged from 7.85 to 8.02.

Blood and tissue sampling

Blood and tissue samples were collected from individual fish exactly after 1 and 48 h of reaching the desirable dissolved oxygen level. Fish were anesthetized with MS 222 (Sigma, USA) and weighed. Blood samples were taken gently from the caudal vein by 1-mL plastic syringe (Hindustan Syringes and Medical Devices Ltd., India) within 1 min and the whole process of blood sampling required <2 min for individual fish after netting. Two different aliquots of blood were used for different analyses. The first aliquot was transferred to a plastic tube coated with ethylene diamine tetraacetate (EDTA) as anticoagulant and was used for respiratory burst activity estimation. A second aliquot was transferred to a plastic tube without EDTA, clot at 4 °C, centrifuged at 1500×*g* for 10 min and collected serum was stored at −20 °C for analyses.

Tissues–muscles, gills and hepatopancreas were immediately frozen with liquid nitrogen and stored at −80 °C for further assays. For the study of nitric oxide synthase, antioxidant system (reduced glutathione) and antioxidant enzymes (glutathione *S*-transferase and glutathione peroxidise), one gram of tissue (10 %) was homogenized in chilled 10 ml phosphate buffer (0.1 M, pH 7.4) using glass/Teflon tissue grinder. The homogenate was centrifuged at 10,500×*g* for 20 min; the supernatant was used for assay. All assays were carried out using Microplate Reader (BioTek, Synergy HT, NY, USA). For gene expression study, brain, gills and hepatopancreas were collected aseptically after 1 and 48 h of reaching the desirable dissolved oxygen level and immediately stored in RNAlater (Sigma-Aldrich, USA) at −20 °C for extraction of total RNA. For all parameters, three replicates were used.

Table 1 Expected and recorded dissolved oxygen levels (±SE) in each treatment during experiment

Treatment	Expected DO (mg/L)	Recorded DO (mg/L)
DO-1	1	0.93 ± 0.02
DO-3	3	2.85 ± 0.02
DO-5	5	5.15 ± 0.08
DO-7	7	7.39 ± 0.03
DO-9	9	8.81 ± 0.03
DO-11	11	11.23 ± 0.02

DO-1, 1 mg/L dissolved oxygen; DO-3, 3 mg/L dissolved oxygen; DO-5, 5 mg/L dissolved oxygen; DO-7, 7 mg/L dissolved oxygen; DO-9, 9 mg/L dissolved oxygen; DO-11, 11 mg/L dissolved oxygen

Abundance of red blood cells

Total erythrocyte counting was performed using an improved Neubauer-ruled hemocytometer (Tripathi et al. 2004). Briefly, blood sample was diluted (1:200) in Hayems's fluid. Then the fluid was allowed to stand in the pipette for 8–10 min before charging into the Neubauer's chamber. Total numbers of red blood cells (RBC) were counted in five secondary square of the centre primary square.

$$\text{RBC}/\mu\text{L} = n \times 10,000$$

where, n = number of RBCs observed in the secondary squares, 10,000 = (200, dilution factor and 50 = volume of fluid in RBC's secondary squares).

Cells were observed in both chambers of the hemocytometer (×40 objective in compound microscope, Carl Ziess, Germany), and the number was averaged to produce the raw RBC count to reduce analytical variation.

Lysozyme

For lysozyme assay, bacteria *Micrococcus lysodeikticus* (MTCC No *106) was cultured in *Staphylococcus* broth (Himedia, Mumbai, India) containing 1 % D-glucose. After 24 h of incubation, the culture was centrifuged and the bacterial pellet was lyophilized. Lysozyme was determined by incubating 10 µL of serum with 1 mL of *Micrococcus lysodeikticus* (20 mg/100 mL) suspended in acetate buffer (0.02 M, pH 5.5) for 60 min at room temperature. The initial absorbance was recorded immediately after addition of sample at 450 nm. The final absorbance was recorded after 60 min of incubation. The standard curve was prepared using hen egg lysozyme (1 mg/mL).

Respiratory burst activity

The fresh blood with EDTA powder was processed for measurement of nitroblue tetrazolium (NBT) within 1 h of collection following the method of Anderson and Siwicki (1995). Reactive oxygen radical production by neutrophils during respiratory burst activity was assayed by the reduction of nitroblue tetrazolium to formazan. Briefly, the blood was mixed with equal volume of 0.2 % NBT (Himedia) and incubated at 25 °C for 30 min. In 25 µL of this mixture, 500 µL of dimethyl formamide (Merck, India) was added to solubilize the reduced formazan product. Then it was centrifuged at 2000×*g* for 5 min and the supernatant was taken. The extent of NBT reduced was measured at 540 nm. Dimethyl formamide was used as the blank.

Nitric oxide synthase

Inducible nitric oxide synthase (iNOS) level of muscles was measured using the method of Lee et al. (2003). The supernatant (100 µL) was mixed with equal volume of Griess reagent (1 % sulphanilamide and 0.1 % naphthylethylenediamine in 5 % phosphoric acid) and incubated at room temperature for 10 min. The absorbance was recorded at 540 nm. The nitrite concentration was determined from the nitrite standard curve and expressed as mmol/mg tissue.

Thiobarbituric acid reactive substances

Thiobarbituric acid reactive substances (TBARS) were measured following the method of Ohkawa et al. (1979). In this process, the end product of lipid peroxidation, the MDA reacts with thiobarbituric acid (TBA). One gram of muscles was homogenized in 9 ml of KCl (1.15 %), and the sample was incubated in 0.6 % TBA (pH 3.5) containing SDS (0.45 %) for 1 h at 100 °C. After cooling, the sample was centrifuged at 825×*g* for 15 min and the absorbance of the supernatant was measured at 532 nm. The standard curve was prepared using 1, 1, 3, 3-tetramethoxy propane, and the result was expressed as µmol MDA/mg protein.

Reduced glutathione

Reduced glutathione (GSH) for muscles, hepatopancreas and gills was determined using the method of Jollow et al. (1974). The collected supernatant was precipitated with 4 % sulfosalicylic acid (Himedia) in 1:1 ratio. The samples were kept at 4 °C for 1 h and then centrifuged at 1500×*g* for 15 min at 4 °C. This supernatant was used for GSH assay. The assay mixture (200 µL) consisted of supernatant, 0.1 M phosphate buffer (pH 7.4) and 5-5-dithiobis-2-nitrobenzoic acid (DTNB, Himedia). Optical density was measured at 412 nm and expressed as nmol GSH/g tissue.

Glutathione *S*-transferase

Glutathione *S*-transferase (GST) activity of muscles and hepatopancreas was measured (Habig et al. 1974). The reaction mixture consisted of 0.1 M phosphate buffer (pH 7.4), 0.60 mM 1-chloro-2-dinitrobenzene (CDNM, Sigma, USA) and 10 mM reduced glutathione (GSH, Himedia). Absorbance was monitored at 340 nm kinetic mode at 25 °C. Activity was expressed as nmol of CDNB/mg protein/min. The molar extinction coefficient is 9.6 × 10^3/M cm.

Glutathione peroxidase

Glutathione peroxidase (GPx) activity of gills and hepatopancreas was measured following the method of Mohandas et al. (1984). The assay mixture consisted of 0.05 M phosphate buffer (pH 7.4), 1 mM (EDTA, Himedia), 1 mM sodium azide (Himedia), 1 U/mL glutathione reductase (Sigma, USA), 1 mM reduced glutathione (GSH, Sigma), 0.2 mM nicotinamide adenine dinucleotide (NADPH, Sigma) and 0.25 mM hydrogen peroxide (H_2O_2, Sigma). The decrease in absorbance was recorded at 340 nm. Activity was expressed as nmol of NADPH/mg protein/min. The molar extinction coefficient is 6.22 × 10^3 M cm.

Gene expression study

RNA isolation and first-strand cDNA synthesis

Total cellular RNA from different tissues of fish (brain, gills and hepatopancreas) was extracted with TRIzol reagent (Invitrogen, USA). RNA concentration was measured with Nanodrop ND-1000 spectrophotometer (Thermo Scientific, USA), and the integrity was assessed by observing the band intensity of RNA on 1 % agarose gel. For the first-strand cDNA synthesis, 1 µg of total RNA was treated with 1 U of

DNase I (Sigma-Aldrich, USA), and reverse transcription was carried out using ProtoScript M-MuLV first-strand cDNA synthesis kit (New England Biolabs, USA). The constitutively expressed housekeeping gene, β-actin, was used both as a positive control and for sample normalization.

Real-time PCR analysis

Quantitative real-time PCR was performed in MicroAmp® Fast Optical 96-well reaction plates with optical adhesive cover in the ViiA-7TM real-time PCR system (Applied Biosystems, USA). Primers for HIF-1α, ATPase 6 and β-actin were designed using Primer 3 software (Table 2). In real-time PCR, amplifications were carried out, in 10 μL reaction volume containing 1 μL of cDNA, 0.25 μL of FW and RV primers (2.5 μM each), 5 μL of 2X Power SYBR® Green PCR Master Mix and 3.5 μL of PCR-grade H_2O. The PCR amplification was performed under the following conditions: 50 °C for 2 min, initial denaturation at 95 °C for 10 min, followed by 45 cycles of 95 °C/15 s, 55 °C/1 min. The reaction carried out without cDNA was used as a negative control. The PCR efficiencies were determined by analysis of serial dilutions of cDNA, and efficiencies were close to 100 % allowing the use of the $2^{-\Delta\Delta CT}$ method for calculation of relative gene expression (Livak and Schmittgen 2001). Specificity of the amplification reaction was analysed using dissociation curves with a temperature range from 60 to 95 °C. The correct size and single-band amplification were confirmed by running the real-time PCR products (8 μL) in agarose gels (1 %) using ethidium bromide.

Statistical analysis

All data were presented as mean ± standard error. Data were analysed using one-way analysis of variance, ANOVA (SPSS 13.0) and Duncan's multiple range (DMR) test (Montgomery 1984). The significance level was accepted at $p < 0.05$.

Results

Catla were acclimated at 5 ± 0.05 mg/L dissolved oxygen and then exposed to both low (1 and 3 mg/L) and high (7, 9 and 11 mg/L) levels of dissolved oxygen. Therefore, 5 ± 0.05 mg/L dissolved oxygen treatment was considered as the normal/control (acclimation) condition. Response of catla to low and high levels of dissolved oxygen was compared with this control one. There was no mortality of fish during experimental period.

Abundance of red blood cells

The number of red blood cells (RBC) decreased in catla exposed at 1 and 3 mg/L dissolved oxygen compared to the control 5 mg/L treatment (Fig. 1) after 1 h of exposure. The number of RBC increased 1.5–1.75-fold in 7–11 mg/L dissolved oxygen treatments compared to the control one after 1 h of exposure. The abundance of RBC reduced significantly in 7, 9 and 11 mg/L dissolved oxygen treatments after 48 h of exposure compared to 1 h exposed fish in respective treatment. There was no significant difference in RBC number in 1, 3 and 5 mg/L treatments after 48 h compared to the 1 h exposed fish in respective treatment.

Lysozyme

Serum lysozyme level reduced significantly after 1 h of exposure of catla in 1 and 3 mg/L dissolved oxygen treatments compared to the control condition (DO-5). The lysozyme activity was 3.50 ± 0.06 mg/mL in

Table 2 Primer sequences used for real-time PCR analysis

Target gene	Primer name	Primer sequence (5′–3′)	Accession number
HIF-1α	HIF 1α Fw	GGAAAGGAGTCTGAGGTATTCT	EF222026.1
	HIF 1α Rv	ACTCTCCAGTTCGTTCTCCTTG	
ATPase 6	ATPase 6 Fw	CCAATTCGCAAGCCCATCAT	JN859669.1
	ATPase 6 Rv	AGGGGGGAGTAGCAGTTGGT	
β-actin	β-actin Fw	AGACCACCTTCAACTCCATCATG	JQ991014.1
	β-actin Rv	CCGATCCAGACAGAGTATTTACG	

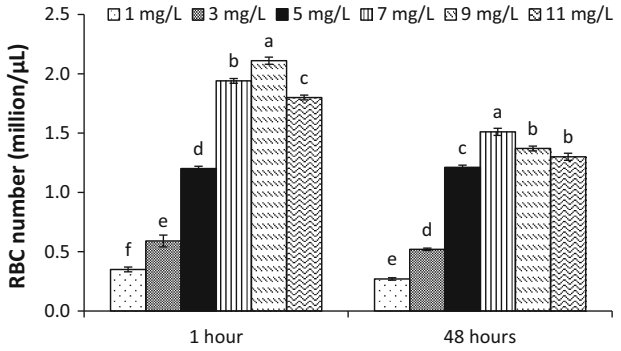


Fig. 1 Abundance of red blood cells in *Catla catla* exposed to various levels of dissolved oxygen. *Vertical bars with different superscripts* are significantly ($p < 0.05$) different ($n = 3$)

control fish at this period. The activity was significantly higher in catla exposed at high levels (7–9 mg/L) of dissolved oxygen compared to the control one. Lysozyme activity increased significantly in all treatments (except DO-5) after 48 h exposure compared to the 1 h exposed fish in the respective treatment (Fig. 2). Significantly lower activity was also found in DO-1 and DO-3 treatments compared to others after 48 h exposure.

Respiratory burst activity

The respiratory burst activity was significantly lower in 1 and 3 mg/L treatments compared to the control catla (DO-5) after 1 h of exposure. The activity increased in fish exposed at high levels of dissolved oxygen compared to the control one. The activity was significantly higher in DO-9 and DO-11 compared to the other treatments in both samples (Fig. 3). Respiratory burst activity reduced 6.8–32.0 % in 48 h exposed fish in 1, 3, 9 and 11 mg/L dissolved oxygen treatments compared to the 1 h exposed fish in the same treatment. The activity was 3.5 % higher in both 5 and 7 mg/L treatments after 48 h of exposure compared to the 1 h exposed fish in the same treatment.

Nitric oxide synthase

This was interesting to observe that nitric oxide synthase (iNOS) level was significantly higher in DO-11 treatment compared to others after 1 and 48 h of exposures. A direct relationship was found between the dissolved oxygen level of water and nitric oxide synthase level in both samples (Fig. 4). Nitric oxide synthase levels in all treatments were significantly higher after 48 h exposure compared to the 1 h exposed fish in the respective treatment.

Thiobarbituric acid reactive substances

Thiobarbituric acid reactive substances (TBARS) level is an indicator of lipid peroxidation of tissues. Significantly lower TBARS was found in DO-5 and DO-7 treatments compared to others. Exposure of catla to low (1 and 3 mg/L) and high (9 and 11 mg/L) levels of dissolved oxygen resulted into higher level of TBARS in the muscles of catla (Fig. 5). TBARS level increased significantly in all 48 h exposed fish regardless of treatments (except DO-5 and DO-7) compared to 1 h exposed fish in respective treatment.

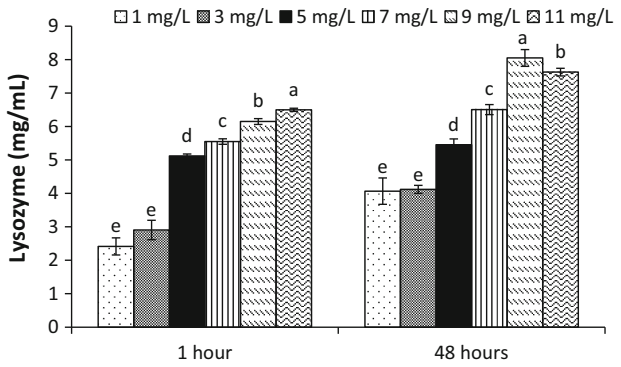


Fig. 2 Serum lysozyme levels of *Catla catla* exposed to various levels of dissolved oxygen. *Vertical bars with different superscripts* are significantly ($p < 0.05$) different ($n = 3$)

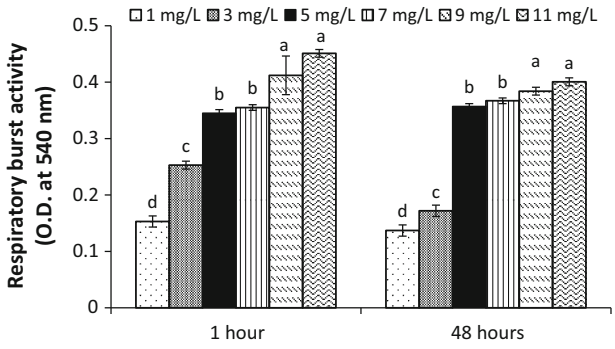


Fig. 3 Respiratory burst activity found in *Catla catla* exposed to various levels of dissolved oxygen. *Vertical bars with different superscripts* are significantly ($p < 0.05$) different ($n = 3$)

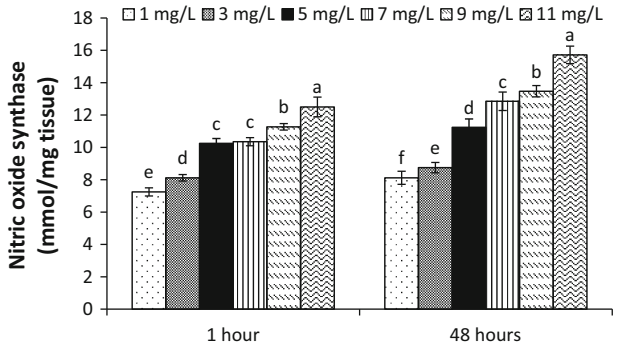


Fig. 4 Nitric oxide synthase levels found in *Catla catla* exposed to various levels of dissolved oxygen. *Vertical bars with different superscripts* are significantly ($p < 0.05$) different ($n = 3$)

Reduced glutathione

Reduced glutathione (GSH) was assayed in muscles, hepatopancreas and gills (Fig. 6a–c). In muscles of catla, reduced glutathione level was significantly higher in DO-5 and DO-7 treatments compared to others after 1 h of exposure. Similar trend was found after 48 h of exposure, except in DO-7. The level was significantly lower in this treatment compared to DO-5. In muscles, GSH level reduced significantly in fish exposed at 7–9 mg/L dissolved oxygen after 48 h compared to the 1 h exposed fish in the respective treatment. Like muscles, GSH level was significantly higher in hepatopancreas of catla exposed at 5 and 7 mg/L of dissolved oxygen compared to the other treatments after 1 h exposure. The level was significantly lower after 48 h of exposure compared to 1 h in all treatments, except DO-5. In gills, GSH level was significantly higher in DO-5 compared to others in both samples. In gills, GSH level reduced after 48 h exposure compared to the 1 h exposed fish regardless of treatment.

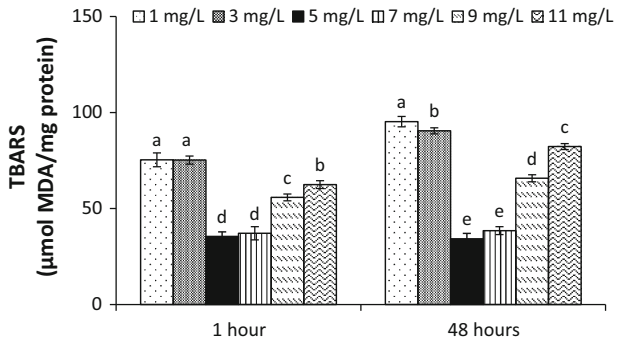


Fig. 5 Effect of various levels of dissolved oxygen on the thiobarbituric acid reactive substances (TBARS) of *Catla catla* after 1 and 48 h of exposure. *Vertical bars with different superscripts* are significantly ($p < 0.05$) different ($n = 3$)

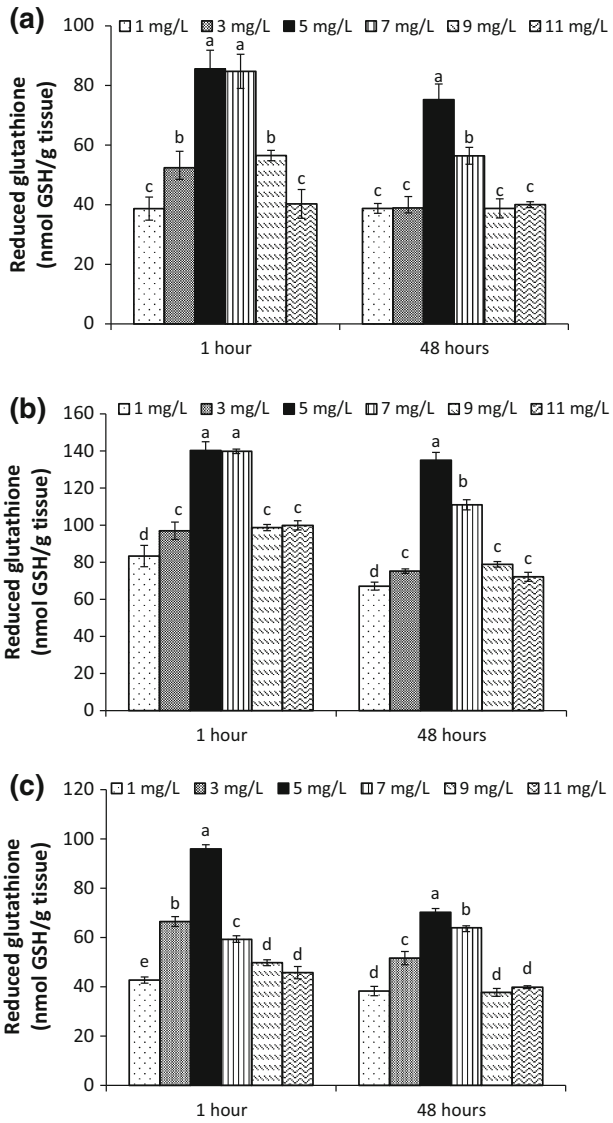


Fig. 6 Effect of various levels of dissolved oxygen on reduced glutathione levels of **a** muscles, **b** hepatopancreas and **c** gills of *Catla catla* after 1 and 48 h of exposure. *Vertical bars with different superscripts* are significantly ($p < 0.05$) different ($n = 3$)

Glutathione *S*-transferase

Glutathione *S*-transferase (GST) level in muscles of catla (Fig. 7a) was significantly lower in DO-5 and DO-7 compared to other treatments after 1 h of exposure. There was no significant difference between DO-5 and DO-7 during this period. In muscles, GST level was significantly higher in DO-1 and DO-3 after

48 h of exposure compared to the 1 h exposed fish in the respective treatment. In hepatopancreas of catla, GST level (Fig. 7b) was significantly higher in DO-1 and DO-3 treatments compared to others after 1 and 48 h of exposure. In hepatopancreas, GST level was significantly higher in all treatments (except DO-5 and DO-7) after 48 h of exposure compared to the respective 1 h exposed fish.

Glutathione peroxidase

In hepatopancreas of catla, glutathione peroxidase (GPx) level was significantly higher in DO-1 and DO-3 treatments compared to DO-5 after 1 h of exposure. There was no significant difference in GPx level between the high dissolved oxygen treatments and the control one (Fig. 8a) during this period. GPx level increased in fish exposed at 9 and 11 mg/L dissolved oxygen treatments after 48 h of exposure compared to the control one. GPx level in hepatopancreas was 7.37–65.78 % higher in 48 h exposed fish compared to 1 h exposed one regardless of treatment (except DO-5). In gills, GPx level was significantly higher in fish exposed at 1 mg/L dissolved oxygen compared to the control one in both samples (8b). The level increased significantly in 48 h exposed catla compared to the 1 h exposed fish in all treatments, except DO-5 and DO-7.

Gene expression

The mRNA level of hypoxia-inducible factor (HIF)-1α was studied in brain, gill and hepatopancreas of catla exposed to six different dissolved oxygen (Fig. 9a, b). In brain, HIF-1α mRNA was increased in 1 and 3 mg/L dissolved oxygen treatments compared to others after 1 h of exposure. In gill and hepatopancreas, HIF-1α mRNA level was significantly higher in DO-1 treatment compared to others after 1 h exposure. The mRNA level was reduced in hepatopancreas of all treatments (except DO-1) compared to DO-5. After 48 h of exposure, HIF-1α mRNA level was significantly higher in gills of DO-3 treatment compared to others. This treatment was followed by DO-11 treatment. The mRNA level was lower in hepatopancreas of all treatments compared to DO-5.

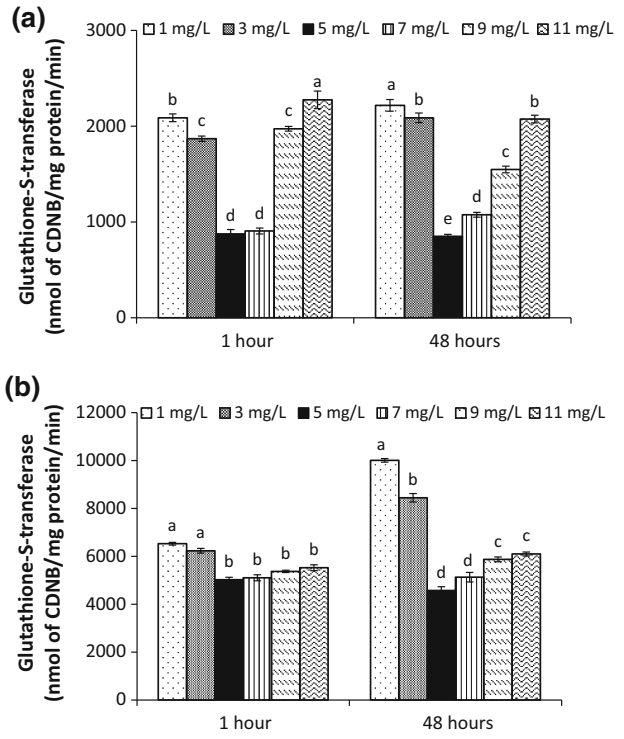


Fig. 7 Glutathione *S*-transferase levels found in **a** muscles and **b** hepatopancreas of *Catla catla* exposed to various levels of dissolved oxygen. *Vertical bars with different superscripts* are significantly ($p < 0.05$) different ($n = 3$)

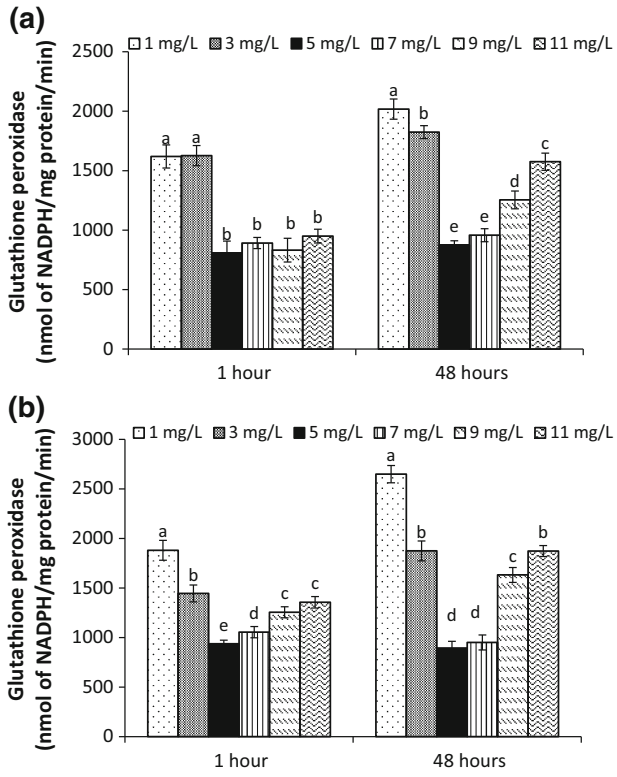


Fig. 8 Glutathione peroxidase level found in **a** hepatopancreas and **b** gills of *Catla catla* exposed to various levels of dissolved oxygen after 1 and 48 h. *Vertical bars with different superscripts* are significantly ($p < 0.05$) different ($n = 3$)

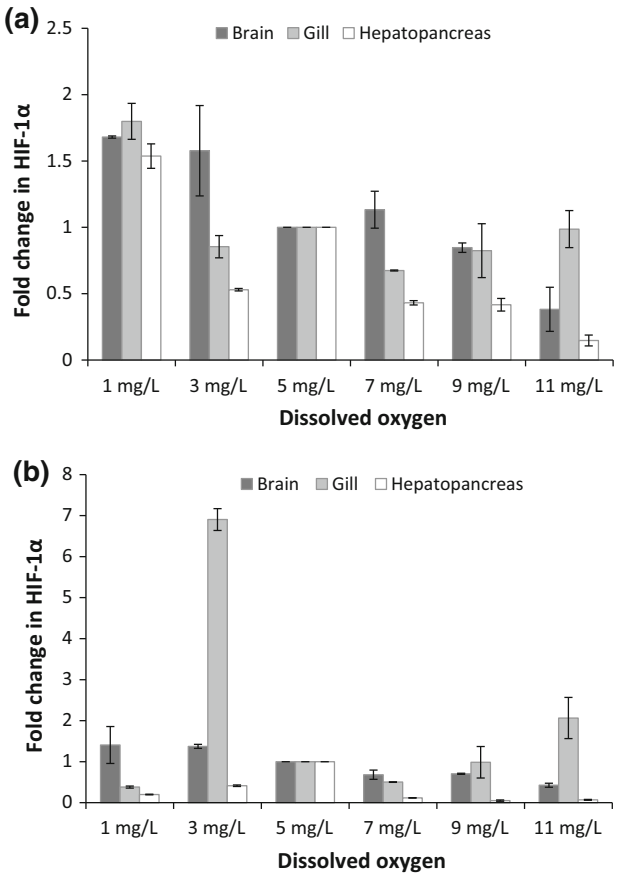


Fig. 9 HIF-1α mRNA levels in brain, gill and hepatopancreas of *Catla catla* exposed to different levels of dissolved oxygen for **a** 1 h and **b** 48 h. The relative expression of the target gene HIF-1α was normalized to the expression of β-actin (internal control) and expressed as fold changes relative to the control group (5 mg/L)

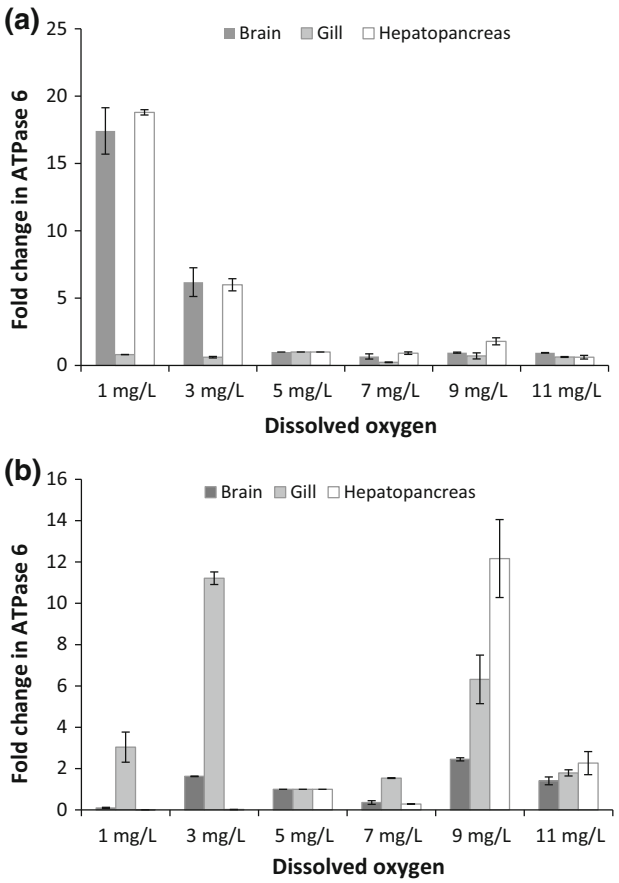


Fig. 10 ATPase 6 mRNA levels in brain, gill and hepatopancreas of *Catla catla* exposed to different levels of dissolved oxygen for **a** 1 h and **b** 48 h. The relative expression of the target gene ATPase 6 was normalized to the expression of β-actin (internal control) and expressed as fold changes relative to the control group (5 mg/L)

The mRNA level of ATPase 6 was significantly higher in brain and hepatopancreas of DO-1 treatment compared to others after 1 h exposure. This treatment was followed by DO-3. The mRNA level of ATPase 6 was decreased in gills of catla regardless of treatments (Fig. 10a). After 48 h of exposure, mRNA level was significantly higher in gill and hepatopancreas of DO-3 and DO-9 treatment, respectively compared to others. In 11 mg/L dissolved oxygen treatment, the mRNA level of ATPase 6 was induced compared to 5 mg/L dissolved oxygen treatment (Fig. 10b).

Discussion

Availability of dissolved oxygen is a critical parameter. The optimum recommended oxygen level for tropical freshwater fish is 5 mg/L (Mallya 2007). In the present study, the exposure of catla at above and below this level showed physiological stress in this species. The number of red blood cells (RBC) is an important parameter as these are associated with the oxygen carrying capacity of the blood. The number of RBC reduced in fish challenged with low dissolved oxygen after 1 h. The abundance of red blood cell increased as the fish was exposed to higher levels of dissolved oxygen during this period. But there was change in the abundance of RBC after 48 h of exposure. In normoxic (5 mg/L) and hypoxic (1 and 3 mg/L) conditions, there was no significant change in RBC abundance between 1 and 48 h samples of same treatment. But in hyperoxic (7–11 mg/L) treatments, there was significant reduction in RBC number after

48 h exposure compared to the sample of 1 h in the same treatment. In juvenile turbot *Scophthalmus maximus*, the number of RBC was higher in 14 mg/L dissolved oxygen treatment compared to the control (7 mg/L) one after 7 days of exposure, but the number reduced significantly in the former after 28 days of exposure (Wu et al. 2014). Both these studies indicated the time-dependent variation in RBC number with response to oxygen stress. In catla, the reduction of number of RBC in 7–11 mg/L treatments after 48 h exposure might be related to less requirement of oxygen transport in fish. This is opposite to the hypoxic conditions. Under hypoxia conditions, increasing the RBC level may help to acquire more oxygen and increase gas transport capacity of the fish blood (Wu et al. 2014). In Amur sturgeon *A. schrenckii*, the abundance of white blood cells and red blood cells increased after 0.5 and 1.5 h exposure at 1 mg/L dissolved oxygen, but there was no significant difference 3 h after hypoxia (Ni et al. 2014). In the present study, the number of RBC was counted at 1 and 48 h. The increase in abundance of RBC was not recorded might be due to the difference in sampling time in the present study. This also might be species-specific response. Rees et al. (2001) found in zebrafish *D. rerio*, the magnitude of the acclimation to hypoxia depended upon the sex of the fish. In hyperoxic condition, RBC abundance reduced after 48 h of exposure. Further study may require to understand the impact of longer duration exposure in hypoxic condition on the abundance of RBC in catla.

The reduced level of serum lysozyme and respiratory burst activity in fish challenged at 1 and 3 mg/L dissolved oxygen were indicators of poor immune system in these treatments. A direct relationship was found between the dissolved oxygen and both parameters, except the serum lysozyme level in 11 mg/L treatment after 48 h of exposure. Fish lysozymes possess a high potential for bacteriocidal or bacteriolytic activity. This plays an important role in the biodefence system against gram-positive and gram-negative bacteria (Saurabh and Sahoo 2008). Lowest level of nitric oxide synthase (iNOS) also showed the impaired immune system of catla exposed at 1 and 3 mg/L dissolved oxygen levels. NOS are a family of enzymes that catalyse the production of cellular signalling molecule nitric oxide. This nitric oxide plays vital role in many biological processes. The inducible isoform iNOS produces large amount of nitric oxide as a defence mechanism. The young fish use innate mechanisms during the first weeks/months of their development, and this may find application for the defence of farmed fish against pathogens at early age (Rombout et al. 2005). In the present study, the elevated levels of lysozyme, respiratory burst activity and NOS indicated the improved defence system of catla in higher dissolved oxygen treatments. But respiratory burst activity reduced in these treatments after 48 h exposure compared to the 1 h exposed fish in the same treatment. In sea bass *Dicentrarchus labrax*, hyperoxygenation of sea water resulted in a twofold increase in immunoglobulins (Scapigliati et al. 1999). The oxygen levels in the environment may modulate the immune response; hypoxia depresses the respiratory burst activity of macrophages and lowers the levels of circulating antibodies, which in turn are elevated by hyperoxia (Watts et al. 2001; Bowden 2008).

Fish maintained at 5 and 7 mg/L dissolved oxygen had less lipid peroxidation compared to the other treatments as the level of TBARS was low in these two treatments. Lipid peroxidation is a well-established mechanism of oxidative damage caused by ROS such as superoxide (O_2^-), OH and hydrogen peroxide (H_2O_2), and the measurement of malondialdehyde (MDA) provides a convenient index of lipid peroxidation (Devasena et al. 2001). Fish challenged with low and high levels of dissolved oxygen (compared to the control condition) were prone to lipid peroxidation in the present study. Lipid peroxidation may bring about protein damage by its end products, MDA and 4-hydroxynonenal (Bhor et al. 2004). Fish tissue contains large quantities of polyunsaturated fatty acids (PUFAs) essential for membrane function (Martinez-Alvarez et al. 2005). Lipid peroxidation is the process of oxidative degradation of PUFA, and its occurrence in biological membranes causes impaired membrane function, structural integrity and inactivation of several membrane-bound enzymes (Goel et al. 2005). Lushchak et al. (2005a) reported that in common carp, TBARS level increased three-fold in hepatopancreas during hypoxic condition. In vitro exposure of rainbow trout plasma and red blood cells to hyperoxia for 5 min resulted in more marked changes in TBARS content (Ritola et al. 2002a, b). In the present study, 48 h exposure resulted in higher lipid peroxidation compared to the 1 h exposed fish in all treatments except DO-5 and DO-7.

It is suggested that increased dissolved oxygen levels increase ROS generation due to enhanced probability of electrons escaped from electron-transport chains to combine with molecular oxygen. However, organisms possess specific adaptive mechanisms to prevent negative consequences of high environmental oxygen levels. In catla, decrease and increase in dissolved oxygen level of water from the control condition (5 mg/L) resulted into lower level of reduced glutathione after 1 and 48 h exposure in all tissues (muscles, hepatopancreas and gills), except muscles of DO-7 treatment after 1 h of exposure. Therefore, it is clear that both decreased and increased levels of external oxygen are an inducer of oxidative stress in catla. The exposure to hyperoxia induced oxidative stress in goldfish (Lushchak et al. 2005b), Atlantic salmon *S. salar* (Olsvik et al. 2005) and Senegal sole *Solea senegalensis* (Salas-Leiton et al. 2009). Maintenance of GSH levels is crucially important in preventing damage to cells exposed to conditions that promote oxidative stress. The cysteine thiol moiety of GSH imparts the antioxidant activity of this molecule. GSH can directly reduce a number reactive oxygen species including $^1O_2$, $HO^{\cdot}$, and O_2^{-} and GSH are oxidized to GSSG in this process. Glutathione may serve as a co-factor for antioxidant enzymes such as glutathione-dependent peroxidases or glutathione *S*-transferases, a second-phase detoxification enzyme (Lushchak 2011). Thus, the depletion of GSH during oxidative stress could have a significant impact on the antioxidant potential of cell (Pompella et al. 2003; Masella et al. 2005).

Glutathione *S*-transferases (GST) represent a major group of detoxification enzymes that catalyses intracellular detoxification reactions, including the inactivation of electrophilic carcinogens by catalysing their conjugation with glutathione (Henderson et al. 1998). In addition, GSTs have endogenous substrates, such as lipid and nucleic acid hydroperoxides and alkenals, which result from the decomposition of lipid hydroxyperoxides (Coles and Kadlubar 2003). Significantly higher level of GST was found in catla exposed at lower and higher levels of dissolved oxygen compared to the control condition. GST level was higher in hepatopancreas compared to the muscles of respective treatment. Oehlers et al. (2007) found that in medaka *Oryzias latipes* hypoxia increased glutathione *S*-transferase level. Elevated levels of GST in hepatopancreas of catla in all treatments (except DO-5 and DO-7) after 48 h of exposure compared to the 1 h exposed fish of the respective treatment indicated higher detoxification mechanism in the tissue to overcome the adverse conditions. This may result into better immune system in fish exposed at elevated dissolved oxygen levels.

Glutathione peroxide (GPx) is a tetrameric enzyme that catalyses the oxidation of glutathione. The enzyme is found in both selenium-containing and selenium-independent forms in the cytosol and mitochondria of animal tissues (Halliwell and Gutteridge 1999). Exposure of catla at low dissolved oxygen resulted in higher value of glutathione peroxidise in hepatopancreas and gills. Longer (48 h) duration exposure caused chronic stress as the GPx level increased in fish maintained above 5 mg/L oxygen level. The level was higher in hepatopancreas compared to gills of respective treatments. This showed tissue-specific expression pattern. The responses of oxidative stress in fishes were highly tissue specific. White muscles have low content of mitochondria and low-intensive oxidative metabolism (Lushchak et al. 2005b). Therefore, it often shows a slight response to oxidative/reductive conditions. On the other hand, aerobic tissues, brain and especially hepatopancreas possess high potential for ROS generation, which seems to be efficiently counter balanced by powerful protective mechanisms to detoxify and repair damaged lipids and proteins.

This study clearly showed that after 48 h of exposure of fish was more stressful for fish compared to the 1 h exposed fish in the same treatments as TBARS levels were elevated in muscles of all treatments, except DO-5. Simultaneously, elevation of GPx level in hepatopancreas of fish in all these treatments indicated stress. This GPx virtually reduced the amount of GSH in most of these treatments. A close connection between oxidized lipids and antioxidant enzymes is proven by time dynamics of these parameters in response to stress. Elevation of lipid peroxidation is often the first reaction to increase ROS generation, but an induction in antioxidant defences, GPx and GST being the main enzymatic ones, causes a quick return of oxidized products to initial level (Lushchak and Bagnyukova 2006). Better detoxification mechanisms at elevated oxygen levels improved immune system of catla. Oxygen free radicals reportedly play a decisive role in the regulation of defence systems. Levels of these oxygen free radicals were

found to be increased in immunocytes during immune responses and the killing of pathogens by phagocytes (Jones et al. 1991). However, reports exploring the effects of generation of oxygen free radicals on immune response are limited. It was revealed that oxygen free radicals may contribute to the immunomodulation and indicated the possible link between oxygen free radicals generation and suppressed immune system during oxidative stress (Koner et al. 1997). Levels of TBARS, reduced glutathione and the activities of antioxidant enzymes clearly showed development of mild oxidative stress under hypoxic conditions in the present study. Glutathione is one more potential candidate because its biosynthesis is stimulated under mild oxidative stress owing to increased expression of glutamate cysteine ligase, a key enzyme for its biosynthesis (Lushchak 2014).

Most studies suggested that HIF levels are regulated via oxygen-dependent breakdown; studies on hypoxia-tolerant vertebrates suggested that HIF mRNA levels may be regulated (Shams et al. 2005; Law et al. 2006; Rissanen et al. 2006). In normoxia- and hypoxia-grown zebra fish *D. rerio*, highest HIF-1α mRNA levels were found in tissues like brain, gill and heart that are important for hypoxic survival (Rytkönen et al. 2014). In the present study, the mRNA level of HIF-1α increased in brain of catla exposed at 1 and 3 mg/L dissolved oxygen after 1 h of exposure. In gill and hepatopancreas of catla, mRNA level of HIF-1α increased in 1 mg/L dissolved oxygen. The mRNA level of HIF-1α increased in gill of catla exposed at 3 and 11 mg/L dissolved oxygen level after 48 h of exposure. This showed tissue-specific expression pattern. Brain is most sensitive to hypoxic condition (≤3 mg/L). The detoxification capacity of hepatopancreas was confirmed from this result. In DO-3 and DO-11 treatments, mRNA level of HIF-1α in gills required longer duration exposure (48 h) for its expression. Gracey et al. (2001) reported tissue-specific patterns of expression reflect the different metabolic roles of tissues during hypoxia in goby fish, *Gillichthys mirabilis*. This was also important to record that like hypoxia, hyperoxic condition was also stressful to catla.

Several studies showed the adaptive response of fish to low oxygen levels. In crucian carp *Carassius carassius*, HIF-1 DNA binding activity and HIF-1 expression in normoxia and hypoxia (0.7 mg/L O_2) were studied at temperatures of 26, 18 and 8 °C (Rissanen et al. 2006). Temperature had a marked influence on HIF-1 in normoxia. Tissue-specific expression pattern was recorded in heart, gills and kidney. HIF is a key transcriptional activator in responses to hypoxia and primary regulator of the production of red blood cells through mediation of the expression of erythropoietin gene (Zhao and Wu 2013). In the present study the mRNA level of HIF-1α increased after 1 h, while the RBC number decreased. This possibly indicates that during hypoxic conditions longer time was required for erythropoiesis as there was no increase in RBC number at least up to 48 h of exposure.

A defence promoting process in hypoxic condition is a drastic suppression of ATP demand, including shutting down energy costly processes like protein synthesis, cell division and ion pumping activity. Another hypoxia defence strategy involves reorganization of metabolic pathways by switching from aerobic oxidation to the glycolytic pathway (Ton et al. 2003). Hypoxia also induced the expression of hepatopancreas genes needed for enhanced anaerobic ATP production of gluconeogenesis. These responses represented an important adaptive strategy enabling *G. mirabilis* to survive under natural conditions of environmental hypoxia (Gracey et al. 2001). In the present study, though initially the mRNA level of ATPase 6 increased in hepatopancreas of catla exposed at DO-1 and DO-3 treatments compared to control one, the mRNA level reduced after 48 h of exposure. These results are comparable with the results of Busk and Boutilier (2005). They observed that anoxia exposure of hepatocytes of eel *Anguilla anguilla* caused an initial decrease in ATP, followed by a stabilization at a new, lower level. In contrast, Krumschnabel et al. (1997) demonstrated that exposure of goldfish hepatocytes to anoxia did not result in a decrease in ATP. In the present study, increased mRNA level of ATPase 6 gene in hepatopancreas after 1 h and decreased mRNA level after 48 h exposure can be considered as the compensatory mechanism to fulfil the ATP requirement needed in various metabolic processes. In the present study, long duration (48 h) exposure of fish to higher levels of dissolved oxygen (DO-9) resulted in up-regulation of ATPase 6 in hepatopancreas. The increase in ATP production must be achieved by coordinate expression of associated proteins encoded by mitochondrial and nuclear genes (Anderson et al. 1981). Carp acclimated at 10 °C

showed two-fold higher ATPase mRNA levels compared to the carp acclimated at 30 °C (Itoi et al. 2003). The present study showed the of ATP metabolism character of the brain, gills and hepatopancreas. Brain is the most sensitive to hypoxic condition as its metabolism relies on majority of ATP formed in the mitochondria through oxidative phosphorylation of adenosine diphosphate (ADP) catalysed by the enzyme ATPase.

Conclusions

The exposure of tropical freshwater fish catla below recommended dose of dissolved oxygen 5 mg/L impaired immune system. This was reflected in the lower values of respiratory burst activity and nitric oxide synthase, whereas lipid peroxidation was higher in fish exposed below and above the 5 mg/L level of dissolved oxygen. In catla, decrease and increase in dissolved oxygen level of water from the control condition resulted into lower level of GSH and increased levels of GST and GPx. Maintenance of GSH levels is crucially important in preventing damage to cells exposed to conditions that promote oxidative stress. The mRNA level of HIF-1α and ATPase increased in treatments with ≤5 mg/L dissolved oxygen just 1 h after exposure. This showed immediate stress effect. Tissue-specific expression showed the different metabolic roles of tissues during hypoxia and hyperoxia in carps. This is clear from the present study that both decreased and increased levels of oxygen in the culture system induced oxidative stress in catla.

Acknowledgments Authors are thankful to Indian Council of Agricultural Research, ICAR, New Delhi, for providing financial support in the form of NFBSFARA project (AS-2001/2010-11) to carry out the research work.

References

Alexander JB, Ingram GA (1992) Noncellular nonspecific defence mechanisms of fish. Annu Rev Fish Dis 2:249–279

Anderson DP, Siwicki AK (1995) Basic haematology and serology for fish health programs. In: Shariff M, Arthur JR, Subasinghe RP (eds) Diseases in Asian Aquaculture II. Manila, Fish Health Section, Asian Fisheries Society

Anderson S, Bankier AT, Barrell BG, de Bruijn MHL, Coulson AR, Drouin J, Eperon IC, Nierlich DP, Roe BA, Sanger F, Schreier PH, Smith AJ, Staden R, Young IG (1981) Sequence and organization of the human mitochondrial genome. Nature 290:457–465

Benita Y, Kikuchi H, Smith AD, Zhang MQ, Chung DC, Xavier RJ (2009) An integrative genomics approach identifies Hypoxia Inducible Factor-1 (HIF-1)-target genes that form the core response to hypoxia. Nucleic Acids Res 37:4587–4602

Bhor VM, Raghuram N, Sivakami S (2004) Oxidative damage and altered antioxidant enzyme activities in the small intestine of streptozotocin-induced diabetic rats. Int J Biochem Cell Biol 36:89–97

Bowden TJ (2008) Modulation of the immune system of fish by their environment. Fish Shellfish Immunol 25:373–383

Brander K (2010) Impacts of climate change on fisheries. J Mar Syst 79:389–402

Busk M, Boutilier RG (2005) Metabolic arrest and its regulation in anoxic eel hepatocytes. Physiol Biochem Zool 78:926–936

Coles BF, Kadlubar FF (2003) Detoxification of electrophilic compounds by glutathione *S*-transferase catalysis: determinants of individual response to chemical carcinogens and chemotherapeutic drugs? BioFactors 17:115–130

D'Avanzo C, Kremer JN (1994) Diel oxygen dynamics and anoxic events in an eutrophic estuary of Waquoit Bay, Massachusetts. Estuaries 17:131–139

Devasena T, Lalitha S, Padma K (2001) Lipid peroxidation, osmotic fragility and antioxidant status in children with acute post-streptococcal glomerulonephritis. Clin Chim Acta 308:155–161

Goel A, Dani V, Dhawan DK (2005) Protective effects of zinc on lipid peroxidation, antioxidant enzymes and hepatic histoarchitecture in chlorpyrifos-induced toxicity. Chem Biol Interact 156:131–140

Gracey AY, Troll JV, Somero GN (2001) Hypoxia-induced gene expression profiling in the euryoxic fish *Gillichthys mirabilis*. Proc Natl Acad Sci USA 98:1993–1998

Graham JB (1990) Ecological, evolutionary, and physical factors influencing aquatic animal respiration. Am Zool 30:137–146

Grecay PA, Stierhoff KL (2002) A device for simultaneously controlling multiple treatment levels of dissolved oxygen in laboratory experiments. J Exp Mar Biol Ecol 280:53–62

Habig WH, Pabst MJ, Jakoby WB (1974) Glutathione *S*-transferases the first enzymatic step in mercapturic acid formation. J Biol Chem 249:7130–7139

Halliwell B, Gutteridge JMC (1989) Free radicals in biology and medicine, 2nd edn. Clarendon Press, Oxford

Halliwell B, Gutteridge JMC (1999) Free radicals in biology and medicine, 3rd edn. Clarendon Press, Oxford

Henderson CJ, Smith AG, Ure J, Brown K, Bacon EJ, Wolf CR (1998) Increased skin tumorigenesis in mice lacking pi class glutathione *S*-transferases. Proc Natl Acad Sci USA 95:5275–5280

Hermes-Lima M (2004) Oxygen in biology and biochemistry: role of free radicals. In: Storey KB (ed) Functional metabolism: regulation and adaptation. Wiley, New Jersey, pp 319–368

Hermes-Lima M, Zenteno-Savın T (2002) Animal response to drastic changes in oxygen availability and physiological oxidative stress. Comp Biochem Physiol C: Toxicol Pharmacol 133:537–556

Hochachka PW, Somero GN (2002) Biochemical adaptation: mechanism and process in physiological evolution, 1st edn. Oxford University Press, New York

Huttula T, Peltonen A, Bilaletdin Ä, Saura M (1992) The effects of climatic change on lake ice and water temperature. Aqua Fenn 22:129–142

Indian Council of Agricultural Research (2013) Handbook of Fisheries And aquaculture, 2nd edn. Indian Council of Agricultural Research, New Delhi, p 1116

Intergovernmental Panel on Climate Change (2007) Climate change 2007: the scientific basis. In: Solomon S et al (eds) Contribution of working group I to the fourth assessment report of the intergovernmental panel on climate change. Cambridge University Press, New York

Itoi S, Kinoshita S, Kikuchi K, Watabe S (2003) Changes of carp F_0F_1-ATPase in association with temperature acclimation. Am J Physiol Regul Integr Comp Physiol 284:R153–R163

Janssens BJ, Childress JJ, Baguet F, Rees J-F (2000) Reduced enzymatic antioxidative defense in deep-sea fish. J Exp Biol 203:3717–3725

Jollow DJ, Mitchell JR, Zampaglione N, Gillette JR (1974) Bromobenzene-induced liver necrosis. Protective role of glutathione and evidence for 3, 4-bromobenzene oxide as the hepatotoxic metabolite. Pharmacology 11:151–169

Jones OTG, Hancock JT, Henderson LM (1991) Oxygen radical production by transformed B lymphocytes. Mol Aspects Med 12:87–92

Koner BC, Banerjee BD, Ray A (1997) Effects of in vivo generation of oxygen free radicals on immune responsiveness in rabbits. Immunol Lett 59:127–131

Krumschnabel G, Schwarzbaum PJ, Biasi C, Dorigatti M, Wieser W (1997) Effects of energy limitation on $Ca2^+$ and K^+ homeostasis in anoxia-tolerant and anoxia-intolerant hepatocytes. Am J Physiol Regul Integr Comp Physiol 273:R307–R316

Kvamme BO, Gadan K, Finne-Fridell F, Niklasson L, Sundh H, Sundell K, Taranger GL, Evensen Ø (2013) Modulation of innate immune responses in Atlantic salmon by chronic hypoxia-induced stress. Fish Shellfish Immunol 34:55–65

Law SH, Wu RS, Ng PK, Richard MK, Kong RY (2006) Cloning and expression analysis of two distinct HIF-alpha isoforms—gcHIF-1alpha and gcHIF-4alpha—from the hypoxia-tolerant grass carp, *Ctenopharyngodon idellus*. BMC Mol Biol 7:15. doi:10.1186/1471-2199-7-15

Lee D-U, Kang YJ, Park MK, Lee YS, Seo HG, Kim TS, Kim CH, Chang KC (2003) Effects of 13-alkyl-substituted berberine alkaloids on the expression of COX-II, TNF-α, iNOS, and IL-12 production in LPS-stimulated macrophages. Life Sci 73:1401–1412

Livak KJ, Schmittgen TD (2001) Analysis of relative gene expression data using real-time quantitative PCR and the $2^{-\Delta\Delta CT}$ method. Methods 25:402–408

Lushchak VI (2011) Environmentally induced oxidative stress in aquatic animals. Aquat Toxicol 101:13–30

Lushchak VI (2014) Free radicals, reactive oxygen species, oxidative stress and its classification. Chem Biol Interact 224:164–175

Lushchak VI, Bagnyukova TV (2006) Effects of different environmental oxygen levels on free radical processes in fish. Comp Biochem Physiol B: Biochem Mol Biol 144:283–289

Lushchak VI, Lushchak LP, Mota AA, Hermes-Lima M (2001) Oxidative stress and antioxidant defenses in goldfish *Carassius auratus* during anoxia and reoxygenation. Am J Physiol Regul Integr Comp Physiol 280:R100–R107

Lushchak VI, Bagnyukova TV, Lushchak OV, Storey JM, Storey KB (2005a) Hypoxia and recovery perturb free radical processes and antioxidant potential in common carp (*Cyprinus carpio*) tissues. Int J Biochem Cell Biol 37: 1319–1330

Lushchak VI, Bagnyukova TV, Husak VV, Luzhna LI, Lushchak OV, Storey KB (2005b) Hyperoxia results in transient oxidative stress and an adaptive response by antioxidant enzymes in goldfish tissues. Int J Biochem Cell Biol 37:1670–1680

Magnuson JJ, Crowder LB, Medvick PA (1979) Temperature as an ecological resource. Am Zool 19:331–343

Mallya YJ (2007) The effect of dissolved oxygen on fish growth in aquaculture. Kingolwira National Fish Farming Centre, Fisheries Division Ministry of Natural Resources and Tourism, Tanzania

Martinez-Alvarez RM, Morales AE, Sanz A (2005) Antioxidant defenses in fish: biotic and abiotic factors. Rev Fish Biol Fisher 15:75–88

Martinovic D, Villeneuve DL, Kahl MD, Blake LS, Brodin JD, Ankley GT (2009) Hypoxia alters gene expression in the gonads of zebrafish (*Danio rerio*). Aquat Toxicol 95:258–272

Masella R, Di Benedetto R, Varì R, Filesi C, Giovannini C (2005) Novel mechanisms of natural antioxidant compounds in biological systems: involvement of glutathione and glutathione-related enzymes. J Nutr Biochem 16:577–586

Mohandas J, Marshall JJ, Duggin GG, Horvath JS, Tiller DJ (1984) Differential distribution of glutathione and glutathione-related enzymes in rabbit kidney: possible implications in analgesic nephropathy. Biochem Pharmacol 33:1801–1807

Montgomery DC (1984) Design and analysis of experiments. Wiley, New York

Ni M, Wen H, Li J, Chi M, Bu Y, Ren Y, Zhang M, Song Z, Ding H (2014) The physiological performance and immune responses of juvenile Amur sturgeon (*Acipenser schrenckii*) to stocking density and hypoxia stress. Fish Shellfish Immunol 36:325–335

Oehlers LP, Perez AN, Walter RB (2007) Detection of hypoxia-related proteins in medaka (*Oryzias latipes*) brain tissue by difference gel electrophoresis and *de novo* sequencing of 4-sulfophenyl isothiocyanate-derivatized peptides by matrix-assisted laser desorption/ionization time-of-flight mass spectrometry. Comp Biochem Physiol C: Toxicol Pharmacol 145:120–133

Ohkawa H, Ohishi N, Yagi K (1979) Assay for lipid peroxides in animal tissues by thiobarbituric acid reaction. Anal Biochem 95:351–358

Olsvik PA, Kristensen T, Waagbø R, Rosseland BO, Tollefsen KE, Baeverfjord G, Berntssen MHG (2005) mRNA expression of antioxidant enzymes (SOD, CAT and GSH-Px) and lipid peroxidative stress in liver of Atlantic salmon (*Salmo salar*) exposed to hyperoxic water during smoltification. Comp Biochem Physiol C: Toxicol Pharmacol 141:314–323

Padilla PA, Roth MB (2001) Oxygen deprivation causes suspended animation in the zebrafish embryo. Proc Natl Acad Sci USA 98:7331–7335

Pamplona R, Costantini D (2011) Molecular and structural antioxidant defenses against oxidative stress in animals. Am J Physiol Regul Integr Comp Physiol 301:R843–R863

Pompella A, Visvikis A, Paolicchi A, deTata V, Casini AF (2003) The changing faces of glutathione, a cellular protagonist. Biochem Pharmacol 66:1499–1503

Rees BB, Sudradjat FA, Love JW (2001) Acclimation to hypoxia increases survival time of zebrafish, *Danio rerio*, during lethal hypoxia. J Exp Zool 289:266–272

Rissanen E, Tranberg HK, Sollid J, Nilsson GE, Nikinmaa M (2006) Temperature regulates hypoxia-inducible factor-1 (HIF-1) in a poikilothermic vertebrate, crucian carp (*Carassius carassius*). J Exp Biol 209:994–1003

Ritola O, Livingstone DR, Peters LD, Lindström-Seppä P (2002a) Antioxidant processes are affected in juvenile rainbow trout (*Oncorhynchus mykiss*) exposed to ozone and oxygen-supersaturated water. Aquaculture 210:1–19

Ritola O, Tossavainen K, Kiuru T, Lindstrom-Seppa P, Molsa H (2002b) Effects of continuous and episodic hyperoxia on stress and hepatic glutathione levels in one-summer-old rainbow trout (*Oncorhynchus mykiss*). J Appl Ichthyol 18:159–164

Rombout J, Huttenhuis HBT, Picchietti S, Scapigliati G (2005) Phylogeny and ontogeny of fish leucocytes. Fish Shellfish Immunol 19:441–455

Rytkönen KT, Prokkola JM, Salonen V, Nikinmaa M (2014) Transcriptional divergence of the duplicated hypoxia-inducible factor alpha genes in zebrafish. Gene 541:60–66

Salas-Leiton E, Cánovas-Conesa B, Zerolo R, López-Barea J, Cañavate JP, Albama J (2009) Proteomics of juvenile Senegal sole (*Solea senegalensis*) affected by gas bubble disease in hyperoxygenated ponds. Mar Biotechnol 11:473–487

Saurabh S, Sahoo PK (2008) Lysozyme: an important defence molecule of fish innate immune system. Aquac Res 39:223–239

Scapigliati G, Scalia D, Marras A, Meloni S, Mazzini M (1999) Immunoglobulin levels in the teleost sea bass *Dicentrarchus labrax* (L.) in relation to age, season, and water oxygenation. Aquaculture 174:207–212

Schrøder MB, Villena AJ, Jørgensen TØ (1998) Ontogeny of lymphoid organs and immunoglobulin producing cells in Atlantic cod (*Gadus morhua* L.). Dev Comp Immunol 22:507–517

Secor DH, Gunderson TE (1998) Effects of hypoxia and temperature on survival, growth, and respiration of juvenile Atlantic sturgeon, *Acipenser oxyrinchus*. Fish Bull 96:603–613

Shams I, Nevo E, Avivi A (2005) Ontogenetic expression of erythropoietin and hypoxia-inducible factor-1 alpha genes in subterranean blind mole rats. FASEB J 19:307–309

Sies H (1991) Role of reactive oxygen species in biological processes. Klin Wochenschr 69:965–968

Stierhoff KL, Targett TE, Grecay PA (2003) Hypoxia tolerance of the mummichog: the role of access to the water surface. J Fish Biol 63:580–592

Storey KB (1996) Oxidative stress: animal adaptations in nature. Braz J Med Biol Res 29:1715–1733

Ton C, Stamatiou D, Liew C-C (2003) Gene expression profile of zebrafish exposed to hypoxia during development. Physiol Genomics 13:97–106

Tripathi NK, Latimer KS, Burnley VV (2004) Hematologic reference intervals for koi (*Cyprinus carpio*), including blood cell morphology, cytochemistry, and ultrastructure. Vet Clin Pathol 33:74–83

Vig E, Nemcsok J (1989) The effects of hypoxia and paraquat on the superoxide dismutase activity in different organs of carp, *Cyprinus carpio* L. J Fish Biol 35:23–25

Watts M, Munday BL, Burke CM (2001) Immune responses of teleost fish. Aust Vet J 79:570–574

Wu Z, You F, Wen A, Ma D, Zhang P (2014) Physiological and morphological effects of severe hypoxia, hypoxia and hyperoxia in juvenile turbot (*Scophthalmus maximus* L.). Aquac Res. doi:10.1111/are.12483

Zhao S, Wu J (2013) Hypoxia inducible factor stabilization as a novel strategy to treat anemia. Curr Med Chem 20:2697–2711

International Journal of Scientific Engineering and Technology
Volume No.4 Issue No.10, pp: 481-485

ISSN :2277-1581
01 Oct. 2015

Relaxing Weighted Clustering Algorithm for Reduction of Clusters and Cluster Head

Vijayanand Kumar
Department of Computer Science and Engineering, Delhi Technological University, New Delhi, India

Abstract: Adhoc clustering in MANET is to divide mobile nodes into different virtual groups. Mobile nodes are allocated geographically adjacent in the cluster. Clustering is done by some rule specific in the network. In this paper, we have concentrated to modify weight based clustering algorithm to improve the performance in this wireless technology. By slight improvement in existing weight based clustering algorithm [1] reduction in cluster as well as cluster head can be observed through experiment. Proposed Algorithm specifies relaxing the weight criteria for isolated cluster head nodes in range of other cluster head as well as reconsidering the nodes in the range which is already participated in cluster formation. Reconsidering the participated node again in clustering formation could help in creation of better cluster, forming better routes as well as in conserving the cluster head energy.

Keywords: Adhoc Networks, Clustering, Clustering Algorithms, NS-2, Weight Based Clustering, Energy Efficient Clustering.

1. INTRODUCTION

Mobile adhoc network is self configuring wireless nodes which communicate in transmission range. Flat and hierarchical topologies are available for arranging the mobile nodes in the network. Mobile adhoc network is infrastructure less network which follows the wireless topology in routing and data forwarding. Mobile node acts as router as well as gateway for other nodes. Clustering is a familiar technique and the cluster formation every group of node is formed together and the arranged in one group which is used to prevents the flood of unnecessary packets and avoids wasting network bandwidth. In this technique, a large network can be divided into several sub-networks with only a few cluster heads maintains the local information. In the flat topology packet flood can be observed but with hierarchical topology control of data packets and messages can be controlled. Hierarchical topology saves network bandwidth, saves energy for mobile nodes, provide better availability of routing option and provide spatial reuse of resources to increase the system capacity. It also has drawbacks such as scaling, stability of the network, dynamic topologies etc. Mobile nodes have many attributes such as mobility, power, compatibility etc. All the static and dynamic behavior must be considered in designing hierarchical topology.

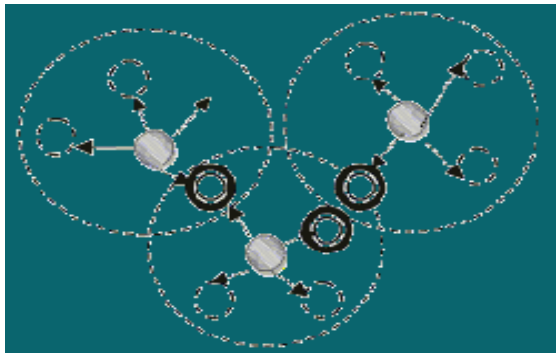


Fig 1:- Example of Cluster Network


Cluster Head (CH)


Gateway node (CN)


Cluster member (CM) / Ordinary Member

This clustering techniques are working with three important aspects which shown in Fig 1. CH plays with superior power in the intra-cluster network which elected by the other member nodes. CH serves the other nodes and perform important role in routing of information from one node to other. Information passes through the cluster head.

Any of the routing techniques such as DSR, AODV, TORA, and DSDV etc can be used in exploring the routes from one node to another. In cluster based routing protocol the route messages are graceful by the following method:

Source → Cluster Head→ Gateway → Cluster Head → Gateway → ⋯ → Destination.

Information can be passed internally to the cluster or to the external cluster better known as intra cluster and inter cluster routing. Clustering mainly of two types overlapping and non-overlapping. Mixed of clustering is also possible in the network. Cluster members can be of one hop or multi hop distance from the cluster head. Many terms such as cluster formation and maintenance, cluster member re-affiliation, ripple effect of clusters and cluster communication has been studied before. Cluster Formation is to invoke such method to find dominant set with cluster head which results in cost effective clustering. Any causes such as dead node, cluster member or cluster head movement results in cluster maintenance.

Moving of cluster member from one cluster to another results in cluster member re-affiliation. Reaffliation of member can cause ripple effect of clusters i.e. invocation of cluster formation.

Section II explains some related clustering algorithms and cost effective clustering criteria. Section III describes the proposed algorithm. Section IV deals with simulation environment and comparative results with the existing weight based clustering algorithms and the conclusion described in Section V.

2. RELATED WORK

The Ad hoc networks topology structure has classified into flat topology structure and hierarchical clustering structure. Due to the dynamic topology of ad hoc, the flat structure results are inefficient. After that, the researchers have proposed the hierarchical clustering structure for ad hoc networks. The clustering techniques can be classified as graph based and geographical based. A number of clustering algorithms have been proposed to choose cluster-heads based on the speed and direction, mobility, energy, position, and the number of neighbors of a given node. These efforts present advantages but also have some drawbacks, such as the high computational overhead for both clustering algorithm execution and update operations. To achieve cost effective clustering below criteria must be considered.

- Minimising re-election of Cluster head.
- Efficient method to find cluster head.
- Reducing the Reclustering or ripple effect by Reclustering.
- Scalable Clustering Scheme.
- Maintenance cost of clustering should be low.
- Load on the distributed nodes must be optimised.
- Network load and cost of communication must be low.
- Minimising the re-affiliation cost.
- Minimising the topology change in clustering.
- Mobility of the node must be considered.
- Power of CH node must be sufficient to serve other nodes.
- Selection of CH and Gateway node must be fast.
- Non Overlapping Structure for Spatial reuse.
- Cluster Size affects communication cost or delay the operation of communication. Greater cluster size have more cost than smaller cluster size.
- Decrease the node, Number of Clusters will be increased.
- Increase in Cluster Head, Increase Hop Distance for data forwarding.
- Form Stable Cluster or Find Stable clustering mechanism.

All above criteria cannot be achieve and considered as NP hard problem of clustering. Most clustering schemes are classified as follow: (a) Dominant set based clustering (b) Low maintenance clustering (c) Mobility aware clustering (d) Energy efficient clustering (e) Load balancing clustering and (f) Combined metrics based clustering. In this paper study of combined metrics based clustering has been presented. Weighted clustering algorithm is one of the combined metrics based clustering.

The **Weighted Clustering Algorithm** (WCA) [1] was originally proposed by M. Chatterjee et al. which obtain 1-hop clusters with one cluster-head. The election of the cluster-head is based on the weight of each node. This algorithm performs with four admissible factors for the cluster head election and maintenance. The four factors are degree difference (Dv), summation of distances (Pv), mobility (Mv) and cumulative time (Tv). Although WCA has proved better performance than all the previous algorithms, it is also has few drawbacks to know the weights of all the nodes before starting the clustering process and CHs rapidly Changing difficulties. As a result, the overhead induced by WCA is very high. The weight value associated to a node 'v' is defined as Wv = W1Dv + W2Pv + W3Mv + W4Tv
A CH algorithm finishes once all the nodes become either cluster head or a member of cluster head. A cluster head consumes more battery power than ordinary node. This algorithm depend few conditions i.e. the distance between members of CH must be less or equal to the transmission range between them. WCA assumption is that a node can support up to δ nodes for better MAC functioning.

WCA Steps for Cluster formation [1]

1. Compute the degree d_v each node v.
2. Compute the degree-difference for every node.
3. Compute the sum of the distances D_v with all neighbors.
4. Compute the average speed of every node; gives a measure of mobility M_v.
5. Compute the total (cumulative) time P_v a node acts as cluster head.
6. Calculate the combined weight W_v for each node $W_v = w_1\Delta_v + w_2D_v + w_3M_v + w_4P_v$.
7. Find min W_v; choose node v as the cluster head, remove all Neighbors of v for further WCA.
8 Repeat steps 2 to 7 for the remaining nodes.

3. PROPOSED WORK

In this section, weight based clustering algorithm has been studied and modified for reduction of cluster as well as reduction of cluster head. We will analyze two scenario of clustering where modification can result in efficient clustering as well as energy can be saved.

Scenario (a): Isolated cluster formation due to minimum weight selection among the nodes.

Step 7 of weighted clustering algorithm [1] could result in isolated cluster. Consider nodes arrangement in table 1. Weight has been taken arbitrary but similar situation also arises while executing in real environment or in network simulation. Range of nodes may or may not be same for this scenario. Assume maximum delta a node can support is (δ) 4.

International Journal of Scientific Engineering and Technology
Volume No.4 Issue No.10, pp: 481-485

ISSN :2277-1581
01 Oct. 2015

Node ID	Weight(Wv)	Nodes in range
1	4	3,4,5
2	3	5,7,6,8
3	7	-
4	8	-
5	9	-
6	12	2
7	10	2
	2	-

Table 1

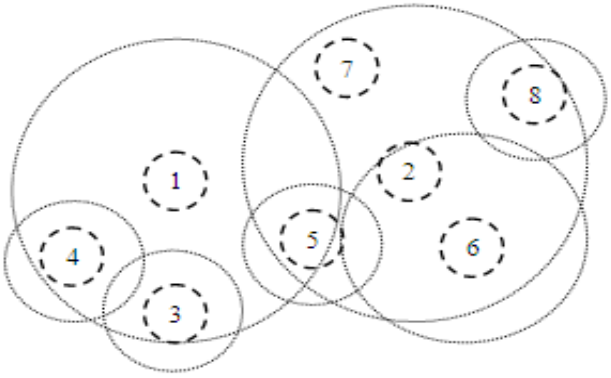


Fig 2:- Cluster architecture before cluster formation.

Running the WCA on above network structure, clustering shown in Fig 3 has been formed for cluster creation process. Cluster head, Member Nodes and gateway nodes are shown in Fig 3. Node_8 has the minimum weight and becomes the cluster head. It has no members in the range so it becomes an isolation node. Node_2 becomes the cluster head after Node_8 since it has more weight than the node_8.Node_1 becomes the next cluster head and node_3 and node_4 becomes its member. Similarly Node_2 serves node_5, node_6 and node_7. Node_8 has no neighbors in the range and hence become isolated cluster as shown in Fig 3.
We also assumed that cluster head can serve up to four nodes. In this case no cluster head is serving the maximum threshold. Here there are two problems isolated cluster head as well as maximum threshold has been not served. Both of the problems can be solved if relaxation is made in minimum weight criteria.

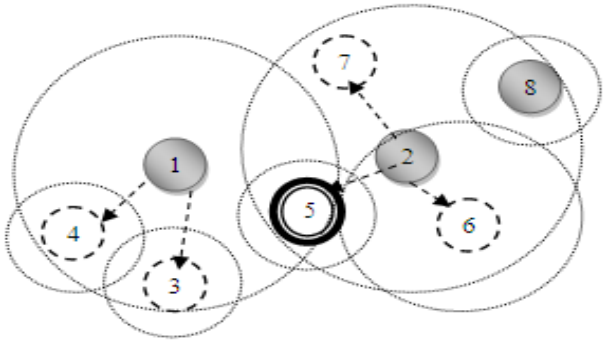


Fig 3:- Cluster Formation with weighted clustering algorithm

Relaxing the already formed isolated cluster head (Node_8) minimum weight criteria and including it in cluster formation again by checking that the cluster head (Node_8) has no neighbors associated and current cluster head node (Node_2) is under threshold, isolated cluster head node (Node_8) becomes member of the next cluster head (Node_2) selected. Since isolated cluster node (Node_8) is not serving any node so there is no need to be a cluster head. Isolated Cluster (Node_8) must be in the range of the next incoming cluster head (Node_2).It is not necessary that immediate node (node_2) with minimum weight in the range elect isolated node as member node. It may take time and turn of next minimum node could be late in cluster head election process due to minimum weight. It will be an exception in the network with minimum weight having no neighbors become a member nodes instead a cluster head. Now the cluster formed will be shown in Fig 4.

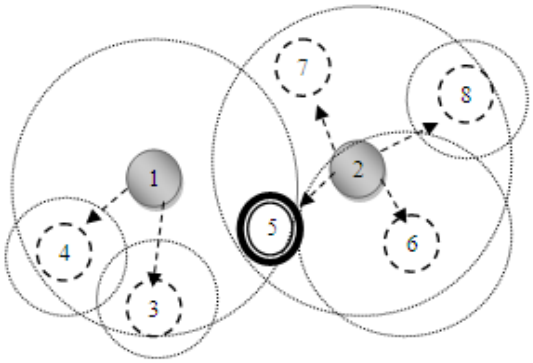


Fig 4:- Cluster Formation after relaxing the minimum weight criteria for isolated nodes.

Such adjustments in the network can help in minimizing the hop count while routing. It reduces the cluster head as well as number of clusters in the network. Less number of clusters in dense network reduces the hop count and intern traffic in the network which is already proven fact.

Scenario (b): Cluster Change of the ordinary or member node if its distance and weight is less than the newly selected cluster head node and become member of new cluster formed.

Energy consumption is more if the node distance is more in communication range. So to save energy already selected member node can be re elected in the cluster formation. Slight change in algorithm can help in achieving the task.
Each node can support maximum threshold to 4 nodes. Node_1 has minimum weight and become cluster head. Neighbor (node_3, node_4, node_8 and node_6) nodes become cluster member. After this cluster Node_7 becomes cluster head according to next minimum weight shown in Fig 5. Once cluster member become part of one cluster it cannot participate in the next cluster head election process but it can be in the neighborhood of other cluster head and it hears the request of cluster election procedure. Small calculation by this member node (node_4) while hearing Node_7 cluster head request can join the

ISSN :2277-1581
01 Oct. 2015

new cluster formed by node_7 cluster head. Node_4 need to check the distance of previous cluster head (node_1) to the new cluster head (node_7) that it's less or more. If node_4 has less distance from node_7 and node_7 can satisfy the maximum threshold as well as node_4 has more weight than Node_7, node_4 joins the cluster formed by Node_7 shown in Fig 6.

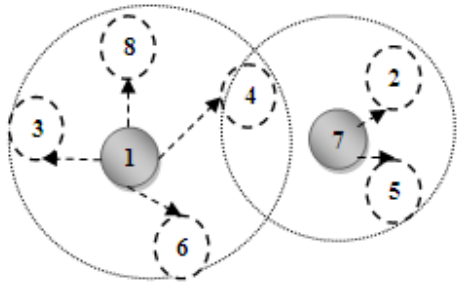


Fig 5:- Initial cluster according to weighted clustering algorithm

Node ID	Weight(Wv)	Nodes in range
1	1	3,4,6,8
2	9	7
3	10	1
4	8	7
5	9	7
6	5	1
7	4	2,4,5
8	12	-

Table 2

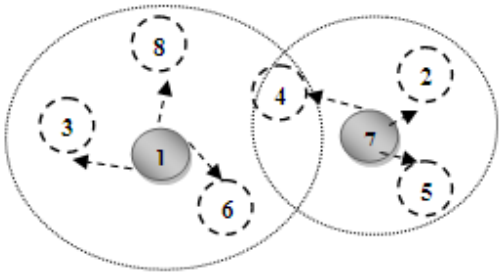


Fig 6:- Node_4 join the cluster formed by Node_7

4. SIMULATION ENVIRONMENT AND RESULTS

A. Introduction

Network Simulator 2 (NS2) is a discrete event simulator targeted at networking research. It provides support for simulation of TCP, routing and multicast protocols over wired and wireless networks. Currently DARPA, NSF and ACIRI support the development of NS. It contains three types of discrete event schedulers: list, heap and hash based calendar. NS2 also provides default implementations for network nodes, links between nodes, routing algorithms, transport level protocols and some traffic generators. Adding functionality to these objects can extend the simulator. NS2 also contains some useful utilities which include Tcl debugger used to debug Tcl scripts and it might become necessary if one is using large scripts to control a simulation. Tcl-debug is not however installed automatically with NS2 but it can be installed later. The major drawback of using Tcl-debug is that it is dependent on used Tcl version and also NS2 version.

B. Simulation Study

In simulation N was chosen to 30 nodes and arrange randomly with X and Y specified. Simulation has been performed with weighted clustering algorithm and weighted clustering after combining scenario (a) and scenario (b).

Parameters	Meaning	Value
N	No of nodes	30
X*Y	Simulation Area	650X500
R	Transmission Range	50-100
Mobility Model	Random Way Point	-
Duration	Simulation time	50Sec
MD	Maximum Displacement	300-400

C. Simulation Results and Discussion

Arrangement of thirty nodes has been done with specifying the coordinates on network simulator. Nodes have been distributed in range of 50 and 100. Weighted Clustering Algorithm has been implemented first; its arrangement in the network area is such that out of 30 nodes 20 nodes become the cluster head and correspondingly 20 clusters. Maximum threshold node to be supported is 4 but none of the cluster head serves maximum threshold. It could be because of arrangement of nodes. Further modified weighted clustering algorithm which includes scenario (a) and scenario (b) on the same network reduce the cluster head to 15 and correspondingly 15 clusters. Result will be variable since it depends on node distribution on the network. It could be possible that network doesn't have isolated node i.e. all nodes are in the range of each other. If the nodes are isolated and fall under scenario (a) definitely could result in reduction of cluster. Scenarios (b) don't reduce the cluster head and cluster size. Its logic is only for better energy conservation or for saving the energy for cluster head since in this case cluster member changes its cluster head identification. Fig 7 and Fig 8 shows the comparison between WCA and WCA with addition of scenario (a) and scenario (b). Since the network is designed randomly such scenarios are likely to take place. This research work has been focused on such issues and further modification to the algorithm for better result in some extra computation time. Computation cost will increase slightly but stability of cluster will increase too. In this WCA computation could have been taken place for avoiding the nodes which has been already participated i.e. already selected cluster member and cluster head will not participate in the cluster formation process but this computation is necessary so that nodes can be added to the cluster. Scenario (a) and (b) could replace this computation for adding in the cluster.

So there is minimum cost of computation here or stay same as original computation cost.

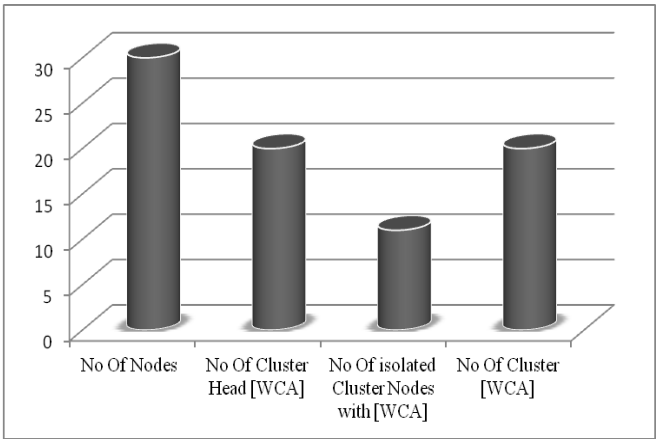


Fig 7:- WCA implementation result

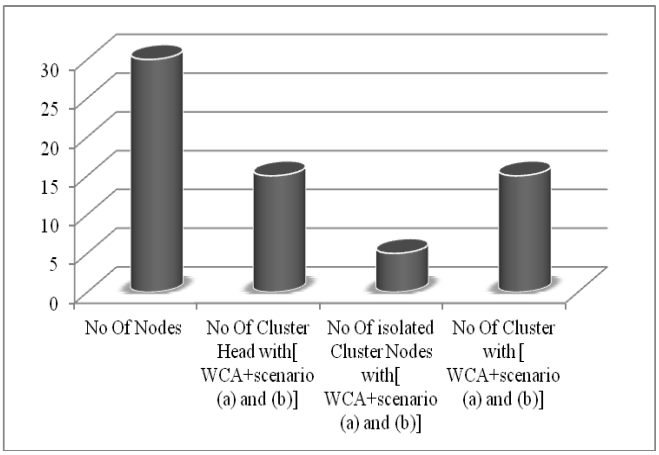


Fig 8:- WCA implementation result after adding scenario(a) and scenario(b)

5. CONCLUSION

Relaxation in weighted clustering algorithm results in better cluster formation. Isolated Cluster head nodes become the cluster member for next selected cluster head due to minimum weight. Isolated node cluster head results due to minimum weight, coming prior in election of cluster head due to minimum weight selection as cluster head, also don't cover any nodes in its range. Since isolated node don't deserve to be cluster head as it is not serving any nodes so it is better to become a cluster member for the next minimum weighted node. For saving the energy further relaxation required for member nodes or ordinary nodes in cluster formation process. Member nodes must join the cluster from which its distance is less from the cluster head. If cluster head covers the other cluster member in the range and it satisfy minimum weight as well as minimum threshold criteria, it must include in its cluster. Practically it is proven fact that as distance from node increases transmission power is required more which results in more energy depletion. So if member nodes are located far from the cluster head it requires more energy to communicate and hence consume more power. So it can be observed by relaxing some of the criteria better cluster formation, energy efficient clustering can be achieved. These methods can be applied in all related weight based clustering to achieve more efficient clustering.

REFRENCES

i. *M Chatterjee, S K Das, D Turgut, "WCA: A Weighted Clustering Algorithm for Mobile Ad Hoc Networks", IEEE Journal of Clustering Computing Vol.5(2),193-204, 2002.*

ii. *C.E. Perkins, ad hoc Networking, Addison-wesley,2001.*

iii. *Yu-Xuan Wang, Forrest Sheng Bao, "An Entropy-Based Weighted Clustering Algorithm and Its Optimization for Ad Hoc Networks," wimob,pp.56, Third IEEE International Conference on Wireless and Mobile Computing, Networking and Communications (WiMob 2007), (2007).*

iv. *A. D. Amis and R. Prakash, "Load-Balancing Clusters in Wireless Ad Hoc Networks," in proceedings of 3rd IEEE ASSET'00, pp. 25–32 (Mar. 2000).*

Journal of Basic and Applied Engineering Research
Print ISSN: 2350-0077; Online ISSN: 2350-0255; Volume 2, Number 14; April-June, 2015 pp. 1214-1219
© Krishi Sanskriti Publications
http://www.krishisanskriti.org/jbaer.html

Sentiment Analysis of Mobile Reviews using Sentiwordnet

Gaurav Dudeja[1] and Kapil Sharma[2]

[1,2]Department of Computer Science Delhi Technological University New Delhi, India
E-mail: [1]gdudeja@gmail.com, [2]kapil@ieee.org

Abstract—*This paper presents our experimental work on a domain specific feature-based for aspect level sentiment analysis of mobile phone reviews. In decision making, the opinions of others have a significant effect on customers ease in making choices regards to online shopping, choosing products, etc. We have devised an rule based domain independent scheme that analyses the textual reviews of a phone and assign a sentiment label on each aspect. The semantic score of subjective sentences is extracted from SentiWordNet Library to calculate their sentiment as positive, negative or neutral based on the textual sentence structure. We have used SentiWordNet library as a dataset with two different approaches of selections comprising of adverbs and verbs,adjectives and n-gram feature extraction. We also used our SentiWordNet library to compute the document level sentiment for each phone reviewed and compared its label with results obtained using Alchemy API. The sentiment label of a phone is also compared with the document level sentiment result. The results obtained show that our approach produces a more accurate sentiment label than the simple document level sentiment analysis.*

1. INTRODUCTION

Sentiment analysis is language process task that uses a approach to spot textual content and categorize it as positive or negative. The unstructured matter knowledge on the net usually carries expression of opinions of users. Sentiment analysis tries to spot the expressions of opinion and mood of writers. a straightforward sentiment analysis rule tries to classify a document as 'positive' or 'negative', supported the opinion expressed in it. The document-level sentiment analysis drawback is basically as follows: Given a collection of documents D, a sentiment analysis rule classifies every document d D into one among the 2 categories, positive and negative. Positive label denotes that the document d expresses a positive opinion and negative label means d expresses a negative opinion of the user. additional refined algorithms try and establish the sentiment at sentence-level, feature-level or entity-level.

There are mainly three types of approaches for sentiment classification of texts: (a) By using a machine learning primarily based text classifier -such as Naïve Thomas Bayes, SVM or kNN- with appropriate feature choice theme; (b) By using the unsupervised semantic orientation scheme of extracting relevant n-grams of the text so treated them either as +ve or -ve and consequentially the document; and (c) By using the SentiWordNet opensource used based online library that gives positive, negative and neutral scores for words. a number of the relevant past works on sentiment classification is found in [1], [2], [3], [4], [5], [6], [7], [8], [9], [10], [11] and [12].

Now a days web of internet hosts an outsized volume of information created by numerous users. Users are currently co-creators of website, instead of being passive customers. The social media is currently a serious a part of the internet. The statistics shows that each four out of five users on the net use some sort of social media. The user contributions to social media vary from blog posts, tweets, reviews and photo or video uploads etc. an outsized quantity of the information on the net is unstructured text. Opinions expressed in social media in sort of reviews or posts represent a very important and attention-grabbing space price exploration and exploitation. With increase in accessibility of opinion resource product reviews, moive reviews, blog reviews, social network tweets, the new difficult task is to mine giant volume of texts and devise appropriate algorithms to know the opinion of others. This info is of very useful and informatial to firms that try and grasp the feedback regarding their product or services. This feedback helps them in taking user choices. additionally to be helpful for firms, the reviews and opinion strip-mined from them, is useful for users in addition. reviews about hotels in a city may help a user going to a city searching a good hotel. Similarly, phone reviews help other users in deciding whether the phone is worth to purchase or not. Similarly, phone reviews facilitate different users choose whether or not the mobile phone is worth for money or not. during this paper we have got tried to explore a new SentiWordNet primarily based theme for each document-level and aspect-level sentiment classification. The document-level classification involves use of various linguistic options (ranging from Adverb+Adjective combination to Adverb+Adjective+Verb combination). we have got additionally devised a new domain specific heuristic for aspect-level sentiment classification of mobile phone reviews. This theme locates the self-opinionated text round the desired aspect feature in an exceedingly review

and computes its sentiment orientation. For a mobile phone, this is used for all the reviews.

The sentiment scores on a particular aspect from all the selected reviews are then aggregated. This process is carried out for all aspects under consideration. Finally a summarized sentiment profile of the mobile phone on all aspects is presented in an easy to visualize and understandable pictorial form. The remaining paper is organized as follows. Section 2 describes the basic approach of uaing SentiWordNet formulation for sentiment classification, along details of our implementation. Section 3 describes the dataset used for classification and performance metrics computed. Section 4 presents the results and the paper concludes with key observations in Section 5.

2. SENTIMENT CLASSIFICATION

We have primarily based our classification formula on the publically avaiable library SentiWordNet [38]. The SentiWordNet approach involves getting sentiment score for every opinion containing term of the text by a search in its library. during this lexical resource every term t occurring in WordNet is associated to a few numerical scores obj(t), pos(t) and neg(t), describing the target, positive and negative polarities of the term, severally. These 3 scores square measure computed by combining the results created by eight ternary classifiers. to create use of SentiWordNet we want to initial extract relevant narrow terms and so search for his or her scores within the SentiWordNet. Use of SentiWordNet needs tons of selections to be taken relating to the linguistic options to be used, deciding what quantity weight is to be to every linguistic feature, and therefore the aggregation technique for consolidating sentiment scores. we have got enforced the SentiWordNet primarily based algorithmic formulation for each document-level and aspect-level sentiment classification.

3. DOCUMENT-LEVEL SENTIMENT CLASSIFICATION

The document level sentiment analysis attempts to analyise the entire document (such as one review) into ‘+ve’ ,‘-ve’ or neutral class. The methodologies based on SentiWordNet focuses the term profile of the review document and concentrate terms having desired POS label (such as adjectives, adverbs or verbs). This obviously shows that before applying the SentiWordNet based formulation; the review text should be applied to a POS tagger which tags each term occurring in the review text. At that point some chose terms (with wanted POS tag) are removed and the opinion score of every extricated term is gotten from the SentiWordNet library. The scores for every removed term in a review are then accumulated utilizing some weightage and accumulation plan. Subsequently two key issues are to choose (a) which POS labels ought to be separated, and (b) how to choose the weightage of scores of distinctive POS labels extricated while registering the total score.

We have investigated with diverse linguistic highlights and scoring plans. Computational Linguists propose that modifiers are great markers of reviews. Case in point, if a review sentence says "The phone is incredible", then utilization of modifier "incredible" lets us know that the phone was loved by the analyst and perhaps he had a superb experience by utilizing it. At times, Adverbs further adjust the sentiment communicated in audit sentences. Case in point, the sentence "The phone is extremely good" communicates a more positive supposition about the phone than the sentence "the phone is great". A related past work [14] has additionally inferred that "Adverb+Adjective" consolidate creates preferred results over utilizing modifiers alone. Subsequently we favored the "adverb+adjective" consolidate over removing "descriptive word" alone. The adverbs are usually used as complements or modifiers. Few more examples of adverb usage are: he ran quickly, only adults, very dangerous trip, very nicely, rarely bad, rarely good etc. In all these examples adverbs modify the adjectives. Though adverbs are of various kinds, but for sentiment classification only adjectives of degree seem useful.

Some past works have recommended misusing the "verb" POS labels in addition to ‘adjective’ for sentiment classification. Here, we have investigated with two semantic highlight determination plans. In one we only concentrate ‘adjectives’ and any ‘adverbs’ going before the selected adjective. In the other one we seperate both ‘adjectives’ and ‘verbs’, along with any ‘adverbs’ going before them. Since, adverbs are changing the scores of succeeding terms, it needs to be chosen as to what extent the sentiment score of an ‘adverb’ should change the succeeding ‘adjective’ or ‘verb’ sentiment score, to obtain higher accuracy. We have chosed the modifying weightage (scaling factor) of adverb score as 0.35, in view on the conclusions reported in [14] and [11]. The other fundamental issue that remains to be addressed is how should the sentiment scores of chosed ‘adverb+adjective’ and ‘adverb+verb’ consolidated be aggregated. For this we have attempted different factors of weight ranging from 10% to 100%, i.e. the ‘adverb+verb’ scores are combined to ‘adverb+adjective’ scores in a weighted way.

In the first plan of utilizing only ‘adverb+adjective’ join, we have picked a scaling element sf = 0.35. This is proportionate to giving just 35% weight to adverb scores. The changes in adjective scores are thus in a fixed proportion to adverb scores. Since we picked a value of scaling variable sf = 0.35, the adjective scores will get a higher priority in the consolidated score. The demonstrative pseudo-code of key steps for this plan i.e. SentiWordNet (AAC) is illustrated below. Here AAC refers to Adverb+Adjective Combine.

```
For each sentence, extract adv+adj combines.
For each extracted adv+adj combine do:
• If adj score=0, ignore it.
• If adv is affirmative, then
  o If score(adj)>0
    ▪ fs_AAC (adv,adj)= min(1,score(adj)+sf*score(adv))
  o If score(adj)<0
    ▪ fs_AAC (adv,adj)= min(1,score(adj)-sf*score(adv))
• If adv is negative, then
  o If score(adj)>0
    ▪ fs_AAC(adv,adj)= max(-1,score(adj)+sf*score(adv))
  o If score(adj)<0
    ▪ fs_AAC(adv,adj)= max(-1,score(adj)-sf*score(adv))
```

Here, adj refers to adjectives and adv refers to adverbs. The last sentiment values (fsAAC) are scaled form of adverb and adjective SentiWordNet scores, where the adverb score is given 35% weightage. The presence of 'Not' is taken care by negating the scores obtained. First of all we picked sentence boundaries of a review and then we process all the sentences. For every sentence we picked the adv+adj joins and then compute their sentiment scores according the scheme described in the 713 pseudo-code. The final document sentiment score is an addition of sentiment scores for every sentences occurring in it. The score value decided the polarity of the review.

```
For each sentence, extract adv+adj and adv+verb combines.
1. For each extracted adv+adj combine do:
• If adj score=0, ignore it.
• If adv is affirmative, then
  o If score(adj)>0
    ▪ f(adv,adj)= min(1,score(adj)+sf*score(adv))
  o If score(adj)<0
    ▪ f(adv,adj)= min(1,score(adj)-sf*score(adv))
• If adv is negative, then
  o If score(adj)>0
    ▪ f(adv,adj)= max(-1,score(adj)+sf*score(adv))
  o If score(adj)<0
  o f(adv,adj)= max(-1,score(adj)-sf*score(adv))
2. For each extracted adv+verb combine do:
    ▪ If verb score=0, ignore it.
    ▪ If adv is affirmative, then
      • If score(verb)>0
        o f(adv,verb)= min(1,score(verb)+sf*score(adv))
      • If score(verb)<0
        o f(adv,verb)= min(1,score(verb)-sf*score(adv))
    ▪ If adv is negative, then
      • If score(verb)>0
        o f(adv,verb)= max(-1,score(verb)+sf*score(adv))
      • If score(verb)<0
        o f(adv,verb)= max(-1,score(verb)-sf*score(adv))
3. f_AAAVC(sentence)=f(adv,adj)+0.3*f(adv,verb)
```

The second usage that we attempted joins both 'adverb+adjective' and 'adverb+verb' sentiment scores. It is same like to the previous scheme in its method of joining adverbs with adjectives or verbs, but it differs in the logic that it counts both adjectives and verbs for chosing the overall sentiment score. We have tried with different aggregation weights for adjective and verb scores and conclud that 30% weight for verb score produces best precision levels. The occurrence of 'not' has been handled in a similar manner as in previous scheme. The indicative pseudo-code of key steps for this scheme, i.e., SentiWordNet (AAAVC) is illustrated below. Here AAAVC refers to Adverb+Adjective and Adverv+Verb Combine.

In this scheme, we compute sentiment score for all 'adverb+adjective' and 'adverb+verb' combines in a sentence and aggregate them together. This is done for all sentences and the document-level sentiment polarity value is determined based on the aggregated sentiment score of the review document.

4. ASPECT-LEVEL SENTIMENT ANALYSIS

The document-level sentiment classification is a reasonable measure of positivity or negativity expressed in a review. However, in selected domains it may be a good idea to explore the sentiment of the reviewer about various aspects of the item in that domain, expressed in that review. Moreover, practically most of the reviews have mixture of positive and negative sentiment about different aspects of the item and it may be difficult and inappropriate to insist on an overall document-level sentiment polarity expressed in a review for the item. Thus, the document-level sentiment classification is not a complete, suitable and comprehensive measure for detailed analysis of positive and negative aspects of the item under review. The aspect-level sentiment analysis allows us to analyze the positive and negative aspects of an item. However, this kind of analysis is often domain specific. The aspect-level sentiment analysis involves the following: (a) identifying which aspects are to be analyzed, (b) locating the opinionated content about that aspect in the review, and (c) determining the sentiment polarity of views expressed about an aspect.

Since we are restricted to phone reviews, a focused domain, we tried to explore the aspect-level sentiment analysis of the phone reviews. The first step was to identify which aspects are worth considering in phone domain. We made an extensive search for identifying the aspects in different phone review sites and phone magazines and worked out a list of aspects. Since a particular aspect is expressed by different words (such as screen size, looks, pricing) by users, we created an aspect-vector for all aspects under consideration. Another example is use of words like camera, audio, volume while referring to multimedia component of a phone. After creating aspect vectors, we parse a review sentence-by-sentence. For each sentence, we look for presence of opinion about an aspect. If there is one, we use the SentiWordNet based approach to

determine its sentiment polarity. This is done for all the sentences in a review and subsequently for all reviews of a phone. The scores for a particular aspect from all the reviews of a phone are aggregated to obtain an opinionated analysis of that aspect.

The sentiment analysis around aspects thus first locates an opinionated content about an aspect in a review and then uses the SentiWordNet based approach to compute its sentiment polarity. We used the SentiWordNet (AAC) scheme for this purpose. When an aspect indicating term (those terms that belong to the aspect vector created in the beginning) is located, we first lookup up to 5-gram backward for occurrence of adjectives or adverb+adjective combines. If no such term is found, we search up to 5-gram forward for their occurrence. In both cases the lookup terminates at 5-gram or sentence boundary whichever is encountered first. Then the sentiment polarity for these terms is computed using the SentiWordNet based formulation for AAC, described earlier.

5. APPROACH

In this section we quickly describe procedures and objectives of this study and we aim to succeed as a result. This study sorted into three stages. Initial phase is the web page crawling phase,in which data is collected from mobile phone review websites. The second stage is the dissecting phase, in which the data is parsed, pprepared and dissected to concentrate valuable information. The third stage is the visualization phase, in which the information is visualized to better understand the results.

6. COLLECTING DATASETS

We have collected 200 reviews each for 200 mobile phones from the popular mobile phone review database website www.gsmarena.com[15].We have labeled all these reviews manually to evaluate performance of implemented algorithmic formulations. Out of 50000 phone reviews collected, 32000 are labeled positive and 18000 are labeled as negative reviews.

7. PERFORMANCE EVALUATION

Keeping in mind the end goal to assess the exactness and execution of our algorithmic definitions, we processed the standard execution measurements of Accuracy, Precision, Recall and Fmeasure. The measure of Accuracy An utilized by us is:

$$A = \frac{\text{Number of Correctly Classified Documents}}{\text{Total Number of Documents}} \quad (1)$$

The equation for F-Measure Fused by us is as follows:

$$Precision\ (l,c) = n_{lc}/n_c \quad (2)$$

$$Recall\ (l,c) = n_{lc}/n_l \quad (3)$$

$$F(l,c) = \frac{2*Recall(l,c)*Precision(l,c)}{Precision(l,c)+Recall(l,c)} \quad (4)$$

$$Overall\ F = \sum_l \frac{n_l}{n} \max\{F(l,c)\} \quad (5)$$

where Nlc is a number of documents with original label l in classified label c;nc is number of documents classified as c and nl is number of documents in original class with label l. The equation for Entropy E used by us is following:

$$E_c = -\sum_l P(l,c) * \log(P(l,c)) \quad (6)$$

$$Overall\ E = \sum_c \frac{n_c * E_c}{n} \quad (7)$$

where, P(l,c) is the probability of documents of characterized class with name c belongs to original class with name l, and n is aggregate number of documents. As we can see from the comparisons above, exactness is measured in rate, though Precision, Recall and F-measure metric qualities range from 0 – 1. A littler worth for entropy metric is a marker of good execution of the calculation. We have additionally assessed slant aftereffects of our information utilizing the Alchemy API [16], to analyze the execution of our calculation.

8. RESULTS

We have explored diverse linguistic highlight selection, weighing and total schemes. For document-level sentiment characterization, we used the SWN (AAC) and SWN (AAAVC) plans. We calculated result of document level sentiment classification of the info collected using both these plans and also using Alchemy API. Table I intorduces the values of performance measurements obtained for our own execution formulaes and Alchemy API.

TABLE I. PERFORMANCE VALUES ON PHONE REVIEW DATASET

Method	Performance measure	Value
SWN (AAC)	Accuracy	77.6%
	F-measure	0.7642532
	Entropy	0.21800485
SWN (AAAVC)	Accuracy	78.7%
	F-measure	0.7737450 6
	Entropy	0.21472746
Alchemy API	Accuracy	77.4%
	F-measure	0.7778397
	Entropy	0.2068102

The table 1 introduces an examination of the conclusion name assignments by our algorithmic plans and the Alchemy API with physically marked information. We can see that out of aggregate number of 32000 real positive reviews, SWN (AAC) marks 29000 as positive, SWN (AAAVC) names 31500 and Alchemy API marks 33521 as positive. Additionally out of 18000 real negative reviews, the three algorithmic details name negative 17600, 16760 and 18000 reviews, separately. The table III presents the rate insightful notion mark task measurements by the three algorithmic plans. As should be obvious from the table, out of 50000 aggregate reviews, the SWN (AAC) marks 82% as positive, SWN (AAAVC) names 82.9% as positive and Alchemy API names 73.4% as positive. So also out of aggregate 50000 reviews, the three algorithmic definitions name negative 18%, 17.1% and 26.6% reviews, individually.

Method	*Phone Review Dataset*	
SWN (AAC)	POS	82%
	NEG	18%
SWN (AAAVC)	POS	82.9%
	NEG	17.1%
Alchemy API	POS	73.4%
	NEG	26.6%

As mentioned earlier, we have explored utilizing different weightage variables for adding the 'adverb+verb' sentiment scores to 'adverb+adjective' sentiment scores. We attempted with distinctive values for weightage variables for 'adverb+verb' consolidate from 10% to 100%.

The document-level sentiment classification results obtained by our algorithmic formual are not only accurate as compared to actual sentiment labels, but are also comparable to the results obtained by Alchemy API. Among the all three methods, SWN (AAAVC) produces the most exact results with verb score weightage factor of 30%. The SWN (AAC) strategy is closer to the performance level of SWN (AAAVC), but it's the later method which has a marginal edge

9. CONCLUSION & OBSERVATION

The document-level plans executed by us include utilization of 'Adverb+Adjective' consolidate only, and utilization of 'Adverb+Verb' combined with the 'Adverb+Adjective' combination. This is done to explore the opinionated value of distinctive linguistic features of a review and discovering a way As a result, many of the sentiment calculation were highly influenced by the tacit assumption is that a review describes about only best aggregate all the opinionated information in a review together to produce the document level sentiment summary. The results demonstrate that joining the sentiment score of 'Adverb+Verb' joins to the commonly used 'Adverb+Adjective' joined further improves the accuracy of sentiment analysis result. The best weightage factor for verb scores got through multiple experimental runs is 30%.

The aspect-level sentiment analysis algorithmic formulation designed by us is a novel and unique way of obtaining a complete sentiment profile of a phone from multiple reviews on different aspects of evaluation. The resultant sentiment profile is informative, easy to understand, and extremely useful for users. Moreover, the algorithmic formulation used for aspect-level sentiment profile is very simple, quick to implement, fast in producing results and does not require any previous training. It can be used on the run and produces very useful and detailed sentiment profile of a phone on different aspects of interest. This part of the implementation can also be used as an add-on step in phone recommendation systems that use content-filtering, collaborative-filtering or hybrid approaches. The sentiment profile can be used as an additional filtering step for designing appropriate phone recommender systems as explored earlier in [17] and [18]. This aspectlevel sentiment profiling is a valuable form of sentiment analysis and subsequent exploitation of information expressed by a large number of users about a particular phone. The only restriction with this aspect-level implementation is that it is domain specific. However, only little changes (in aspect vectors) would be required to use this algorithmic formulation in a different domain.

Our experimental work makes two important contributions. First, it explores the use of 'Adverb+Verb' combine with 'Adverb+Adjective' combine for document-level sentiment classification of a review. Second, it proposes a new feature-based heuristic scheme for aspect-level sentiment classification of a phone. The aspect level sentiment classification produces an accurate and easy to understand sentiment profile of a phone on various aspects of interest. Interestingly, the aspect-level sentiment profile result is congruent to the document level sentiment classification of reviews of a phone. Though, the aspect-level sentiment profile produces a more focused and accurate sentiment summary of a particular phone and is more useful for the users.

REFERENCES

[1] M.A. Hearst, "Untangling text data mining," Proceedings of the 37th annual meeting of the Association for Computational Linguistics on Computational Linguistics, 1999, pp. 3-10.

[2] D.J. Orre, P. Gerstl, and R. Seiffert, "Text mining: finding nuggets in mountains of textual data," Proceedings of the fifth ACM SIGKDD international conference on Knowledge discovery and data mining, 1999, pp. 398-401.

[3] P. Falinouss, "Stock trend prediction using news articles: a text mining approach," Lule{å} tekniska universitet, 2007.

[4] M. Sharp, "Text mining," Rutgers University, School of Communication, Information and Library Studies, Allen, J. Natural Language Understanding, Second Edition. Redwood City, CA: Benjamin/Cummings, 2001, pp. 1-12.

[5] A. Khan, B. Baharudin, L.H. Lee, and K. Khan, "A Review of Machine Learning Algorithms for Text-Documents Classification," Journal of Advances in Information Technology, vol. 1, 2010, pp. 4-20.

[6] A. Khan, B. Baharudin, and K. Khan, "Sentiment Classification from Online Customer Reviews Using Lexical Contextual Sentence Structure," Communications in Computer and Information Science, Software Engineering and Computer Systems,, Springer Verlag, 2011, pp. 317-331.

[7] S. Chakrabarti, "Data mining for hypertext: A tutorial survey," ACM SIGKDD Explorations Newsletter, vol. 1, 2000, pp. 1-11.

[8] R. Kosala and H. Blockeel, "Web mining research: A survey," ACM SIGKDD Explorations Newsletter, vol. 2, 2000, pp. 1-15.

[9] J.M. Wiebe, "Tracking point of view in narrative," Internation Journal of Computational Linguistics, vol. 20, 1994, pp. 233-287.

[10] J. Wiebe, T. Wilson, R. Bruce, M. Bell, and M. Martin, "Learning subjective language," Internation Journal of Computational linguistics, vol. 30, 2004, pp. 277-308.

[11] J. Wiebe and E. Riloff, "Creating subjective and objective sentence classifiers from unannotated texts," Computational Linguistics and Intelligent Text Processing, 2005, pp. 486-497.

[12] J.M. Wiebe, "Learning subjective adjectives from corpora," Proceedings of the National Conference on Artificial Intelligence, 2000, pp. 735-741.

[13] B. Pang and L. Lee, "Opinion mining and sentiment analysis," Foundations and Trends Int. J Comp Sci. Emerging Tech Vol-2 No 4 August, 2011 550 in Information Retrieval, vol. 2, 2008, pp. 1-135.

[14] B. Pang, L. Lee, and S. Vaithyanathan, "Thumbs up: sentiment classification using machine learning techniques," Proceedings of the ACL-02 conference on Empirical methods in natural language processing-Volume 10, 2002, pp. 79-86.

[15] S.M. Kim and E. Hovy, "Determining the sentiment of opinions," Proceedings of the 20th international conference on Computational Linguistics, 2004, pp. 1367-1374.

[16] J.M. Wiebe, "Identifying subjective characters in narrative," Proceedings of the 13th conference on Computational linguistics-Volume 2, 1990, pp. 401-406.

[17] A. Esuli and F. Sebastiani, "Determining term subjectivity and term orientation for opinion mining," Proceedings the 11th Meeting of the European Chapter of the Association for Computational Linguistics (EACL-2006), 2006, pp. 193-200.

[18] S.M. Kim and E. Hovy, "Automatic detection of opinion bearing words and sentences," Companion Volume to the Proceedings of the International Joint Conference on Natural Language Processing (IJCNLP), 2005, pp. 61-66.

[19] S. Bethard, H. Yu, A. Thornton, V. Hatzivassiloglou, and D. Jurafsky, "Automatic extraction of opinion propositions and their holders," 2004 AAAI Spring Symposium on Exploring Attitude and Affect in Text, 2004, pp. 2224-2236.

[20] P. Turney, "Thumbs up or thumbs down? Semantic orientation applied to unsupervised classification of reviews," Proceedings of the 40th Annual Meeting of the Association for Computational Linguistics (ACL'02), 2002, pp. 417-424.

[21] S. Argamon, K. Bloom, A. Esuli, and F. Sebastiani, "Automatically determining attitude type and force for sentiment analysis," Human Language Technology. Challenges of the Information Society, 2009, pp. 218-231.

[22] L. Polanyi and A. Zaenen, "Contextual valence shifters," Computing attitude and affect in text: Theory and applications, 2006, pp. 1-10.

[23] S. Hariharan, R. Srimathi, M. Sivasubramanian, and S. Pavithra, "Opinion mining and summarization of reviews in web forums," Proceedings of the Third Annual ACM Bangalore Conference, 2010, pp. 1-4.

[24] C.W.K. Leung and S.C.F. Chan, "Sentiment Analysis of Product Reviews," Encyclopedia of Data Warehousing and Mining Information Science Reference,, 2008, pp. 1794-1799.

[25] A. Andreevskaia and S. Bergler, "Mining WordNet for fuzzy sentiment: Sentiment tag extraction from WordNet glosses," Proceedings of EACL, 2006, pp. 209-216.

[26] M. Koppel and J. Schler, "The importance of neutral examples for learning sentiment," Computational Intelligence, vol. 22, 2006, pp. 100-109.

[27] T. Zagibalov and J. Carroll, "Unsupervised classification of sentiment and objectivity in Chinese text," IJCNLP, 2008, pp. 304-311.

[28] B. Pang and L. Lee, "Seeing stars: Exploiting class relationships for sentiment categorization with respect to rating scales," Proceedings of the ACL, 2005, pp. 115-124.

[29] A.B. Goldberg and X. Zhu, "Seeing stars when there aren't many stars: Graph-based semi-supervised learning for sentiment categorization," Proceedings of the First Workshop on Graph Based Methods for Natural Language Processing, 2006, pp. 45-52.

[30] X. Zhu and A.B. Goldberg, "Kernel regression with order preferences," PROCEEDINGS OF THE NATIONAL CONFERENCE ON ARTIFICIAL INTELLIGENCE, 2007, pp. 681-686.

[31] A. Andreevskaia and S. Bergler, "When specialists and generalists work together: Overcoming domain dependence in sentiment tagging," Proceedings of ACL-08: HLT, 2008, pp. 290-298.

[32] C.W.K. Leung, S.C.F. Chan, and F. Chung, "Integrating collaborative filtering and sentiment analysis: A rating inference approach," Proceedings of The ECAI 2006 Workshop on Recommender Systems, 2006, pp. 62-66.

[33] P.D. Turney, "Mining the web for lexical knowledge to improve keyphrase extraction: Learning from labeled and unlabeled data," Int. J Comp Sci. Emerging Tech Vol-2 No 4 August, 2011 551 Journal of Artificial Intelligence Research, Arxiv preprint cs/0212011, 2002, pp. 1-34.

[34] A. Esuli and F. Sebastiani, "Determining the semantic orientation of terms through gloss classification," Proceedings of the 14th ACM international conference on Information and knowledge management, 2005, pp. 617-624.

[35] C.O. Alm, D. Roth, and R. Sproat, "Emotions from text: machine learning for text-based emotion prediction," Proceedings of the conference on Human Language Technology and Empirical Methods in Natural Language Processing, 2005, pp. 579-586.

[36] T. Wilson, J. Wiebe, and P. Hoffmann, "Recognizing contextual polarity in phrase-level sentiment analysis," Proceedings of the conference on Human Language Technology and Empirical Methods in Natural Language Processing, 2005, pp. 347-354.

[37] http://google.com

[38] http://sentiwordnet.isti.cnr.it

[39] http://www.sentiwordnet.isti.cnr.it

[40] http://www.gsmarena.com

Circuits and Systems, 2015, 6, 237-251
Published Online November 2015 in SciRes. http://www.scirp.org/journal/cs
http://dx.doi.org/10.4236/cs.2015.611024

Single CDBA Based Voltage Mode Bistable Multivibrator and Its Applications

Rishi Pal[1], Rajeshwari Pandey[2*], Neeta Pandey[2], Ramesh Chandra Tiwari[1]

[1]Department of Physics, Mizoram University, Aizawl, India
[2]Department of Electronics and Communication Engineering, Delhi Technological University, Delhi, India
Email: rishi.dcp@gmail.com, *rpandey@dce.ac.in, neetapandey@dce.ac.in, ramesh_mzu@rediffmail.com

Received 19 September 2015; accepted 13 November 2015; published 16 November 2015

Copyright © 2015 by authors and Scientific Research Publishing Inc.
This work is licensed under the Creative Commons Attribution International License (CC BY).
http://creativecommons.org/licenses/by/4.0/
Open Access

Abstract

In this paper, current differencing buffered amplifier (CDBA) based bistable multivibrators are introduced. Each presented circuit is constructed using single CDBA as the basic active building block and three resistors. Two applications namely an astable and a monostable multivibrator are also realized to demonstrate the usefulness of the proposed bistable multivibrators. The presented circuits are simulated using PSPICE from Cadence Orcad16.2 to verify their functionality. Simulation results agree well with the theoretical analysis.

Keywords

Schmitt Trigger, Bistable Multivibrator, CDBA, Monostable Multivibrator

1. Introduction

Inherent wide bandwidth which is virtually independent of closed loop gain, greater linearity, and large dynamic range are the key performance features of current mode technique [1]. The CDBA is one such active element which inherits these advantages. In addition, it is free from parasitic capacitances [2] and hence is appropriate for high frequency operation. It provides further flexibility to the designers, enabling a variety of circuit designs, as it can operate in both current and voltage mode [3].

Bistable multivibrator, commonly known as Schmitt trigger, finds extensive applications in the fields of communication systems, instrumentation measurement systems, and power conversion control circuits [4]. It is commonly employed in monostable multivibrator [4]-[7], square wave generator [8]-[12], pulse width modulator (PWM) [13] [14], etc. Several implementations of the Schmitt triggers using different high-performance active building blocks have been proposed in open literature [15]-[19]. Conventional voltage-mode bistable multi-

*Corresponding author.

How to cite this paper: Pal, R., Pandey, R., Pandey, N. and Tiwari, R.C. (2015) Single CDBA Based Voltage Mode Bistable Multivibrator and Its Applications. *Circuits and Systems*, **6**, 237-251. http://dx.doi.org/10.4236/cs.2015.611024

vibrators [15] employ an op-amp with a positive feedback. Current mode building blocks based voltage output bistable multivibrators are presented in [16]-[19]. Schmitt trigger based on two operational transconductance amplifiers (OTAs) and two resistors is presented in [16] wherein the output amplitude and threshold level can be independently/electronically tuned. Schmitt triggers based on current conveyors are presented in [17] [18] which use only single active element and their outputs are temperature-insensitive. Bistable multivibrator configurations using single operational transresistance amplifier (OTRA) are proposed in [19] which provide both Clockwise (CW) and counter clock wise (CCW) hysteresis functions. A compartaive statement of the existing voltage mode schmitt triggers is reported in **Table 1**.

It may be observed from the table that

- the op-amp based structures [15] though provide voltage output at appropriate impedance level yet the constant gain-bandwidth product and lower slew rate of the op-amps limit their high frequency operations.
- the structure proposed in [16] provides temperature sensitive output
- the configurations of [16]-[18] provide voltage output at high impedance and hence require a buffer to drive the voltage input circuits. This increases the component count in the circuit.
- the structures presented in [17] [18] provide only CW hysteresis
- the OTRA based structures[19] can be used both for voltage and current inputs, however output can be only voltage type
- the CDBA based structure provides further flexibility as it can be driven by both voltage and current inputs and can provide both voltage and current outputs

Above discussion suggests that CDBA based design is one of the most suitable choice. To the best of authors' knowledge no CDBA based schmitt trigger circuit is available in literature. Thus this paper aims at introducing new CW and CCW Schmitt Triggers, using single CDBA and three resistors which will provide further flexibility to circuit designers. The PSPICE simulation results are also shown, which are in correspondence to the theoretical analysis. To show the usefulness of the presented circuits, the applications of the Schmitt triggers as square wave/triangular wave generator and monostable multivibrator are introduced.

The remaining paper is organized as follows. In Section 2 the function of a CDBA is introduced followed by the description of proposed circuits. The PSPICE simulations and experimental results to investigate the circuit performances are presented in Section 3 which are in confirmation with the theoretical propositions. In Section 4, application examples of the proposed circuits are given. The concluding remarks are presented in Section 5.

2. Circuit Description

The circuit symbol of CDBA is shown in **Figure 1** and the port characteristics are given by Equation (1)

$$\begin{bmatrix} I_Z \\ V_W \\ V_p \\ V_n \end{bmatrix} = \begin{bmatrix} 0 & 0 & 1 & -1 \\ 1 & 0 & 0 & 0 \\ 0 & 0 & 0 & 0 \\ 0 & 0 & 0 & 0 \end{bmatrix} \begin{bmatrix} V_Z \\ I_W \\ I_p \\ I_n \end{bmatrix} \tag{1}$$

Table 1. Comparison of existing voltage mode schmitt triggers.

Ref.	No. of active blocks used	No. of passive components	Hysteresis type	Output type	Output Impedance	Temperature sensitivity
[15]	1 Op-amp	3R	CW, CCW	Voltage	Low	No
[16]	2 OTA	2R	CW	Voltage	High	Yes
[17]	1 CC II+	3R	CW	Voltage	High	No
[18]	1CC II	3R	CW	Voltage	high	No
[19]	1 OTRA	2R	CW, CCW	Voltage	Low	No
Proposed	1 CDBA	3R	CW, CCW	Voltage	Low	No

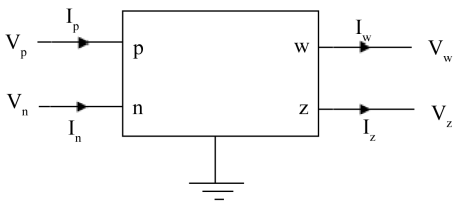


Figure 1. Block diagrammatic representation of CDBA.

2.1. The CW Schmitt Trigger

The proposed CW Schmitt Trigger configuration is shown in **Figure 2(a)**. The Input is provided through a small resistance R_1 at n terminal of the CDBA and output v_o is taken across w terminal. A high value resistance R_Z is connected at the z terminal of the CDBA which forces the circuit into saturation. Resistor R_2 forms a positive feedback loop to the 'p' input of the CDBA. Thus, the CDBA output saturates either at $+V_{sat}$, the positive saturation level or at the negative saturation level $-V_{sat}$. This circuit realizes the CW hysteresis characteristic as shown in **Figure 2(b)**.

For the CW hysteresis operation, the output V_o is initially assumed to be at the positive saturation level V_{sat}^{+}. The current I_p and I_n of CDBA are given by

$$I_p = \frac{V_o}{R_2} \tag{2}$$

$$I_n = \frac{V_i}{R_1} \tag{3}$$

As V_i increases from zero, V_o remains at V_{sat}^{+} until V_i reaches the upper threshold voltage V_{TH} thereby changing the output level from V_{sat}^{+} to V_{sat}^{-}. This output level is maintained as long as V_i is greater than the lower threshold voltage V_{TL}. Assuming that V_o is at V_{sat}^{+} and V_i is smaller than V_{TH} initially, I_p can be determined from Equation (3) as

$$I_p = \frac{V_{sat}^{+}}{R_2} \tag{4}$$

As v_i increases, current I_n gets closer to I_p and when I_n exceeds I_p, the output V_o switches to its negative saturation level V_{sat}^{-}. From Equations (3) and (4), the upper threshold voltage V_{TH} can be computed when I_p is equal to I_n and can be expressed as

$$V_{TH} = V_{sat}^{+}\frac{R_1}{R_2} \tag{5}$$

The current of p terminal can now be computed as

$$I_p = \frac{V_{sat}^{-}}{R_2} \tag{6}$$

However, I_n remains same as Equations (3). By equating I_p and I_n the lower threshold voltage V_{TL} can be determined as

$$V_{TL} = V_{sat}^{-}\frac{R_1}{R_2} \tag{7}$$

The output level will switch back to V_{sat}^{+} once I_p gets more positive than I_n.

2.2. The CCW Schmitt Trigger

The CCW Schmitt Trigger is shown in **Figure 3(a)** wherein, the input voltage is connected at p terminal of CDBA. The currents I_p and I_n can be computed as

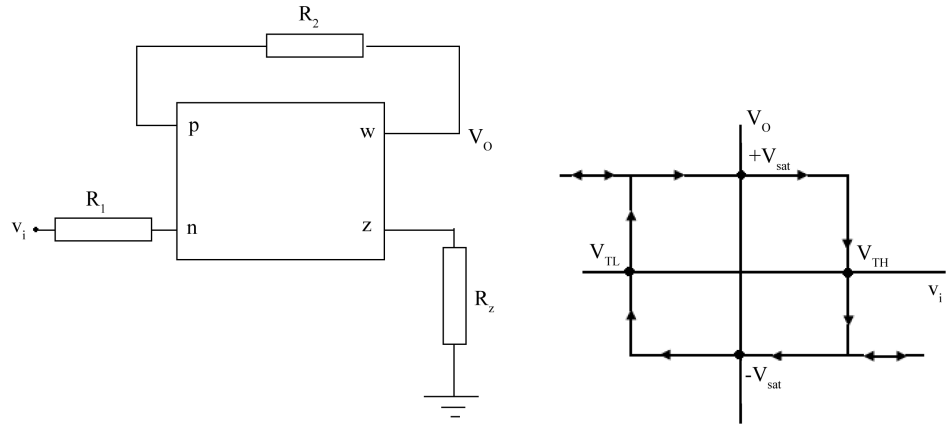


Figure 2. (a) CW Schmitt Trigger; (b) CW Hysteresis Curve.

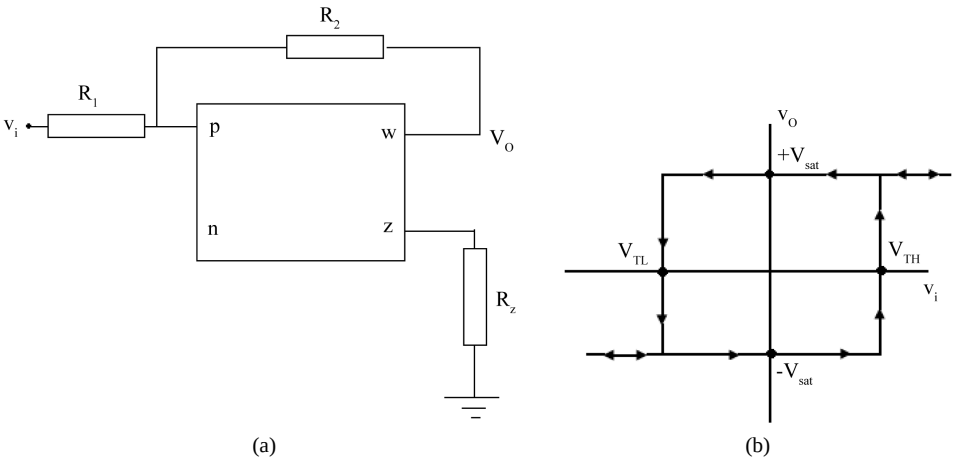


Figure 3. (a) CCW Schmitt Trigger; (b) CCW Hysteresis Curve.

$$I_p = \frac{V_i}{R_1} + \frac{V_o}{R_2} \tag{8}$$

$$I_n = 0 \tag{9}$$

Assuming that V_o is at V_{sat}^+ and V_i is initially larger than V_{TL}, then V_{TL} can be computed as

$$V_{TL} = V_{sat}^+ \frac{R_1}{R_2} \tag{10}$$

When V_i is smaller than V_{TL}, output V_o switches to V_{sat}^-. With increasing V_i, I_p also increases and forces the output to change its state when I_p exceeds I_n. The upper threshold voltage V_{TH} can thus be derived as

$$V_{TH} = V_{sat}^- \frac{R_1}{R_2} \tag{11}$$

Hysteresis Curve for CCW Schmitt Trigger is shown in **Figure 3(b)**.

2.3. Schmitt Trigger with Reference Voltage

For the circuits shown in **Figure 2(a)** and **Figure 3(a)** the $V_{TH} = -V_{TL}$ and hence the switching voltage (V_{ST}) defined as $(V_{TH} + V_{TL})/2$ is zero. Some applications require that V_{TH} and V_{TL} both should either be positive or nega-

tive resulting in finite value of V_{ST}. This can be accomplished by adding a reference voltage to the circuit of **Figure 2(a)** and **Figure 3(a)** which results in following four configurations

1. CW Schmitt Trigger with positive V_{ST}, shown in **Figure 4(a)**,
2. CW Schmitt Trigger with negative V_{ST}, depicted in **Figure 4(b)**,
3. CCW Schmitt Trigger with positive V_{ST}, given in **Figure 5(a)**,
4. CCW Schmitt Trigger with negative V_{ST}, shown in **Figure 5(b)**.

For the circuit of **Figure 4(a)** I_p and I_n are given as

$$I_p = \frac{V_o}{R_2} + \frac{V_{dc}}{R_s} \tag{12}$$

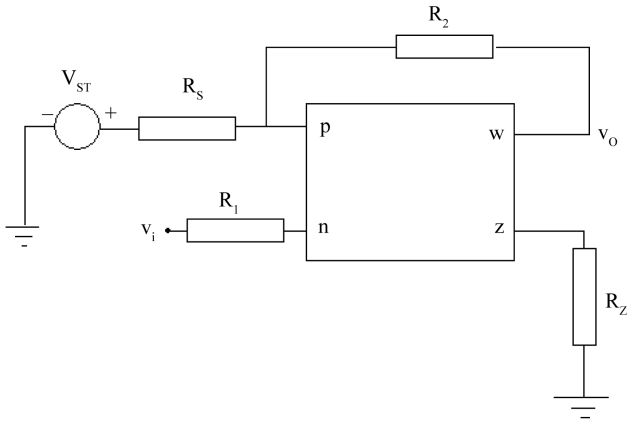
$$I_n = \frac{V_i}{R_1} \tag{13}$$

Using routine analysis the V_{TH} and V_{TL} can be computed as

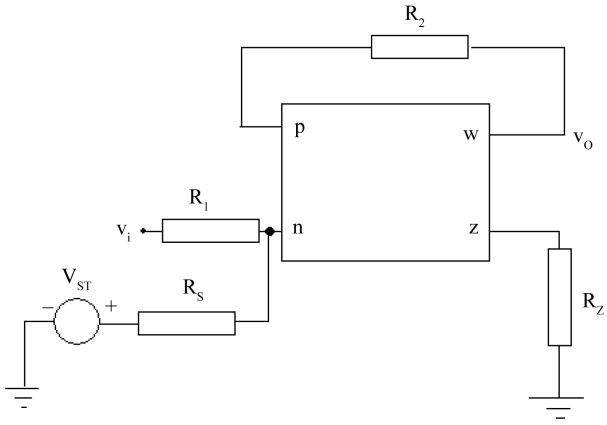
$$V_{TH} = V_{ST} + V_{sat}^{+} \frac{R_1}{R_2} \tag{14}$$

$$V_{TL} = V_{ST} + V_{sat}^{-} \frac{R_1}{R_2} \tag{15}$$

where

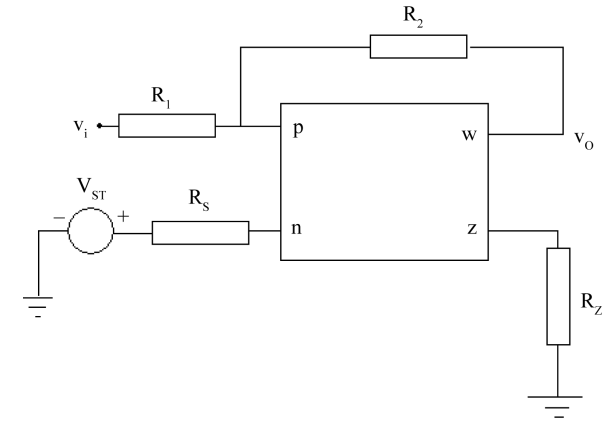


(a)

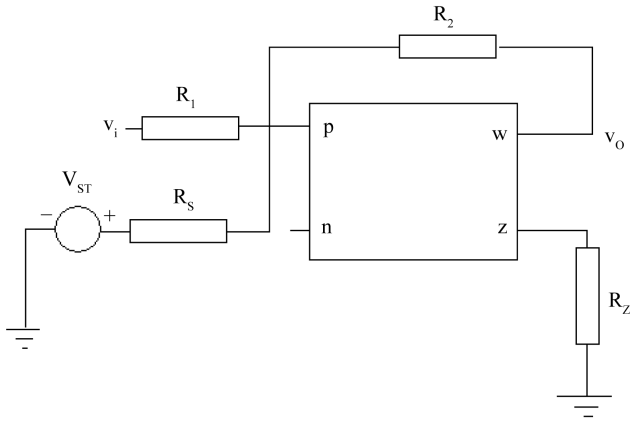


(b)

Figure 4. (a) CW Schmitt Trigger with positive V_{ST}; (b) CW Schmitt Trigger with negative V_{ST}.



(a)



(b)

Figure 5. (a) CCW Schmitt Trigger with positive V_{ST}; (b) CCW Schmitt Trigger with negative V_{ST}.

$$V_{ST} = \frac{R_1}{R_S} V_{dc} \tag{16}$$

Similarly the V_{TH} and V_{TL} for negative switching, as given in **Figure 4(b)**, can be derived as

$$V_{TH} = -V_{ST} + V_{sat}^{+} \frac{R_1}{R_2} \tag{17}$$

$$V_{TL} = -V_{ST} + V_{sat}^{-} \frac{R_1}{R_2} \tag{18}$$

For CCW Schmitt Trigger with positive switching voltage, the threshold voltages V_{TH} and V_{TL} are given by Equations (14) and (15) respectively whereas for CCW configuration with negative switching voltage are given in Equations (17) and (18) respectively.

3. Simulation and Experimental Results

To validate the theoretical predictions, the proposed bistable multivibrator circuits have been simulated using PSPICE. The CDBA is realized using current feedback operational amplifier (CFOA) IC AD 844 as shown in **Figure 6** [2]. PSPICE Macro model of CFOA IC AD 844AN [20] is used for simulations and supply voltages used are ±10 V.

Figure 7(a) shows the simulation results of CW Configuration for R_Z = 500 kΩ, R_1 = 5 kΩ, R_2 = 10 kΩ. The

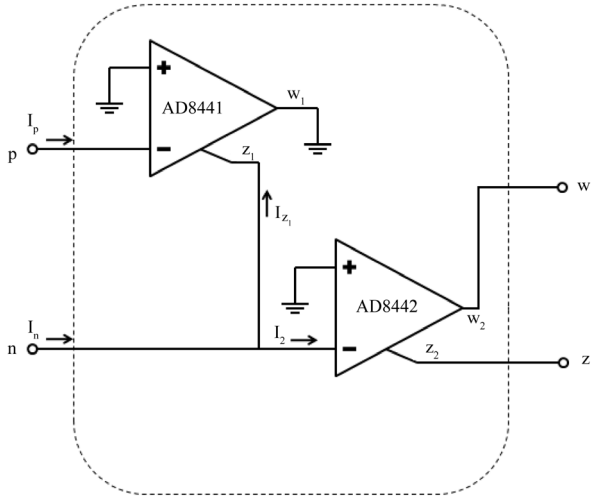
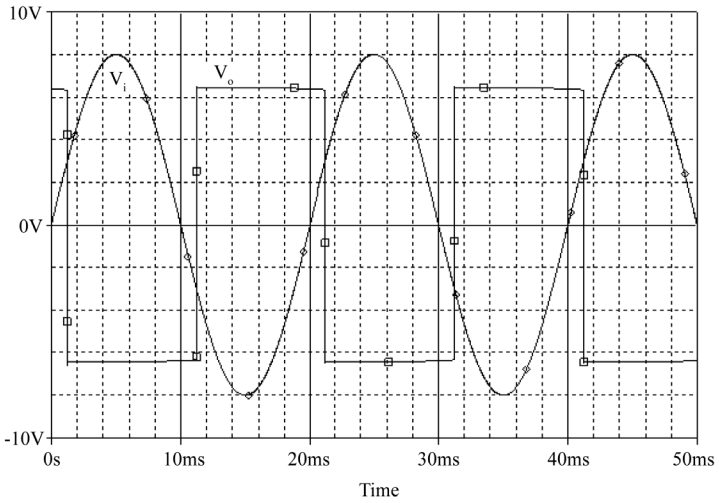
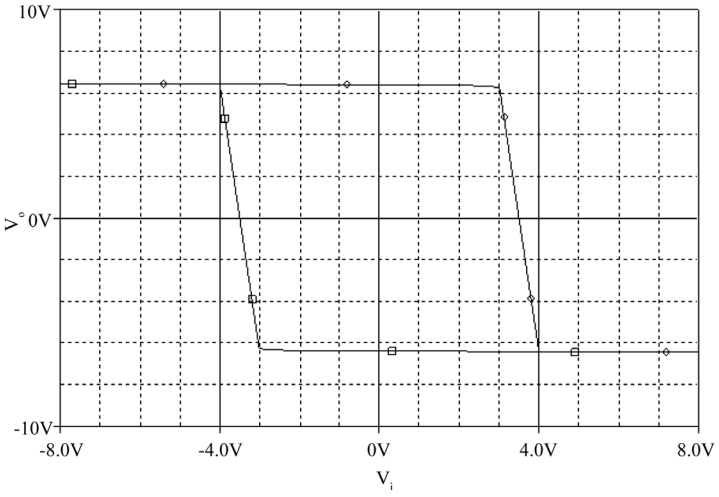


Figure 6. CFOA based implementation of CDBA [2].



(a)



(b)

Figure 7. (a) Output of the CW Schmitt Trigger; (b) CW Hysteresis Curve.

saturation levels are ±6.3 V. The input voltage is a 50 Hz sinusoid with signal swing from −8 V to +8 V. The simulated threshold levels are ±3 V which are in accordance with the theoretically computed value of ±3.15 V. **Figure 7(b)** shows the hysteresis curve for CW configuration. The results for CCW configuration are depicted in **Figure 8** wherein, the component values and supply voltages are chosen same as that for the CW operation.

The transient responses for CW and CCW configurations are shown in **Figure 9(a)** and **Figure 9(b)** respectively for an input frequency of 250 KHz.

The frequency response of CW Schmitt Trigger is shown in **Figure 10** having 3 dB bandwidth as 2.6 MHz.

Transient response for CCW for positive switching voltage is shown in **Figure 11(a)** for V_{TH} = 6 V and V_{TL} = 2 V and corresponding transfer characteristics is shown in **Figure 11(b)**. The component values are computed as R_Z = 500 kΩ, R_1 = 3.17 kΩ, R_S = 4.6 kΩ, R_2 = 10 kΩ and V_{dc} = 5 V. Transient response and hysteresis curve for CW configuration with negative switching voltage for V_{TH} = 6 V and V_{TL} = 2 V are shwon in **Figure 12(a)** and **Figure 12(b)** respectively. The simulated results are in close agreement with theoretical values for both the configurations.

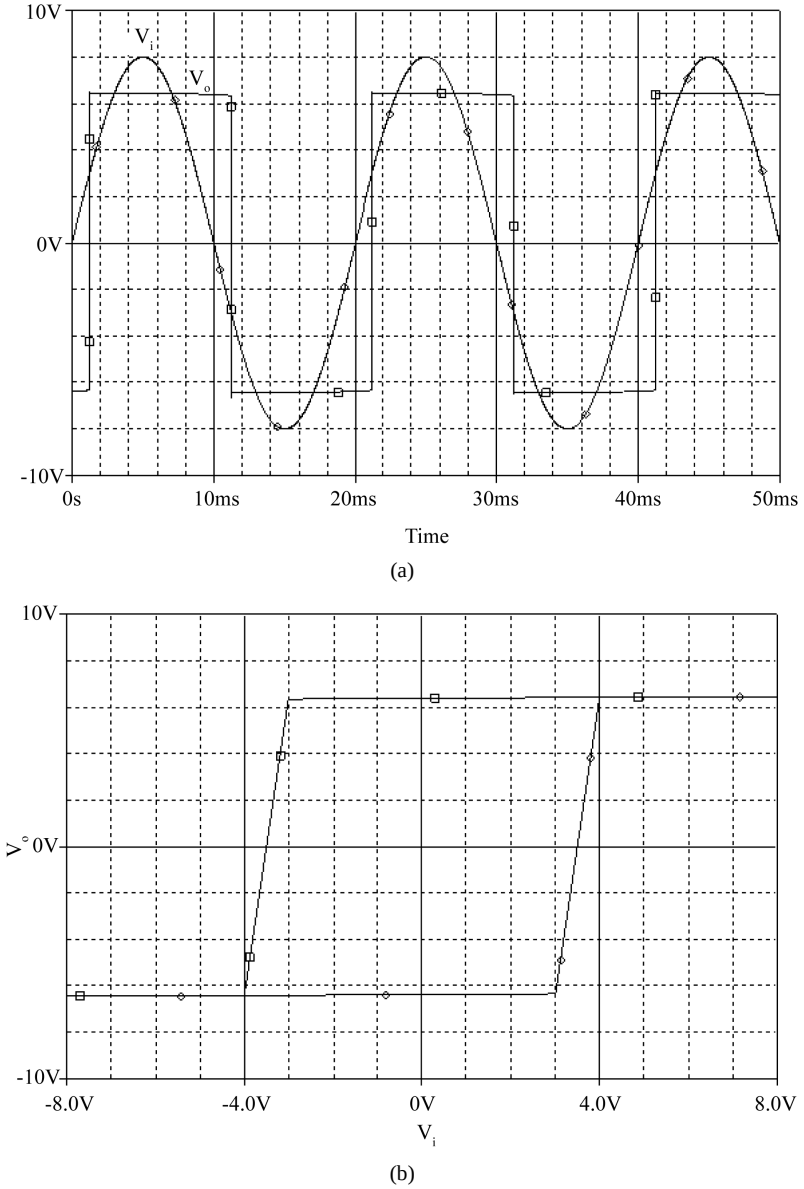
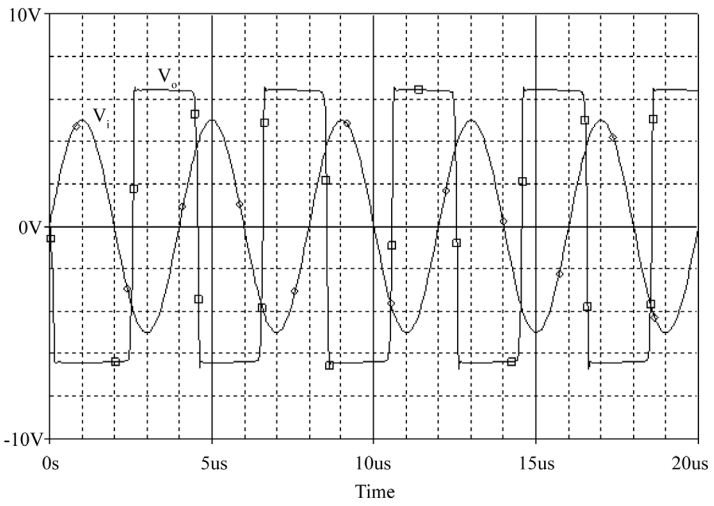
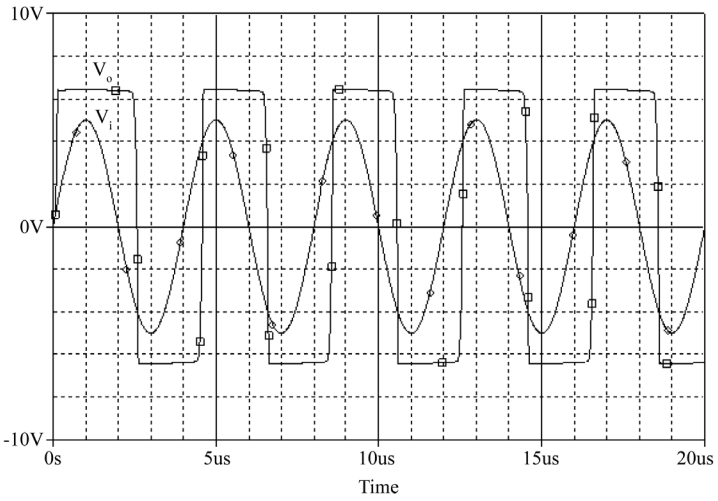


Figure 8. (a) Output of the CCW Schmitt Trigger; (b) CCW Hysteresis Curve.



(a)



(b)

Figure 9. Outputs for 250 KHz input signal (a) CW output; (b) CCW output.

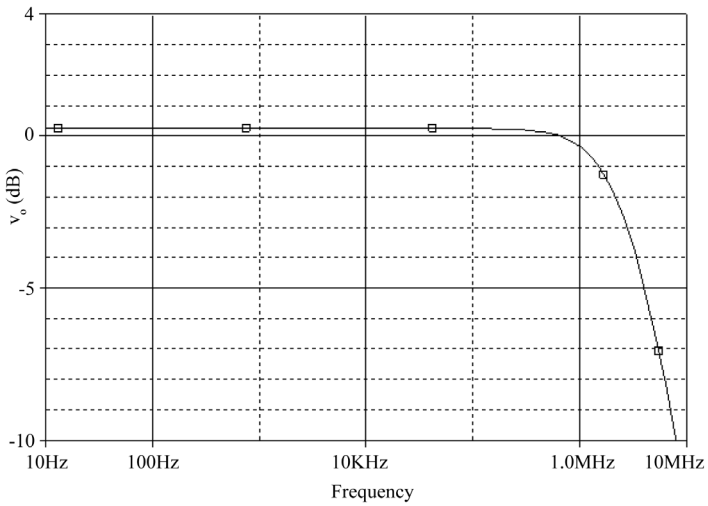


Figure 10. Frequency response of CW Schmitt Trigger.

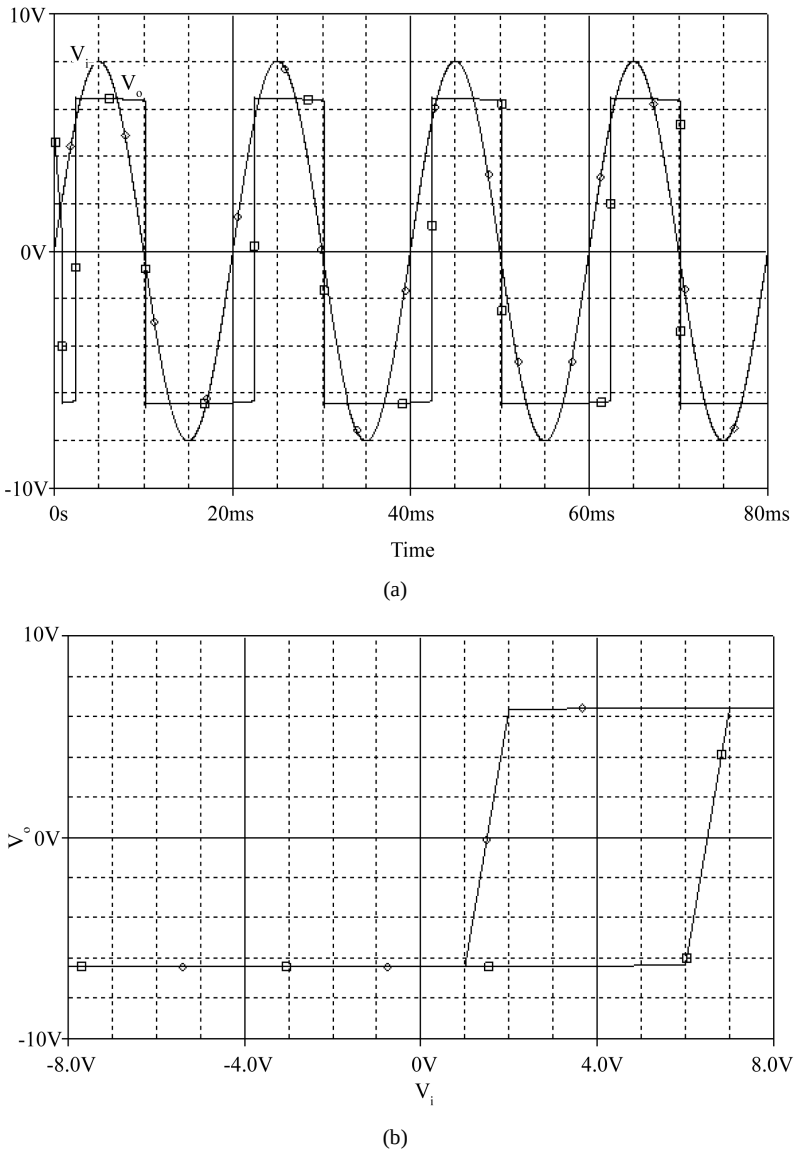
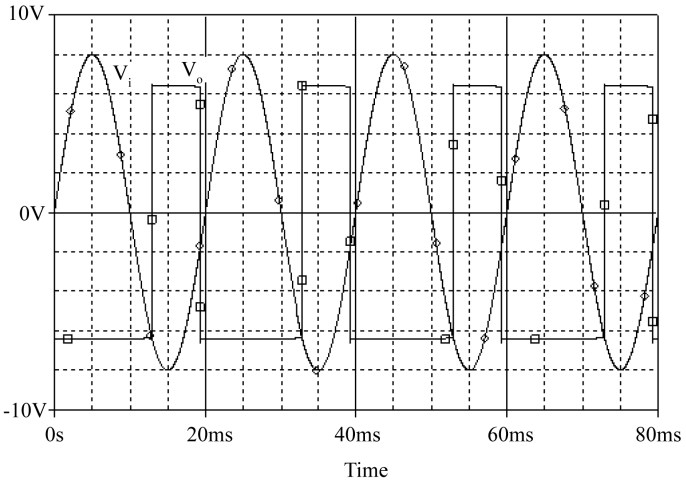


Figure 11. (a) CCW output with positive switching voltage; (b) CCW Hysteresis Curve with positive switching voltage.

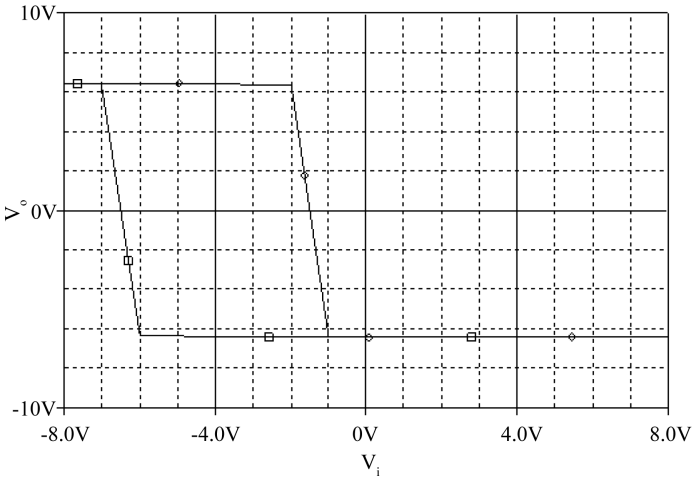
Figure 13(a) shows the experimental results of CW Configuration for R_Z = 100 kΩ, R_1 = 4.7 kΩ, R_2 = 4.7 kΩ with supply voltage of ±12 V. The saturation levels are ±10 V. The input voltage is a 1 KHz sinusoid with signal swing from −10 V to +10 V. The observed threshold levels are ±10 V which are same as the theoretically computed value. **Figure 13(b)** shows the hysteresis curve for CW configuration and the experimental output for CCW configuration for an applied input voltage of 6 KHz sinusoid with signal swing from −10 V to +10 V is presented in **Figure 13(c)**. The component values are chosen as R_Z = 100 kΩ, R_1 = 4.7 kΩ, R_2 = 4.7 kΩ and supply voltages are ±8 V. Observed saturation voltages are ±6 V giving threshold voltages as ±6 V and are equal to theoretical values.

4. Applications

In the following subsections two well known applications of Schmitt trigger namely triangular/square wave Generator and monostable multivibrators are developed to demonstarte the utility of proposed work in circuit applications.

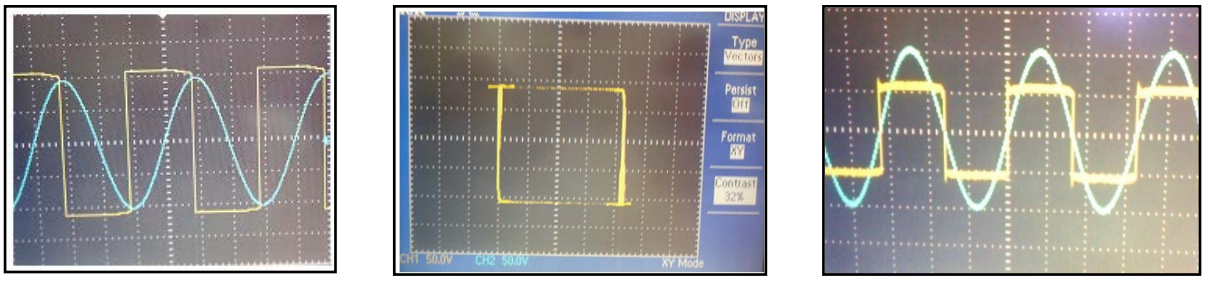


(a)



(b)

Figure 12. (a) CW output with negative switching voltage; (b) CW hysteresis curve with negative switching voltage.



(a) (b) (c)

Figure 13. Experimental results (a) output of CW Schmitt Trigger; (b) hysteresis curve for CW configuration; (c) output of CCW Schmitt Trigger.

4.1. Triangular/Square Wave Generator

The circuit of CDBA Schimitt trigger based triangular/square wave generator is shown in **Figure 14**. The circuit can be viewed as two cascaded blocks. The circuitry comprising of CDBA I is a Schmitt trigger, while the cir-

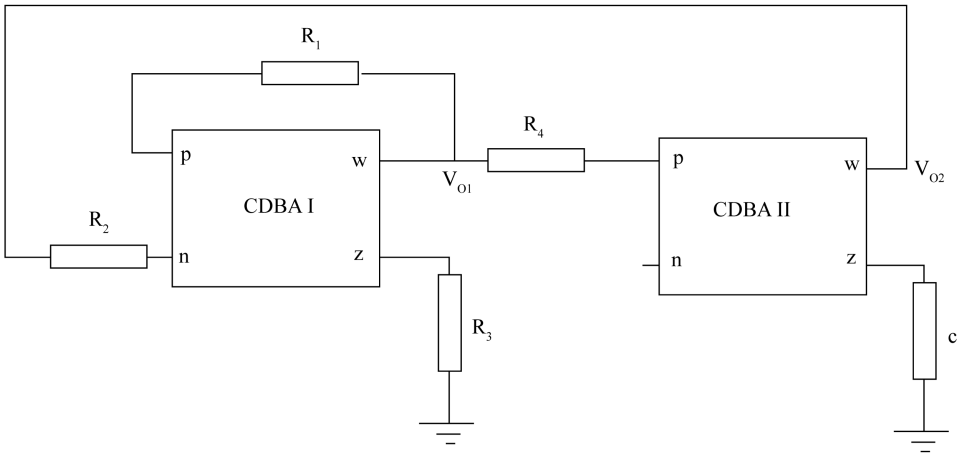


Figure 14. Triangular/square wave generator.

cuit comprising of CDBA II, is a simple integrator. The Schmitt trigger continuously compares the current I_{p1} and I_{n1} and accordingly the output V_{o1} swings repetitively between positive saturation level V_{sat}^{+} and negative saturation level V_{sat}^{-}. Assuming initially the output V_{o1} to be at V_{sat}^{+}, which is input to integrator, will charge the capacitor and would result in output voltage V_{o2} that is linearly rising. As a result the current I_{n1} will rise and when exceeds I_{p1} the output V_{o1} switches to V_{sat}^{-}. Now capacitor would begin to charge in opposite direction resulting in a negative ramp output at V_{o2}. As soon as I_{n1} falls below I_{p1}, V_{o1} switches back to V_{sat}^{+} and V_{o2} become a positive going ramp again. For Schmitt trigger the V_{TH} and V_{TL} can be computed as V_{sat}^{+} R_2/R_1 and V_{sat}^{-} R_2/R_1 respectively. Using the routine analysis the time period of the waveform can be computed as

$$T = 4V_{TH}R_4C/V_{sat}^{+} = 4R_2R_4C/R_1 \tag{19}$$

This gives frequency of oscillation as

$$f_o = 1/T = R_1/4R_2R_4C \tag{20}$$

The simulated square wave output V_{o1} and triangular output V_{o2} are shown in **Figure 15** for R_1 = 10 kΩ, R_2 = 100 Ω, R_3 = 20 kΩ, R_4 = 5 kΩ, and C = 1 μF.

4.2. Monostable Multivibrator

The realization of the monostable multivibrator is shown in **Figure 16**. The positive feedback loop is completed using the capacitor and a resistor. Under stable state the V_c is clamped by diode. To ensure the stable-state operation, R_Z must be high enough to make output voltage V_o switch to positive saturation level V_{sat}^{+}. Under sable state, ignoring the diode drop, the currents I_z and I_p are given by

$$I_Z = V_{sat}^{+}/R_Z \tag{21}$$

$$I_p = V_o/R_F = V_{sat}^{+}/R_F \tag{22}$$

Now if a positive-edge triggering signal I_{trig} is applied at terminal n of CDBA, the circuits enter into the quasi-stable State. As I_n is more positive than I_p the output voltage V_o jumps to V_{sat}^{-} and C starts to discharge through R_F. In the quasi-stable state, the expressions of I_p and I_z are given by

$$I_Z = V_Z/R_Z = V_{sat}^{-}/R_Z \tag{23}$$

$$I_p = \left(V_{sat}^{-} - V_C\right)/R_Z \tag{24}$$

And capacitor discharging equation can be expressed as

$$v_C = V_{sat}^{-}\left(1 - e^{-\left(\frac{t-T_1}{R_FC}\right)}\right) \tag{25}$$

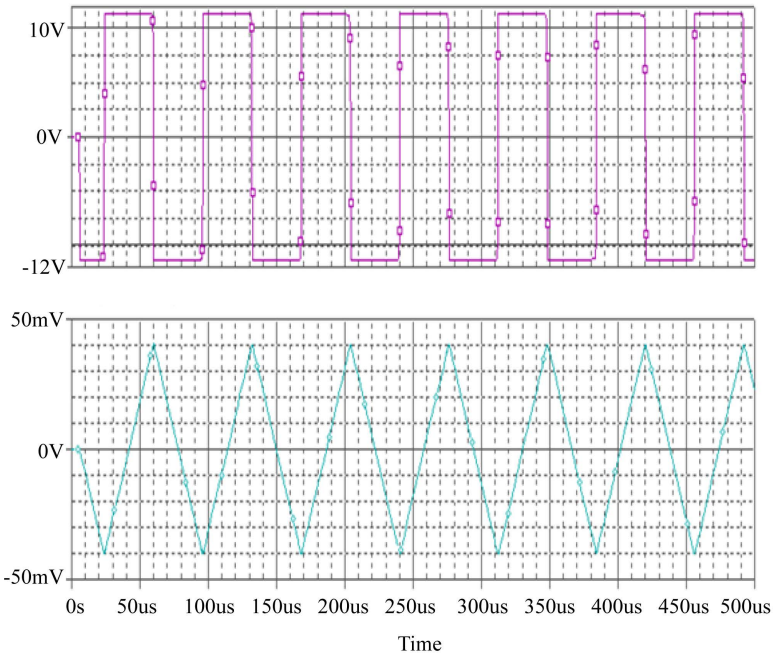


Figure 15. Output of triangular/square wave generator.

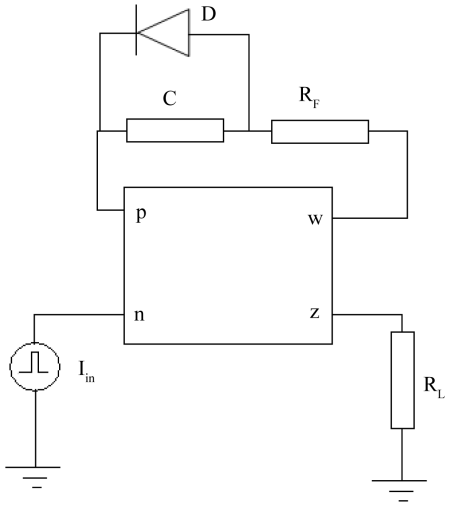


Figure 16. Monostable multivibrator.

at $t = T_2$ the capacitorvoltage reaches the threshold voltage V_{TL}, when output voltage switches back to V_{sat}^{+}. V_{TL} can be derived by equating Equations (23) and (24) and is given by

$$V_{TL} = V_{sat}^{-}\left(1 - R_F / R_Z\right) \tag{26}$$

From Equations (25) and (26) the pulse width T $(T_2 - T_1)$ for which the circuit remains in quasi stable sate can be computed as

$$T = R_F C \ln \frac{R_F}{R_Z} \tag{27}$$

Figure 17 shows the output of monostable multivibrator for R_F = 20 kΩ, R_Z = 500 kΩ, C = 10 nF having T = 59 μs as against calculated value of 64 μs.

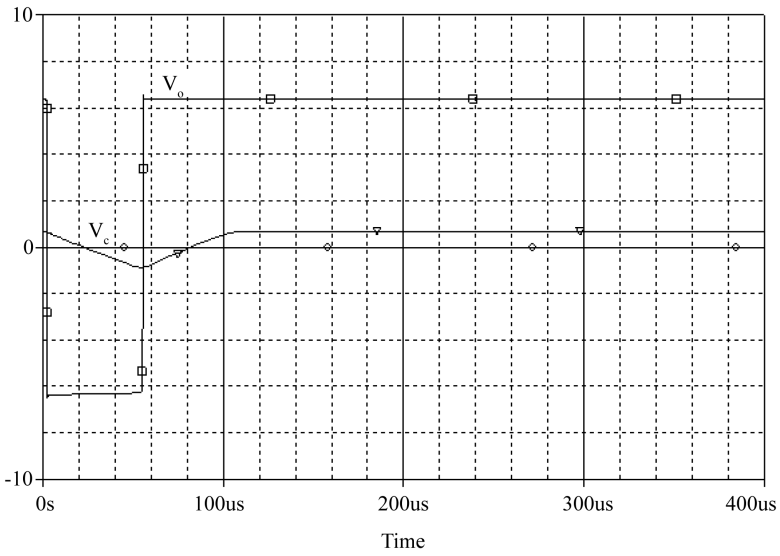


Figure 17. Output of monostable multivibrator.

5. Conclusion

In this paper single CDBA based bistable multivibrator configurations are proposed which include CW, CCW Schmitt Triggers with and without reference voltage. Two applications namely square wave/triangular wave generator and monostable multivibrator are realized to demonstrate the usefulness of the proposed bistable multivibrators. The simulation and experimental results are found to be in close agreement to theoretical predictions. The proposed configurations are one of the best choices for voltage mode applications. Also, due to inherent flexibility of signal usage in CDBA the proposed configurations can easily be extented to current/transimpedance/transadmittance mode depending upon the applications.

References

[1] Toumazou, C., Lidgey, F.J. and Haigh, D.G. (1990) Analogue IC Design: The Current Mode Approach. Peter Peregrinus Ltd., London.

[2] Acar, C. and Ozuguz, S. (1999) A New Versatile Building Block: Current Differencing Buffered Amplifier Suitable for Analog Signal Processing Filters. *Microelectronics Journal*, **30**, 157-160. http://dx.doi.org/10.1016/S0026-2692(98)00102-5

[3] Cakir, C. and Cicekoglu, O. (2008) Low-Voltage High-Performance CMOS Current Differencing Buffered Amplifier (CDBA). *Proceedings of IEEE PRIME Conference*, Istanbul, 22 June 2008-25 April 2008, 37-40. http://dx.doi.org/10.1109/rme.2008.4595719

[4] Chien, H.-C. and Lo, Y.-K. (2011) Design and Implementation of Monostable Multivibrators Employing Differential Voltage Current Conveyors. *Microelectronics Journal*, **42**, 1107-1115. http://dx.doi.org/10.1016/j.mejo.2011.07.005

[5] Chung, W.-S., Cha, H.-W. and Kim H.-J. (2002) Current-Controllable Monostable Multivibrator Using OTAs. *IEEE Transactions on Circuits and Systems I*, **49**, 703-705. http://dx.doi.org/10.1109/TCSI.2002.1001963

[6] Lo, Y.-K. and Chien, H.-C. (2006**)** Current-Mode Monostable Multivibrators Using OTRAs. *IEEE Transactions on Circuits and Systems II*: *Express Briefs*, **53**, 1274-1278. http://dx.doi.org/10.1109/TCSII.2006.882361

[7] Lo, Y.-K. and Chien, H.-C. (2007) Single OTRA-Based Current Mode Monostable Multivibrator with Two Triggering Modes and a Reduced Recovery Time. *IET Circuits, Devices & Systems*, **1**, 257-261. http://dx.doi.org/10.1049/iet-cds:20060359

[8] Almashary, B. and Alhokail, H. (2000) Current-Mode Triangular Wave Generator Using CCIIs. *Microelectronics Journal*, **31**, 239-243. http://dx.doi.org/10.1016/S0026-2692(99)00106-8

[9] Siripruchyanun, M. and Wardkein, P. (2001) Temperature Insensitive and Electronically Adjustable Square/Triangular Wave Generation Based on Novel Schmitt trigger Oscillator. *Proceedings of ISIC*2001 9*th International Symposium on Integrated Circuits, Devices and Systems*, 219-222.

[10] Hung, W.-S., Kim, H., Cha, H.-W. and Kim, H.-J. (2005) Triangular/Square-Wave Generator with Independently Controllable Frequency and Amplitude. *IEEE Transactions on Instrumentation and Measurement*, **54**, 105-109. http://dx.doi.org/10.1109/TIM.2004.840238

[11] Haque, A.S., Hossain, M.M., Davis, W.A., Russell, H.T. and Carter, R.L. (2008) Design of Sinusoidal, Triangular, and Square Wave Generator Using Current Feedback Operational Amplifier (CFOA). 2008 *IEEE Region* 5 *Conference*, Kansas City, 17-20 April 2008, 1-5. http://dx.doi.org/10.1109/tpsd.2008.4562735

[12] Pal, D., Srinivasulu, A., Demonsthenous, A., Pal, B.B. and Das, B.N. (2009) Current Conveyor-Based Square/Triangular Waveform Generators with Improved Linearity. *IEEE Transactions on Instrumentation and Measurement*, **58**, 2174-2180. http://dx.doi.org/10.1109/TIM.2008.2006729

[13] Siripruchyannun, M. and Wardkein, P. (2003) A Fully Independently Adjustable, Integrable Simple Current Controlled Oscillator and Derivative PWM Signal Generator. *The IEICE Transactions on Fundamentals of Electronics, Communications and Computer Sciences*, **E86-A**, 3119-3126.

[14] Kim, H., Kim, H.J. and Chung, W.S. (2007) Pulsewidth Modulation Circuits Using CMOS OTAs. *IEEE Transactions on Circuits and Systems I*: *Regular Papers*, **54**, 1869-1878. http://dx.doi.org/10.1109/TCSI.2007.904677

[15] Sedra, A.S. and Smith, K.C. (2004) Microelectronic Circuits. 4th Edition, Oxford University Press, New York.

[16] Kim, K., Cha, H.W. and Chung, W.S. (1997) OTA-R Schmitt Trigger with Independently Controllable Threshold and Output Voltage Levels. *Electronics Letters*, **33**, 1103-1105. http://dx.doi.org/10.1049/el:19970786

[17] Diutaldo, G., Palumbo, G. and Pennisi, S. (1995) A Schmitt Trigger by Means of a CCII+. *International Journal of Circuit Theory and Applications*, **23**, 161-165. http://dx.doi.org/10.1002/cta.4490230207

[18] Del, S.R., Marcellis, A.D., Ferri, G. and Stornelli, V. (2007) Low Voltage Integrated Astable Multivibrator Based on a Single CCII. *Proceedings of* 2007 *PhD Research in Microelectronics and Electronics Conference*, Bordeaux, 2-5 July 2007, 177-180.

[19] Lo, Y.K., Chien, H.C. and Chiu, H.J. (2008) Switch-Controllable OTRA-Based Bistable Multivibrators. *IET Circuits, Devices & Systems*, **2**, 373-382. http://dx.doi.org/10.1049/iet-cds:20080011

[20] Macromodel of AD 844 in PSPICE library. http://espice.ugr.es/espice/src/modelos_subckt/Anal%C3%B3gicos/ad844.cir

Volume 3, Issue 3 (2015) 524-535 ISSN 2347 - 3258
International Journal of Advance Research and Innovation

Thermal Performance Improvements of Vapour Compression Refrigeration System Using Eco Friendly Based Nanorefrigerants in Primary Circuit

R. S. Mishra, Rahul Kumar Jaiswal
Department of Mechanical Engineering, Delhi Technological University, Delhi, India

Article Info

Article history:
Received 12 July 2015
Received in revised form
20 July 2015
Accepted 28 August 2015
Available online 15 September 2015

Keywords
First law Efficiency Improvement,
Energy-Exergy Analysis,
Nano refrigerants,
Ecofriendly Refrigerant,
Vapour Compression Refrigeration System,
Second Law (Exergetic Efficiency) Improvement

Abstract

Now a days nano refrigerants are being considered as a most efficient heat transfer fluids having superior heat transfer properties than conventional refrigerants in various thermal applications. Refrigerant based nano fluid termed as "Nanorefrigerant" have the great potential for improve thing first law thermal performance in terms of coefficient of performance in the refrigeration and air conditioning system. The thermo physical properties by addition of different nanoparticle mixed with eco friendly refrigerant are analyzed and their effects on the coefficient of performance (C.O.P.) have been reported in this paper. The thermal modeling have been done for the same cooling load and same geometry parameter for all nanoparticles and refrigerant combination mixture in the vapour compression refrigeration based chiller system having two concentric tube type heat exchanger as evaporator and condenser. The experimental results are indicating the thermal conductivity, dynamic viscosity and density of nanorefrigerant (different nanoparticle i.e. Cu, Al_2O_3,CuO and TiO_2 with eco friendly refrigerant R134a,R407c and R404A) increased about 15 to 94 %, 20% and 12 to 34 % respectively compared to base refrigerant on the other hand specific heat of nanorefrigerant is slightly lower that the base refrigerant. Moreover Al_2O_3/R134a nanorefrigerant shows highest C.O.P. of 35%. R404A and R407 with different nanoparticle show enhancement in C.O.P. about 3 to 14 % and 3 to 12 % respectively. Therefore application of nanorefrigerant in refrigeration and air conditioning system is most required to improve the performance of the system.

Nomenclature

COP	Coefficient of performance
COPt	Global coefficient of performance
Cp	Specific heat (J/kg K)
D	Diameter (m)
h	Specific enthalpy (J/kg)
k	Thermal conductivity (W/m K)
L	Length (m)
M	Mass flow rate (kg/s)
N	compressor speed (r.p.m.)
P	Power consumption (W)
p	Pressure (Pa)
Q	Volumetric rate of flow (m3/s)
q	Heat transfer rate (W)
q"	Heat Flux (W/m2)
r	Radius (m)
S	Area (m2)
T	Temperature (K)
t	Time (s)
U	Overall heat transfer coefficient (W/m2 K)
VG	Geometric compressor volume (m3)
v	Velocity (m/s)
x	Refrigerant quality
X n,o	nanoparticle/oil suspension concentration

Suffixes

air	Environment
avg	Brine/nanofluid
C	Compressor
e	Evaporation
i	Inner
in	Input
k	Condensation
l	Liquid
M	Metal
o	Outer
out	Output
r	Refrigerant
sat	Saturated
V	Vapor
w	Water
nf	Nanofluid
m	Base fluid
p	Nanoparticle
ϕ	volume fraction
n	nanoparticle
o	Lubricating oil
f	Saturated liquid
G	Saturated vapour
nb	Nucleate boiling
wn	Nanoparticle concentration in nanoparticle oil suspension

Greek symbols

α	Heat transfer coefficient (W/m^2 K)
λ	Phase change latent heat (J/kg)
μ	Dynamic viscosity (Pa s)
η_v	Compressor volumetric efficiency

Corresponding Author,
E-mail address: professor_rsmishra@yahoo.co.in
All rights reserved: http://www.ijari.org

η_{is} Compressor isentropic efficiency
η_G Global electromechanical compressor efficiency
ρ Density (kg/m^3)
σ Surface tension (N/m)

1. Introduction

Now a days refrigeration and air conditioning system are more important for industrial and domestic appliances. These systems consume more electricity than the other. Lots of research have been done till now to reduce the power consumption of refrigeration and air conditioning system. Nanofluid is a new kind of heat transfer medium, containing nanoparticles (1–100 nm) which are uniformly and stably distributed in a base fluid. These distributed nanoparticles, generally a metal or metal oxide greatly enhance the thermal conductivity of the nanofluid, increases conduction and convection coefficients, allowing for more heat transfer. Nanofluids have been considered for applications as advanced heat transfer fluids for almost two decades. However, due to the wide variety and the complexity of the nanofluid systems, no agreement has been achieved on the magnitude of potential benefits of using nanofluids for heat transfer applications. Compared to conventional solid–liquid suspensions for heat transfer intensifications, nanofluids having properly dispersed nanoparticles possess the following advantages:

- High heat transger surface area between particle and fluid.
- High dispersion stability with Brownian motion of particles.
- Reduced pumping power as compared to pure liquid to achieve equivalent heat transfer intensification.
- High specific surface area and therefore more heat Reduced particle clogging as compared to conventional slurries, thus promoting system miniaturization.
- Adjustable properties including thermal conductivity and surface wettability by varying particle concentrations to suit different applications.

The first test with nanofluids gave more encouraging features than they were thought to possess. The four unique features observed are listed below.

- Abnormal enhancement of thermal conductivity. The most important feature observed in nanofluids was an abnormal rise in thermal conductivity, far beyond expectations and much higher than any theory could predict.
- Stability**.** Nanofluids have been reported to be stable over months using a stabilizing agent.
- Small concentration and Newtonian behavior. Large enhancement of conductivity was achieved with a very small concentration of particles that completely maintained the Newtonian behavior of the fluid. The rise in viscosity was nominal; hence, pressure drop was increased only marginally.
- Particles size dependence. Unlike the situation with microslurries, the enhancement of conductivity was found to depend not only on particle concentration but also on particle size. In general, with decreasing particle size, an increase in enhancement was observed.

The above potentials provided the thrust necessary to begin research in nanofluids, with the expectation that these fluids will play an important role in developing the next generation of cooling technology. The result can be a highly conducting and stable nanofluid with exciting newer applications in the future.

1.1. Nanofluids and its Thermo Physical Property

Thermo physical properties of the nanofluids are quite essential to predict their heat transfer behavior. It is extremely important in the control for the industrial and energy saving perspectives. There is great industrial interest in nanofluids. Nanoparticles have great potential to improve the thermal transport properties compared to conventional particles fluids suspension, millimetre and micrometer sized particles. In the last decade, nanofluids have gained significant attention due to its enhanced thermal properties. Experimental studies show that thermal conductivity of nanofluids depends on many factors such as particle volume fraction, particle material, particle size, particle shape, base fluid material, and temperature. Amount and types of additives and the acidity of the nanofluid were also shown to be effective in the thermal conductivity enhancement. The transport properties of nanofluid: dynamic thermal conductivity and viscosity are not only dependent on volume fraction of nanoparticle, also highly dependent on other parameters such as particle shape, size, mixture combinations and slip mechanisms, surfactant, etc. Studies showed that the thermal conductivity as well as viscosity both increases by use of nanofluid compared to base fluid. So far, various theoretical and experimental studies have been conducted and various correlations have been proposed for thermal conductivity and dynamic viscosity of nanofluids. However, no general correlations have been established due to lack of common understanding on mechanism of nanofluid. As compared with the experimental studies on thermal conductivity of nanofluids, there are limited rheological studies reported in the literature for viscosity. Different models of viscosity have been used by researchers to model the effective viscosity of nanofluid as a function of volume fraction.

1.2. Applications of Nanofluids

The novel and advanced concepts of nanofluids offer fascinating heat transfer characteristics compared to conventional heat transfer fluids. There are considerable researches on the superior heat transfer properties of nanofluids especially on thermal conductivity and convective heat transfer. Applications of nanofluids in industries such as heat exchanging devices appear promising with these characteristics. Kostic reported that nanofluids can be used in following specific areas:

- Heat-transfer nanofluids.
- Tribological nanofluids.
- Surfactant and coating nanofluids.
- Chemical nanofluids.
- Process/extraction nanofluids.
- Environmental (pollution cleaning) nanofluids.
- Bio- and pharmaceutical-nanofluids.
- Medical nanofluids (drug delivery and functional tissue–cell interaction).

- *Design of nanofluid*

In light of all the mentioned nanofluid property trends, development of a heat transfer nanofluid requires a complex approach that accounts for changes in all important thermophysical properties caused by introduction of nanomaterials to the fluid. Understanding the correlations between nanofluid composition and thermo-physical Properties is the key for engineering nanofluids with desired properties. The complexity of correlations between Nanofluid parameters and properties described in the previous section indicates that manipulation of the system performance requires prioritizing and identification of critical parameters and properties of nanofluids. Systems engineering is an interdisciplinary field widely used for designing and managing complex engineering projects, where the properties of a system as a whole, may greatly differ from the sum of the parts' properties. Therefore systems engineering can be used to prioritize nanofluid parameters and their contributions to the cooling performance.

The decision matrix is one of the systems engineering approaches, used here as a semi quantitative technique that Allows ranking multi-dimensional nanofluid engineering options .It also offers an alternative way to look at the Inner workings of a nanofluid system and allows for design choices addressing the heat transfer demands of a given Industrial application.

2. Literature Review

Buzelin & Amico [1] developed an intelligent refrigeration system to reduce energy consumption in industrial refrigeration systems is proposed and introduced. A typical industrial refrigeration system was conceived, built and modified in the laboratory, receiving a novel power law control system, which utilizes a frequency inverter. The operation and energy consumption of the system operating either with the new control system or with the traditional on-off control were compared to realistically quantify the obtained gains. In this manner, the measured temperature data acquired from several points of both systems and the energy consumption in kW h during a 24 h experimental run period are compared. Jwo et al. [2] conducted studies on a refrigeration system replacing R-134a refrigerant and polyester lubricant with a hydrocarbon refrigerant and mineral lubricant. The mineral lubricant included added Al_2O_3 nanoparticles to improve the lubrication and heat-transfer performance. Their studies show that the 60% R-134a and 0.1 wt % Al_2O_3 nanoparticles were optimal. Under these conditions, the power consumption was reduced by about 2.4%, and the coefficient of performance was increased by 4.4%. Peng et al. [3] conducted experimental on the nucleate pool boiling heat transfer characteristics of refrigerant/oil mixture with diamond nano particles. The refrigerant used was R113 and the oil was VG68. They found out that the nucleate pool boiling heat transfer coefficient of R113/oil mixture with diamond nanoparticles is larger than the R113/oil mixture. They also proposed a general correlation for predicting the nucleate pool boiling heat transfer coefficient of refrigerant/oil mixture with nanoparticles, which well satisfies their experimental results. Henderson et al. [4] conducted an experimental analysis on the flow boiling heat transfer of R134a based nanofluids in a horizontal tube. They found excellent dispersion of CuO nanoparticle with R134a and POE oil and the heat transfer coefficient increases more than 100% over baseline R134a/POE oil results. Bobbo et al. [5] conducted a study on the influence of dispersion of single wall carbon nanohorns (SWCNH) and Ti2O3 on the tribological properties of POE oil together with the effects on the solubility of R134a at different temperatures. They showed that the tribological behaviour of the base lubricant can be either improved or worsen by adding nanoparticles. On the other hand the nanoparticle dispersion did not affect significantly the solubility. Bi et al. [6] conducted an experimental study on the performance of a domestic refrigerator using Ti2O3 -R600a nanorefrigerant as working fluid. They showed that the Ti2O3-R600a system worked normally and efficiently in the refrigerator and an energy saving of 9.6%. They too cited that the freezing velocity of nano refrigerating system was more than that with pure R600a system. The purpose of this article is to report the results obtained from the experimental studies on a vapour compression system. Lee et al. [7] investigated the friction coefficient of the mineral oil mixed with 0.1 vol.% fullerene nanoparticles, and the results indicated that the friction coefficient decreased by 90% in comparison with rawlubricant, which lead us to the conclusion that nanoparticles can improve the efficiency and reliability of the compressor. Wang and Xie [8] found that Ti2O3 nanoparticles could be used as additives to enhance the solubility between mineral oil and hydrofluorocarbon (HFC) refrigerant. The refrigeration systems using the mixture of R134a and mineral oil appended with nanoparticles Ti2O3, appeared to give better performance by returning more lubricant oil back to the compressor, and had the similar performance compared to the systems using polyol-ester (POE) and R134a. In the present study the refrigerant selected is R600a and the nanoparticle is alumina. Isobutane (R600a) is more widely adopted in domestic refrigerator because of its better environmental and energy performances. In this paper, a new refrigerator test system was built up according to the National Standard of India. A domestic R600a refrigerator was selected. Al2O3-R600a nano-refrigerant was prepared and used as working fluid. The energy consumption test and freeze capacity test were conducted to compare the performance of the refrigerator with nano-refrigerant and pure refrigerant so as to provide the basic data for the application of the nanoparticles in the refrigeration system. Heris et al.,[9] investigated laminar flow convective heat transfer through circular tube with constant wall temperature boundary condition for nanofluids containing CuO and Al2O3 oxide nanoparticles in water as base fluid. The experimental apparatus consisting of a test chamber constructed of 1 m annular tube with 6 mm diameter inner copper tube and with 0.5 mm thickness and 32 mm diameter outer stainless steel tube. Nanofluid flows inside the inner tube while saturated steam enters annular section, which creates constant wall temperature boundary condition. The fluid after passing through the test section enters heat exchanger in which water was used as cooling fluid. The experimental results emphasized that the single phase correlation with nanofluids properties (Homogeneous Model) was not able to predict heat transfer coefficient

enhancement of nanofluids. The comparison between experimental results obtained for CuO/ water and Al2O3 / water nanofluids indicated that heat transfer coefficient ratios for nanofluid to homogeneous model in low concentration were close to each other but by increasing the volume fraction, higher heat transfer enhancement for Al2O3/water was observed. They concluded that heat transfer enhancement by nanofluid depends on several factors including increment of thermal conductivity, nanoparticles chaotic movements, fluctuations and interactions. Hwang et al., [10] investigated the convective heat transfer coefficient of Al_2O_3 /water based nanofluid. In their experiment nanofluid considered flowing through circular tube having 1.812 mm inside diameter and maintaining constant heat flux for fully developed laminar regime. Al_2O_3 /water based nanofluids with various volume % concentration 0.01% to 0.3% are manufactured with two-step method. They have also obtained the thermo physical property of nanofluid such as density, viscosity, heat capacity and thermal conductivity. They have concluded that the convective heat transfer coefficient enhancement occurs with 0.01 and 0.3 vol % concentration of nanoparticle in fully developed laminar regime and heat transfer enhancement about 8 % obtained under the same Reynolds number of base fluid. They also concluded that enhancement in heat transfer coefficient were much higher that the thermal conductivity enhancement at the same vol % concentration of nanoparticle. Sharma et al.,[11] investigated to evaluate friction factor and heat transfer coefficient with a inserted twisted tape in the flow region of tube with Al_2O_3 nanofluid they have consider a test section of L/D ration 160 and 1.5m length. For uniform heating test section were wrapped with 1 KW .The aluminum strip having 0.018mm width and 1mm thick are used. Test section is subjected to 180° twist holding both end of test section in lathe machine obtaining 5, 10 and 15 twist ratio. Their result show enhancement in heat transfer coefficient with Al_2O_3 nanoparticle into the base fluid compare to the base water. The heat transfer coefficient was 23.7 % higher that the water at Reynolds number 9000.Yu et al., [12] investigated the heat transfer coefficient of silicon carbide nanoparticle having diameter 170nm and 3.7 vol % suspended into the pure water and found that an increment in heat transfer coefficient about 50-60 % compared to host fluid. Their test section was stainless steel tube with 4.76 mm outside diameter and 2.27 inside diameter. Their test rigs have heat exchanger flow meter horizontal tube, pre heater as a closed loop system. They concluded that enhancement is 14-32 % higher that the predicted value for single phase turbulent correlation of heat transfer. Also they found that the pressure loss is little lower than the Al_2O_3 water nanofluid. Torii and Yang [13] investigated the heat transfer coefficient of suspended diamond nanoparticle into the host fluid by maintaining constant heat flux. Their test section contains a flow loop, a digital flow meter, a pump, a reservoir and a tank. The test is prepared stainless steel tube having 4.3 mm outer diameter 4.0 mm inner diameter and 1000 mm length. The whole is heated with a dc electrode heater considering joule heating. They reported that (i) the heat transfer performance of nanofluid increases with the suspension of diamond nano particle into the water compared to pure water. (ii) Reynols number variation influence the enhancement occurs in heat transfer coefficient. Rea et al., [14] investigated the heat transfer coefficient and viscous pressure loss for Al_2O_3 /water and zirconia-water nanoparticle based nanofluid flowing loop. The stainless steel vertical heated test section considered having outer diameter of 6.4 mm, an inner diameter of 4.5 mm and 1.01 m length. The test section 8 T type thermocouples sheathed and insulated electrically and soldered onto the outside wall of the tube along axial direction 5, 16, 30,44, 58, 89 and 100 cm from heated inlet section of the test facility. to measure the fluid temperatures Two same T-type thermocouples were inserted into the flowing passage of the channel after and before of the test section. They observed that the heat transfer coefficients increased 17% and 27%, in fully developed region compare to base water. The heat transfer of zirconia–water nanofluid increases by approx 2% at 1.32 vol. % in the inlet region and 3% at 1.32 vol % in the fully developed region. The observed pressure loss for nanofluids was higher than the base water having good agreement with predicted model for laminar flow. Murshed et al.[15] carried out experiments with spherical and rod-shaped TiO_2nanoparticles. The spherical particles were 15 nm in diameter and the rod-shaped particles were 10 nm in diameter and 40 nm in length. The base fluid was deionized water. The measurement method was transient hot wire. It should be mentioned here that they used oleic acid and cetyltrimethyl ammonium bromide (CTAB) surfactants (0.01 to 0.02 vol %). They maintained a nearly neutral (pH 6.2 to 6.8) suspension. For the first time, a nonlinear correlation between the volume fraction and conductivity enhancement was observed here at lower concentrations. This is interesting with respect to the temperature effect and pure metallic particles. They found that the conductivity enhancement was higher for rod-shaped particles than for spherical particles. Enhancement up to 29.7% was found with 5% spherical particles and up to 32.8% with rod-shaped particles. They attributed this to the higher shape factor (n =6) of the rods than of the spheres (n =3) in the Hamilton–Crosser [16] model. Xuan and Li [17] were first to show a significant increase in the turbulent heat transfer coefficient. They found that at fixed velocities, the heat transfer coefficient of nanofluids containing Cu nanoparticles at 2.0 vol% was improved by as high as 40% compared to the host water. The Dittus–Boelter correlation failed to obtain the improved experimented heat transfer behavior of nanofluids. Recent unpublished work shows that the effect of particle size and shape and dispersion becomes predominant in enhancing heat transfer in nanofluids. Even greater heat transfer effects are expected for nanofluids produced by the one-step process. Therefore, there is great potential to "engineer" ultra-energy-efficient heat transfer fluids by choosing the nanoparticle material as well as by controlling particle size, shape, and dispersion.

3. Performance Improvement Methodology

To increase thermal performance of vapour compression refrigeration system (VCRS) by improving 1st law efficiency in terms of coefficient of performance because the heat absorption is depending on many factors in terms of geometric parameters of the heat exchanger's thermo physical properties of the absorbing fluid, heat

transfer rate, thermal conductivity of fluid, specific heat,density and viscosity etc. all these property can be enhance by the suspension of nanoparticle (100 nm - 10µm) in the base fluid (i.e. nanofluid) and nanoparticle suspended in the refrigerant called nanorefrigerent. Applications of nanorefrigerent in the VCRS instead of conventional refrigerant can inhances the thermal property of the system. Thus 1st law efficiency (i.e. C.O.P) can be increased and the power consumption for the same load can be reduced also cost saving achieved.

4. Vapour Compression Refrigeration System Modeling

In this paper to evaluate the performance parameter of VCRS using nanorefrigerent following model and formulation for each component of VCRS is used as shown in following Fig.-1

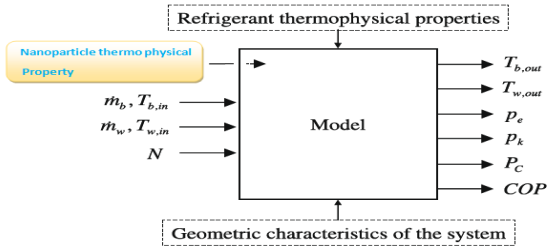


Fig: 1. Vapour Compression Refrigeration System Model

In this model we have taken only five variable and nanoparticle physical property with geometric parameter of the complete system (assumed) as input variable for the VCRS. These variables, together with the thermo physical properties of the refrigerant, nanoparticle and geometric characteristics of the VCRS (vapour compression refrigeration system) are used to obtain the evaporation and condensing pressure and brine, water outlet temp. Power consumption, energy efficiency and exergy efficiency of VCRS. Thus we will be able to evaluate the performance of VCRS by changing the operating parameter on the system performance so that we can optimize the performance of the VCRS.The schematic structure of the model proposed for this investigation is presented in Fig. 1 where it can be seen that the model input variable are brine inlet temperature in the evaporator, water inlet temperature in the condenser, compressor speed, types of refrigerant, mass flow rate of brine, water and geometric parameter of the heat exchanger (Evaporator and Condenser) and used to evaluate the performance of VCRS without nanofluid. When we go to compute the performance of VCRS using nano fluid an additional input parameter is required i.e. type of nanoparticle, diameter of nanoparticle, thermo physical property of nanofluid/nanoparticle (thermal conductivity, specific heat, density). The proposed model is basically a VCRS based chiller machine in which two concentric tube (copper) heat exchanger is used for evaporating and condensing operation. In this model refrigerant is supposed to flow in inner side of the evaporator tube and brine in annuli side as shown in fig-2. And water flow in inner side of the condenser tube and refrigerant in the annuli side as shown in fig-.2. The input parameter taken initially to compute the performance of VCRS using nanofluid and without nanofluid is given below.

Input variable	
Type of Refrigerant	R$=R404A
RPM of compressor	N=2900 {rpm}
Brine inlet Temperature	Tb_in =25+273.15 {K}
Water inlet Temperature	Tw_in=25+273.15 {K}
Mass flow rate of brine	m_b=0.006 {kg/s}
Mass flow rate of water	m_w=0.006 {kg/s}
Air Temperature	T_air=30+273.15 {K}
Inlet pressure of brine	Pb_in=2{bar}
Inlet pressure of water	Pw_in=2{bar}
Air Pressure	P_air=1.01325 {bar}
Acceleration due to gravity	g=9.81{m/s2}
Ambient Temperature	T_ambient=298{K}
Inside dia. of brine tube in evaporator	D_bie=0.013875 {m}
Inside dia. of refrigerant tube in evaporator	D_rie=0.007525 {m}
Outside dia. of refrigerant tube in evaporator	D_roe=0.009525 {m}
Geometric Parameter	
Inside dia. of brine tube in evaporator	D_bie=0.013875 {m}
Inside dia. of refrigerant tube in evaporator	D_rie=0.007525 {m}
Outside dia. of refrigerant tube in evaporator	D_roe=0.009525 {m}
Length of tube in evaporator	L_e=0.76 {m}
Surface area of evaporator	S_e=3.14*(D_roe)*L_e {m2}
Geometric compressor volume	V_g =5.79E-06 {m3}
Inside dia. of refrigerant tube in condenser 3-4	D_rik=0.013875 {m}
Inside radius of refrigerant tube in condenser 3-4	r_rik=D_rik/2 {m}
Inside dia. of water tube in condenser 3-4	D_wik=0.007525 {m}
outside dia. of water tube in condenser 3-4	{D_wok=0.009525 {m}}
outside radius of water tube in condenser 3-4	r_wok=D_wok/2 {m}
Length of tube in condenser 3-4	L_k=1.05 {m}
outside dia. of water tube in condenser 3-4	D_wok=0.00508 {m}
Surface area of condenser 3-4	S_k=3.14*(D_wok)*L_k {m2}
Inside dia. of refrigerant tube in condenser 2-3	D_ri23=0.007525 {m}
Inside radius of refrigerant tube in condenser 2-3	r_ri23=D_ri23/2 {m}
Outside dia. of	D_ro23=0.009525 {m}

refrigerant tube in condenser 2-3	
Outside radius of refrigerant tube in condenser 2-3	r_ro23=D_ro23/2 {m}
Length of tube in condenser 2-3	L_23=0.6 {m}
Surface area of condenser 2-3	S_23=3.14*D_ro23*L_23 {m2}
Inside dia. of Capillary Tube	D_cap=0.0006 {m}
Fouling in the tubes	R_TFO=0.000086 {m2 K/W}

Using these inputs and the main characteristics of the compressor and heat exchangers, the model compute the operating pressures (without considering pressure drops), secondary fluids output variables and the energy performance. The property of nanorefrigerant/refrigerant and the thermo-physical properties of secondary fluids are evaluated by using software

4.1. Vapor Compression System Modeling

The model contain of a set of below equations based on physical laws showing the main parts of the system, as shown Properly (Schematically) in Fig.(2).

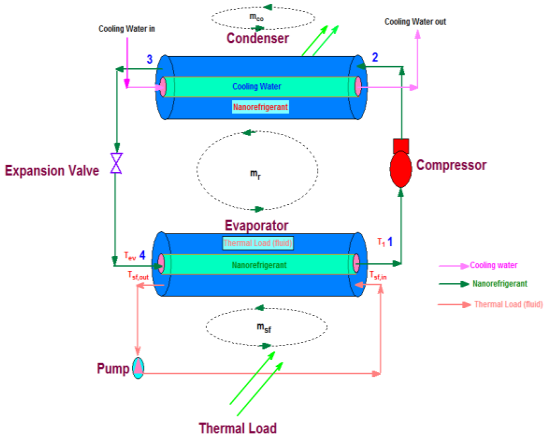


Fig: 2. Schematic Diagram of Vapour Compression Refrigeration System Model

The nanorefrigerant/refrigerant states are numbered in Fig. 3. To compute nanorefrigerant/refrigerant mass flow rate *(m_r)* Eq. (1) is used, where the compressor volumetric efficiency (η_v) is shown as a function of operating pressure and compressor speed (*N*) as shown in Eq. (2). For simplicity, *(ρ_1)* is the nanorefrigerant/refrigerant density taken is the one corresponding to the saturated condition.

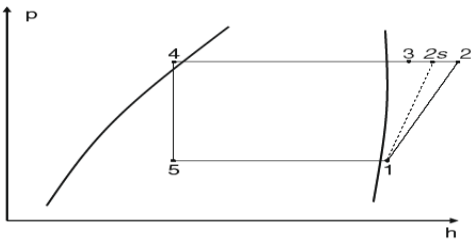


Fig: 3. Vapor Compression Cycle

Vapor at the evaporating pressure and V_g is the geometric compressor volume.

$$m_r = \eta_v \cdot \rho_1 \cdot V_g \cdot N \quad (1)$$

$$\eta_v = 1 + C - C \cdot \left[\frac{P_k}{P_e}\right]^{\left[\frac{1}{n_1}\right]} \quad (2)$$

$$C = \frac{V_{suction}}{V_{discharge}}$$

Where,

P_k & P_e is the condenser pressure and evaporator pressure. $V_{Suction}$ & $V_{Discharge}$ is the suction volume and discharge volume of compressor. n_1 is the index of expansion.

Based upon energy balance quation for condenser, evaporator, compressior and expainsion device a linear/non linear equation based simulation programm is prepared and solved. For nanofluid property calculations following equations are used.

4.2. Nanofluid/Nanorefrigerant Property Calculation

Direct suspension of nanoparticle into base refrigerant through appropriate method and procedure and then calculate the thermo physical property of nanorefrigerant with the help of following equation and that property is used to compute the performance of vapour compression refrigeration system (VCRS). To compute the performance of VCRS with nanoparticle based nanorefrigerant we use thermo physical property of nanorefrigerant instead of pure refrigerant as below.

Thermal conductivity of nanorefrigerant

Thermal conductivity of nanorefrigerant is computed by using Sitprasert correlation [18] this relation consider the effect of temperature dependence interfacial layer of nanofluid as below,

$$K_{r,n} = \frac{(K_p - k_l)\cdot\phi\cdot k_l\cdot(2\cdot\beta_1^3 - \beta^3 + 1) + (K_p + 2\cdot k_l)\cdot\beta_1^3\cdot(\phi\cdot\beta^3\cdot(k_l - K_r) + K_r)}{\beta_1^3\cdot(K_p + 2\cdot k_l) - ((K_p - k_l)\cdot\phi\cdot(\beta_1^3 + \beta^3 - 1))} \quad (3)$$

K r,n is the thermal conductivity of nanorefrigerant. Φ is the volume % suspension of nanoparticle into the pure refrigerant.

Kp is the thermal conductivity of nanoparticle.

Kl is the interfacial thermal conductivity can be obtained using eq. (4)

$$\beta = 1 + \frac{t}{r_p}$$

$$\beta_1 = 1 + \frac{t}{2\cdot r_p}$$

$$t = 0.01\cdot(T_e - 273)\cdot r_p^{0.35}$$

$$k_l = C\cdot K_r\cdot\frac{t}{r_p} \quad (4)$$

Where t is the interfacial layer thickness. Kr is the thermal conductivity of pure refrigerant at liquid face. rp is the radius of nanoparticle in nanometer

C is constant its value 30 for Al2O3, CuO and 10 for TiO2, 100 for Cu.

Viscosity of nanorefrigerant

The viscosity of nanorefrigerant is computed using Brinkman correlation [19]

$$\mu_{r,n} = \mu_r \cdot \frac{1}{(1-\phi)^{2.5}}$$

Where μ r,n is the viscosity of nanorefrigerant. μ r is the viscosity of liquid pure refrigerant

Density of nanorefrigerant

The density of nanorefrigerant is calculated using Pak and Cho [20]

$$\rho_{h,r} = \phi \cdot \rho_p + (1-\phi) \cdot \rho_r$$

Where

$\rho_{n,r}$ is the density of nanorefrigerant

ρ_p is the nanoparticle density.

ρ_r is the density of liquid refrigerant

Specific heat of nanorefrigerant

Specific heat of nano refrigerant is computed using Pak and Cho[20]

$$Cp_{r,n} = (1-\phi) \cdot Cp_{r,l} + \phi \cdot Cp_p$$

Where Cp r,n is the specific heat of nanorefrigerant. Cp r,l id the specific heat of liquid pure refrigerant. Cp p is the nano particle specific heat. And other parameter/property of nanorefrigerant is calculated using following equation.

$$Re_{r,n} = G_n \cdot \frac{D_i}{\mu_{r,n}}$$

$$Re_r = G_r \cdot \frac{D_i}{\mu_r}$$

$$Pr_{r,n} = Cp_{r,n} \cdot \frac{\mu_{r,n}}{K_{r,n}}$$

$$Pr_r = Cp_{r,l} \cdot \frac{\mu_r}{K_r}$$

$$\alpha_{conv,r,n} = N_{u,r,n} \cdot \frac{K_{r,n}}{D_i}$$

$$\alpha_{conv,r} = N_{u,r} \cdot \frac{K_r}{D_i}$$

$$\alpha_{LV,nr} = F_n \cdot \alpha_{conv,r,n} + S_n \cdot \alpha_{nb,r,n}$$

$$\alpha_{nb,r,n} = 207 \cdot \frac{K_{r,n}}{BD_n} \cdot \left[\frac{q'' \cdot BD_n}{K_{r,n} \cdot T_e}\right]^{0.674} \cdot \left[\frac{\rho_{G,n}}{\rho_{r,n}}\right]^{0.581} \cdot Pr_{r,n}^{0.533}$$

$$BD_n = 0.51 \cdot \left[\frac{2 \cdot \sigma}{g_g \cdot (\rho_{r,n} - \rho_{G,n})}\right]^{0.5}$$

$$F_n = 53.64 \cdot \left[\frac{q''}{G_n \cdot h_{fg}}\right]^{0.314} \cdot X_{tt,n}^{-0.839}$$

$$G_n = \rho_{h,r} \cdot V_r$$

$$X_{tt,n} = \left[\frac{1-x}{x}\right]^{0.9} \cdot \left[\frac{\rho_{G,n}}{\rho_{r,n}}\right]^{0.5} \cdot \left[\frac{\mu_{r,n}}{\mu_{G,n}}\right]^{0.1}$$

$$S_n = 0.927 \cdot \left[\left(\frac{1-x}{x}\right)^{0.8} \cdot \left(\frac{\rho_{G,n}}{\rho_{r,n}}\right)^{0.5}\right]^{0.319}$$

Where Re r,n is the Reynold number of nanorefrigerant. Pr,n Prandle number of nanorefrigerant. Gr is the mass flux of nanorefrigerant Xtt,n is the martinelli parameter of nanorefrigerant.

X is the vapour quality of nanorefrigerant. BDn is the bubble diameter of nanorefrigerant. Sn is suppression factor of of nanorefrigerant. q" is the heat flux received by the nanorefrigerant in the evaporator.

Vr is the velocity of nanorefrigerant in the evaporator

All these property are used to compute the performance of VCRS using nanorefrigerant in the above equation from (1) to (28). Thus we can find out the performance of VCRS using nanorefrigerant in primary circuit. In this research direct suspension of nanoparticle into the base refrigerant is proposed and effect of various input parameter of the proposed model on the performance of VCRS is computed using nanofluid (nanorefrigerant) and without nanofluid are shown in result and discussion chapter.

5. Results and Discussion

A computational program has been developed to solve non linear system equations of vapour compression refrigeration cycle by considering nano-refrigerant flowing in the primary circuit of the enaporater and water into the secondary circuit of the evaporator. Theoretical analysis has been done using EES software for nanorefrigerant flowing in primary circuit and R718 (water) flowing in secondary circuit of VCRS and results are given below.

5.1. Thermo Physical Property of Nanorefrigerant

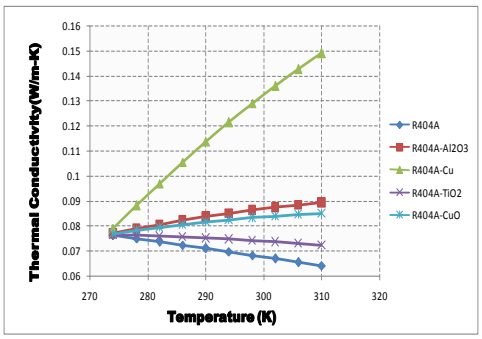


Fig: 4. Variation of Thermal conductivity with Temperature of R404A using different nanoparticles

Thermo physical property of base refrigerant using nanoparticle suspended into base refrigerant at 5 Vol % are shown below.

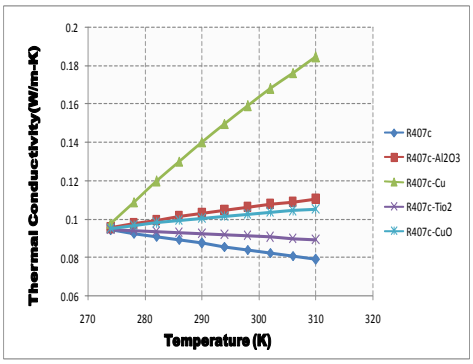


Fig: 5. Variation of Thermal conductivity with Temperature of R407c using different nanoparticles

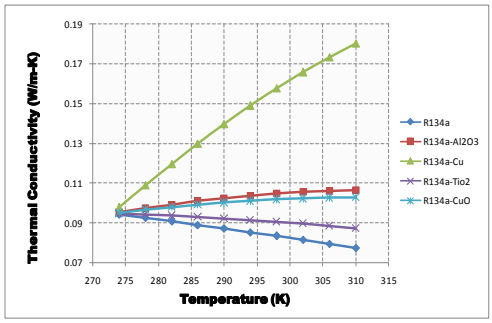


Fig: 6. Variation of Thermal conductivity with Temperature of R134a using different nanoparticles

Fig: 4, Fig: 5 and Fig: 6 show the enhancement in thermal conductivity of nanorefrigerant when different kind of nanoparticle is suspended into the host refrigerant. The enhancement factor varies from 0.06 to 2 for different nanoparticle.from the Fig we can see that cu nanoparticle have more EF at higher temperature which value is approx 2.

5.1.1. Effect of volume fraction on Thermo physical property of nanorefrigerant with different nanoparticle (at 280K temperature)

Thermal conductivity shown in Fig 5.4 is defined as the ratio of thermal conductivity of nanorefrigerant (pure refrigerant mixed with nanoparticle) to the thermal conductivity of pure refrigerant.

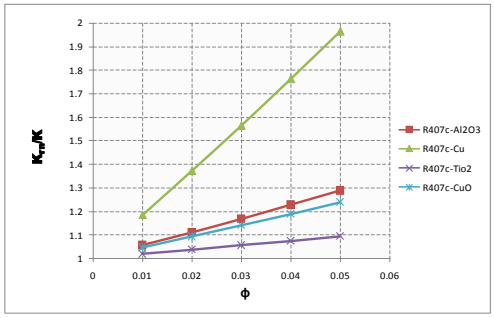


Fig: 7. Variation of Thermal conductivity Ratio with volume fraction (ϕ) of R134a using different nanoparticles

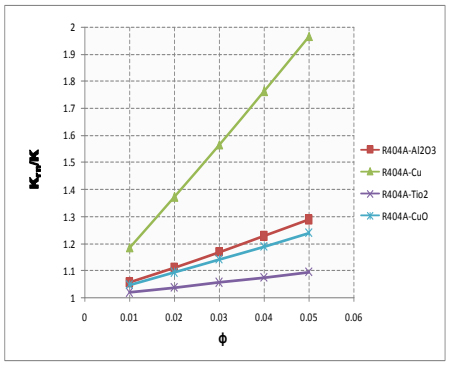


Fig: 8. Variation of Thermal conductivity Ratio with volume fraction (ϕ) of R404A using different nanoparticles

Fig (4) to Fig.(.)6 Shows that conductivity ratio of pure refrigerant to nanorefrigerant increases with increasing concentration of nanoparticle into the host refrigerant. From the fig we can see that Cu nanoparticle based nanorefrigerant have higher cond. Ratio than other nanoparticle and have approx two times higher than base refrigerant at 5 vol % concentration.

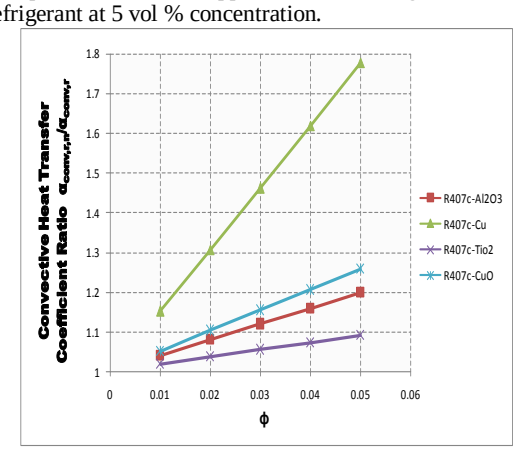


Fig: 9. Variation of Convective heat transfer coefficient ratio with volume fraction (ϕ) of R407c using different nanoparticles

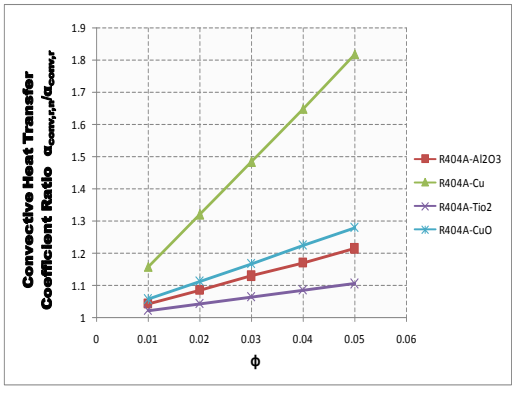


Fig: 10. Variation of Convective heat transfer coefficient ratio with volume fraction (ϕ) of R134a using different nanoparticles

Convective heat transfer coefficient ratio shown in Fig (7), Fig. (8) and Fig. (9) is defined as the ratio of

Convective heat transfer coefficient of nanorefrigerant (nanoparticle mixed with pure refrigerant) to the Convective heat transfer coefficient of pure refrigerant. The heat transfer Enhancement Factor shown in Figs (10), Fig. (11) and Fig.(12) is defined as the ratio of heat transfer coefficient of nano-refrigerant (nanoparticle mixed with pure refrigerant) to the heat transfer coefficient of pure refrigerant.

Fig (7) to Fig. (9) shows the convective heat transfer coefficient Ratio increases by increasing the concentration of nanoparticle. and copper nanoparticle based nanorefrigerant have highest convective heat transfer coefficient ratio than other particle its value ranges from 1 to 1.7.

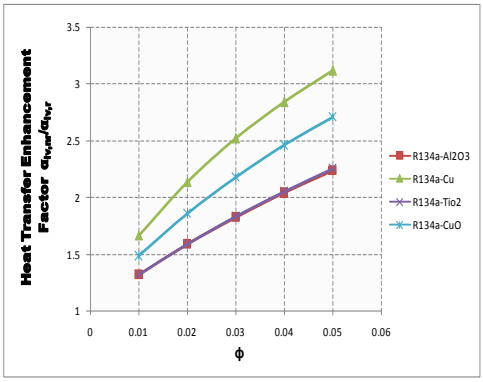


Fig: 11. Variation of Heat transfer Enhancement Factor with volume fraction (ϕ) of R134a using different nanoparticles

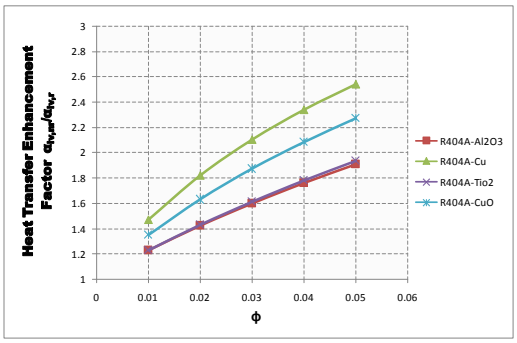


Fig: 12. Variation of Heat transfer Enhancement Factor with volume fraction (ϕ) of R404A using different nanoparticles

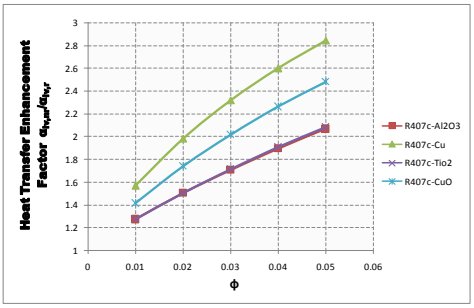


Fig: 13. Variation of Heat transfer Enhancement Factor with volume fraction (ϕ) of R407c using different nanoparticles

5.2. Effect of nanoparticle volume fraction (ϕ) on the 1st law of thermodynamics (C.O.P.) of VCRS

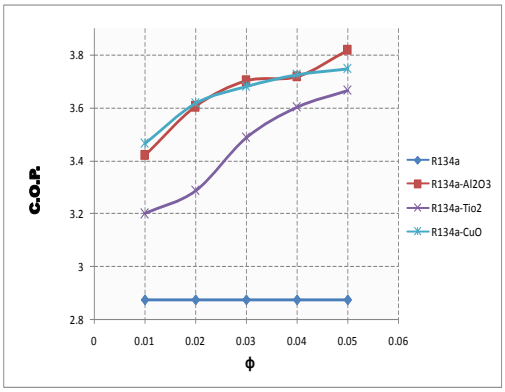


Fig: 14. Variation of C.O.P with volume fraction (ϕ) of VCRS with R134a using different nanoparticles

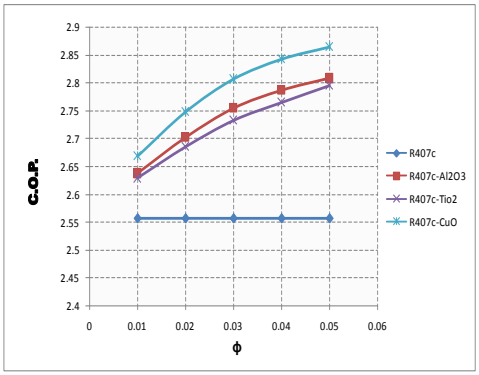


Fig: 15. Variation of C.O.P with volume fraction (ϕ) of VCRS with R407c using different nanoparticles

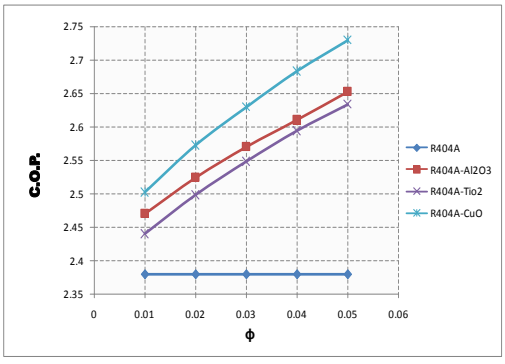


Fig: 16. Variation of C.O.P with volume fraction (ϕ) of VCRS with R404A using different nanoparticles

Fig (13) to Fig.(15) shows that C.O.P. enhancement of VCRS is achieved by using nanorefrigerant as a working fluid in VCRS. Fig-19 show that the maximum second law performance enhancement theoretically achieved about 35 % with combination of R134a with copper and 32% using R134a and Al2O3 nanoparticles at 5 vol % based nanorefrigerant. C.O.P. enhancements of VCRS with different combination of nanorefrigerant are given in tables 5.1(a)-5.1(c) as given below.

Table: 1(a). Enhancement in C.O.P using R-134a nanorefrigerant of VCRS

Refrigerant		R134a	
Nanoparticle	Volume Fraction (ϕ)	C.O.P.	% Enhancement
	0	2.82	-
Al_2O_3	0.01	3.421	21.3%
	0.02	3.604	27.8%
	0.03	3.701	31.2%
	0.04	3.717	31.8%
	0.05	3.817	35.4%
TiO_2	0.01	3.287	16.6%
	0.02	3.488	23.7%
	0.03	3.603	27.8%
	0.04	3.666	30.0%
	0.05	3.691	30.9%
CuO	0.01	3.464	22.8%
	0.02	3.616	28.2%
	0.03	3.681	30.5%
	0.04	3.725	32.1%
	0.05	3.748	32.9%

Table: 1(b). Enhancement in C.O.P using R407c nanorefrigerant of VCRS

Refrigerant		R407c	
Nanoparticle	Volume Fraction (ϕ)	C.O.P.	% Enhancement
	0	2.556	-
Al_2O_3	0.01	2.637	3.2%
	0.02	2.702	5.7%
	0.03	2.755	7.8%
	0.04	2.787	9.0%
	0.05	2.808	9.9%
TiO_2	0.01	2.629	2.9%
	0.02	2.685	5.0%
	0.03	2.733	6.9%
	0.04	2.765	8.2%
	0.05	2.795	9.4%
CuO	0.01	2.669	4.4%
	0.02	2.748	7.5%
	0.03	2.806	9.8%
	0.04	2.842	11.2%
	0.05	2.864	12.1%

Table: 1(c). Enhancement in C.O.P using R404a + nanorefrigerant of VCRS

Refrigerant		R404A	
Nanoparticle	Volume Fraction (ϕ)	C.O.P.	% Enhancement
	0	2.379	-
Al_2O_3	0.01	2.47	3.8%
	0.02	2.524	6.1%
	0.03	2.536	6.6%
	0.04	2.558	7.5%
	0.05	2.653	11.5%
TiO_2	0.01	2.44	2.6%
	0.02	2.498	5.0%
	0.03	2.548	7.1%
	0.04	2.594	9.0%
	0.05	2.634	10.7%
CuO	0.01	2.502	5.2%
	0.02	2.572	8.1%
	0.03	2.63	10.6%
	0.04	2.683	12.8%
	0.05	2.73	14.8%

5.3. Effect of nanoparticle volume fraction (ϕ) on the Exergy destruction ratio of VCRS

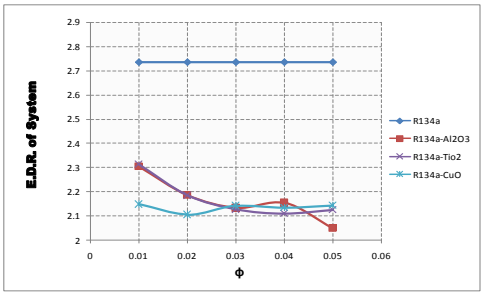


Fig: 17. Variation of Exergy destruction ratio with volume fraction (ϕ) of VCRS with R134a using different nanoparticles

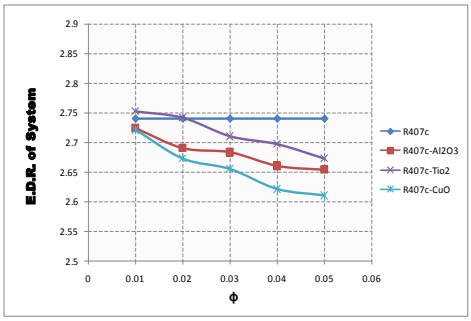


Fig: 18. Variation of Exergy Destruction ratio with volume fraction (ϕ) of VCRS with R407c using different nanoparticles

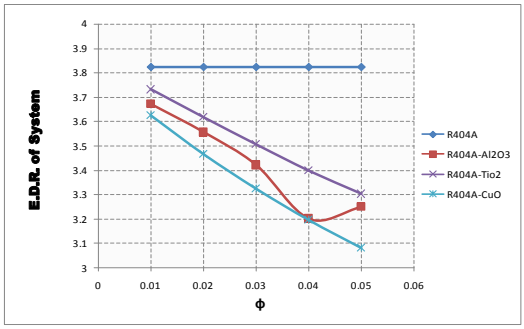


Fig: 19. Variation of Exergy destruction ratio with volume fraction (ϕ) of VCRS with R404a using different nanoparticles

Fig (17) to Fig (19) shows that the Eexergy.Destruction Ratio of VCRS is reduced by using nanofluid (nanoparticle based nanorefrigerant)

5.4. Effect of nanoparticle volume fraction (ϕ) on the 2nd law efficiency of VCRS

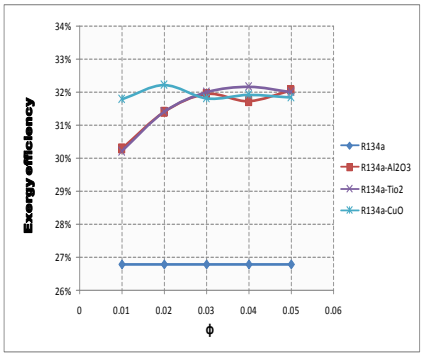


Fig: 20. Variation of Exergy Efficiency with volume fraction (ϕ) of VCRS with R134a using different nanoparticles

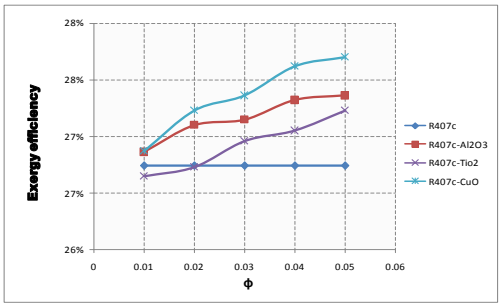


Fig: 21. Variation of Exergy Efficiency with volume fraction (ϕ) of VCRS with R407c using different nanoparticles

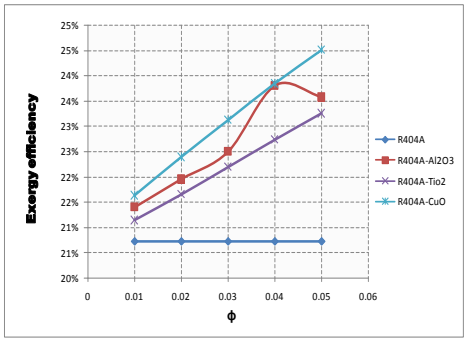


Fig: 22. Variation of Exergy Efficiency with volume fraction (ϕ) of VCRS with R404A using different nanoparticles

Fig (20) to Fig (22) shows that exergetic efficiency (i.e. 2nd Law efficiency) is increased by using nanorefrigerant and the exergetic effiency (i.e. 2nd law efficiency) of vapour compression refrigeration system using nanorefrigerant R134a/CuO is much higher than the other nanorefrigerant having value approx 35%.

6. Conclusions & Recommendations

It has been observed that the use of nano-refrigerants instead of pure refrigerant in vapour compression refrigeration cycle the thermal performances of nanorefrigerant enhances significantly as well as the performance of refrigeration system. The following conclusion have been drawn from present investigations

1. Use of nanoparticles enhances thermal performance of vapour compression refrigeration system from 8% to 35 % using nanorefrigerant in primary circuit.
2. Use of nanoparticles enhances the thermal performance of vapour compression refrigeration system from 7 to 21 % using nanofluid in secondary circuit.
3. Maximum enhancement in the performance was observed using R134a/ Cu nano-refrigerant in primary circuit and water in secondary circuit of VCRS.
4. Lowest enhancement in performance was observed using R404A/TiO_2 nanorefrigerant in primary circuit and water in secondary circuit of VCRS.

References

[1] L.O.S. Buzelin, S.C. Amicoa, J.V.C. Vargasa, J.A.R. Parise, Experimental development of an intelligent refrigeration system, International Journal of Refrigeration, 28, 2005 165–175

[2] Jwo et.al, Effect of nano lubricant on the performance of Hydrocarbon refrigerant system. J. Vac. Sci. Techno. B, 27(3), 2009, 1473-1477

[3] Hao Peng et.al., Nucleate pool boiling heat transfer characteristics of refrigerant/oil mixture with diamond nano parti cles. International Journal of Refrigeration, 33, 2010, 347-358.

[4] Henderson et al. Experimental analysis on the flow boiling heat transfer of R134a based nanofluids in a horizontal tube, IJHMT, 53, 2010, 944-951.

[5] S. Bobbo et.al, Influence of nanoparticles dispersion in POE oils on lubricity and R134a solubility. International Journal of Refrigeration, 33, 2010, 1180-1186

[6] Shengshan Bi, Performance of a Domestic Refrigerator using TiO2-R600a nano-refrigerant as working fluid, Int J of Energy Conservation and Management, Vol. 52, 2011, 733-737

[7] K Lee, YJ Hwang, S Cheong, L Kwon, S Kim, J. Lee, Performance evaluation of nano-lubricants of fullerene nanoparticles in refrigeration mineral oil. Current Applied Phys 2009, 9:128–31.

[8] RX Wang, HB. Xie, A refrigerating system using HFC134a and mineral lubricant appended with N-TiO_2 (R) as working Fluids. In: Proceedings of the 4th international symposium on HAVC, Tsinghua University; 2003

[9] S.Z. Heris, S.G. Etemad, M.N. Esfahany, Experimental investigation of oxide nanofluids laminar flow convective heat transfer, Int. Commun. Heat and Mass Transfer, 33, 2006, 529535.

[10] K Lee, YJ Hwang, S Cheong, L Kwon, S Kim, J. Lee, Performance evaluation of nano-lubricants of fullerene

nanoparticles in refrigeration mineral oil. Curr Appl Phys, 2009, 9:128–31.
[11] A. Sharma, S. Chakraborty, Semi-analytical solution of the extended Graetz problem for combined electro osmotically and pressure-driven microchannel flows with stepchange in wall temperature, Int. J. Heat Mass Transf. 51, 2008, 4875-4885.
[12] W. Yu, D.M. France, D.S. Smith, D. Singh, E.V. Timofeeva, J. L. Routbort, Heat transfer to a silicon carbide/water nanofluid, Int. J. Heat Mass Transf 52, 2009, 3606-3612.
[13] S. Torii, W. J. Yang, Heat transfer augmentation of aqueous suspensions of nanodiamonds in turbulent pipe flow, J. Heat Transf. 131, 2009, 043203-1 - 043203-5
[14] U. Rea, T. McKrell, L.W. Hu, J. Buongiorno, Laminar convective heat transfer and viscous pressure loss of alumina-water and zirconia-water nanofluids, Int. J. Heat Mass Transf. 52, 2009, 2042-2048
[15] S. M. S. Murshed, K. C. Leong, C. Yang, Enhanced thermal conductivity of TiO_2-water based nanofluids, Int. J. Therm. Sci., 44, 2005, 367–373.
[16] R. L. Hamilton, O. K. Crosser, Thermal conductivity of heterogeneous two component systems, I & EC Fundam., 1(3), 1962, 187–191.
[17] Y. Xuan, Q. Li, Investigation on convective heat transfer and flow features of nanofluids, J. Heat Transfer, 125, 2003 151–155.
[18] C. Sitprasert, P. Dechaumphai, A thermal conductivity model for nanofluid including effect of temperature – dependent interfacial layer, Res 11(6), 2009, 1465-1476
[19] H. Brinkman, The viscosity of concentrated suspensions and solution J chem. Physics 20, 1952.
[20] B. C. Pak, Y. I. Cho, hydrodynamics and heat transfer study of dispersed fluid with submicron metallic oxide particle Exp. Heat transfer, 11(2), 1998, 151-170

Volume 3, Issue 3 (2015) 498-502 ISSN 2347 - 3258
International Journal of Advance Research and Innovation

Thermodynamic Analysis of Heat Pipe Using Ammonia, Water and Ethanol with a View to Being Used in Refrigeration

Ankit Dwivedi, R. S. Mishra
Department of Mechanical Engineering, Delhi Technological University, Delhi, India

Article Info

Article history:
Received 10 July 2015
Received in revised form
20 July 2015
Accepted 28 August 2015
Available online 15 September 2015

Keywords

Ammonia,
Ethanol,
Heat Pipe

Abstract

Heat pipe was developed by NASA for space applications, and this device can be used in simple refrigeration systems, which will have a great impact on the size of the system. Several working fluids can be used in the heat pipe along with the different available material in the designs of the pipe. In this research work several parameters of a heat pipe are observed varying the design conditions alongside the working fluid in the heat pipe which are Water, Ammonia and Ethanol analysed on software. The design conditions are kept as it would be in a commonly used refrigeration system. The capacity of the system is varied and analysis is done. The capacity can be enhanced without much change in the size. Also the temperature of working becomes more or less constant. Water turns out to be a very effective working fluid in a heat pipe with the view of refrigeration when the temperature of working increases.

1. Introduction: Heat Pipes

1.1 History

Heat Pipes were developed particularly for space applications ' by the NASA. One principle problem in space applications was to transport the heat from inside to the outside, on the grounds that the heat conduction in a vacuum is exceptionally restricted. So there was a need to create a quick and viable approach to transport heat, without having the impact of gravity. The thought behind is to make a flow field which transports heat from one spot then onto the next by mode of convection, in light of the fact that convective heat exchange is much quicker than conduction. These days, heat pipes are utilized in many applications, where one has restricted space and the need of a high heat flux. Obviously, it is still being used in space applications, yet it is likewise utilized as a part of heat exchange systems, cooling of PCs, cell telephones and cooling of solar based collectors.

1.2 Principle of Working

The fundamental of heat pipes is dependent of evaporation and condensation. At the hot side, the working liquid is evaporated and at the cool side it condenses. As every material has different properties, it's required to choose the set of material properly. At the source the cool fluid is evaporated, the hot vapour stream is a while later transported to the sink where the vapour condenses again and is transported back to the source. The issue of this procedure is the space utilization; consequently it was important to build up a compacter approach to transport heat with the indicated procedure. The thought of a Heat Pipe is presently to incorporate the complete convective transport in one channel, where the vapour stream is in the centre of the pipe and the floe happens to be on the outside of the barrel. Heat exchange is so efficient that fundamentally it is a direct result of the low heat resistance because of the convective stream, as explained earlier. This low heat resistance is because of little effective length of heat exchange through strong porous wick walls.

Corresponding Author,
E-mail address: professor_rsmishra@yahoo.co.in
All rights reserved: http://www.ijari.org

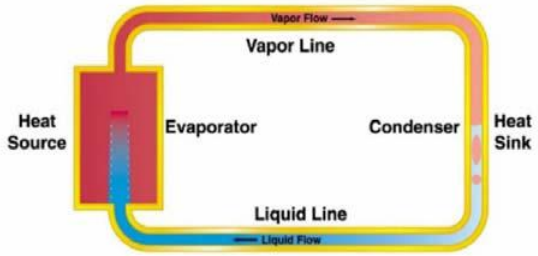


Fig: 1. Circular Process of a Heat Pipe [2]

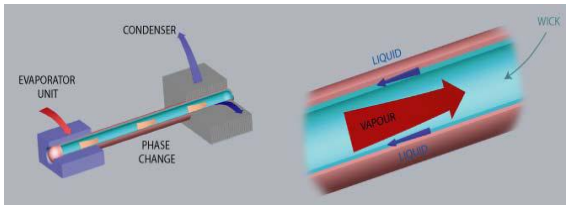


Fig: 2. Concept of Heat Pipe [2]

1.3 Key Features of Heat Pipe

- Very high heat transfer capacity in a simple system.
- Allows several Heat Transport passes, avoids a single point breakdown.
- Smaller units, no bulky pressure vessel.
- Valves, pumps or compressors are not required.
- Can be started cold, no need of preheat.
- High temperatures allow very high efficiency operation, almost constant temperature process.

1.4 The Selection of the Working fluid in the Heat Pipe

The Fluids used in the Heat Pipe are chosen on the basis of their merit:

1. Water
2. Ammonia
3. Ethanol

Also these fluids are very easily available. These also show the best Figure of Merit to be used in heat pipe

applications. These fluids are cheap and non toxic in nature. Ethanol is flammable so it's used must be strictly observed.

The latent heat of vaporisation and condensation is also a very big deciding factor for the fluid in heat pipe. The working liquid must have great thermo-physical properties at the predetermined operational temperature and weight. Working liquid must have high wettability, surface tension and other attractive thermo-physical properties incorporating a high fluid thermal conductivity, high inert enthalpy of vaporization, low fluid viscosity, and a low vapour viscosity.

1.5 Limitations

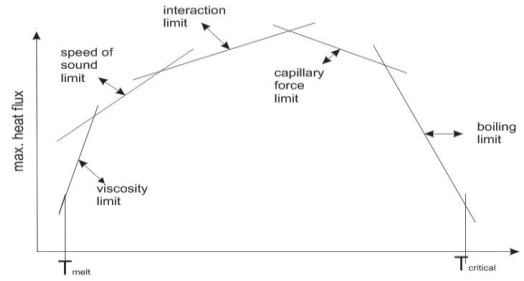


Fig: 3. Limitations of a Heat Pipe [2]

- **Melting Temperature:** One can't utilize a heat pipe below the melting temperature.
- **Viscosity Limit:** The viscosity of the liquid is too high for being transported at low temperatures and low pressures.
- **Sonic Limit:** It is critical for high temperature, where the vapour could conceivably achieve the velocity of sound while leaving the source.
- **Capillary limit:** When the capillary force is definitely not fulfilling the required force transport the fluid
- **Interaction limit:** This breaking point is associated with open channels, where the vapour can be diverted by the vapour, because of high speed contacts.
- **Boiling cut off:** The fluid forms bubbles which close the capillaries, it's not an issue for open channel structures
- **Critical temperature:** Beyond the critical temperature the concept of vapour and liquid seizes to exist.

2. Literature Review

P. Yeunyongkul et al.[2010] conducted set of experiments for which the results of closed loop oscillating heat pipe (CLOHP) condenser was connected to vapor compression refrigeration. In which two cons of split sort ventilation system were considered [1]. ***Fabian Korn et al. [2012]*** performed several vital experiments on heat pipes to establish it to be one of the most effective procedures to transport thermal energy from one point to another, mostly used for cooling [2]. ***Sameer Khandekar et al. [2010]*** performed experiments on the global thermal performance modeling of Pulsating Heat Pipes (PHPs) requires local, spati-o-temporally coupled, flow and heat transfer information during the characteristic, self-sustained thermally driven oscillating Taylor bubble flow, under different operating conditions[3]. ***Jozef Hužvár, Patrik Nemec et al. [2007]*** used heat pipe, observed its basic principles and operating limits. High temperature heat pipes were evaluated for use in energy conversion applications such as fuel cells, gas turbine re-combustors, and Stirling cycle heat sources, with the resurgence of space nuclear power, additional applications include reactor heat removal elements and radiator elements [4]. ***R.Z. Wanget al. [2008]*** added heat pipes in adsorption water chiller or ice maker initials. His work showed that the adsorption refrigerators are very efficient [5]. ***Pracha Yeunyongkul et al.[2009]*** aimed at experimentally investigating the application of a closed loop oscillating heat pipe (CLOHP) as the condenser for a vapor compression refrigeration system[6]. ***R. Rajashree et al. [1990]*** went through a numerical analysis of an unsteady, viscous, laminar, incompressible, two dimensional heat and mass transfer, in the vapour gas region of gas loaded circular heat pipe [7].

In the case of heat pipe an analysis based on multiple easily available working fluid, with different working conditions can be done. For an example liquid Sodium is not a vital fluid to be used for common refrigerating plants, where fluids as methanol, ethanol, water ammonia etc can make the use of heat pipe in the main stream. Also the main parameters of a heat pipe such as cross-sectional area of the wick, Heat Transfer Factor etc can be analysed on the basis of varying design variables such as operating temperature, pore radius, wick permeability, wick material, maximum heat to be transported etc. Along with being used in the VCR system it can be used in an ejector type refrigerating unit and vapour absorption and Electrolux and may enhance the performance of these systems. In the case of observing the changes brought by a regenerative heat exchanger and a flash gas removing chamber along with two stage compression without inter-cooling with eco-friendly refrigerants a comparison with Simple VCR cycle can be observed and same for the VARS cycle can be done.

3. Systems Description

The system has to have a capacity of 10 TR increasing up to 50 TR at the evaporator temperature also the evaporator temperature will be observed from 253K to 273K. Considering the surrounding situation of the country the condenser temperature will be varied from 313K to 328K.In the study the condenser used in the VCRS will be replaced by a Heat pipe of a chosen wick material 30 mesh screens. The effect of the size change will be observed with the application of heat pipe. Also three different fluids for heat pipe namely Water, Ammonia and Ethanol will be checked for their merits and what effect would they have on the design of heat pipe. The heat taken by the condenser will now be absorbed by the heat pipe and a direct comparison for the size of these two components would be sought after. The length of tubes in the evaporator and condenser and the effective length of the heat pipe are kept 1 meter in length. A software analysis is done.

4. Performance Parameters

Figure of Merit (MF_h): The figure of merit is the ratio of the product of density, surface tension and latent heat of evaporation to the dynamic viscosity of the fluid at saturated liquid state. As it can be seen clearly the Figure of Merit is the ratio of the thermo-physical properties it is dependant only on the temperature of working. So its variation is observed with the variation of temperature between the working limits of the condenser of the system ie. 40 °C to 55 °C.

$MF_h=\rho_l \sigma h_{fg}/\mu_l$

Where:

ρ_l is the density of liquid in heat pipe in kg/m^3,

σ is the surface tension of the fluid in N/m,

h_{fg} is the latent heat of vaporization at heat pipe temperature in kJ/kg, and

μ_l is the viscosity of the liquid in Pa-s.

Maximum Heat transfer (Q_{max}) (Capillary Limitation): It's the maximum heat that can be transferred on the basis of capillary limitation.

$Q_{max}= (MF_h)(A_w k_{hp}/L_{eff})\{(2/r_p)-(\rho_l g L_{eff} \sin\phi / \sigma)\}$

where:

MF_h is the Figure of Merit in kW/m^2,

A_w is the cross sectional area of wick in m^2,

k_{hp} is the Permeability of the wick material in m^2,

L_{eff} is the effective length of the heat pipe in m,

r_p is the pore radius in m,

g is the acceleration due to gravity in m/s^2, and

Φ is the inclination angle in degrees.

Heat Transfer Factor: Heat transfer factor is another factor in the analysis which will affect the size of the heat pipe. It depends on permeability, pore radius, Figure of Merit and the wick area. Its unit is W-m, and plays an important in the designing of a heat pipe.

$HTF= (2* MF_h* A_w* k_{hp}/r_p)$

The symbols have usual predefined meaning.

5. Results and Discussions

The analysis will show which one of the three fluids will work better at higher temperatures with a higher capacity of absorbing heat, with smallest size.

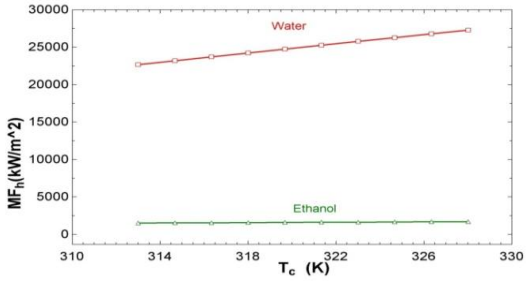


Fig: 4. Variation of Figure of Merit and Heat pipe temperature for Water and Ethanol [8]

Fig 4 shows a comparison between Figure of Merit and Heat pipe temperature for Water and Ethanol. The least Merit is related to the Ethanol while Water has substantially large value with rise in the temperature the figure of merit of water shows a rise while for ethanol it has a constant value.

In another analysis the variation in wick area (A_w) is observed with the operating temperature (T_c) and the Figure of Merit (MF_h).

The difference between the wick area required for Ethanol and Ammonia can be observed very easily, whereas the same required for Ammonia and water are comparable. Size is affected by the wick area required per unit effective length. Fig 5 and Fig 6 prove that with rise in temperature the wick cross-sectional area required is least for water as a working fluid.

The Refrigerating capacity is a very important parameter in any refrigeration plant. The capacity must be enhanced, size and the power consumption must be reduced to obtain a desired result. Hence the wick area with respect to the maximum heat absorbed by the heat pipe (Q_{max}) and the Refrigerating capacity is studied

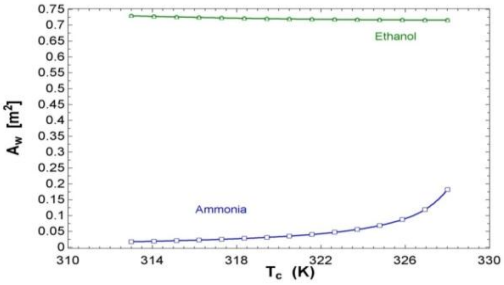


Fig: 5. Variation of Wick Area with operating temperature of heat pipe for Ethanol and Ammonia [8]

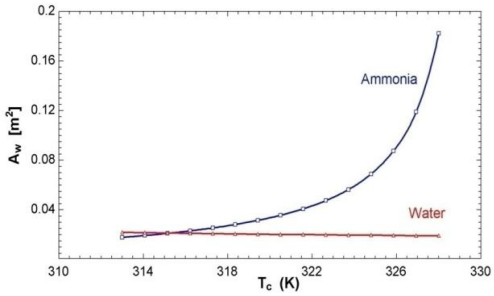


Fig: 6: Variation of Wick Area with operating temperature of heat pipe for Ammonia and Water [8]

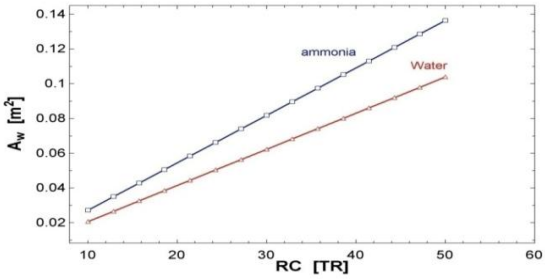


Fig: 7. Variation of Wick area with refrigerating capacity for Ammonia and Water [8]

The wick areas for Ammonia and Water are comparable and close enough. But water proves out to be better in this analysis. The separate variation for Ethanol is also shown.

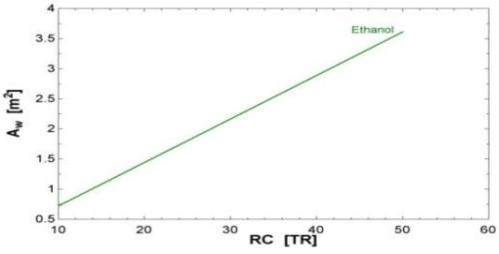


Fig: 8: Variation of Wick area with refrigerating capacity for Ethanol [8]

It is evident from Fig 7 and Fig 8 that water is giving a lesser area of heat pipe for the same capacity of the plant. The capacity can be increased and further analysis can be done.

Inclination angle of the heat pipe also affects the wick area required in the heat pipe. The inclination angle (ϕ) is measured in degrees. Variations obtained are as follows:

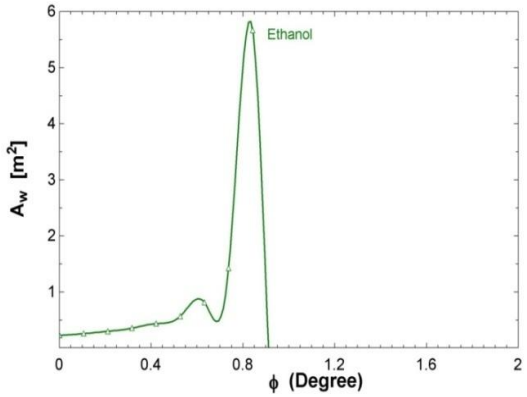


Fig: 9: Variation of Wick Area with Inclination Angle for Ethanol [8]

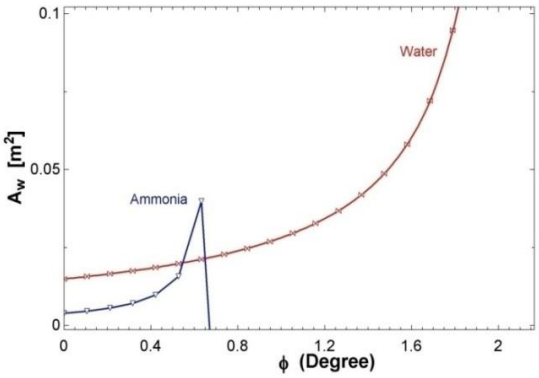


Fig: 10: Variation of Wick Area with Inclination Angle for Ammonia and Water [8]

Fig 9 and Fig 8 show the variation of the wick area with the inclination angle. It can be observed that as the inclination angle is increased area for water increases rapidly.

The plot for Water, Ammonia and Ethanol is obtained.

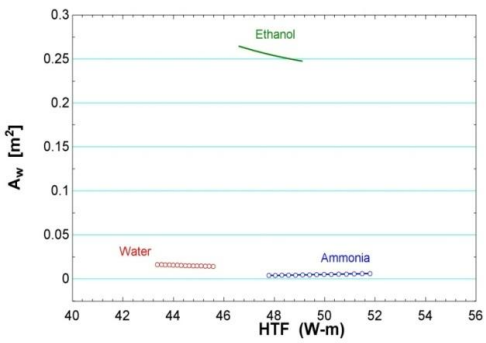


Fig: 11. Overlay Plot for Water, Ammonia and Ethanol [8]

Fig11 shows the variation of area with heat transfer factor .Area required for Ethanol is maximum and minimum with Ammonia. The Heat Transfer Factor is largest for the Ammonia and smallest for Water.

Another analysis is conducted to obtain the effect of pore radius r_p on the wick area. Parametric tables are presented as follows. The tables show respectively the relation between the A_w and r_p Water, Ammonia and Ethanol. The widest range of acceptable inclination angles is obtained for water, where as for ammonia area tends to negative for higher values of angle.

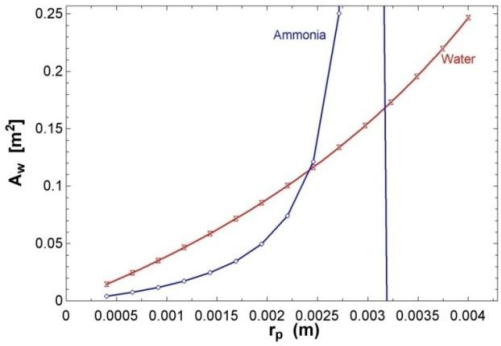


Fig: 12: Plot between Wick Area and Pore Radius for Ammonia and Water [8]

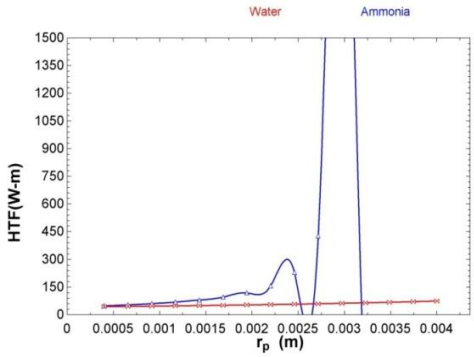


Fig: 13: Plot between HTF and Pore Radius for Ammonia and Water [8]

Fig: 12 shows the variation of wick cross-sectional area and pore radius with water and ammonia. For Water with increase in the pore radius the cross-sectional area goes on increasing but for Ammonia after a point it reduces. Fig 13 shows the variation of heat transfer factor and pore radius. For Water the heat transfer factor is more or less constant with the pore radius.

The heat pipe in this analysis replaces the conventional condenser which is deemed to be one of the essential parts of the refrigeration cycle. Be it a VCRS cycle or a VARS cycle condenser has always been there. The main advantage of a heat pipe is that it can be observed that its size will not be very huge even if the capacity of the system has to be enhanced. In this analysis Parametric Tables are prepared for condenser area, wick area, evaporator area with varying operating temperatures and refrigerating capacity and maximum heat transferred in heat pipe and condenser. The purpose is to show the difference in the condenser size,

evaporator size and wick area of a heat pipe all the three having unit length.

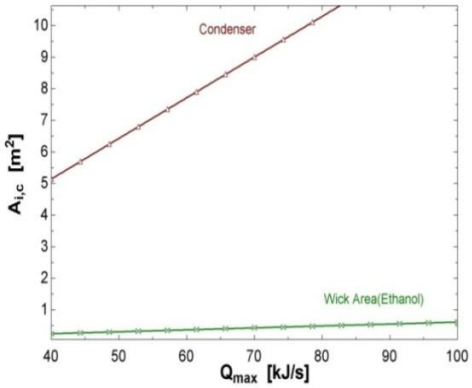


Fig: 14. Variation of Condenser area and wick area with heat capacity [8]

Fig 14 shows that the cross-sectional area of the wick is very small when compared to the heat transfer area of the condenser which result reduced size and capacity of the plant will also will be high.

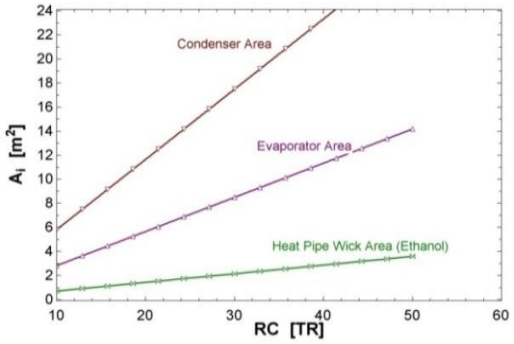


Fig: 15: Variation of condenser, evaporator and wick area with refrigerating capacity[8]

Fig: 15 shows the variation of areas of all the three heat exchangers that can be used in the system

6. Conclusions

From the results of the above research work the following conclusions can be made:

- The Figure of Merit of the working fluids Ammonia has the largest and Ethanol has the least merit. But Water shows the best possible results for the operating temperature of the heat pipe.
- As the temperature of heat pipe raises the merit of Water and Ethanol show increase and for Ammonia it decreases. As the
- Figure of Merit increases, the required cross-sectional area of the wick decreases.Expected variations have been observed between working temperature and wick cross-sectional area ie. with increase in temperature the area increases. For Ammonia it has a sharp rise as the temperature decreases and for Water and Ethanol the area is almost constant.
- As the capacity of refrigeration is increased maximum wick area is required by Ethanol and the least is for water. The same variations can be observed between the Heat transfer Factor and Wick Cross-sectional area.
- Angle of inclination also has an interesting effect on the on the area of the wick, so the inclination has to be chosen to optimize the heat transfer, the wick area and the cost of the heat pipe.
- For the range of temperature we are dealing with maximum heat transfer factor has been obtained for Ammonia, and the area will be the maximum for the Ethanol. With increase in the pore radius the area first increases then decreases after a certain limit, hence it has to be chosen optimally. The heat transfer factor also shows a similar variation with the pore radius.
- With increasing capacity the wick area increases slightly when compared to the increase in a conventional condenser. The low wick area will render a small overall area of heat pipe.

In Future work mixture of different working fluids can be experienced with, along with different nano-particles. Also there is a scope of optimization for different types of heat pipe working on the refrigerating conditions. Different materials for the construction of the heat pipe will also be studied for their suitability for being used in refrigeration plants

References

[1] N. Kammuang-lue, P. Sakulchangsatjatai, P. Terdtoon, P. Yeunyongkul, Experimental Investigation of the Closed Loop Oscillating Heat Pipe Condenser for Vapor Compression Refrigeration, Journal of Applied Science and Engineering, 15(2), 2012, 117-18

[2] F. Korn, Heat Pipes and its Applications, Project Report 2008 MVK160 Heat and Mass Transport, Lund, Sweden, 2008

[3] J. Bonjour, F. Lefèvre, S. Khandekar, P. K. Panigrahi, Local Hydrodynamics of Flow In A Pulsating Heat Pipe: A Review, Frontiers in Heat Pipes (FHP), 1, 2010

[4] J. Hužvár, P. Nemec, Mathematical Calculation of Total Heat Power of the Sodium Heat Pipe, APVV - 0517 – 07.

[5] R. Z. Wang, Efficient adsorption refrigerators integrated with heat pipes, Applied Thermal Engineering, 28, 2008, 317–326

[6] P. Sakulchangsatjatai, P. Terdtoon, P. Yeunyongkul, Mathematical Model of the Optimum Heat Pipe Heat Exchanger for a Condenser of Vapor-Compression Refrigeration Cycle, Energy Research Journal, 1(2), 2010, 104-110

[7] R. Rajashree, K.S. Rao, **A** Numerical Study of the Performance of Heat Pipe, Indian Journal of Pure and Applied Mathematics, 21(1): 1990, 95-108

[8] A. Dwivedi, Thermodynamic Analysis of Vapour Compression Refrigeration System Using a Heat Pipe, Masters Degree in Delhi Technological University, 2015, 20-48

Defence Science Journal, Vol. 65, No. 6, November 2015, pp. 500-507, DOI : 10.14429/dsj.65.8385
© 2015, DESIDOC

X-ray Diffraction Analysis of Severely Cold Deformed Hypereutectoid Steel Wire

S.S. Bargujer[*,#], N.M. Suri[#], and R.M. Belokar[#]

[*]*Ordnance Cable Factory, Chandigarh - 160 002, India*
[#]*PEC University of Technology, Chandigarh - 160 012, India*
[*]*E-mail: bargujer@yahoo.com*

ABSTRACT

Hypereutectoid steel wire rod of diameter 6.40 mm is lead patented in lead bath of an electric powered furnace and then it is cold drawn through converging conical dies in a die sequence up to 2.50 mm diameter. The drawn wires subjected to different true strain are analysed using line profile X-ray diffraction methods. The classical Williamson-Hall plot as well as modified Williamson-Hall plot of drawn wire specimens of different true strain is plotted. The theoretical as well as experimental value of *q* is evaluated. The *q* is a parameter which depends up on elastic constant of the crystal and type of dislocations. The changes in nature of dislocations from edge dislocations to screw dislocations are calculated against true strain and are verified by scanned electron microscopy's micrograph of drawn wire.

Keywords: Hypereutectoid steel wire, Williamson-Hall plot, spring, true strain, x-ray diffraction, elastic constant and full width half maximum, FWHM

1. INTRODUCTION

The detailed study on lead patenting and wire drawing of pearlitic steel wire[1-2] has been carried out by analysing SEM/TEM micrograph but limited study has been reported on hypereutectoid steel wire drawing process by X-ray diffraction (XRD) methods so far. XRD analysis has been done on Cu[3-7], ferritic-pearlitic steel[8], Aluminium[9-10] martensitic steel[11-12], pearlitic steel[13-15], nickle[16], FeN[17], 10Cr-5W heat resistant steels[18]. The elaborate study on elastic constants[19] for hypereutectoid steel and dislocations contrast factors[20-22] of cubic crystals is available in literature. The present study is carried out to correlate the mechanical properties, microstructural changes as well as detailed X-ray diffraction line profile analysis for better understanding of cold drawing process of hypereutectoid steel wires.

The springs[23] are used in the arms and ammunitions[24] for performing specific task. A few example of application of hypereutectoid steel wire which are used for manufacturing springs are of diameter 0.35 mm, 0.45 mm, 0.50 mm, 0.60 mm, 0.70 mm, 0.90 mm, 1.00 mm, 1.20 mm, 1.25 mm, 1.30 mm, 1.40 mm, 1.50 mm, 2.00 mm, 2.30mm, 2.50 mm, 2.80 mm, 3.00 mm, 4.50 mm and 5.00 mm. These wires are used in various springs for 0.22″ revolver, 0.32″ pistol, 5.56 mm INSAS rifle, 30-06 sporting rifle, tear gas gun, MCIWS weapon, pump action gun, double barrel breach loading gun, 7.62 mm rifle, 12.7 mm AD gun, ILG gun, PRG gun, and 30 mm Cannon, T-72 Tank gun, etc.

The lead patented hypereutectoid steel wire has a very fine alternate layer of ferrite and cementite lamellae. These alternate layers in fine pearlite cannot be resolved under optical microscope. Hypereutectoid steel wire does not have any cementite network on its grain boundary. The lamellas of ferrite and cementite have same orientation in individual pearlite colony but each pearlite colony has different and random orientation of lamellas from its neighbour's pearlite colonies. The hypereutectoid steel wire has higher ultimate tensile strength (UTS) and torsion strength as compared to other steel.

2. EXPERIMENTAL WORK

The chemical composition of hypereutectoid steel wire rod used in the study is mentioned in Table 1. The initial diameter of lead patented wire rod is 6.40 mm. The sample is subjected to cold wire drawing process and mechanical properties are recorded after drawing from each die. The results are mentioned in Table 2. The selected samples for X-ray analysis are of 6.40 mm, 5.80 mm, 5.30 mm, 4.40 mm, 3.60 mm, 3.0 mm, and 2.50 mm diameter.

Table 1. Chemical composition of wire rod

Carbon	Manganese	Silicon	Sulphur	Phosphorous
0.88	0.48	0.20	0.005	0.006

The plot of ultimate tensile strength (UTS) vs. true strain for drawn sample is shown in Fig. 1(a). The bar chart indicating the contribution percentage in the gain of UTS of wires by lead patenting process and wire drawing process are shown in Fig. 1(b). The Fig. 1(c) show the swirling of lamellar structure due to wire drawing strain. The average grain size number of lead patented wire rod of diameter 6.40 mm is 9.5. The average grain size number is calculated using optical microscopic image by standard method.

Received 24 January 2015, revised 20 October 2015, online published 10 November 2015

Table 2. Draw dies sequence of wire

Diameter of wire	Ultimate tensile strength (MPa)	Ultimate torsion strength (nos. of turn)
6.4	1378.34	24
5.8	1486.84	26
5.3	1531.1	28
4.8	1592.09	28
4.4	1599.73	26
4.0	1742.35	40
3.6	1777.73	24
3.3	1870.03	23
3.0	1896.18	25
2.7	2004.13	24
2.5	2069.1	25

3. RESULTS AND DISCUSSION

The X-ray diffraction line profile analysis is done by Philip PAN XPRT analysis X-ray diffraction (XRD) machine having copper as X-ray generating source. The W. H. Bragg carried out experimentation on X-ray diffraction of various materials and found that the incident beam, the normal to diffraction plane and the transmitted beam are always coplanar. The angle between the diffracted beam and the transmitted beam is always twice of the diffraction angle. According to Bragg's law: $d = \lambda/2\sin\theta$. Where, d is inter-planer spacing, normally called as d-spacing, λ is wavelength of X-rays and θ is diffraction angle. XRD of a pearlitic steel wire mainly display peak generated from ferrite phase. The XRD graphs of samples subjected to various degree of cold working are as shown in Fig. 2 (a) - 2(e).

3.1 X-ray Peak Analysis

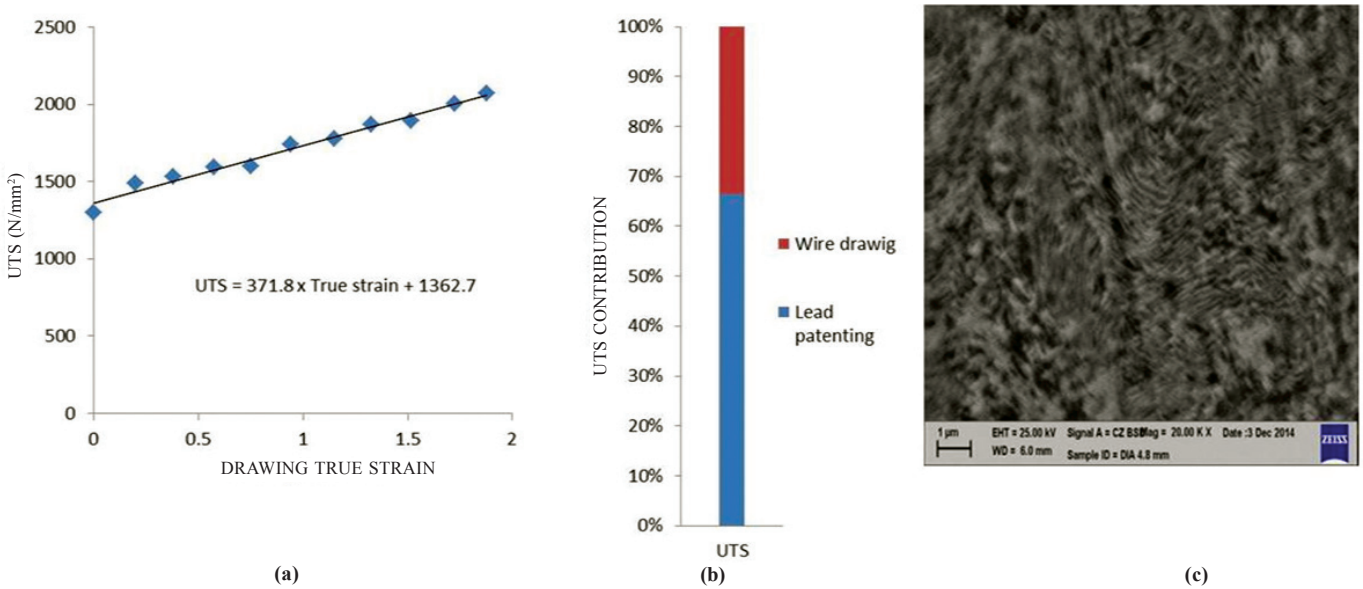
Peaks in XRD plots are identified by using Bragg's law and crystal geometry of ferrite phase of steel. In b.c.c. crystal, d_{hkl} of an hkl plane = $a/(h^2+k^2+l^2)^{1/2}$. Where, a is unit cell dimension and is equal to 4 $r/(3)^{1/2}$. Where, r is atomic radius of ferrite. The indexing of diffraction peaks is done on the basis of structural factor using equation $\lambda/4a^2 = \sin\theta_{hkl}/(h^2+k^2+l^2)$ = constant. For b.c.c. crystals, those diffraction planes which satisfies the condition $h+k+l$ = even are only producer of the constructive peaks in XRD.

The plot of FWHM vs. true strain for different diffraction planes is shown in Fig. 3. The plot indicates that FWHM increases almost linearly with increase in true strain although rate of increase is slightly differ from plane to plane as indicated in Fig. 3. The maximum increase in FWHM is noticed at 310 diffraction plane.

The broadening of diffraction lines due to non-uniformity of strain is obtained by the Bragg's law as: $b = -2(\Delta d/d)\tan\theta$. Where b is broadening due to fractional variation in Bragg plane spacing, $\Delta d/d$. When a heat treated metal is cold worked, its diffraction lines become broader. The broadening of diffraction lines is due to particle size or due to strain becomes a point of controversy. The separation of the size and strain components can be done by plotting $B\,Cos\theta$ as a function of $Sin\theta$. Where, B is FWHM of a peak. This plot of $B\,Cos\theta$ vs. $Sin\theta$ is known as classical Williamson-Hall plot and implicitly assumes that peak shapes are Lorentzian.

3.2 The Classical Williamson-Hall Plot

The classical Williamson-Hall plot for steel wire samples are plotted at different true strain in Fig. 4 (a) - 4(g). In a classical Williamson-Hall plot, X-axis represents $B\,(Cos\theta)\,/\lambda$ and Y-axis represents $Sin\theta/\lambda$. The Scherrer equation can be used to find out the broadening of peak width due to crystallite size or strain broadening. The Scherrer equation is as: $B\,\text{Cos}\,\theta = K\,\lambda\,/\,L + 4\,\varepsilon\,Sin\,\theta$. Where, first part of equation indicates the role of crystallite size in broadening of peak and the value of



(a) (b) (c)

Figure 1. (a) UTS vs drawing true strain plot, (b) Bar chart shows the contribution of lead patenting process and wire drawing process in UTS of wire, and (c) SEM micrograph showing the dominance of swirling of lamellar at 0.5753 drawing true strain, respectively.

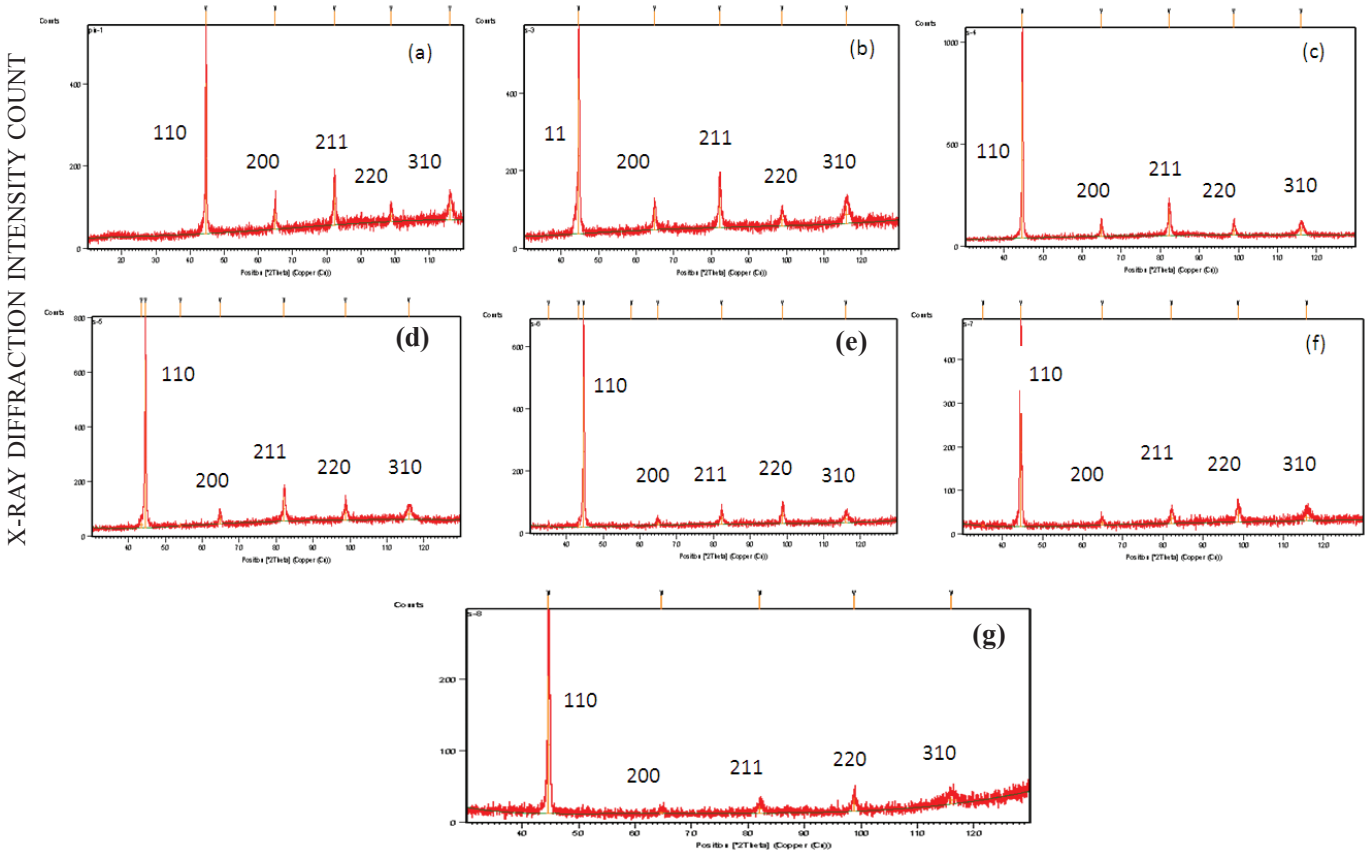


Figure 2. (a)-(g): X-ray diffraction line profile of 6.40 mm, 5.80 mm, 5.30 mm, 4.40 mm, 3.60 mm and 3.00 mm, and 2.50 mm diameter wire, respectively.

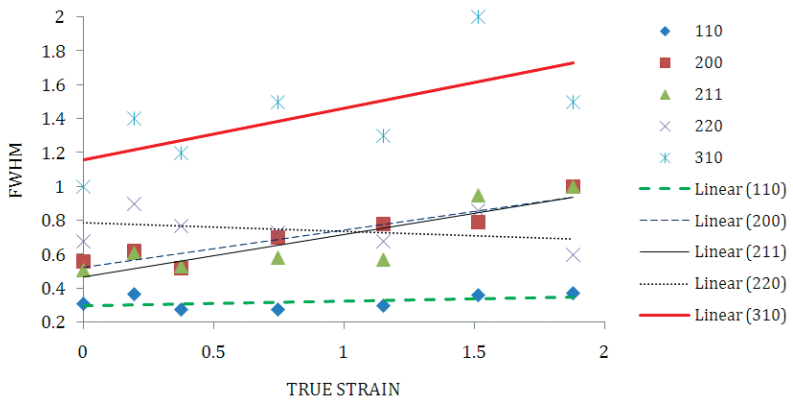


Figure 3. FWHM vs. true strain plot for plane having 110, 200, 211, 220 and 310 diffraction planes.

this part is given by linear interception on *Y* axis. The second part of equation indicates the role of strain in broadening of peak and is equal to slope of linear plot. The crystallite size is calculated using data from XRD figures with the help of Scherrer equation. The crystallite size is 57.32 nm, 56.679 nm, 52.51 nm, 43.57 nm and 42.21 nm at drawn true strain nil, 0.743, 1.150, 1.515, and 1.880, respectively. This indicates that the increase in drawn true strain results in decrease in crystallite size.

According to Modified Williamson-Hall equation, the line broadening of diffraction profile with increasing diffraction order is caused by dislocations in strain anisotropy. The FWHM of the diffraction profile as per modified Williamson-hall plot is:

$\Delta K \sim = \gamma / d + (\pi M^2 b^2)/ 2 * \rho^{1/2} * K^2 C + O (K^4 C^2)$

where $\gamma = 0.90$ for ferrite. d = size parameter. ρ = average dislocation density. b = length of Burgur's vector of dislocation and is equal to 0.248 nm for pearlitic steel. M = a constant which depends upon effective outer cut-off radius of dislocation and is determined from Fourier coefficient. C = contrast factor of dislocation. O = higher order term in K^4C^2. $\Delta K = Cos\ \theta\ [\Delta (2\theta)] / \lambda$, where $\Delta (2\theta)$ is FWHM of diffraction peak and $H^2 = (h^2k^2 + h^2l^2 + k^2l^2)/(h^2 + k^2 + l^2)$.

Average dislocation contrast factor of un-textured cubic polycrystalline $C = C_{h00} (1\text{-}qH^2)$, where C_{h00} is average

Table 3. $C_{pure\ edge}$ and $C_{pure\ screw}$ for different diffraction plane *g*

g	(110), (220)	(200)	(211)	(310)
$C_{pure\ edge}$	0.1795	0.1861	0.1795	0.1837
$C_{pure\ screw}$	0.1057	0.2522	0.1056	0.0758

dislocation contrast factor for *h00* reflections. *q* is a parameter which depends up on elastic constant of the crystal and type of dislocations, i.e., edge or screw dislocations. The contrast factors C_{h00} for different diffraction vector *g* for pure edge dislocations and pure screw dislocations of ferrite is calculated using ANZIC software and are mentioned in Table 3.

3.3 Theoretical Methods for Determination of *q*

The value of *q* is a function of elastic constants of steel. The average polycrystalline elastic constants for α-Fe are taken from Kim[19], *et al*. The values of c_{11}, c_{12}, c_{44} for hypereutectoid steel are 231.5 GPa, 135.0 GPa, and 116.0 GPa, respectively. The theoretical value of *q* is determined by using Eqn (9).

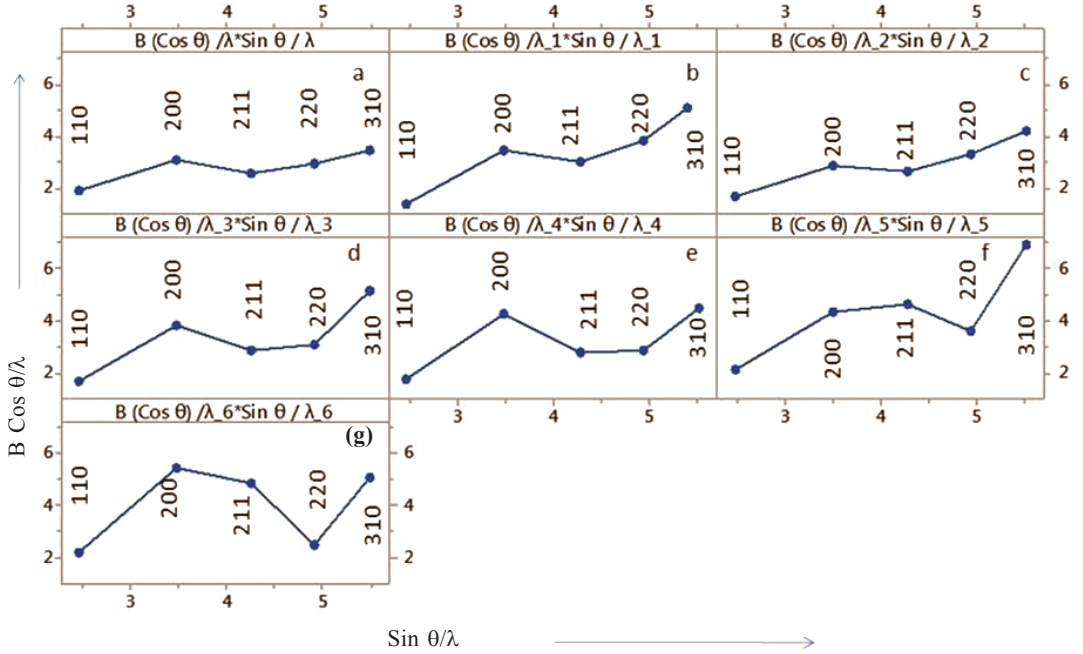


Figure 4. (a)-(g): The classical Williamson-Hall plot for hypereutectoid steel wire as lead patented and at 0.1968, 0.3771, 0.7493, 1.1507, 1.5153, and 1.8800 true strain, respectively.

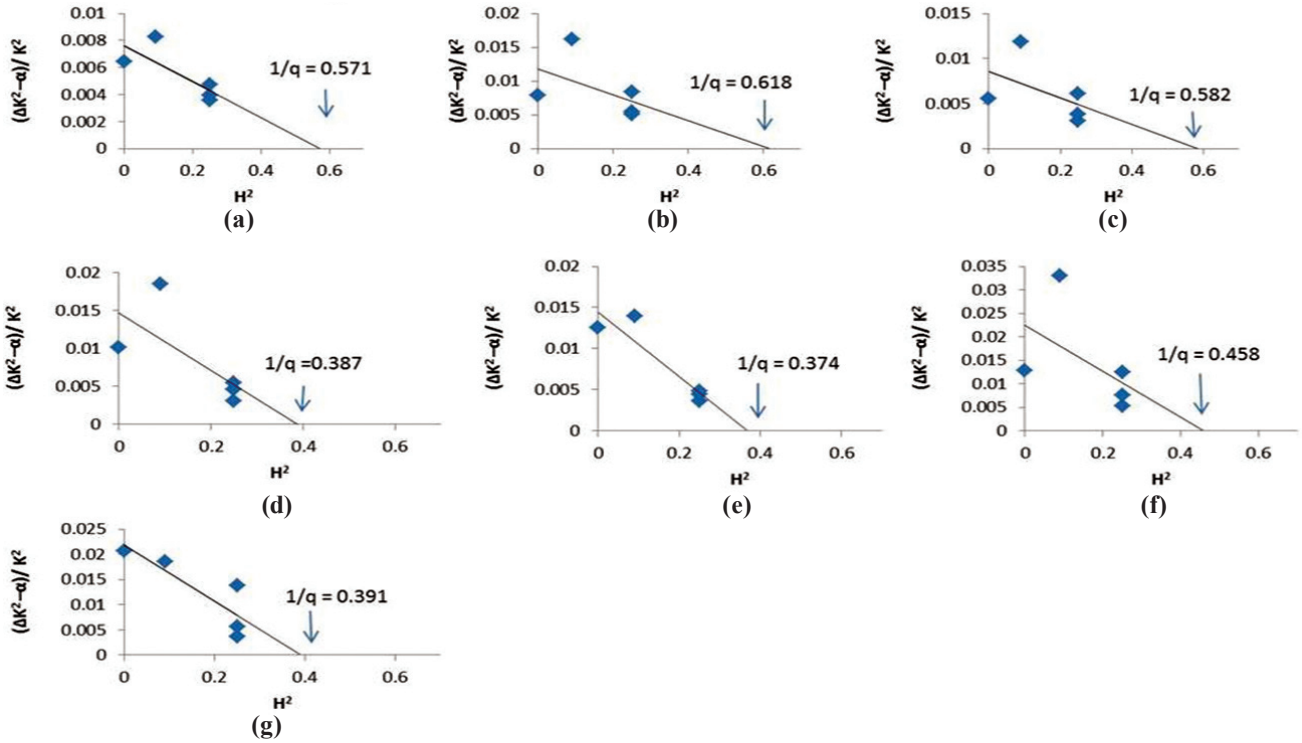


Figure 5. (a)-(g): Experimental value of *q* for hypereutectoid steel wire drawn to true strain of 0.00, 0.1968, 0.3771, 0.7493, 1.1507, 1.5153, and 1.8800 with average crystallite size 70 nm, 63 nm, 57 nm, 48 nm, 39 nm, 32 nm, and 27 nm are 1.750, 1.618, 1.717, 2.578, 2.669, 2.183, and 2.555, respectively.

Table 4. The parameters *a, b, c, d* for c_{12}/c_{44} ratio equal to 1 and 2

Type of dislocation	c_{12}/c_{44}	*a*	*b*	*c*	*d*
Screw	1	8.6590	0.3730	0.0424	-6.074
Screw	2	6.0725	0.4338	0.0415	-3.5021
Edge	1	7.2361	0.9285	0.1359	-5.7484
Edge	2	8.8331	0.8241	0.1078	-7.0570

Table 5. The calculated value of q_{screw} and q_{edge} for different ratio c_{12}/c_{44}

A_i	c_{12}/c_{44}	q_{screw}	q_{edge}
2.416	1	2.674	1.280
2.416	2	2.647	1.783
2.416	1.163	2.669	1.362

$q = a[1- exp.(-A_i/b)] + cA_i + d$. (T. Ungar[20] *et. al.*).
where, A_i is a Zener constant, which depends upon the elastic constant and $A_i = 2c_{44}/(c_{11}-c_{22})$. The value of parameters *a, b, c, d* for above equation are taken from Table 8 and 9 of Ungar[20], *et. al*. and the same are reproduced in Table 4. The calculated values of *q* in case of screw dislocations and edge dislocations in b.c.c. crystal system are mentioned in Table 5.

3.4 Experimental Methods for Determination of *q*

The experimental method used for determination of *q* is based on equation 12 proposed by Ungar[20], *et.al.* are shown in Fig. 5(a-g). The equation is $[(\Delta K)^2–\alpha]/ K^2 = \beta C_{h00}(1-qH^2)$. Where, $\alpha = (0.9/D)^2$ and $\beta = \pi M^2 b^2 \rho/2$. *D* is average particle size. *M* is a constant which depends on the effective outer cut off radius of dislocations. $K = 2\sin\theta/\lambda$, ΔK is FWHM. The interception point on x-axis by best regression line gives the value of $1/q$.

3.5 Evaluation of C_{actual} by using q_{exp}

The C_{actual} is calculated by using simple lever rule with $q_{exp.,}$ q_{th}^{edge} and q_{th}^{Screw} and are mentioned in Table 6.

3.6 Modified Williamson- Hall Plots

The modified Williamson- Hall plots predicts that if strain broadening of diffraction profile in drawn steel wires is caused by dislocations then $(KC)^{1/2}$ will have binomial relationship with FWHM. The modified Williamson- Hall plots of hypereutectoid steel wires at different true strain are shown in Fig. 6 (a-g). The slope of modified Williamson-Hall plot shows an increasing trend from Fig. 6(a) to 6(g). This demonstrates that the numbers of dislocations increases with increase in true strain.

The character of prevailing dislocation can be described using equation 7 of Movaghar Garabagh[12], *et. al.* as: $f^{edge} = 1 - f^{screw} = (q_{th}^{Screw} - q_{exp}) / (q_{th}^{Screw} - q_{th}^{edge})$. Where, f^{edge} and f^{screw} is fraction of edge and screw type dislocations respectively. q_{th}^{Screw} and q_{th}^{edge} is theoretical *q* value for screw and edge type dislocations respectively. q_{exp} is experimental value of *q*. The fraction of pure edge dislocations and pure screw dislocations at various true drawn strains are mentioned in Table 7.

Initially the value of q_{exp} shows an increasing trend till maxima is achieved then slightly decreases trend as shown by dotted line in the Fig. 7. The SEM micrograph shown in Fig. 1(c) and Fig. 7 confirms that the screw dislocations increase initially till maxima is achieved with increase in true strain and then slightly decreases.

Table 6. The calculated value C_{actual} of for different true strain and diffraction plane

Wire diameter (in mm)	True strain	q_{exp}	Diffraction plane	$c_{pure\ edge}$	$c_{pure\ screw}$	c_{actual}
6.40	0.00	1.750	110	0.1795	0.1057	0.1576
			200	0.1861	0.2522	0.2056
			211	0.1795	0.1056	0.1575
			220	0.1795	0.1057	0.1576
			310	0.1837	0.1995	0.1883
5.80	0.1968	1.618	110	0.1795	0.1057	0.1650
			200	0.1861	0.2522	0.1990
			211	0.1795	0.1056	0.1650
			220	0.1795	0.1057	0.1650
			310	0.1837	0.1995	0.1867
5.30	0.3771	1.717	110	0.1795	0.1057	0.1594
			200	0.1861	0.2522	0.2040
			211	0.1795	0.1056	0.1594
			220	0.1795	0.1057	0.1594
			310	0.1837	0.1995	0.1879
4.40	0.7493	2.578	110	0.1795	0.1057	0.1108
			200	0.1861	0.2522	0.2475
			211	0.1795	0.1056	0.1107
			220	0.1795	0.1057	0.1108
			310	0.1837	0.1995	0.1983
3.60	1.1507	2.669	110	0.1795	0.1057	0.1057
			200	0.1861	0.2522	0.2521
			211	0.1795	0.1056	0.1056
			220	0.1795	0.1057	0.1057
			310	0.1837	0.1995	0.1994
3.00	1.5153	2.183	110	0.1795	0.1057	0.1331
			200	0.1861	0.2522	0.2275
			211	0.1795	0.1056	0.1331
			220	0.1795	0.1057	0.1331
			310	0.1837	0.1995	0.1936
2.50	1.8800	2.555	110	0.1795	0.1057	0.1121
			200	0.1861	0.2522	0.2464
			211	0.1795	0.1056	0.1120
			220	0.1795	0.1057	0.1121
			310	0.1837	0.1995	0.1981

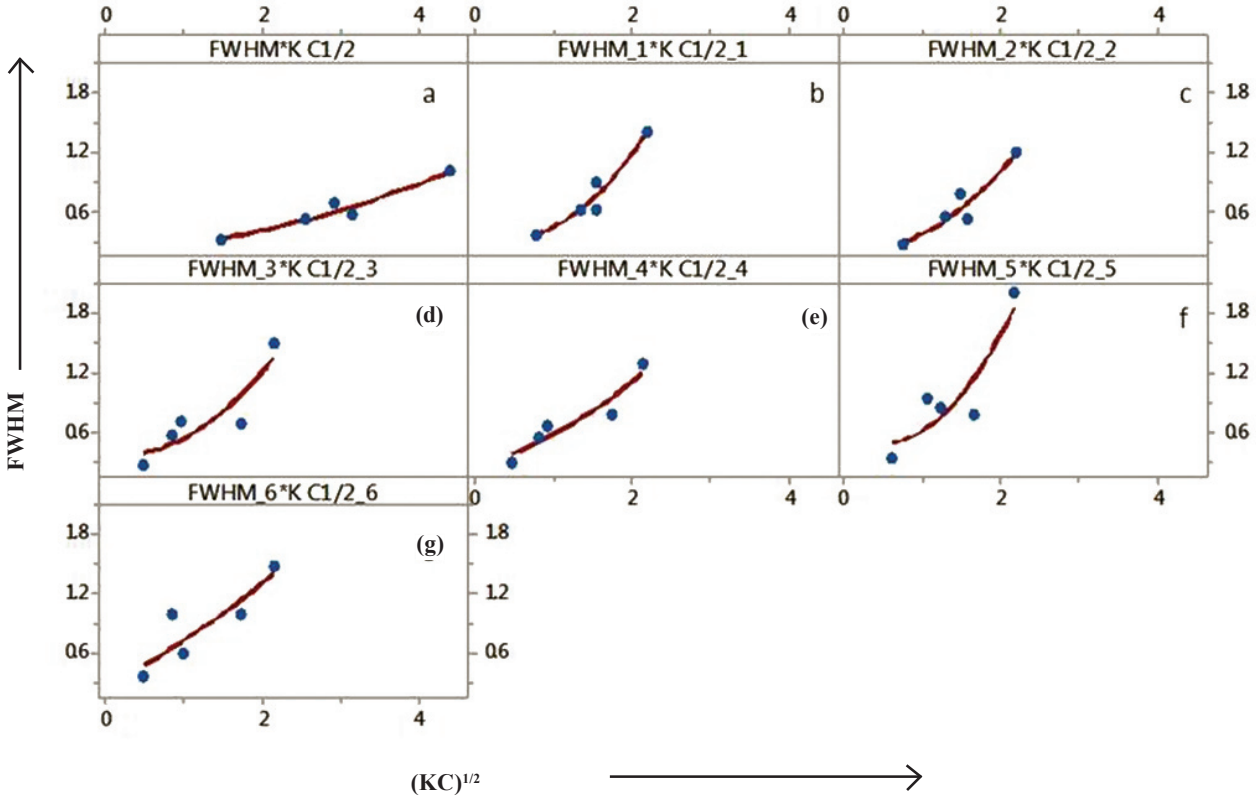


Figure 6. (a)-(g): The Modified Williamson-hall plot for hypereutectoid steel wire as lead patented and at 0.1968, 0.3771, 0.7493, 1.1507, 1.5153, and 1.8800 true strain, respectively.

Table 7. The fraction of pure edge and pure screw dislocations at different true strain

Wire diameter	True drawn strain	q_{exp}	q_{th}^{edge}	q_{th}^{Screw}	f^{edge}	f^{screw}
6.40	0.0000	1.750	1.362	2.669	0.7035	0.2964
5.80	0.1968	1.618	1.362	2.669	0.8044	0.1955
5.30	0.3771	1.717	1.362	2.669	0.7287	0.2712
4.40	0.7493	2.578	1.362	2.669	0.0701	0.9298
3.60	1.1507	2.660	1.362	2.669	0.0005	0.9994
3.00	1.5153	2.183	1.362	2.669	0.3722	0.6277
2.50	1.8800	2.555	1.362	2.669	0.0877	0.9122

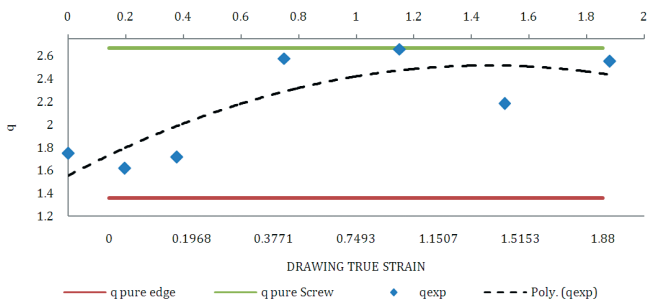


Figure 7. The plot of q_{exp}, $q_{pure\ edge}$ and $q_{pure\ screw}$ *vs* drawing true strain along with trend line for q_{exp}.

4. CONCLUSION

The tensile strength of patented drawn wires increases linearly with increase in true strain as: UTS = 371.8 x True strain + 1362.7. Approximately 66 percent of total UTS are gained by lead patenting process and 34 percent of total UTS are gained by wire drawing process. The drawn wire sample shows that FWHM of the peaks increases with increase in true strain. The classical Williamson-Hall plot of drawn wire specimens shows that broadening of peaks are due to drawing true strain as well as fine microstructure of hypereutectoid steel wire. The value of q by experimental method shows good agreements with theoretical method. The exact contribution of edge and screw dislocations in q value has been found out with increasing drawn true strain. It is observed that with increase in drawn true strain, there is increase in screw type dislocations and reductions in edge type dislocations till approximately 1.515 drawn true strain. After that a marginal decrease in screw type dislocations and increases in edge type dislocations with further increases in strain. The modified Williamson-Hall plot of drawn wire specimens shows that strain anisotropy in drawn samples is mainly due to dislocations.

REFERERCES

1. Elwazri, A.M.; Wanjara, P. & Yue, S. The effect of microstructure characteristics of pearlite on the mechanical properties of hypereutectoid steel. *Mater. Sci. Eng. A,* 2005,**404**, 91-98. doi: 10.1016/j.msea.2005.05.051.

2. Zhang, X.; Godfrey, A.; Huang, X.; Hansen, N. & Liu, Q. Microstructure and strengthening mechanisms in cold-drawn pearlitic steel wire. *Acta Materialia*, 2011, **59**, 3422-3430. doi: 10.1016/j.actamat.2011.02.017.
3. Ungar, T.; Gubicza, J.; Rabarik, G. & Borebely, A. Crystallite size distribution and dislocation structure determined by diffraction profile analysis: principles and practical application to cubic and hexagonal crystals. *J. Appl. Crystallography*, 2001, **34**,298-310. doi: 10.1107/S0021889801003715.
4. Ungar, T.; Gubicza, J.; Hanak, P. & Alexandrov, I. Densities and character of dislocations and size-distribution of sub grain in deformed metal by X-ray diffraction profile analysis. *Mater. Sci. Eng. A*, 2001, **319-321**, 274-278. doi: 10.1016/S0921-5093(01)01025-5.
5. Gubicza, J.; Rabarik, G.; Goren-Muginstein, G.R.; Rosen, A.R. & Ungar, T. The density and the character of dislocations in cubic and hexagonal polycrystals determined by X-ray diffraction. *Mater. Sci. Eng. A*, 2001, **309-310**, 60-63. doi: 10.1016/S0921-5093(00)01666-X.
6. Dragomir-Cernatescu, I.; Gheorghe, M.; Thadhani, N. & Snyder, R. L. Dislocation densities and character evolution in copper deformed by rolling under liquid nitrogen from X-ray peak profile analysis. JCPDS-International Centre for Diffraction Data, Advance in X-ray Analysis, 2005, **48**, 67-72. doi:10.1524/zksu.2008.0013.
7. Ungar, T.; Ott, S.; Borbely, A. & Weertman, J. R. Dislocations, grain size and planar faults in nanostructured copper determined by high resolution X-ray diffraction and a new procedure of peak profile analysis. *Acta Materialia*, 1998, **46**(12), 3693-3699. doi: 10.1016/S1359-6454(98)00001-9.
8. Simek, D.; Rafaja, D.; Motylenko, Klemm, V.; Ullrich, C.; Oswald, A. & Schmidtchen, R. The exploitation of X-ray diffraction in characterization of strength of hot-rolled and cold-drawn ferritic-pearlitic steel. *Mater. Struct.*, 2011, **18** (3), 178-183.
9. Goodarzy, M.H.; Arabi, H.; Boutorabi, M.A.; Seyedein, S.H. & Shahrokhi, H. Dislocations structure and scattering phenomenon in crystalline cell size 2024 AL alloy deformed by one pass ECAP at room temperature. *Iranian J. Mater. Sci. Eng.*, 2014, **11**(1), 27-38. doi: 10.1016/S1003-6326(14)63245-3.
10. Rezvanifar, A. & Zandrahimi, M. Evaluation of dislocation structure and crystallite size in worn AL –SI alloy by X-ray diffraction. *Iranian J. Mater. Sci. Eng.*, 2010, **7**(1), 32-38.
11. Takebayashi, S.; Kunieda, T.; Yoshinaga, N.; Ushioda, K. & Ogata, S. Comparison of the dislocation density in martensitic steels evaluated by some X-ray diffraction methods. *ISIJ International*, 2010, **50** (6), 875-882. doi.org/10.2355/isijinternational. 50.875.
12. Garabagh, M.R.M.; Nedjad, S.H.; Shirazi, H.; Mobarekeh, M.I. & Ahmadabadi, M.N. X-ray diffraction peak profile analysis aiming at better understanding of the deformation process and deformed structure of a martensitic steel. *Thin Solid Films*, 2008, **516**, 8117-8124. doi:10.1016/j.tsf.2008.04.019.
13. Kriska, M.; Tacq, J.; Acker, K.V.; Seefeldt, M. & Petegem, S.V. Neutron and X-ray diffraction study of residual and internal stress evolution in pearlitic steel during cold drawing. *J. Phy.*, Conference Series, 2012, **340**, 1-7. doi:10.1088/1742-6596/340/1/012101.
14. Sato, S.; Wagatsuma, K.; Ishikuro, M.; Kwon, E.-P.; Tashiro, H. & Suzki, S. Precise characterization of dislocations and cementite in pearlitic steels at different drawing strains using X-ray diffraction. *ISIJ International*, 2013, **53**(4), 673-679. doi: 10.2355/isijinternational.53.673.
15. Chakarborty, J.; Maiti, T.; Ghosh, M.; Das, G. & Chandra, S. Cementite dissolution in cold drawn pearlitic steel wires: role of dislocations. *Mater. Sci. Forum*, 2014, **768-769**, 304-312. doi: 10.4028/www.scientific.net/MSF.768-769.304.
16. Kamminga, J.-D. & Seijbel, L.J. Diffraction line broadening analysis if broadening is caused by both dislocations and limited crystallite size. *J. Res. National Inst. Standard Technol.* 2004, **109**, 65-74. doi:10.6028/ jres.109.005
17. Leineweber, A. & Mittemeijer, E. J. Anisotropic strain-like broadening due to composition variations. JCPDS – International Centre for Diffraction Data, Advances in X-ray Analysis, 2003,**46**, 43-48. doi:10.1.1.296.962
18. Cong, Z. & Murata, Y. Dislocation density of lath martensite in 10Cr-5W heat resistant steels. *Mater. Trans.*, 2011, **52**(12), 2151-2154. doi: 10.2320/ matertrans.M2011201.
19. Kim, S.A. & Johnson, W.L. Elastic constants and internal friction of martensitic steel, ferritic-pearlitic steel and α-iron. *Mater. Sci. Eng. A*, 2007, **452-453**, 633-639. doi*:* 10.1016/j.msea.2006.11.147.
20. Ungar, T.; Dragomir, I.; Revesz, A. & Borbely, A. The contrast factors of dislocations in cubic crystals: the dislocation model of strain anisotropy in practice. *J. Appl. Crystallography*, 1999, **32**, 992-1002. doi*:* 10.1107/S0021889899009334.
21. Dragomir, I.C. & Ungar. T. The dislocations contrast factors of cubic crystals in the Zener constant range between zero and unity. *Powder Diffraction,* 2002, **17**(2), 104-111. doi:10.1154/1.1471520.
22. Martinez-Garcia, J.; Leoni, M. & Scardi, P. Analytical expression for dislocation contrast factor of ‹011›, {100} cubic slip system: Application to Cu_2O. *Physical Review* B, 2007, **76**, 174117, 1-8.
23. Yadav, R. A. Establishment of a spring formula for low temperature use of spring. *Def. Sci. J.*, 1974, **25**, 69-76. doi: 10.14429/dsj.25.6596.
24. Chatterjee, D.P. Steels in Ordnance Factories. *Def. Sci. J.*, 1960, **10**(2A), 40-44. doi: 10.14429/dsj.10.7651

CONTRIBUTORS

Mr Shamsher Singh Bargujer did his BTech (Mechanical Engineering) from Regional Engineering College, Kurukshetra, in 1997 and ME (Thermal Engineering) from Delhi College of Engineering, Delhi, in 1999. Currently pursuing his PhD in Production Engineering from PEC University of Technology, Chandigarh. Presently, he is working as Assistant Works Manager and Divisional Officer of quality control at Ordnance Cable Factory, Chandigarh. He worked in area of defence production, planning and quality control since 2002. All experimentation in this study is carried out by him and manuscript compiled by him.

Dr Narender M. Suri did his graduation in Production Engineering from GBP University of Technology, Pantnagar, in 1990 and post-graduation in Industrial Metallurgy from IIT, Roorkee, in 1995. Obtained his PhD in Welding Engineering from IIT, Delhi in 2005. Presently, he is the head of Production engineering department. His area of specialisation is welding engineering, casting technology, material science and operation research. He has published more than 20 research paper in international and national journals. He is member of ISTE. He carried out analysis of XRD diffraction peaks. He also carried out detail discussion on results and concluded the manuscript.

Dr Rajendra M. Belokar did his graduation from Amravati University, Amravati, in 1987. He did post-graduation and PhD from PEC University of Technology, Chandigarh, in 1999 and 2010 respectively. Presently, he is associate professor in Production Engineering, PEC University ofTechnology, Chandigarh. He published more than 70 research papers in national and international journals. He published one book and two books are in press. He is Sr. Member SME (USA), M.I.E, C. Eng (I), LM-ISTE, Member-INVEST, and Member APICS (USA). He framed the manuscript and plotted all relevant plots in the manuscript.